



# **Surface-Crack Growth: Models, Experiments and Structures**

**Reuter/Underwood/  
Newman, editors**



**STP  
1060**

STP 1060

# ***Surface-Crack Growth: Models, Experiments, and Structures***

*Walter G. Reuter, John H. Underwood, and James C. Newman, Jr.,  
editors*



ASTM  
1916 Race Street  
Philadelphia, PA 19103

## Library of Congress Cataloging-in-Publication Data

Surface-crack growth: models, experiments, and structures/ Walter G. Reuter, John H. Underwood, and James C. Newman, Jr., editors.

(STP: 1060

"The symposium on Surface-Crack Growth: Models, Experiments, and Structures was held in Sparks, Nevada, 25 April 1988"—Foreword.

Includes bibliographies and index.

ISBN 0-8031-1284-X

1. Surfaces (Technology)—Congresses. 2. Fracture mechanics—Congresses. 3. Materials—Cracking—Congresses. I. Reuter, Walter G., 1938– . II. Underwood, John H., 1941– . III. Newman, James, C., Jr., 1942– . IV. Symposium on Surface-Crack Growth: Experiments, and Structures (1988: Sparks, Nev.)

TA418.7.S84 1990

620.1'26—dc20

89-49360

CIP

Copyright© by AMERICAN SOCIETY FOR TESTING AND MATERIALS 1990

### NOTE

The Society is not responsible as a body,  
for the statements and opinions  
advanced in this publication.

### Peer Review Policy

Each paper published in this volume was evaluated by three peer reviewers. The authors addressed all of the reviewers' comments to the satisfaction of both the technical editor(s) and the ASTM Committee on Publications.

The quality of the papers in this publication reflects not only the obvious efforts of the authors and the technical editor(s), but also the work of these peer reviewers. The ASTM Committee on Publications acknowledges with appreciation their dedication and contribution of time and effort on behalf of ASTM.



J. L. Swedlow

1935–1989

## Dedication

*Dr. Swedlow was one of a rather small but very active group in the early history of Committee E24 on Fracture Testing. Professor Swedlow served in a variety of roles including researcher, organizer, initiator, and expeditor within Committee E24 and within related applied mechanics and fracture mechanics activities.*

*Professor Swedlow's services to Committee E24 include membership on Fracture Mechanics Test Methods Subcommittee (1965–1973); Representative to International Congress on Fracture (1969– ); National Symposium Task Group (1972–1989), Chairman (1977–1989); Executive Committee (1973– ). Jerry was the chairman of the organizing committee for the first National Symposium on Fracture Mechanics to be held away from Lehigh University (1970). In subsequent years, Jerry served on the organizing committees of three additional National Symposia and cochairman of the ninth symposium. For many years until his death, Jerry was responsible to Committee E24 for the organizational oversight of all National Symposia. He played a crucial role, along with a few others, in assuring the very high quality and vigor that we have come to associate with these Symposia. In a related activity, Professor Swedlow for the past 20 years served as editor of the Reports of Current Research for the International Journal of Fracture.*



*Professor Swedlow was also a member of Committee D30 on High Modulus Fibers and Their Composites from 1972 to 1975. During that time, Jerry participated in some of the earliest work on the establishment of test methods and analysis models for the fracture mechanics behavior of graphite/epoxy composites. That initial work is still cited by those active in the research area.*

*Professor Swedlow's involvement in Committee E24 research activities was primarily focused on the nature of elastoplastic responses of materials with cracks. One of Jerry's principal research concerns in this work was to match numerical responses to experimental data. He established the importance of a proper understanding of uniaxial stress-strain curve development in being able to establish meaningful correlation. Additionally, he was an early contributor regarding the development of ductile fracture criteria and the influence of crack front curvature on plane strain fracture toughness measurements. One of his earliest and abiding research interests related to these issues was that of the three-dimensional character of elastic and elasto-plastic response of cracked bodies. As part of this activity Jerry was involved in studies of the behavior of surface cracks. Some of his contributions in this field are identified in the first paper in this publication. He made numerous presentations within the task group Structure of Committee E24, as well as the National Symposia.*

*Committee E24 has recognized the many diverse and critical contributions made by Professor Swedlow. In recognition of these, ASTM conferred upon Jerry the singular honor of Fellow of ASTM in 1984. Jerry was also this year named the first recipient of the Committee E24 Fracture Mechanics Medal Award.*

*A keen interest in and dedication to the goals of ASTM Committee E24 stands as an example to all of us who will commit to the development and application of research findings through professional associations.*

*T. A. Cruse*

## Foreword

The symposium on Surface-Crack Growth: Models, Experiments, and Structures was held in Sparks, Nevada, 25 April 1988. The symposium was sponsored by ASTM Committee E24 on Fracture Testing, Walter G. Reuter, Idaho National Engineering Laboratory, John H. Underwood, U.S. Army Benet Laboratories, and James C. Newman, Jr., NASA Langley Research Center, presided as symposium cochairmen and are editors of this publication.

# Contents

<b>Overview</b>	1
<b>MODELS AND EXPERIMENTS (MONOTONIC LOADING)</b>	
<b>A Surface Crack Review: Elastic and Elastic-Plastic Behavior—D. M. PARKS</b>	9
<b>Evaluation of Finite-Element Models and Stress-Intensity Factors for Surface Cracks Emanating from Stress Concentrations—P. W. TAN, I. S. RAJU, K. N. SHIVAKUMAR, AND J. C. NEWMAN, JR.</b>	34
<b>Tabulated Stress-Intensity Factors for Corner Cracks at Holes Under Stress Gradients—R. PEREZ, A. F. GRANDT, JR., AND C. R. SAFF</b>	49
<b>Fracture Analysis for Three-Dimensional Bodies with Surface Crack—LI YINGZHI</b>	63
<b>On the Semi-Elliptical Surface Crack Problem: Detailed Numerical Solutions for Complete Elastic Stress Fields—A. F. BLOM AND B. ANDERSSON</b>	77
<b>Analysis of Optical Measurements of Free-Surface Effects on Natural Surface and Through Cracks—C. W. SMITH, M. REZVANI, AND C. W. CHANG</b>	99
<b>Optical and Finite-Element Investigation of a Plastically Deformed Surface Flaw Under Tension—J. C. OLINKIEWICZ, H. V. TIPPUR, AND F. P. CHIANG</b>	112
<b>Extraction of Stress-Intensity Factor from In-Plane Displacements Measured by Holographic Interferometry—J. W. DALLY, C. A. SCIAMMARELLA, AND I. SHAREEF</b>	130
<b>Fracture Behavior Prediction for Rapidly Loaded Surface-Cracked Specimens—M. T. KIRK AND E. M. HACKETT</b>	142
<b>Measurements of CTOD and CTOA Around Surface-Crack Perimeters and Relationships Between Elastic and Elastic-Plastic CTOD Values—W. G. REUTER AND W. R. LLOYD</b>	152
<b>Surface Cracks in Thick Laminated Fiber Composite Plates—S. N. CHATTERJEE</b>	177
<b>Surface Crack Analysis Applied to Impact Damage in Thick Graphite/Epoxy Composite—C. C. POE, JR., C. E. HARRIS, AND D. H. MORRIS</b>	194

## FATIGUE CRACK GROWTH

<b>Experimental Evaluation of Stress-Intensity Solutions for Surface Flaw Growth in Plates—D. K. CARTER, W. R. CANDA, AND J. A. BLIND</b>	215
<b>A Novel Procedure to Study Crack Initiation and Growth in Thermal Fatigue Testing—N. J. MARCHAND, W. DORNER, AND B. ILSCHNER</b>	237
<b>Observations of Three-Dimensional Surface Flaw Geometries During Fatigue Crack Growth in PMMA—W. A. TROHA, T. NICHOLAS, AND A. F. GRANDT, JR.</b>	260
<b>Some Special Computations and Experiments on Surface Crack Growth—M. PRODAN AND J. C. RADON</b>	287
<b>Influences of Crack Closure and Load History on Near-Threshold Crack Growth Behavior in Surface Flaws—J. R. JIRA, D. A. NAGY, AND T. NICHOLAS</b>	303
<b>Growth of Surface Cracks Under Fatigue and Monotonic Increasing Load—L. HODULAK</b>	315
<b>Experimental Investigation of Subcritical Growth of a Surface Flaw—M. RAMULU</b>	333
<b>Measurement and Analysis of Surface Cracks in Tubular Threaded Connections—A. NEWPORT AND G. GLINKA</b>	348
<b>Propagation of Surface Cracks in Notched and Unnotched Rods—M. CASPERS, C. MATTHECK, AND D. MUNZ</b>	365
<b>Theoretical and Experimental Analyses of Surface Fatigue Cracks in Weldments—X. NIU AND G. GLINKA</b>	390
<b>Author Index</b>	415
<b>Subject Index</b>	417

## Overview

---

Over the past 30 years, substantial effort has been devoted to developing techniques and standards for measuring fracture toughness and subcritical crack growth. These methods use specimens containing two-dimensional (2-D), through-the-thickness flaws because of their relative ease of fabrication and the availability of accepted analytical and numerical solutions. However, many defects observed in practice, and often responsible for failures or questions regarding structural integrity, are three-dimensional (3-D) surface flaws. The efficiency of data generated from standard specimens containing 2-D defects in predicting crack growth behavior of 3-D flaws, including crack initiation, subcritical crack growth, and unstable fracture, is a major concern. An important alternative is use of data obtained from surface flawed specimens. Resolving these issues is a goal of activities within Subcommittee E24.01 on Fracture Mechanics Test Methods, a subcommittee of ASTM E24 on Fracture Testing.

The first significant review of the status of research being conducted on surface cracks was the ASME symposium "The Surface Crack: Physical Problems and Computational Solutions" organized by Professor J. L. Swedlow in 1972. The review presented here is the culmination of a joint effort of ASTM E24 and SEM (Society for Experimental Mechanics), initiated in 1986, to identify the international state-of-the-art of research on surface flaws. The joint effort has resulted in two symposia. Papers from the first symposium, held at the Fall 1986 SEM meeting in Keystone, Colorado, were published in *Experimental Mechanics*, Vol. 28, No. 2, June, and No. 3, September 1988. The papers in this Special Technical Publication were presented at a symposium held at the Spring 1988 ASTM E24 meeting in Sparks, Nevada, and cover much of the state-of-the-art research being conducted on the behavior of surface flaws.

The papers included in this publication cover: (a) analytical and numerical models for stress-intensity factor solutions, stresses, and displacements around surface cracks; (b) experimental determination of stresses and displacements due to applied loads under either predominately elastic stress conditions or elastic-plastic conditions; and (c) experimental results related to fatigue crack growth. The subject matter is very broad, ranging from linear elastic fracture mechanics to nonlinear elastic fracture mechanics, and includes weldments and composites. Areas where additional research is needed are also identified. For example, considerable progress has been made on the comparison of fatigue crack growth rates, but a number of questions are still unanswered. Also, the ability to accurately predict behavior of a surface crack is generally limited to predominately elastic stress conditions; considerable research is required for surface cracks under elastic-plastic conditions.

Some of the critical areas addressed in the volume are: (a) differences in constraint for 2-D through-thickness cracks and 3-D surface cracks; (b) applicability of  $J_{Ic}$ ,  $K_{Ic}$ , CTOD, and  $da/dN$  test data obtained from 2-D cracks to surface cracks; and (c) applicability of surface crack testing and analysis to composites, ceramics, and weldments. This overview describes the state of the art, as well as identifying the researchers presently pursuing specific topics. The papers are grouped into two sections: Models and Experiments (Monotonic Loading) and Fatigue Crack Growth.

### Models and Experiments (Monotonic Loading)

The first two papers are reviews of the important numerical analysis procedures that have been applied to the surface-crack problem. Parks describes a variety of surface-crack analysis methods, including crack-front variation of  $K$  for elastic conditions and  $J$ -integral for nonlinear conditions, and line-spring and plastic-hinge models of surface-cracked pipes. He identifies two areas in need of further study, crack-tip blunting and its effect on shear deformation through to the back surface, and free surface effects on the loss of constraint for shallow cracks. Tan, Raju, Shivakumar, and Newman give an evaluation of finite-element methods and results for the common, and difficult, problem of a surface crack at a stress concentration, such as a hole. Values of  $K$  were calculated for a variety of geometries using both nodal force and virtual crack-closure methods. A related configuration was also analyzed, that of a surface crack at a semicircular edge notch in a tensile loaded plate, for comparison with "benchmark" results obtained in the United States and abroad for this geometry.

Three papers then continue the emphasis on numerical stress analysis of surface crack configurations to obtain crack front  $K$  values. Perez, Grant, and Saff use a weight function method and finite-element results from prior work to obtain tabular results for a variety of configurations of the corner crack at a hole. They describe a superposition method which can be used to analyze problems with very complex stress fields. Yingzhi uses a high order 3-D finite-element method to calculate  $K$  for surface-crack configurations with tension and bending loads. The calculations require fewer degrees of freedom than prior work in the literature, and the results agree well with that work. Blom and Andersson use the  $p$ -version of the finite-element method to calculate the elastic stress field in surface cracked plates with different values of Poisson's ratio. The emphasis is on the intersection of the surface crack with the free surface. Near the free surface and for Poisson's ratio near 0.5, the problem becomes more complex.

The next three papers involve aspects of optical stress analysis applied to the surface-crack problem. Smith, Rezvani, and Chang performed photoelastic stress freezing tests of naturally grown through-thickness and surface cracks in bending specimens. Their tests and associated analysis were used to study the difficult problem of free surface effects. As in Blom and Andersson's work, complexities arise, possibly because the photoelastic results were not "sufficiently close to the free surface." The paper by Olinkiewicz, Hareesh, and Chiang combines moiré and finite-element methods to obtain the deformation fields of a plastically deformed surface crack loaded in tension. The authors evaluate  $J$  from both experimental results and from finite elements and find that they are essentially equivalent. Dally, Sciammarella, and Shareef use holographic interferometry and Westergaard series analyses to determine stresses and displacements around a surface crack. The experimentally determined singularity of the stress field (of  $K$ ) at the free surface is found to be close to, but in excess of, 0.5, in agreement with some analytical results from the literature.

Kirk and Hackett investigated dynamic loading of surface-cracked specimens. They compared results from drop-tower loaded, through-cracked, bend specimens containing deep and shallow cracks to results from dynamically-loaded, shallow, surface-cracked specimens, all of embrittled high strength steel. The critical  $J$  at failure for shallow through cracks gave good predictions of surface crack behavior, whereas the critical  $J$  for deep through cracks underpredicted the surface crack results.

Reuter and Lloyd performed a comprehensive experimental study of crack-tip-opening displacement (CTOD), crack-tip-opening angle (CTOA), and crack growth for tension-loaded A710 steel plates with surface cracks of various configurations. They compared their results to center-of-rotation models and numerical solutions of CTOD around the

crack front. Good agreement between experimental and numerical CTOD values was demonstrated. Relationships between CTOD, and CTOA and between CTOA and crack growth were also described.

The last two papers of the section on monotonic models and experiments involved surface cracks in composite materials. Chatterjee describes analysis of surface cracks in transversely isotropic and orthotropic composites and gives correction factors to obtain  $K$  for these types of composites from isotropic  $K$  results from the literature. He also compares the results from test data from the literature for thick laminated fiber composites with analytical predictions for failure. The outermost layers of many composites with surface cracks are observed to fail first, unlike similar configurations in metals. Poe, Harris, and Morris describe predictions of residual tensile strength of thick graphite/epoxy laminates using surface crack analysis. Impact damage in this material was represented by a semielliptical surface crack of the same width and depth as the damaged area of broken fibers; the crack plane was nearly perpendicular to the fiber direction. Following a first stage of failure, well predicted by surface crack analysis, a second stage of failure occurred in which damaged layers delaminate from undamaged layers. The second stage failure was predicted using a maximum strain failure criteria.

### Fatigue Crack Growth

Over the past decade, the stress-intensity factor concept ( $\Delta K$  against crack-growth rate) has been shown to correlate quite well with fatigue-crack growth rates for three-dimensional crack configurations under constant-amplitude loading. In order to extend these concepts to more complex loadings and to other structural configurations, much more research is needed to characterize the behavior of surface cracks. The papers in this section extend the application of LEFM concepts to study of fatigue-crack growth of surface cracks in a wide variety of materials and in several structural configurations. The materials covered include aluminum alloys, a titanium alloy, two superalloys, PMMA and a variety of steels. In several applications, the alternating current potential drop (ACPD) technique was used to monitor the growth of surface cracks and an interferometric-displacement technique was used to monitor crack-surface profiles. The nature of the surface crack, however, is truly three dimensional. In through-thickness cracks, one may be able to use a single value of stress intensity and a single crack-opening stress to correlate fatigue-crack growth rates, but for surface cracks the three-dimensional variations around the crack front must be considered. Two numerical methods have been used in these papers to calculate stress-intensity factor variations. They are the finite-element and weight-function methods. A knowledge of the variation of stress-intensity factors and triaxial constraint conditions around the crack front is necessary to develop improved life and strength predictions for surface cracks. The papers in this section have been grouped into four topic areas, stress-intensity factor evaluations during fatigue-crack growth, three-dimensional crack closure and constraint, small-crack behavior, and applications.

Several papers compared crack-growth rates for surface cracks and those of either compact or bend specimens. Carter, Canda, and Blind evaluated several stress-intensity factor solutions for surface cracks and correlated fatigue crack-growth rate data with compact specimen data on an aluminum alloy. For a given stress-intensity factor range, their rates were well within a factor of 2. The slope of their  $\Delta K$ -rate curve from their surface-crack data, however, was different than the slope from the compact specimen data. The data agreed in magnitude around  $12 \text{ MPa m}^{1/2}$ . Their surface cracks tended to show the presence of a "cusp" where the crack intersected the plate surface. They found, however, that the

Raju-Newman stress-intensity factor equations predicted surface-crack growth and crack shape changes reasonably well compared with experimental results. Prodan and Radon, using a novel method of comparing surface-crack growth with compact specimen data, also made a similar conclusion on a fine-grain structural steel. Caspers, Mattheck, and Munz made stress-intensity factor calculations for surface cracks in cylindrical bars under tension and bending loads using a weight-function method. In contrast to point values of stress-intensity factors, they evaluated the "local average" technique proposed by Cruse and Besuner. Fatigue-crack growth rate measurements made on a Cr-Mo steel compared very well with rates measured on four-point notch bend specimens (rates generally within about 30%).

Jira, Nagy, and Nicholas found that crack-growth rate data measured on surface cracks and on compact specimens correlated well for a titanium alloy using a closure-based  $\Delta K_{\text{eff}}$ . They determined crack-opening loads from compliance measurements made at the crack mouth using a laser-interferometry displacement gauge. The effective stress-intensity factor range correlated data quite well for the four types of load histories used to reach a threshold condition. Using a transparent polymer (PMMA), Troha, Nicholas, and Grandt observed three different closure behaviors for surface-cracked specimens. During loading, a surface crack would open first at the maximum depth location. At a slightly higher load, the crack mouth region would then open. This opening load produced the least amount of scatter on a  $\Delta K_{\text{eff}}$ -rate correlation compared to two other definitions of opening load. The crack-front region at the plate surface would be the last region to open. These distinct behaviors are in part caused by the three-dimensional constraint developed around the surface-crack front. Plane-strain conditions around the maximum depth location cause lower opening loads in comparison to the plane-stress regions where the crack intersects the plate surface. A discussion of these constraint variations around the crack front was presented by Hodulak. The triaxiality or constraint factor presented by Hodulak is defined as the ratio of the hydrostatic stress to the effective (von Mises) stress. A knowledge of this constraint factor, or other constraint factors with other definitions, as a function of crack size, crack shape and loading is needed to predict fatigue-crack closure behavior and subsequent crack growth, and to predict the location of fracture initiation around a three-dimensional crack configuration.

Marchand, Dörner, and Ilschner used an advanced ACPD system to study crack initiation and growth under cyclic thermal histories in two superalloys. The initiation of microcracks, 10 to 50  $\mu\text{m}$  in length, could be detected. The specimen used in this study was a double-edge wedge specimen simulating the leading and trailing edges of a gas turbine airfoil. Ramulu studied the initiation and growth of small cracks in "keyhole" compact specimens of an aluminum alloy. This specimen is a standard compact specimen with a hole drilled at the end of the starter notch. Indents (about 250  $\mu\text{m}$  deep) were made at the center of the notch root to act as crack starters. A scanning electron microscope was used to perform fractographic analyses of striation spacings to determine the growth rates for small cracks. The classical "small" crack effect was observed, that is, the small cracks showed initial rapid growth with a minimum rate occurring at about 1 to 2 mm of crack growth.

The remaining papers in this section are concerned with the application of surface-crack methodology to cracks in threaded connections and in welded joints made of steel. Newport and Glinka conducted tests and analyses on surface cracks in tubular threaded connections, while Niu and Glinka conducted tests and analyses on surface cracks in T-butt welded joints. The experimental and analytical approaches were nearly the same in these papers. An advanced ACPD technique was used to monitor the growth of surface cracks (both depth and length). A weight-function method proposed by Petroski and Achenbach was employed to calculate the stress-intensity factors for surface cracks in these structural



configurations. A comparison was made between theoretical and experimentally determined stress-intensity. Experimental stress intensities were determined from measured rates and a  $\Delta K$ -rate curve for the material of interest. For the butt-weld cracks the theoretical and experimental values compared quite well, but the values for the threaded connection cracks showed some large differences. Several reasons were given for the large differences: there is a lack of suitable crack-growth rate data for the test specimen material, local stress concentrations at the thread root are strongly dependent upon thread load and pre-load on the cylinder, and the weight-function method was derived for a flat plate.

### *Symposium Cochairmen and Editors*

*Walter G. Reuter*

Idaho National Engineering Laboratory  
Idaho Falls, ID 83415-2218

*John H. Underwood*

U.S. Army Benet Laboratories  
Watervliet, NY 12189

*James C. Newman, Jr.*

NASA Langley Research Center  
Hampton, VA 23665

## **Models and Experiments (Monotonic Loading)**

David M. Parks<sup>1</sup>

## A Surface Crack Review: Elastic and Elastic-Plastic Behavior

---

**REFERENCE:** Parks, D. M., "A Surface Crack Review: Elastic and Elastic-Plastic Behavior," *Surface-Crack Growth: Models, Experiments, and Structures*, ASTM STP 1060, W. G. Reuter, J. H. Underwood, and J. C. Newman, Jr., Eds., American Society for Testing and Materials, Philadelphia, 1990, pp. 9–33.

**ABSTRACT:** The development and application of various analytical and computational procedures have provided important information regarding the crack-front fields, and associated cracking phenomena, in engineering structures typified by surface crack configurations. Major features of the formulation of several of these numerical approaches are discussed along with certain particular results which have been obtained by using them, with emphasis on surface crack applications.

**KEY WORDS:** fracture mechanics, surface cracks, corner singularities, numerical methods, singular integral/finite-element hybrid methods, virtual crack extension, domain integral methods, line-spring model, linear-elastic fracture mechanics (LEFM), elastic-plastic fracture mechanics, *J*-integral, Hutchinson-Rice-Rosengren, (HRR) singularities, HRR dominance

Just over 15 years have passed since the publication of *The Surface Crack: Physical Problems and Computational Solutions* [1], the proceedings of what was perhaps the first fracture symposium devoted specifically to the physical and analytical complexities of this practically important class of crack configurations. Since then, the analytical and experimental understanding and characterization of part-through surface cracks and, indeed, of fracture mechanics have made significant progress. Nonetheless, the particular three-dimensional (3-D) challenges (still) offered by these special fracture problems have substantially retarded progress toward rendering their treatment as "routine" fracture-mechanics applications.

The scope of mechanics and material behavior phenomena relevant to a discussion of fracture in general, or surface cracks in particular, is too broad to review in the current format. However, it is possible to survey major developments in both the analysis and the experimental characterization of surface flaws in order to understand both "where we are" as well as what remains to be achieved. Here we attempt such a survey, focused more on the analytical aspects, but also drawing upon experimental results.

In discussing "analytical" aspects of the surface crack, we are immediately struck by the fact that the geometrical complexity of three dimensions all but precludes closed-form continuum analysis, so that computational/analytical *tools* become the means for constructing solutions. The array of such tools, as well as their adaptability, power, and precision, has vastly expanded in recent years.

<sup>1</sup> Associate professor, Department of Mechanical Engineering, Massachusetts Institute of Technology, Cambridge, MA 02139.

The major use to which these tools have been put is the quantification of asymptotically dominant crack-front stress and deformation fields. In the context of the surface crack, this includes, for example, the variation of crack-front stress-intensity factors  $K_I(s)$ ,  $K_{II}(s)$ , and  $K_{III}(s)$  of linear-elastic fracture mechanics (LEFM), and the  $J$ -variation,  $J(s)$ , in nonlinear (elastic) fracture mechanics (NLEFM) for quasi-stationary crack fronts. If such single-parameter asymptotic characterizations actually *dominate* the complete near-crack front fields (including the zone of operative microfracture processes) in a surface-cracked geometry, then crack growth exhibited in the surface crack may be expected to be "similar" to that obtained in, for example, a through-cracked "two-dimensional" (2-D) laboratory specimen of the same material loaded to the same dominant asymptotic field strength. Indeed, such correlations form the practical basis of nearly all fracture-mechanics approaches.

At least three important caveats regarding the justification of dominant singularity-based cracking correlations between through-crack and surface-crack configurations should be noted. First, the notion of maintaining single-parameter "dominance" of the crack-tip fields driving microstructural fracture processes such as void growth and cleavage is somewhat fuzzily defined. For example, it is difficult to answer precisely the question, "When is the plastic zone too large to use LEFM?" Careful interpretation of information generated by experimental and analytical studies of the surface crack can, however, provide guidance as to inherent parametric limits of applicability of dominant singularity approaches. Second, the gradients in deformation intensity along surface crack fronts are often substantially greater than in nominally 2-D through-crack geometries. This feature can stabilize the process of cracking. Finally, it is implicitly assumed in fracture-mechanics-based correlations of cracking that there are "similar" distributions of operable fracture process sites along respective crack fronts. This assumption can be questioned in cases such as cleavage fracture of steel, where microstructural distribution statistics of coarse carbide cleavage nuclei can have important effects on, for example, scatter in fracture toughness.

In the next section, several of the tools for fracture analysis of surface cracks are reviewed. In this sense, "tool" is broadly interpreted, including special results in linear elasticity, numerical implementations of domain or conservation integrals for  $J$ -analysis, and simplified models such as the line-spring and plastic hinge idealizations of part-through circumferentially cracked pipe sections. The author's choice of topics is subjective, but the intent is to address methods and results of greatest demonstrated or potential applicability to surface crack modeling and analysis. The third section reviews recent studies on the effects of crack geometry, material strain hardening level, and load magnitude on the degree of  $J$ -based asymptotic dominance in tensile-loaded surface-cracked plates loaded into the plastic regime. The conclusion addresses major developments needed to better deal with surface cracks in practice.

### Analytical/Computational Tools

Three classes of analytical/computational tools are seen as having major or potentially major impact on the understanding of the mechanics of surface cracks. These are identified as dealing with linear elasticity, with virtual crack extension formulations for  $J$  evaluation, and with the development of simplified models. Each class of tool is reviewed. One of the most important mechanics tools of all, the finite-element method *per se*, is too multifaceted to review here.

#### Linear-Elastic Fracture Mechanics

Many conceptual aspects of fracture mechanics are common to linear elastic, as well as nonlinear material behavior, so analytical procedures based on them are likewise indepen-

dent of material behavior. On the other hand, special properties of solutions in linear elasticity, such as superposition, can be exploited effectively by specially tailored tools. In view of the overwhelming preponderance and relative importance of linear elastic behavior in engineering aspects of surface cracks, several specialized approaches have been developed.

**Background**—For isotropic linear elastic response, the asymptotic crack tip fields at any point  $s$  along a 3-D crack front can be characterized by the variation with  $s$  of three stress-intensity factors,  $K_I(s)$ ,  $K_{II}(s)$ , and  $K_{III}(s)$ . Let the linear feature representing the crack front have a continuously turning tangent vector  $t(s) = e_3$ , local crack plane normal  $n(s) = e_2$ , and curve bi-normal  $b(s) = e_1$ . Let local cartesian coordinates emanating from the crack front be  $x_i$ . For material points in the 1,2 plane located a distance  $r = (x_1^2 + x_2^2)^{1/2}$  from the origin at angle  $\theta = \tan^{-1}(x_2/x_1)$  counterclockwise from the  $e_1$  axis, components of the asymptotic stress tensor,  $\sigma_{ij}$ , are given by

$$\sigma_{ij}(r, \theta; s) \rightarrow \frac{K_I(s)f_{ij}^I(\theta) + K_{II}(s)f_{ij}^{II}(\theta) + K_{III}(s)f_{ij}^{III}(\theta)}{(2\pi r)^{1/2}} \quad (1)$$

as  $r \rightarrow 0$ .

Here the dimensionless tensor components  $f_{ij}^I$ ,  $f_{ij}^{II}$ , and  $f_{ij}^{III}$  are known functions of their argument [2]. Similarly, the near tip displacement vector  $u$  is given by

$$u(r, \theta; s) - u^0(s) \rightarrow \sqrt{\frac{r}{2\pi}} \left[ \frac{K_I(s)g^I(\theta, \nu) + K_{II}(s)g^{II}(\theta, \nu)}{E'} + \frac{K_{III}(s)g^{III}(\theta, \nu)}{2G} \right] \quad (2)$$

as  $r \rightarrow 0$ , where the  $g$ -functions are also known. In Eq 2,  $u^0(s)$  is a rigid translation of the crack tip,  $G$  is shear modulus, and  $E' = E/(1 - \nu^2)$  is the plane-strain tensile modulus, where  $\nu$  is Poisson's ratio and  $E$  is Young's modulus.

The task of engineering stress analysis in LEFM is to evaluate numerically  $K_I(s)$  [and  $K_{II}(s)$ ,  $K_{III}(s)$ , if present] for a given body containing crack(s) of a given shape and size, subject to various loadings. There are many methods for obtaining such calibrations. While exact elasticity solutions have been obtained for many configurations, the complexity of 3-D surface crack geometries has required the use of numerical methods such as singular integral equations, boundary integral equations, finite differences, and the finite-element method. Subsequently, we discuss particular features of special analytical/numerical methods in elastic fracture-mechanics analysis, with particular attention to applications in surface cracks.

**Singular Integral Formulations**—A powerful tool for 2-D elastic crack analysis is based on the representation of a crack by a continuous distribution of dislocations. The technique can be notionally appreciated by considering the opening profile of a crack along the  $x_1$  axis as approximated by a finite number of opening (and closing) "steps." Each step is formally equivalent to an edge dislocation of Burger's vector  $b(x_1)$ . In the limit of an infinite number of infinitesimal steps,  $db(x_1) = \mu(x_1) dx_1$ , the crack problem is described by the dislocation density,  $\mu(x_1)$ . Many 2-D crack problems have been solved in closed form by the use of distributions of dislocations to formulate a singular integral equation. For more complicated problems, effective numerical techniques for solving the singular integral equations have been developed by Erdogan and Gupta [3]. The density  $\mu(x_1)$  has a square-root singularity at the ends of the cut, and the strength is proportional to  $K_I$  at the respective ends. Thus  $K_I$  can be directly determined from  $\mu$ . This procedure is readily generalized to include mixed modes, curved or multiple cracks, etc.

An important limitation of such techniques, however, has been the difficulty associated with finite boundaries (other than the cracks themselves). Recently, Annigeri and Cleary

[4] (see also Refs 5–7) have developed an effective combination of dislocation and finite-element techniques for elastic analysis. Termed SIFEH (singular integral, finite-element hybrid), the method requires only a modestly refined finite-element grid, sufficient to model the “no-crack” fields and external boundary conditions, while the singular integral equation “substructure(s)” models the crack(s). The resulting set of equations can be symbolically written as

$$\begin{bmatrix} K & G \\ S & C \end{bmatrix} \begin{bmatrix} U^{FE} \\ D \end{bmatrix} = \begin{bmatrix} F \\ T \end{bmatrix} \quad (3)$$

where

$K$ ,  $U^{FE}$ , and  $F$  = stiffness matrix, nodal displacements, and forces of the finite-element portion of the model, respectively,

$D$  = set of discretized dislocation variables,

$C$  = collocation “self-stiffness” of the dislocation substructure,

$T$  = discretized crack surface traction, if present, and

$S$  and  $G$  = interaction matrices between the finite-element and singular integral substructures, respectively.

It is important to note that they connect only *boundary* nodes of the finite-element mesh to the dislocation array; thus the “finite-element substructure” could just as well be a no-crack boundary integral mesh. The key idea is that the *total* field quantities—displacement, strain, etc.—at any point in the body are the superposition of those calculated from finite-element interpolation at that point, plus those due to the distribution of dislocations.

For 2-D studies of mixed-mode crack propagation, the method is ideally suited, since only the 1-D “cracked” substructure need be recomputed for the next configuration [4,6]. It is clear that this technique for analysis of mixed-mode crack growth has great advantages over more traditional techniques, such as finite-element rezoning.

Related formulations have been recently extended to 3-D elastic crack configurations through use of a distribution of dipole singularities in conjunction with a finite-element substructure [7]. The primary technical difference in the 2-D singular integral over the crack *plane* which arises in 3-D applications is the choice of the fundamental singular field. In 3-D, dipoles derived from Kelvin solutions of opposing point forces initially separated by an infinitesimal distance are chosen. The infinite strains occurring within the dipoles are mathematically equivalent to the displacement discontinuity associated with relative motion of the crack faces, and near the crack front,  $K_i(s)$ , etc., are identified from  $u(r, \pi; s) - u(r, -\pi; s)$  by means of Eq 2.

The integral equation is highly singular, and special procedures for numerical evaluation must be devised. Results to date are limited to planar crack geometry. Surface cracks have been successfully analyzed using this method [8], and it is likely that the relative efficiency of rezoning 2-D crack domains, as compared with 3-D finite-element or even standard boundary-element discretizations, will make this method particularly effective in parametric studies of crack shape. Should suitable means for dealing with nonplanar crack surfaces be devised, this could prove to be essentially the only practical way to follow general 3-D mixed-mode crack growth.

Another approach to 3-D singular integral crack formulations in bonded plane-layered media is based on approximate Green’s functions [9]. Fares [9] demonstrated a generalized image method for constructing convergent expansions of Green’s functions for problems in planar media. Thus, these kernels automatically satisfy global boundary conditions (to the order of the expansion), and there is no need for a macrogeometric substructure to

“fix” the boundary conditions, as in Ref 7. Fares [9] obtained good agreement with the Raju and Newman [10] surface-crack solutions for tension. Fares’ method is limited to essentially infinite planar domains, so additional geometric complications such as holes and nearby edge boundaries cannot be handled. The SIFEH formulation of Keat [8] also made use of the more sophisticated singular fields of dipoles in the interior of an isotropic linear elastic half-space bonded to a dissimilar elastic half-space. In the degenerate case of vanishing moduli, traction-free boundary conditions are automatically satisfied by the singular fields, thereby reducing the burden placed on the regular boundary discretization in accurately enforcing (total) boundary conditions. Fares’ singular fields carry this one step further by satisfying boundary conditions on two infinite parallel interfaces.

*Corner Singularities in LEFM*—The nature of the elastic singularity at the intersection of a crack front with a traction-free surface changes to one of spherical coordinates centered at the intersection. This problem has been studied by a number of investigators [11–14], but even a moderately complete understanding of these singularities and their zones of dominance has yet to emerge. For Mode I loading of a crack making normal incidence with a free surface, it appears, however, that the order of the corner singularity is generally weaker than  $-\frac{1}{2}$ . Thus a strict view of  $K_I$  as the strength of the *square-root* singularity indicates that, at such points,  $K_I$  should vanish in a thin boundary layer.

A recent examination of the linear-elastic corner singularity and its zone of dominance in a particular class of problems has been made by Nakamura and Parks [15]. They considered a large “thin” plate of thickness  $t$  containing a through-crack of length much greater than  $t$ , remotely loaded in plane stress by a (2-D) Mode I stress-intensity factor,  $K_I^{\text{far}}$ . For several values of  $\nu$ , they obtained the local (3-D) variation of  $K_I(x_3)$  through the plate thickness. Maximum local values of  $K_I$  occurred on the centerplane with a slow but monotone decrease as the free surface was approached, until reaching a distance of approximately  $0.02t$  from the free surface. Within this near surface region,  $K_I$  decreased rapidly with decreasing distance from the free surface. Benthem [12] formally showed that the order,  $\lambda$ , of the corner singularity in *spherical* coordinate,  $\rho$ , ( $\sigma \propto \rho^{-\lambda}$ ), can be asymptotically consistent with a square-root singularity in *cylindrical* coordinate,  $r$ , providing the strength of the square-root singularity varies with distance,  $z$  beneath the free surface as  $K_I(z) \sim z^{1/2-\lambda}$ . In general,  $\lambda$  varies with  $\nu$ , and Nakamura and Parks’ computations, shown in Fig. 1, are in excellent agreement with such an interpretation. On the free surface, the angular dependence of in-plane stress components given by Benthem [11] is also in excellent agreement with that obtained in Ref 15.

Asymptotic corner solutions for *antisymmetric* loading of perpendicularly intersecting cracks [13,14] show that  $\lambda > \frac{1}{2}$  for  $\nu > 0$ , so the local strengths of  $K_{II}(z)$  and  $K_{III}(z)$  become unbounded as  $z \rightarrow 0$ , and results consistent with this interpretation have been also found by Nakamura and Parks [16] when remote Mode II loading was applied.

More general understanding of the details of the 3-D stress fields near crack-front/free surface intersections, or near points where a 3-D crack front crosses a bi-material boundary (for example, a reactor vessel cladding) is not shown. The order of the spherical singularity depends also on the angle of incidence between the free surface and the prolongation of the crack tangent [14].

Nakamura and Parks [15] noted that plate thickness  $t$  was the only geometric length scale in their problem and that the corner field dominated over  $\sim 0.03t$ , for nonnegative  $\nu$ . They conjectured that, if the crack front radius of curvature,  $\rho_{\text{crack front}}$ , at the free-surface intersection was the corresponding relevant length scale for surface cracks, then perhaps the corner singularity would dominate over 3% of this length. They also noted that, for semielliptical crack shapes, with depth  $a$  and total surface length  $2c$ , the estimated region of dominance was only  $(a/t) \cdot (a/c) \cdot (t/33)$ . The validity of this conjecture awaits sufficiently refined analysis.

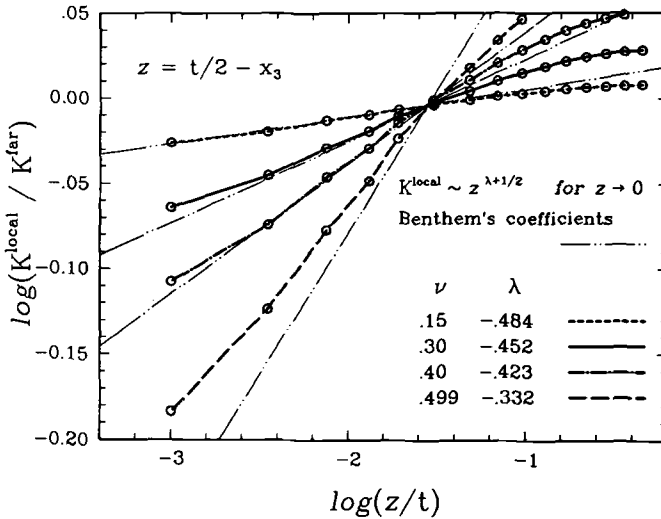


FIG. 1—Normalized  $K^{\text{local}}$  variation across the thickness of a thin elastic plate, plotted for the various Poisson's ratios against distance from free surface ( $z$ ) normalized by plate thickness ( $t$ ) (log-log scale). Small circles represent midlocation of element layers along crack front. Benthem's singularity exponents are shown in inset. Slopes of straight lines correspond to corner singularity solutions [15].

### Virtual Crack Extension and Domain Integrals

One of the most broadly applicable and widely used computational tools in fracture-mechanics analysis is based on virtual perturbations of the crack front. This approach has permitted very accurate evaluations of  $J(s)$  to be obtained in 3-D configurations such as surface cracks while using relatively coarse discretizations. Early finite-element implementations due to Parks [17], although effective, resorted to cumbersome numerical differencing to perform calculations and were poorly suited to deal with thermal strain. deLorenzi [18] interpreted the method as a (virtual) mapping and obtained a compact expression for evaluating energy perturbations. Subsequently, thermal loads and kinetic energy have been rigorously incorporated into a crack energy flux by Shih and co-workers. In view of the historically central role of quasi-static "potential energy differences" in fracture mechanics and of the importance of this method in surface crack analysis, the following simplified derivation of deLorenzi's results is presented.

*A Derivation*—An assessment of the strength of the crack-tip singular fields in a wide variety of material models can be made from appropriate "energetic" comparisons with respect to crack length. For stationary cracks in elastic and hyperelastic "equivalent" models of rate independent elastic-plastic behavior, the fundamental energetic relation between two adjacent equilibrium solutions differing only by a small crack-front perturbation  $\delta\ell(s)$  is

$$\int_{\text{crack front}} J(s) \delta\ell(s) ds = -\delta_e \pi \quad (4)$$

where the variation (with respect to crack front,  $\ell$ ) in the potential energy,  $\pi$ , of the system can be decomposed into that part due to stress working power, plus that due to the variation of prescribed loadings. In certain instances, global potentials for each of these terms



may exist, but this is not necessarily the case. Nonetheless, the variations  $\delta_\epsilon(\dots)$  of the quantities do exist. We will adopt this symbol as a formal operator in the derivation. The deformation work is

$$W = \int_V \mathcal{W} dV \quad (5)$$

where

$$\mathcal{W} = \int_0^{\epsilon_m - \epsilon_{th}} \sigma : d\epsilon_m \quad (6)$$

Here  $\sigma$  and  $\epsilon_m$  are work-conjugate stress and “mechanical” strain measures. The integral for  $\mathcal{W}$  is understood to be evaluated along the actual load history in elastic-plastic materials. The mechanical strain,  $\epsilon_m$ , is taken as the difference between “kinematic” strain

$$\epsilon = \frac{1}{2}(\nabla u + (\nabla u)^T) \quad (7)$$

and the thermal strain,  $\epsilon_{th}$ . We take  $\epsilon_{th}$  to depend upon the instantaneous temperature distribution,  $T(x)$ , in a way decoupled from the mechanical action. For isotropic response with constant coefficient of linear thermal expansion,  $\alpha$ ,  $\epsilon_{th} = \alpha[T(x) - T_0]1$ , where  $T_0$  is a uniform reference temperature.

The variation of  $W$  is

$$\delta_\epsilon W = \int_V \left( \delta_\epsilon \mathcal{W} + \mathcal{W} \frac{\delta_\epsilon(dV)}{dV} \right) dV \quad (8)$$

Because of the symmetry of  $\sigma$ , the first term in the integrand can be written as

$$\delta_\epsilon \mathcal{W} = \sigma : \delta_\epsilon(\nabla u - \epsilon_{th}) \quad (9)$$

deLorenzi [18] has interpreted the variation with respect to geometric parameters as a perturbation mapping of reference coordinates  $x$  into new coordinates  $\hat{x} = x + \delta\ell q(x)$ . Here, for  $x = x(s)$  on the crack front,  $\delta\ell(s) = \delta\ell q(x(s)) \cdot b(s)$ , and  $q(x)$  is otherwise arbitrary in the interior of  $V$ . In the old coordinates, the gradient operator  $\nabla$  is defined in terms of field differentials,  $d(\dots)$ , by

$$d(\dots) = dx \cdot \nabla(\dots) \quad (10)$$

for arbitrary fields  $(\dots)$ . In the new coordinates,

$$d\hat{x} = dx + \delta\ell dx \cdot \nabla q \quad (11)$$

and the perturbed gradient operator is

$$\hat{\nabla} = \nabla + \delta_\epsilon \nabla \quad (12)$$

By requiring  $d(\dots) = d\hat{x} \cdot \hat{\nabla}(\dots)$ , we recover, to first order in  $\delta\ell$ ,

$$\delta_\epsilon \nabla(\dots) = -\delta\ell \nabla q \cdot \nabla(\dots) \quad (13)$$

Thus,

$$\delta_\ell \mathcal{W} = -\delta\ell \sigma : (\nabla u \cdot \nabla q) - \sigma : \delta_\ell \epsilon_{th} \quad (14)$$

and

$$\frac{\delta_\ell(dV)}{dV} = \delta\ell \nabla \cdot q = \delta\ell 1 : \nabla q \quad (15)$$

The variation in the thermal strain is

$$\delta_\ell \epsilon_{th}(T(x)) = \frac{\partial \epsilon_{th}}{\partial T} \delta_\ell T = \frac{\partial \epsilon_{th}}{\partial T} (\nabla T \cdot \delta\ell q) \quad (16)$$

A second contribution to the energy perturbation is that due to prescribed loads

$$\begin{aligned} \delta_\ell L &= \int_{S_t} t \cdot \delta_\ell u \, dS + \int_V f \cdot \delta_\ell u \, dV \\ &= -\delta\ell \left\{ \int_{S_t} t \cdot \nabla u \cdot q \, dS + \int_V f \cdot \nabla u \cdot q \, dV \right\} \end{aligned} \quad (17)$$

where it is understood that tractions  $t$  are prescribed on the portion  $S_t$  of the boundary and body forces  $f$  (per unit volume) are prescribed in  $V$ . On combining and rearranging terms, we obtain

$$\frac{-\delta_\ell \pi}{\delta\ell} = \left\{ \begin{aligned} &\int_V dV \left[ (\nabla u \cdot \sigma - \mathcal{W} 1) : \nabla q + \left( \sigma : \frac{\partial \epsilon_{th}}{\partial T} \nabla T - f \cdot \nabla u \right) \cdot q \right] \\ &-\int_{S_t} t \cdot \nabla u \cdot q \, dS \end{aligned} \right\} \quad (18)$$

This rather general result was first obtained (without thermal straining) by deLorenzi, and the thermal strain terms were first added by Bass et al. [19]. A simple derivation using the (virtual) crack tip energy flux has been given by Shih and co-workers, who note connections with prior implementations of the virtual crack extension (VCE) method. The present derivation limited attention at the outset to quasi-static conditions. However, Shih and co-workers [20,21] have demonstrated the theory and implementation of VCE-like calculations for dynamic crack problems.

An infinity of crack-front perturbations can be considered by arbitrarily choosing different functions,  $q$ . In practice, it suffices to interpolate a finite number,  $R$ , of crack-front perturbations  $q^R(x)$  in terms of nodal values

$$q^R(x) = \sum_P N^P(x) Q^{RP} \quad (19)$$

where  $N^P$  denotes nodal shape functions within the elements and  $Q^{RP}$  are nodal values (at node ' $P$ ') of  $q^R$ . Here  $R$  is the number of nodal locations along the crack front. Corresponding to each  $q^R(x)$ , there is an associated perturbation of the crack front  $\delta\ell^R(s) = q^R(x(s)) \cdot b(s)$ , where  $b(s) = e_i(s)$  is crack-front bi-normal vector (see text prior to Eq 1). From separate evaluations of Eq 18 for each of the  $R$ -independent crack locations,  $R$ -independent

evaluations,  $-\delta_\ell \pi^R$ , can be obtained. Corresponding to each of these values is the particular weighted average of Eq 1

$$-\delta_\ell \pi^R = \int_{\text{crack front}} J(s) \delta \ell^R(s) ds \quad (20)$$

Finally, the (sought-for) distribution  $J(s)$  can be discretized by 1-D shape functions along the crack front as

$$J(s) = \sum_{M=1}^R N^M(s) J^M \quad (21)$$

where  $J^M$  is the local value of  $J$  at nodal location  $M$  on the crack front (crack-front coordinate  $s^M$ ). When Eqs 20 and 21 are inserted into Eq 1 for each  $R$ , and then equated with the evaluation of  $-\delta_\ell \pi^R$  in Eq 18, there results the simple algebraic equation

$$\sum_{M=1}^R \left[ \int_{\text{crack front}} N^M(s) N^P(s) (Q^{RP} \cdot B^P) ds \right] J^M = -\delta_\ell \pi^P \quad (22)$$

It is understood in Eq 22 that  $Q^{RP} \cdot B^P = \delta \ell$  if  $P = R$  and is equal to zero otherwise. Thus, the magnitude  $\delta \ell$  is truly virtual and can be symbolically factored from the left side of Eq 18 for equating with the quotient form (Eq 18) which forms the right side of Eq 22. The matrix in Eq 22 is small, banded, symmetric, and positive definite, and can be easily solved for the consistent nodal  $J^M$  values. Further discussion of the numerical details of implementation of this domain integral version of the virtual crack extension method can be found in Ref 20.

### *Simplified Models*

The geometric and parametric complexities of surface crack problems remain as formidable obstacles for "exact" continuum solutions, even if they are obtained with the aid of powerful computers executing sophisticated computational algorithms. In engineering practice, there is great need for simplified mechanics models of surface crack behavior which approximately account for major observed features. However, the scope and quantitative effects of the assumptions made in constructing a simplified model may be difficult to determine *a priori*. There is also an element of "style" to modeling; one person's "model" may be another's "empirical correlation."

If we bear these points in mind, attention is limited to two classes of simplified models which have had great impact on the understanding of surface crack behavior: the line-spring and the plastic hinge idealization of part through circumferentially cracked pipes in bending.

*Line-Spring Analysis of Surface-Cracked Shells*—"Part-through" cracks in plates and shells are an important class of surface crack configurations encountered in engineering practice. Although detailed 3-D analysis of these problems (using, for example, the VCE method) is possible, such detailed modeling generally requires extensive computational time and (equally important!) large amounts of data preparation in the form of mesh generation and input deck creation. Some time ago, Rice and Levy [22] introduced a simplified "line-spring" model for approximate analysis of such problems, which Parks and co-workers and others have recently applied and extended. In general,  $K$  and  $J$  results from

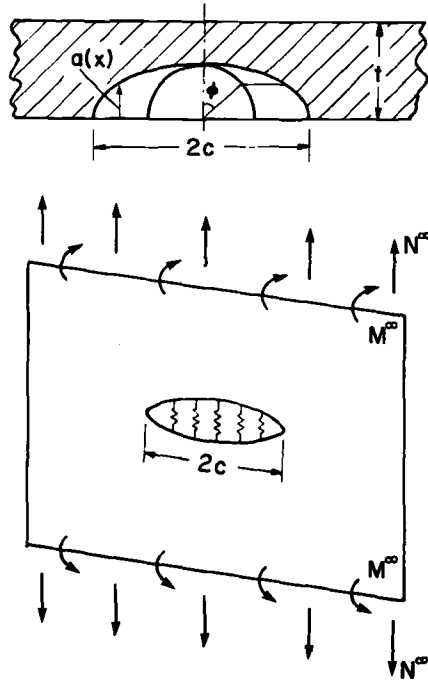


FIG. 2—Schematic cross section of a surface crack with varying depth  $a(x)$  and projected length  $2c$  in a shell of thickness  $t$ .

the solutions compare favorably (say, within  $\sim 10\%$  or so) with results of detailed continuum solutions, but typically involve *one to two orders of magnitude* less computer and data preparation time. We briefly highlight the main features of the model.

Consider the surface-cracked plate of thickness  $t$  shown schematically in Fig. 2. The presence of the surface crack introduces an additional compliance into the structure which is accounted for in the model by introducing a distributed foundation along the cut of length equal to the surface projection,  $2c$ , of the surface crack. In symmetric structures, the generalized shell resultants which the foundation transmits are a moment  $M$  and a membrane force  $N$  per unit length. Work-conjugate variables are relative separation,  $\delta$ , and relative rotation,  $\theta$ , of the two sides of the model through-crack. The compliance of the distributed foundation at any position  $s$  along the cut depends on local crack depth,  $a(s)$ , at that point. More precisely, the foundation compliance at  $s$  is equated to the "cracked" compliance of a single-edge notched (SEN) specimen of the same material having thickness  $t$  and crack depth  $a$  equal to  $a(s)$ , and subject to combined tension and bending.

Let the force variables ( $N, M$ ) be denoted by  $Q_\alpha$ ,  $\alpha = 1, 2$  and work-conjugate displacements  $(\delta, \theta) = q_\alpha$ . Total and incremental displacements are additively decomposed into elastic and plastic parts

$$q_\alpha = q_\alpha^e + q_\alpha^p \quad (23)$$

and

$$dq_\alpha = dq_\alpha^e + dq_\alpha^p \quad (24)$$

Elastic displacements,  $q_\alpha^e$ , are related to  $Q_\beta$  via

$$q_\alpha^e = P_{\alpha\beta} Q_\beta \quad (25)$$

where the matrix  $P_{\alpha\beta}$  is obtained from  $K_I$  calibrations of the SEN specimen using energy/compliance relations derived by Rice [23]. Normalized components of  $P_{\alpha\beta}$  are given by

$$\begin{aligned} E'P_{11} &= 2\pi K_{11} \\ tE'P_{12} &= tE'P_{21} = 12\pi K_{12} \\ t^2E'P_{22} &= 72\pi K_{22} \end{aligned} \quad (26)$$

where

$$K_{\alpha\beta} = \int_0^{a/t} \xi \cdot F_\alpha(\xi) \cdot F_\beta(\xi) d\xi \quad (27)$$

and the assumed stress-intensity factor calibration of the SEN specimen under tension and bending is

$$K_I = \sqrt{\pi\alpha} \times \left[ \frac{N}{t} \cdot F_1(a/t) + \frac{6M}{t^2} \cdot F_2(a/t) \right] \quad (28)$$

Approximate formulae for the functions  $F_\alpha$  can be obtained, for example, from Tada et al. [24].

For elastic response, the line-spring has been generalized to include mixed-mode loading on a surface-crack [24]. Within the context of the line-spring,  $K_{II}$  loading of a surface-cracked shell is due to the transverse shear force  $V$ , which is generally relatively small compared to typical membrane forces. Mode III loading of the line-spring is caused by both the membrane shear force  $Q$  and the twisting moment,  $T$ , in the shell. The respective work-conjugate displacements are the jump  $\Delta_t$  (across the spring) of in-plane displacement tangent to the cut and in relative rotation component,  $\phi$ , in the tangent plane but orthogonal to cut tangent vector. Energy analyses similar to those leading to the Mode I compliance components  $P_{\alpha\beta}$  would formally suggest that an off-diagonal coupling term,  $C_{45}$ , appear in the Mode III block compliance

$$\begin{bmatrix} \Delta_t \\ \phi \end{bmatrix} = \begin{bmatrix} C_{44} & C_{45} \\ C_{54} & C_{55} \end{bmatrix} \begin{bmatrix} Q \\ T \end{bmatrix} \quad (29)$$

However, Desvaux [25] has demonstrated that inaccurate solutions can arise unless  $C_{45}$  is set to zero. "Physical" arguments in support of this procedure were also given.

Two procedures have evolved for evaluating the plastic displacements,  $q_\alpha^p$ , if they are present. The first method, initially suggested by Rice [26], is based on an incremental or flow theory of plasticity and has been developed and applied by Parks [27], Parks and White [28], and White et al. [29]. Recently Shawki et al. [30] used pure power-law deformation theory calibrations [31] of a semi-infinite crack approaching the boundary of a half-space with the remaining ligament subject to tension and bending to estimate  $q_\alpha^p$  in moderately deeply cracked SEN and line-spring calculations.

The calibrated spring compliances are embedded in a structural model of the surrounding shell, loads are applied, and the resulting statically indeterminate system of equations is solved for kinematic variables, including  $q_a(s)$ . These variables, in conjunction with the spring compliances, provide the generalized forces  $Q_a(s)$ .

Finally, in either elastic-plastic model, the "payoff" lies in the estimation of crack parameter  $J(s)$  along the crack front. In Mode I, the local  $J$ -integral is taken as the sum of elastic and plastic parts

$$J(s) = J^e(s) + J^p(s) \quad (30)$$

where

$$J^e = K_1^2/E' = Q_a k_a k_\beta Q_\beta/E' \quad (31)$$

and  $k_a(a(s)/t)$  are related to the SEN stress-intensity factor coefficients  $F_a$  of Eq 28. For incremental plasticity formulations, an evolution law for  $J^p$  comes from

$$dJ^p = m \cdot \sigma_{\text{flow}} \cdot d\delta_t^p \quad (32)$$

where  $m$  is a dimensionless scalar (ranging from roughly 1 to 2, depending on load ratio),  $\sigma_{\text{flow}}$  is the ligament-average tensile flow strength (in general dependent on strain hardening), and the plastic increment of crack-tip opening displacement,  $d\delta_t^p$ , is calculable from  $dq_a^p$  [28]. In the case of deformation theory power-law models of plasticity,  $J^p$  is taken as an explicit function of  $Q_a$ ,  $t - a$  and power-law material constants [31,30]. The latter authors show that some improvement in the transitional loading regime, when  $J^e$  and  $J^p$  are roughly equal, can be obtained by using a plasticity-adjusted "effective" crack length,  $a_e \geq a$ , in the elastic compliances and in  $J^e$ .

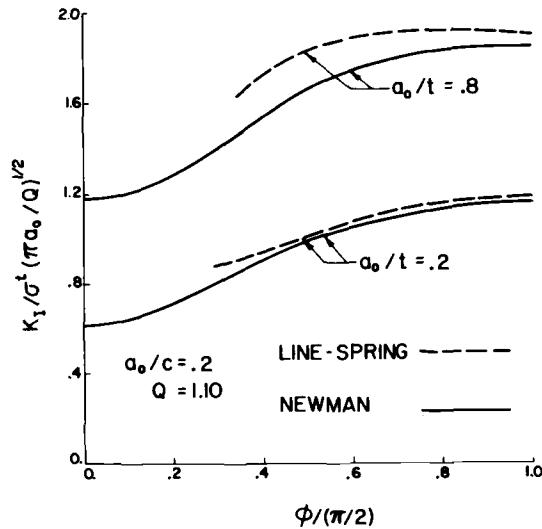


FIG. 3—Normalized stress-intensity distribution for semielliptical surface cracks in a tensile-loaded plate: line-spring, and continuum finite-element solutions. (Finite-element solutions are those of Raju and Newman [10].)

Good agreement has been obtained between line-spring calculations and a number of continuum analyses. Figure 3 shows the distribution of  $K_I$  along a semielliptical crack front in a large plate subject to tension  $\sigma$ , at infinity. The deepest penetration of the ellipse is  $a_0$ . The elliptic angle  $\phi$  parametrizes position along the crack front, with  $\phi = 0$  at the center line and  $\phi = \pi/2$  at the free surface. Also shown are Raju and Newman's [10] 3-D finite-element results.

Figure 4 [30] shows power-law line-spring and 3-D VCE calculations of centerplane  $J$  versus tensile load curves for a surface cracked plate. The power-law exponent (plastic strain  $\propto$  stress <sup>$n$</sup> ) was  $n = 10$  (see also Eq 37). The agreement is excellent, as was the variation along the crack front at all points except very near the corner, a point where the line-spring model has no basis.

*Plastic Hinges in Circumferentially Cracked Pipe*—The operational definition of  $J$  as related to the difference between load/load-point-displacement curves of otherwise identical bodies having slightly different crack profiles has played an important role in the development of NLEFM. A generalization of Eq 4 provides, for imposed displacement,  $q$

$$\bar{J} \delta A = \int_0^{q_c} [Q(q_c; \ell) - Q(q_c; \ell + \delta \ell(s))] dq_c \quad (33)$$

where work-conjugate generalized force is  $Q$ , and the arguments indicate that it depends on both the "cracked" part of imposed displacement,  $q_c$ , and the crack front "shape,"  $\ell(s)$ .  $\bar{J}$  is an "average" crackfront value for  $J$  over that portion of the front where the crack fronts differ by the infinitesimal amount  $\delta \ell(s)$ . The difference in crack plane area is

$$\delta A = \int_{\text{crack front}} \delta \ell(s) ds \quad (34)$$

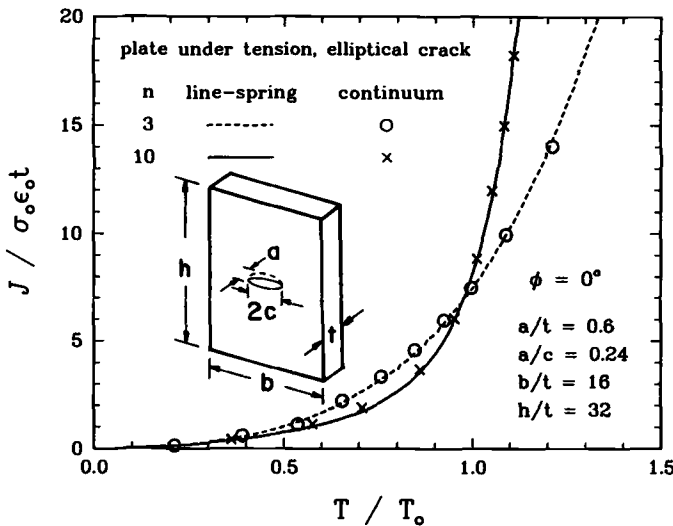


FIG. 4—Normalized  $J$  versus normalized load for a tension-loaded plate of Ramberg-Osgood power law hardening material containing a part through semielliptical surface flaw. Continuum finite-element and power-law line-spring finite-element solutions are shown for hardening exponents  $n = 5$  and  $10$  [30].

The right side of Eq 33 can formally be evaluated in the rigid/ideally plastic limit, where the integrands are the limit loads for each crack front and are independent of the magnitude of imposed displacement. Thus

$$\bar{J} = q_c^{\ell} \frac{Q_{\text{limit}}(\ell) - Q_{\text{limit}}(\ell + \delta\ell)}{\delta A} \quad (35)$$

Equations such as Eq 35 (first obtained in Ref 32) have been widely used in the fracture analysis of ductile fracture in nuclear piping [33–37]. For circumferentially cracked thin pipes of radius  $R$  and thickness  $t$  subject to bending moment,  $M$ , it is elementary to obtain a lower bound estimate of the section neutral axis and limit moment as functions of crack geometry, and the generalized displacement is hinge rotation. Using a perturbation technique based on Eq 35, Pan [35,36] showed that in constant depth part through surface cracks of large angular extent, there was a marked trend for larger notional  $\bar{J}$  values near midplane than at other locations around the crack front. The reason is geometrically clear; a ligament patch of area  $\delta A$  carrying flow stress  $\sigma_0$  is much more effective in reducing the limit-load bending moment if it is farther from the neutral axis. The  $\bar{J}$ -variation inferred from this simple model is surprisingly realistic when the crack front spans 180 deg.

Using assumed functional dependencies relating load to displacement, Pan [36] also extended this perturbation formalism to derive effective scaling laws for the plastic part of local  $\bar{J}$  as

$$\bar{J}^p = \frac{-\delta Q_{\text{limit}}}{\delta A Q_{\text{limit}}} \int_0^{q_c^{\ell}} Q dq_c^{\ell} \quad (36)$$

where  $\delta Q_{\text{limit}}$  is the numerator in Eq 35.

Finally, Pan has shown how this technique, along with an assumed material resistance curve in the form of a  $\bar{J}$  versus  $\Delta a$  relation, qualitatively predicts the initially stable, then abruptly unstable penetration of the surface crack in these geometries, as observed experimentally by Wilkowski and reported in Ref 37.

The predictive capabilities of this model are at least partly fortuitous; for example, the shape of the  $\bar{J}$  curve and attendant crack advance along the crack front would not be correct in tensile loaded plates. On the other hand, the qualitative features of this extremely simple model are at once both remarkably realistic and comprehensible.

### HRR Dominance in Tensile-Loaded Surface Cracks

Dominant singularity correlations of cracking have inherent parametric limits of applicability. For  $J$ -based applications in largely yielded plane strain geometries, these are fairly well understood, but for applications to 3-D geometries such as surface cracks, much less is known. Here we review recent work on understanding of the establishment and loss of  $J$ -based asymptotic dominance along tensile-loaded surface crack fronts.

#### Background

In the analysis of monotonically loaded bodies undergoing significant nonlinear (plastic) deformation, it is convenient to consider an “equivalent” nonlinear elastic material model which coincides with the plastic response of the material under conditions of proportional



stressing. A fairly general phenomenological power law model of nonlinear uniaxial behavior is

$$\epsilon = \alpha \epsilon_0 \cdot (\sigma/\sigma_0)^n \quad (37)$$

Here  $\epsilon$  and  $\sigma$  are strain and stress, respectively, and material parameters are  $\sigma_0$ , an effective yield stress;  $\epsilon_0 = \sigma_0/E$  ( $E$  is Young's modulus), a reference yield strain;  $n$ , the strain hardening exponent; and  $\alpha$ , a dimensionless factor. This relation is tensorially generalized using  $J_2$  deformation theory plasticity to provide the (plastic) strain,  $\epsilon_{ij}$ , as

$$\epsilon_{ij} = \alpha \epsilon_0 \cdot \frac{3}{2} (\sigma_e/\sigma_0)^{n-1} s_{ij}/\sigma_0 \quad (38)$$

where  $s_{ij}$  is the stress deviator, and  $\sigma_e = \sqrt{3s_{ij}s_{ij}/2}$  is the Mises equivalent tensile stress. Small geometry change asymptotic analysis of a symmetrically loaded, mathematically sharp crack front in such a material leads, as  $r \rightarrow 0$ , to the crack tip fields

$$\sigma_{ij}(r, \theta; s) \rightarrow \sigma_0 \cdot [J(s)/(\alpha \epsilon_0 \sigma_0 I_n r)]^{1/n+1} \cdot \tilde{\sigma}_{ij}(\theta, n) \equiv \sigma_{ij}^{HRR} \quad (39)$$

$$\epsilon_{ij}(r, \theta; s) \rightarrow \alpha \epsilon_0 \cdot [J(s)/(\alpha \epsilon_0 \sigma_0 I_n r)]^{n/n+1} \cdot \tilde{\epsilon}_{ij}(\theta, n) \equiv \epsilon_{ij}^{HRR} \quad (40)$$

Here  $\tilde{\sigma}_{ij}$  and  $\tilde{\epsilon}_{ij}$  are dimensionless functions of their arguments, and  $I_n(n)$  is a normalizing factor. These fields were determined by Hutchinson [38] and Rice and Rosengren [39] and are collectively referred to as the HRR singular fields. For fixed material properties, the magnitude of these fields is given solely by the value of the parameter  $J(s)$ . When the HRR fields truly dominate the complete crack-tip fields over distances large compared to crack-tip blunting and fracture process zone, it is a natural and continuous extension of LEFM methodology to correlate crack extension with  $J$ . For a recent review of this approach, see Ref 40.

The asymptotic fields (Eqs 39 to 40) do not apply *too* close to the crack tip, since effects of finite geometry change (blunting) have been neglected. An effective crack-tip opening displacement,  $\delta_t$ , can be defined from the HRR fields as the crack separation where  $\pm 45$ -deg lines emanating from the crack tip intercept the crack faces (Shih [41])

$$\delta_t = d_n(\alpha \epsilon_0, n) \cdot \frac{J}{\sigma_0} \quad (41)$$

This estimate of crack tip blunting is in good agreement with finite deformation numerical solutions (McMeeking [42]). The length scale  $\delta_t$  measures the finitely deforming region not accounted for in Eqs 39 and 40. Furthermore, since ductile void growth is inherently a finite strain fracture process, this scale implicitly defines the fracture process zone as well. Under conditions of small-scale yielding (SSY) in plane strain, finite deformation studies [42,43] show that the asymptotic fields (Eqs 39 to 40) *do* exist at distances near the tip but greater than  $\sim 5\delta_t$ .

Finite-element studies [43,44] provided quantitative insight into conditions under which the asymptotic fields (Eqs 39 to 40) likely dominate the crack-tip region for plane-strain geometries such as center-cracked tension, and edge-cracked bend and tension specimens. This work provided guidance as to minimum specimen dimensions (analogous to those assuring well-contained yielding in standard fracture toughness testing) so that critical experimentally determined material properties such as  $J_{Ic}$  and  $J_R$  ( $\Delta a$ ), would be both

conservative and relatively insensitive to other features of testing procedure. In large-scale yielding, these size restrictions have been formalized by requiring that the ratio of ligament size,  $\ell$ , to the crack tip similarity length,  $J/\sigma_0$ , satisfies

$$\mu \equiv \frac{\ell}{J/\sigma_0} \geq \mu_{cr} \quad (42)$$

where  $\mu_{cr}$  is a "critical" lower limit. For low hardening materials,  $\mu_{cr} \approx 25$  for bending, while for predominant ligament tension,  $\mu_{cr} \approx 200$ . Shih [45] has shown that for sufficiently deep edge cracks,  $\mu_{cr}$  varies smoothly, with the ratio of tension to bending, between these limits.

### *HRR Dominance in Surface Cracks*

Understanding of corresponding necessary conditions for HRR-dominance in largely yielded surface crack configurations remains slight. Brocks and Olschewski [46] provided nonlinear finite-element studies of 3-D crack configurations along with certain assessments of HRR-dominance, but the mesh fineness used was far less than in the 2-D studies cited. Brocks and Noack [47] have further emphasized the loss of HRR dominance under fully plastic conditions for an interior axial surface crack in a pressurized cylinder.

Recently, Parks and Wang [48] analyzed wide plates under remote uniaxial tension of magnitude  $\sigma^\infty$  normal to a centrally located part-through surface crack. The plates had thickness  $t$ , total width  $2b$ , and total length  $2h$ . The surface cracks considered were semi-elliptical in shape, with maximum penetration  $a$  and total surface length  $2c$ . Figure 5a shows one quarter of the structural geometry, including the global coordinates ( $X, Y, Z$ ). In the post-processing of the data obtained near the crack front, local coordinates ( $x, y, z$ ), indicated in Fig. 5b, were used. The parametric angle  $\phi$  locating positions along the semielliptical crack front given by  $(X/c)^2 + (Z/a)^2 = 1$  is also shown. The local  $z$ -axis is tangent to the crack front, and the local  $y$ -axis, which coincides with the global  $Y$ -axis, is normal to the crack plane.

Plate geometrical ratios were  $b/t = 8$  and  $h/t = 16$ . The crack depths considered were moderately deep; a semicircular crack front (denoted SC) had  $a/t = 0.5$  and  $a/c = 1$ , while

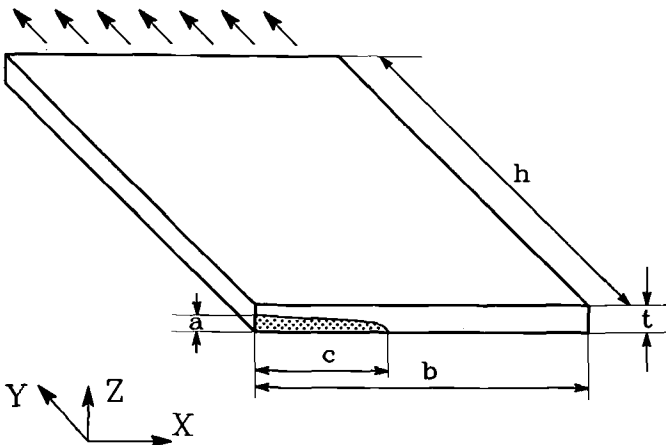


FIG. 5a—Schematic view of one-fourth of surface-cracked plate, showing global coordinate axes.

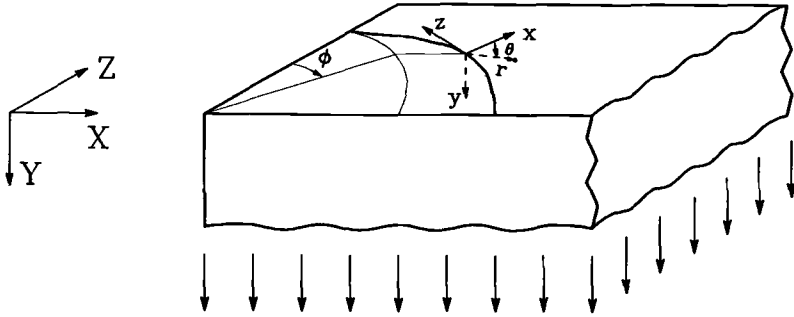


FIG. 5b—Global view of local coordinate system, along semielliptical crack front.

a semielliptical crack front (denoted SE) had  $a/t = 0.6$  and  $a/c = 0.24$ . These ratios match the experimental geometries of Epstein et al. [49]. Loading was imparted to the body by imposing uniform displacements  $U_Y$  at the remote boundary,  $Y = h$ , along with the symmetry conditions. Overall loading was characterized by the average remote stress,  $\sigma^\infty \equiv P/2bt$ , where  $P$  was the total load applied to the complete specimen. The constitutive model used was  $J_2$  deformation theory plasticity based on the Ramberg-Osgood power law form. Calculations were performed for strain-hardening exponents of both  $n = 5$  (high hardening) and  $n = 10$  (moderately low hardening).

$J(s)$  values were determined using the VCE method as modified in version 4-6 of the ABAQUS [50] finite-element program following the work of Li, Shih, and Needleman [51] and Shih et al. [20,21] on domain integral methods (see also the subsection on Virtual Crack Extension and Domain Integrals [p. 14]). Domain independence in the computed  $J$ -values can be an indicator of the overall accuracy of VCE calculations. In all cases,  $J(s)$  values obtained from six domains agreed to within 4%. Local stress values were sampled at both the reduced Gauss points and (from extrapolations) the nodal points.

Figure 6 (semielliptical [SE], top, and semicircular [SC], bottom) shows normalized center plane ( $\phi = 0$ )  $J$  values versus  $\sigma^\infty/\sigma_0$ . Each figure contains results for both strain-hardening exponents. At low stress,  $\sigma^\infty/\sigma_0 \leq \sim 0.5$ , the two curves coincide, and  $J$  is essentially the elastic value  $K_I^2/E'$ . Linear elastic  $J$  calculations (not shown) were typically within 5% of those given by Raju and Newman [10]. At intermediate stress levels,  $0.5 \leq \sigma^\infty/\sigma_0 \leq \sim 0.9$ ,  $J$ -values for  $n = 5$  were slightly greater than for  $n = 10$ . At higher load, the trend reversed due to the rapid increase of  $J$  in the  $n = 10$  material.

Figure 7 shows that the *shape* of the distribution of  $J$  along the crack front in these problems is relatively insensitive to stress level and degree of strain hardening. Three curves of  $J(\phi)$ , normalized by centerplane ( $J_{\phi=0}$ ) values of Fig. 6 are shown versus  $\phi$  for both the SE and SC geometries. At the lowest load level shown for each geometry, the shape of the distribution is essentially the same as the linear elastic case. Even at fully plastic conditions,  $\sigma^\infty/\sigma_0 \sim 1$ , the shape of each geometry's normalized  $J$ -distribution has changed very little. Distributions at intermediate load levels (not shown for purposes of clarity) essentially interpolate the small distance between elastic and fully plastic curves. Presumably, elastic-plastic  $J_{\phi=0}$  versus load curves, in conjunction with LEFM profiles of  $K^2$  versus  $\phi$  (for example, Ref 10), would permit accurate evaluation of  $J$  at any point along such crack fronts at any load level.

The degree to which the complete local crack-front fields agree with the asymptotic singular fields (Eqs 39 to 40) is a measure of the dominance of the latter. Parks and Wang presented detailed comparisons for the normal stress component  $\sigma_{yy}$  directly ahead of the

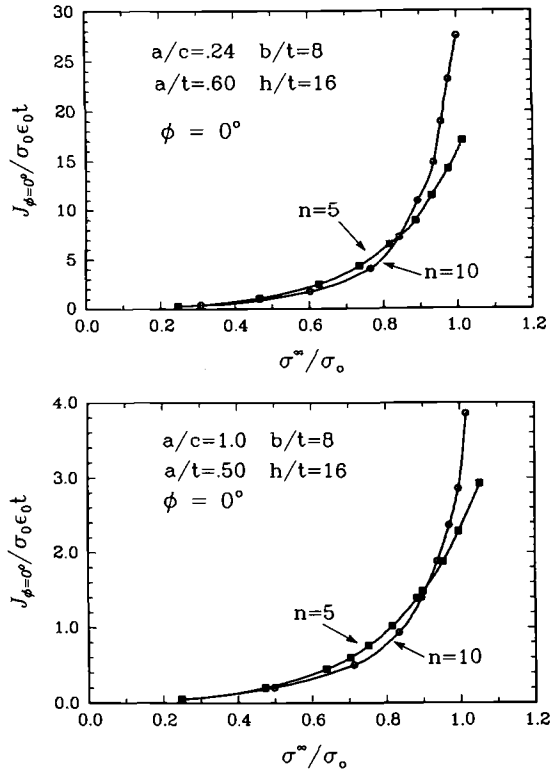


FIG. 6—Normalized center plane ( $\phi = 0$  deg)  $J$  versus remote stress: (top) semielliptical crack; (bottom) semicircular crack [48].

crack front,  $\theta = 0$ , as in Refs 43 to 45, to illustrate the existence and subsequent loss of HRR dominance in plane strain geometries.

Figure 8 shows  $\sigma_{yy}(r, \theta = 0; \phi = 0)$ , normalized by the corresponding HRR value of Eq 39 versus  $r$ , normalized by  $J/\alpha\sigma_0\epsilon_0$ , for the SE geometry with  $n = 10$ . The normalizing stress field  $\sigma_{HRR}(r)$  was determined from Eq 39 using  $J_{\phi=0}$ . Curves are shown for seven levels of remote stress, as well as a curve obtained from mathematical small-scale yielding (SSY). The latter curve was obtained from a 2-D plane strain analysis of a large circular domain, remotely loaded by the linear elastic  $K_I$  field. Details of this procedure can be found, for example, in Rice and Tracey [52]. Returning to the figure, it is seen that, at lower loads, the local stress profile is near, but slightly beneath the SSY results, which in turn, fall slightly below the precise HRR fields corresponding to the abscissa value of unity. At higher applied stress, the normalized stress profiles decay steadily, then rapidly, from HRR dominance.

The data of Fig. 8 have been replotted in Fig. 9 as stress, normalized by SSY stress, versus  $r$  normalized by  $\delta_i$  as calculated from Eq 41. The magnitudes of the normalized stress are closer to unity, and the closeness of the data points to the (neglected) crack tip blunting zone is evident. At the highest load levels, the stress at points nearest the tip is within 85% of the SSY value; this agreement occurs deep within the blunting zone and must be disregarded. A more realistic assessment of asymptotic dominance can be made

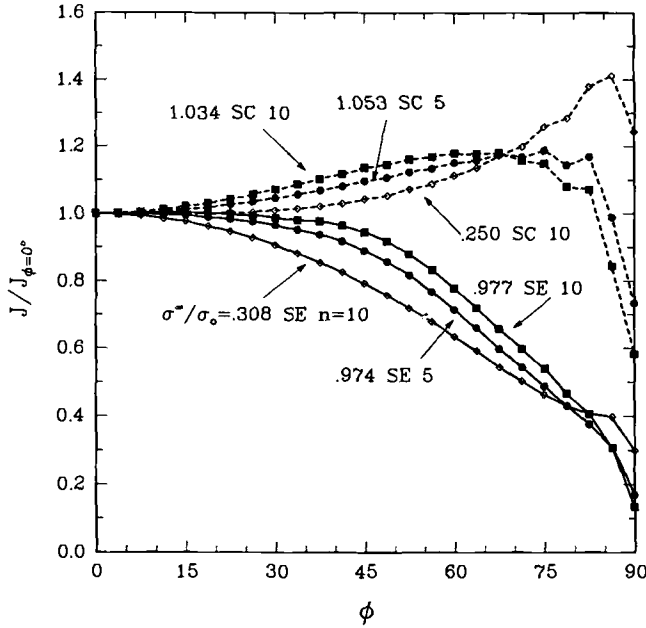


FIG. 7—Crack front  $J$ , normalized by center-plane values, for both semielliptical and semicircular crack fronts at various stress levels [48].

by examining the agreement at a few multiples of  $\delta_i$ , just outside the region affected by large geometry change.

For the centerplane data, this is done as Fig. 10, which shows the local  $\sigma_{yy}$  normalized by the SSY value, versus  $\sigma^\infty/\sigma_0$ . Curves are shown for material points at varying multiples of  $\delta_i$  from the crack tip. In the load range  $0.4 < \sigma^\infty/\sigma_0 < \sim 0.75$ ,  $\sigma_{yy}/\sigma_{ssy}$  decreases linearly. Indeed, this portion of the respective curves extrapolates back to unity at vanishing applied

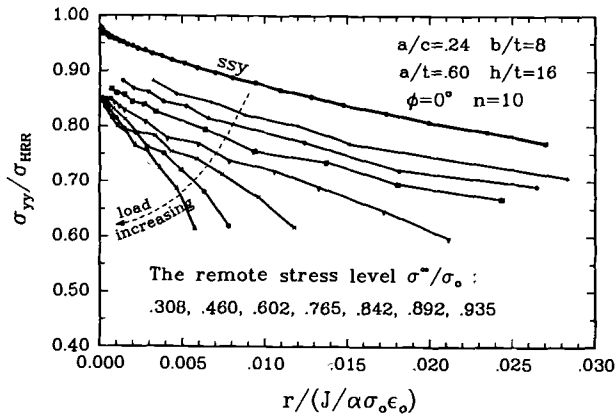


FIG. 8—Center plane ( $\phi = 0$  deg) normal stress ahead of crack tip, normalized by corresponding plane strain HRR values, versus normalized distance from crack tip. Curves are shown for a semielliptical crack front loaded to various applied stress levels [48].

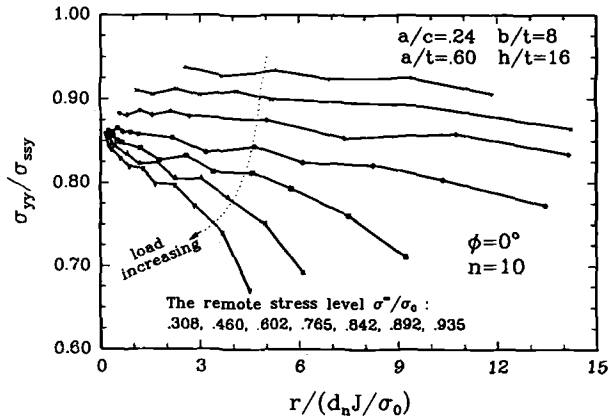


FIG. 9—Center plane ( $\phi = 0$  deg) normal stress ahead of crack tip, normalized by small-scale yielding (SSY) values, versus distance from crack tip normalized by crack-tip opening displacement (CTOD) as obtained from HRR fields, at various remote stress levels [48].

stress—that is, under small-scale yielding! At higher applied load, near  $\sigma^\infty/\sigma_0 = 0.8$ , the divergence from dominance becomes rapid. Points furthest from the crack tip are the first to feel the effects of the impinging fully plastic flow fields. Regardless of the distance chosen, it is clear that substantial deviation from SSY (and, implicitly, HRR) dominance is felt at  $\phi = 0$  in this problem near  $\sigma^\infty = 0.9\sigma_0$ .

Parks and Wang illustrated the effects of other variables on both the gradual and ultimate loss of HRR dominance. Figure 11 compares the decrease of  $\sigma_{yy}/\sigma_{ssy}$  with  $\sigma^\infty/\sigma_0$  at various locations along the SE and SC crack fronts, for the case of  $n = 10$ . The curve is arbitrarily drawn for points 66, from the tip. The SC geometry is more resistant to abrupt loss of dominance in the fully plastic regime than the SE configuration. The decrease from SSY dominance continues to be linear along the SC crack front up to  $\sigma^\infty = 1.04\sigma_0$ . The trend of decreasing dominance with decreasing  $\phi$  is also followed in this crack geometry.

The marked difference in fully plastic dominance displayed by these two crack geome-

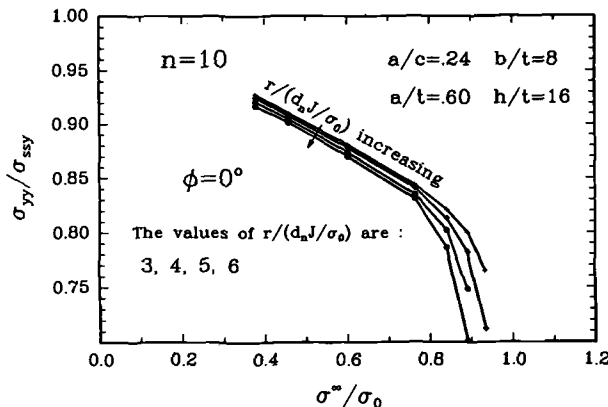


FIG. 10—Center Plane ( $\phi = 0$  deg) normal stress, normalized by SSY values, versus normalized remote stress, at various normalized distances from crack tip [48].

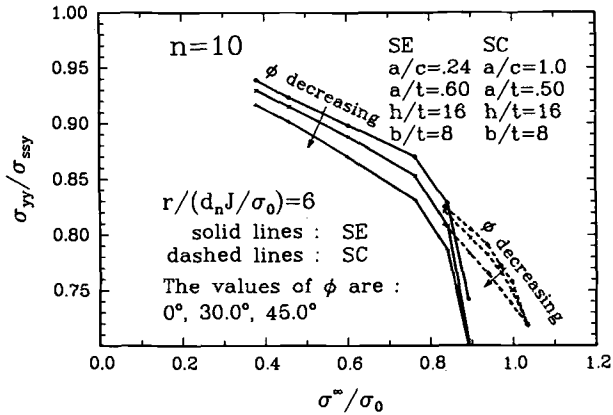


FIG. 11—Normalized stress at 6 CTOD ahead of crack tip, normalized by SSY values, versus normalized remote stress for semielliptical (SE) and semicircular (SC) surface cracked geometries, at various locations ( $\phi$ ) along the crack front [48].

tries is due to the relative ease with which deformation can focus into plane strain-like behavior. Once the surrounding material reaches flow conditions, the long, relatively constant depth ligament near the center of the SE readily accommodates the lightly constrained in-plane flow typical of a single-edge crack under tension. In contrast, the minimum ligament depth and crack-front radius of curvature are equal in the SC geometry, and no such planar modes of flow are available. Hence, relative HRR dominance is retained to higher stress levels in the SC geometry. Indeed, experimental evidence consistent with this conclusion has been provided by Epstein et al. [49].

A related point concerns the effect of crack-front position on loss of dominance. At larger  $\phi$  values in the SE specimen, the ability of deformation to focus into low constraint planar deformation bands is less than at  $\phi = 0$ . Brocks and Noack [47] have noted this feature in a fully plastic axially cracked cylinder and suggested that the relatively higher constraint near  $\phi \approx 75$  deg could be in part responsible for “canoe-shaped” ductile crack growth patterns often observed on surface crack fronts, this despite the fact that the (now) notional  $J_{\phi=0}$  exceeded  $J_{\phi=75 \text{ deg}}$  in the fully plastic regime. The calculations of Parks and Wang are in agreement with this suggestion, though additional effects such as anisotropy of initiation and tearing toughness in rolled plate material may also be important.

## Summary

We have reviewed progress in analysis and modeling of surface crack configurations. Mathematical tools of varying degrees of sophistication have been developed and applied to surface crack problems. Which major issues remain to be addressed?

The main challenge in linear elastic analysis is following general mixed-mode cracking in 3D. It was suggested that this class of problems can be effectively attacked only with singular integral boundary element hybrid schemes, but further development is required in performing the delicate integrations over nonplanar 2D domains. A secondary topic in LEFM is the further clarification of the fields where crack fronts intersect free surfaces or bi-material interfaces.

In the small-scale yielding regime, when LEFM nominally dominates crack front behavior, there nonetheless remain issues of concern. Fracture toughness values inferred from

tests of surface-cracked specimens are sometimes higher than those obtained from through-cracked (CT) specimens. This seems especially so for cases where the maximum  $K_I$  value along the surface crack front occurs on (near) the free surface, and the value there is appreciably greater than at maximum penetration. In such cases, it is likely that crack-front plastic constraint is being relieved by the presence of the nearby free surface, so higher loads must be applied to achieve "critical" conditions.

At higher loads, the  $J$  distributions of NLEFM can characterize crack-front fields, but this approach also fails to provide a single dominant crack loading parameter in the fully plastic regime. When dominance is lost, it will be necessary to consider the effects of the *complete* local stress and deformation fields in driving local processes of fracture. The level of detail and sophistication which such an approach may involve could vary, ranging from detailed continuum damage mechanics based on approximate void growth kinetics, to simplified line-spring or hinge models including constraint-dependent crack growth models based on crack opening angle, crack opening displacement, and so on.

Corner fields in plastic material are virtually unexplored. The relaxed near surface constraint leads to prominent crack tip blunting at the free surface intersection, and often the crack locally branches into a forked configuration. This shear localization at the corner often "sets up" the crack trajectory for lateral growth as a full slant through-crack after back surface penetration has occurred.

Near free surface effects are expected to be important in characterizing loss of HRR dominance for the practically important case of shallow surface cracks loaded to general yielding.

Finally, aspects of material inhomogeneity due to, for example, welding have not been adequately treated in fracture-mechanics theory, including surface-crack geometries, yet these features are likely sites for fracture.

Given both the technological impetus to better understand these and other features of surface-crack behavior and the collective body of fracture expertise, the pace of progress is likely to be sufficiently rapid that another major symposium devoted to this topic will not wait 15 more years to occur.

### Acknowledgments

This work was supported by the Office of Basic Energy Sciences, Department of Energy, under Grant No. DE-FG02-85ER13331. Computations were performed on an Alliant FX-8 computer obtained under DARPA Grant No. N00014-86-K-0768 and on a Data General MV-10000 computer donated to Massachusetts Institute of Technology by the Data General Corporation. The ABAQUS finite-element program was made available under academic license from Hibbitt, Karlsson, and Sorensen, Inc., Providence, Rhode Island.

### References

- [1] *The Surface Crack: Physical Problems and Computational Solutions*, J. L. Swedlow, Ed., American Society of Mechanical Engineers, New York, 1972.
- [2] Rice, J. R., "Mathematical Analysis in the Mechanics of Fracture," *Fracture*, Vol. 2, H. Liebowitz, Ed., Academic Press, New York, 1968, pp. 191-311.
- [3] Erdogan, F. and Gupta, G. D., "On the Numerical Solution of Singular Integral Equations," *Quarterly of Applied Mathematics*, Vol. 29, No. 4, 1972, pp. 525-534.
- [4] Annigeri, B. S. and Cleary, M. P., "Surface Integral Finite Element Hybrid (SIFEH) Method for Fracture Mechanics," *International Journal for Numerical Methods in Engineering*, Vol. 20, 1984, pp. 869-885.



- [5] Annigeri, B. S., "Surface Integral Finite Element Hybrid Method for Localized Problems in Continuum Mechanics," D. Sc. thesis, Department of Mechanical Engineering, Massachusetts Institute of Technology, Cambridge, MA, 1984.
- [6] Wium, D. J. W., Buyukozturk, O., and Li, V. C., "Hybrid Model for Discrete Cracks in Concrete," *Journal of Engineering Mechanics*, American Society of Civil Engineers, Vol. 110, 1984, pp. 1211-1229.
- [7] Keat, W. D., Annigeri, B. S., and Cleary, M. P., "Surface Integral and Finite Element Hybrid Method for Two- and Three-Dimensional Fracture Mechanics Analysis," *International Journal of Fracture*, Vol. 36, 1988, pp. 35-53.
- [8] Keat, W. D., "Surface Integral and Finite Element Hybrid Method for the Analysis of Three-Dimensional Fractures," Ph.D. thesis, Department of Mechanical Engineering, Massachusetts Institute of Technology, Cambridge, MA, 1989.
- [9] Fares, N., "Green's Functions for Plane-Layered Elastostatic and Viscoelastic Regions with Applications to 3-D Crack Analysis," Ph.D. thesis, Department of Civil Engineering, Massachusetts Institute of Technology, Cambridge, MA, 1987.
- [10] Raju, I. S. and Newman, J. C., Jr., "Stress Intensity Factors for a Wide Range of Semi-Elliptical Surface Cracks in Finite-Thickness Plates," *Engineering Fracture Mechanics*, Vol. 11, 1979, pp. 817-829.
- [11] Benthem, J. P., "Three-Dimensional State of Stress at the Vertex of a Quarter-Infinite Crack in a Half-Space," Report WTHD No. 74, Department of Mechanical Engineering, Delft University of Technology, Delft, the Netherlands, 1975.
- [12] Benthem, J. P., "State of Stress at the Vertex of a Quarter-Infinite Crack in a Half-Space," *International Journal of Solids and Structures*, Vol. 13, 1977, pp. 479-492.
- [13] Benthem, J. P., "The Quarter-Infinite Crack in a Half-Space: Alternative and Additional Solutions," *International Journal of Solids and Structures*, Vol. 16, 1980, pp. 119-130.
- [14] Břazant, Z. P. and Estensorro, L. F., "Surface Singularity and Crack Propagation," *International Journal of Solids and Structures*, Vol. 15, 1979, pp. 405-426.
- [15] Nakamura, T. and Parks, D. M., "Three-Dimensional Stress Field Near the Crack Front of a Thin Elastic Plate," *Journal of Applied Mechanics*, American Society of Mechanical Engineers, Vol. 55, 1988, pp. 805-813.
- [16] Nakamura, T. and Parks, D. M., "Anti-Symmetrical 3D Stress Field Near the Crack Front of a Thin Elastic Plate," *International Journal of Solids and Structures*, in press.
- [17] Parks, D. M., "The Virtual Crack Extension Method for Nonlinear Material Behavior," *Computer Methods in Applied Mechanics and Engineering*, Vol. 12, 1977, pp. 353-364.
- [18] deLorenzi, H. G., "On the Energy Release Rate and the  $J$ -Integral for 3-D Crack Configurations," *International Journal of Fracture*, Vol. 19, 1982, pp. 183-193.
- [19] Bass, B. R., Bryan, R. H., Bryson, J. W., and Merkle, J. G., "Applications of Energy Release Rate Techniques to Part-Through Cracks in Experimental Vessels," *Journal of Pressure Vessel Technology*, American Society of Mechanical Engineers, Vol. 104, 1982, pp. 308-316.
- [20] Nakamura, T., Shih, C. F., and Freund, L. B., "Three-Dimensional Transient Analysis of a Dynamically Loaded Three-Point-Bend Ductile Fracture Specimen," *Nonlinear Fracture Mechanics, ASTM STP 995*, American Society for Testing and Materials, Philadelphia, 1989, pp. 217-241.
- [21] Moran, B. and Shih, C. F., "Crack Tip and Associated Domain Integrals from Momentum and Energy Balance," *Engineering Fracture Mechanics*, Vol. 27, 1987, pp. 615-642.
- [22] Rice, J. R. and Levy, N., "The Part-Through Surface Crack in an Elastic Plate," *Journal of Applied Mechanics*, American Society of Mechanical Engineers, Vol. 39, 1972, pp. 185-194.
- [23] Rice, J. R., "Some Remarks on Elastic Crack Tip Fields," *International Journal of Solids and Structures*, Vol. 8, 1972, pp. 751-758.
- [24] Tada, H., Paris, P. C., and Irwin, G. R., *The Stress Analysis of Cracks Handbook*, Fracture Proof Design, Saint Louis, MO, 1985.
- [25] Desvaux, G. J., "The Line-Spring Model for Surface Flaw, an Extension to Mode II and Mode III," M. Sc. thesis, Department of Mechanical Engineering, Massachusetts Institute of Technology, Cambridge, MA, 1985.
- [26] Rice, J. R., "The Line-Spring Model for Surface Flaws," *The Surface Crack: Physical Problems and Computational Solutions*, J. L. Swedlow, Ed., American Society of Mechanical Engineers, New York, 1972, pp. 171-185.
- [27] Parks, D. M., "The Inelastic Line-Spring: Estimates of Elastic-Plastic Fracture Mechanics Parameters for Surface-Cracked Plates and Shells," *Journal of Pressure Vessel Technology*, American Society of Mechanical Engineers, Vol. 103, 1981, pp. 246-254.

- [28] Parks, D. M. and White, C. S., "Elastic-Plastic Line-Spring Finite Elements for Surface-Cracked Plates and Shells," *Journal of Pressure Vessel Technology*, American Society of Mechanical Engineers, Vol. 104, 1982, pp. 287-292.
- [29] White, C. S., Ritchie, R. O., and Parks, D. M., "Ductile Growth of Part-Through Surface Cracks: Experiment and Analysis," *Elastic-Plastic Fracture: Second Symposium, Volume I—Inelastic Crack Analysis*, ASTM STP 803, C. F. Shih and J. P. Gudas, Eds., American Society for Testing and Materials, Philadelphia, 1984, pp. I-384-I-409.
- [30] Shawki, T. G., Nakamura, T., and Parks, D. M., "Line-Spring Analysis of Surface Flawed Plates Using Deformation Theory," *International Journal of Fracture*, Vol. 41, 1989, pp. 23-38.
- [31] Shih, C. F. and Hutchinson, J. W., "Combined Loading of a Fully Plastic Ligament Ahead of an Edge Crack," *Journal of Applied Mechanics*, American Society of Mechanical Engineers, Vol. 53, 1986, pp. 271-277.
- [32] Bucci, R. J., Paris, P. C., Landes, J. D., and Rice, J. R., "J-Integral Estimation Procedures," *Fracture Toughness*, ASTM STP 514, American Society for Testing and Materials, Philadelphia, 1972, pp. 40-69.
- [33] Tada, H., Paris, P. C., and Gamble, R. M., "A Stability Analysis of Circumferential Crack for Reactor Piping," *Fracture Mechanics: Twelfth Conference*, ASTM STP 700, American Society for Testing and Materials, Philadelphia, 1980, pp. 296-313.
- [34] Zahoor, A. and Kanninen, M. F., "A Plastic Fracture Instability Analysis of Wall Breakthrough in a Circumferentially Cracked Pipe Subjected to Bending Loads," *Journal of Engineering Materials and Technology*, American Society of Mechanical Engineers, Vol. 103, 1981, pp. 194-200.
- [35] Pan, J., "Some Considerations on Estimation of Energy Release Rates for Circumferentially Cracked Pipes," *Journal of Pressure Vessel Technology*, American Society of Mechanical Engineers, Vol. 106, 1984, pp. 391-398.
- [36] Pan, J., "Estimation of Energy Release Rates and Instability for a Pipe With a Circumferential Surface Crack Subjected to Bending," *Journal of Pressure Vessel Technology*, American Society of Mechanical Engineers, Vol. 108, 1986, pp. 33-40.
- [37] Kanninen, M. F. et al., "Instability Predictions for Circumferentially Cracked Type 304 Stainless Steel Pipes Under Dynamic Loading," EPRI Project T118-2, Vols. 1 and 2, Final Report, Electric Power Research Institute, Palo Alto, CA, 1982.
- [38] Hutchinson, J. W., "Singular Behaviour at the End of a Tensile Crack in a Hardening Material," *Journal of the Mechanics and Physics of Solids*, Vol. 16, 1968, pp. 13-31.
- [39] Rice, J. R. and Rosengren, G. F., "Plane Strain Deformation Near a Crack Tip in a Power Law Hardening Material," *Journal of the Mechanics and Physics of Solids*, Vol. 16, 1968, pp. 1-12.
- [40] Hutchinson, J. W., "Fundamentals of the Phenomenological Theory of Nonlinear Fracture Mechanics," *Journal of Applied Mechanics*, American Society of Mechanical Engineers, Vol. 50, 1983, pp. 1042-1051.
- [41] Shih, C. F., "Relationships Between the J-Integral and the Crack Opening Displacement for Stationary and Extending Cracks," *Journal of the Mechanics and Physics of Solids*, Vol. 29, 1981, pp. 305-326.
- [42] McMeeking, R. M., "Finite Deformation Analysis of Crack-Tip Opening in Elastic-Plastic Materials and Implications for Fracture," *Journal of the Mechanics and Physics of Solids*, Vol. 25, 1977, pp. 357-381.
- [43] McMeeking, R. M. and Parks, D. M., "On Criteria for J-Dominance of Crack Tip Fields," *Elastic-Plastic Fracture*, ASTM STP 668, J. D. Landes, et al., Eds., American Society for Testing and Materials, Philadelphia, 1979, pp. 175-194.
- [44] Shih, C. F. and German, M. D., "On Requirements for a One-Parameter Characterization of Crack Tip Fields by the HRR Singularity," *International Journal of Fracture*, Vol. 17, 1981, pp. 27-43.
- [45] Shih, C. F., "J-Dominance Under Plane Strain Fully Plastic Conditions: the Edge Crack Subject to Combined Tension and Bending," *International Journal of Fracture*, Vol. 29, 1985, pp. 73-84.
- [46] Brocks, W. and Olschewski, J., "On J-Dominance of Crack-Tip Fields in Largely Yielded 3D Structures," *International Journal of Solids and Structures*, Vol. 22, 1986, pp. 693-708.
- [47] Brocks, W. and Noack, H.-D., "J-Integral and Stresses at an Inner Surface Flaw in a Pressure Vessel," *International Journal of Pressure Vessels and Piping*, Vol. 31, 1988, pp. 187-203.
- [48] Parks, D. M. and Wang, Y.-Y., "Elastic-Plastic Analysis of Part-Through Surface Cracks," *Analytical, Numerical, and Experimental Aspects of Three-Dimensional Fracture Processes*, ASME AMD-91, A. J. Rosakis et al., Eds., American Society of Mechanical Engineers, New York, 1988, pp. 19-32.

- [49] Epstein, J. S., Lloyd, W. R., and Reuter, W. G., "Three-Dimensional CTOD Measurements of Elastic-Plastic Surface Flaws," *Analytical, Numerical, and Experimental Aspects of Three-Dimensional Fracture Processes*, ASME AMD-91, A. J. Rosakis et al., Eds., American Society of Mechanical Engineers, New York, 1988, pp. 33-49.
- [50] *ABAQUS, User's Manual, Version 4-6*, Hibbitt, Karlsson, and Sorensen, Inc., Providence, RI, 1987.
- [51] Li, F. Z., Shih, C. F., and Needleman, A., "A Comparison of Methods for Calculating Energy Release Rate," *Engineering Fracture Mechanics*, Vol. 21, 1985, pp. 405-421.
- [52] Rice, J. R. and Tracey, D. M., "Computational Fracture Mechanics," *Numerical and Computer Methods in Structural Mechanics*, S. J. Fenves et al., Eds., Academic Press, New York, 1973, pp. 585-623.

P. W. Tan,<sup>1</sup> I. S. Raju,<sup>1</sup> K. N. Shivakumar,<sup>1</sup> and  
J. C. Newman, Jr.<sup>2</sup>

## Evaluation of Finite-Element Models and Stress-Intensity Factors for Surface Cracks Emanating from Stress Concentrations

---

**REFERENCE:** Tan, P. W., Raju, I. S., Shivakumar, K. N., and Newman, J. C., Jr., "Evaluation of Finite-Element Models and Stress-Intensity Factors for Surface Cracks Emanating from Stress Concentrations," *Surface-Crack Growth: Models, Experiments, and Structures*, ASTM STP 1060, W. G. Reuter, J. H. Underwood, and J. C. Newman, Jr., Eds., American Society for Testing and Materials, Philadelphia, 1990, pp. 34-48.

**ABSTRACT:** This paper presents an evaluation of the three-dimensional finite-element models and methods used to analyze surface cracks at stress concentrations. Previous finite-element models used by Raju and Newman for surface and corner cracks at holes were shown to have "ill-shaped" elements at the intersection of the hole and crack boundaries. These ill-shaped elements tended to make the model too stiff and, hence, gave lower stress-intensity factors near the hole-crack intersection than models without these elements. Improved models, without these ill-shaped elements, were developed for a surface crack at a circular hole and at a semicircular edge notch. Stress-intensity factors were calculated by both the nodal-force and virtual-crack-closure methods. Both methods and different models gave essentially the same results. Comparisons made between the previously developed stress-intensity factor equations and the results from the improved models agreed well except for configurations with large notch-radii-to-plate-thickness ratios.

Stress-intensity factors for a semi-elliptical surface crack located at the center of a semicircular edge notch in a plate subjected to remote tensile loadings were calculated using the improved models. A wide range in configuration parameters was considered. The ratio of crack depth to crack length ranged from 0.4 to 2; of crack depth to plate thickness from 0.2 to 0.8; and of notch radius to plate thickness from 1 to 3. The finite-element or nonsingular elements models employed in the parametric study had singularity elements all along the crack front and linear-strain (eight-noded) elements elsewhere. The models had about 15 000 degrees of freedom. Stress-intensity factors were calculated by using the nodal-force or virtual-crack-closure method.

**KEY WORDS:** crack, surface cracks, crack propagation, fracture, stress analysis, fatigue (materials), stress-intensity factors, finite elements, boundary-layer region

### Nomenclature

- a* Half-depth of surface crack along notch root
- b* Width of plate

<sup>1</sup> Research scientist, senior scientist, and senior scientist, respectively, Analytical Services and Materials, Inc., 107 Research Drive, Hampton, VA 23666.

<sup>2</sup> Senior scientist, Materials Division, NASA Langley Research Center, Mail Stop 188E, Hampton, VA 23665-5225.

- $c$  Length of surface crack from notch root
- $F_{sn}$  Stress-intensity boundary-correction factor
- $h$  Half-height of plate
- $K$  Stress-intensity factor (Mode I)
- $Q$  Shape factor for elliptical crack
- $r$  Radius of the semicircular notch or circular hole
- $S$  Remote uniform tensile stress
- $t$  Half-thickness of plate
- $x, y, z$  Cartesian coordinate system
- $\nu$  Poisson's ratio
- $\phi$  Parametric angle of ellipse

Surface and corner cracks can occur in many structural components. These cracks can cause premature failure of landing gear of aircraft, spars, stiffeners, and other reinforcements. Accurate stress analyses of these crack components are needed for reliable prediction of crack-growth rates and fracture strengths.

Surface and corner cracks in plates have received considerable attention in the literature in the past 16 years [1–20]. Various methods: finite-element method with singularity elements [3,4,8,10,12,13,17,19], finite-element method with displacement hybrid elements [5,6], alternating method [1,2,7,9], finite-element-alternating method [14,15,18,20], and boundary-integral equation method [11], were used to obtain stress-intensity factors for these cracked components. Stress-intensity factor equations were obtained by fitting empirical equations to the stress-intensity factors obtained from numerical analyses [16,17].

Surface and corner cracks at holes have received much less attention than surface cracks in plates. Smith and Kullgren [9] and Raju and Newman [12] analyzed corner cracks from a circular hole by the alternating method and the finite-element method (with singularity elements), respectively. Nishioka and Atluri [15,18] analyzed corner cracks from a circular hole and corner cracks in a lug by the finite-element-alternating method. The stress-intensity factors by all of the previously mentioned methods agreed well with one another [12,15], except in the region where the crack intersected the hole boundary. In this region, the stress-intensity factors from Raju and Newman [12,16] showed a precipitous “drop-off.” The stress-intensity factors calculated by other investigators (see Refs 9 and 15) did not show the large drop-off near the hole-crack intersection. Thus, the primary purpose of this paper is to investigate the reasons for the large drop in the stress-intensity factors where a surface crack meets a hole or notch boundary. In this investigation, an evaluation of the previously developed finite-element models used by Raju and Newman [12,16] and of the methods used to determine the stress-intensity factors was performed.

The second purpose of this paper is to present stress-intensity factors for a semielliptical surface crack located at the center of a semicircular edge notch in a finite thickness plate. This crack configuration has not been analyzed in the literature. The plates were subjected to remote tension loads and a wide range in configuration parameters were considered. The ratio of crack depth along the notch root to crack length away from the notch root ( $a/c$ ) ranged from 0.4 to 2; the ratio of crack depth to plate thickness ( $a/t$ ) ranged from 0.2 to 0.8; and the ratio of notch radius to plate thickness ( $r/t$ ) ranged from 1 to 3. The  $r/t$  ratio of 3 was chosen because this particular configuration was tested in an Advisory Group for Aerospace Research and Development (AGARD) study on short-crack growth behavior [21].

### Three-Dimensional Finite-Element Analysis

A three-dimensional finite-element analysis was used to calculate the Mode I stress-intensity factor variations along the crack front for a surface crack emanating from the center of a semicircular edge notch (or a circular hole) in a plate subjected to tensile loading, as shown in Fig. 1. In these analyses, Poisson's ratio was assumed to be 0.3.

Due to symmetry, only one quarter of the specimen was modeled for the notch configuration. Symmetry conditions on the  $x = 0$  plane were used to model the circular hole configuration. A typical model is shown in Fig. 2. This model has eight wedges on the crack plane and four layers on the hole. Six-noded pentahedral singularity elements or eight-noded nonsingular elements were used along the crack front and eight-noded hexahedral elements were used elsewhere. The finite-element models were subjected to remote tensile loading on the  $y = h$  plane. Stress-intensity factors were calculated using the nodal-force method or the virtual crack-closure technique (VCCT). Details of the formulation of these types of elements, the nodal-force method, and the VCCT are given in Refs 8, 10, 12, 22, and 23. Details on the development of the finite-element models will be discussed later.

### Stress-Intensity Factor

The remote tensile loads cause only Mode I deformations. The Mode I stress-intensity factor  $K$  for any location along the crack front was taken to be

$$K = S(\pi a/Q)^{1/2} F_{sn}(a/t, a/c, r/t, \phi) \quad (1)$$

The half-height of the plate,  $h$ , and width,  $b$ , were chosen large enough to have a negligible effect on stress-intensity factors ( $h/b \geq 2$  and  $r/b \approx 0.05$ ). Values of  $F_{sn}$ , the boundary-correction factor, were calculated along the crack front for various combinations of parameters ( $a/t$ ,  $a/c$ ,  $r/t$ , and  $\phi$ ). The crack dimensions and parametric angle,  $\phi$ , are defined in Fig. 1. The shape factor for an ellipse,  $Q$ , is given by the square of the complete elliptic integral of the second kind. Empirical expressions for  $Q$  (taken from Ref 10) were

$$Q = 1 + 1.464(a/c)^{1.65} \quad \text{for } a/c \leq 1 \quad (2a)$$

$$Q = 1 + 1.464(c/a)^{1.65} \quad \text{for } a/c > 1 \quad (2b)$$

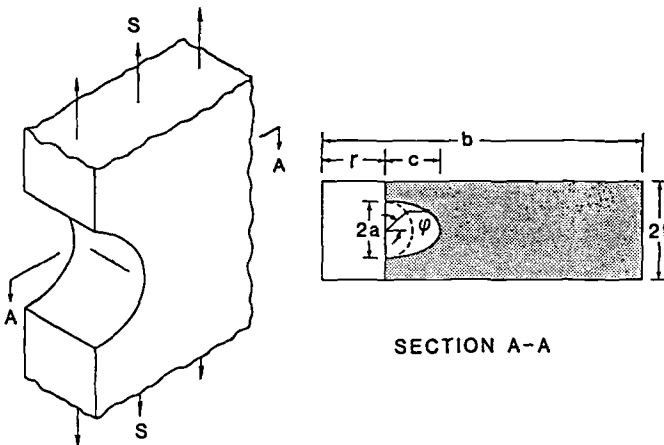


FIG. 1—Specimen configuration and loading.

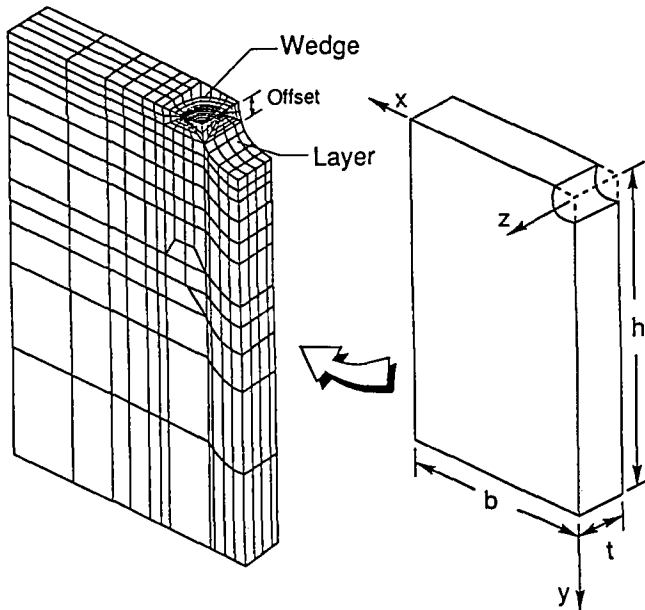


FIG. 2—Typical finite-element model.

### *Evaluation of Finite-Element Models and Methods*

Stress-intensity factor distributions in Refs 12 and 16 for surface and corner cracks at a hole showed a precipitous “drop-off” near the region where the crack meets the hole boundary. This drop-off was believed to have been caused by the “boundary-layer” effect. However, comparisons (see Refs 9 and 15) with other solutions in the literature showed that the stress-intensity factors calculated by other investigators did not exhibit this large drop-off near the boundary-layer region. Therefore, a study was carried out to determine whether this drop-off is an artifact of the modeling or is a real behavior. The models used in Refs 12 and 16 were reexamined. This examination revealed that the procedures used to generate the solids produced models with some “ill-shaped” elements in the region where the crack intersects the hole boundary. These ill-shaped elements were produced when the “wedge” region along the crack plane was connected directly to the “layer” region to model the hole or notch. For  $r/t = 1$ , the elements in the region where the crack meets the hole boundary had aspect ratios (ratio of largest to smallest dimension) of about 150. The aspect ratio of these elements increased linearly as the  $r/t$  ratio increased, that is, for  $r/t = 3$  the aspect ratio was 450!

The “ill-shaped” elements do not have any influence on the results if they are in regions of small stress gradients. However, they tend to produce a stiffer model if they are located in regions of large stress gradients. Because these elements were found in the region where the crack intersects the hole boundary, an investigation was undertaken to study the influence of these ill-shaped elements on the stress-intensity factor solutions. Three different finite-element models were developed and two different methods were used to extract the stress-intensity factors from the finite-element solutions.

**Models**—Model A used finite-element patterns that were similar to those used in Refs 12 and 16 with the “ill-shaped” elements near the hole-crack intersection. Model B was a newly developed finite-element model similar to Model A but without ill-shaped elements

Both Models A and B used a polar mesh and singularity elements around the crack front, as shown in Fig. 2. Model C, on the other hand, used a rectangular mesh and nonsingular elements around the crack front. Also, Model C did not have any ill-shaped elements near the hole-crack intersection. In Models B and C, the ill-shaped elements were avoided by not directly connecting the wedge region to the layer region near the hole-crack intersection. A small offset (between  $0.03r$  and  $0.1r$ ) was used before the layers were added to model the hole or notch configuration (Fig. 2). The  $x$ -coordinates of the nodes in the "offset" region were adjusted so that they lie on the circular boundary.

Two different in-house (National Aeronautics and Space Administration [NASA], Langley) computer programs, discussed in Refs 12 and 22, were used to analyze the various models. The different computer programs were used to verify the consistency of the results and to determine whether any undetected errors existed in the computer codes and analyses.

In Models A and B, pentahedron singularity elements were used all along the crack front and eight-noded hexahedron elements were used to model the rest of the solid. Furthermore, a 3 by 3 by 3 Gaussian integration scheme was used to form the element stiffness matrices. In Model C, nonsingular eight-noded hexahedron elements were used everywhere to model the solid. A 2 by 2 by 2 Gaussian integration scheme and reduced integration for the shear terms [22] were used in conjunction with Model C. In contrast to Models A and B, where the models had a polar-mesh pattern around the crack front, Model C had a rectangular-mesh pattern around the crack front.

*Methods*—Two methods for extracting stress-intensity factors from the solutions were also studied. The methods were the nodal-force method [8,10,12] and the virtual-crack-closure technique (VCCT) [23]. In the nodal-force method, the forces normal to the crack plane and ahead of the crack front were used to calculate the stress-intensity factors. This method does not require the assumption of either plane stress or plane strain to obtain the stress-intensity factor. The VCCT calculates the strain-energy release rate using the forces normal to the crack plane and ahead of the crack front and the relative displacements of the crack faces behind the crack front. The stress-intensity factor is then obtained from the calculated strain-energy release rate by assuming either plane-strain or plane-stress conditions. Plane-strain conditions were used everywhere along the crack front except where the crack meets the notch surface ( $\phi = 90$  deg). At this location, plane-stress conditions were used. These types of assumptions along the crack front are widely used in the literature [4,11,13,23,24].

*Comparison of Stress-Intensity Factors*—Three specimen configurations with  $r/t = 1$  or 3 were chosen in the evaluation study. All configurations had a semicircular ( $a/c = .1$ ) crack with an  $a/t$  ratio of 0.2. One configuration had a surface crack emanating from a circular hole ( $r/t = 1$ ), while the other configurations had a surface crack emanating from a semicircular edge notch ( $r/t = 1$  and 3). All models had 14 wedges to model the crack plane and 10 layers to model the notch. Models A and B had about 15 000 degrees of freedom (dof) while Model C had about 18 000 dof.

Figure 3 presents the stress-intensity factor distributions along the crack front from Models A, B, and C for a surface crack located at the center of a circular hole with  $r/t = 1$ . The results from Models B and C agreed well (within 1.5%) with each other all along the crack front. Model A, with the "ill-shaped" elements (circular symbols [16]), gave stress-intensity factors that were lower than the results from the other models. The discrepancy was quite large for  $\phi > 60$  deg. The results from Models B and C do not show the large drop-off exhibited by Model A.

The solid curve is an empirical equation for a surface crack at a circular hole that was based on previous finite-element results [16]. Comparison with the present finite-element



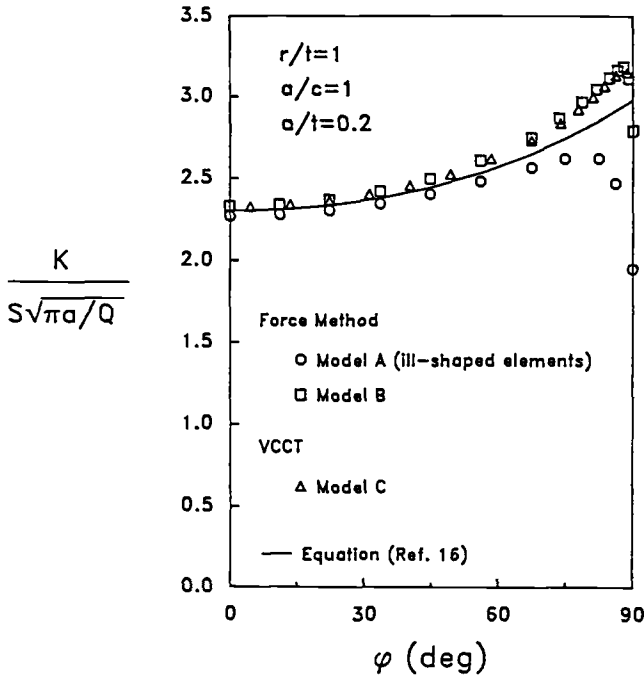


FIG. 3—Comparison of results for a surface crack emanating from the center of a circular hole, using various models and methods for  $r/t = 1$ .

results suggests that the equation is still accurate (within 5%) for this crack configuration, although a slight modification would be necessary near the hole-crack intersection.

Figures 4 and 5 present stress-intensity factors for the same crack shape and size as shown in Fig. 3 ( $a/c = 1$ ;  $a/t = 0.2$ ) but for a surface crack at a semicircular edge notch with  $r/t$  ratios of 1 and 3, respectively. The nodal-force results from models with and without ill-shaped elements (Models A and B, respectively) differed all along the crack front for  $r/t = 1$  (Fig. 4). Again, the largest discrepancies occurred for  $\phi > 60$  deg. However, the nodal-force results (Model B) were in good agreement with results from Model C using the VCCT for  $r/t$  ratios of 1 and 3. The maximum difference between these two sets of results was only about 2%.

Again, the solid curves in these figures show stress-intensity factors calculated from an empirical equation [25]. This equation was previously fitted to finite-element results for a surface crack at a hole [16] but adjusted for the stress concentration differences between a hole and a notch. Comparison with the present finite-element results (Fig. 4) suggests that the equation is still accurate for this crack configuration although a slight modification would, again, be necessary near the hole-crack intersection (maximum difference at this location was about 5%). However, for  $r/t = 3$ , the equation consistently underestimated the stress-intensity factors (3 to 13%), as shown in Fig. 5. A reason for the lower estimate is probably because the equation was extrapolated to  $r/t$  values beyond those used in fitting the equation ( $0.5 \leq r/t \leq 1$ ). Thus, a modification to the equations is required for crack configurations with the  $r/t$  ratios greater than unity.

*Discussion*—Recall that the nodal-force method was used to extract the stress-intensity factors from the models with and without the ill-shaped elements (Model A and B, respec-

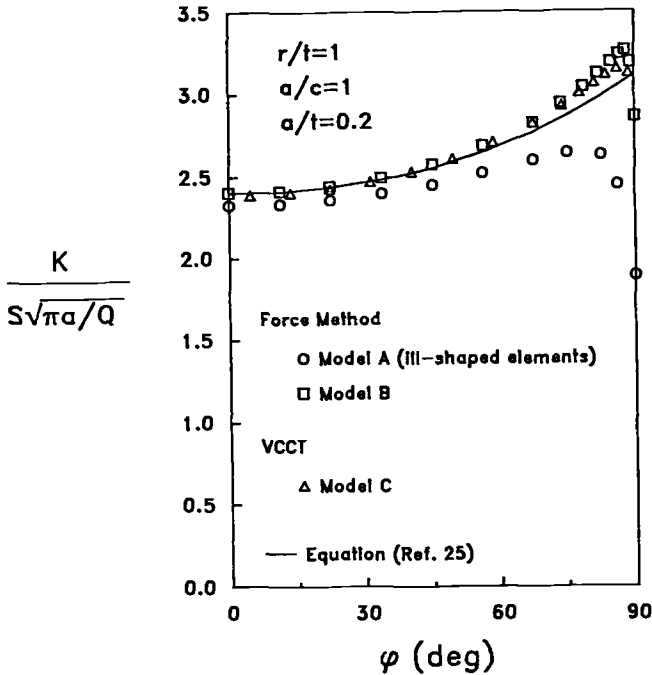


FIG. 4—Comparison of results for a surface crack emanating from the center of a semi-circular notch, using various models and methods for  $r/t = 1$ .

tively). On the other hand, the VCCT was used in conjunction with Model C. All models without the ill-shaped elements gave nearly the same stress-intensity factors all along the crack front. This suggests that the two methods of extracting stress-intensity factors are reliable, provided that the models are well behaved. The models with the “ill-shaped” elements tended to make the model too stiff and, hence, gave lower stress-intensity factors than models without these elements. Therefore, improved finite-element models that were similar to those used in Refs 12 and 16 but did not contain any ill-shaped elements were developed for a wide range in configuration parameters. These new models, in conjunction with the nodal-force method or the VCCT, were used to analyze a surface crack at a semi-circular edge notch herein. These models had about 15 000 dof. The results obtained with these models are discussed in the following section.

#### Stress-Intensity Factor Solutions for Surface Crack at Semicircular Edge Notch

A surface crack emanating from a semicircular edge notch in a plate subjected to remote tensile loading was considered herein. A wide range in crack sizes ( $a/t$ ), crack shapes ( $a/c$ ), and notch sizes ( $r/t$ ) were analyzed. The ranges in crack and notch parameters were

$$\begin{aligned} a/t &= 0.2, 0.5, \text{ and } 0.8 \\ a/c &= 0.4, 1, \text{ and } 2 \\ r/t &= 1, 2, \text{ and } 3 \end{aligned}$$

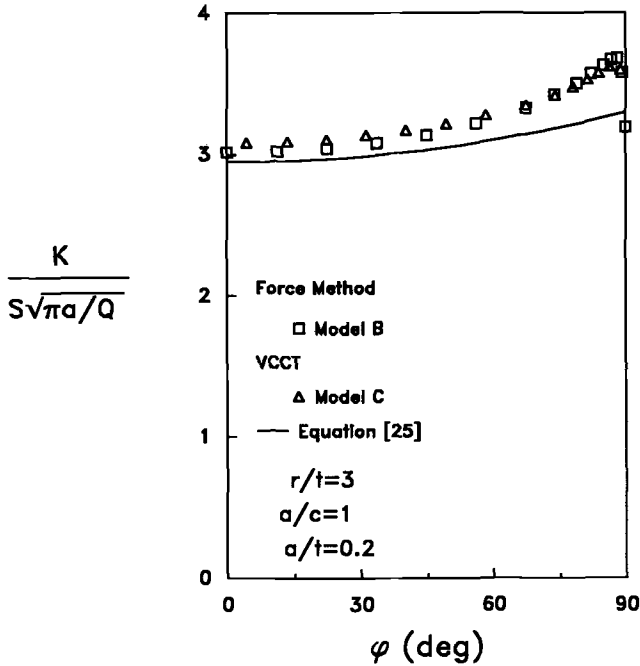


FIG. 5—Comparison of results for a surface crack emanating from the center of a semi-circular notch, using various models and methods for  $r/t = 3$ .

These particular crack configurations were chosen to cover the range of crack shapes and sizes that have been observed to grow in experiments. Note that the  $r/t = 3$  configuration corresponds to a specimen used in an AGARD study on short cracks (see Refs 21 or 25). For each combination of parameters, stress-intensity factors were obtained all along the crack front.

The normalized stress-intensity factors obtained with the three-dimensional finite-element analyses are presented in Tables 1–3. Typical results are shown and discussed herein.

The normalized stress-intensity factor variations all along the crack front for the AGARD short-crack specimen with  $r/t = 3$  are shown in Figs. 6 and 7 for various crack shapes ( $a/c = 0.4$  and 1, respectively). In these figures, the inserts show part of the crack plane with the relative size of the notch, half-thickness of the plate, and the various crack shapes and sizes considered. For both crack shapes, the maximum normalized stress-intensity factors occurred near the intersection of the crack front and the notch boundary ( $\phi = 90$  deg). This trend is expected because the crack front lies in a region that is influenced by the notch. Hence, surface cracks would be expected to grow more along the bore of the notch than away from the notch and approach an  $a/c$  ratio greater than unity. Experiments on surface cracks at notches [21,25] tend to support this observation.

Figure 8 shows the normalized stress-intensity factor variations along the crack front for a semielliptical surface crack with an  $a/c$  ratio of 2 and  $r/t = 1$ . In this case, the normalized stress-intensity factors are largest at the maximum crack length from the notch root ( $\phi = 0$  deg). For deep cracks ( $a/t = 0.8$ ), the normalized stress-intensity factors are nearly con-

TABLE 1—Boundary-correction factors,  $F_{sn}$ , for semielliptical surface crack emanating from center of a semicircular notch in a plate under tension ( $r/t = 1$ ;  $F_{sn} = K/[S(\pi a/Q)^{1/2}]$ ).

$a/c$	$\phi$ , deg	$a/t$		
		0.2	0.5	0.8
0.4 <sup>a</sup>	0.0	1.113	0.869	0.833
	22.5	1.284	0.997	0.967
	45.0	1.678	1.296	1.274
	67.5	2.190	1.733	1.774
	78.8	2.567	2.129	2.232
	84.9	2.809	2.445	2.631
	88.0	2.938	2.655	2.951
	90.0	2.727	2.548	2.944
1 <sup>a</sup>	0.0	2.402	1.865	1.697
	22.5	2.442	1.904	1.716
	45.0	2.574	2.046	1.841
	67.5	2.826	2.355	2.211
	78.8	3.043	2.646	2.599
	84.9	3.192	2.858	2.898
	88.0	3.263	2.975	3.089
	90.0	2.858	2.656	2.826

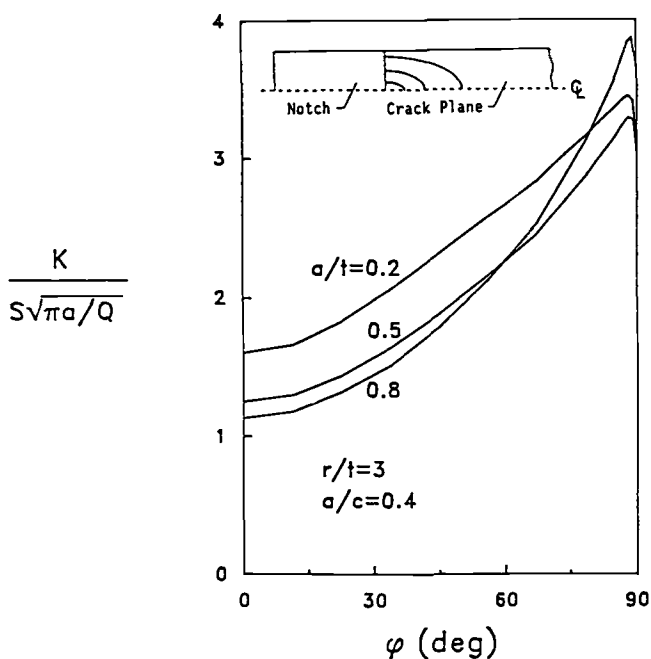
<sup>a</sup> Nodal-force method and Model B.FIG. 6—Boundary correction-factor distributions along crack front for semielliptical surface crack ( $a/c = 0.4$ ) at the center of the notch root.

TABLE 2—Boundary-correction factors,  $F_{sn}$ , for semielliptical surface crack emanating from center of a semicircular notch in a plate under tension ( $\tau/t = 2$ ;  $F_{sn} = K/[S(\pi a/Q)^{1/2}]$ ).

$a/c$	$\phi$ , deg	$a/t$		
		0.2	0.5	0.8
0.4 <sup>a</sup>	0.0	1.405	1.081	0.989
	22.5	1.613	1.245	1.156
	45.0	2.070	1.634	1.553
	67.5	2.596	2.174	2.207
	78.8	2.943	2.595	2.764
	84.9	3.151	2.880	3.182
	88.0	3.252	3.044	3.469
	90.0	2.982	2.844	3.347
1 <sup>a</sup>	0.0	2.789	2.316	2.128
	22.5	2.822	2.357	2.152
	45.0	2.929	2.497	2.303
	67.5	3.138	2.780	2.715
	78.8	3.323	3.028	3.105
	84.9	3.454	3.201	3.378
	88.0	3.509	3.285	3.533
	90.0	3.052	2.885	3.161

<sup>a</sup> Nodal-force method and Model B.TABLE 3—Boundary-correction factors,  $F_{sn}$ , for semielliptical surface crack emanating from center of a semicircular notch in a plate under tension ( $\tau/t = 3$ ;  $F_{sn} = K/[S(\pi a/Q)^{1/2}]$ ).

$a/c$	$\phi$ , deg	$a/t$		
		0.2	0.5	0.8
0.4 <sup>a</sup>	0.0	1.603	1.253	1.131
	22.5	1.831	1.442	1.325
	45.0	2.318	1.882	1.788
	67.5	2.839	2.460	2.534
	78.8	3.167	2.878	3.135
	84.9	3.361	3.145	3.559
	88.0	3.452	3.290	3.834
	90.0	3.151	3.044	3.655
1 <sup>a</sup>	0.0	3.017	2.592	2.429
	22.5	3.045	2.630	2.454
	45.0	3.138	2.761	2.610
	67.5	3.328	3.022	3.032
	78.8	3.503	3.251	3.421
	84.9	3.629	3.411	3.685
	88.0	3.679	3.482	3.829
	90.0	3.192	3.040	3.398
2.0 <sup>b</sup>	4.5	2.229	2.115	2.031
	22.5	2.154	2.057	2.004
	45.0	1.960	1.909	1.928
	67.5	1.773	1.776	1.851
	80.0	1.745	1.765	1.854
	84.0	1.762	1.788	1.884
	87.0	1.825	1.819	1.920
	89.0	1.808	1.823	1.929

<sup>a</sup> Nodal-force method and Model B.<sup>b</sup> Virtual crack-closure technique and Model C.

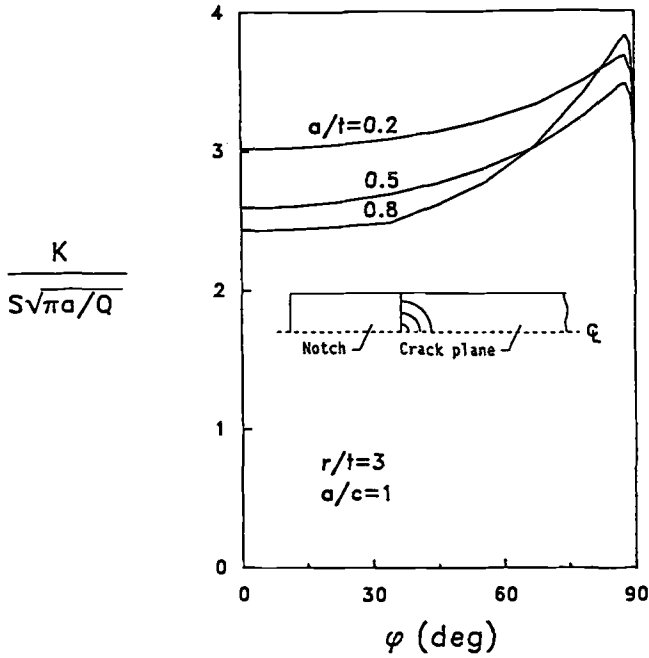


FIG. 7—Boundary-correction factor distributions along crack front for semicircular surface crack ( $a/c = 1.0$ ) at the center of the notch root.

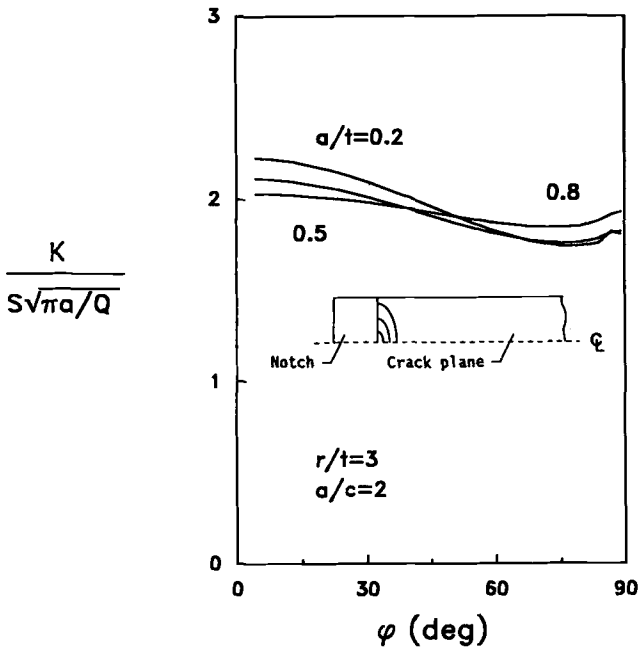


FIG. 8—Boundary-correction factor distributions along crack front for semielliptical surface crack ( $a/c = 2.0$ ) at the center of the notch root.

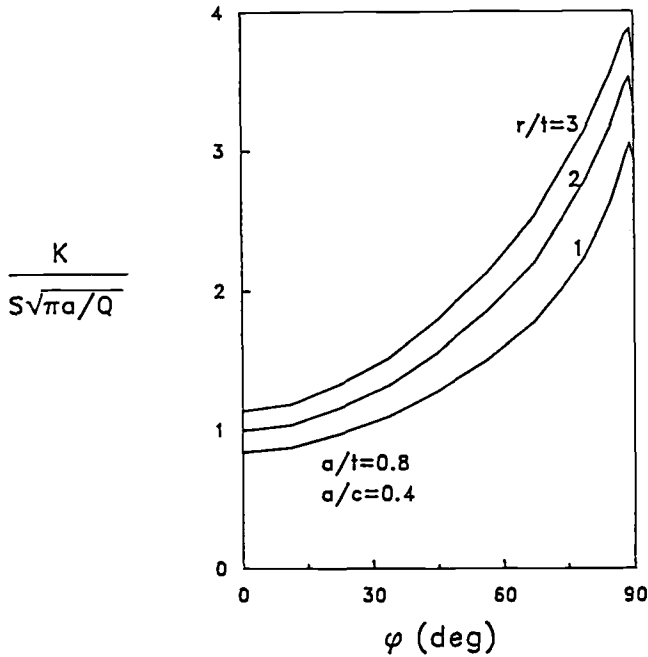


FIG. 9—Effect of  $r/t$  on the distribution of boundary-correction factors for a deep semielliptical surface crack at the center of the notch root.

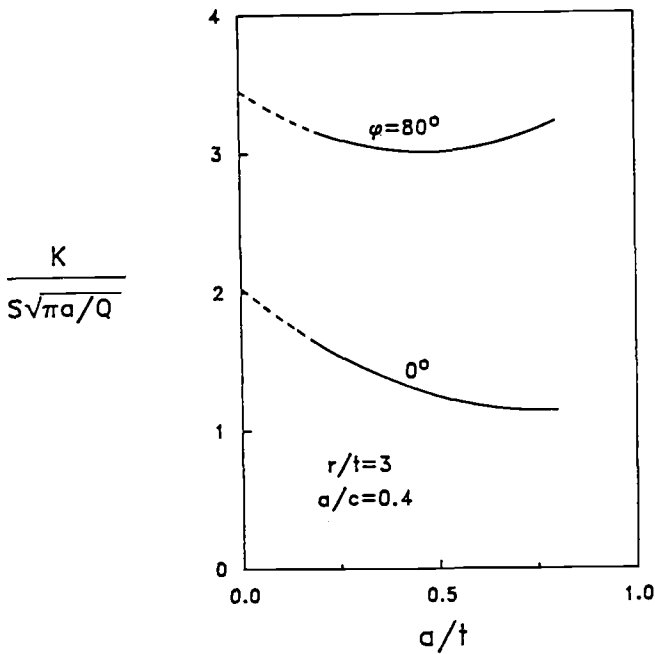


FIG. 10—Effect of crack size on boundary-correction factors at the end of the major and near the end of the minor axes ( $\psi = 0$  deg and 80 deg).

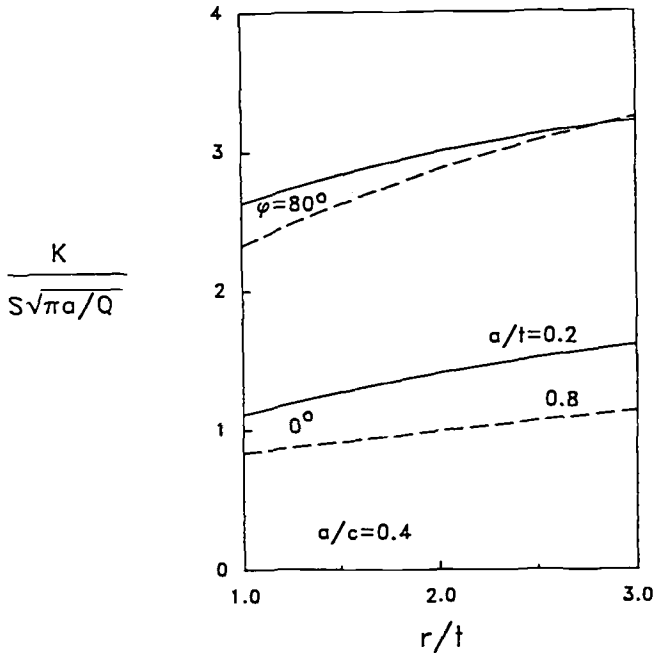


FIG. 11—Effect of notch size on boundary-correction factors for a semielliptical surface crack at the end of the major and near the end of the minor axes ( $\psi = 0$  deg and 80 deg).

stant all along the crack front. (Note that the results presented herein for  $a/c = 2$  were obtained from Model C and the VCCT [23].)

The variation of normalized stress-intensity factors all along the crack front for various  $r/t$  ratios with  $a/c = 0.4$  and  $a/t = 0.8$  is shown in Fig. 9. As expected, larger values of notch radii (higher  $r/t$  ratios) gave higher values of normalized stress-intensity factors for the same crack shape and size. This trend is expected because the crack surfaces are subjected to a higher normal stress component for the larger  $r/t$  values. Similar trends were observed for all crack shapes and sizes analyzed and, hence, the results are not shown.

Figure 10 presents the normalized stress-intensity factors at two locations along the crack front as a function of  $a/t$  for two different crack configurations. The stress-intensity factors at  $\phi = 0$  deg and near the end of the other axis ( $\phi = 80$  deg) are presented. The 80-deg location was selected to avoid the boundary-layer region. Finite-element results were obtained for  $a/t$  ratios of 0.2, 0.5, and 0.8. The limiting solutions for a surface crack at a notch as  $a/t$  approaches zero were estimated from stress-intensity factor equations for a surface crack in a plate [16] and a stress concentration factor of 3.17 [25].

The normalized stress-intensity factors at  $\phi = 0$  and 80 deg are shown in Fig. 11 as a function of notch size ( $r/t$ ) for an  $a/c$  ratio of 0.4. The results for the shallow crack ( $a/t = 0.2$ ) are shown as solid curves, whereas the results for a deep crack ( $a/t = 0.8$ ) are shown as dashed curves. These figures show that larger size notches (higher  $r/t$  ratios) tend to give higher normalized stress-intensity factor at both ends of the crack.

### Concluding Remarks

An evaluation of the finite-element models and methods used to extract stress-intensity factors from finite-element solutions for surface cracks at stress concentrations was per-



formed. Previous finite-element models used by Raju and Newman for surface and corner cracks at holes were shown to have "ill-shaped" elements at the intersection of the hole and crack boundaries. These ill-shaped elements tended to make the models too stiff and, hence, gave lower stress-intensity factors near the hole-crack intersection than models without these elements. The improved models employed eight-noded elements and stress-intensity factors were calculated by both the nodal-force and virtual crack-closure methods. Both methods and different models, without the ill-shaped elements, gave essentially the same results.

Comparisons made between the previously developed stress-intensity factor equations and the results from the improved models agreed well (within 5%) for configurations with notch-radius-to-plate-thickness ( $r/t$ ) ratios less than 2. Larger discrepancies were shown for an  $r/t$  ratio of 3. Here, the stress-intensity factor equations gave results that were 3 to 13% lower than the results from the improved models for a semielliptical surface crack at a semicircular edge notch.

Stress-intensity factors for semielliptical surface cracks emanating from the center of a semicircular edge notch in a plate subjected to remote tensile loading were obtained by three-dimensional finite-element analyses. A wide range of crack shapes, crack sizes, and notch-radius-to-plate-thickness ratios was considered. The range of crack sizes, defined by crack-depth-to-plate-thickness ( $a/t$ ), considered was 0.2 to 0.8. The range of crack shapes, defined by the ratio of crack length along the notch to the crack length away from the notch root ( $a/c$ ), considered was 0.4 to 2. The range of notch sizes, defined by the notch-radius-to-plate-thickness ( $r/t$ ), considered was 1 to 3. The configuration with  $r/t = 3$  was chosen because this is the configuration that was tested in an AGARD cooperative test program on growth of short cracks at notches.

- [1] Shah, R. C. and Kobayashi, A. S., "On the Surface Flaw Problem," *The Surface Crack: Physical Problems and Computational Solutions*, J. L. Swedlow, Ed., American Society of Mechanical Engineers, 1972, pp. 79–142.
- [2] Smith, F. W., "The Elastic Analysis of the Part-Circular Surface Flaw Problem by the Alternating Method," *The Surface Crack: Physical Problems and Computational Solutions*, J. L. Swedlow, Ed., American Society of Mechanical Engineers, 1972, pp. 125–152.
- [3] Tracey, D. M., "30 Elastic Singularity Element for Evaluation of  $K$  Along an Arbitrary Crack Front," *International Journal of Fracture*, Vol. 9, 1973, pp. 340–343.
- [4] Tracey, D. M., "Finite Element for Three-dimensional Elastic Crack Analysis," *Nuclear Engineering and Design*, Vol. 26, 1974.
- [5] Atluri, S. N. and Kathiresan, K., "An Assumed Displacement Hybrid Finite Element Model for Three-dimensional Linear Elastic Fracture Mechanics Analysis," *Proceedings*, 12th Annual Meeting of the Society of Engineering Science, University of Texas, Austin, TX, 1975.
- [6] Kathiresan, K., "Three-dimensional Linear Elastic Fracture Mechanics Analysis by a Displacement Hybrid Finite Element Model," Ph.D. thesis, Georgia Institute of Technology, Atlanta, 1976.
- [7] Kobayashi, A. S. and Enetanya, A. N., "Stress Intensity Factor of a Corner Crack," *Mechanics of Crack Growth, ASTM STP 590*, American Society for Testing and Materials, Philadelphia, 1976, pp. 477–495.
- [8] Raju, I. S. and Newman, J. C., Jr., "Improved Stress-Intensity Factors for Semi-Elliptical Surface Cracks in Finite-Thickness Plates," NASA TM X-72825, National Aeronautics and Space Administration, Washington, DC, 1977.
- [9] Smith, F. W. and Kullgren, T. E., "Theoretical and Experimental Analysis of Surface Cracks Emanating from Fastener Holes," AFFDL-TR-76-104, Air Force Flight Dynamics Laboratory, Wright-Patterson Air Force Base, OH, 1977.
- [10] Raju, I. S. and Newman, J. C., Jr., "Stress-Intensity Factors for a Wide Range of Semi-Elliptical Surface Cracks in Finite-Thickness Plates," *Engineering Fracture Mechanics*, Vol. 11, No. 4, 1979, pp. 817–829.

- [11] Heliot, J., Labbens, R. C., and Pellissier-Tanon, A., "Semi-elliptical Surface Cracks Subjected to Stress Gradients," *Fracture Mechanics, ASTM STP 677*, C. W. Smith, Ed., American Society for Testing of Materials, Philadelphia, 1979, pp. 341–364.
- [12] Raju, I. S. and Newman, J. C., Jr., "Stress-Intensity Factors for Two Symmetric Corner Cracks," *Fracture Mechanics, ASTM STP 677*, C. W. Smith, Ed., American Society of Testing and Materials, Philadelphia, 1979, pp. 411–430.
- [13] Pickard, A. C., "Stress-Intensity Factors for Cracks with Circular and Elliptic Crack Fronts—Determined by 3D Finite Element Methods," PNR-90035, Rolls-Royce Limited, May 1980.
- [14] Nishioka, T. and Atluri, S. N., "Analytical Solution for Embedded Elliptical Cracks, and Finite Element-Alternating Method for Elliptical Surface Cracks, Subjected to Arbitrary Loadings," *Engineering Fracture Mechanics*, Vol. 17, 1983, pp. 247–268.
- [15] Nishioka, T. and Atluri, S. N., "An Alternating Method for Analysis of Surface Flawed Aircraft Structural Components," *AIAA Journal*, American Institute of Aeronautics and Astronautics, Vol. 21, 1983, pp. 749–757.
- [16] Newman, J. C., Jr., and Raju, I. S., "Stress-Intensity Factor Equations for Cracks in Three-Dimensional Finite Bodies," *Fracture Mechanics: Fourteenth Symposium. Volume I: Theory and Analysis, ASTM STP 791*, J. C. Lewis and G. Sines, Eds., American Society for Testing and Materials, Philadelphia, 1983, pp. I-238–I-265.
- [17] Newman, J. C., Jr., and Raju, I. S., "Stress-Intensity Factor Equations for Cracks in Three-Dimensional Finite Bodies Subjected to Tension and Bending Loads," NASA TM-85793, National Aeronautics and Space Administration, Washington, DC, April 1984.
- [18] Atluri, S. N. and Nishioka, T., "Computational Methods for Three-dimensional Problems of Fracture," *Computational Methods in Mechanics of Fracture*, Chapter 7, S. N. Atluri, Ed., North Holland, Amsterdam, 1986, pp. 230–287.
- [19] Raju, I. S. and Newman, J. C., Jr., "Finite-Element Analysis of Corner Cracks in Rectangular Bars," NASA TM-89070, National Aeronautics and Space Administration, Washington, DC, 1987.
- [20] Raju, I. S., Atluri, S. N., and Newman, J. C., Jr., "Stress-Intensity Factors for Small Surface and Corner Cracks in Plates," presented at the 20th National Symposium on Fracture Mechanics, Lehigh University, Bethlehem, PA, 23–25 June 1987.
- [21] Newman, J. C., Jr., and Edwards, P. R., "Short-Crack Growth Behaviour in an Aluminum Alloy—An AGARD Cooperative Test Programme," AGARD Report No. 732, Advisory Group for Aerospace Research and Development, 1988.
- [22] Chermahini, R. G., Shivakumar, K. N., and Newman, J. C., Jr., "Three-Dimensional Finite-element Simulation of Fatigue-Crack Growth Closure," *Mechanics of Fatigue Crack Closure, ASTM STP 982*, J. C. Newman, Jr., and W. Elbe, Eds., American Society for Testing and Materials, Philadelphia, 1988.
- [23] Shivakumar, K. N., Tan, P. W., and Newman, J. C., Jr., "A Virtual Crack-Closure Technique For Calculating Stress-Intensity Factors For Cracked Three Dimensional Bodies," *International Journal of Fracture*, Vol. 36, 1988, pp. R43–R50.
- [24] Raju, I. S., Shivakumar, K. N., and Crews, J. H., Jr., "Three-Dimensional Elastic Analysis of a Composite Double Cantilever Beam Specimen," AIAA-87-0864, AIAA/ASME/ASCE/AHS, 27th Structures, Structural Dynamics, and Materials Conference, Monterey, CA., 6–8 April 1987.
- [25] Swain, M. H. and Newman, J. C., Jr., "On the Use of Marker Loads and Replicas for Measuring Growth Rates for Small Cracks," *Fatigue Crack Topography*, AGARD-CP-376, Advisory Group for Aerospace Research and Development, 1984, pp. 12.1–12.17.

## Tabulated Stress-Intensity Factors for Corner Cracks at Holes Under Stress Gradients

**REFERENCE:** Perez, R., Grandt, A. F., Jr., and Saff, C. R., "Tabulated Stress-Intensity Factors for Corner Cracks at Holes Under Stress Gradients," *Surface-Crack Growth: Models, Experiments, and Structures*, ASTM STP 1060, W. G. Reuter, J. H. Underwood, and J. C. Newman, Jr., Eds., American Society for Testing and Materials, Philadelphia, 1990, pp. 49–62.

**ABSTRACT:** The objective of this paper is to present stress-intensity factors,  $K$ , for corner cracks at holes in a tabulated format which can be used to calculate  $K$  for general stress fields. Stress-intensity factors were obtained with the weight function method for various stress gradients and crack sizes. The paper also describes a superposition procedure to generate  $K$  for general stress distributions by using the data presented. This tabulated information is intended to expand the existing database of reference stress-intensity factors. Results were compared with other published solutions in order to evaluate the analysis procedure. In general, the difference between solutions was within 10%.

**KEY WORDS:** stress-intensity factor, corner crack, weight function, stress gradients

The computation of stress-intensity factors ( $K$ ) for the corner crack at the hole illustrated in Fig. 1 is a difficult three-dimensional problem. The stress-intensity factor not only depends on the flaw shape and size, but also varies along the crack perimeter. In addition,  $K$  is a function of the load condition and the resulting stress distribution on the  $x$ - $y$  plane. When a plate with a hole is loaded in tension, the resulting unflawed stress field varies mainly in the direction away from the hole. In plate bending, the stress field displays significant gradients away from the hole and through the thickness. More complex stress distributions involve thermal gradients and residual stresses. This paper is intended to fulfill the need for  $K$  solutions in the case of specialized load conditions.

The weight function method was used to generate stress-intensity factors for different crack sizes under basic stress gradients. Results for the basic gradients can be combined by superposition to obtain  $K$  for more complex load situations.

### Weight Function Method

Bueckner [1] and Rice [2] have developed a technique in which information from a reference load case determines stress-intensity factors for an alternate load situation of interest. The desired  $K$  is calculated with the following weight function relation for a through the thickness crack of length  $a$

$$K = \frac{H}{K_r} \int_0^a \sigma(x) \frac{\partial u_r(x,a)}{\partial a} dx \quad (1)$$

<sup>1</sup> Lead engineer and section chief, respectively, McDonnell Aircraft Company, St. Louis, MO 63166.

<sup>2</sup> Professor and head, School of Aeronautics and Astronautics, Purdue University, West Lafayette, IN 47907.

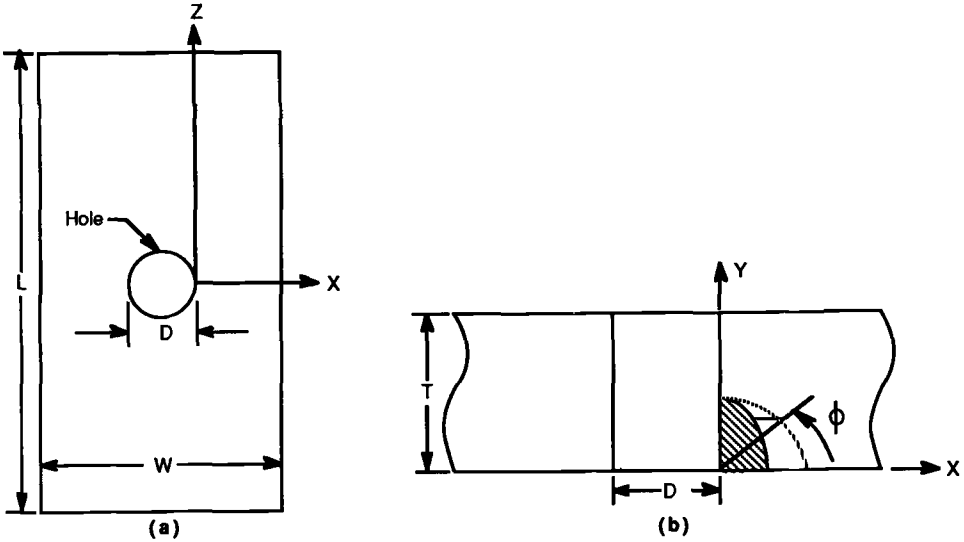


FIG. 1—Schematic representation of corner cracked hole.

where

- $K_r$  = stress-intensity factor for the reference case,
- $u_r$  = crack opening displacement for the reference case,
- $\sigma(x)$  = unflawed stress distribution acting on the crack plane for the new load situation,
- $x$  = coordinate in the direction of crack growth, and
- $H$  = elastic modulus  $E$  for plane stress;  $E/(1 - \nu^2)$  for plane strain.

For three-dimensional problems such as corner cracks, these relations need to be modified to consider changes in crack area, rather than length. Weight function relations were derived for surface flaws by Mattheck et al. [3]. Similar equations were derived for corner cracks at holes in Ref 4. The change in crack surface area due to growing an amount  $dc$  or  $da$  is illustrated in Fig. 2 for a corner flawed hole. For this geometry, the surface area increments are

$$dS_x = \frac{\pi}{4} a \, dc \quad (2)$$

$$dS_y = \frac{\pi}{4} c \, da \quad (3)$$

The effective stress-intensity factors  $\bar{K}_x$  and  $\bar{K}_y$  associated with the  $x$  and  $y$  directions are defined in Ref 3 by

$$\bar{K}_x = \frac{H}{\bar{K}_{rx}} \int \sigma(x, y) \frac{\partial u_r}{\partial S_x} dS \quad (4)$$

$$\bar{K}_y = \frac{H}{\bar{K}_{ry}} \int \sigma(x, y) \frac{\partial u_r}{\partial S_y} dS \quad (5)$$

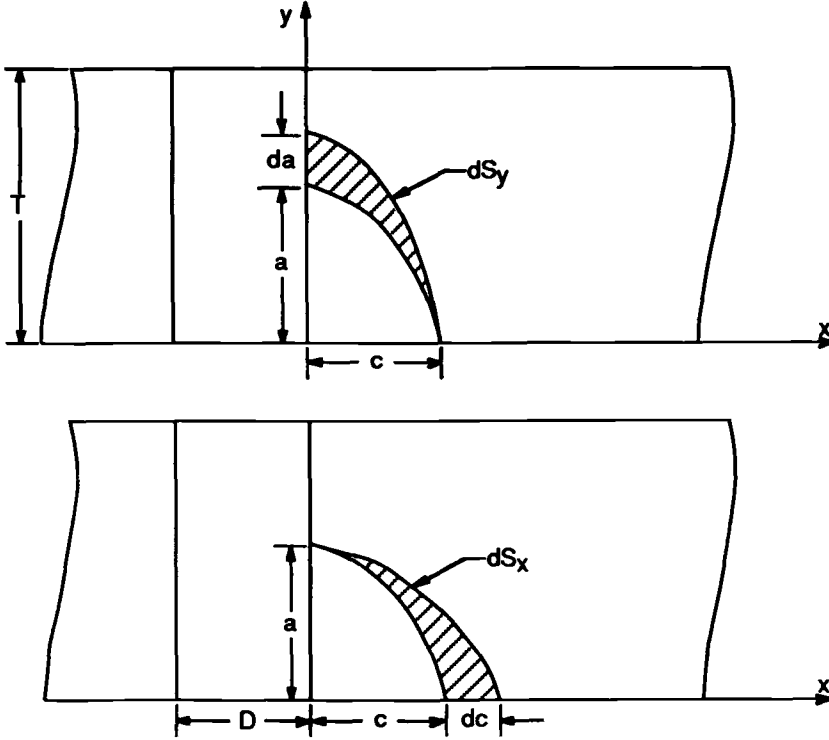


FIG. 2—Two-degree-of-freedom corner crack at a hole model.

Combining Eqs 2 to 5 give

$$\bar{K}_x = \frac{H}{\bar{K}_{rx}} \frac{4}{\pi a} \int_{y=0}^a \int_{x=0}^{x(y)} \sigma(x,y) \frac{\partial u_r}{\partial c} dx dy \quad (6)$$

$$\bar{K}_y = \frac{H}{\bar{K}_{ry}} \frac{4}{\pi c} \int_{y=0}^a \int_{x=0}^{x(y)} \sigma(x,y) \frac{\partial u_r}{\partial a} dx dy \quad (7)$$

These relations represent a two-degree-of-freedom model since stress-intensity factors are associated with two directions,  $x$  and  $y$ . Thus, the stress-intensity factor along the crack front is calculated in the region near the bore of the hole and at the free surface.

The weight functions in Eqs 6 and 7 are composed of three main parts. First, the crack opening displacement  $u_r$  for the reference load case is required. A model was formulated by Mattheck et al. [3] in which a three-dimensional surface flaw is assumed to behave as a series of compatible through-the-thickness cracks. The crack opening displacement of each through-the-thickness crack is then obtained from its known  $K$  solutions as demonstrated by Petroski and Achenbach [5]. These models were adapted to the corner crack at a hole geometry of interest here.

The second component in the weight function calculation involves defining the reference

stress-intensity factors  $\bar{K}_x$  and  $\bar{K}_y$ . Cruse and Besuner [6] formulated the root-mean-square relations

$$\bar{K}_x^2 = \frac{1}{\Delta S_x} \int_{\Delta S_x} K^2(\Phi) d[(\Delta S_x(\Phi))] \quad (8)$$

$$\bar{K}_y^2 = \frac{1}{\Delta S_y} \int_{\Delta S_y} K^2(\Phi) d[\Delta S_y(\Phi)] \quad (9)$$

The changing stress-intensity factor  $K(\Phi)$  is obtained from the Newman and Raju [7] solutions for corner cracks at holes under remote tension. In Eqs 8 and 9,  $\Delta S_x$  and  $\Delta S_y$  are numerical equivalents to  $dS_x$  and  $dS_y$  in Eqs 2 and 3, and  $\Phi$  is the parametric angle which defines the location of points along the crack front as defined in Fig. 1.

The final piece of information necessary in the weight function method is the unflawed stress distribution  $\sigma(x,y)$  acting perpendicular to the crack plane for the load situation of interest. The following section presents stress-intensity factors obtained with the weight function for various basic stress gradients. The section also describes how these results can be combined to solve for  $K$  in complex load situations.

### Stress-Intensity Factor Calculations

Stress-intensity factors were computed with the weight function for corner cracks under each of the following basic stress gradients  $\sigma(x,y)$

$$\begin{matrix} s \\ s(x/R) & s(y/T) \\ s(x/R)^2 & s(x/R)(y/T) & s(y/T)^2 \\ s(x/R)^3 & s(x/R)^2(y/T) & s(x/R)(y/T)^2 & s(y/T)^3 \end{matrix} \quad (10)$$

where

- $s$  = coefficient of each stress term,
- $R$  = hole radius, and
- $T$  = plate thickness.

Stress-intensity factors due to each term  $s(x/R)^m (y/T)^n$  are identified as

$$\begin{matrix} & & \bar{K}_{00} \\ & \bar{K}_{10} & \bar{K}_{01} \\ \bar{K}_{20} & \bar{K}_{11} & \bar{K}_{02} \\ \bar{K}_{30} & \bar{K}_{21} & \bar{K}_{12} & \bar{K}_{03} \end{matrix} \quad (11)$$

The factors  $\bar{K}_{mn}$  were nondimensionalized in the form

$$\bar{M}_{mn} = \frac{\bar{K}_{mn}}{s \sqrt{\pi a}} \quad (12)$$

where  $a$  is the crack length along the hole. Factors  $\bar{M}_{mn}$  can be used to solve for  $K$  in the case of complex stress gradients. To illustrate this, consider a general stress distribution represented by the polynomial

$$\sigma(x,y) = A_{00} + A_{10}(x/R) + A_{01}(y/T) + A_{20}(x/R)^2 + A_{11}(x/R)(y/T) + A_{02}(y/T)^2 + \dots \quad (13)$$

where  $A_{mn}$  are the polynomial coefficients for the general case. Superimposing the stress-intensity factors  $\bar{K}_{mn}^*$  due to each polynomial term  $A_{mn}(x/R)^m(y/T)^n$  results in

$$\bar{K} = \sum \bar{K}_{mn}^* \quad (14)$$

where  $m = 0, 1, 2, 3$  and  $n = 0, 1, 2, 3$ . Each term  $\bar{K}_{mn}^*$  can be determined from the tabulated factors defined by Eq 12 and the coefficients of Eq 13 as

$$\bar{K}_{mn}^* = \bar{M}_{mn} A_{mn} \sqrt{\pi a} \quad (15)$$

Substituting Eq 15 into Eq 14 gives

$$\bar{K} = \sqrt{\pi a} \sum \bar{M}_{mn} A_{mn} \quad (16)$$

Factors  $\bar{M}_{mn}$  are presented in Tables 1–3 for cracks with ratios  $a/c = 1.1, 1.5, 2.0$ , and lengths  $a/T = 0.2, 0.4, 0.6, 0.8, 1.0$ .  $\bar{M}_{mnx}$  and  $\bar{M}_{mny}$  correspond to  $\bar{K}_x$  and  $\bar{K}_y$ . Each table contains information for a different hole diameter to plate thickness ratios  $D/T$ ;  $D/T = 1.0, 1.5$ , and  $2.0$ , respectively. Factors  $\bar{M}_{mnx}$  and  $\bar{M}_{mny}$  may be used to calculate stress-intensity factors for any load case if the unflawed hoop stress is expressed as the polynomial in Eq 13. This hoop stress can be determined by finite elements or some other stress analysis technique.

With the procedure just mentioned, a list of stress-intensity factors for various crack sizes under a complex load can be generated. This list can be used to obtain  $K$  for intermediate cracks by interpolation. In Ref 4, this interpolation procedure was used to calculate  $K$  repeatedly during crack growth calculations.

### Example Problem

This example illustrates how the information in Tables 1–3 can be used to calculate stress-intensity factors for a crack under a complex load situation. Consider a corner crack with dimensions  $a/T = 0.4$  and  $a/c = 1.5$  emanating from a hole in a plate with a hole diameter to thickness ratio  $D/T = 1.0$ . The plate has a width to diameter ratio  $W/D = 5$  and is subjected to pure bending. The unflawed stress distribution caused by the bending load was determined by finite elements and is expressed as the polynomial

$$\begin{aligned} \sigma(x,y) = \sigma_{\text{nom}} [2.19 - 2.3334 (x/R) + 1.4369 (x/R)^2 \\ - 4.38 (y/T) + 4.6669 (x/R)(y/T) \\ - 2.8737 (x/R)^2(y/T)] \end{aligned} \quad (17)$$

where

- $\sigma_{\text{nom}}$  = nominal bending stress on the surface =  $M(T/2)/I$ ,
- $M$  = bending moment,
- $T/2$  = distance from the neutral axis to the surface, and
- $I$  = moment of inertia.

TABLE 1—Nondimensional stress-intensity factors  $\bar{M}_{mn} = \bar{K}_{mn}/s\sqrt{\pi a}$  for corner crack at holes ( $D/T = 1.0$ ) loaded with a crack face pressure  $s(x/R)^m(y/T)^n$ .

a/T	a/c	$\bar{M}_{00x}$	$\bar{M}_{00y}$	$\bar{M}_{10x}$	$\bar{M}_{10y}$	$\bar{M}_{01x}$
0.2	1.1	0.63169	0.71057	0.14424	0.09098	0.04952
0.4		0.66222	0.72093	0.29986	0.18235	0.10300
0.6		0.70407	0.75056	0.46971	0.28179	0.16251
0.8		0.75698	0.80140	0.65893	0.39715	0.23026
1.0		0.81952	0.87680	0.86840	0.53083	0.30798
0.2	1.5	0.61347	0.63555	0.09738	0.05960	0.04731
0.4		0.62768	0.64286	0.19976	0.11952	0.09650
0.6		0.65226	0.66469	0.30835	0.18360	0.14937
0.8		0.68552	0.70334	0.42582	0.25679	0.20762
1.0		0.72755	0.76171	0.55508	0.34455	0.27311
0.2	2.0	0.58577	0.56531	0.06745	0.03995	0.04468
0.4		0.59031	0.56984	0.13617	0.07955	0.09001
0.6		0.60394	0.58420	0.20824	0.12131	0.13754
0.8		0.62500	0.61027	0.28493	0.16774	0.18869
1.0		0.65300	0.64968	0.36738	0.22150	0.24486

a/T	a/c	$\bar{M}_{01y}$	$\bar{M}_{20x}$	$\bar{M}_{20y}$	$\bar{M}_{11x}$	$\bar{M}_{11y}$
0.2	1.1	0.08586	0.03866	0.01705	0.01027	0.01011
0.4		0.17484	0.15981	0.06788	0.04236	0.04060
0.6		0.27204	0.37202	0.15644	0.09845	0.09368
0.8		0.38350	0.68999	0.29270	0.18186	0.17423
1.0		0.51754	1.12535	0.48892	0.29567	0.28950
0.2	1.5	0.07899	0.01874	0.00818	0.00683	0.00679
0.4		0.16031	0.07698	0.03269	0.02792	0.02727
0.6		0.24797	0.17722	0.07491	0.06416	0.06259
0.8		0.34683	0.32411	0.13909	0.11707	0.11557
1.0		0.46300	0.52471	0.23243	0.18888	0.19093
0.2	2.0	0.07224	0.00963	0.00413	0.00468	0.00467
0.4		0.14608	0.03884	0.01632	0.01888	0.01862
0.6		0.22428	0.08887	0.03717	0.04311	0.04249
0.8		0.31034	0.16147	0.06829	0.07813	0.07772
1.0		0.40822	0.25880	0.11231	0.12497	0.12665

In order for  $\bar{K}_x$  to be determined, the factors  $\bar{M}_{mn}$  (found in Table 1 for  $D/T = 1$ ,  $a/T = 0.4$ , and  $a/c = 1.5$ ) and the coefficients  $A_{mn}$  (from Eq 17) are substituted into Eq 16 as

$$\begin{aligned}
 \bar{K}_x &= \sqrt{\pi a} \sum \bar{M}_{mn} A_{mn} \\
 &= \sigma_{\text{nom}} \sqrt{\pi a} [(0.62768)(2.1900) - (0.19976)(2.3334) \\
 &\quad + (0.07698)(1.4369) - (0.09650)(4.3800) \\
 &\quad + (0.02792)(4.6669) - (0.00995)(2.8737)] \\
 \bar{K}_x &= 0.6982 \sigma_{\text{nom}} \sqrt{\pi a}
 \end{aligned}$$



TABLE 1—Continued.

a/T	a/c	$\bar{M}_{02x}$	$\bar{M}_{02y}$	$\bar{M}_{30x}$	$\bar{M}_{30y}$	$\bar{M}_{21x}$
0.2	1.1	0.00542	0.01262	0.01115	0.00380	0.00254
0.4		0.02244	0.05149	0.09177	0.03011	0.02086
0.6		0.05280	0.11997	0.31851	0.10369	0.07206
0.8		0.09912	0.22451	0.78435	0.25822	0.17595
1.0		0.16466	0.37641	1.59132	0.53698	0.35384
0.2	1.5	0.00512	0.01172	0.00392	0.00133	0.00122
0.4		0.02086	0.04767	0.03222	0.01065	0.00995
0.6		0.04825	0.11049	0.11079	0.03648	0.03410
0.8		0.08902	0.20532	0.26911	0.09009	0.08239
1.0		0.14572	0.34057	0.54306	0.18795	0.16501
0.2	2.0	0.00480	0.01082	0.00150	0.00051	0.00062
0.4		0.01934	0.04386	0.01210	0.00399	0.00499
0.6		0.04423	0.10098	0.04147	0.01359	0.01703
0.8		0.08066	0.18583	0.10023	0.03322	0.04097
1.0		0.13040	0.30413	0.20020	0.06817	0.08143

a/T	a/c	$\bar{M}_{21y}$	$\bar{M}_{12x}$	$\bar{M}_{12y}$	$\bar{M}_{03x}$	$\bar{M}_{03y}$
0.2	1.1	0.00175	0.00103	0.00138	0.00069	0.00201
0.4		0.01398	0.00849	0.01113	0.00570	0.01640
0.6		0.04809	0.02943	0.03842	0.02003	0.05726
0.8		0.11874	0.07197	0.09480	0.04994	0.14251
1.0		0.34485	0.14519	0.19565	0.10328	0.29764
0.2	1.5	0.00086	0.00068	0.00093	0.00065	0.00187
0.4		0.00689	0.00555	0.00752	0.00527	0.01524
0.6		0.02358	0.01906	0.02586	0.01823	0.05298
0.8		0.05777	0.04614	0.06338	0.04471	0.13102
1.0		0.11881	0.09255	0.13002	0.09121	0.27078
0.2	2.0	0.00045	0.00046	0.00065	0.00060	0.00174
0.4		0.00353	0.00373	0.00518	0.00486	0.01409
0.6		0.01202	0.01275	0.01771	0.01665	0.04865
0.8		0.02919	0.03070	0.04305	0.04041	0.11923
1.0		0.05919	0.06113	0.08722	0.08147	0.24334

In a similar manner,  $\bar{K}_y$  is found by substituting factors  $\bar{M}_{mny}$  and the coefficients  $A_{mn}$  into Eq 16

$$\bar{K}_y = \sqrt{\pi a} \sum \bar{M}_{mny} A_{mn}$$

$$\bar{K}_y = 0.5813 \sigma_{\text{nom}} \sqrt{\pi a}$$

If stress-intensity factors for a different crack are needed, another set of factors  $\bar{M}_{mnx}$  and  $\bar{M}_{mny}$  is obtained from Table 1 for the new crack dimensions  $a/T$  and  $a/c$ . In addition, an alternate load condition will result in a different set of stress gradient coefficients  $A_{mn}$  in Eq 17.

TABLE 2—Nondimensional stress-intensity factors  $\bar{M}_{mm} = \bar{K}_{mm}/s\sqrt{\pi a}$  for corner cracks at holes ( $D/T = 1.5$ ) loaded with a crack face pressure  $s(x/R)^m(y/T)^n$ .

$a/T$	$a/c$	$\bar{M}_{00x}$	$\bar{M}_{00y}$	$\bar{M}_{10x}$	$\bar{M}_{10y}$	$\bar{M}_{01x}$
0.2	1.1	0.63958	0.73112	0.09686	0.06244	0.05007
0.4		0.66956	0.74516	0.20083	0.12526	0.10425
0.6		0.71578	0.77869	0.31576	0.19347	0.16547
0.8		0.77604	0.83505	0.44580	0.27290	0.23644
1.0		0.84686	0.91731	0.59139	0.36817	0.31804
0.2	1.5	0.62475	0.65380	0.06569	0.04088	0.04808
0.4		0.63919	0.66722	0.13451	0.08251	0.09826
0.6		0.66533	0.69361	0.20779	0.12697	0.15252
0.8		0.70238	0.73717	0.28796	0.17775	0.21305
1.0		0.74955	0.80108	0.37716	0.23865	0.28188
0.2	2.0	0.59793	0.58013	0.04560	0.02733	0.04551
0.4		0.60452	0.59164	0.09211	0.05496	0.09208
0.6		0.61927	0.61141	0.14087	0.08425	0.14107
0.8		0.64235	0.64253	0.19306	0.11682	0.19414
1.0		0.67334	0.68706	0.24965	0.15449	0.25288

$a/T$	$a/c$	$\bar{M}_{01y}$	$\bar{M}_{20x}$	$\bar{M}_{20y}$	$\bar{M}_{11x}$	$\bar{M}_{11y}$
0.2	1.1	0.08780	0.01728	0.00781	0.00689	0.00690
0.4		0.17929	0.07121	0.03103	0.02840	0.02770
0.6		0.27972	0.16619	0.07129	0.06628	0.06382
0.8		0.39613	0.30977	0.13317	0.12324	0.11883
1.0		0.53743	0.50797	0.22249	0.20174	0.19801
0.2	1.5	0.08081	0.00841	0.00374	0.00460	0.00463
0.4		0.16503	0.03446	0.01503	0.01879	0.01869
0.6		0.25621	0.07933	0.03442	0.04328	0.04291
0.8		0.35973	0.14548	0.06382	0.07928	0.07928
1.0		0.48218	0.23643	0.10652	0.12857	0.13116
0.2	2.0	0.07378	0.00433	0.00188	0.00316	0.00318
0.4		0.15047	0.01745	0.00751	0.01276	0.01277
0.6		0.23233	0.03991	0.01717	0.02916	0.02924
0.8		0.32295	0.07259	0.03156	0.05299	0.05358
1.0		0.42660	0.11661	0.05188	0.08505	0.08744

### Evaluation

Stress-intensity factors obtained by using the tables were compared with calculations based on solutions by Newman and Raju [7] and the slice synthesis technique developed by Saff and Sanger [8]. Figure 3 illustrates one set of comparisons involving plates in bending with the stress distribution represented by Eq 17. The nondimensional stress-intensity factors  $\bar{K}_x/\sigma_{nom}\sqrt{\pi a}$  and  $\bar{K}_y/\sigma_{nom}\sqrt{\pi a}$  are graphed versus crack length  $a/T$  for an  $a/c$  ratio of 1.5 and  $D/T = 1$ . Although all three solutions display similar trends, there are differences between results based on the weight function and the other solutions.

TABLE 2—Continued.

$a/T$	$a/c$	$\bar{M}_{02x}$	$\bar{M}_{02y}$	$\bar{M}_{30x}$	$\bar{M}_{30y}$	$\bar{M}_{21x}$
0.2	1.1	0.00547	0.01287	0.00332	0.00116	0.00113
0.4		0.02273	0.05261	0.02724	0.00917	0.00930
0.6		0.05383	0.12289	0.09469	0.03141	0.03223
0.8		0.10191	0.23104	0.23412	0.07796	0.07911
1.0		0.17069	0.38963	0.47716	0.16195	0.16000
0.2	1.5	0.00520	0.01196	0.00117	0.00041	0.00054
0.4		0.02124	0.04889	0.00960	0.00326	0.00445
0.6		0.04931	0.11370	0.03300	0.01115	0.01528
0.8		0.09146	0.21204	0.08032	0.02745	0.03703
1.0		0.15060	0.35325	0.16261	0.05712	0.07447
0.2	2.0	0.00488	0.01103	0.00045	0.00015	0.00028
0.4		0.01977	0.04502	0.00362	0.00122	0.00224
0.6		0.04538	0.10415	0.01239	0.00418	0.00765
0.8		0.08306	0.19247	0.02996	0.01020	0.01843
1.0		0.13484	0.31631	0.05995	0.02090	0.03674

$a/T$	$a/c$	$\bar{M}_{21y}$	$\bar{M}_{12x}$	$\bar{M}_{12y}$	$\bar{M}_{03x}$	$\bar{M}_{03y}$
0.2	1.1	0.00080	0.00069	0.00094	0.00070	0.00204
0.4		0.00635	0.00570	0.00757	0.00578	0.01672
0.6		0.02176	0.01984	0.02609	0.02044	0.05853
0.8		0.05367	0.04884	0.06447	0.05140	0.14637
1.0		0.11078	0.09921	0.13348	0.10717	0.30757
0.2	1.5	0.00039	0.00046	0.00064	0.00066	0.00191
0.4		0.00315	0.00374	0.00514	0.00536	0.01560
0.6		0.01075	0.01287	0.01767	0.01864	0.05440
0.8		0.02629	0.03129	0.04333	0.04598	0.13500
1.0		0.05404	0.06309	0.08903	0.09437	0.28026
0.2	2.0	0.00020	0.00031	0.00044	0.00061	0.00177
0.4		0.00161	0.00252	0.00354	0.00496	0.01443
0.6		0.00550	0.00863	0.01214	0.01708	0.05006
0.8		0.01336	0.02084	0.02956	0.04163	0.12318
1.0		0.02709	0.04165	0.05998	0.08432	0.25245

All of the solutions used to generate the curves in Fig. 3 involve approximations which are a primary cause of the difference in results. The components in the weight function which include approximations are the crack-opening displacement model and the unflawed stress distribution of the load case being analyzed. In general, the difference between the weight function solution and the references was within 20%. There is a larger percentage difference in Fig. 3b for  $a/T$  greater than 0.7, but this is attributed to the lower values of  $\bar{K}_y$  for these larger cracks.

The data presented on the tables were also compared with results obtained by Grandt and Kullgren [9] using the finite-element alternating method. They determined  $K$ 's for

TABLE 3—Nondimensional stress-intensity factors  $\bar{M}_{mm} = \bar{K}_{mm}/s\sqrt{\pi a}$  for corner cracks at holes ( $D/T = 2.0$ ) loaded with a crack face pressure  $s(x/R)^m(y/T)^n$ .

a/T	a/c	$\bar{M}_{00x}$	$\bar{M}_{00y}$	$\bar{M}_{10x}$	$\bar{M}_{10y}$	$\bar{M}_{01x}$
0.2	1.1	0.64902	0.74954	0.07338	0.04797	0.05073
0.4		0.68027	0.77018	0.15204	0.09683	0.10589
0.6		0.72943	0.80972	0.23943	0.15006	0.16871
0.8		0.79507	0.87334	0.33935	0.21233	0.24246
1.0		0.87326	0.96481	0.45250	0.28754	0.32917
0.2	1.5	0.63571	0.66960	0.04987	0.03136	0.04884
0.4		0.65261	0.69042	0.10223	0.06386	0.10022
0.6		0.68098	0.72339	0.15810	0.09884	0.15610
0.8		0.72133	0.77397	0.21960	0.13896	0.21892
1.0		0.77309	0.84599	0.28862	0.18726	0.29102
0.2	2.0	0.60885	0.59300	0.03464	0.02092	0.04626
0.4		0.61885	0.61149	0.07017	0.04249	0.09413
0.6		0.63612	0.63784	0.10750	0.06563	0.14481
0.8		0.66187	0.67574	0.14760	0.09155	0.20004
1.0		0.69613	0.72763	0.19134	0.12166	0.26159

a/T	a/c	$\bar{M}_{01y}$	$\bar{M}_{20x}$	$\bar{M}_{20y}$	$\bar{M}_{11x}$	$\bar{M}_{11y}$
0.2	1.1	0.08962	0.00981	0.00450	0.00521	0.00528
0.4		0.18411	0.04033	0.01797	0.02149	0.02128
0.6		0.28856	0.09421	0.04132	0.05028	0.04915
0.8		0.41064	0.17611	0.07733	0.09390	0.09173
1.0		0.56014	0.28999	0.12948	0.15454	0.15336
0.2	1.5	0.08245	0.00478	0.00215	0.00348	0.00354
0.4		0.16969	0.01958	0.00871	0.01427	0.01438
0.6		0.26500	0.04510	0.02004	0.03292	0.03315
0.8		0.37405	0.08284	0.03726	0.06049	0.06144
1.0		0.50398	0.13499	0.06232	0.09848	0.10196
0.2	2.0	0.07517	0.00246	0.00108	0.00239	0.00242
0.4		0.15459	0.00994	0.00435	0.00970	0.00982
0.6		0.24036	0.02275	0.01001	0.02224	0.02260
0.8		0.33619	0.04142	0.01848	0.04050	0.04160
1.0		0.44666	0.06667	0.03048	0.06521	0.06815

$$\begin{aligned}\sigma(x) &= s \\ \sigma(x) &= s(x/R) \\ \sigma(x) &= s(x/R)^2 \\ \sigma(x) &= s(x/R)^3\end{aligned}$$

Figure 4 presents a comparison in the case of  $\sigma(x) = s(x/R)$ . Stress-intensity factors were nondimensionalized on this figure as  $\bar{K}_x/s\sqrt{D}$  and  $\bar{K}_y/s\sqrt{D}$  where  $D$  is the hole diameter. The difference between the weight-function solution and Ref 9 was within 5%. Similar agreement was observed for other gradients  $\sigma(x) = s(x/R)^m$ .

TABLE 3—Continued.

$a/T$	$a/c$	$\bar{M}_{02x}$	$\bar{M}_{02y}$	$\bar{M}_{30x}$	$\bar{M}_{30y}$	$\bar{M}_{21x}$
0.2	1.1	0.00554	0.01310	0.00141	0.00050	0.00064
0.4		0.02309	0.05386	0.01156	0.00398	0.00527
0.6		0.05491	0.12632	0.04019	0.01363	0.01828
0.8		0.10458	0.23856	0.09959	0.03384	0.04501
1.0		0.17638	0.40442	0.20366	0.07037	0.09144
0.2	1.5	0.00527	0.01218	0.00050	0.00018	0.00031
0.4		0.02165	0.05013	0.00408	0.00142	0.00253
0.6		0.05047	0.11716	0.01404	0.00486	0.00868
0.8		0.09402	0.21955	0.03422	0.01199	0.02109
1.0		0.15559	0.36755	0.06942	0.02496	0.04255
0.2	2.0	0.00495	0.01122	0.00019	0.00007	0.00016
0.4		0.02019	0.04613	0.00154	0.00053	0.00127
0.6		0.04656	0.10736	0.00528	0.00182	0.00435
0.8		0.08559	0.19949	0.01279	0.00447	0.01052
1.0		0.13954	0.32959	0.02562	0.00918	0.02101

$a/T$	$a/c$	$\bar{M}_{21y}$	$\bar{M}_{12x}$	$\bar{M}_{12y}$	$\bar{M}_{03x}$	$\bar{M}_{03y}$
0.2	1.1	0.00046	0.00052	0.00072	0.00070	0.00208
0.4		0.00366	0.00431	0.00580	0.00587	0.01709
0.6		0.01254	0.01505	0.02003	0.02086	0.06004
0.8		0.03093	0.03724	0.04959	0.05278	0.15080
1.0		0.06397	0.07608	0.10300	0.11082	0.31851
0.2	1.5	0.00022	0.00035	0.00049	0.00066	0.00194
0.4		0.00181	0.00283	0.00394	0.00546	0.01597
0.6		0.00622	0.00979	0.01360	0.01908	0.05594
0.8		0.01523	0.02388	0.03345	0.04729	0.13945
1.0		0.03135	0.04836	0.06894	0.09756	0.29088
0.2	2.0	0.00012	0.00024	0.00033	0.00062	0.00179
0.4		0.00093	0.00191	0.00271	0.00507	0.01476
0.6		0.00318	0.00657	0.00935	0.01752	0.05150
0.8		0.00776	0.01593	0.02286	0.04290	0.12737
1.0		0.01577	0.03195	0.04655	0.08729	0.26235

An experimental evaluation of the weight function method is documented in Ref. 4. Stress-intensity factors generated with the weight function were used successfully to predict corner crack growth at holes. The comparisons described in Ref. 4 involved plates under cyclic bending loads.

## Conclusion

Tabulated stress-intensity factors for corner cracks at holes were generated with the weight function method. The crack sizes analyzed were  $a/T = 0.2, 0.4, 0.6, 0.8$ , and  $1.0$

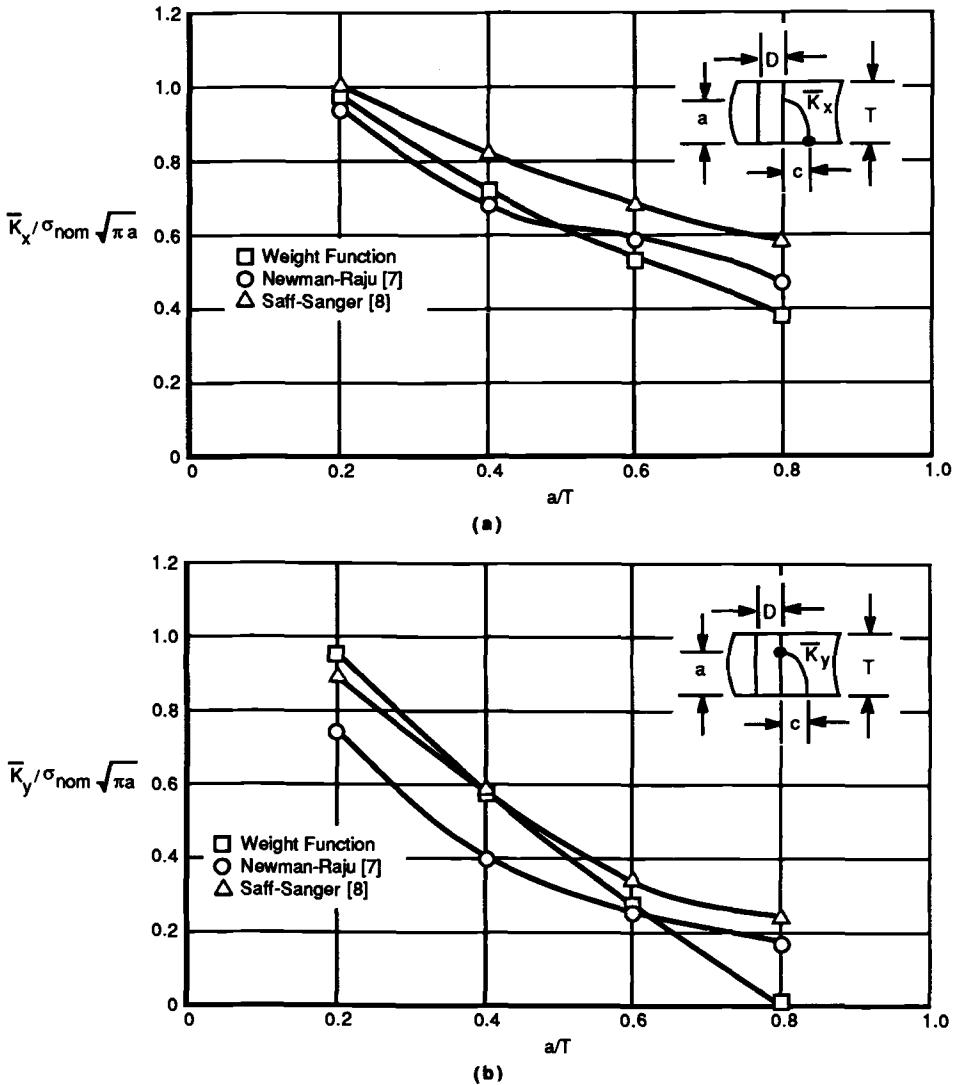


FIG. 3—Comparison of corner crack stress-intensity factors for a plate in bending ( $a/c = 1.5$ ).

with shape ratios  $a/c = 1.1, 1.5$ , and  $2.0$ . Hole diameter to plate thickness ratios  $D/T$  were  $1, 1.5$ , and  $2$ . Solutions were obtained for basic stress gradients of the form

$$\sigma(x, y) = s(x/R)^m (y/T)^n$$

A method of superposition can be used for combining the tabulated data in order to analyze problems with more complex stress fields. There is favorable agreement between the results presented here and other published solutions. The tabulated results are intended to increase the available solutions for corner cracks at holes under complex load conditions.

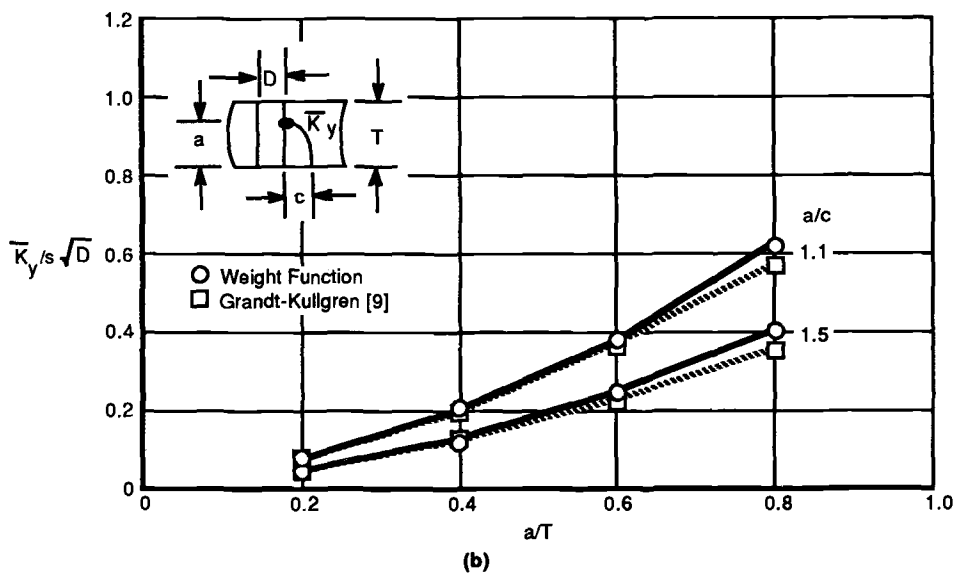
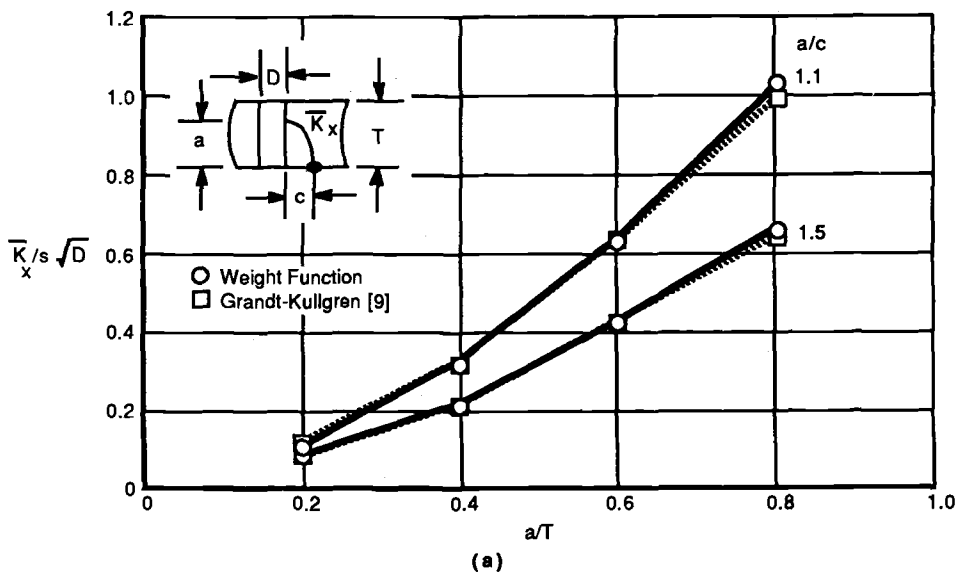


FIG. 4—Nondimensional stress-intensity factors due to a crack face pressure  $\sigma(x) = s(x/R)$  computed for various corner crack sizes.

#### Acknowledgments

Portions of this research were sponsored by the U.S. Air Force Office of Scientific Research, Air Force Systems Command under Grant No. AFOSR-85-0106. The authors wish to thank Professor B. M. Hillberry of Purdue University for providing the finite-element software.

## References

- [1] Bueckner, H. F., "A Novel Principle for the Computation of Stress-Intensity Factors," *Zeitschrift für Angewandte Mathematik und Mechanik*, Vol. 50, 1970, pp. 529-546.
- [2] Rice, J. R., "Some Remarks on Elastic Crack-Tip Stress Fields," *International Journal of Solids Structures*, Vol. 8, 1972, pp. 751-758.
- [3] Mattheck, C., Morawietz, P., and Munz, D., "Stress-Intensity Factors at the Surface and at the Deepest Point of a Semi-Elliptic Surface Crack in Plates Under Stress Gradients," *International Journal of Fracture*, Vol. 23, 1983, pp. 201-212.
- [4] Perez, R., Ray, S. K., and Grandt, A. F., Jr., "Application of a Weight Function Method to Predict the Fatigue Life of Corner Cracked Holes Loaded in Bending," *Engineering Fracture Mechanics*, Vol. 28, No. 3, 1987, pp. 283-291.
- [5] Petroski, H. J. and Achenbach, J. D., "Computation of the Weight Function from a Stress-Intensity Factor," *Engineering Fracture Mechanics*, Vol. 10, 1978, pp. 257-266.
- [6] Cruse, T. A. and Besuner, P. M., "Residual Life Prediction for Surface Cracks in Complex Structural Details," *Journal of Aircraft*, Vol. 12, No. 4, 1975.
- [7] Newman, J. C., Jr., and Raju, I. S., "Stress-Intensity Factor Equations for Cracks in Three Dimensional Finite Bodies Subjected to Tension and Bending," NASA Technical Memorandum 85793, National Aeronautics and Space Administration, Washington, DC, April 1984.
- [8] Saff, C. R. and Sanger, K. B., "Part-Through Flaw Stress-Intensity Factors Developed by a Slice Synthesis Technique," *Fracture Mechanics: Fifteenth Symposium, ASTM STP 833*, R. J. Sanford, Ed., American Society for Testing and Materials, Philadelphia, 1984, pp. 23-43.
- [9] Grandt, A. F., Jr., and Kullgren, T. E., "Tabulated Stress-Intensity Factor Solutions for Flawed Fastener Holes," *Engineering Fracture Mechanics*, Vol. 18, No. 2, 1983, pp. 435-451.



# Fracture Analysis for Three-Dimensional Bodies with Surface Crack

---

**REFERENCE:** Li Yingzhi, "Fracture Analysis for Three-Dimensional Bodies with Surface Crack," *Surface-Crack Growth: Models, Experiments, and Structures*, ASTM STP 1060, W. G. Reuter, J. H. Underwood, and J. C. Newman, Jr., Eds., American Society for Testing and Materials, Philadelphia, 1990, pp. 63–76.

**ABSTRACT:** This paper deals with fracture analyses in three-dimensional bodies containing a surface crack. A general solution of stress-strain fields at the crack tip is proposed. Based on the stress-strain fields obtained, a high-order, three-dimensional special element is established to calculate the stress-intensity factors in a plate with surface crack. The variation of stress-intensity factors with geometric parameters is investigated.

**KEY WORDS:** three-dimensional, surface crack, fracture, local-global analysis, eigenfunction expansion, stress-strain field

Since Irwin first proposed an approximate solution of surface crack problems in 1962 [1], various methods have been proposed to improve Irwin's solution. Many researchers have used the alternating method [2–9], Rice and Levy proposed the line spring model concept [10], Marcal used the three-dimensional finite-element method [11], and Nisitani and other researchers have developed the body-force method [12,13]. Many research results before 1972 have been collected in Ref 14.

In 1979, Newman and Raju collected the results of 13 investigators' research work and published their results of three-dimensional finite-element analysis by using nearly 7000 degrees of freedom [15,18]. Their formulas have been adopted by the American Society for Testing and Materials (ASTM) [19]. Meanwhile, many Chinese investigators studied this subject and also achieved significant gains [20,21]. Folias, Benthem et al. [22–24] have obtained significant results by studying the singularity at the vertex of surface crack.

To sum up, in the past 20 years, many investigators have made great progress in this area. In spite of the progress noted above, there are still many aspects which should be improved. As far as I know, the research on stress-strain fields along the crack tip is insufficient. Only the first term of stress-strain fields was found; the whole fields are elusive. Therefore, it is important to seek the stress-strain fields along the crack tip: it can provide a foundation for numerical analyses.

In this paper, the so-called "local-global analysis" is used to deal with three-dimensional body fracture analyses. The strategy can be expressed as follows:

1. Introduce a special coordinate transformation with parameters  $r, \theta, \phi$ . In this way, the semi-ellipse boundary condition can be simplified as  $\theta = \pm \pi$ .

<sup>1</sup> Academic visitor, Department of Engineering Science, Oxford University, Oxford, OX1 3PJ, U.K. On leave from Institute of Mechanics, Chinese Academy of Sciences, Beijing, China.

2. Establish the governing equations in curvilinear coordinates. Use the eigenexpansion method to find a set of eigenfunctions which satisfy the crack boundary condition.
3. Based on the stress strain fields at crack tip, a high-order three-dimensional special element is established to determine the unknown coefficients of expansion.

### Governing Equations in Curvilinear Coordinates

#### Coordinate Transformation

Consider a half space containing a semi-elliptical crack, with its normal in the  $y$ -direction. It has semi-axes  $a$  and  $b$  in the  $x, z$  direction respectively (Fig. 1). Introduce a special transformation with parameters  $r, \theta, \phi$ , the crack boundary condition can be specified as  $\theta = \pm\pi$ .

The new coordinate system can be established in the following way: Let axis  $y'$  parallel to axis  $y$ , and the new origin  $o'$  moves along the crack front. Axes  $o'x'$  and  $o'z'$  are the normal and tangent of the ellipse, respectively. Denote  $\phi$  as the angle between axes  $o'x'$  and  $ox$  and introduce a polar coordinate  $r, \theta$  in plane  $x'o'y'$ . The relation between new and old coordinate systems can be expressed in the form

$$\begin{aligned} x &= \frac{a \cos \phi}{(1 - e^2 \sin^2 \phi)^{1/2}} + r \cos \theta \cos \phi \\ y &= r \sin \theta \\ z &= \frac{b^2 \sin \phi}{a(1 - e^2 \sin^2 \phi)^{1/2}} + r \cos \theta \sin \phi \end{aligned} \quad (1)$$

where  $e^2 = (a^2 - b^2)/a^2$  and  $e$  denotes the centrifugal ratio of ellipse.

From Eq 1 the gage coefficients and Christoffel coefficients can be calculated. Hence, the three-dimensional equations in curvilinear coordinate are established.

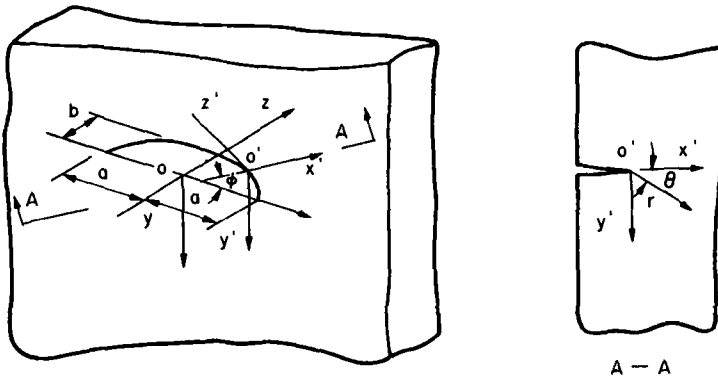


FIG. 1—Coordinate transformation.

### Governing Equation in Curvilinear Coordinates

The equilibrium equations in curvilinear coordinates are

$$\begin{aligned}
 \frac{\partial \sigma_r}{\partial r} + \frac{\partial \sigma_{r\theta}}{r \partial \theta} + \frac{\sigma_r - \sigma_\theta}{r} + \frac{1}{\Phi} \left[ \frac{\partial \sigma_{r\phi}}{\partial \phi} + (\sigma_r - \sigma_\phi) \cos \theta - \sigma_{r\theta} \sin \theta \right] &= 0 \\
 \frac{\partial \sigma_{r\theta}}{\partial r} + \frac{\partial \sigma_\theta}{r \partial \theta} + \frac{2\sigma_{r\theta}}{r} + \frac{1}{\Phi} \left[ \frac{\partial \sigma_{\theta\phi}}{\partial \phi} + \sigma_{r\theta} \cos \theta + (\sigma_\phi - \sigma_\theta) \sin \theta \right] &= 0 \\
 \frac{\partial \sigma_{r\phi}}{\partial r} + \frac{\partial \sigma_{\theta\phi}}{r \partial \theta} + \frac{\sigma_{r\phi}}{r} + \frac{1}{\Phi} \left[ \frac{\partial \sigma_\phi}{\partial \phi} + 2(\sigma_{r\theta} \cos \theta - \sigma_{\theta\phi} \sin \theta) \right] &= 0
 \end{aligned} \tag{2}$$

where

$$\Phi = \frac{b^2}{a(1 - e^2 \sin^2 \phi)^{3/2}} + r \cos \theta$$

denotes the Lamé coefficient in the  $\phi$ -direction.

The geometric equations are obtained in the form

$$\begin{aligned}
 \epsilon_r &= \frac{\partial u_r}{\partial r} \\
 \epsilon_\theta &= \frac{\partial u_\theta}{r \partial \theta} + \frac{u_r}{r} \\
 \epsilon_\phi &= \frac{1}{\Phi} \left( \frac{\partial u_\phi}{\partial \phi} + u_r \cos \theta - u_\theta \sin \theta \right) \\
 \epsilon_{r\theta} &= \frac{\partial u_r}{r \partial \theta} + \frac{\partial u_\theta}{\partial r} - \frac{u_\theta}{r} \\
 \epsilon_{r\phi} &= \frac{\partial u_r}{\Phi \partial \phi} + \frac{\partial u_\phi}{\partial r} - \frac{u_\phi}{\Phi} \cos \theta \\
 \epsilon_{\theta\phi} &= \frac{\partial u_\theta}{\Phi \partial \phi} + \frac{\partial u_\phi}{r \partial \theta} + \frac{u_\phi}{\Phi} \sin \theta
 \end{aligned} \tag{3}$$

The Hooke's law can be written as

$$\begin{aligned}
 E\epsilon_r &= (1 + \nu)\sigma_r - \nu\Theta \\
 E\epsilon_\theta &= (1 + \nu)\sigma_\theta - \nu\Theta \\
 E\epsilon_\phi &= (1 + \nu)\sigma_\phi - \nu\Theta
 \end{aligned} \tag{4}$$

$$G\varepsilon_{r\theta} = \sigma_{r\theta}$$

$$G\varepsilon_{r\phi} = \sigma_{r\phi}$$

$$G\varepsilon_{\theta\phi} = \sigma_{\theta\phi}$$

By substituting Eqs 3 and 4 into Eq 2, we can establish the governing equations

$$\begin{aligned} 2(1-\nu) \left( \frac{\partial^2 u_r}{\partial r^2} + \frac{\partial u_r}{r \partial r} - \frac{u_r}{r^2} \right) + (1-2\nu) \frac{\partial^2 u_r}{r^2 \partial \theta^2} + \frac{\partial^2 u_\theta}{r \partial r \partial \theta} - (3-4\nu) \frac{\partial u_\theta}{r^2 \partial \theta} \\ + \frac{1}{\Phi} \left[ \frac{\partial^2 u_\phi}{\partial r \partial \phi} + 2(1-\nu) \frac{\partial u_r}{\partial r} \cos \theta - \frac{\partial u_\theta}{\partial r} \sin \theta - (1-2\nu) \left( \frac{\partial u_r}{r \partial \theta} - \frac{u_\theta}{r} \right) \sin \theta \right] \\ + \frac{1}{\Phi^2} \left[ - (3-4\nu) \frac{\partial u_\phi}{\partial \phi} \cos \theta - 2(1-\nu)(u_r \cos \theta - u_\theta \sin \theta) \cos \theta + (1-2\nu) \frac{\partial^2 u_r}{\partial \phi^2} \right] \\ - \frac{1}{\Phi^3} \frac{3(1-2\nu)b^2 e^2 \sin \phi \cos \phi}{a(1-e^2 \sin^2 \phi)^{5/2}} \left( \frac{\partial u_r}{\partial \phi} - u_\phi \cos \theta \right) = 0 \end{aligned} \quad (5a)$$

$$\begin{aligned} \frac{\partial^2 u_r}{r \partial r \partial \theta} + (3-4\nu) \frac{\partial u_r}{r^2 \partial \theta} + (1-2\nu) \left( \frac{\partial^2 u_\theta}{\partial r^2} + \frac{\partial u_\theta}{r \partial r} - \frac{u_\theta}{r^2} \right) + 2(1-\nu) \frac{\partial^2 u_\theta}{r^2 \partial \theta^2} \\ + \frac{1}{\Phi} \left[ \frac{\partial^2 u_\phi}{r \partial \theta \partial \phi} + \frac{\partial u_r}{r \partial \theta} \cos \theta - 2(1-\nu) \left( \frac{\partial u_\theta}{r \partial \theta} + \frac{u_r}{r} \right) \sin \theta - \frac{u_\theta}{r} \cos \theta + (1-2\nu) \frac{\partial u_\theta}{\partial r} \cos \theta \right] \\ + \frac{1}{\Phi^2} \left[ (1-2\nu) \frac{\partial^2 u_\theta}{\partial \phi^2} + (3-4\nu) \frac{\partial u_\phi}{\partial \phi} \sin \theta + 2(1-\nu)(u_r \cos \theta - u_\theta \sin \theta) \sin \theta \right] \\ - \frac{1}{\Phi^3} \frac{3(1-2\nu)b^2 e^2 \sin \phi \cos \phi}{a(1-e^2 \sin^2 \phi)^{5/2}} \left( \frac{\partial u_\theta}{\partial \phi} + u_\phi \sin \theta \right) = 0 \end{aligned} \quad (5b)$$

$$\begin{aligned} \frac{\partial^2 u_\phi}{\partial r^2} + \frac{\partial u_\phi}{r \partial r} + \frac{\partial u_\phi}{r^2 \partial \theta^2} + \frac{1}{\Phi} \left[ \frac{1}{(1-2\nu)} \left( \frac{\partial^2 u_r}{\partial r \partial \phi} + \frac{\partial^2 u_\theta}{r \partial \theta \partial \phi} + \frac{\partial u_r}{r \partial \phi} \right) + \frac{\partial u_\phi}{\partial r} \cos \theta - \frac{\partial u_\phi}{r \partial \theta} \sin \theta \right] \\ + \frac{1}{\Phi^2} \left[ \frac{2(1-\nu)}{1-2\nu} \frac{\partial^2 u_\phi}{\partial \phi^2} + \frac{3-4\nu}{1-2\nu} \frac{\partial u_r}{\partial \phi} \cos \theta - \frac{3-4\nu}{1-2\nu} \frac{\partial u_\theta}{\partial \phi} \sin \theta - u_\phi \right] \\ - \frac{1}{\Phi^3} \frac{6(1-\nu)e^2 b^2 \sin \phi \cos \phi}{a(1-2\nu)(1-e^2 \sin^2 \phi)^{5/2}} \left( \frac{\partial u_\phi}{\partial \phi} + u_r \cos \theta - u_\theta \sin \theta \right) = 0 \end{aligned} \quad (5c)$$

The boundary condition at the crack edge are

$$\sigma_\theta = 0, \quad \sigma_{r\theta} = 0, \quad \sigma_{\theta\phi} = 0 \quad (6)$$

### The Eigenfunction Expansion

The governing Eqs 5a to 5c are partial-differential equations with variable coefficients which are very difficult to solve directly. Since only the stress-strain fields at crack tip are of interest, the asymptotic technique can be usefully introduced. That is, when  $r \rightarrow 0$ ,  $1/\Phi$  can be expanded in the form

$$\frac{1}{\Phi} = \frac{1}{\frac{b^2}{a(1 - e^2 \sin^2 \phi)^{3/2}} + r \cos \theta} = \frac{a}{b^2} (1 - e^2 \sin^2 \phi)^{3/2} \left[ 1 - r \cos \theta \frac{a}{b^2} (1 - e^2 \sin^2 \phi)^{3/2} + \dots \right] \quad (7)$$

Define the dimensionless parameters to be

$$\rho = \frac{r}{b^2}, \quad v_r = \frac{u_r}{b^2}, \quad v_\theta = \frac{u_\theta}{b^2}, \quad v_\phi = \frac{u_\phi}{b^2}$$

and introduce a new sign  $\Psi = (1 - e^2 \sin^2 \phi)^{3/2}$ , the governing equations can be expanded and handled readily.

### *Eigenfunction Expansion*

First, we expand dimensionless displacements  $v_r, v_\theta, v_\phi$  in double eigenexpansion series

$$\begin{aligned} v_r &= \sum_{\lambda} \sum_n \rho^{\lambda+n} a_n(\theta, \phi; \lambda) = \sum_{\lambda} \rho^{\lambda} [a_0(\theta, \phi; \lambda) + \rho a_1(\theta, \phi; \lambda) + \dots] \\ v_\theta &= \sum_{\lambda} \sum_n \rho^{\lambda+n} b_n(\theta, \phi; \lambda) = \sum_{\lambda} \rho^{\lambda} [b_0(\theta, \phi; \lambda) + \rho b_1(\theta, \phi; \lambda) + \dots] \\ v_\phi &= \sum_{\lambda} \sum_n \rho^{\lambda+n} c_n(\theta, \phi; \lambda) = \sum_{\lambda} \rho^{\lambda} [c_0(\theta, \phi; \lambda) + \rho c_1(\theta, \phi; \lambda) + \dots] \end{aligned} \quad (8)$$

By substitution of Eq 8 into the governing Eq 5a to 5c and the boundary conditions 6, the asymptotic governing equations and boundary conditions can be found, according to the terms which have the same order of  $\rho$ . The eigenvalue can be found from the governing equations and boundary conditions of zero order. These give

$$\lambda = \pm \frac{n}{2} \quad (n = 0, 1, 2, \dots) \quad (9)$$

From the condition of finite strain energy, the negative value should be disregarded. Therefore, the double eigenexpansion series can be reduced into a single eigenexpansion series

$$v_r = \sum_{n=0}^{\infty} \rho^{n/2} a_n(\theta, \phi) \quad v_\theta = \sum_{n=0}^{\infty} \rho^{n/2} b_n(\theta, \phi) \quad v_\phi = \sum_{n=0}^{\infty} \rho^{n/2} c_n(\theta, \phi) \quad (10)$$

If one substitutes Eq 10 into the governing Eq 5 and the boundary Eq 6, the asymptotic equations can be found. From the asymptotic expression, the asymptotic solution of  $v_r, v_\theta, v_\phi$  can be obtained term by term.

*Solution of Dimensionless Displacements*

The asymptotic solution can be derived by summing up the infinite series. However, the first few terms usually suffice to yield satisfactory results. We find

(a) Zero order ( $n = 0$ )

$$\begin{aligned}a_0 &= K_0 \cos \theta + L_0 \sin \theta \\b_0 &= -K_0 \sin \theta + L_0 \cos \theta \\c_0 &= P_0\end{aligned}\tag{11}$$

where  $K_0$ ,  $L_0$ ,  $P_0$  denote the translational motion along  $o'x'$  direction,  $o'y'$  direction, and  $o'z'$  direction, respectively. It should be noted that  $K_0$ ,  $L_0$ , and  $P_0$  are all functions of coordinate  $\phi$ .

(b) First order ( $n = 1$ )

$$\begin{aligned}a_1 &= K_1 \left[ \cos \frac{3}{2} \theta - (5 - 8\nu) \cos \frac{\theta}{2} \right] + L_1 \left[ \sin \frac{3}{2} \theta - \frac{1}{3} (5 - 8\nu) \sin \frac{\theta}{2} \right] \\b_1 &= -K_1 \left[ \sin \frac{3}{2} \theta - (7 - 8\nu) \sin \frac{\theta}{2} \right] + L_1 \left[ \cos \frac{3}{2} \theta - \frac{1}{3} (7 - 8\nu) \cos \frac{\theta}{2} \right] \\c_1 &= Q_1 \sin \frac{\theta}{2}\end{aligned}\tag{12}$$

(c) Second order ( $n = 2$ )

$$\begin{aligned}a_2 &= K_2 (1 - 2\nu + \cos 2\theta) - \nu \Psi (P'_0 + K_0) \\b_2 &= -K_2 \sin 2\theta + N_2 \\c_2 &= P_2 \cos \theta - \Psi L'_0 \sin \theta\end{aligned}\tag{13}$$

(d) Third order ( $n = 3$ )

$$\begin{aligned}a_3 &= K_3 \left[ \cos \frac{5}{2} \theta + (3 - 8\nu) \cos \frac{\theta}{2} \right] + L_3 \left[ \sin \frac{5}{2} \theta + \frac{1}{5} (3 - 8\nu) \sin \frac{\theta}{2} \right] \\&\quad + \Psi \left\{ \frac{1}{4} K_1 \left[ (3 - 8\nu) \cos \frac{3}{2} \theta - \frac{1}{3} (13 - 96\nu + 128\nu^2) \cos \frac{\theta}{2} \right] \right. \\&\quad \left. + \frac{1}{12} L_1 \left[ (3 - 8\nu) \sin \frac{3}{2} \theta - \frac{1}{15} (107 + 96\nu - 128\nu^2) \sin \frac{\theta}{2} \right] - \frac{2}{15} (1 + 4\nu) Q'_1 \sin \frac{\theta}{2} \right\} \\b_3 &= -K_3 \left[ \sin \frac{5}{2} \theta - (9 - 8\nu) \sin \frac{\theta}{2} \right] + L_3 \left[ \cos \frac{5}{2} \theta - \frac{1}{5} (9 - 8\nu) \cos \frac{\theta}{2} \right] \\&\quad + \Psi \left\{ -\frac{1}{4} K_1 \left[ (5 - 8\nu) \sin \frac{3}{2} \theta + \frac{1}{3} (55 - 192\nu + 128\nu^2) \sin \frac{\theta}{2} \right] \right. \\&\quad \left. + \frac{1}{12} L_1 \left[ (5 - 8\nu) \cos \frac{3}{2} \theta - \frac{1}{15} (79 - 192\nu + 128\nu^2) \cos \frac{\theta}{2} \right] - \frac{4}{15} (1 - 2\nu) Q'_1 \cos \frac{\theta}{2} \right\}\end{aligned}\tag{14}$$

$$c_3 = Q_3 \sin \frac{3}{2} \theta + \Psi \left[ -\frac{2}{3} (7 - 8\nu) K'_2 \cos \frac{3}{2} \theta + 2 \left( K'_2 \cos \frac{\theta}{2} + \frac{1}{3} L'_2 \sin \frac{\theta}{2} \right) + \frac{1}{4} Q_1 \sin \frac{\theta}{2} \right]$$

(e) Fourth order ( $n = 4$ )

$$\begin{aligned} a_4 = & K_4 \left[ \cos 3\theta + \frac{1}{3} (1 - 4\nu) \cos \theta \right] + L_4 \left[ \sin 3\theta + (1 - 4\nu) \sin \theta \right] + \left[ -\Psi^{4/3} \frac{3}{4} \nu e^2 \sin 2\phi L'_0 \right. \\ & + \Psi \frac{\nu}{2} N_2 + \Psi^2 \frac{\nu}{2} L''_0 \left. \right] \sin \theta + \left\{ \Psi^{4/3} (K'_0 - P_0) \frac{1 - \nu}{4} e^2 \sin 2\phi - \Psi \left[ \frac{1 + 2\nu}{6} P'_2 \right. \right. \\ & + \frac{1}{3} (1 - \nu)(2 + \nu) K_2 \left. \right] + \Psi^2 \left[ \frac{1}{6} (1 + \nu)(2 + \nu) K_0 - \frac{1}{6} (1 - \nu) K''_0 \right. \\ & \left. \left. + \frac{1}{6} (3 + 2\nu + \nu^2) P'_0 \right] \right\} \cos \theta \\ b_4 = & -K_4 \left[ \sin 3\theta - \frac{1}{3} (5 - 4\nu) \sin \theta \right] + L_4 \left[ \cos 3\theta - (5 - 4\nu) \cos \theta \right] \\ & - \left[ -\Psi^{4/3} \frac{3}{4} \nu e^2 \sin 2\phi L'_0 + \Psi \frac{\nu}{2} N_2 + \Psi^2 \frac{\nu}{2} L''_0 \right] \cos \theta - \left\{ \Psi^{4/3} (K'_0 - P_0) \frac{1 + \nu}{4} e^2 \sin 2\phi \right. \\ & - \Psi \left[ \frac{1 - 2\nu}{6} P'_2 + \frac{1}{3} (1 - \nu)(2 - \nu) K_2 \right] + \Psi^2 \left[ \frac{1}{6} (1 + \nu)(2 - \nu) K_0 - \frac{1}{6} (1 + \nu) K''_0 \right. \\ & \left. \left. + \frac{1}{6} (3 + 2\nu - \nu^2) P'_0 \right] \right\} \sin \theta \end{aligned} \quad (15)$$

$$\begin{aligned} c_4 = & P_4 \cos 2\theta + \frac{1}{2} (-\Psi N'_2 + \Psi^2 L'_0) \sin 2\theta + \Psi^{4/3} \frac{3}{4} e^2 \sin 2\phi (P'_0 + K_0) \\ & - \frac{1}{2} \Psi \left( \frac{1}{2} P_2 + K'_2 \right) - \frac{1}{2} \Psi^2 \left( -\frac{1}{2} P_0 + P'_0 + \frac{3}{2} K'_0 \right) \end{aligned}$$

where  $(\gamma = \partial(\ )/\partial\phi$ , and  $(\gamma'' = \partial^2(\ )/\partial\phi^2$ .

With the asymptotic solution of displacements  $v_r$ ,  $v_\theta$ ,  $v_\phi$  known, the stress-strain fields at crack tip can be derived using Eqs 3 and 4.

### Calculation of the Stress-Intensity Factors in Plate with a Surface Crack

Finite-element method has found wide application in engineering. It has been proved to be a very powerful method. However, it is expensive to tackle three-dimensional fracture analysis. In this paper, three means are used to improve its ability:

1. Based on the stress-strain fields above, a high-order special element is established. This not only improves the accuracy of results, but also reduces the number of degrees of freedom.
2. Apart from the region connecting the special element, thick-shell isoparametric elements are used to substitute three-dimensional elements.
3. A condensation technique is adopted to solve the large linear algebraic equations.

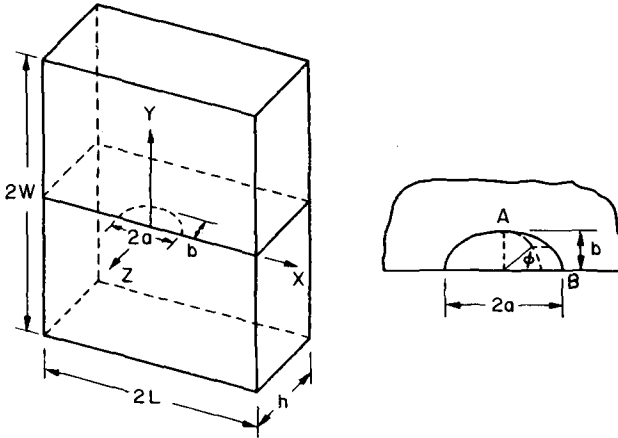


FIG. 2—Plate containing surface crack.

### Finite-Element Mesh and Special Element

Consider a plate with a semi-elliptical surface crack (Fig. 2); the finite-element mesh is shown in Fig. 3.

The number of degrees of freedom we adopted is equal to 838 and almost equals one tenth of that Newman and Raju adopted.

A series expansion of the displacements in the neighborhood of the crack is used to establish the stiffness matrix of a special element having the correct asymptotic behavior. The coefficients of expansion are used as the generalized displacement vector of the special element. It should be emphasized that the coefficients of expansion  $K_0, K_1, K_2, \dots$  in Eqs 11 to 15 are still functions of coordinate  $\phi$ , and they must be discretized first. Second, the special element is incorporated into standard elements by satisfying the condition requiring that both the special element and the standard elements have same displacements at each common node. Furthermore, the stress-intensity factors can be determined directly from the coefficients of the special element.

### Numerical Examples

In order to check the manipulation and validate the code, we reevaluated Newman and Raju's results. In Ref 17, they proposed an expression of stress-intensity factors for a plate containing a surface crack (Fig. 2)

$$K_i = \sigma_i \sqrt{\frac{\pi b}{Q}} F_i\left(\frac{b}{h}, \frac{b}{a}, \frac{a}{L}, \phi\right) \quad (i = 1, 2) \quad (16)$$

where  $F_i(b/h, b/a, a/L, \phi)$  denotes dimensionless stress-intensity factor and  $i = 1$  denotes tension case, while  $i = 2$  denotes bending case.

The value for  $F_i(0.6, 0.6, 0.2, \phi)$  is calculated and compared with that of Newman and Raju's (Table 1 and Fig. 4). In Figs. 4a and 4b, it can be seen that, at the deepest Point A, the error for tension is 0.37% and for bending 1.81%. Meanwhile, according to our results, the stress-intensity factors dropped dramatically near the plane surface. This means that



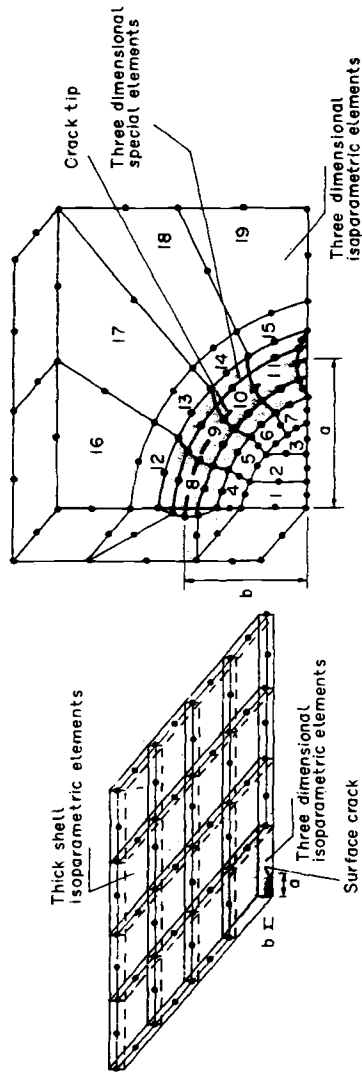


FIG. 3—Finite-element mesh.

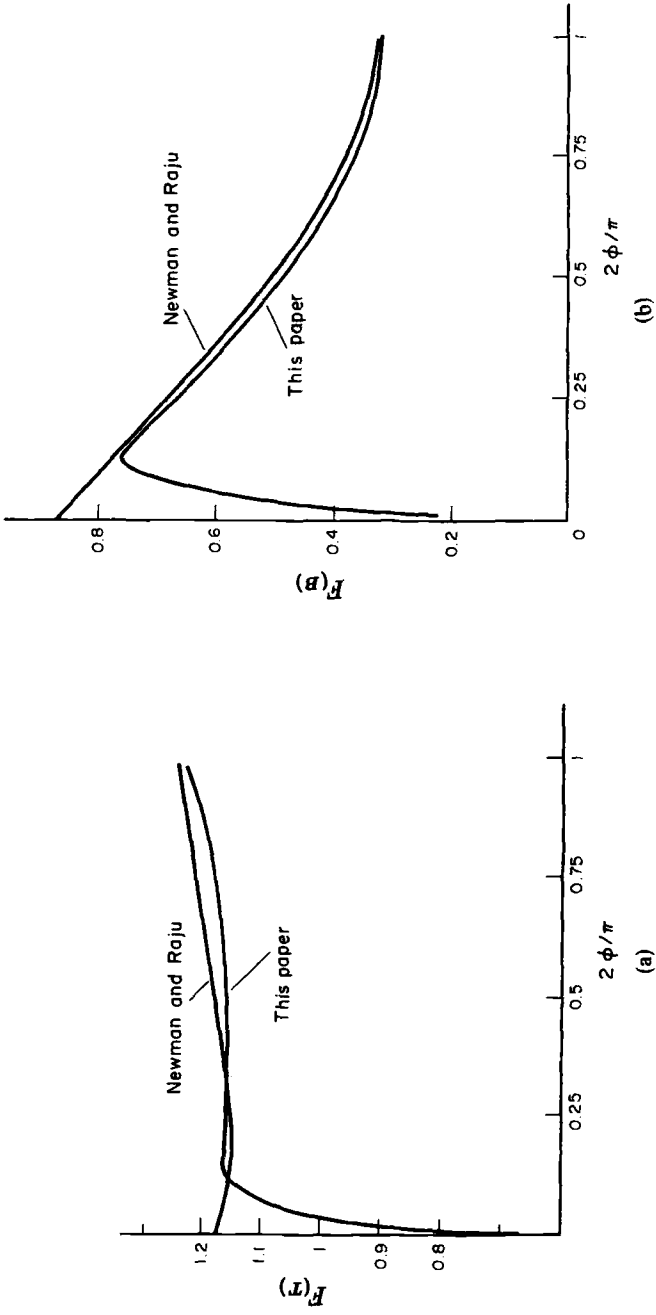


FIG. 4—Compare our results with Ref 17: (a) tension and (b) bending.

TABLE 1—Dimensionless stress-intensity factors  $F_i = \frac{K_I}{\sigma_i \sqrt{\frac{\pi b}{Q}}}$  in plate with surface crack

$$\left( \frac{a}{L} = 0.2, \quad \frac{a}{w} = 0.2, \quad \frac{b}{a} = 0.6, \quad \frac{b}{h} = 0.6, \quad \nu = 0.3 \right).$$

$\frac{2\phi}{\pi}$	Tension		Bending	
	This Paper	Ref 17	This Paper	Ref 17
0.000	0.253	1.172	0.151	0.862
0.125	1.148	1.149	0.764	0.779
0.250	1.150	1.142	0.640	0.676
0.375	1.159	1.160	0.570	0.587
0.500	1.160	1.182	0.486	0.504
0.625	1.162	1.202	0.410	0.430
0.750	1.178	1.218	0.364	0.370
0.875	1.198	1.227	0.334	0.331
1.000	1.225	1.230	0.322	0.317

there is a boundary layer near the plane surface. Our results compare favorably with the experimental data given by Ruiz et al. [25].

The variations of stress-intensity factors with geometric parameters are investigated. Compare the results in Table 2 (Fig. 5) and the formula for finite width correction given in Ref 17, that is

$$f_w = \left[ \sec \left( \frac{\pi a}{2L} \sqrt{\frac{b}{h}} \right) \right]^{1/2} \quad (17)$$

it can be seen that Eq 17 gives a reasonable value when  $a/L < 0.25$  and the error is less than 5%. However, when  $a/L > 0.25$ , Eq 17 gives a smaller value, especially for bending case. It is necessary that another more reasonable formula be proposed for finite width

TABLE 2—Variation of the dimensionless stress-intensity factors with plate width

$$\left( \frac{a}{w} = 0.2, \quad \frac{b}{h} = 0.6, \quad \frac{b}{a} = 0.6, \quad \nu = 0.3 \right).$$

$\frac{2\phi}{\pi}$	$\frac{a}{L} = 0.15$		$\frac{a}{L} = 0.20$		$\frac{a}{L} = 0.25$		$\frac{a}{L} = 0.30$		$\frac{a}{L} = 0.40$	
	Tension	Bending	Tension	Bending	Tension	Bending	Tension	Bending	Tension	Bending
0.000	0.250	0.151	0.253	0.151	0.265	0.160	0.283	0.171	0.304	0.187
0.125	1.134	0.760	1.148	0.764	1.184	0.788	1.244	0.810	1.344	0.840
0.250	1.136	0.620	1.150	0.640	1.188	0.662	1.240	0.682	1.324	0.740
0.375	1.148	0.562	1.159	0.570	1.198	0.604	1.254	0.640	1.332	0.684
0.500	1.148	0.474	1.160	0.486	1.196	0.508	1.244	0.548	1.320	0.592
0.625	1.150	0.400	1.162	0.410	1.192	0.430	1.236	0.468	1.312	0.524
0.750	1.152	0.356	1.178	0.364	1.192	0.386	1.248	0.428	1.322	0.483
0.875	1.168	0.330	1.198	0.334	1.210	0.360	1.264	0.400	1.340	0.448
1.000	1.215	0.320	1.225	0.322	1.255	0.342	1.304	0.377	1.383	0.427

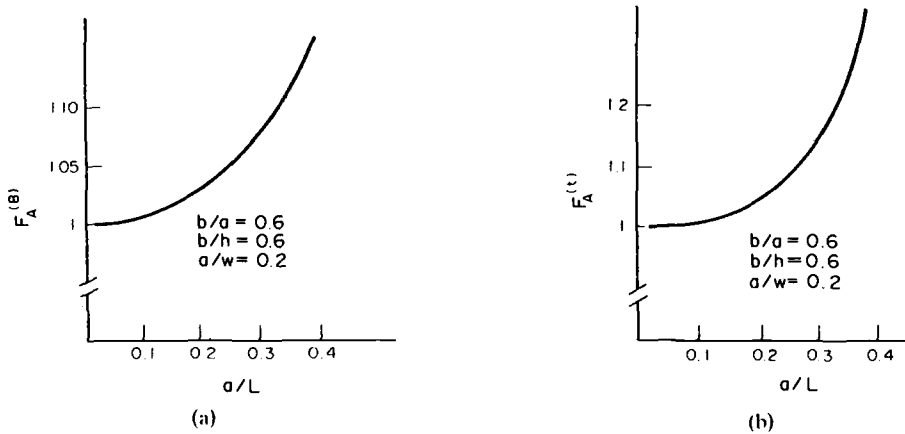


FIG. 5—(a) Variation of  $F_{(T)}$  with plate width (tension, at Point A), and (b) variation of  $F_{(B)}$  with plate width (bending, at Point A).

correction. In Table 3 and Fig. 6, the variation of stress-intensity factors is shown for a range of value of  $(2\phi)/\pi$ . It may be seen that these values decrease with increasing  $b/h$  for the bending case, and increase with increasing  $b/h$  for the tension case.

### Conclusion

1. In this paper the so-called local-global analysis is used to deal with three-dimensional fracture-mechanics problems. A general solution of stress-strain fields at crack tip, including Mode I, II, III, is proposed.

2. A special coordinate transformation is proposed to seek the general solution. This method is suitable not only for the semi-elliptical crack, but also for arbitrary configuration.

3. Based on the stress-strain fields obtained, a high-order, three-dimensional special element is established. It improves the accuracy of calculation and reduces the number of

TABLE 3—Variation of dimensionless stress-intensity factors with plate thickness

$$\left( \frac{a}{L} = 0.2, \quad \frac{a}{w} = 0.2, \quad \frac{b}{a} = 0.6, \quad \nu = 0.3 \right).$$

$\frac{2\phi}{\pi}$	$\frac{b}{h} = 0.2$		$\frac{b}{h} = 0.4$		$\frac{b}{h} = 0.6$		$\frac{b}{h} = 0.75$	
	Tension	Bending	Tension	Bending	Tension	Bending	Tension	Bending
0.000	0.215	0.153	0.241	0.153	0.253	0.161	0.264	0.148
0.125	0.944	0.766	1.080	0.764	1.148	0.764	1.192	0.742
0.250	0.976	0.732	1.098	0.680	1.150	0.640	1.184	0.560
0.375	1.010	0.750	1.120	0.676	1.159	0.570	1.200	0.496
0.500	1.036	0.756	1.130	0.632	1.160	0.486	1.192	0.396
0.625	1.062	0.744	1.140	0.584	1.162	0.410	1.180	0.260
0.750	1.086	0.748	1.160	0.572	1.178	0.364	1.200	0.212
0.875	1.104	0.764	1.194	0.570	1.198	0.334	1.220	0.170
1.000	1.130	0.792	1.212	0.568	1.225	0.322	1.243	0.128

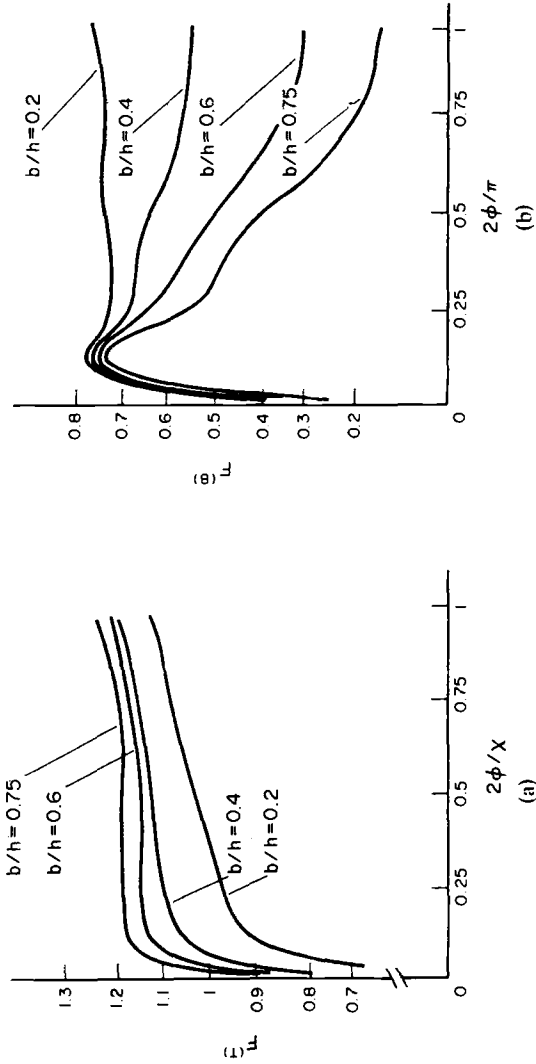


FIG. 6—(a) Variation of  $F_T$  with plate thickness (tension), and (b) variation of  $F_B$  with plate thickness (bending).

degree of freedom by a big margin. The number of degrees of freedom we adopted is only one tenth that adopted by Newman and Raju.

4. The stress-intensity factors in a finite-size plate with surface crack are calculated. Compared with Newman and Raju's results, the error is less than 5%. In the near-surface area, the results we obtained also agree with the experimental data very well.

### Acknowledgment

The author wishes to thank Professor Li Minhua, Professor Liu Chuntu, and Professor He Ming Yuan for their guidance, encouragement, and helpful discussion.

### References

- [1] Irwin, G. R., *Journal of Applied Mechanics*, Vol. 29, No. 4, 1962, pp. 651-654.
- [2] Smith, F. W., "Stress Near a Semicircular Edge Crack," Ph.D. dissertation, University of Washington, Seattle, 1966.
- [3] Smith, F. W. and Alavi, M. J., *Journal of Engineering Fracture Mechanics*, Vol. 1, 1969.
- [4] Thresher, R. W. and Smith, F. W., *Journal of Applied Mechanics*, Vol. 39, No. 1, 1972.
- [5] Shah, R. C. and Kobayashi, A. S., *Engineering Fracture Mechanics*, Vol. 3, No. 1, 1971.
- [6] Smith, F. W., *International Journal of Fracture Mechanics*, Vol. 12, No. 1, 1976.
- [7] Paris, P. C. and Sih, G. C. in *Fracture Toughness Testing and Its Applications*, ASTM STP 381, American Society for Testing and Materials, Philadelphia, 1965, p. 51.
- [8] Kobayashi, A. S. and Moss, W. L. in *Proceedings, 2nd International Conference on Fracture Mechanics*, 1969, p. 31.
- [9] Smith, F. W., Emery, A. F., and Kobayashi, A. S., *Journal of Applied Mechanics*, Vol. 34, 1967, p. 952.
- [10] Rice, J. R. and Levy, N. J., *Journal of Applied Mechanics*, Vol. 39, No. 1, 1972, p. 185.
- [11] Marcal, V., *The Surface Crack: Physical Problems and Computational Solutions*, J. L. Swedlow, Ed., 1972.
- [12] Nisitani, H., *Mechanics of Fracture*, G. C. Sih, Ed., Vol. 5, Nordhoff International Publishing, Leyden, The Netherlands.
- [13] Isida, M., Noguchi, H., and Yoshida, T., *International Journal of Fracture Mechanics*, Vol. 26, 1984, pp. 157-188.
- [14] *The Surface Crack: Physical Problems and Computational Solutions*, J. L. Swedlow, Ed., 1972.
- [15] Newman, J. C., Jr., in *Part-Through Crack Fatigue Life Prediction*, ASTM STP 687, J. B. Chang, Ed., American Society for Testing and Materials, Philadelphia, 1979, pp. 16-42.
- [16] Raju, I. S. and Newman, J. C., Jr., NASA TND-8414, National Aeronautics and Space Administration, Washington, DC, 1977.
- [17] Newman, J. C., Jr., and Raju, I. S., NASA TP-1578, National Aeronautics and Space Administration, Washington, DC, 1979.
- [18] Raju, I. S. and Newman, J. C., Jr., *Engineering Fracture Mechanics*, Vol. 11, 1979, pp. 817-829.
- [19] *Annual Book of ASTM Standards*, American Society for Testing and Materials, Philadelphia, 1983.
- [20] Cui Zhenyuan, J. in *Proceedings of ICF International Symposium on Fracture Mechanics*, Beijing, 1983, pp. 485-493.
- [21] Lo Zudas, "An Approximate Method for Calculating Three-Dimensional Stress-Intensity Factors," Technical Report of Shanghai Jiaotong University, Shanghai, 1978.
- [22] Folias, F. S., *Journal of Applied Mechanics*, Vol. 42, No. 3, 1975, pp. 663-674.
- [23] Benthem, J. P., *International Journal of Solid Structures*, Vol. 16, No. 2, 1980.
- [24] Tadahiko, K., Yoshinibu, F., and Kiyohiko, K. in *Fracture Mechanics and Technology*, G. C. Sih and C. L. Chow, Eds., Hong Kong, Vol. 2, 1977.
- [25] Ruiz, C. and Epstein, J., *International Journal of Fracture Mechanics*, Vol. 28, 1985, pp. 231-238.
- [26] Li, Yingzhi, "The Stress-Strain Fields at the Crack Tip in Three-Dimensional Bodies Containing a Surface Crack and the Calculation of Stress-Intensity Factors," Ph.D. dissertation, Institute of Mechanics, Chinese Academy of Sciences, Beijing, 1986.

## On the Semi-Elliptical Surface Crack Problem: Detailed Numerical Solutions for Complete Elastic Stress Fields

---

**REFERENCE:** Blom, A. F. and Andersson, B., "On the Semi-Elliptical Surface Crack Problem: Detailed Numerical Solutions for Complete Elastic Stress Fields," *Surface-Crack Growth: Models, Experiments, and Structures*, ASTM STP 1060, W. G. Reuter, J. H. Underwood, and J. C. Newman, Jr., Eds., American Society for Testing and Materials, Philadelphia, 1990, pp. 77-98.

**ABSTRACT:** The  $p$ -version of the finite-element method together with carefully designed meshes is used to obtain accurate numerical solutions for complete elastic stress fields in a linearly elastic plate containing a semi-elliptical surface crack for two materials having a Poisson's ratio of 0.3 and 0.499, respectively. *A priori* known convergence properties are used to estimate bounds for the error in the numerical solutions. The calculated displacements are believed to be accurate at all points located not closer than  $0.001a$ ,  $a$  being the crack size, from the crack front.

It is demonstrated that pointwise values for the traditional edge stress-intensity factors  $K_I$  are readily obtained with very high accuracy even when a very simple mesh and a modest computational effort are used. So-called vertex and vertex-edge intensity factors are derived which together with numerically determined eigenfunctions fully characterize the complete solution in the vicinity of the vertex where the crack front intersects with the stress-free surface.

For the nearly incompressible material, the second-order vertex intensity factor strongly influences the solution close to the vertex. In fact, the first-order vertex intensity factor, under different boundary conditions, may be of negligible importance (except for extremely small distances from the vertex). The size of the domain where the vertex singularity strongly influences the solution is of the order  $0.02a$ .

**KEY WORDS:** fracture mechanics,  $p$ -version finite-element method (FEM), surface crack, elastic stress fields, edge stress-intensity factor, vertex intensity factor, vertex-edge intensity factor, incompressibility, boundary layers

The problem of determining stress-intensity factors for elliptical surface cracks in structural members has, due to its technical importance, received considerable attention. Due to the complexity of the problem, numerical methods have generally been used. Displacement and hybrid formulations of the finite-element method and the boundary element method are numerical methods often employed for the purpose of determining stress-intensity factors.

The accuracy in computed edge stress-intensity factors generally attainable is, at best, in the order of a few percent [1]. Exhaustive reviews describing computational procedures [2] and handbooks summarizing computed data [3,4] are available.

<sup>1</sup> Head, Fatigue and Fracture, and head, Computational Mechanics, respectively, Structures Department, The Aeronautical Research Institute of Sweden, P.O. Box 11021, S-161 11 Bromma, Sweden.

Despite considerable effort, the elliptical surface crack problem has not been satisfactorily solved from either a theoretical or a practical point of view. It is well known that close to vertices of the domain (for example, close to the point where the elliptical crack front intersects with the stress-free surface), the standard square-root stress singularity does not apply. Based on experimental data available [5,6], it is believed that the size of the domain where standard linear elastic fracture mechanics (LEFM) does not apply is strongly dependent on the Poisson's ratio.

The sizes of such domains and the principal behavior of the exact solutions close to a vertex have not been clarified; consequently, suitable intensity factors have neither been defined nor computed.

The objective of the present paper is to discuss briefly the behavior of the exact solution close to vertices and, further, to compute a few accurate numerical solutions for the complete elastic stress fields close to edges and vertices for the problem of a plate with a semi-elliptical surface crack subject to tensile loading. Linearly elastic small strain and small displacement conditions are assumed.

The accuracy and reliability in computed data are questions of primary importance in any computation. In the present paper, the  $p$ -version of the finite-element method has been used to derive solutions for increasing orders of approximation  $p$  [7]. The reliability in computed data then, in our case, can be judged by comparing the set of solutions generated.

### Behavior of Exact Solutions

The plate with the symmetrically located semi-elliptical surface crack shown in Fig. 1 is considered. Plate properties are assumed isotropic and linearly elastic.

A uniform tensile stress  $\sigma_0$  is applied on the faces  $z = \pm h$ . According to regularity theories developed in Ref 8, the exact solution to this elastomechanical problem may be found in the sum of smooth functions and functions which have singular derivatives at edges and corners of the domain.

In the case of the Laplace equation, the properties of these functions are well characterized within the framework of functional analysis. For the equations of elastomechanics, properties of the solution are not known in such detail. The general character of the solu-

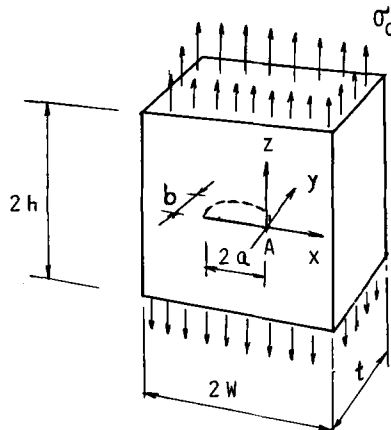


FIG. 1—Plate of width  $2W$ , height  $2H$ , and thickness  $t$  with semi-elliptical surface crack.



tion will be assumed to have the same character as has the Laplace equation [8,9], since detailed mathematical proofs are lacking.

Consider first the behavior of the solution near the crack front but not too close to Vertex A (Fig. 1).

The leading term in the expansion of the displacements  $u_i$  close to the crack front can then be written as [10]

$$u_i = K_I(x_3) \cdot r^{1/2} f_i(\varphi) + O(r) \quad (1)$$

where  $(r, \varphi, x_3)$  defines a curvilinear coordinate system with the  $x_3$ -axis coinciding with the elliptical crack front and  $(r, \varphi)$  being polar coordinates. The function  $K_I(x_3)$  is the Mode I edge stress-intensity function to be determined and  $f_i(\varphi)$  are known functions.

Consider now the behavior of the solution on the surface of a small spherical subdomain with radius  $\rho$  having its origin at Vertex A (Fig. 2). The solution close to Vertex A is of the type

$$u_i = \rho^{\lambda_i} w_i(\phi, \theta) + \text{smoother terms} \quad (2)$$

where the eigenvalue  $\lambda_i > -\frac{1}{2}$  (for finite strain energy) can be obtained by solving the eigenvalue problem discussed in Refs 11 and 12. The three edges with origin at Vertex A are defined by  $(\rho, 0, \pi/2)$ ,  $(\rho, 2\pi, \pi/2)$  and  $(\rho, \phi, 0)$  in the spherical coordinate system  $(\rho, \phi, \theta)$ . These edges are geometrical discontinuities close to which the functions  $w_i(\phi, \theta)$  are less smooth. The strongest singularity is at the edge  $(\rho, \phi, \theta)$  (the crack front) where the stresses exhibit the well-known square-root singularity.

In order for one to characterize the solution near a vertex, knowledge about  $\lambda_i$  and the functions  $w_i(\phi, \theta)$  would be needed. While the functions  $w_i(\phi, \theta)$  have to be determined numerically, it is advantageous to split the functions  $w_i(\phi, \theta)$  into their regular and non-regular parts. The functions  $w_i(\phi, \theta)$  may then be characterized, for example for fracture-mechanics purposes, by a few constants.

As an example, we consider, since an analytical solution is available, the solution of the Laplace equation, Eq 3, on the spherical domain shown in Fig. 2 with boundary conditions  $u = 0$  on crack faces and  $u = 0$  on the surface  $y = 0$ .

$$\Delta u = 0 \quad (3)$$

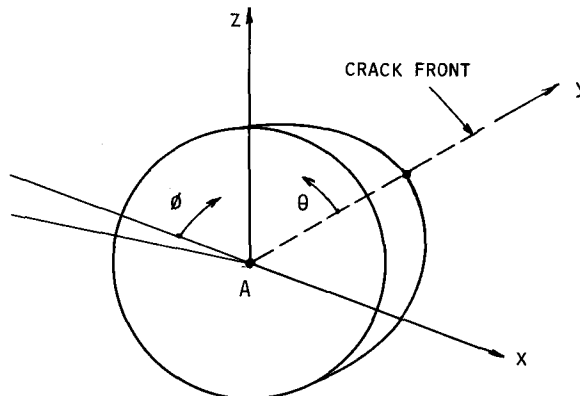


FIG. 2—Spherical subdomain with radius  $\rho$  having origin at Vertex A.  $(\rho, \phi, \theta)$  are spherical coordinates.

The leading term in the analytical solution is [13]

$$u = C\rho^\lambda \cdot w(\phi, \theta) \quad (4)$$

where

$$\lambda = 3/2$$

$$w(\phi, \theta) = (\sin\theta)^{1/2} \cos\theta \sin(\phi/2)$$

Close to the edge  $(\rho, \phi, 0)$ , that is, for small  $\theta$ , the solution  $u$  exhibits a square-root singularity (as in elastomechanics), while close to the edges  $(\rho, 0, \pi/2)$  and  $(\rho, 2\pi, \pi/2)$  the solution  $u$  is proportional to  $\rho_x^2$ ,  $\rho_x$  being the distance to the edge considered [9,13]. The solution given by Eq 4 may then be written in its regular and nonregular parts as<sup>2</sup> [9]

$$\begin{aligned} u = & D_1 \cdot \rho^{\lambda_1} \cdot v_1(\phi, \theta) \\ & + D_2 \cdot \chi_y(\rho_y) \cdot y^{\lambda_1-\lambda_2} \cdot \rho_y^{\lambda_2} \cdot v_2(\phi) \\ & + D_3 \cdot \chi_x(\rho_x) \cdot x^{\lambda_1-\lambda_3} \cdot \rho_x^{\lambda_3} \cdot v_3(\phi, \theta) \end{aligned} \quad (5)$$

Here  $\rho_x$  and  $\rho_y$  are distances to the  $x$ - and  $y$ -axes, respectively,  $\chi_x$  and  $\chi_y$  are cut-off functions infinitely smooth and with function values 1 at the edges and 0 at a distance from the edges. The eigenvalues are

$$\lambda_1 = 3/2, \quad \lambda_2 = 1/2, \quad \lambda_3 = 2 \quad (6)$$

and the smooth functions  $v_2(\phi)$ ,  $v_3(\phi, \theta)$  defining the angular behavior close to the edges are

$$\begin{aligned} v_2(\phi) &= \sin(\phi/2) \\ v_3(\phi, \theta) &= \sin 2\psi \end{aligned} \quad (7)$$

where  $\sin 2\psi = \sin 2\theta \cdot \sin \phi / (\cos^2 \theta + \sin^2 \theta \sin^2 \phi)$ .

The function  $v_1(\phi, \theta)$  is identical to  $w(\phi, \theta)$  (Eq 4) except in the neighborhood of the three edges.

The advantage of replacing Eq 4 with Eq 5 is that the singular character of the exact solution is explicitly defined in Eq 5. Close to the crack front, gradients of  $u$  are infinite and

$$(D_2 \cdot y^{\lambda_1-\lambda_2})$$

is the intensity function defining the variation of the solution  $u$  close to the crack front near Vertex A.

Close to the two edges  $(\rho, 0, \pi/2)$  and  $(\rho, 2\pi, \pi/2)$  gradients of  $u$  are finite since  $\lambda_3 = 2$  and thus of less interest from an engineering point of view. It is, however, interesting to note that the intensity function  $(D_3 x^{-1/2})$  goes to infinity close to the vertex. Obviously, the constant  $D_3$  being an "intensity factor of the intensity function" could be used to characterize the solution  $u$  near Vertex A.

<sup>2</sup> Babuška, I., private communication, December 1987.

Now, returning to our elastomechanical problem, the displacements  $u_i$  can also in this case be written

$$\begin{aligned} u_i = & D_1 \cdot \rho^{\lambda_1} \cdot w_{1i}(\phi, \theta) \\ & + D_2 \cdot \chi_y(\rho_y) \cdot y^{\lambda_1 - \lambda_2} \cdot \rho_y^{\lambda_2} \cdot w_{2i}(\phi) \\ & + D_3 \cdot \chi_x(\rho_x) \cdot x^{\lambda_1 - \lambda_3} \cdot \rho_x^{\lambda_3} \cdot w_{3i}(\phi, \theta) + \text{higher-order terms} \end{aligned} \quad (8)$$

The functions  $w_{ji}$  are smooth. The eigenvalues  $\lambda_i$  which depend on the Poisson's ratio  $\nu$  are given in the section on Determination of Eigenvalues  $\lambda_i$ . The eigenvalue  $\lambda_3$  is 1 (for all  $\nu$ -values), implying that there is no stress singularity close to the edges  $(\rho, 0, \pi/2)$  and  $(\rho, 2\pi, \pi/2)$ . Hence the determination of the constants  $D_1$  and  $D_2$  close to the vertex will suffice.

### The $p$ -Version of the Finite-Element Method

In the standard version of the finite-element method, the  $h$ -version, the degree  $p$  of the interpolation polynomials is fixed to a low value (normally  $p = 1$  or  $p = 2$ ). By increasing the number of finite elements used, the desired solution accuracy can be obtained. In the  $p$ -version of the finite-element method, a fixed mesh is used and convergence is obtained by increasing the degree  $p$  of the interpolation polynomials used [7].

The finite-element program STRIPE [14], which is based on a  $p$ -version of the finite-element method, has been used for the present computations. Finite-element models used are built up of brick elements and prismatic elements.

The interpolation polynomials used are minimally conforming and correspond to piecewise complete polynomials of order  $p$  together with a few monomial terms of degree higher than  $p$ . Finite-element-approximations of order  $1 \leq p \leq 15$  are allowed. The order of approximation  $p$  in each element may be the same (uniform  $p$ -extensions) or may be assigned automatically in a self-adaptive way.

The number of interpolation functions in brick and prismatic finite elements are for uniform  $p$ -extensions given in Table 1. The number of degrees of freedom are three times the number of interpolation functions used.

Domains of complex shape may be modeled with a few elements by use of so-called blended function mapping [15]. This type of geometrical transformations is rejected when

TABLE 1—Number of interpolation functions used in the STRIPE-code for different orders of approximation  $p$  in case of uniform  $p$ -extensions.

Order of Approximation, $p$	Number of Functions	
	Brick Element	Prismatic Element
1	8	6
2	20	15
3	32	26
4	50	42
5	72	64
6	105	93
7	144	130
8	192	176
9	250	232
10	319	299

the  $h$ -version of the finite-element method is employed, since rigid-body rotations and translations cannot be exactly modeled. When blended function mapping is applied in combination with the  $p$ -version, this error decreases exponentially with increasing order or approximation  $p$ .

So-called locking effects, a notorious problem when one uses the  $h$ -version, do not exist in the  $p$ -version of the finite-element method. In the case of near incompressibility, a rigorous proof of this property of the  $p$ -version of the finite-element method is given in Ref 16.

Finally, it should be noted that no *a priori* knowledge of the behavior of the solution close to edges and vertices has been introduced into the finite-element interpolation functions used.

### Convergence Properties of the $p$ -Version of the Finite-Element Method

Questions concerning convergence properties of the discretization scheme used are of vital importance when one is judging the reliability of the computed data. In Refs 9, 17, and 18, error bounds are given for the  $p$ -version of the finite-element method. The error  $e$  in elastic energy in the solution is bounded by

$$\|e\|_E^2 \leq C \cdot p^{-2\alpha} \quad (9)$$

where

$$\alpha = \min \left( \lambda_1 + \frac{1}{2}, \lambda_2 \right) \quad (10)$$

It is important to note that asymptotically, the convergence properties of the finite-element method depend on the strength of the edge or the vertex singularity. For domains of isotropic material and with crack-like defects ( $\lambda_2 = \frac{1}{2}$ ), as studied in the present research, it seems that the line singularity will govern the solution since  $\lambda_1$  most likely is greater than zero.

The constant  $C$  in Eq 9 depends on the exact solution  $u$ , the domain investigated, and the mesh used, but is independent of the order of the approximation  $p$ .

For large values of  $p$ , the asymptotic rate of convergence is entered and the error  $e$  is given approximately by

$$\|e\|_E^2 = C P^{-2\alpha} \quad (11)$$

The  $p$ -level for which Eq 11 approximately applies is mesh dependent. Numerical experience from solutions of two- and three-dimensional problems in linear elasto-mechanics [14,18] has indicated that when fairly uniform meshes are used, the asymptotic rate of convergence is entered at low  $p$ -levels ( $p > 3$ ).

Optimal meshes for the  $p$ -version of the finite-element method, that is, meshes giving the highest accuracy for a given computational effort, should be graded near point and line singularities [14,18,19]. Grading of the elements should be such that the element sizes are in geometric progression (factor about 6) with the smallest elements where the stress gradients are largest. The pre-asymptotic rate of convergence is exponential when such meshes are used, which leads to high accuracy for a given computational effort.

In the section on Determination of Eigenvalues  $\lambda_n$ , the determination of the vertex eigen-

value  $\lambda_1$  is briefly discussed. We will be interested in an estimate of the error in  $\lambda_1$  when solving a generalized eigenvalue problem of the type

$$[K]x = \lambda_1[B]x + [B_{12}]x \quad (12)$$

where matrices  $[K]$ ,  $[B]$ , and  $[B_{12}]$  are derived using the  $p$ -version of the finite-element method.<sup>3</sup>

In Ref 20 it has been shown that the error  $\Delta\lambda_1$  in calculated eigenvalues, when employing the  $p$ -version of the finite-element method, is bounded by

$$|\Delta\lambda_1| \leq C p^{-4\alpha} \quad (13)$$

This rate of convergence is exactly twice that given by Eq 9. For large  $p$ -values, the following equation approximately applies

$$|\Delta\lambda_1| = C p^{-4\alpha} \quad (14)$$

Equations 11 and 14 may be used to estimate the error in the computed values, provided that three solutions for different orders of approximation  $p$  are available. By solving the set of three nonlinear equations, we may determine the unknowns  $\Delta\lambda_1$ ,  $C$ , and  $\alpha$  where  $\Delta\lambda_1$  is the estimate for the error in the eigenvalue  $\lambda_1$ .

### Calculation of Stress-Intensity Factors

The technique developed in Ref 14 will be used for the calculation of pointwise values of the edge stress-intensity factors. This method is a generalization of the contour integral method [21] used for solution of two-dimensional problems in elastomechanics.

An infinitely thin slice perpendicular to the crack front is considered (Fig. 3). By using the Maxwell-Betti reciprocity theorem, knowledge about the principal character of the near crack-tip stress distribution (equations above), and a suitable choice of an additional load system, one arrives at the following expression for the Mode I stress intensity factor

$$K_I = \int_{\Gamma} (T_i u_i^{Ex} - T_i^{Ex} u_i) dT + \int_S \left( \frac{\partial T_i}{\partial x_3} u_i^{Ex} - T_i^{Ex} \frac{\partial u_i}{\partial x_3} \right) \quad (15)$$

In Eq 15,  $u_i^{Ex}$  and  $T_i^{Ex}$  are displacements and tractions for an arbitrarily selected load system [14,21]. By substituting displacements and tractions obtained from the finite-element solution for  $u_i$  and  $T_i$  in Eq 15, we can obtain an estimate for the true stress-intensity factor.

The first integral on the right-hand side of Eq 15 is that obtained when using the contour integral method in two-dimensional elastomechanics, while the second integral considers the variation of field quantities along the crack front.

The term  $\partial T_i / \partial x_3$  occurring in the surface integral implies that second-order derivatives of the finite-element solution have to be calculated. Since the exact solution is smooth along a (smooth) curved crack front (for smooth load distributions) and the  $p$ -version of the finite-element method converges rapidly for such cases, the error in the numerical solution will, for higher  $p$ -levels, still be dominated by the square-root singularity.

<sup>3</sup> See footnote 2.

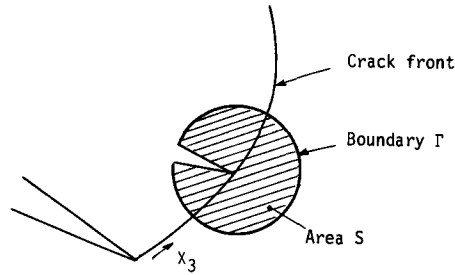


FIG. 3—Slice perpendicular to crack front used for determination of Mode I stress-intensity factors.

### Determination of Eigenvalues $\lambda_i$

The eigenvalues  $\lambda_i$  used to characterize the solution close to the vertex A ( $\lambda_1$ ) and the edges ( $\lambda_2$  and  $\lambda_3$ ) may be determined from local three- and two-dimensional analyses, respectively. The two-dimensional problem has been treated in Ref 22, while the three-dimensional problem has been treated in Refs 11 and 12. In Table 2, eigenvalues  $\lambda_i$  reported in these references are summarized.

For materials having a Poisson's ratio  $\nu$  of 0.3, there are several independent investigations arriving at the value 0.548 for the eigenvalue  $\lambda_1$ . For the incompressible material ( $\nu = 0.5$ ), the solution  $\lambda_1 = 0.668$  by Benthem [11] seems to be the only one available.

The numerical determination of the fundamental eigenvalue  $\lambda_1$  may be formulated as a standard eigenvalue problem of the form given by Eq 12.<sup>4</sup> The finite-element program [14] has been modified and used to compute the eigenvalue  $\lambda_1$  for the cases  $\nu = 0.3$  and  $\nu = 0.499$ . Table 3 summarizes data for  $\lambda_1$  obtained using an eight-element finite-element mesh and different orders of approximation  $p$ .

Results shown in Table 3 for  $\nu = 0.3$  are in good agreement with data reported in Refs 11 and 12. For the nearly incompressible material, however, the present estimation of  $\lambda_1$  is larger than that given by Benthem [11]. By using a 32-element mesh, eigenvalues  $\lambda_1$  were estimated to 0.547 and 0.681 for a Poisson's ratio of 0.3 and 0.499, respectively (uniform  $p = 7$  was used). We conclude that the value  $\lambda_1 = 0.668$  given in Ref 11 for the case  $\nu = \frac{1}{2}$  seems to be somewhat low.

### A Model Problem

The principal character of the exact solution close to Vertex A has been discussed above and characteristic eigenvalues  $\lambda_i$  have been determined. In order to quantify explicitly the influence of the vertex singularity on the overall solution, we have singled out a model problem for investigation.

As the model problem, the domain ( $-h < x < h$ ,  $0 < y < 2h$ ,  $-h < z < h$ ) shown in Fig. 4 is considered. Uniform traction loading  $T_z = \sigma_0$  and  $T_z = -\sigma_0$  on the faces  $z = h$  and  $z = -h$ , respectively, is used. Two isotropic materials with modulus of elasticity  $E$  and Poisson's ratios of 0.3 and 0.499 are considered, respectively. The finite-element mesh used is graded towards the crack front and the point where the crack front intersects with the stress-free surface [23]. The mesh has 14 elements in four layers along the  $y$ -axis (in

<sup>4</sup> See footnote 2.

TABLE 2—Eigenvalues  $\lambda_1$  characterizing solution close to Vertex A.

	Poisson's Ratio		
	0	0.3	0.5
$\lambda_1$	0.5	0.548	0.668
$\lambda_2$	0.5	0.5	0.5
$\lambda_3$	1.0	1.0	1.0

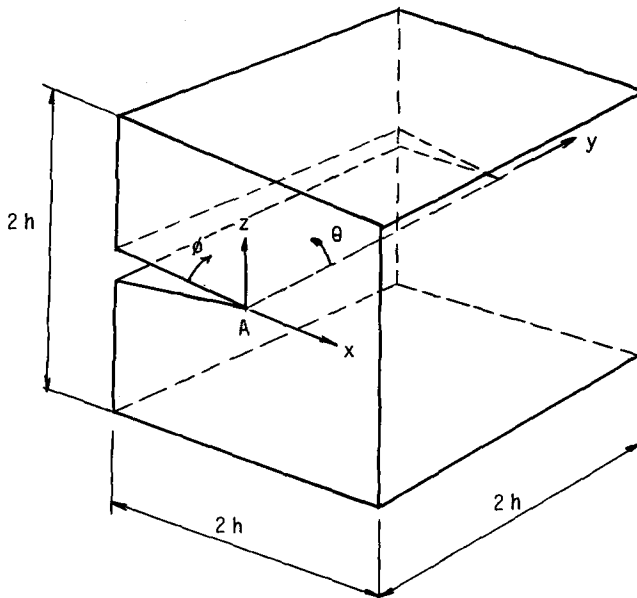


FIG. 4—Cube-shaped domain with symmetrically located crack.

TABLE 3—Computed eigenvalues  $\lambda_1$  using different orders of approximation  $p$  and an eight-element mesh. Error estimate  $\Delta\lambda_1$  is computed from Eq 14.

$p$	$\nu = 0.3$		$\nu = 0.499$	
	$\lambda_1$	$\lambda_1 + \Delta\lambda_1$	$\lambda_1$	$\lambda_1 + \Delta\lambda_1$
4	0.580	...	0.768	...
5	0.570	...	0.716	...
6	0.565	0.549	0.701	0.690
7	0.561	0.544	0.695	0.688
8	0.558	0.546	0.689	0.679
9	0.556	0.547	...	...
10	0.555	0.547	...	...

all 56 elements). The four layers are at sections  $y = 0.003375 h$ ,  $y = 0.0225 h$ ,  $y = 0.15 h$  and  $y = h$ , respectively (due to symmetry, only one quarter of the domain needs to be modeled in the analysis). The grading towards Vertex A thus is about 6. This grading is used towards the crack-tip in the  $xz$ -planes, too. Solutions have been derived for  $p = 2$  to  $p = 8$  using uniform  $p$ -extensions. The largest finite-element model has about 15 000 deg of freedom.

In Fig. 5, the  $z$ -displacements  $u_3/\sqrt{\rho}$  at the crack face ( $\phi = 0$ ) are plotted in a  $^{10}\log - ^{10}\log$  scale, for the case  $\nu = 0.499$ , as function of the distance  $\rho$  to Vertex A for different angles  $\theta$ . For small values of the radius  $\rho$ , where the exact solution is well approximated by the leading term in the expansion of  $u_i$  (Eq 2), a straight line with slope  $(\lambda_1 - \frac{1}{2})$  should be obtained. The set of curves shown in Fig. 5 are nearly parallel and straight lines in the range  $0 < \rho/h < 0.15$  with slopes  $0.177 \pm 0.001$  (at least for  $\theta > 10$  deg). The numerical results shown in Fig. 5 are in agreement with the assumption that the leading term of the exact solution is that given by Eq 2. The value  $\lambda_1 = 0.677 \pm 0.001$  obtained from the Fig. 5 differs only slightly from the value  $\lambda_1 = 0.679$  given in Table 3. In the following, the value  $\lambda_1 = 0.677$  will be used when evaluating data obtained from the analyses of the surface crack problem.

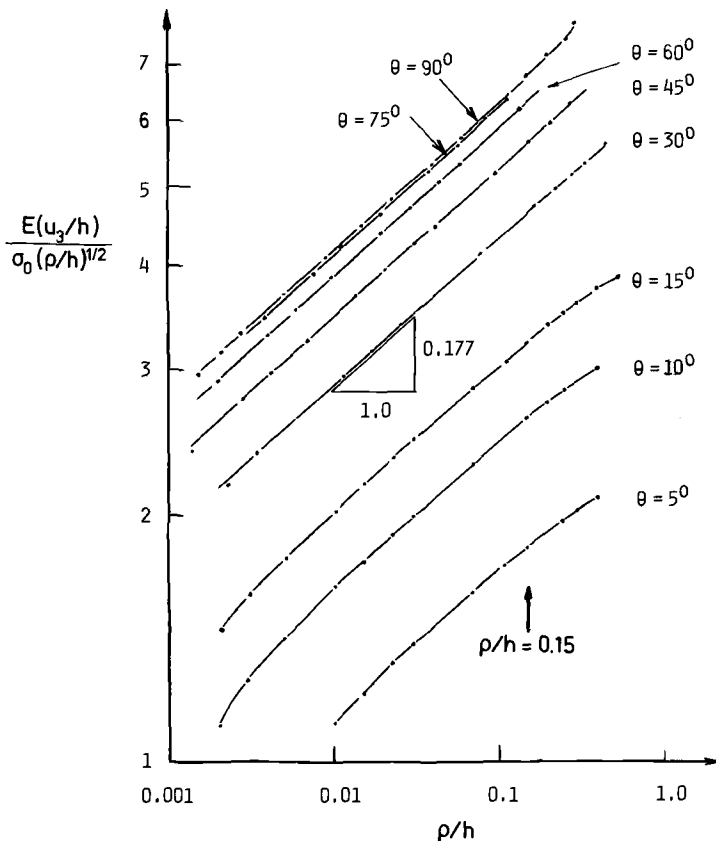


FIG. 5—Calculated  $z$ -displacement  $u_3$  at crack face for cube-shaped domain with edge crack having linear elastic material properties with modulus  $E$  and with Poisson's ratio 0.499.



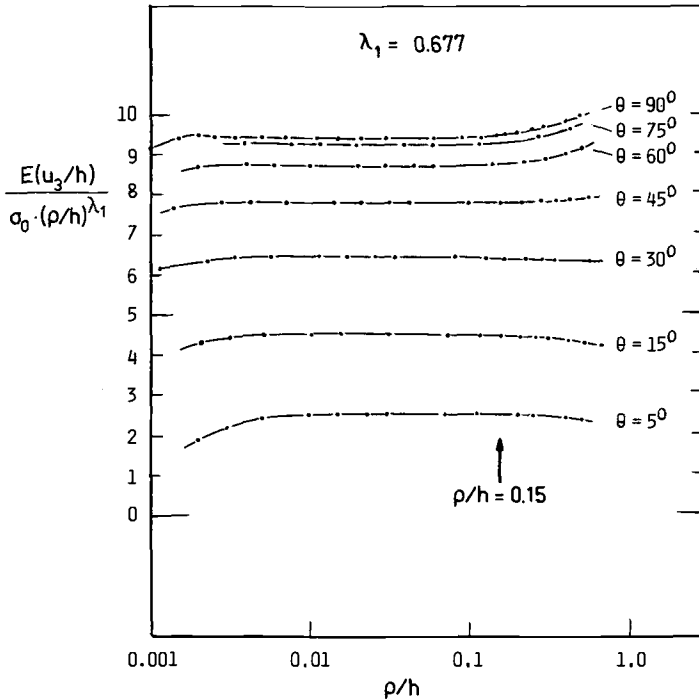


FIG. 6—Calculated z-displacement obtained using 56-element mesh and uniform  $p$ -distribution  $p = 8$  for nearly incompressible material with  $\nu = 0.499$ .

Note that no assumption whatsoever about the behavior of the solution close to Vertex A and the crack front has been made in the finite-element analyses.

The reliability in computed data has been judged to be good by comparing different solutions of different orders of approximation  $p$  [23]. Results in Figs. 5 and 6 indicate that the numerical solution available is accurate over a length scale covering almost three orders of magnitude.

The size of the domain where the vertex singularity governs the solution, and where standard LEFM does not apply, is of special interest. The size of this domain will in the present paper be estimated from graphs showing half the crack-opening displacement  $u_z$  versus a function of the distance to the vertex. By a proper choice of this function, a set of straight lines will be obtained in the  $\rho$ -interval where the leading term of Eq 2 well approximates the displacements. The size of the domain of interest will be determined visually by inspection of the graphs included in the present paper. A slight deviation from a straight line will be interpreted as if the leading term of Eq 2 no longer well approximates the displacements.

Figure 6 clearly shows that this domain is relatively large ( $0 < \rho/h < 0.15$ ) for this load case and the nearly incompressible material considered. In case of materials having  $\nu = 0.3$ , however, this domain is considerably smaller, as indicated in Figs. 7 and 8. In fact, the size of the domain, which is of the order  $\rho/h < 0.03$ , is so small that the numerical accuracy is not completely satisfactory even with the finite-element model having about 15 000 deg of freedom.

The eigenvalue  $\lambda_1$  can from Fig. 7 be estimated to 0.560–0.565, which differs considerably from the value 0.548 [11,12] given in Table 2.

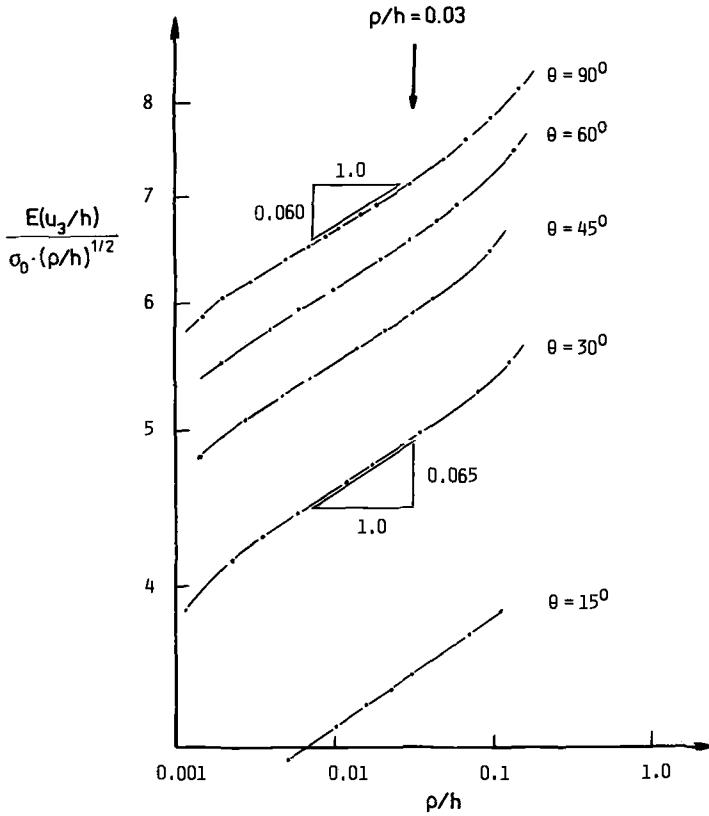


FIG. 7—Computed  $z$ -displacement on crack surface for cube-shaped domain with edge crack for material with  $\nu = 0.3$ .

The variation of the stress-intensity factor along the crack front has been calculated using the technique described in the previous section. Table 4 summarizes the data obtained. For the case of  $\nu = 0.3$ , the calculated stress-intensity factors exhibit a satisfactory convergence with increasing order of approximation  $p$ . For the nearly incompressible material the convergence is poorer. The reason for this behavior is that a special technique is needed to extract accurate values for the normal stresses (but not the shear stresses, the deviatoric stresses, or the displacements) in the case of nearly incompressible material properties. This technique has not been used in the present analyses.

In Eq 8, the constant  $D_2$  was used to characterize the solution close to the crack front near Vertex A. We now define the vertex-edge intensity factor  $S_E$  for the edge  $(\rho, \phi, 0)$  as

$$S_E = \lim_{y \rightarrow 0} \frac{K_I(y/h)}{(y/h)^{\lambda_1 - \lambda_2}} \quad (16)$$

where  $\lambda_1 = 0.548$  and  $0.677$  for  $\nu = 0.3$  and  $0.499$ , respectively, and  $\lambda_2 = \frac{1}{2}$ .

Figure 9 shows the variation of the stress-intensity factor close to Vertex A for the two materials considered. The vertex-edge intensity factor,  $S_E/(\sigma_0 \sqrt{\pi h})$ , can from this figure

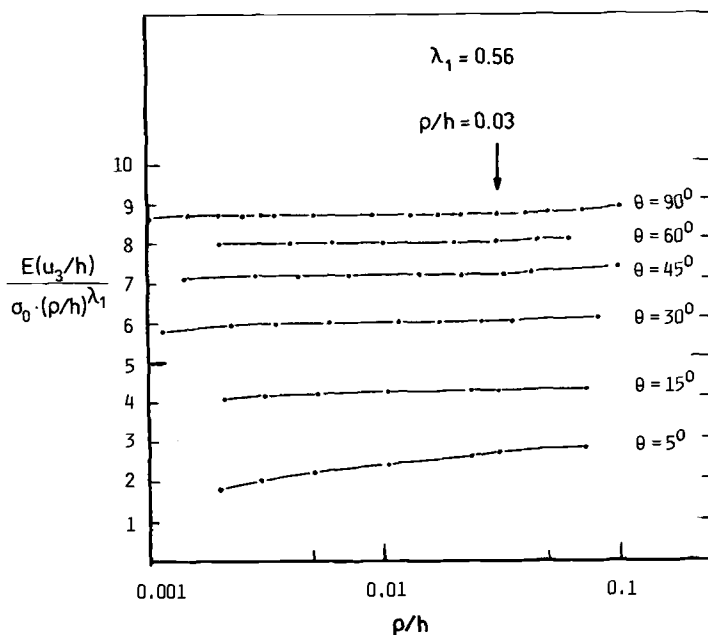


FIG. 8—Computed  $z$ -displacements on crack surface plotted as function of distance  $\rho$  to Vertex A for case  $\nu = 0.30$ .

TABLE 4—Calculated stress-intensity factors  $K_I(y/h)/(\sigma_0 \sqrt{h})$  for two materials and different orders of approximation  $p$ .

$p$	Coordinates, $y/h$				
	$1.7 \times 10^{-3}$	$11.2 \times 10^{-3}$	$86.3 \times 10^{-3}$	0.575	1.0
POISSON'S RATIO 0.3					
2	3.54	3.87	4.29	4.75	4.74
3	3.83	4.30	4.81	5.35	5.36
4	3.89	4.32	4.82	5.35	5.44
5	3.98	4.47	4.99	5.54	5.60
6	4.00	4.47	4.99	5.54	5.60
7	4.03	4.48	5.02	5.57	5.63
8	4.03	4.48	5.02	5.57	5.63
POISSON'S RATIO 0.499					
2	0.37	-1.27	-6.39	-13.72	-16.85
3	-0.74	0.60	5.80	0.96	1.44
4	2.25	2.63	1.63	-0.39	2.88
5	1.71	3.66	3.71	4.14	3.93
6	2.35	3.37	3.17	4.10	4.73
7	2.22	3.51	4.38	5.62	5.56
8	2.39	3.36	4.36	5.50	5.78

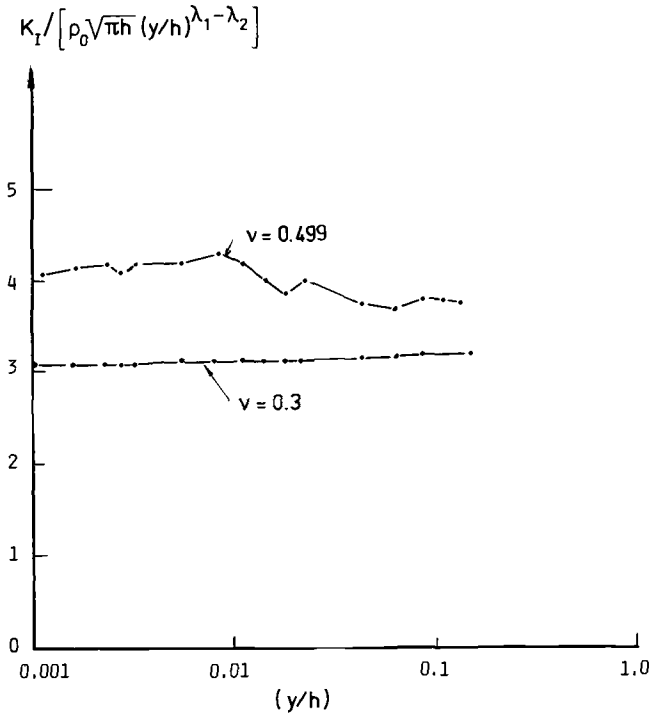


FIG. 9—Calculated stress-intensity factor  $K_I$  as function of distance  $y$  to Vertex A. Finite-element solution is obtained using uniform  $p$ -distribution  $p = 8$ .

be estimated to 3.1 and 4.1 units for  $\nu = 0.3$  and 0.499, respectively. The stress-intensity factors obtained for  $\nu = 0.499$  are less accurate of reasons discussed above. For the case  $\nu = 0.3$ , however, the results seem reliable. For this case the edge stress-intensity factor  $K_I(y/h)$  close to Vertex A is approximately given by

$$K_I(y/h) = 3.1 \sqrt{\pi h} (y/h)^{\lambda_1 - \lambda_2}, \quad y/h < 0.1 \quad (17)$$

with  $\lambda_1 = 0.548$  and  $\lambda_2 = \frac{1}{2}$ .

### The Semi-Elliptical Surface Crack Model

The domain shown in Fig. 1 with  $a/b = 2$ ,  $h/w = 2$ ,  $t/b = 4$ , and  $w/a = 4$  is considered. Due to symmetry, only one quarter of the plate needs to be analyzed. Two finite-element meshes have been used to study this problem. The first mesh, shown in Fig. 10a, has 80 elements and is graded close to the vertex where the crack front intersects with the stress-free surface. Solutions obtained with this mesh give accurate information about the solution close to the vertex.

A second mesh having 22 elements (Fig. 10b) is used to demonstrate the simplicity of mesh design and the accuracy obtainable by employing the  $p$ -version of the finite-element method in a practical situation.

The two meshes have three cylindrical layers of elements located at distances of about  $0.003a$ ,  $0.02a$ , and  $0.10a$ , respectively, from the crack front. Thus, elements located at the

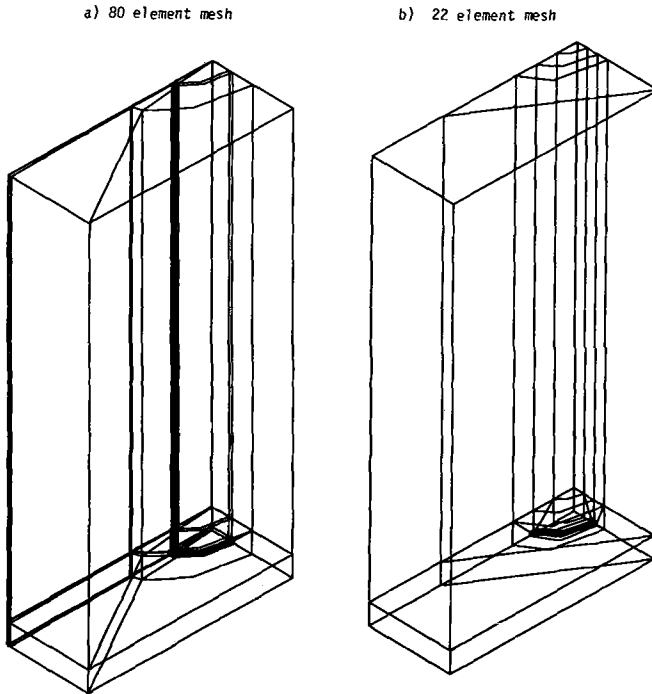


FIG. 10—Finite-element models for analysis of plate with semi-elliptical surface crack: (a) 80-element mesh; (b) 22-element mesh.

crack front in the two meshes have aspect ratios of the order 1000, which is perfectly acceptable with the  $p$ -version of the finite-element method.

For the coarse mesh, only one element edge is used to model the entire crack-front! So-called blended function mapping [15] is used to model the elliptical shape of the crack front exactly.

Edge stress-intensity factors have been computed along the elliptical crack front from Eq 15. The section (Fig. 3) used when evaluating the line and surface integral is perfectly perpendicular to the crack front and of size  $0.02a$  by  $0.01a$ .

Calculated stress-intensity factors are presented in form of engineering magnification factors  $M(\psi)$ , defined for  $a/b = 2$  as

$$M(\psi) = \frac{1.211}{\sigma_0 \sqrt{\pi b}} K_I(\psi) \quad (18)$$

where  $\psi$  is the so-called elliptical angle [24]. Table 5 summarizes data obtained using the two meshes for different orders of approximation  $p = 2, 3, \dots, 7$ .

In Fig. 11, data from Table 5b are compared with a "best estimate" of the stress-intensity variation along the flaw border [24]. The bands shown above and below the curve give an estimate of the uncertainty which was believed in Ref 24 to be about 3%.

Calculated stress-intensity factors obtained for  $p = 7$  with the 22-element mesh and the 80-element mesh are in close agreement in the interval  $0 \text{ deg} < \psi < 75 \text{ deg}$ . Close to the

TABLE 5a—Calculated magnification factor  $M(\psi)$  obtained with 80-element mesh for Poisson's ratio 0.499.

$p$	Elliptical Angle $\psi$ , degrees											
	0.0	9.6	19.1	28.7	38.3	47.8	57.4	66.9	76.5	80.8	85.1	88.6
2	0.84	-1.37	-1.55	-0.82	-0.08	0.09	-0.39	-0.83	-0.26	-0.50	0.73	1.13
3	2.03	1.89	2.05	2.09	2.02	1.98	2.09	2.29	-0.04	2.18	2.24	1.36
4	2.61	0.87	0.84	1.06	1.06	0.89	0.84	1.05	0.33	0.58	0.77	0.79
5	2.06	1.64	1.54	1.46	1.42	1.49	1.60	1.52	1.22	1.19	1.24	0.97
6	1.28	1.08	0.99	0.98	0.99	0.99	0.98	0.85	0.92	0.73	0.72	0.73
7	1.36	1.35	1.33	1.27	1.19	1.19	1.18	1.08	1.03	0.99	0.96	0.88

TABLE 5b—Calculated magnification factor  $M(\psi)$  obtained with 80-element mesh for Poisson's ratio 0.3.

$p$	Elliptical Angle $\psi$ , degrees											
	0.0	9.6	19.1	28.7	38.3	47.8	57.4	66.9	76.5	80.8	85.1	88.6
2	0.93	0.87	0.85	0.85	0.84	0.83	0.79	0.75	0.74	0.75	0.75	0.76
3	1.08	1.05	1.04	1.02	0.99	0.95	0.91	0.87	0.86	0.87	0.88	0.89
4	1.08	1.05	1.03	1.01	0.98	0.94	0.90	0.87	0.84	0.85	0.86	0.87
5	1.12	1.10	1.08	1.06	1.03	0.99	0.94	0.90	0.87	0.88	0.89	0.90
6	1.11	1.10	1.08	1.06	1.02	0.98	0.94	0.90	0.88	0.87	0.88	0.90
7	1.12	1.11	1.09	1.07	1.03	0.99	0.95	0.91	0.88	0.88	0.89	0.91

TABLE 5c—Calculated magnification factor  $M(\psi)$  obtained with 22-element mesh for Poisson's ratio 0.3.

$p$	Elliptical Angle $\psi$ , degrees											
	0.0	9.0	18.0	27.0	36.0	49.5	58.5	67.5	76.5	81.0	85.5	90.0
2	0.99	0.86	0.80	0.77	0.77	0.77	0.78	0.77	0.76	0.76	0.76	0.78
3	1.10	1.06	1.03	0.99	0.96	0.91	0.89	0.88	0.89	0.91	0.93	0.98
4	1.12	1.05	1.02	1.00	0.98	0.93	0.89	0.86	0.86	0.87	0.89	0.92
5	1.13	1.10	1.07	1.05	1.03	0.98	0.94	0.90	0.88	0.89	0.90	0.93
6	1.12	1.10	1.08	1.06	1.03	0.98	0.94	0.89	0.88	0.89	0.91	0.93
7	1.12	1.11	1.09	1.07	1.04	0.99	0.95	0.91	0.88	0.89	0.91	0.93

vertex, however, only the 80-element mesh give reliable results. Both solutions are in close agreement with data reported in Ref 24.

For a Poisson's ratio of 0.3, the calculated edge intensity factors converge rapidly with increasing  $p$ -levels, leading to virtually identical results for  $p > 4$ . For the case of the nearly incompressible material, however, the convergence behavior is less good. By using a different technique for computing edge intensity factors, one can avoid the problem of the low quality of the normal stresses in case of incompressibility.<sup>5</sup> Such a technique<sup>6</sup> is currently being implemented in the finite-element system described in Ref 14.

<sup>5</sup> See footnote 2.

<sup>6</sup> See footnote 2.

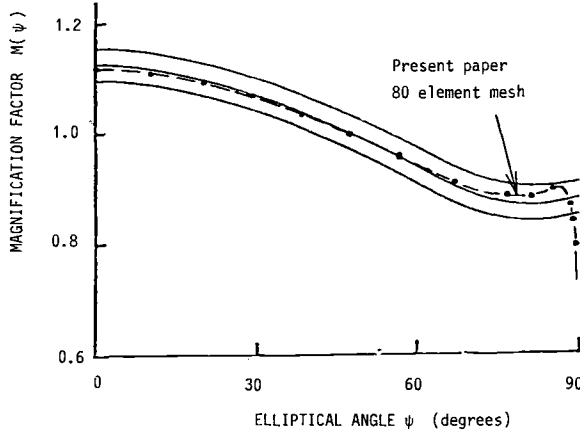


FIG. 11—Calculated magnification factor  $M$  for  $p = 7$  and  $\nu = 0.3$ .

We next consider the behavior of the solution close to Vertex A (Fig. 1).

In order to characterize the solution over what may be a microstructurally significant distance from Vertex A (Fig. 1), we found it necessary to consider not only the leading term in the expansion of  $u_i$ . If the two leading terms are considered, and the crack front is straight, the displacements  $u_i$  may be written [9]

$$u_i = \frac{b\sigma_0}{E} (S^{(1)}(\rho/b)^{\lambda_1^{(1)}} w_i^{(1)}(\phi, \theta) + S^{(2)}(\rho/b)^{\lambda_1^{(2)}} w_i^{(2)}(\phi, \theta)) + \text{smoother terms} \quad (19)$$

The function  $w_i^{(2)}$  has the same characteristics as has  $w_i^{(1)}$  (see the section on Behavior of Exact Solutions). The eigenvalues  $\lambda_1^{(2)}$  have been estimated by solving Eq 12, to 1.218 and 1.000 for  $\nu = 0.3$  and  $\nu = 0.499$ , respectively. There are (independently of  $\nu$ ) two additional eigenvalues  $\lambda_1^{(3)} = 1$  and  $\lambda_1^{(4)} = 1$  corresponding to a rigid body rotation around the  $z$ -axis and a uniform stress  $\sigma_x = \text{constant}$ , respectively. The corresponding two eigenfunctions do not contribute to the  $z$ -displacement used here to estimate the size of the domain of interest. Consequently, these two functions have not been specifically defined in Eq 19.

We are not aware of any theoretical justification that the expansion given by Eq 19 should apply also for the curved crack front studied in the present paper. While mathematical proofs are lacking, we will assume that Eq 19 applies also to a curved crack front for distances  $\rho$  from the vertex which are small compared to the radius of curvature of the crack front. For the cases studied, the results given below support this hypothesis.

By plotting

$$u_3/\rho^{\lambda_1^{(1)}} \text{ versus } \rho^{\lambda_1^{(2)} - \lambda_1^{(1)}}$$

one expects a straight line in the  $\rho$ -interval where the  $z$ -displacement is well approximated by the first two terms in the expansion of  $u_3$ . Figure 12 shows such a plot for the surface crack problem in case of the material with  $\nu = 0.3$ . The set of curves corresponding to different angles  $\theta$  are straight lines in the region  $\rho/b < 0.08$ , at least for  $\theta \geq 30$  deg, indicating that the solution close to the vertex could be well approximated by the two leading terms in the expansion of  $u_i$ .

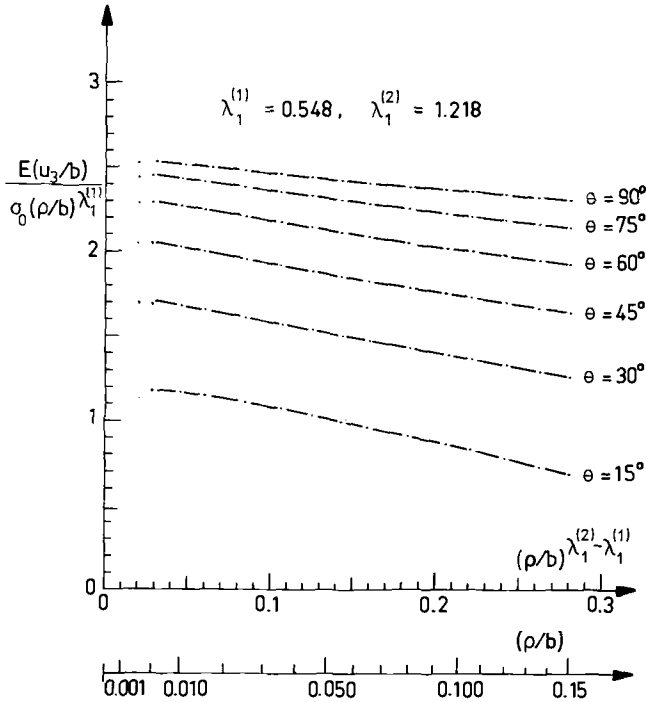


FIG. 12—Calculated  $z$ -displacements obtained using 80-element mesh and uniform  $p$ -distribution  $p = 7$  for  $\nu = 0.30$ .

The vertex-edge intensity factor  $S_E/\sigma_0 \sqrt{\pi b}$  has been determined graphically from Eq 16, using  $h = b$ , to 0.95 units. The edge stress-intensity factor  $K_I$  is then (for  $\nu = 0.3$ ) close to Vertex A approximately given by

$$K_I(y) = 0.95 \sigma_0 \sqrt{\pi b} (y/b)^{\lambda_1 - \lambda_2} \quad \text{for } y/b < 0.01 \quad (20)$$

with  $\lambda_1$  and  $\lambda_2$  as in Eq 17.

For the nearly incompressible material, the domain where the solution  $u_i$  is well approximated by the leading term in Eq 19 is extremely small (Fig. 13). This result seems to contradict those obtained in the model study described in the previous section, where it was found that the higher the Poisson's ratio, the larger is this domain.

The reason for this apparent contradiction is that the size of this domain is very strongly dependent on the boundary conditions. This conclusion has been arrived at by applying different simple load systems on the structure shown in Fig. 4. For example, by applying a linearly varying traction force  $T_x = (2z - h) \sigma_0/h$  and  $T_x = -(2z - h) \sigma_0/h$  on the faces  $x = -h$  and  $z > 0$  and  $z < 0$ , respectively, one will find that the leading term of Eq 19 approximates the solution  $u_i$  well only in a spherical domain with radius  $\rho$  less than  $0.1 \times 10^{-3} h$ . If we apply the simple tensile loading discussed in the previous section, the size of this domain is about  $0.15 h$ .

Our assumption that Eq 19 should apply also for a curved crack front is tentative because the influence of the crack front curvature on higher-order terms in the expansion of  $u_3$  near the vertex is not theoretically known. The numerical data shown in Fig. 13, however, clearly indicate that for  $\theta \geq 30$  and  $\rho < 0.03$  the curves are straight lines. For



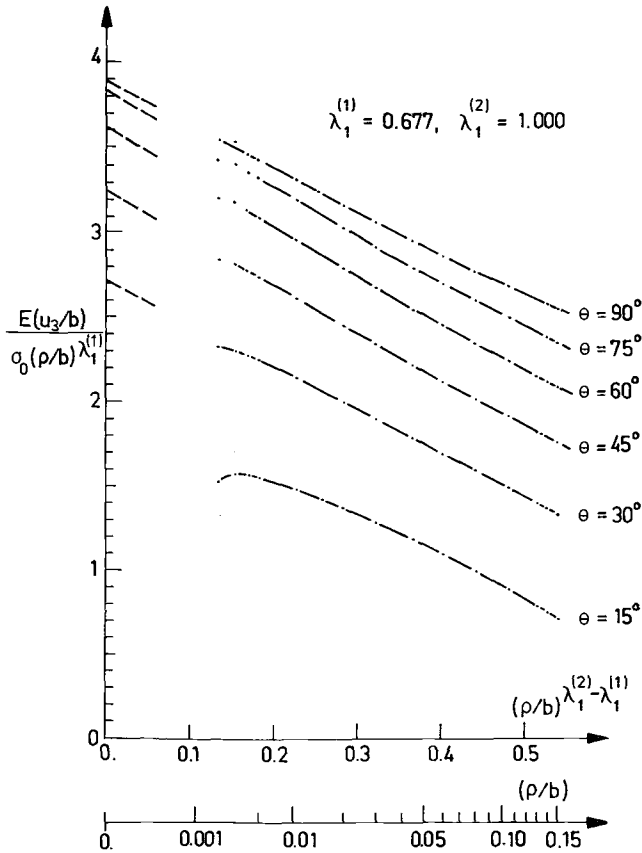


FIG. 13—Calculated  $z$ -displacements obtained using 80-element mesh and uniform  $p$ -distribution  $p = 7$  for nearly incompressible material with  $\nu = 0.499$ . For  $\rho/b < 0.01$ , solutions are obtained with 30-element mesh with uniform  $p = 9$ . Dashed lines are extrapolated values.

angles  $\theta < 30$  deg and  $\rho < 0.01$ , rays  $\theta = \text{constant}$  are located very close to the curved crack front leading to errors of unknown magnitude. In order for us to verify the reliability of the computed data, a box-shaped domain  $1.85 \leq x/b \leq 2.15$ ,  $0 \leq y/b \leq 0.15$ , and  $0 \leq z/b \leq 0.15$  was studied with a 30-element mesh, using displacement boundary conditions from the solution for  $p = 7$  obtained with the 80-element mesh (Fig. 10a).

The solution for uniform  $p = 9$  (each finite element has 250 nodes) was, for  $0.01 < \rho/b < 0.15$  and  $90 \text{ deg} \geq \theta \geq 15 \text{ deg}$ , found to be indistinguishable from that shown in Fig. 13. For  $\rho/b < 0.01$ , the results obtained support the hypothesis that the solution  $u_i$  is well approximated by the two leading terms in the expansion of  $u$ .

By extrapolating the straight lines to  $\rho = 0$  (Fig. 13), we obtain an estimate for  $S^{(1)} w_3^{(1)}(0, \theta)$  (compare Eq 19). Since the function  $w_3^{(1)}(0, \theta)$  is available, we can estimate the constant  $S^{(1)}$  [the constant  $S^{(2)}$  can be estimated from the slopes of the straight lines with known values of  $w_3^{(2)}(0, \theta)$ ]. The eigenfunction  $w_3^{(1)}(\phi, \theta)$  is obtained, except from an arbitrary constant, from Eq 12. We select this constant such that

$$w_3^{(1)}(0, \pi/2) = 1 \quad (21)$$

TABLE 6—Estimated value of parameter  $S^{(1)}$  from Fig. 13 for semi-elliptical surface flaw problem for the case  $\nu = 0.499$ .

Angle $\theta$ , deg	$w_3^{(1)}(0, \theta)$	Estimated Value for $S^{(1)}$
90	1.000	3.89
75	0.982	3.90
60	0.926	3.91
45	0.828	3.91
30	0.685	3.96

The estimated value for  $S^{(1)}$  obtained in this way should be independent of the curve (that is  $\theta$ -angle) used in Fig. 13, provided that our numerical solution is accurate and that the near-vertex solution is well approximated by the two terms on the right-hand side of Eq 19. Data given in Table 6 show that the estimated value of  $S^{(1)}$  indeed with good approximation is independent of the  $\theta$ -angle used in Fig. 13 for estimation of  $S^{(1)}$ . The values for the eigenfunction  $w_3^{(1)}(\phi, \theta)$  have been determined from Eqs 12 and 21 using an eight-element mesh and uniform  $p = 8$ .

For the model problem studied in the previous section, the parameter  $S^{(1)}$  can be estimated to 9.5 units using data from Fig. 6. Also in this case, the value for  $S^{(1)}$  is virtually independent of the  $\theta$ -angle used for the estimation of  $S^{(1)}$ .

To this end, the results shown in Figs. 12 and 13 appear to be accurate and reliable and consistent with the assumption that the near-vertex solution is well approximated by the two first terms on the right-hand side of Eq 19 in case of the semi-elliptical surface crack problem.

### Concluding Remarks

The objective of the present paper is twofold. The first objective is to demonstrate the simplicity, reliability, efficiency, and accuracy obtainable when the  $p$ -version of the finite-element method is employed to solve three-dimensional fracture-mechanics problems.

1. The simplicity of mesh design is exemplified in Fig. 10*b*. In fact the total time needed to manually prepare the mesh, boundary condition data, etc., was only 2 h.
2. The reliability in computed data can be judged from the sequence of solutions obtained. Since there are no locking effects, nearly incompressible materials may be analyzed. Some care has to be taken when evaluating stress-intensity factors for the nearly incompressible material.<sup>7</sup> This was, as discussed previously, not done in the present study.
3. The  $p$ -version is very economic if both computer costs and costs for input data preparation are considered. For example, the six solutions given in Table 5*c* needed only five CPU-hours on an Apollo 4000 work station. The three solutions for  $p = 5, 6$ , and 7 are virtually the same and have been derived only in order to demonstrate the reliability in computed data. In a practical situation, only the solution for  $p = 5$  would be needed. Such a computation requires only one CPU-hour on an Apollo 4000 work station.
4. A very high accuracy is obtainable in practical situations when the  $p$ -version of the finite-element method is employed in combination with a properly graded mesh. For

<sup>7</sup> See footnote 2.

the problems studied here, it seems as if it has been possible to obtain accurate solutions over a length scale covering almost three orders of magnitude.

The second objective is to give detailed numerical solutions for the complete elastic stress fields for the semi-elliptical surface crack problem. Our interest is focused on the behavior of the solution close to the crack front. As in standard LEFM, we have tried to characterize the solution in terms of stress-intensity factors. The calculated values of the edge stress-intensity factor  $K_I$ , not too close to Vertex A, were found to be in good agreement with benchmark data reported in the literature [24]. The set of solutions obtained with the two meshes and the different orders of approximation  $p$  (for  $p > 4$ ) verifies the data given in Ref 24.

Close to Vertex A, the edge stress-intensity factor  $K_I$  does not characterize the solution. The size of the domain where standard fracture mechanics methodology is not applicable is of course of greatest interest. In the present paper we have used simple graphical methods to visualize the behavior of the solution close to Vertex A and, further, to estimate the size of the domain where the vertex singularity dominates the solution.

For a material with a Poisson's ratio of 0.3, our results indicates that the displacements at Vertex A are well approximated by an expression of the type

$$u_i = \frac{b\sigma_0}{E} S^{(1)}(\rho/b)^{\lambda_1^{(1)}} w_i^{(1)}(\phi, \theta) \quad (22)$$

only in a very small region  $\rho/b < 0.01$  (Fig. 12). The value for  $\lambda_1$  obtained in this study for  $\nu = 0.3$  is in good agreement with that given in Ref 11. A vertex-edge intensity factor  $S_E$  used to characterize the edge intensity factor close to Vertex A has been defined and its value was estimated.

Another intensity parameter  $S$  characterizing the general behavior of the solution at the vertex (Eq 20) was estimated from Fig. 13 for the nearly incompressible material. General methods for extraction of vertex  $S$ , vertex-edge  $S_E$ , and edge  $K_I$  intensity factors are currently being implemented in the STRIPE-code [14]. This project is part of a joint project with Professor Ivo Babuška at the University of Maryland.

For the nearly incompressible material the situation is more complex. We have found that for certain simple load systems the domain where the leading term of the vertex singularity governs the solution is very large (for example,  $\rho/h < 0.15$  for the model problem studied in the previous section), while for other equally simple load systems this domain seems to be extremely small.

For the semi-elliptical surface crack problem, the size of this domain is very small as compared to the crack size. This is not to say that the influence of the vertex is confined to a vanishingly small region. Instead, the first and second vertex eigenfunctions seem to characterize the solution well over a distance of the order  $0.03b$  from the vertex.

The experimental data reported in Refs 5 and 6 indicate that for nearly incompressible materials, the vertex singularity strongly influences the overall solution. This is in agreement with our findings. An important addition, however, is that the leading term of the expansion might—depending on boundary conditions—be of negligible importance for the overall behavior of the solution close to the vertex (but not very close to the vertex).

From a fracture mechanics point of view, the highly stressed region may be confined to a volume so small that in many cases it might be smaller than microstructurally characteristic lengths (the second eigenfunction discussed above corresponds to an almost uniform stress distribution, since  $\lambda_1^{(2)} = 1.000$ ). The establishment of a mechanistic design philosophy applicable for crack initiation and crack growth close to a vertex in incompressible materials may thus turn out to be difficult.

## References

- [1] Newman, J. C., Jr., "A Review and Assessment of the Stress-Intensity Factors for Surface Cracks," *Part-Through Crack Fatigue Life Prediction*, ASTM STP 687, J. B. Chang, Ed., American Society for Testing and Materials, Philadelphia, 1979, pp. 16-42.
- [2] *Computational Methods in the Mechanics of Fracture*, S. N. Atluri, Ed., Elsevier Science Publishers B.V., Amsterdam, the Netherlands, 1986.
- [3] Rooke, D. P. and Cartwright, D. J., *Compendium of Stress Intensity Factors*, Her Majesty's Stationery Office, London, 1976.
- [4] *Stress Intensity Factors Handbook*, Y. Murakami, Ed., Pergamon Press, Oxford, U.K., 1987.
- [5] Smith, C. W., Oloosebikan, O., and Lloyd, W. R., "Free Surface Effects on Stress Singularities in Cracked Bodies," *Role of Fracture Mechanics in Modern Technology*, G. C. Sih, H. Nisitani, and T. Ishihara, Eds., North-Holland, Elsevier Science Publishers B.V., Amsterdam, the Netherlands, 1987, pp. 617-627.
- [6] Ruiz, C. and Epstein, J., "On the Variation of the Stress Intensity Factor along the Front of a Surface Flaw," *International Journal of Fracture*, Vol. 28, 1985, pp. 231-238.
- [7] Babuška, I., "The  $p$ - and  $h$ - $p$  Versions of the Finite Element Method. The State of the Art," *Technical Note BN-1156*, Institute for Physical Science and Technology, University of Maryland, Maryland, Sept. 1986. Also to appear in *Proceedings of Finite Element Workshop*, R. Voigt, Ed., Springer Verlag, Berlin.
- [8] Grisvard, P., *Elliptic Problems in Nonsmooth Domains*, Pitman, Boston, 1985.
- [9] Dorr, M. R., "The Approximation of Solutions of Elliptic Boundary-Value Problems via the  $p$ -Version of the Finite Element Method," *SIAM Journal of Numerical Analysis*, Vol. 23, 1986, pp. 58-76.
- [10] Kassir, M. K. and Sih, G. C., "Three-Dimensional Stress Distribution around an Elliptical Crack under Arbitrary Loading," *Transactions, American Society of Mechanical Engineers, Journal of Applied Mechanics*, 1966, pp. 601-611.
- [11] Benthem, J. P., "State of Stress at the Vertex of a Quarter-Infinite Crack in a Half-Space," *International Journal of Solids and Structures*, Vol. 13, 1977, pp. 479-492.
- [12] Bazant, Z. P. and Estenssoro, L. F., "Surface Singularity and Crack Propagation," *International Journal of Solids and Structures*, Vol. 15, 1979, pp. 405-426.
- [13] Walden, H. and Kellogg, R. B., "Numerical Determination of the Fundamental Eigenvalue for the Laplace Operator on a Spherical Domain," *Journal of Engineering Mathematics*, Vol. 11, 1977, pp. 299-318.
- [14] Andersson, B. and Falk, U., "Self-Adaptive Analysis of Three-Dimensional Structures using a  $p$ -Version of Finite Element Method," *Computers and Structures*, in press.
- [15] Gordon, W. J. and Hall, C. A., "Transfinite Element Methods: Blending-Function Interpolation over Arbitrary Curved Element Domains," *Numerische Mathematik*, Vol. 21, 1973, pp. 109-129.
- [16] Vogelius, M., "An Analysis of the  $p$ -Version of the Finite Element Method for Nearly Incompressible Materials. Uniformly Valid, Optimal Error Estimates," *Numerical Mathematics*, Vol. 41, 1983, pp. 39-53.
- [17] Babuška, I. and Suri, M., "The Optimal Convergence Rate of the  $p$ -Version of the Finite Element Method," *SIAM Journal of Numerical Analysis*, Vol. 24, 1987, pp. 750-776.
- [18] Babuška, I. and Szabo, B. A., "On the Rate of Convergence of the Finite Element Method," *International Journal of Numerical Methods Engineering*, Vol. 18, 1982, pp. 323-341.
- [19] Szabo, B. A., "Mesh Design for the  $p$ -Version of the Finite Element Method," Report WU/CCM-85/2, Washington University, St. Louis, MO, 1985.
- [20] Babuška, I. and Osborn, J. E., "Estimate for the Errors in Eigenvalue and Eigenvector Approximation by Galerkin Methods, with Particular Attention to the Case of Multiple Eigenvalues," Technical Note BN-1056, Institute for Physical Science and Technology, University of Maryland, College Park, Maryland, Nov. 1986.
- [21] Szabo, B. A. and Babuška, I., "Computation of the Amplitude of Stress Singular Terms for Cracks and Reentrant Corners," Report WU/CCM-86/1, Washington University, St. Louis, MO, 1986.
- [22] Williams, M. L., "Stress Singularities Resulting from Various Boundary Conditions in Angular Corners of Plates in Extension," *Journal of Applied Mechanics*, Vol. 19, 1952, pp. 526-528.
- [23] Szabo, B. A., "Estimation and Control of Error Based on  $p$ -Convergence," *Accuracy Estimates and Adaptive Refinements in Finite Element Computations*, I. Babuška, O. C. Zienkiewicz, J. Gago, and E. R. de A. Oliveira, Eds., Wiley, New York, 1986, pp. 61-78.
- [24] McGowan, J. J., "A Critical Evaluation of Numerical Solutions to the Benchmark Surface Flaw Problem," *SESA Monograph*, Society for Experimental Stress Analysis, 1980.

## Analysis of Optical Measurements of Free-Surface Effects on Natural Surface and Through Cracks

---

**REFERENCE:** Smith, C. W., Rezvani, M., and Chang, C. W., "Analysis of Optical Measurements of Free-Surface Effects on Natural Surface and Through Cracks," *Surface-Crack Growth: Models, Experiments, and Structures, ASTM STP 1060*, W. G. Reuter, J. H. Underwood, and J. C. Newman, Jr., Eds., American Society for Testing and Materials, Philadelphia, 1990, pp. 99–111.

**ABSTRACT:** After briefly reviewing the algorithms used to convert experimental data into fracture parameters, experimental results are presented from experimental studies conducted on both compact bending specimens containing mutually grown "thumbnailed" cracks through the thickness and naturally grown surface flaws in wide plates. Results are compared with analytical results and are used to explain certain phenomena observed with both thumbnailing of cracks in compact bending specimen and in the analyzing of surface flaws.

**KEY WORDS:** fracture mechanics, optical stress analysis, crack border-free surface intersection effects, experimental stress-intensity factors, dominant eigenvalues

It has been established, both analytically [1,2] and experimentally [3,4], that, when cracks intersect free surfaces at right angles, the inverse square-root stress singularity is lost and that this effect is most significant in nearly incompressible materials. Using compact<sup>2</sup> bending experiments, the first author and his colleagues have validated two optical methods, frozen stress photoelasticity, and high-density moiré interferometry for measuring the order of the dominant singularity near the free surface in nearly incompressible materials [5]. When applied to straight through cracks in polyurethane, moiré interferometric measurements suggest a strong effect at the free surface accompanied by a severe constriction of the zone controlled by the dominant singularity [6]. However, when data are averaged through the plate thickness photoelastically, the linear-elastic fracture-mechanics result is recovered. Moreover, when applied to surface flaws, although reasonable values of the singularity order are obtained photoelastically, efforts to introduce a "corresponding" stress-intensity factor appear to yield ultraconservative results [7].

This paper attempts to present an overview of results of experimental studies to date as well as new studies conducted on both compact bending specimens containing naturally extended "thumbnailed" cracks through the thickness and naturally grown surface flaws in wide plates. Also, where appropriate, results will be compared with analytical results and will be used to suggest explanations for certain phenomena observed with both thumbnailing of cracks in compact bending specimens and in the analyzing of surface flaws.

<sup>1</sup> Alumni professor, graduate research assistant, and graduate research assistant, respectively, Department of Engineering Science and Mechanics, Virginia Polytechnic Institute and State University, Blacksburg, VA 24061.

<sup>2</sup> The word "compact" refers to a single edge cracked specimen thick enough to induce plane strain in a compact specimen.

### Prior Studies

Prior experimental studies have dealt almost exclusively with crack fronts which intersected free surfaces at right angles. Most experiments were conducted on either "artificial" straight front cracks in compact bending specimens under four-point loading [8-11] or naturally grown surface flaws in large flat plates of finite thickness [5,11]. In both cases, the crack border-free surface intersection angle was always 90 deg. The methods of analysis employed, frozen stress and moiré interferometry, yield measurements of the maximum in-plane shearing stress, and the in-plane displacement field, respectively. The methods themselves are well established, but when employed to obtain near tip data for fracture parameter evaluation, they require some refinements in order to achieve good results. These experimental details are briefly described in the Appendix.

Once the measurements are made, it is necessary to develop algorithms for converting the measurements into fracture parameters. For the right-angle intersection studies, Benthien [2] has provided variables separable eigenfunction series expansions for both the stresses and displacements near the crack front-free surface intersection point in the free surface. This solution, together with algorithms developed for linear-elastic fracture mechanics (LEFM) analysis were used as guides in developing the algorithms for use near the free surface. The LEFM algorithms are used in the interior of the body where the lowest eigenvalue, or order of the stress singularity,  $\lambda_r = 1/2$ . Near the free surface where  $\lambda_r$  changes, a "variable eigenvalue" algorithm is used. Since these same algorithms will be employed in the present study, they will be briefly reviewed before proceeding further.

### Analytical Considerations

#### LEFM Algorithms

By choosing a data zone sufficiently close to the crack tip that a Taylor Series Expansion of the nonsingular stresses can be truncated to the leading terms, one may write, for a straight front crack [12] (Fig. 1 where  $t$  direction is constant)

$$\sigma_{ij} = \frac{K_I}{(2\pi r)^{1/2}} f_{ij}(\theta) - \sigma_{ij}^0(\theta), \quad i, j = 1, 2 \quad (1)$$

where

$\sigma_{ij}$  = stress components in the  $x_1x_2$  plane normal to the crack border,  
 $K_I$  = Mode I stress-intensity factor, and  
 $r, \theta$  = polar coordinates with origin at the crack tip.

Along  $\theta = \pi/2$ , the stress fringes spread under Mode I load (Fig. 2) and one has, for the case where  $(\sigma^0)^2$  is small relative to  $8\tau_{\max}^2$  (see Ref 12) (where  $\sigma^0$  is proportional to the contribution of the nonsingular stress to the maximum shear stress,  $\tau_{\max}$  in the  $x_1x_2$  plane)

$$\tau_{\max} = \frac{K_I}{(8\pi r)^{1/2}} + \frac{\sigma^0}{\sqrt{8}} \quad (2)$$

Now defining an "apparent" stress-intensity factor (SIF),

$$K_{AP} = \tau_{\max}(8\pi r)^{1/2} \quad (3)$$

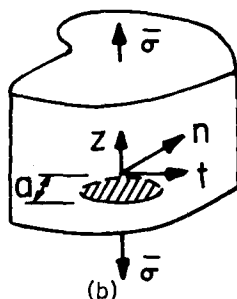
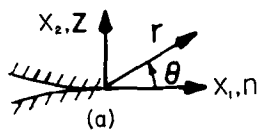


FIG. 1—Near-tip problem geometry and notation.

and normalizing with respect to  $\bar{\sigma}(\pi a)^{1/2}$  where  $\bar{\sigma}$  represents the remote stress and  $a$  the crack length, one has

$$\frac{K_{Ap}}{\bar{\sigma}(\pi a)^{1/2}} = \frac{K_I}{\bar{\sigma}(\pi a)^{1/2}} + \frac{\sigma^0}{\bar{\sigma}} \left( \frac{r}{a} \right)^{1/2} \quad (4)$$

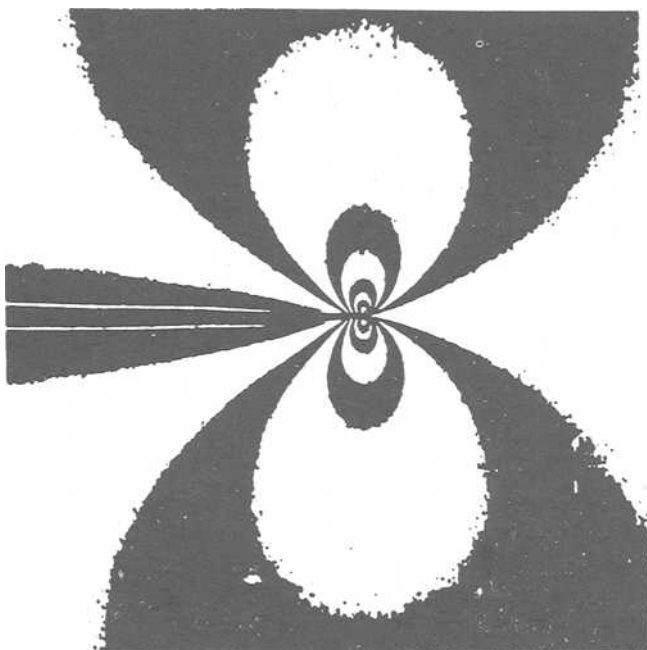


FIG. 2—Near-tip Mode I stress fringe pattern.

which suggests an elastic linear zone (ELZ) in a plot of

$$\frac{K_{Ap}}{\bar{\sigma}(\pi a)^{1/2}}$$

versus  $(r/a)^{1/2}$  with a slope of  $\sigma^0/\bar{\sigma}$ . Experience shows this zone to lie between  $(r/a)^{1/2}$  values of approximately 0.2 to 0.4 (or above) in two-dimensional problems. By extracting optical data from this zone and extrapolating across a near tip nonlinear zone, one can obtain an accurate estimate of  $K_I/\bar{\sigma}(\pi a)^{1/2}$ . This is illustrated in Fig. 3 for two slices at different locations in a compact bending specimen. This approach may be directly extended to three-dimensional (3-D) problems involving curved crack fronts by replacing  $i, j$  values of 1, 2 by  $n, z$  where the  $nz$  plane is normal to the crack border at each point along the flaw border and the  $nzt$  coordinate system is a local cartesian system which follows the crack border (Fig. 1). In 3-D problems, the outer boundary of the data zone is usually restricted to  $(r/a)^{1/2} \approx 0.4$  or less.

In the frozen stress algorithm, the effect of the nonsingular stress was included since it was independent of  $r$ . However, one may, for sufficiently small values of  $r$ , neglect the effect of the  $\sigma^0$  terms in the displacement field equations. Thus, along  $\theta = \pi/2$ , for a 3-D problem, one may write

$$u_z = C'(K_I)_{Ap} r^{1/2} \quad (5)$$

and extrapolate the linear part of  $u_z/C'r^{1/2}$  versus  $r^{1/2}$  to the origin as before.

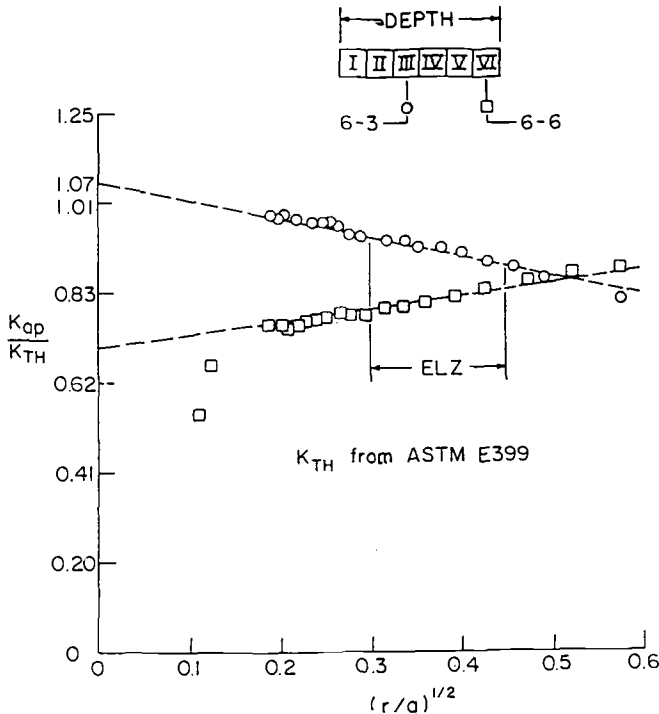


FIG. 3—Determination of  $K_I$  from near-tip data.



### Variable $\lambda$ Algorithms

Using Benthems analysis and the LEFM results as a guide, one can construct the following functional forms for the near tip  $\sigma_{ij}$  and  $u_i$

$$\sigma_{ij} = \frac{F_{ij}(\lambda_\sigma, \theta)}{r_\sigma^\lambda} - \sigma_{ij}^0 \quad (i, j = n, z) \quad (6)$$

where  $\sigma_{ij}^0 = \sigma^0$  for  $i, j = n$  and zero for all other values of  $i, j$

$$u_i = D_i(\theta)r^{\lambda_u} \quad (7)$$

where  $\lambda_\sigma$  and  $\lambda_u$  represent the lowest dominant eigenvalues in the local stress and displacement field equations, respectively, and  $\lambda_\sigma = |1 - \lambda_u|$ . Here similar functional forms are implied near the crack tip for  $\sigma_{ij}$  and  $u_i$  as in LEFM, but  $\lambda$  is undetermined. From Eq 7, one may, along  $\theta = \pi/2$ , write

$$u_z = D_z r^{\lambda_u}$$

$$\log u_z = \log D_z + \lambda_u \log r \quad (8)$$

(all logs are natural)

and determine  $\lambda_u$  from a plot of  $\log u_z$  versus  $\log r$  in the linear range.

Independent determination of  $\lambda_\sigma$  may also be carried out, but the procedure is not as straightforward due to the presence of the second term in Eq 6 and the highly 3-D nature of the near-tip stress state at the free surface. If one evaluates  $\tau_{\max}$  from Eq 6 along  $\theta = \pi/2$  as done in LEFM, one obtains

$$\tau_{\max}^{nz} = \frac{\lambda_\sigma K_{\lambda_\sigma}}{\sqrt{2\pi}r^{\lambda_\sigma}} + \frac{\sigma^0}{2} \sin(\lambda_\sigma + 1) \frac{\pi}{2} = \lambda_\sigma \frac{(K_{\lambda_\sigma})Ap}{\sqrt{2\pi}r^{\lambda_\sigma}} \quad (9)$$

where  $K_{\lambda_\sigma}$  may be designated a stress eigenfactor. Defining  $\tau_0 = (\sigma^0/2) \sin(\lambda_\sigma + 1)(\pi/2)$ , one obtains

$$\log(\tau_{\max}^{nz} - \tau_0) = \log \left\{ \frac{\lambda_\sigma K_{\lambda_\sigma}}{\sqrt{2\pi}} \right\} - \lambda_\sigma \{\log r\} \quad (10)$$

Thus, if one can determine  $\tau_0$ , one can plot  $\log(\tau_{\max}^{nz} - \tau_0)$  versus  $\log r$  and obtain  $\lambda_\sigma$  as the slope of the linear range. Since LEFM is expected to prevail away from the free surface, one may conjecture that the value of  $\tau_0$  as determined from LEFM away from the free surface should suffice as an adequate correction for the nonsingular field effect except near the free surface. Data for such a determination of  $\tau_0$  is shown in Fig. 4 for an interior slice from a surface flaw where  $\lambda_\sigma \approx 0.5$ .

From Eq 2, one sees that, in LEFM,  $\tau_0 = \sigma^0/\sqrt{8}$ . Thus  $\tau_0$  can be determined from the slope of the normalized  $K_{Ap}$  versus  $r^{1/2}$  graph.

### Experimental Results

In addition to the prior studies on straight front cracks and surface flaws described above, experiments were conducted on "thumbnail" shaped natural cracks grown in com-

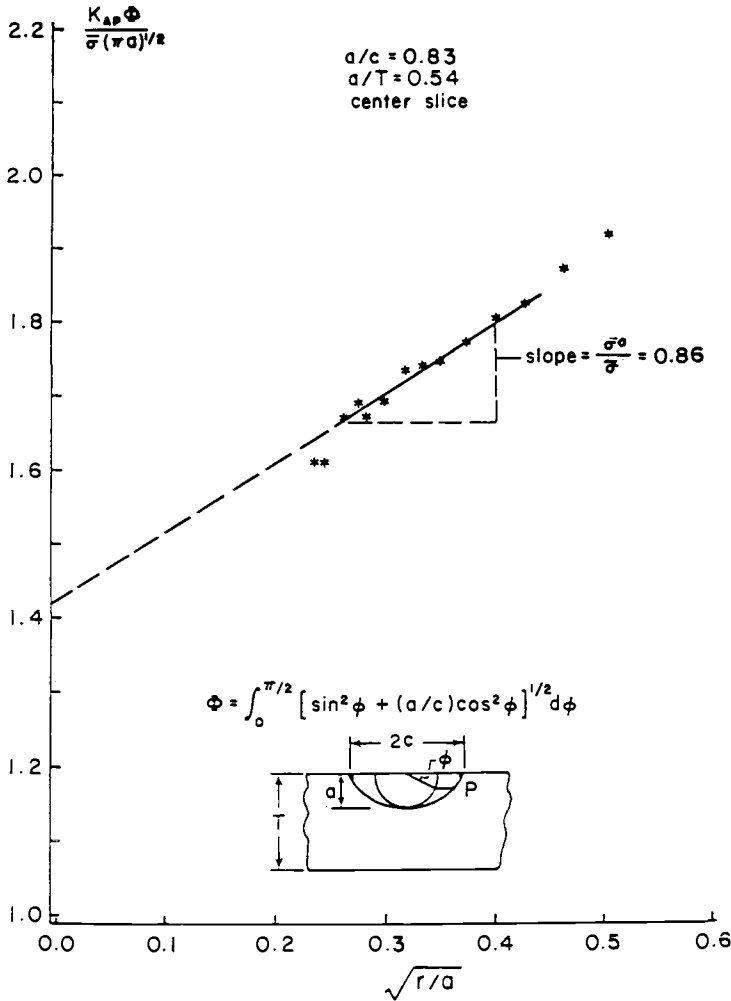


FIG. 4—Determination of nonsingular effect in LEFM.

pact bending specimens. Crack front shapes and free-surface intersection angles are given for these tests in Fig. 5.

Frozen stress slices removed from one side of the centerline of the crack front were oriented parallel to the free surface, and those on the other side (except for the surface slice) were oriented normal to the crack border. The difference in the resulting values of  $\lambda_s$  obtained using Eq 10 due to slice orientation for the interior slices appeared to be insignificant. The average value of  $\lambda_s$  obtained from the two surface slices was 0.315, which compares favorably with Benthem's value of 0.33 for a 90 deg intersection angle. The average boundary intersection angle here was 104 deg.

Takukada [13] used a boundary integral approach to extract the singularity orders from surface flaws in a half space intersecting the free surface at arbitrary angles. A comparison of moiré results at the free surfaces of compact bending specimens containing "thumb-nailed" cracks with Takukada's results is given in Table 1.

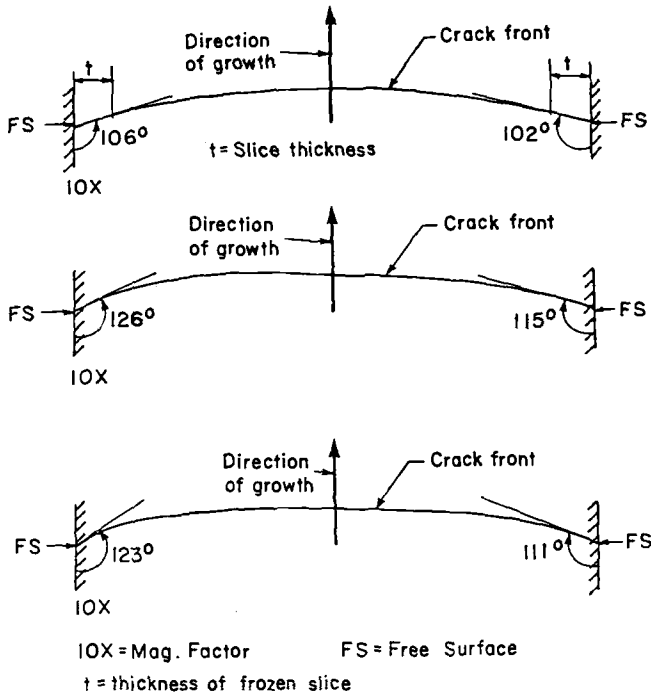


FIG. 5—Shape of "thumbnail" crack in compact bending specimen with boundary intersection angles.

In his analysis, Benthem obtained a value of  $\lambda_u = 0.67$  at the free surface for the case  $\alpha = 90$  deg. Clearly, Takakuda's analysis suggests that increasing  $\alpha$  above 90 deg will result in a decreasing value of  $\lambda_u$ . The algorithm used for obtaining experimental values of  $\lambda_u$  was based upon  $\alpha = 90$  deg and led to experimental values of  $\lambda_u$  which were higher than predicted by Takakuda. However, if one introduces as a simple modification factor  $\cos(\alpha - 90 \text{ deg})$  into the algorithm, results are found to be much closer to Takakuda's results, as shown in Table 1.

It has been suggested, that, when a crack thumbnails, it is attempting to restore the LEFM condition ( $\lambda_u = \frac{1}{2}$ ) along its border. If true, then  $\lambda_u$  should have a physical lower limit of 0.5. The preceding experimental data would seem to support this conjecture.

However, the authors feel that further collaborative experiments would be necessary to verify this conjecture.

TABLE 1—Values at  $\lambda_u$

Test No.	$\alpha$ deg	$\lambda_u$ (Analysis)	$\lambda_u$ (Experiment)	$\lambda_u$ (Experiment) $\cos(\alpha - 90 \text{ deg})$
1 Sp.A	111	0.49	0.57	0.53
2 Sp.A	115	0.47	0.54	0.49
3 Sp.B	126	0.40	0.60	0.49
AVG	117	0.45	0.57	0.50

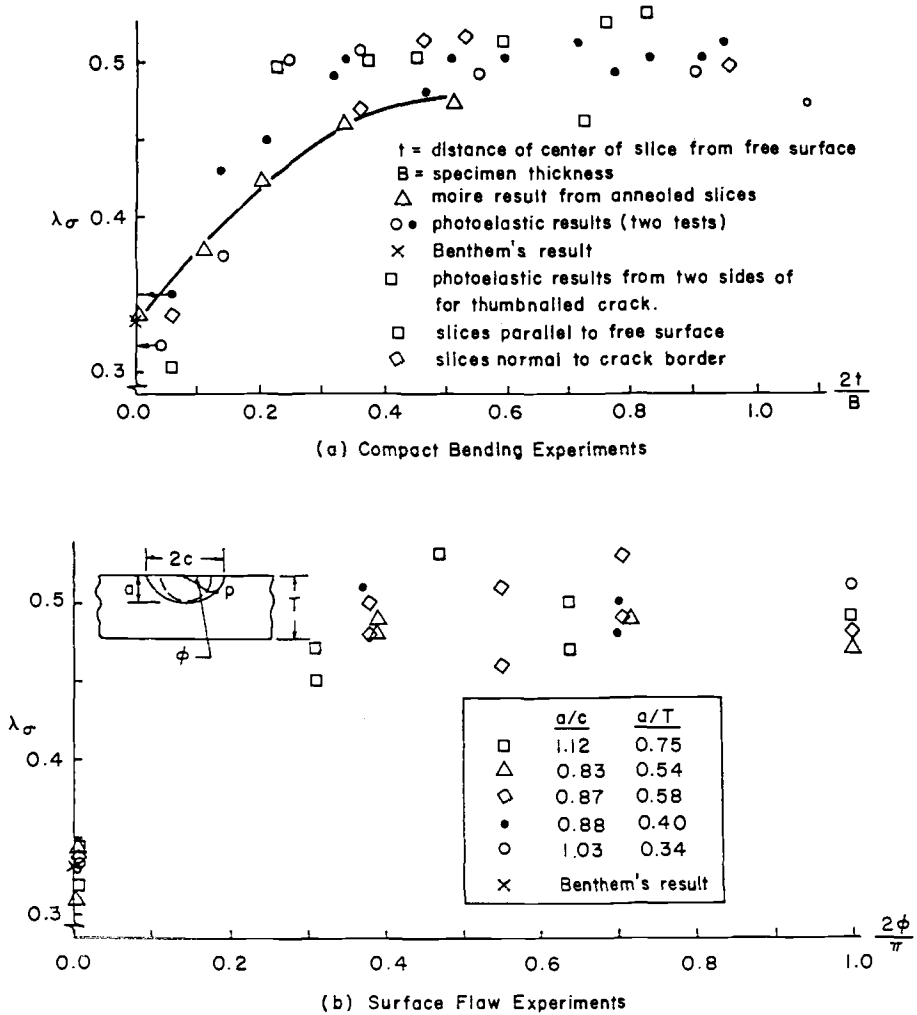


FIG. 6—Summary of results for determination of  $\lambda$ .

A summary of all of the results obtained to date on  $\lambda$  determination is presented in Fig. 6. A study of Fig. 6 leads one to the following observations:

1. Benthem's solution appears very accurate for the 90 deg crack front free surface intersection angle for both straight front and surface flaws.
2. A transition zone in  $\lambda$  occurs near the boundary.
3. Thumbnailing apparently alters the value of  $\lambda$  at the free surface and may be doing so in such a way as to restore the LEFM condition.

### Practical Application

In order to adapt measured variations in  $\lambda$  at the free surface to the framework of LEFM, we have suggested in prior work the use of a quantity  $K_{cor}$ , the "corresponding"

stress-intensity factor, which replaces the quantity  $(K_{\sigma})_{Ap}/r^{1/2}$  by  $(K_{cor})_{Ap}/r^{1/2}$  so that the dimensions of the SIF are restored.  $K_{cor}$  becomes the SIF which would exist if the free-surface effect were not present and the above dimensional substitution leads to [7]

$$K_{cor} = \frac{K}{2\lambda_s} \quad (11)$$

Using only thickness averaged photoelastic data through a surface slice, we can compare SIF distributions from photoelastic data with finite-element results and  $K_{cor}$  distributions in Fig. 7 for a surface flaw. Since the use of  $K_{cor}$  should eliminate the effect of the free surface, we would expect a smooth distribution with near zero slope at the free surface, since elimination of the free surface effect should produce an SIF curve which should be symmetric with respect to the ordinate. This obviously does not occur. A possible explanation may be that neither the finite-element results nor the photoelastic result are suffi-

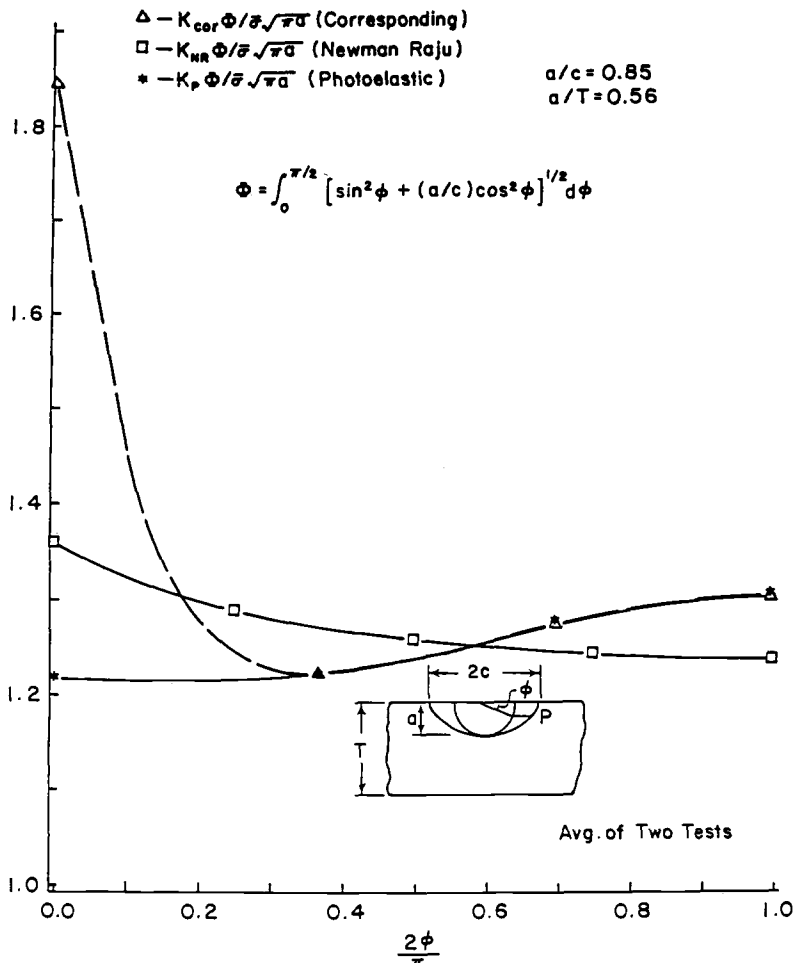


FIG. 7—Normalized SIF distributions.

ciently close to the free surface to capture a sharp downturn in the SIF distribution suggested by some analysts.

The photoelastic result is obtained from shear stresses reduced somewhat by the free-surface effect but using the LEFM algorithm ( $\lambda_e = \frac{1}{2}$ ). The finite-element result ignores any change in  $\lambda_e$  from a value of one half.

In view of these results, it would appear more practical to use the photoelastic result at the free surface unless and until accurate moiré data are obtained for the free surface itself.

Finally, thumbnailing of straight front cracks seems to reduce  $\lambda_e$  from its value for  $\alpha = \pi/2$  toward the LEFM result. This latter effect needs further study.

### *Acknowledgments*

The authors wish to acknowledge the contributions of their colleagues as noted in the text and the support of the U.S. Air Force Astronautics Laboratory under Contract No. F04611-87-C-0057.

## APPENDIX

### **Optical Methods of Analysis**

When optical methods are applied to cracked body problems, some equipment modifications may be anticipated in order to enhance near-tip measurement. They will now be briefly described.

#### *Frozen Stress Analysis*

This method of analysis was introduced by Oppel [14] in 1936. It involves the use of a transparent plastic which exhibits, in simplest concept, diphasic mechanical and optical properties. That is, at room temperature, its mechanical response is viscoelastic. However, above its "critical" temperature, its viscous coefficient vanishes, and its behavior becomes purely elastic, exhibiting a modulus of elasticity of about 0.2% of its room temperature value and a stress fringe sensitivity of 20 times its room temperature value. Thus, if the photoelastic models are loaded above critical temperature, cooled under load, and then the load is removed, only negligible elastic recovery occurs at room temperature and the stress fringes and deformations produced above critical temperature are retained. Moreover, the "frozen model" may be sliced without altering its condition.

In order to determine useful optical data from frozen stress analysis, one needs to suppress deformations near the crack tip in the photoelastic material in its rubbery state above critical temperature and to be able to produce the same crack shape and size produced in the prototype. In order for one to accomplish the first objective, applied loads are kept very small, and a polariscope modified to accommodate the tandem application of partial mirror fringe multiplication and Tardy compensation is employed. Such a polariscope is pictured in Fig. 8. Normally, fifth multiples of fringe patterns are read to a tenth of a fringe, thus providing adequate data within about 1 mm of the crack tip to two hundredths of a fringe order.

Natural crack shapes are obtained by introducing a starter crack at the desired location in the photoelastic model of the structure before stress freezing by striking a sharp blade held normal to the crack surface with a hammer. The starter crack will emanate from the blade tip and propagate dynamically a short distance into the model and then arrest. Further growth to the desired size is produced when loaded monotonically above critical temperature. The shape of the crack is controlled by the body geometry and loads. By comparing crack shapes grown in photoelastic models by this process to those grown under

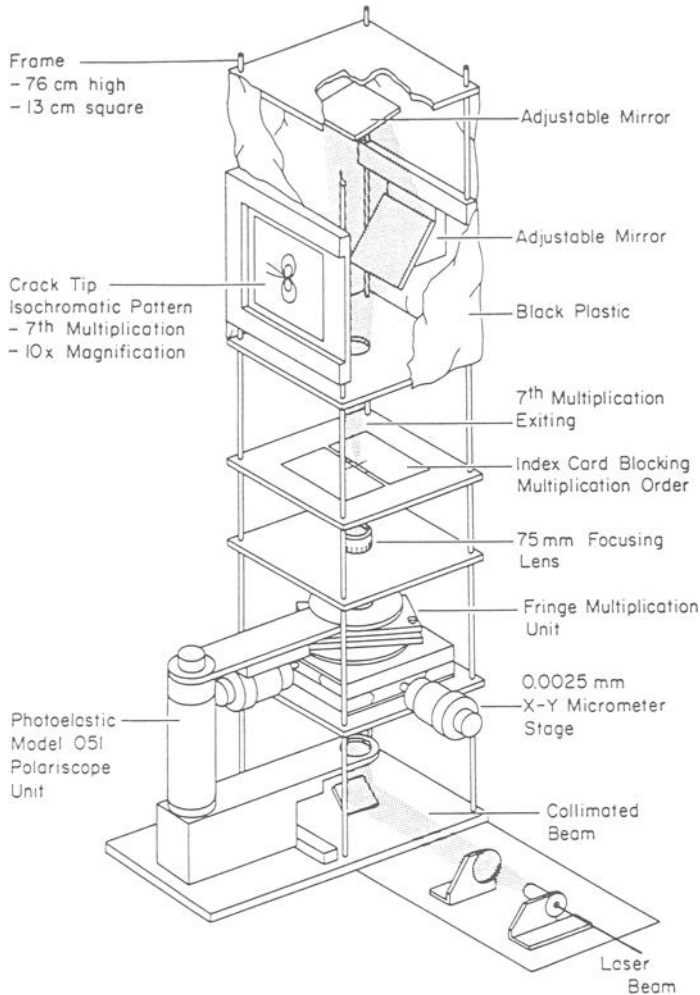


FIG. 8—Refined polariscope.

tension-tension fatigue loads in steel, researchers [15] have obtained excellent correlation even when some crack closure was present on the free surface of the latter. It appears that the cracked body geometry and loads control the crack shape in thick, isotropic bodies and that the stress ratio  $R$  (as long as it is positive) and plasticity or closure effects are of secondary importance.

Artificial cracks are made by machining into the body a desired shape, maintaining a V-notch tip with an included angle not exceeding 30 deg. With this angle, near-tip stress fields are essentially the same as for branch cuts.

Removal of thin slices of material which are oriented mutually orthogonal to the crack front and the crack plane locally and analysis of these slices will yield the distribution of the maximum shear stress in the  $nz$  plane of Fig. 1. Then, by computing this stress from the near-tip Mode I singular stress field equations, including the contribution of the regular stresses in the near tip zone as constants, one can arrive at an algorithm for extracting the SIF for each slice.

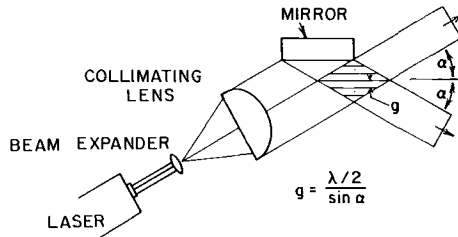


FIG. 9—Virtual grating.

### Moiré Interferometry

This method of analysis was introduced by Weller et al. [16] in 1948. As was the case with the frozen stress method, some modification of the usual approach is desirable in order to obtain accurate near tip data. In the present case, a "virtual" grating was constructed optically by reflecting part of an expanded laser beam from a mirror so as to intersect the unreflected part of the beam, forming walls of constructive and destructive interference which serve as the master grating (Fig. 9). The specimen grating, a reflective-phase grating, is viewed through the virtual grating as it (the former) deforms in order to see the moiré fringes proportional to the in-plane displacement normal to the grating. By photographing the moiré fringe patterns produced on the surface of a frozen slice after it has been annealed to its stress free state, one can measure the inverse of the displacement fields produced in the plane of the slice by stress freezing. Since our interest here focuses heavily upon surface effects, note that the photoelastic data yield information which is averaged through the thickness of a single slice which is usually of the order of 0.50 mm, while the moiré data yield data from the surface itself upon which the moiré grating was placed.

It follows that frozen stress data from a surface slice will closely represent free-surface information only if there is little change in this information through the slice thickness.

Details of the above methods are found in Refs 12 and 17.

### References

- [1] Benthem, J. P., "On an Inverse Theorem for Conical Regions of Elasticity," *Journal of Elasticity*, Vol. 9, No. 2, 1979, pp. 159-169.
- [2] Benthem, J. P., "The Quarter Infinite Crack in a Half Space: Alternative and Additional Solutions," *International Journal of Solids and Structures*, Vol. 16, 1980, pp. 119-130.
- [3] Smith, C. W. and Epstein, J. S., "Measurement of Three Dimensional Effects in Cracked Bodies," *Proceedings of 5th International Conference on Experimental Mechanics*, June 1984, pp. 102-110.
- [4] Smith, C. W., Theiss, T. J., and Rezvani, M., "Experimental Analysis of Crack Front-Free Surface Intersection Phenomena," *Proceedings of 11th Canadian Congress on Applied Mechanics*, Vol. 1, 1987, pp. 180-181.
- [5] Smith, C. W. and Rezvani, M., "Measurement of Boundary Effects in Surface Flaws," *Application at Advanced Strain Measurement Techniques*, British Society of Strain Measurement, Whittle's Publishing, Caithness, U.K.
- [6] Smith, C. W., Rezvani, M., and Theiss, T. J., "Boundary Effects on Stress Singularities in Cracked Bodies," *Proceedings of 1987 Annual Conference on Experimental Mechanics*, 1987, pp. 215-220.
- [7] Smith, C. W. and Rezvani, M., "Intersection of Surface Flaws with Free Surfaces," *Fracture Mechanics: Perspectives and Directions*, Vol. 20, ASTM STP 1020, American Society for Testing and Materials, Philadelphia, 1989, pp. 317-326.
- [8] Smith, C. W., Olasebikan, O., and Lloyd, W. R., "Free Surface Effects on Stress Singularities in Cracked Bodies," *Proceedings of an International Conference on the Role of Fracture Mechanics in Modern Technology*, North Holland, Amsterdam, New York, Tokyo, 1987, pp. 617-628.



- [9] Smith, C. W., Olasebikan, O., and Lloyd, W. R., "Boundary Effects in Fracture Mechanics," *Proceedings of 1985 Annual Conference on Experimental Mechanics*, June 1985, pp. 113-118.
- [10] Smith, C. W. and Epstein, J. S., "Boundary Layer Measurements in Cracked Body Problems," *Proceedings of SECTAM XII*, 1984, pp. 355-360.
- [11] Smith, C. W. and Epstein, J. S., "Measurements of Near Tip Fields Near the Right Angle Intersection of Straight Front Cracks," *Modelling Problems in Crack Tip Mechanics*, Martinus-Nijhoff, Amsterdam, the Netherlands, 1984, pp. 325-334.
- [12] Smith, C. W., "Use of Three-Dimensional Photoelasticity and Progress in Related Areas," Chapter 1, *Experimental Techniques in Fracture Mechanics 2*, Society for Experimental Stress Analysis (now Society for Experimental Mechanics), monograph, A. S. Kobayashi, Ed., Iowa State Press, Ames, IA, pp. 3-58.
- [13] Takakuda, K., "Stress Singularities Near Crack Front Edges," *Bulletin, Japan Society of Mechanical Engineers*, No. 236, Feb. 1985, pp. 225-231.
- [14] Oppel, G., "Polarisationsoptische Untersuchung Raumlicher Spannungs und Dehnungszustände," *Forschung aus dem Gebiete des Ingenieurwesens*, Vol. 7, 1936, pp. 240-248.
- [15] Smith, C. W., "Measurement of Three-Dimensional Effects in Cracked Reactor Vessel Components," *Transactions of the 8th International Conference on Structural Mechanics in Reactor Technology*, Vol. 6, Aug 1985.
- [16] Weller, R. and Shepard, B. M., "Displacement Measurement by Mechanical Interferometry," *Proceedings of Society for Experimental Stress Analysis*, Vol. 6, No. 1, 1948, pp. 35-38.
- [17] Smith, C. W. and Kobayashi, A. S., "Experimental Fracture Mechanics," Chapter 20, *Handbook on Experimental Mechanics*, A. S. Kobayashi, Ed., Society for Experimental Mechanics, Prentice-Hall, Englewood Cliffs, NJ, 1987, pp. 891-956.

## Optical and Finite-Element Investigation of a Plastically Deformed Surface Flaw Under Tension

**REFERENCE:** Olinkiewicz, J. C., Tippur, H. V., and Chiang, F. P., "Optical and Finite-Element Investigation of a Plastically Deformed Surface Flaw Under Tension," *Surface-Crack Growth: Models, Experiments, and Structures*, ASTM STP 1060, W. G. Reuter, J. H. Underwood, and J. C. Newman, Jr., Eds., American Society for Testing and Materials, Philadelphia, 1990, pp. 112-129.

**ABSTRACT:** A combined moiré method has been used to experimentally obtain three-dimensional surface deformations in a plastically deformed tensile strip containing a surface flaw. A finite-element approach using experimentally obtained displacements as boundary conditions is followed to investigate the interior deformation fields and to study several parameters of interests such as  $J$ , crack-tip singularity and  $J$ , crack-mouth opening displacement equivalence for a chosen specimen geometry.

**KEY WORDS:** surface flaw, plasticity, optical methods, finite-element analysis, work hardening,  $J$ -integral, singularity

Much of the previous research on surface flaws has been in the area of elastic analysis of surface crack configurations under different types of loading. Early works of Irwin [1], Kobayashi and Moss [2], Rice and Levy [3], Newman and Raju [4,5], Smith and Sorensen [6], and Smith et al. [7], have aimed at describing stress-intensity factor distribution along semielliptical crack fronts with some consideration given to crack-tip plasticity. Elastic-plastic analysis of such crack configurations has also been undertaken by several investigators [8-14]. The main thrust in all these has been to characterize fracture parameters such as  $K$  or  $J$ , growth of plastic zone and deformation fields, using either experimental or numerical approaches.

The present work employs a combined optical and numerical scheme for analyzing fully plastic deformation fields ahead of a part circular surface notch in a hardening alloy (Al 5052-H32) under tension. Whole-field three-dimensional (3-D) deformations were measured on the surfaces of a tension specimen using combined moiré method [15]. Experimental results have been used as boundary conditions in a nonlinear finite-element (FE) analysis to study the interior deformation fields. Approximate  $J$  values have been calculated using experimental as well as experimental FE results. Equivalence of  $J$  and crack-mouth opening displacement (CMOD) is considered. The crack-tip singularity is empirically described by simple polynomial functions.

<sup>1</sup> Research assistant, research assistant, and leading professor, respectively, Laboratory for Experimental Mechanics Research, State University of New York at Stony Brook, Stony Brook, NY 11794-2300.

### Experimental Method

A combined grating method is used to study the problem of a part-circular surface notch in an aluminum plate under tension. The technique incorporates a combination of in-plane and projection moiré methods to simultaneously obtain all three displacement components ( $u$ ,  $v$ , and  $w$ ) on both the front (crack) and back surfaces. In order to measure in-plane displacements, a 20 lpmm ( $1/p$ ,  $p$  = pitch) cross grating is photoprinted on the front and back surfaces of the specimen. In addition, a line grating of approximately 4 to 8 lpmm ( $1/p'$ ) is projected onto both of the surfaces to obtain the out-of-plane displacements. The optical arrangement used for this purpose is shown schematically in Fig. 1a. Collimated light impinges on a line grating to produce regular and diffracted wavefronts, which are collected by a field lens. A diffraction spectrum in the form of equally spaced bright dots or diffraction orders is formed at its focal plane where a mask blocks out all but the  $\pm 1$  diffraction orders. These diffraction orders are collected by a third-field lens to form two nearly collimated beams with an angle  $2\alpha$  between them. Within the intersecting beams there exists a standing wave of pitch  $[\lambda/(2 \sin \alpha)]$  where  $\lambda$  is the wavelength of light. Due to the angular parameter  $\beta$  of the projection system, the pitch of the grating on the specimen surface is

$$p' = \frac{\lambda}{2 \sin \alpha \cos \beta} \quad (1)$$

All these gratings are recorded by single exposures prior to loading (master or reference grating) as well as at various load levels (deformed gratings). Figure 1b shows a typical recorded grating in which the fine dots correspond to the photoprinted cross grating whose intensity is modulated by the low-frequency projected grating.

Optical spatial filtering [15,16] is used to separate the  $u$ ,  $v$ , and  $w$  displacement fields for each applied load. The set up used for this purpose is schematically shown in Fig. 2a. When a matched pair of deformed and undeformed gratings is placed in a converging beam of light a diffraction spectrum such as the one shown in Fig. 2b is produced at the focal plane of the transform lens. A mask is placed in this plane to block all but the appropriate diffraction order such that the corresponding displacement field ( $u$ ,  $v$ , or  $w$ ) is displayed at the image plane of the reconstruction lens. The displacements are governed by

$$u = N_1 p \quad (2)$$

$$v = N_2 p \quad (3)$$

$$w = \frac{N_3 p'}{\tan \beta} \quad (4)$$

$N_1$ ,  $N_2$ , and  $N_3 = 0, \pm 1, \pm 2, \dots$ , where  $N_1$ ,  $N_2$ ,  $N_3$  are the fringe orders.

### Experimental Results and Discussion

Three crack configurations have been studied using the above method. Specimens 50.8 mm wide by 6.35 mm thick (Fig. 3) were machined from aluminum 5052-H32 sheet stock such that the rolling direction is transverse to the loading axis. Material characteristics (Fig. 3b) were obtained from a uniaxial tension test (Young's modulus  $E = 6700 \text{ kg/mm}^2$ , yield

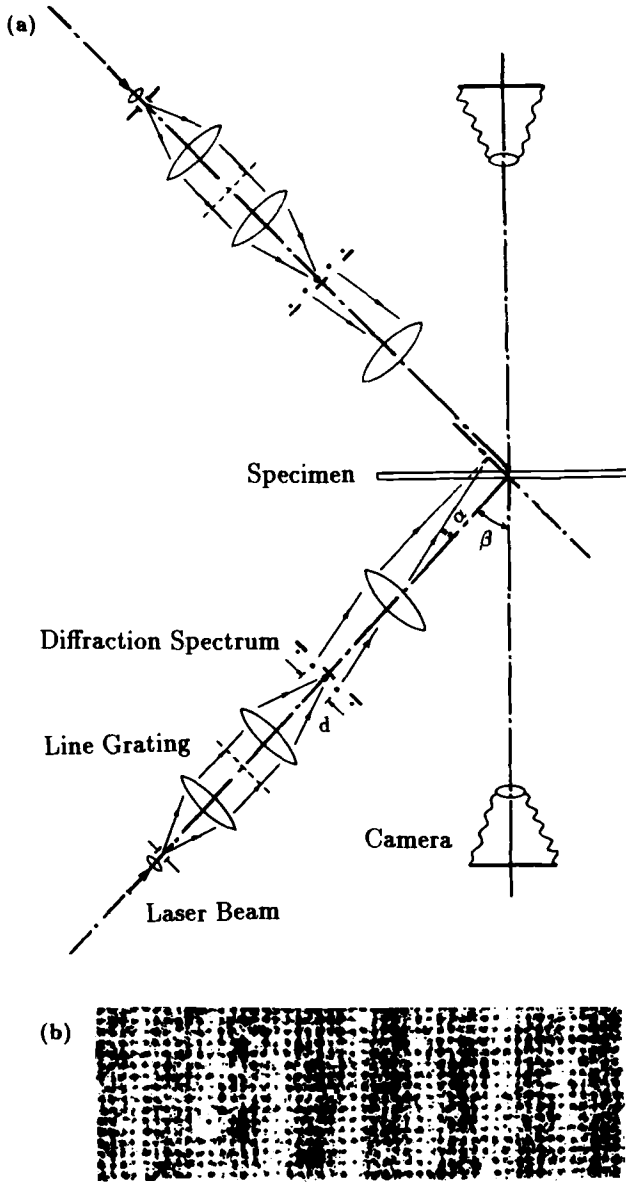


FIG. 1—(a) Optical arrangement for combined moiré method; (b) enlarged recorded grating.

stress  $\sigma_0 = 14.3 \text{ kg/mm}^2$ , and hardening exponent  $n = 6.4$ ). The surface flaws were created using a 25.4-mm-diameter, 0.20-mm-thick saw blade, resulting in a square notch tip profile. Three different surface notch depths, namely,  $a = 4, 3$ , and  $2 \text{ mm}$ , have been studied. These crack depths correspond to the ratios  $(a/t) = 0.63, 0.47, 0.31$  and  $(a/c) = 0.43, 0.36, 0.29$  where  $c$  and  $t$  are the half surface crack length and the thickness of the specimen, respectively. The specimens were subjected to monotonically increasing far-field stress lev-

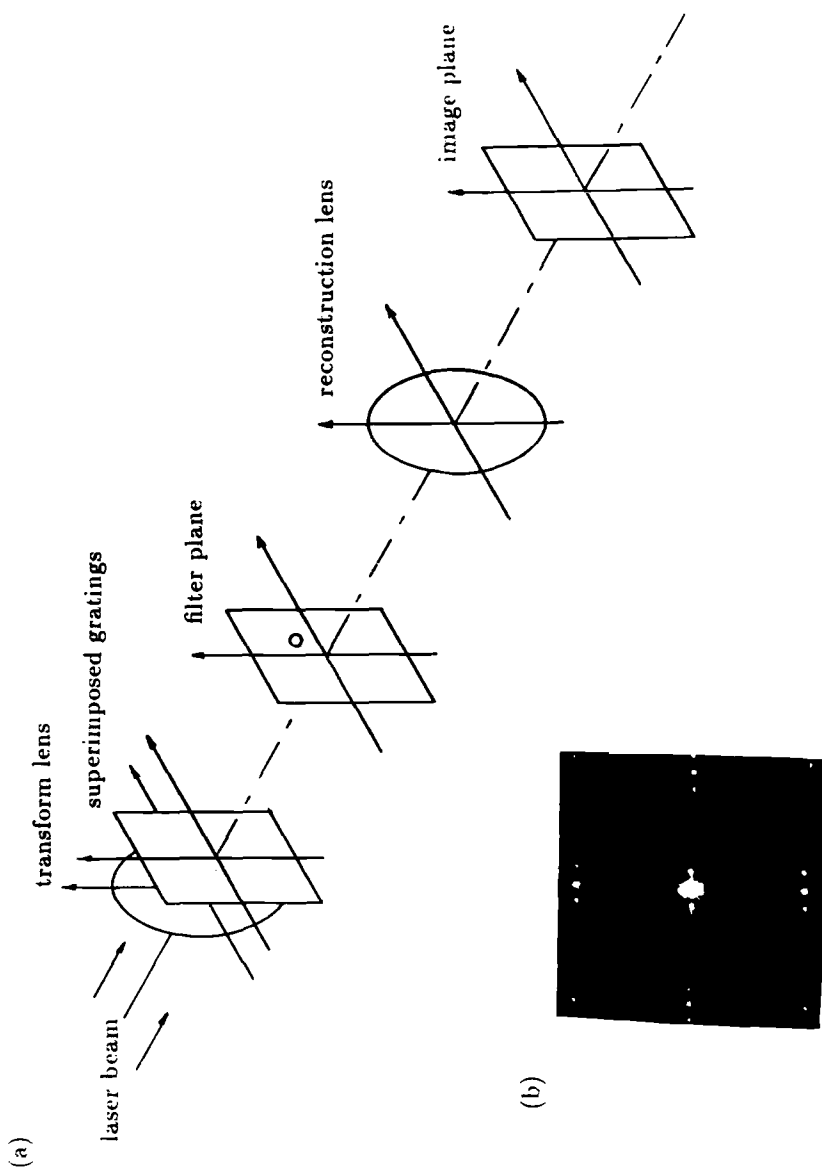


FIG. 2—(a) Schematic for optical spatial filtering; (b) diffraction spectrum.

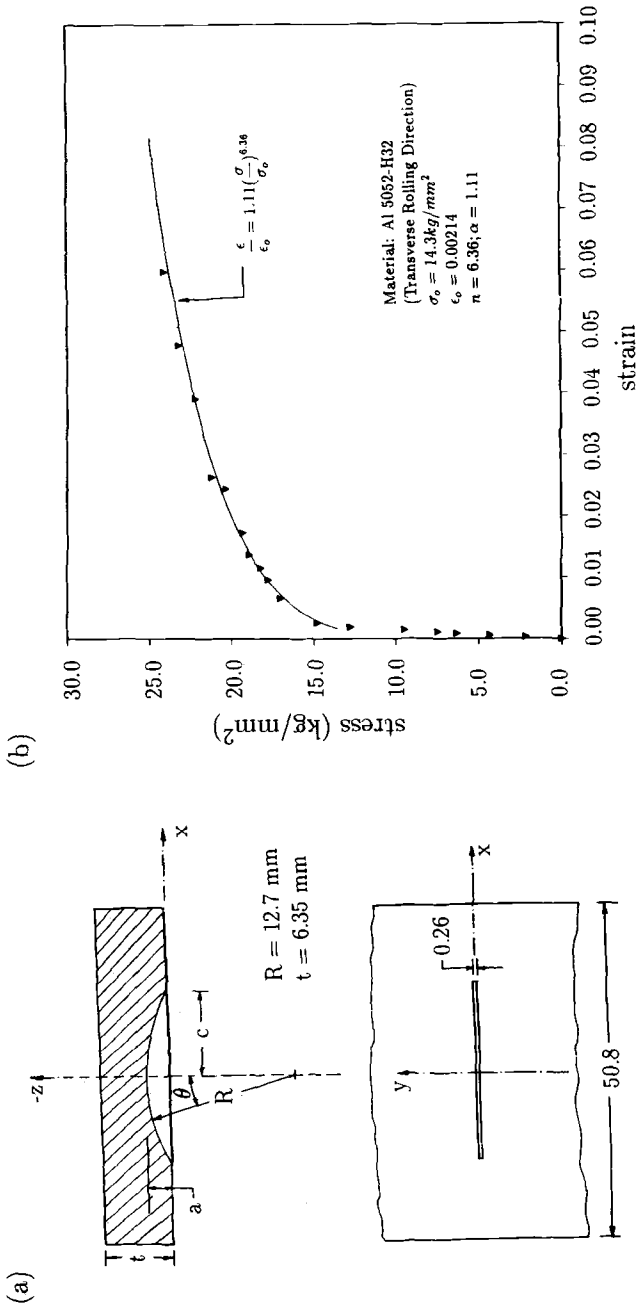


FIG. 3—(a) Specimen geometry; (b) material calibration curve.

els well beyond the yield stress of the material. Contours of constant displacement corresponding to far-field stress ( $\sigma_\infty$ ) =  $1.12\sigma_0$ ,  $1.28\sigma_0$ , and  $1.36\sigma_0$  for the 4, 3, and 2-mm-deep cracks, respectively, are shown in Figs. 4a and 4b. Displacement fields are shown for only one half of the plate due to the symmetry of the problem. Fringe sensitivity for  $u$  and  $v$  fields is 0.0508 mm/fringe, while for  $w$  field it varies from 0.0365 mm/fringe to 0.0742 mm/fringe, as noted in the figure.

Numerical differentiation, using one-dimensional smoothed cubic splines, is performed on the experimental displacement data to obtain displacement gradients and hence strain components. Representative plot of contours of  $\epsilon_{yy}$  are shown in Fig. 5a for the front and back surfaces of the specimen having a crack depth  $a = 4$  mm at far field stress  $\sigma_\infty = 1.12\sigma_0$ . Higher magnitudes of strain are noted at a distance away from the crack plane on the back surface which is consistent with results reported in other investigations [8,9]. Displacement and strains for the three geometries are compared in Figs. 5b and 5c, along the line ( $x = 0, y, z = -t$ ). In Fig. 5b, back surface out-of-plane displacement  $w$  normalized with CMOD has been plotted. CMOD values are calculated from fringe orders experimentally obtained at the crack mouth. As one would expect, deeper back surface dimples were observed for crack configurations with larger ( $a/t$ ) at lower far-field applied stress levels. In Fig. 5c, variation of ( $\epsilon_{yy}/\epsilon_\infty$ ) with respect to  $y$  is shown for each of the geometries. Also, the location of maximum opening strain on the back surface is closer to the crack plane for deeper notches, as might be anticipated because of the decreased ligament lengths.

Using the method followed by King et al. [12], values of  $J$  for a contour on the ( $y - z$ ) plane enclosing the deepest point of the crack were calculated for each of the specimen geometries. The contour considered is path #(1) shown in Fig. 6a.  $J$  is given by

$$J = \int_c W dy - T_k \frac{\partial u_k}{\partial x_3} ds \quad (5)$$

and an additional area term

$$J_A = - \int_A \frac{\partial}{\partial x_1} \left[ \sigma_{1k} \frac{\partial u_k}{\partial x_3} \right] ds \quad (6)$$

for strain energy density  $W$ , traction vector  $T_k$ , displacement vector  $u_k$ , the arc length  $s$  measured along contour  $c$ , and  $A$  the area enclosed by the line contour. Assuming that the contribution to  $J$  is predominantly due to the components of displacement  $u_2$  (or  $v$ ), stress  $\sigma_{yy}$  and strain  $\epsilon_{yy}$  terms, only the following two terms were considered in calculating  $J$ :

$$W = \int_0^{y_y} \sigma_{yy} d\epsilon_{yy} \quad (7)$$

$$T_2 \frac{\partial u_2}{\partial z} = \sigma_{yy} \frac{\partial v}{\partial z} \quad (8)$$

where  $\sigma_{yy}$  is determined from the average strain for the front and back surfaces and the displacement gradient is considered constant through the thickness.

Using the experimental measurements, values of  $J$  have been calculated for different load levels. Equivalence of  $J$  and CMOD is considered.  $J$  and CMOD have been plotted

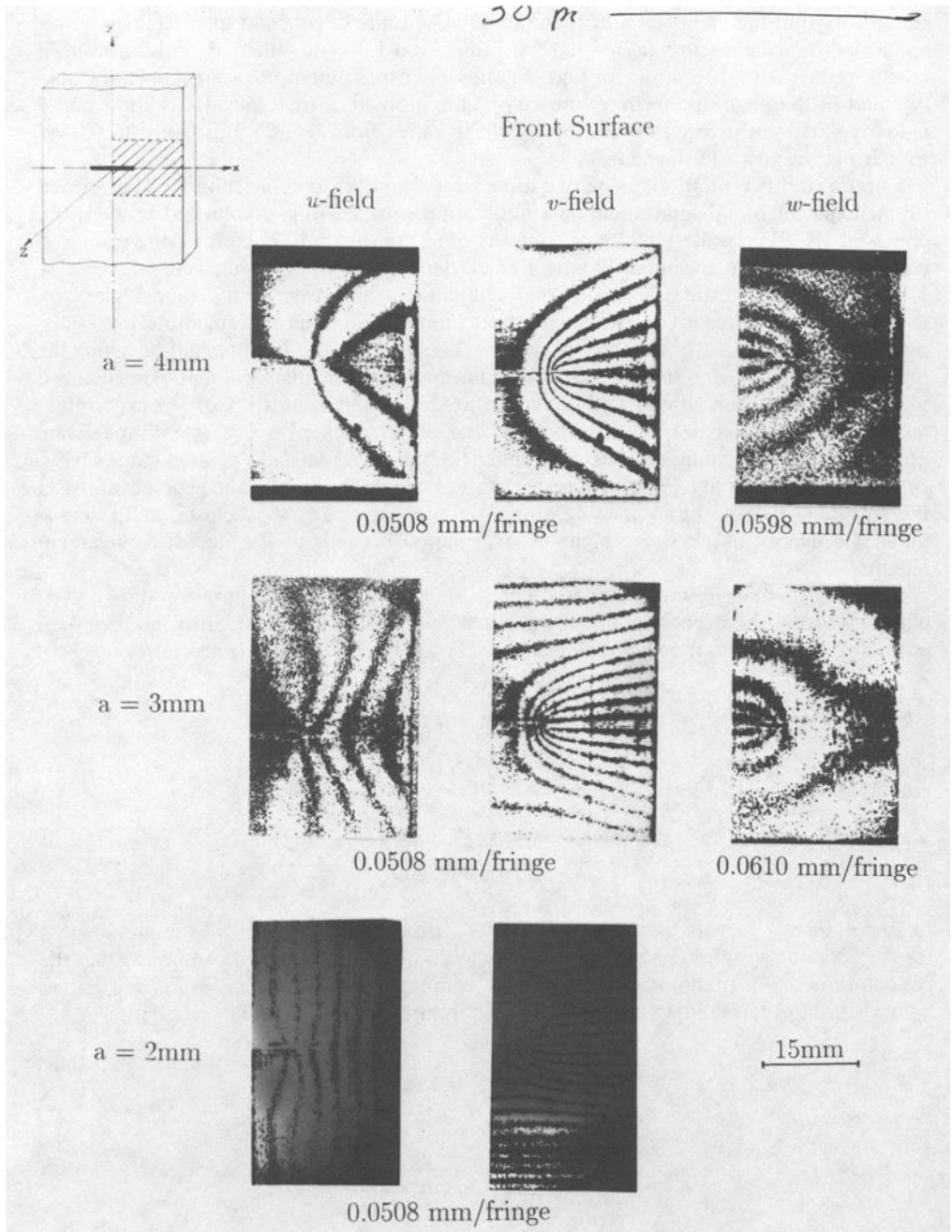


FIG. 4a—Experimental displacement fields on front surface.



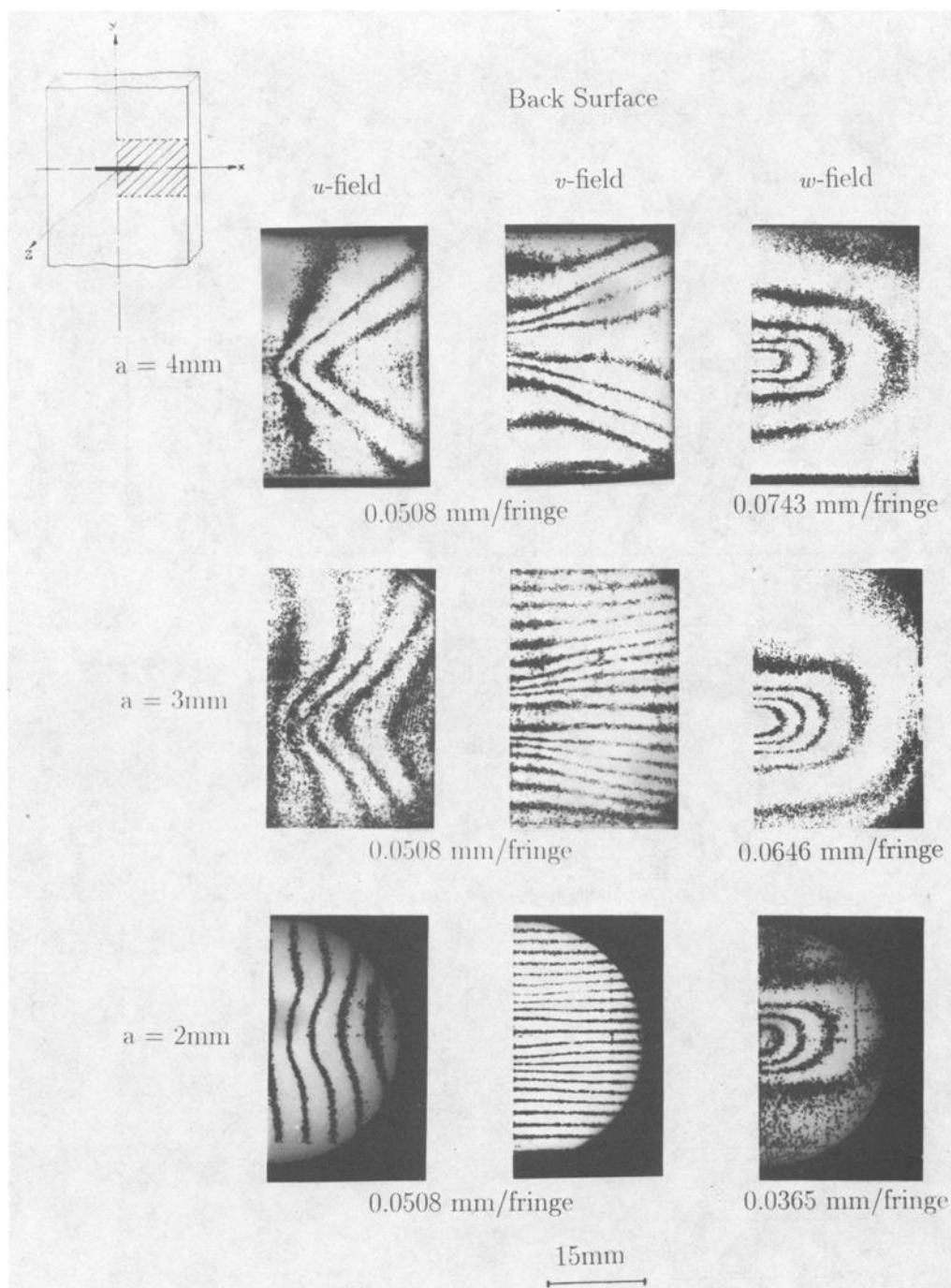


FIG. 4b—Experimental displacement fields on back surface.

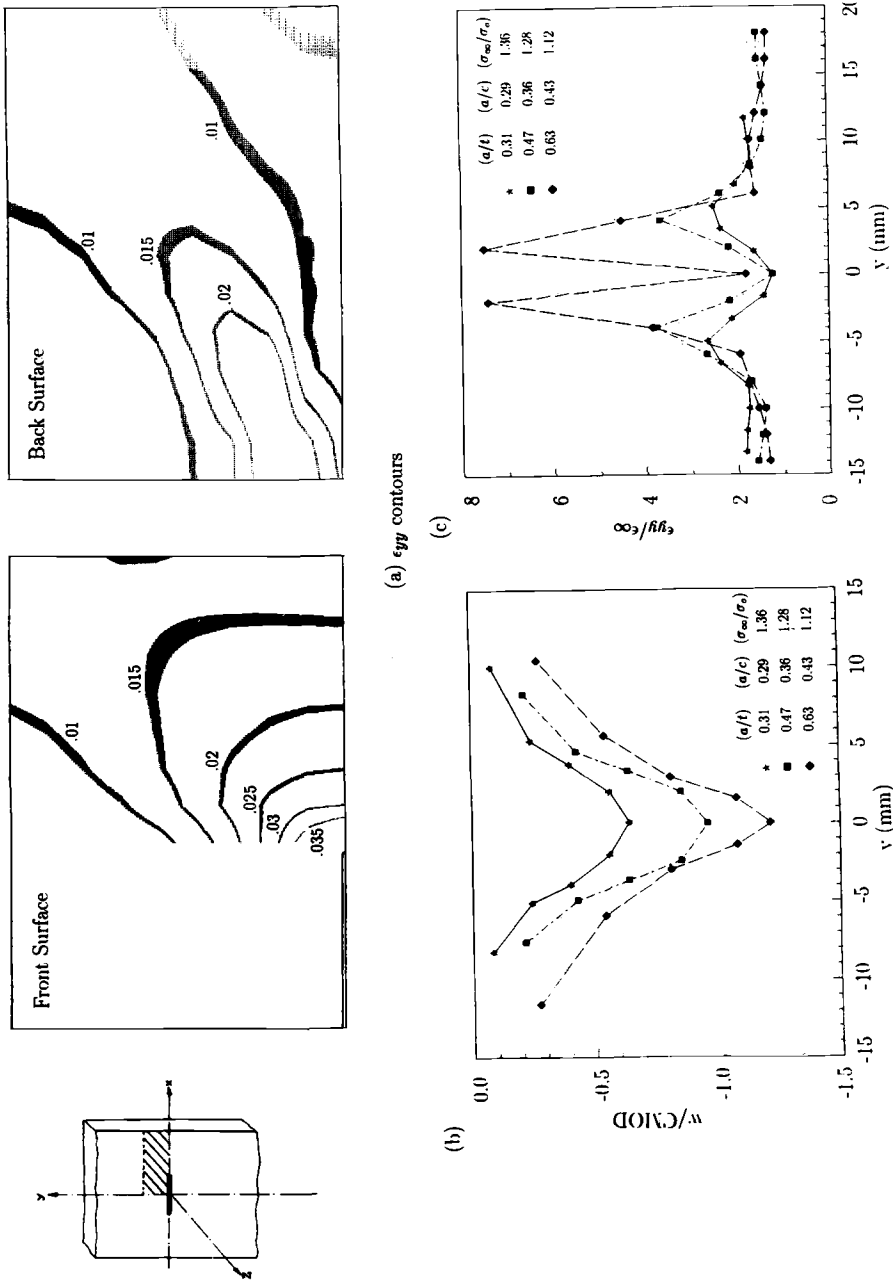


FIG. 5—(a) Experimental  $\epsilon_{yy}$  contours; (b)  $w/CMOD$  versus  $y$ ; (c)  $\epsilon_{yy}/\epsilon_{\infty}$  versus  $y$ .

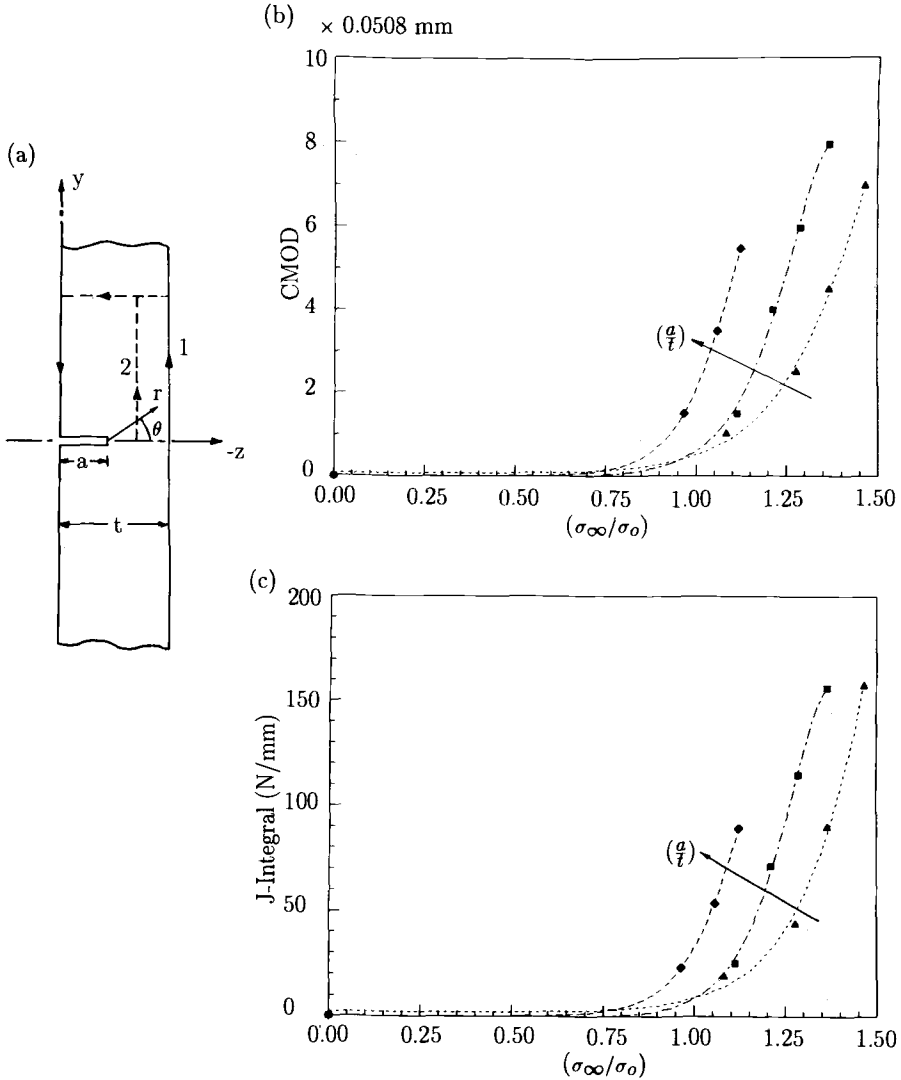


FIG. 6—(a) Integration paths considered to calculate approximate J; (b), (c) J — CMOD equivalence curves.

against normalized far field stress in Figs. 6b and 6c. Definite similarity in trends have been observed in each case where fitted curves are of the same form given by

$$J\left(\frac{\sigma_\infty}{\sigma_0}\right) = A_1 + A_2\left(\frac{\sigma_\infty}{\sigma_0}\right)^n + A_3\left(\frac{\sigma_\infty}{\sigma_0}\right)^{2n} \quad (9)$$

$$\text{CMOD}\left(\frac{\sigma_\infty}{\sigma_0}\right) = B_1 + B_2\left(\frac{\sigma_\infty}{\sigma_0}\right)^n + B_3\left(\frac{\sigma_\infty}{\sigma_0}\right)^{2n} \quad (10)$$

where  $n$  is the hardening exponent of the material and the coefficients  $A_i$ ,  $B_i$  depend on the crack configuration. Also, as noted earlier by Parks et al. [11], in his line-spring models, as  $(a/t)$  increases, curves of  $J$  versus  $(\sigma_\infty/\sigma_0)$  move to the left. A similar trend is obvious in the (CMOD) plots as well.

### Finite-Element Model

An integrated experimental-finite element technique, developed successfully by Hareesh and Chiang [17] for elastoplastic crack-tip analysis, has been applied to probe the interior of this three-dimensional (3-D) crack geometry. Experimentally obtained displacements are used as boundary conditions in a nonlinear finite-element model. The material nonlinearity is incorporated into the calculations using experimentally obtained uniaxial tensile stress-strain data. The 3-D FE model is based on small strain approximation and deformation theory of plasticity. The initial stress method is used to account for the material nonlinearity. Eight-node linear brick elements with three degrees of freedom per node corresponding to displacement components in the  $x$ ,  $y$ , and  $z$  directions are used. Numerical integration is performed at eight gaussian locations in each element.

The specimen with  $a = 4$ -mm-deep crack and deformations corresponding to far field applied stress  $\sigma_\infty = 1.12\sigma_0$  is chosen for FE analysis. Due to the symmetry of the problem, only one quarter of the plate is analyzed. The model considered extends to the boundary of the plate in the  $x$ -direction, to a distance 17.5 mm in the  $y$ -direction and through-the-thickness of the material. It is made up of twelve identical layers of nodes, unequally spaced in the  $y$ -direction. The overall model consists of 1518 elements and 6012 degrees of freedom. Symmetry boundary conditions are applied to the  $(x - z)$  and  $(y - z)$  planes of the model. Experimentally obtained displacements are applied as boundary conditions for nodes on  $(x, y = 17.5 \text{ mm}, z)$  plane. It was assumed that all three displacement fields vary linearly through the thickness.

### Finite-Element Results and Discussion

In Fig. 7, the calculated  $v$  displacement and  $\epsilon_{yy}$  strains are plotted as contours on the front and back surfaces of the model. When these are compared with their experimental counterparts (Figs. 4 and 5), good correlation between the two results becomes evident. Experimental and numerical front and back surface  $w$  displacements are plotted along the slice  $(x = 0, y)$  in Figs. 8a and 8b. Trends are similar in both sets of results although the out-of-plane displacements obtained by the finite-element method are somewhat higher in magnitude. Also, in Fig. 8c, the variation of opening strain  $\epsilon_{yy}$  with respect to distance from the crack plane is shown. Higher maximum values of strain are observed for experimental results than for finite-element analysis, although maximum strains are noted at a distance of approximately 3 mm from the crack plane in both cases. The discrepancies between the two could be attributed to the size of the elements in the  $y$ -direction.

Since finite-element results on the surface compare well with experimental results, investigation is continued into the interior of the material. Figure 9 shows contours of constant displacement  $w$  and strain  $\epsilon_{yy}$  on the crack plane  $(x, y = 0, z)$  along with the undeformed and deformed finite element mesh used in the study. Similarly, in Fig. 10, contours of  $v$  displacement and strain  $\epsilon_{yy}$  are shown for the plane  $(x, y = 0, z)$  as well as the undeformed and deformed mesh on the midplane of the specimen. Strain contours on this plane may be compared with the results of Ayres [8] and Levy et al. [9], who plotted the progression of plastic zone for increasing far field loads below the limit load of the material. In an effort to characterize the singularity ahead of the crack tip, effective stress  $\sigma_{eff}$  and effective strain

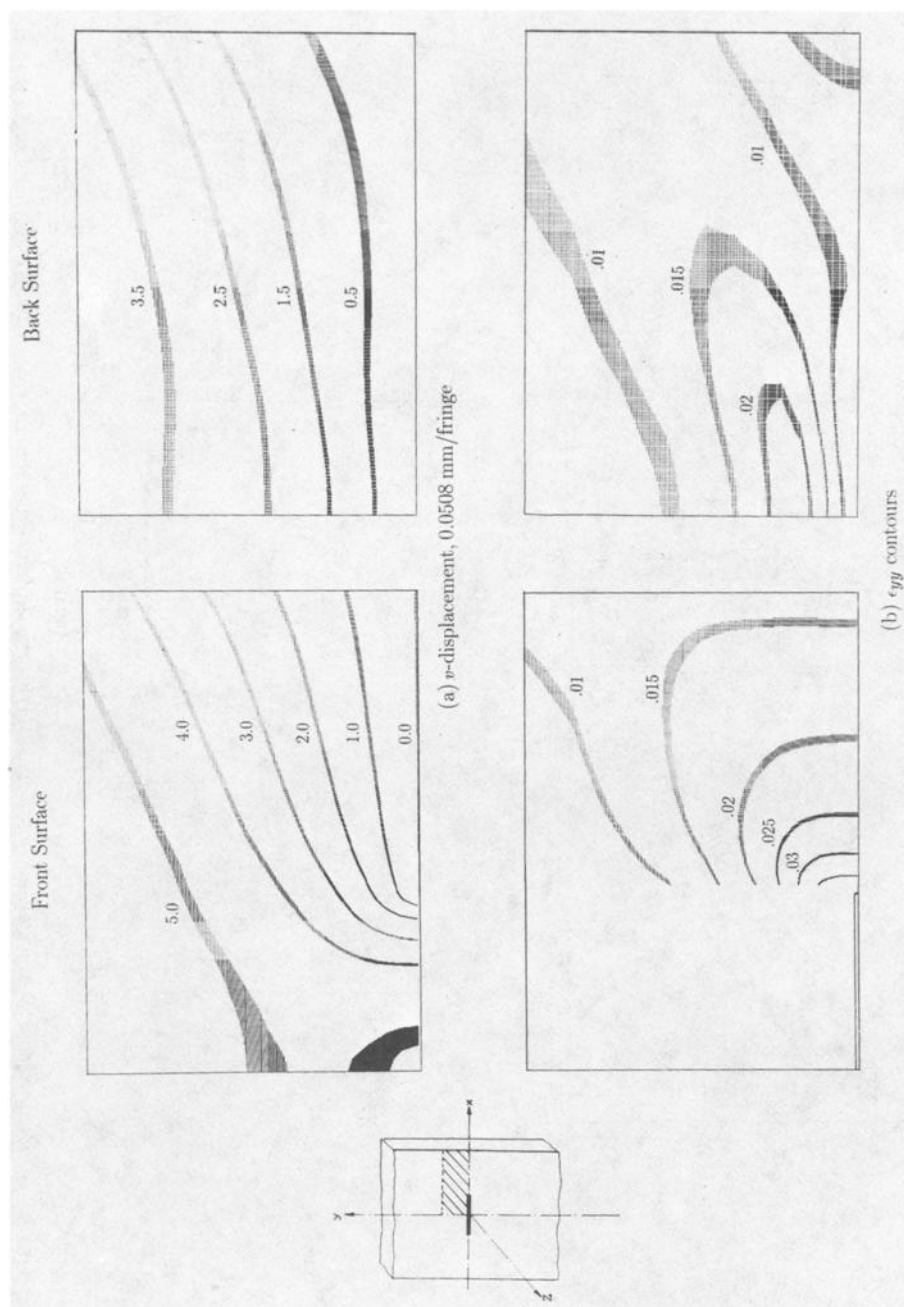


FIG. 7—Numerical (a)  $v$ -displacement contours (b)  $\epsilon_{yy}$  contours,  $a = 4 \text{ mm}$ .

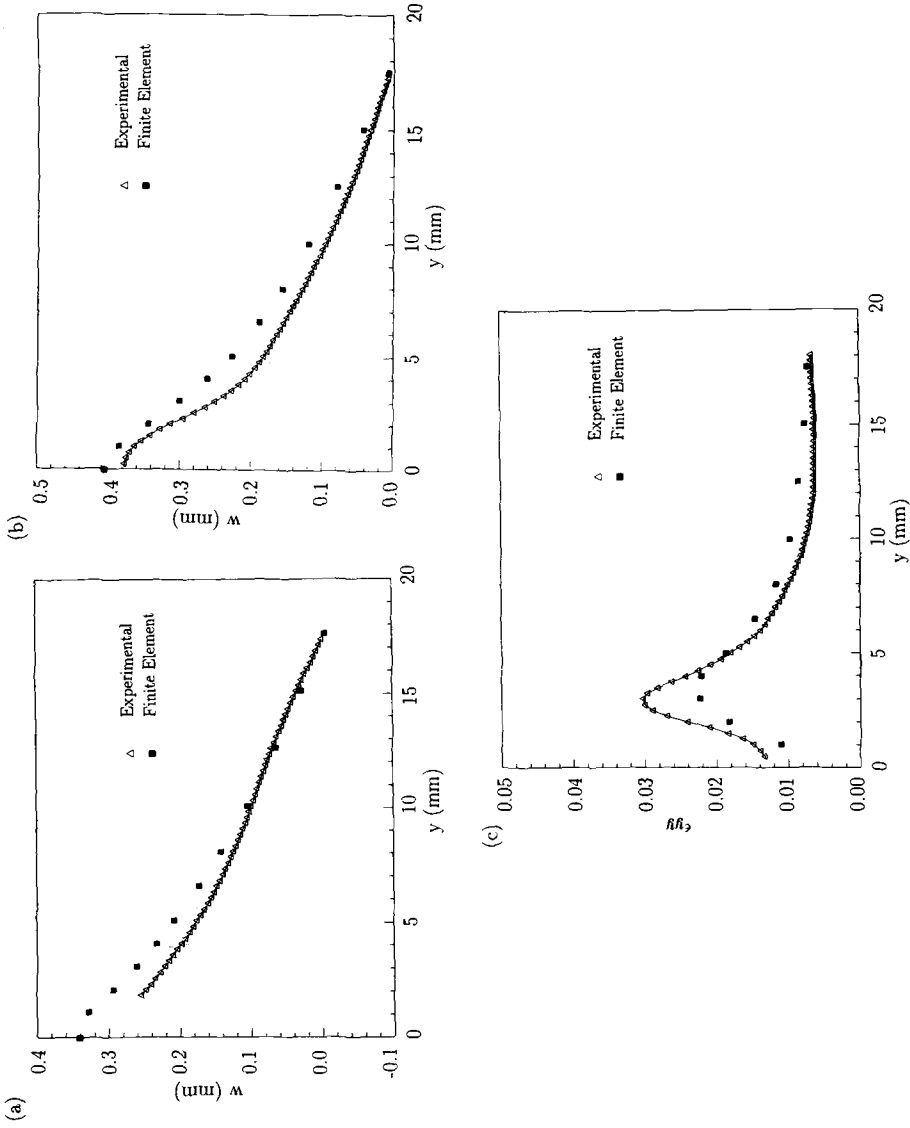


FIG. 8—Comparison of experimental and finite element: (a)  $w$ -displacements (front surface); (b)  $w$ -displacements (back surface); (c)  $\epsilon_{yy}$  (back surface),  $a = 4$  mm.

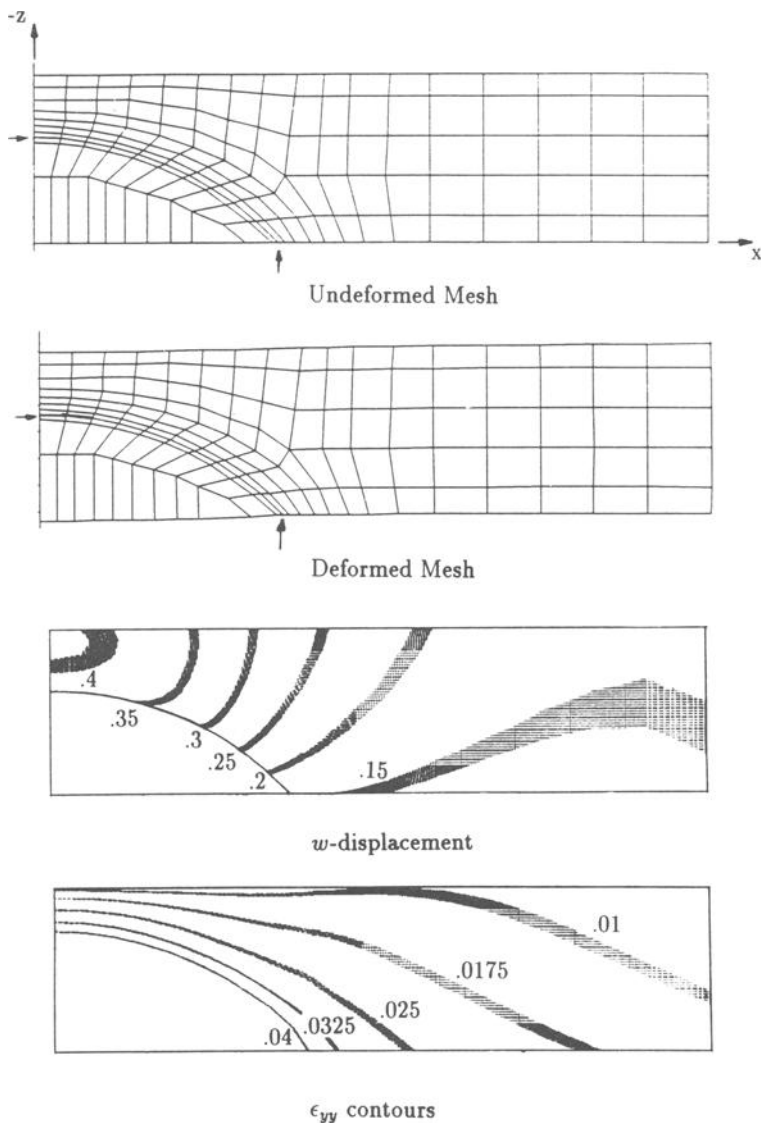


FIG. 9—Deformation fields on  $(x - z)$  plane,  $a = 4$  mm.

$\epsilon_{eff}$  are plotted against distance from the crack tip  $r$  in Fig. 11, for various angles to the crack plane,  $\theta$ . In each case, the fitted curve was of the form

$$\frac{\sigma_{eff}}{\sigma_{\infty}} = \sum_{i=0}^{i=2} F_i r^{(i-b)/n} \quad (11)$$

$$\frac{\epsilon_{eff}}{\epsilon_{\infty}} = \sum_{i=0}^{i=2} G_i r^{(i-b)} \quad (12)$$

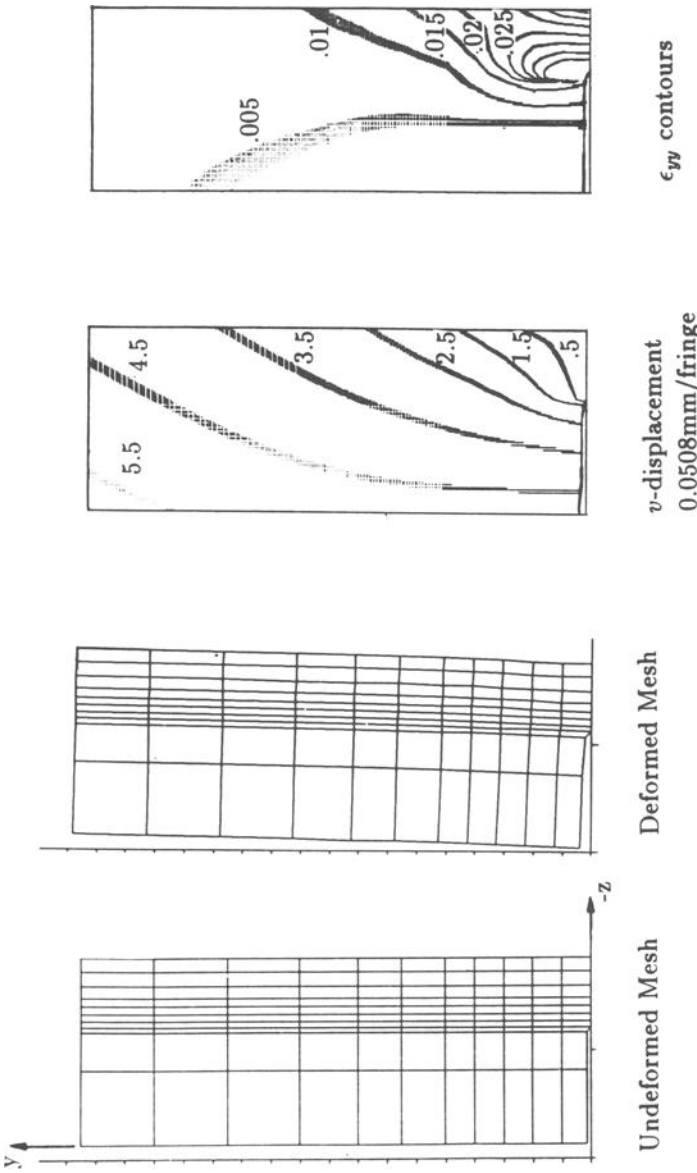


FIG. 10—Deformation fields on ( $y - z$ ) plane,  $a = 4$  mm.



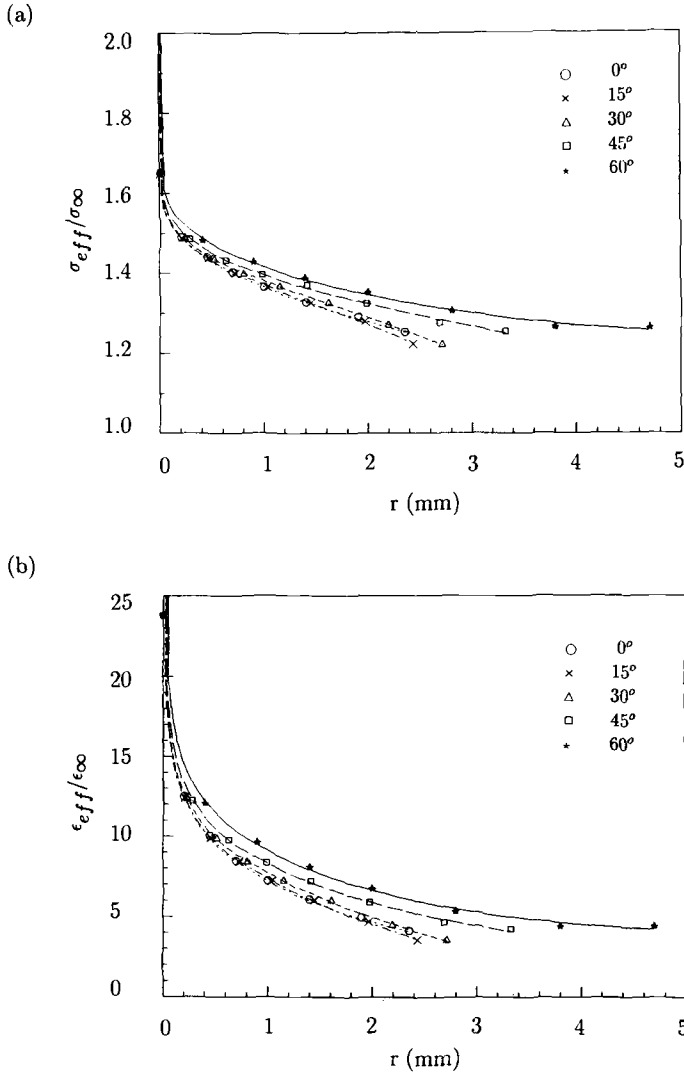


FIG. 11—(a) Effective stress distribution on (y - z) plane,  $a = 4$  mm; (b) effective strain distribution on (y - z) plane,  $a = 4$  mm.

where the constants  $F_i$  and  $G_i$  are different for different  $\theta$  and the exponent  $b$  ( $= 0.2$  for  $a = 4$  mm) may be a constant dependent on the hardening index  $n$  of the material and crack geometry. In the above polynomials, the first term denotes the strength of the associated singularity while the rest of the terms account for the far field stresses and strains. In addition,  $J$ -integral is calculated from the finite-element results by the previously described method for two different contours (paths Nos. 1 and 2 in Fig. 6a) for comparison to the values obtained from the experimental results. Approximate  $J$ -integral evaluated from experimental results for  $a = 4$  mm and  $\sigma_{\infty} = 1.12\sigma_0$  is 89.0 N/mm. Corresponding  $J$  from finite-element results are 88.2 N/mm and 89.3 N/mm for integration paths Nos. 1 and 2,

respectively. By using plane strain HRR equations for  $v$  displacement,  $J$ -integral was estimated from

$$\left[ \frac{v}{\bar{v} \alpha \epsilon_0 r} \right]^{(n+1)/n} \alpha \sigma_0 \epsilon_0 I_n r \rightarrow J \quad \text{as } r \rightarrow 0 \quad (13)$$

Extrapolated values of  $J$  for various  $\theta$  range from 80 to 125 N/mm. This approach is similar to the one followed by Levy et al. [9] to determine stress-intensity factor  $K$  for a similar surface flaw configuration.

## Conclusions

We have optically measured 3-D surface deformations in a plastically deformed sheet containing a part circular surface flaw when subjected to tension. Measured displacements were then used as boundary conditions in a finite-element model to obtain the interior deformations ahead of the crack front. Approximate  $J$  values have been calculated using the experimental measurements as well as FE results.  $J$ -CMOD equivalence is considered based on the similarity in their variations for different load levels. Effective stress and strain distributions along various angles in the interior of the material on the ( $x = 0, y, z$ ) plane are described by polynomial functions containing one singular term in an effort to empirically describe the crack-tip singularity in terms of hardening index and crack configuration.

## Acknowledgments

Dr. James Tasi's help in providing us with a part of the computational time at Cornell National Supercomputing Facility during the course of the investigation is greatly appreciated.

This work is financially supported by ONR Mechanics Division (Dr. Y. Rajapakse, Scientific Officer), Contract No. N0001482K0566, and NSF Solid and Geo-Mechanics Program (Dr. K. Thirumalai, Program Director), Grant No. MEA8403912.

## References

- [1] Irwin, G. R., "Crack Extension Force for a Part-Through Crack in a Plate," *Journal of Applied Mechanics*, Vol. 29, 1962, pp. 651-654.
- [2] Kobayashi, A. S. and Moss, W. L., "Stress Intensity Magnification Factors for Surface Flawed Tension Plate and Notched Round Tension Bar," *Fracture 1969, Proceedings, 2nd International Conference on Fracture*, P. L. Pratt, Ed., 1969, pp. 31-45.
- [3] Rice, J. R. and Levy, N., "The Part-Through Surface Crack in an Elastic Plate," *Journal of Applied Mechanics*, 1972, pp. 185-194.
- [4] Raju, I. S. and Newman, J. C., "Stress-Intensity Factors for a Wide Range of Semielliptical Surface Cracks in Finite Thickness Plates," *Engineering Fracture Mechanics*, Vol. 11, 1979, pp. 817-829.
- [5] Newman, J. C. and Raju, I. S., "An Empirical Stress-Intensity Factor Equation for the Surface Crack," *Engineering Fracture Mechanics*, Vol. 15, No. 1-2, 1981, pp. 185-192.
- [6] Smith, F. W. and Sorensen, D. R., "The Semi-Elliptical Surface Crack—A Solution by the Alternating Method," *International Journal of Fracture*, Vol. 12, No. 1, 1976, pp. 47-57.
- [7] Smith, C. W., Peters, W. H., Kirby, G. C., and Andonian, A., "Stress-Intensity Distribution for Natural Flaw Shapes Approximating 'Benchmark' Geometries," *Fracture Mechanics (13th Conference)*, ASTM STP 743, Richard Roberts, Ed., American Society for Testing and Materials, Philadelphia, 1981, pp. 422-437.

- [8] Ayres, D. J., "A Numerical Procedure for Calculating Stress and Deformation Near a Slit in a Three-Dimensional Elastic-Plastic Solid," *Engineering Fracture Mechanics*, Vol. 2, 1970, pp. 87-106.
- [9] Levy, N., Marcal, P. V., and Rice, J. R., "Progress in Three-Dimensional Elastic-Plastic Stress Analysis for Fracture Mechanics," *Nuclear Engineering and Design*, Vol. 17, 1971, pp. 64-75.
- [10] Francis, P. H., Davidson, D. L., and Forman, R. G., "An Experimental Investigation in the Mechanics of Deep, Semi-Elliptical Surface Cracks into Mode-I Loading," *Engineering Fracture Mechanics*, Vol. 4, 1972, pp. 617-635.
- [11] Parks, D. M. and White, C. S., "Elastic-Plastic Line Spring Finite Elements for Surface Cracked Plates and Shells," *Journal of Pressure Vessel Technology*, Vol. 104, 1982, pp. 287-292.
- [12] King, R. B., Cheng, Y. W., Read, D. T., and McHenry, H. I., "J-Integral Analysis of Surface Cracks in Pipeline Steel Plates," *Elastic-Plastic Fracture: Second Symposium. Volume I: Inelastic Crack Analysis*, ASTM STP 803, American Society for Testing and Materials, Philadelphia, C. F. Shih and J. P. Gudas, Eds., 1983, pp. 1444-1457.
- [13] Read, D. T., McHenry, H. I., and Petrovski, B., "Elastic Plastic Models of Surface Cracks in Tensile Panels," *Proceedings of the SEM Fall Conference on Experimental Mechanics*, 1986, pp. 210-216.
- [14] Reuter, W. G. and Epstein, J. S., "Experimental Measurements of CTOD for Two Surface Cracks Configurations," *Proceedings of the SEM Fall Conference on Experimental Mechanics*, 1986, pp. 263-269.
- [15] Chiang, F. P. and Hareesh, T. V., "Three-Dimensional Crack Tip Deformation: An Experimental Study and Comparison to HRR Field," *International Journal of Fracture*, Vol. 36, 1988, pp. 243-257.
- [16] Chiang, F. P., "Techniques of Optical Spatial Filtering Applied to the Processing of Moiré Fringe Patterns," *Experimental Mechanics*, Nov. 1969, pp. 523-526.
- [17] Hareesh, T. V. and Chiang, F. P., "Integrated Experimental-Finite Element Approach for Studying Elasto-Plastic Crack Tip Fields," *Journal of Engineering Fracture Mechanics*, Vol. 31, No. 3, 1988, pp. 451-461.

## Extraction of Stress-Intensity Factor from In-Plane Displacements Measured by Holographic Interferometry

---

**REFERENCE:** Dally, J. W., Sciammarella, C. A., and Shareef, I., "Extraction of Stress-Intensity Factor from In-Plane Displacements Measured by Holographic Interferometry," *Surface-Crack Growth: Models, Experiments, and Structures*, ASTM STP 1060, W. G. Reuter, J. H. Underwood, and J. C. Newman, Jr., Eds., American Society for Testing and Materials, Philadelphia, 1990, pp. 130-141.

**ABSTRACT:** Utilizing the well-known Westergaard approach in conjunction with Goursat-Kolosov series stress functions, suitable series solutions are developed for stresses and displacements around the crack tip. In-plane displacement data from the entire field near the crack tip are obtained by holographic interferometry. Measurement errors in the experimental data are minimized by the least-squares method. Series solution of displacements together with experimental data is used to establish the loss of inverse square-root singularity at the free surface-crack border intersection. Experimental results are compared with the analytical results from recent studies, and a good correlation is found between analytical and experimental values.

**KEY WORDS:** holographic interferometry, in-plane displacements, surface stress-intensity factor, free surface-crack border intersection, holographic moiré, stress singularity, eigenvalue

Several investigators have made considerable progress [1-5] toward determining the stress-intensity factor  $K_I$  from photoelastic measurements by utilizing isochromatic data in the field adjacent to the crack tip. The advantage of this approach is that measurements can be made away from the crack tip, where errors resulting from imperfections in crack tip geometry, nonlinearities, mixed plane-stress plane-strain, and gradient effects are minimized. Because the measurements are made in the adjacent field, it is necessary to account for the total stress or displacement field and to utilize a representation of the stress or displacement field which contains several terms in addition to the singularity term.

However, the photoelastic methods are severely limited when it becomes necessary to determine the stress-intensity factors in metals or other opaque materials. In such cases, the experimentalist has limited options, one of which is the use of in-plane displacement data obtained by coherent optical methods such as moiré [6-9], speckle [10,11], or holographic interferometry [12,13]. It is possible to determine  $K_I$  from these measurements with a minimum of error by extending the methods already established for photoelasticity.

<sup>1</sup> Professor, Department of Mechanical Engineering, University of Maryland at College Park, College Park, MD 20742.

<sup>2</sup> Professor, Department of Mechanical Engineering, Illinois Institute of Technology, Chicago, IL 60616.

<sup>3</sup> Assistant professor, Department of Manufacturing Engineering, Bradley University, Peoria, IL 61625.

The goal of this paper is to develop a series solution to the stresses and displacements around the crack tip and utilize them to find the stress-intensity factor along the flaw border in the interior. The paper also demonstrates how in-plane displacement data from the entire field, obtained by holographic interferometry, can be used with series solution to establish the loss of inverse square-root crack tip stress singularity at the free surface-crack border intersection.

### Analytical Technique

Muskhelishvili [14] has shown that the stresses and displacements in a plane body can be represented in terms of Goursat-Kolosov stress functions as

$$\sigma_x = 2\operatorname{Re}\Phi'(z) - x\operatorname{Re}\Phi''(z) - y\operatorname{Im}\Phi''(z) - \operatorname{Re}X''(z) \quad (1a)$$

$$\sigma_y = 2\operatorname{Re}\Phi'(z) + x\operatorname{Re}\Phi''(z) + y\operatorname{Im}\Phi''(z) + \operatorname{Re}X''(z) \quad (1b)$$

$$\tau_{xy} = x\operatorname{Im}\Phi''(z) - y\operatorname{Re}\Phi''(z) + \operatorname{Im}X''(z) \quad (1c)$$

$$u = \frac{1}{2G} \left[ \left( \kappa \right) \operatorname{Re}\Phi(z) - x\operatorname{Re}\Phi'(z) - y\operatorname{Im}\Phi'(z) - \operatorname{Re}X'(z) \right] \quad (1d)$$

$$v = \frac{1}{2G} \left[ \left( \kappa = 3 - 4\nu \right) \operatorname{Im}\Phi(z) + x\operatorname{Im}\Phi'(z) - y\operatorname{Re}\Phi'(z) + \operatorname{Im}X'(z) \right] \quad (1e)$$

where  $\Phi$  and  $X$  are functions of  $z = x + iy$

$$\Phi' = \frac{d}{dt} \Phi \quad \text{and} \quad \Phi'' = \frac{d}{dt} \Phi'$$

Further

$$\kappa = 3 - 4\nu \quad \text{for plane strain} \quad (2a)$$

and

$$\kappa = \frac{3 - \nu}{1 - \nu} \quad \text{for plane stress} \quad (2b)$$

where  $\nu$  is the Poisson's ratio.

The Goursat Stress functions are expressed as power series in terms of  $z$  as

$$\Phi = \sum_{n=0}^{\infty} R_n z^{\lambda_n} \quad (3a)$$

and

$$X' = \sum_{n=0}^{\infty} (\lambda_n + 1) S_n z^{\lambda_n} \quad 3b$$

Sih and Liebowitz [15] have determined the displacement field corresponding to the first two terms of the power series expansion (that is,  $n = 0$  and 1). First, in this approach, two terms are not sufficient for extracting accurate information from adjacent field. Second, even if suitable series equations for  $u$  and  $v$  displacements are developed by following the method of Sih and Liebowitz, yet they would be limited because Goursat-Kolosov stress functions are not well known to the experimental community.

Therefore, in the current investigation, the well-known Westergaard [16] approach for determination of stresses and displacements will be applied, in conjunction with Sanford's [17] method. In the study by Sanford, the Goursat-Kolosov stress functions were replaced by  $Z$  and another stress function  $\eta$ , both functions of  $z$ , where

$$2\Phi' = Z - \eta \quad (4a)$$

$$\eta = 2\Phi'' + X'' \quad (4b)$$

where

$$Z = \sum_{n=0}^N \frac{A_n}{n - \frac{1}{2}} z^{n-1/2} \quad \text{with } n = 0, 1, 2, 3, \dots \quad (5a)$$

and

$$\eta = \sum_{m=0}^M \alpha_m z^m \quad \text{with } m = 0, 1, 2, 3, \dots \quad (5b)$$

The integers  $N$  and  $M$  are selected so that a sufficient number of terms are included to adequately describe the stresses and displacements in the adjacent field.

Substituting Eqs 4 into Eqs 1, the stresses and displacements are obtained as

$$\sigma_x = \operatorname{Re} Z - 2 \operatorname{Re} \eta - y \operatorname{Im} Z' + y \operatorname{Im} \eta' \quad (6a)$$

$$\sigma_y = \operatorname{Re} Z + y \operatorname{Im} Z' - y \operatorname{Im} \eta' \quad (6b)$$

$$\tau_{xy} = \operatorname{Im} \eta - y \operatorname{Re} Z' + y \operatorname{Re} \eta' \quad (6c)$$

$$u = \frac{1}{2G} \left[ \left( \kappa \right) \operatorname{Re}(\tilde{Z} - \tilde{\eta}) - x \operatorname{Re}(Z - \eta) - y \operatorname{Im}(Z - \eta) \right. \\ \left. - 2 \operatorname{Re} \tilde{\eta} + \operatorname{Re} \int z(Z' - \eta') dz \right] \quad (6d)$$

$$v = \frac{1}{2G} \left[ \left( \kappa \right) \operatorname{Im}(\tilde{Z} - \tilde{\eta}) + x \operatorname{Im}(Z - \eta) - y \operatorname{Re}(Z - \eta) \right. \\ \left. + 2 \operatorname{Im} \tilde{\eta} - \operatorname{Im} \int z(Z' - \eta') dz \right] \quad (6e)$$

where

$$\tilde{Z} = \int Z dz, \quad \tilde{\eta} = \int \eta dz, \quad \frac{d}{dz} Z = Z', \quad \text{and} \quad \frac{d}{dz} \eta = \eta' \quad (6f)$$

It is evident from a comparison of Eqs 1 with Eqs 6 that the substitution of the functions  $Z$  and  $\eta$  for the functions  $\Phi$  and  $X$  has simplified slightly the expressions for the stresses and greatly complicated the expressions for the displacements.

Substituting Eqs 5 into Eqs 6 and using the Moivre relationship

$$z^p = r^p(\cos p\theta + i \sin p\theta)$$

gives the stresses and displacements in a form convenient for use in analysis of adjacent field data as

$$\sigma_x = \sum_{n=0}^N A_n r^{n-1/2} \left\{ \frac{2}{2n-1} \cos(n - \frac{1}{2})\theta - \sin \theta \sin(n - \frac{1}{2})\theta \right\} - \sum_{m=0}^M \alpha_m r^m \{2\cos m\theta - m\sin \theta \sin(m-1)\theta\} \quad (7a)$$

$$\sigma_y = \sum_{n=0}^N A_n r^{n-1/2} \left\{ \frac{2}{2n-1} \cos(n - \frac{1}{2})\theta + \sin \theta \sin(n - \frac{1}{2})\theta \right\} - \sum_{m=0}^M \alpha_m r^m m\sin \theta \sin(m-1)\theta \quad (7b)$$

$$\tau_{xy} = \sum_{n=0}^N -A_n r^{n-1/2} \sin \theta \cos(n - \frac{1}{2})\theta + \sum_{m=0}^M \alpha_m r^m \{\sin m\theta + m\sin \theta \cos(m-1)\theta\} \quad (7c)$$

$$u = \frac{1}{4G} \left[ \sum_{n=0}^N A_n r^{n+1/2} \left\{ \left( \frac{4\kappa - 4n - 2}{4n^2 - 1} \right) \cos(n + \frac{1}{2})\theta - \frac{2}{2n-1} \cos(n - \frac{1}{2})\theta \right\} + \sum_{m=0}^M \alpha_m r^{m+1} \left\{ - \left( \frac{\kappa + m + 2}{m+1} \right) \cos(m+1)\theta + \cos(m-1)\theta \right\} \right] \quad (7d)$$

$$v = \frac{1}{4G} \left[ \sum_{n=0}^N A_n r^{n+1/2} \left\{ \left( \frac{4\kappa - 4n + 2}{4n^2 - 1} \right) \sin(n + \frac{1}{2})\theta + \frac{2}{2n-1} \sin(n - \frac{1}{2})\theta \right\} + \sum_{m=0}^M \alpha_m r^{m+1} \left\{ - \left( \frac{\kappa - m - 2}{m+1} \right) \sin(m+1)\theta - \sin(m-1)\theta \right\} \right] \quad (7e)$$

It must be noted that in the foregoing Eq 7, the truncated power series for  $Z$  utilizes inverse square-root singularity, which is the eigenvalue required to insure that the upper and lower surface of a semi-infinite crack occupying the negative  $x$ -axis are free of tractions.

Although the inverse square-root crack tip singularity form was noted by several investigators including Williams [18], Irwin [19], and Kassir and Sih [20]; it was recognized in early 1970s by Sih [21] that the square-root singularity existed only in the interior and it vanishes gradually as the flaw surface-crack border is reached. Folias [22] investigated the transition zone from interior to free surface and noted the loss of inverse square-root singularity and its dependence on Poisson's Ratio. These results were further confirmed by Bazant and Estenssoro [23] and Benthem [24,25]. Benthem, in his excellent work involving three-dimensional separation of variables for a quarter infinite crack, noted a loss of inverse square-root singularity and found the eigenvalue of the distance from the crack tip to be Poisson ratio dependent. Smith and Epstein [26], in a recent experimental study involving three-dimensional photoelasticity and high-density moiré, observed a three-dimensional boundary-layer effect near a free surface crack border intersection, indicating a divergence from classical a stress-intensity factor (SIF) with its inverse square-root singularity.

In the present investigation, since holographic interferometric technique was used to measure the in-plane displacements on the free surface near the crack tip, it would be more meaningful to modify Eq 5a by replacing  $\frac{1}{2}$  by a variable  $\lambda$  and seek the value of  $\lambda$  which best satisfies the experimentally measured displacements. The substitution of modified Eqs 5 in Eqs 7 leads to the stresses and displacements being expressed as

$$\sigma_x = \sum_{n=0}^N A_n r^{n-\lambda} \left\{ \frac{\cos(n-\lambda)\theta}{n-\lambda} - \sin\theta \sin(n-\lambda-1)\theta \right\} - \sum_{m=0}^M \alpha_m r^m \{ 2\cos m\theta - m\sin\theta \sin(m-1)\theta \} \quad (8a)$$

$$\sigma_y = \sum_{n=0}^N A_n r^{n-\lambda} \left\{ \frac{\cos(n-\lambda)\theta}{n-\lambda} + \sin\theta \sin(n-\lambda-1)\theta \right\} - \sum_{m=0}^M \alpha_m r^m m\sin\theta \sin(m-1)\theta \quad (8b)$$

$$\tau_{xy} = \sum_{n=0}^N -A_n r^{n-\lambda} \sin\theta \cos(n-\lambda-1)\theta + \sum_{m=0}^M \alpha_m r^m \left\{ \sin m\theta + m\sin\theta \cos(m-1)\theta \right\} \quad (8c)$$

$$u = \frac{1}{4G} \left[ \sum_{n=0}^N \frac{A_n r^{n-\lambda+1}}{n-\lambda} \left\{ \left( \frac{\kappa+n-\lambda}{n-\lambda+1} \right) \cos(n-\lambda+1)\theta - \cos(n-\lambda-1)\theta \right\} + \sum_{m=0}^M \alpha_m r^{m+1} \left\{ - \left( \frac{\kappa+m+2}{m+1} \right) \cos(m+1)\theta + \cos(m-1)\theta \right\} \right] \quad (8d)$$

$$v = \frac{1}{4G} \left[ \sum_{n=0}^N \frac{A_n r^{n-\lambda+1}}{n-\lambda} \left\{ \left( \frac{\kappa-n+\lambda}{n-\lambda+1} \right) \sin(n-\lambda+1)\theta + \sin(n-\lambda-1)\theta \right\} + \sum_{m=0}^M \alpha_m r^{m+1} \left\{ - \left( \frac{\kappa-m-2}{m+1} \right) \sin(m+1)\theta - \sin(m-1)\theta \right\} \right] \quad (8e)$$

### Least-Squares Method

For a certain fixed value of  $\lambda$ , the equations for the displacements are linear in terms of the unknown coefficients  $A_n$  and  $\alpha_m$ . The number  $P$  of unknowns which are to be deter-



mined are  $N + M + 2$ , and it is possible to select  $P$  data points and to directly solve the system of linear equations for the unknown coefficients. However, it is more appropriate to employ  $Q$  data points (where  $Q \gg P$ ) and to minimize measurement errors.

If we consider a moiré pattern either obtained by a conventional procedure or by holographic moiré, the  $v$  component of the displacement field can be expressed as

$$v_e(r_q, \theta_q) = pN_q(r_q, \theta_q) \quad (9)$$

where  $p$  is the pitch of the grid and  $r_q$  and  $\theta_q$  are radial and angular position of the Moiré fringe order  $N_q$  at the data point  $q$ .

Next, consider the square of the difference  $S$ ,

$$S = \sum_{q=1}^Q (v - v_e)^2 \quad (10)$$

where  $v$  and  $v_e$  denote the theoretical and experimental displacements, respectively, over the adjacent field with some preference for the regions above and below the crack where  $v_e$  is the largest.

Equation 8e for analytically computed displacement  $v$  can be conveniently expressed as

$$v = \frac{1}{4G} \left\{ \sum_{n=0}^N A_n f_n(r, \theta, \lambda) + \sum_{m=0}^M \alpha_m g_m(r, \theta) \right\} \quad (11a)$$

where

$$f_n(r, \theta, \lambda) = \frac{r^{n-\lambda+1}}{n-\lambda} \left\{ \left( \frac{\kappa - n + \lambda}{n - \lambda + 1} \right) \sin(n - \lambda + 1)\theta + \sin(n - \lambda - 1)\theta \right\} \quad (11b)$$

and

$$g_m(r, \theta) = r^{m+1} \left\{ - \left( \frac{\kappa - m - 2}{m + 1} \right) \sin(m + 1)\theta - \sin(m - 1)\theta \right\} \quad (11c)$$

Substituting Eqs 9 and 11 into Eq 10 yields

$$S = \sum_{q=1}^Q \left[ \frac{1}{4G} \left\{ \sum_{n=0}^N A_n f_n(r, \theta, \lambda) + \sum_{m=0}^M \alpha_m g_m(r, \theta) \right\} - pN(r, \theta) \right]^2 \quad (12)$$

To minimize the error in determining  $A_n$ ,  $\alpha_m$ , and  $\lambda$ , the least-squares procedure requires that

$$\frac{\partial S}{\partial(A_n, \alpha_m, \lambda)} = 0 \quad (13)$$

Differentiating Eq 12 and using Eq 13 gives a system of  $P + 1$  equations, where the first  $P$  equations are linear in terms of unknown coefficients  $A_m$  and  $\alpha_m$  for a particular value of  $\lambda$  and the  $(P + 1)$ th equation obtained by differentiating  $S$  with respect to  $\lambda$  is nonlinear.

In order to solve the system of  $P + 1$  equations, the  $P$  linear equations obtained by differentiating  $S$  with respect to  $A_n$  and  $\alpha_m$  are expressed as

$$[u]\{x\} = \{y\} \quad (14)$$

where the matrix  $[u]$  is given by

$$\begin{bmatrix} \Sigma f_0^2 & \Sigma f_0 f_1 & \dots & \dots & \Sigma f_0 f_N & \Sigma f_0 g_0 & \Sigma f_0 g_1 & \dots & \dots & \Sigma f_0 g_M \\ \Sigma f_1 f_0 & \Sigma f_1^2 & \dots & \dots & \Sigma f_1 f_N & \Sigma f_1 g_0 & \Sigma f_1 g_1 & \dots & \dots & \Sigma f_1 g_M \\ \dots & \dots & \dots & \dots & \dots & \dots & \dots & \dots & \dots & \dots \\ \dots & \dots & \dots & \dots & \dots & \dots & \dots & \dots & \dots & \dots \\ \Sigma f_N f_0 & \Sigma f_N f_1 & \dots & \dots & \Sigma f_N^2 & \Sigma f_N g_0 & \Sigma f_N g_1 & \dots & \dots & \Sigma f_N g_M \\ \\ \Sigma g_0 f_0 & \Sigma g_0 f_1 & \dots & \dots & \Sigma g_0 f_N & \Sigma g_0^2 & \Sigma g_0 g_1 & \dots & \dots & \Sigma g_0 g_M \\ \Sigma g_1 f_0 & \Sigma g_1 f_1 & \dots & \dots & \Sigma g_1 f_N & \Sigma g_1 g_0 & \Sigma g_1^2 & \dots & \dots & \Sigma g_1 g_M \\ \dots & \dots & \dots & \dots & \dots & \dots & \dots & \dots & \dots & \dots \\ \dots & \dots & \dots & \dots & \dots & \dots & \dots & \dots & \dots & \dots \\ \Sigma g_M f_0 & \Sigma g_M f_1 & \dots & \dots & \Sigma g_M f_N & \Sigma g_M g_0 & \Sigma g_M g_1 & \dots & \dots & \Sigma g_M^2 \end{bmatrix} \quad (15)$$

and the matrices  $\{x\}$  and  $\{y\}$  are given by

$$\{x\} = \begin{Bmatrix} A_0 \\ A_1 \\ \dots \\ \dots \\ A_N \\ \alpha_0 \\ \alpha_1 \\ \dots \\ \dots \\ \alpha_M \end{Bmatrix} \quad \text{and} \quad \{y\} = 4G \begin{Bmatrix} \Sigma v_e f_0 \\ \Sigma v_e f_1 \\ \dots \\ \dots \\ \Sigma v_e f_N \\ \Sigma v_e g_0 \\ \Sigma v_e g_1 \\ \dots \\ \dots \\ \Sigma v_e g_M \end{Bmatrix} \quad \begin{matrix} \text{(left) (16)} \\ \text{(right) (17)} \end{matrix}$$

where

$$\Sigma = \sum_{q=1}^Q$$

is the summation over the data field.

For a suitably chosen initial value of  $\lambda$ , the solution for the unknown coefficients  $A_n$  and  $\alpha_m$  is given by

$$\{x\} = [u]^{-1}\{y\} \quad (18)$$

Then the computed coefficients  $\{x\}$  are substituted in the  $(P + 1)$ th equation to satisfy

$$\frac{\partial S}{\partial \lambda} = \sum_{q=1}^Q \left[ \left[ \frac{1}{4G} \left\{ \sum_{n=0}^N A_n f_n(r, \theta, \lambda) + \sum_{m=0}^M \alpha_m g_m(r, \theta) \right\} - pN(r, \theta) \right] \left\{ \frac{1}{4G} \sum_{n=0}^N A_n f'_n(r, \theta, \lambda) \right\} \right] = 0 \quad (19)$$

If Eq 19 is not satisfied with the initial guess of  $\lambda$  and the corresponding computed coefficients  $\{x\}$ , then a new value of  $\lambda$  is appropriately chosen and a new set of coefficients  $\{x\}$  are obtained to be used in satisfying Eq 19. This process of selection of suitable  $\lambda$  and the computation of the corresponding coefficients  $\{x\}$  is continued until Eq 19 is completely satisfied.

### Experimental Technique

The double-beam illumination technique has been used to obtain the displacement field on the surface of a polyvinyl chloride (PVC) pipe. The pipe properties are Young's modulus  $E = 2964$  MPa, Poisson's ratio  $\nu = 0.35$ , outer diameter  $d_o = 48.514$  mm, inner diameter  $d_i = 40.640$  mm.

The sensitivity of the optical setup for the double-beam illumination is given by  $\delta = \lambda / 2\sin\alpha$ , where laser wave length  $\lambda$  is equal to  $6328 \text{ \AA}$  and the angle of incidence  $\alpha$  is equal to  $17.5$  deg.

The displacement field is projected on the tangent plane to the cylinder along a generatrix that coincides with the crack line as shown in Fig. 1. The crack length  $2C$  is  $18.5$  mm and its depth  $a$  is  $0.5$  mm.

The state of stress of the surface crack in the pipe is three-dimensional (3-D), and there are no rigorous solutions known for such cracks. For an infinitely long and shallow crack, one can apply the stress-intensity factor corresponding to the single-edge notched plate. Kobayashi [27] has shown that for the infinitely long and shallow crack, the normalized stress-intensity factor for the cylinder coincides with the values corresponding to the single-edge notched plate.

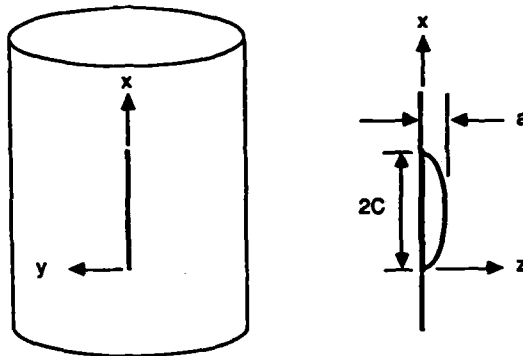


FIG. 1—Coordinate system of a crack in PVC pipe.

A double-exposure hologram was taken of the PVC pipe subjected to internal pressure of 348.5 kPa. The displacement pattern corresponding to the fringes projected in the  $y$ -axis direction is shown in Fig. 2. The crack tip location can be easily recognized by analyzing the geometry of the moiré field. Due to internal pressure in the pipe and in the absence of a flaw, moiré fringes are formed parallel to the pipe generatrix. However, the presence of

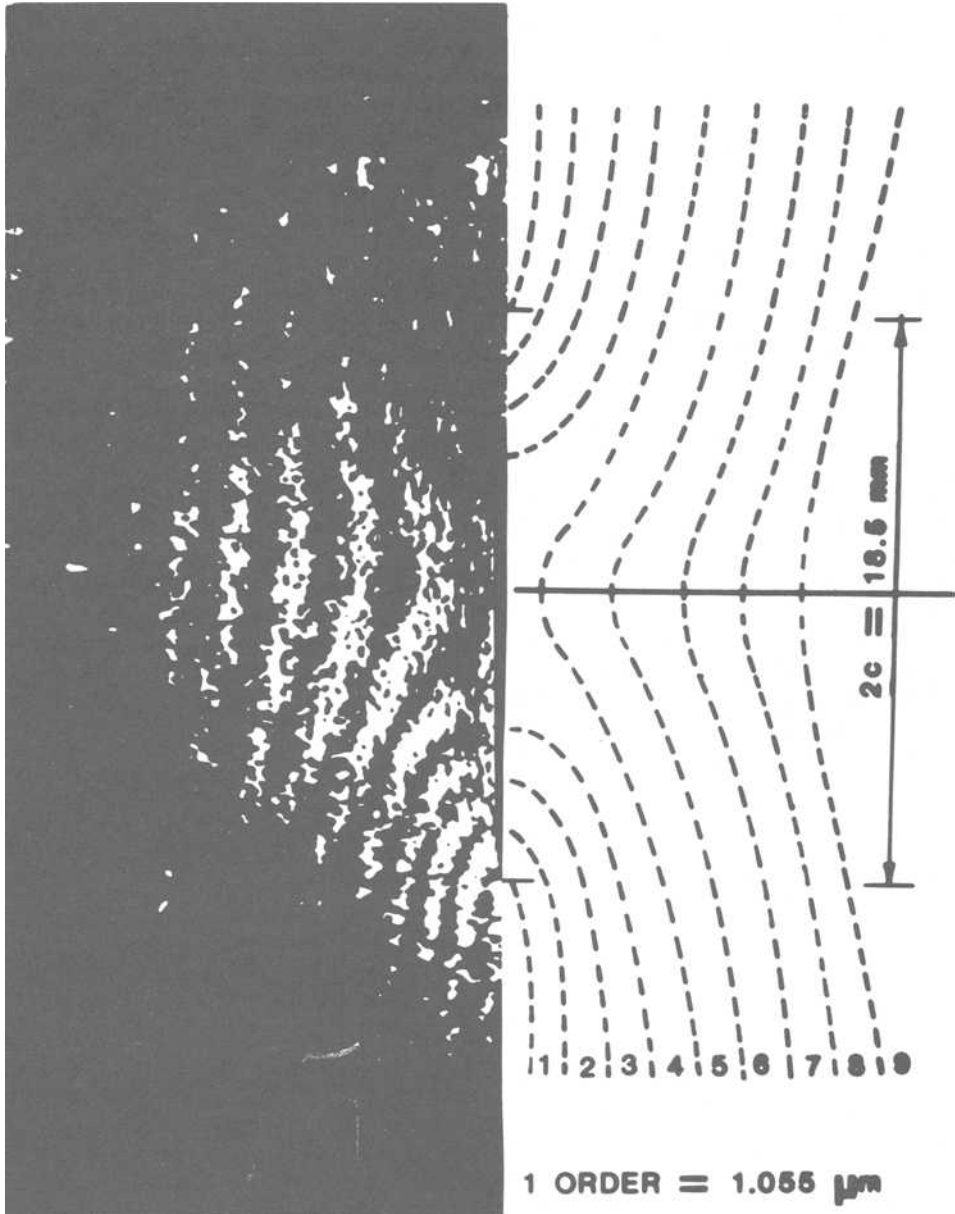


FIG. 2—Moiré fringes obtained by double-exposure holography.

a crack introduces a perturbation and the fringes lose their linearity, as vividly seen in Fig. 2.

One of the rules of interpretation of moiré patterns, as a consequence of continuity of displacements, is that the Moiré fringes of different order do not intersect. Consequently, one must assume that the two intersecting fringes belong to the same order and therefore the region that they enclose will have a line of zero strain along the line of symmetry (therefore, crack-tip regions have very high strains in the  $y$ -direction), the fringes belong to different order, and they are only joining in appearance. Truly, the field of displacement is discontinuous at the crack tip, and since the strains become infinite, the moiré fringes show a singularity at the corresponding point. The fact that two different order fringes seem to join indicate presence of an extremely high strain.

## Results

Following the procedure described in the least-squares technique, a general-purpose computer code is produced for simultaneous solution of Eqs 18 and 19. Apart from material properties, the program seeks values of  $M$ ,  $N$ , and  $Q$ . In the case of PVC pipe,  $M$  and  $N$  were taken to be 7, and  $Q$  was equal to 27.

The simultaneous solution of Eqs 18 and 19 provides a value of  $\lambda$  equal to 0.5515, as distinct from  $\lambda = 0.5$ . This establishes the loss of inverse square-root singularity on the surface and reconfirms the work of several investigators [21–26]. Benthem [24,25], Bazant and Estenssoro [23], and Smith and Epstein [26] obtained the values of  $\lambda$  as shown in Table 1.

This establishes that the series solution technique developed in this present work could complement the experimental results in accurate calculation of the loss of inverse square-root singularity at the crack front free surface intersection point.

## Discussion

The results given in Table 1 correspond to the eigenvalues of the displacement field  $\lambda_{us}$ , which are related to the eigenvalues of the stress field through the relationship  $\lambda_\sigma = 1 - \lambda_{us}$ .

Furthermore, the values in Table 1 correspond to the crack fronts free surface intersection angle  $\alpha = 90$  deg between the crack front and the free surface, while the results of this investigation correspond to an angle  $\alpha = 6$  deg. Takakuda [28], applying the boundary integral approach, gets the singularity orders from surface flaw in a half space intersecting the surface at arbitrary angles. Figure 3 shows Takakuda's results for a surface crack subjected to internal pressure, as a function of the intersection angle of the crack front with the free surface, and for different Poisson's ratios. It is evident that these results do not

TABLE 1—Values of  $\lambda$  obtained by various investigators.

Poisson's Ratio, $\nu$	Benthem (Theory)	Bazant (Theory)	Smith (Experimental)	Present (Experimental)
0.15	0.5164	0.516	...	...
0.30	0.5481	0.546	...	...
0.35	...	...	...	0.55
0.40	0.5871	0.587	0.58	...
0.48	...	...	0.63	...
0.50	0.6619	...	...	...

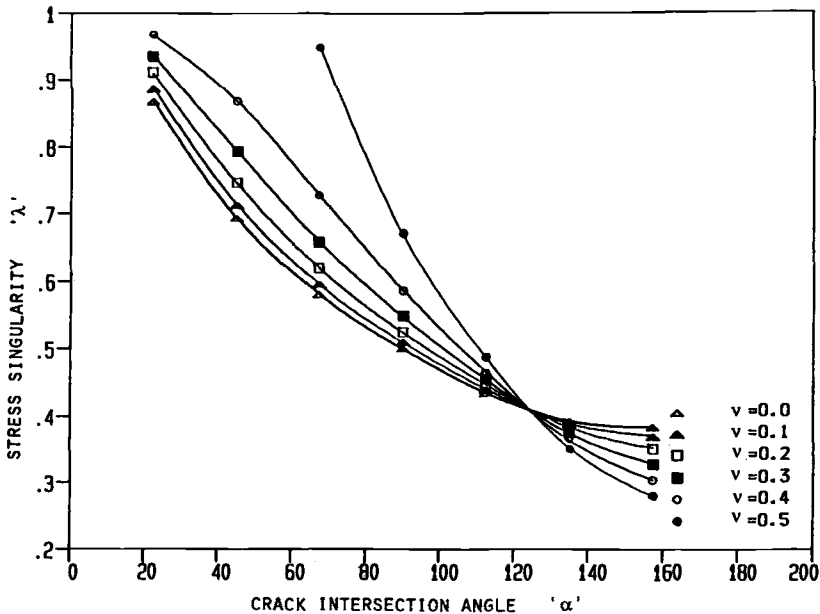


FIG. 3—Variation of stress singularity  $\lambda$  with crack front free surface intersection angle  $\alpha$  as per Takakuda [28].

agree with the experimental value found in the present investigation. Independently of the form of the algorithm used to obtain the value of the singularity, the experimental results give values of the singularity close but in excess of 0.5, whereas Takakuda's results predict a singularity close to 1 for an angle  $\alpha$  tending to zero. In view of the complexity of the solution of a surface crack problem, it is not easy to find the reason of this discrepancy. If one considers the value of Benthem for  $\alpha = \Pi/2$  as a correct value and one takes the experimental value as a good value, the singularity appears not to be greatly influenced by the angle  $\alpha$ .

## References

- [1] Etheridge, J. M. and Dally, J. W., "A Critical Review of Methods for Determining Stress-Intensity Factors from Isochromatic Fringes," *Experimental Mechanics*, Vol. 17, No. 6, 1977, pp. 248-254.
- [2] Smith, C. W., "Use of Optical Methods in Stress Analysis of Three-Dimensional Cracked Body Problems," *Journal of Optical Engineering*, Vol. 21, No. 4, 1982, pp. 66-703.
- [3] Sanford, R. J. and Dally, J. W., "A General Method for Determining Mixed-Mode Stress-Intensity Factors from Isochromatic Fringe Patterns," *Engineering Fracture Mechanics*, Vol. 11, No. 4, 1979, pp. 621-633.
- [4] Godutos, E. E. and Theocaris, P. G., "A Photoelastic Determination of Mixed-Mode Stress-Intensity Factors," *Experimental Mechanics*, Vol. 18, 1978, pp. 87-97.
- [5] Dally, J. W., "Dynamic Photoelastic Studies of Fracture," *Experimental Mechanics*, Vol. 19, No. 10, 1979, pp. 349-367.
- [6] Post, D., "Developments in Moiré Interferometry," *Journal of Optical Engineering*, Vol. 21, No. 3, 1982, pp. 458-467.
- [7] Rossmanith, H. P., "Analysis of Crack-tip Moiré Fringe Patterns," *International Journal of Fracture*, Vol. 21, No. 2, 1983, pp. 83-106.

- [8] Liu, H. W., and Ke, J. S., "Moiré Method," *Experimental Techniques in Fracture Mechanics*, Vol. 2, A. S. Kobayashi, Ed., SESA Monograph, Society for Experimental Stress Analysis, No. 2, 1975, pp. 111-165.
- [9] Nicolletto, G., Post, D., and Smith, C. W., "Moiré Interferometry for High Sensitivity Measurements in Fracture Mechanics," *Proceedings of the 1982 SESA/JSME Joint Conference on Experimental Mechanics*, Hawaii, Society of Experimental Stress Analysis/Japan Society of Mechanical Engineers, 1982, pp. 266-270.
- [10] Sharpe, W. H., Jr., "Coherent Optical Methods of Stress-Intensity Factor Measurement," *Proceedings of the 1982 SESA/JSME Joint Conference on Experimental Mechanics*, Hawaii, Society of Experimental Stress Analysis/Japan Society of Mechanical Engineers, 1982.
- [11] Barker, D. B. and Fourney, M. E., "Displacement Measurement in the Interior of 3-D Bodies Using Scattered Light Speckle Patterns," *Experimental Mechanics*, Vol. 16, No. 6, 1976, pp. 209-214.
- [12] Sciammarella, C. A., "Holographic Moiré, An Optical Tool for the Determination of Displacements, Strains, Contours, and Slopes of Surfaces," *Optical Engineering*, Vol. 21, No. 3, 1982, pp. 447-457.
- [13] Dally, J. W., Sciammarella, C. A., and Shareef, I., "Determination of the Stress-Intensity Factor  $K_I$  from In-Plane Displacement Measurements," *Proceedings of the Fifth International Congress on Experimental Mechanics*, Montreal, Canada, 1984, pp. 122-126.
- [14] Muskhelishvili, N. I., *Some Basic Problems of the Mathematical Theory of Elasticity*, Nordhoff Ltd, Groningen, the Netherlands, 1953, pp. 104-161.
- [15] Sih, G. C. and Liebowitz, H., "Mathematical Theory of Brittle Fracture," *Fracture*, Vol. 2, Academic Press, New York, 1968, pp. 91-93.
- [16] Westergaard, H. M., "Bearing Pressures and Cracks: Bearing Pressures Through a Slightly Waved Surface or Through a Nearly Flat Part of a Cylinder, and Related Problems of Cracks," *Journal of Applied Mechanics*, Vol. 6, 1937, pp. A49-A53.
- [17] Sanford, R. J., "A Critical Re-Examination of the Westergaard Method for Solving Opening Mode Crack Problems," *Mechanics Research Communications*, Vol. 6, 1979, pp. 289-294.
- [18] Williams, M. L., "On the Stress Distribution at the Base of a Stationary Crack," *Journal of Applied Mechanics*, 1957, pp. 109-114.
- [19] Irwin, G. R., "Analysis of Stresses and Strains Near the End of a Crack Traversing a Plate," *Journal of Applied Mechanics*, Vol. 24, 1957, pp. 361-364.
- [20] Kassir, M. K. and Sih, G. C., "Three-Dimensional Stress Distribution Around an Elliptical Crack Under Arbitrary Loadings," *Journal of Applied Mechanics*, Vol. 33, No. 3, 1966, pp. 601-611.
- [21] Sih, G. C., "A Review of the Three-Dimensional Stress Problems for a Cracked Plate," *International Journal of Fracture Mechanics*, Vol. 7, No. 1, 1971, pp. 35-59.
- [22] Folias, E. S., "On the Three-Dimensional Theory of Cracked Plates," *Journal of Applied Mechanics*, Vol. 42, No. 3, 1975, pp. 663-674.
- [23] Bazant, Z. P. and Estenssoro, L. F., "Stress Singularity and Propagation of Cracks at their Intersection with Surfaces," Structures Engineering Report 77-12/480, Department of Civil Engineering, Northwestern University, Evanston, IL, Dec. 1977.
- [24] Benthem, J. P., "State of Stress at the Vertex of a Quarter-Infinite Crack in a Half-Space," *International Journal of Solids Structures*, Vol. 13, 1977, pp. 479-492.
- [25] Benthem, J. P., "The Quarter-Infinite Crack in a Half Space; Alternate and Additional Solutions," *International Journal of Solids Structures*, Vol. 16, 1980, pp. 119-130.
- [26] Smith, C. W. and Epstein, J. S., "Measurement of Three-Dimensional Effects in Cracked Bodies," *Proceedings of the Fifth International Congress on Experimental Mechanics*, Montreal, Canada, 1984.
- [27] Kobayashi, A. S., "Fracture Mechanics," *Experimental Techniques in Fracture Mechanics*, A. S. Kobayashi, Ed., Iowa State University Press, Ames, IA, 1973.
- [28] Takakuda, K., "Stress Singularities Near Crack Front Edges," *Bulletin of Japan Society of Mechanical Engineers*, Vol. 28, No. 236, 1985, pp. 225-231.

## Fracture Behavior Prediction for Rapidly Loaded Surface-Cracked Specimens

---

**REFERENCE:** Kirk, M. T. and Hackett, E. M., **Fracture Behavior Prediction for Rapidly Loaded Surface-Cracked Specimens,"** *Surface-Crack Growth: Models, Experiments, and Structures, ASTM STP 1060*, W. G. Reuter, J. H. Underwood, and J. C. Newman, Jr., Eds., American Society for Testing and Materials, Philadelphia, 1990, pp. 142-151.

**ABSTRACT:** The feasibility of predicting the fracture behavior of surface cracks from shallow cracked bend specimens was investigated. The material studied was a high-strength steel stress relief embrittled to various levels of Charpy-V notch impact toughness. Material toughness was quantified in terms of the J-integral at total specimen failure ( $J_{crit}$ ), using both deeply notched and shallow-notched bend bars (single-edge notch bend) [SE(B)] dynamically loaded in a drop tower impact testing machine. These data were compared with the fracture behavior of rapidly pressure loaded part-through surface cracked bend [PS(B)] specimens, which had a shallow surface flaw introduced at the specimen midspan. For highly embrittled material (Charpy V-notch energy (CVE) between 10 J and 24 J),  $J_{crit}$  values measured using shallow crack SE(B) specimens were consistently higher than deep crack  $J_{crit}$  values due to the shorter crack size, as well as increased plastic energy dissipation within the specimen. These higher  $J_{crit}$  values served as better predictors of the PS(B) fracture performance than did comparable deep crack values. Even though  $J_{crit}$  cannot be considered a geometry independent measure of fracture toughness for shallow through cracks, values of this parameter determined using test specimens containing them appear to have considerable engineering utility for predicting the fracture behavior of part-through surface flaws.

**KEY WORDS:** J-integral, dynamic loading, fracture mechanics, elastic-plastic fracture, short crack, surface crack

The value of the J-integral at or near the onset of ductile crack growth has been recognized for some time to be an appropriate single-parameter measurement of upper-shelf fracture toughness, provided certain criteria are satisfied. These criteria—associated with maintenance of a Hutchinson-Rice-Rosengren (HRR) singularity at the crack tip—are typically satisfied in laboratory experiments by testing deeply cracked ( $a/W$  between 0.50 and 0.75) specimens loaded primarily in bending. In this case, the HRR singularity continues to exist past net section yield due to a high-stress triaxiality at the crack tip [1]. Using slip line field analysis, Matsoukas, Cotterell, and Mai [2] have determined that the crack tip stress triaxiality decreases with decreasing crack size. This reduction manifests itself experimentally as an increase in the observed fracture toughness with decreasing initial crack depth [3-5].

You and Knott [6] experimentally demonstrated that, for a given maximum crack depth, fracture initiation toughness measured using bend specimens containing shallow through flaws compares well with that measured at the maximum depth of semielliptical

<sup>1</sup> Mechanical engineer and materials engineer, respectively, David Taylor Research Center, Annapolis, MD 21402.



surface flaws. This observation may be used to advantage during fracture safety analyses of structures containing shallow surface flaws by using the techniques of Sumpter [7]. Sumpter has suggested that toughness levels for surface cracks may be quantified in terms of the J-integral by testing bend specimens with through flaws of similar depth. Sumpter derived  $J$  formulas for specimens of this type which compare well with elastic-plastic finite-element results. This approach sacrifices the specimen independent properties of  $J_{Ic}$  values determined with deeply cracked specimens in favor of a more accurate engineering approximation to the fracture resistance of surface flaws typically encountered in service.

In this investigation, the feasibility of using this approach for a high-strength steel alloy stress relief embrittled to various levels of Charpy V-notch impact toughness was investigated. Material toughness was quantified in terms of the J-integral at total specimen failure ( $J_{crit}$ ), using both deeply notched and shallow-notched bendbars dynamically loaded in a drop tower impact testing machine. These data were compared to the fracture behavior of rapidly pressure loaded part-through surface cracked bend specimens, which had a shallow surface flaw introduced at the specimen midspan.

### Material Investigated

Typical chemical composition and strength properties for high-strength steel are given in Table 1. The subject of this investigation was the fracture tolerance of this alloy in a stress relief embrittled condition. In high-strength steel, stress relief embrittlement changes the typical high-energy dissipation upper shelf fracture mode (transgranular fracture by microvoid coalescence) to a low-energy dissipation intergranular fracture mode. This change reduces the material fracture resistance, as illustrated by the reduction of the Charpy V-notch energy (CVE) with time held at the embrittling temperature, as shown in Fig. 1. For purpose of correlation of  $J_{crit}$  values, the average CVE will be used as a qualitative index of the degree of material embrittlement. This use of CVE is only appropriate when the fracture mode does not vary with specimen size or type, as was the case for this material.

TABLE 1—*Typical chemical composition and strength properties<sup>a</sup> of high-strength steel.*

Element	Weight %
C	0.08
Mn	0.67
Si	0.31
P	0.02
S	0.014
Cr	1.52
Ni	3.1
Mo	0.43
Cu	0.2
V	0.003
Ti	0.001
0.2% Offset yield strength, MPa	574
Ultimate tensile strength, MPa	674
Elongation, %	24
Reduction in area, %	66

<sup>a</sup>Strength properties measured using round tensile specimens of 50.8-mm gage length and 12.8-mm diameter.

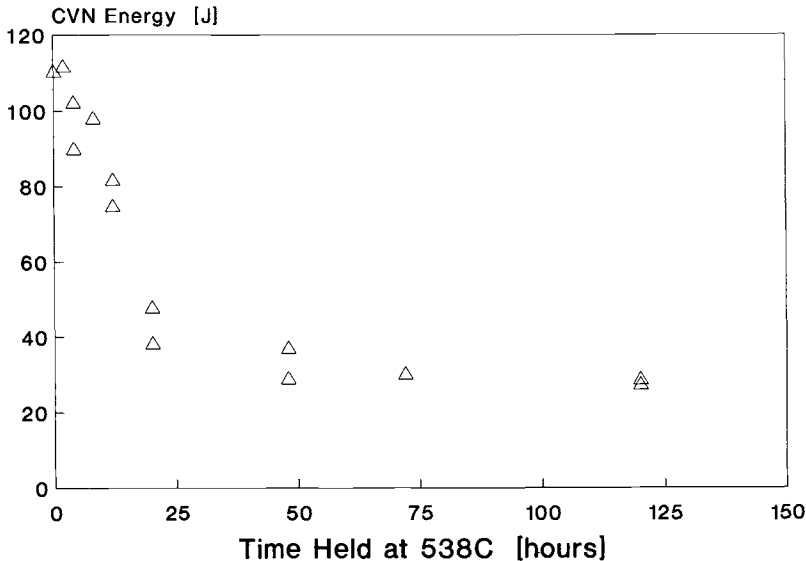


FIG. 1—Stress relief embrittlement of high-strength steel as evidenced by reduction of CVE with time held at the embrittling temperature.

### Experimental Approach and J-Integral Formulas

#### Deep Cracked Single-Edge Notch Bend [SE(B)]

Three-point bend specimens (Fig. 2a) having initial precrack depths between 0.66 and 0.70  $a/W$  and nominal thicknesses of 25.4 mm and 50.8 mm were tested. All specimens were dynamically loaded in a drop tower using the procedures developed by Hackett and Joyce [8]. Load was measured during the test using strain gages attached at the quarter span points of the specimen and wired to form a full bridge. The relation between the bridge output and the applied load was established prior to each test by statically loading the specimen in the elastic regime. Hackett, Joyce, and Shih [9] have determined that loads determined in this manner compare well with those measured with a load cell, even in the post-yield regime. Crack opening displacement was also measured using a capacitance transducer placed in the notch. The  $J_{crit}$  value was calculated using the formula due to Rice [10]

$$J_{crit} = 2 \cdot A/B_{net} \cdot b_0 \quad (1)$$

where

- $A$  = area under the load versus load line displacement curve,
- $B_{net}$  = minimum specimen thickness, and
- $b_0$  = remaining ligament.

Load line displacement was calculated from the measured crack opening displacement (COD) by multiplying by the factor 1.16, determined by Kirk and Hackett [11] to relate these two quantities for wrought high-strength steel specimens having the same initial crack length. It should be noted that the stress-strain properties of this material are quite similar to those of the material considered herein.

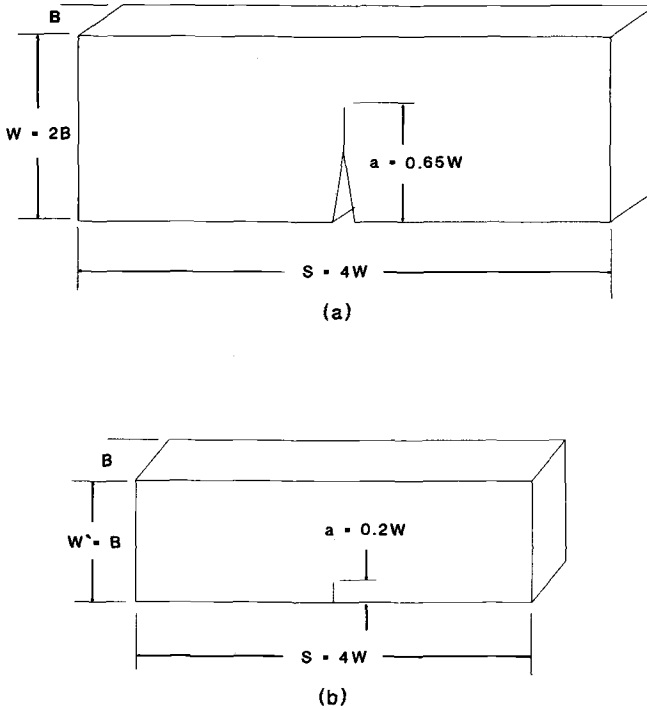


FIG. 2—SE(B) specimens; (a) deep crack; (b) shallow crack.

### Shallow Cracked SE(B)

The shallow-cracked three-point bend specimen (Fig. 2b) was designed consistent with the criteria forwarded for the subsidiary bend specimen in British Standard Methods for COD Testing (BS 5762). The specimen thickness (50.8 mm) was the same as the structure whose fracture behavior was to be predicted, while the precrack depth ( $a/W = 0.20$  to  $0.23$ ) was slightly deeper than the surface crack of interest. In this case, the “structure” referred to is the part-through surface cracked bend specimen described in the next section.

All shallow cracked SE(B)s were tested in a manner similar to that described previously for the deeply cracked specimens. For these specimens, load line displacement was calculated from the displacement measured using a noncontacting eddy-current transducer positioned 50.8 mm from the loading point. As with the load, the relation between the output of these transducers and the actual load line displacement was determined by statically loading each specimen in the elastic region prior to testing. For these specimens, the load line displacement was approximately 1.8 times larger than that recorded by the eddy current transducer.

The formula proposed by Sumpter [7] was used to calculate  $J_c$  for specimens of this type. This formula is

$$J_c = \frac{K^2 \cdot (1 - \nu^2)}{E} + \frac{n_p \cdot U_p}{B \cdot b_0} \quad (2)$$

where

$K$  = linear elastic stress-intensity factor calculated from maximum applied load,

$\nu$  = Poisson's ratio,

$E$  = Young's modulus,

$B$  = specimen thickness,

$b_0$  = initial remaining ligament

$U_p$  = plastic component of the area under the load versus load line displacement trace, and

$$n_p = 0.32 + 12.0(a/W) - 49.5(a/W)^2 + 99.8(a/W)^3 \text{ for } a/W < 0.282$$

$$= 2.0 \text{ for } a/W \geq 0.282.$$

Sumpter demonstrated that  $J$  values thus calculated lie within 10% of  $J$  values computed using a numerical contour integration in a homogeneous specimen having normalized crack lengths ranging from 0.1 to 0.5.

#### *Part-Through Surface Cracked Bend Specimens, PS(B)*

Figure 3 shows the part-through surface cracked bend, PS(B), specimen employed in this investigation. A semielliptical surface flaw of approximately 16.5-mm (0.65 in.) surface extent and 6.35-mm (0.25 in.) depth was introduced at the midspan of each specimen by fatigue extension from an electro-discharge machined notch. Subsequent to fatigue crack-ing, the beams were welded into carrier plates of high-strength steel. Strain gages were placed along the specimen midspan on the cracked side to record the development of strain during the test. Specimens were then bolted into a test die, which left only the test section free to deform. Loading was accomplished by rapidly applying a pressure pulse to the uncracked surface. The maximum  $J$  value applied to the specimen was calculated from the maximum recorded strain using Turner's Engineering- $J$  approach [12], which expresses  $J$  as a function of applied strain as follows

$$J = (e/e_y)^2 \cdot [1 + 0.5 \cdot (e/e_y)^2] \cdot G \text{ for } e/e_y \leq 1.2 \quad (3a)$$

$$= 2.5 \cdot [(e/e_y) - 0.2] \cdot G \quad \text{for } e/e_y > 1.2 \quad (3b)$$

where

$$G = Y^2 \cdot S_{yd}^2 \cdot (a/E),$$

$e$  = maximum applied strain,

$a$  = maximum crack depth,

$E$  = Young's modulus,

$S_{yd}$  = dynamic yield stress,

$e_y = S_{yd}/E$ , and

$Y = K/(S \cdot a^{1/2})$ , linear elastic shape factor.

The solution of Newman and Raju [13] for a semielliptical surface crack in a plate subjected to combined tension and bending loads was used to determine the appropriate  $Y$  values. When the specimen failed across the remaining ligament, strain data were sometimes lost. In these cases, the maximum applied strain was calculated from the severity of the applied pressure pulse based on data obtained from similar specimens for which all data were recorded.

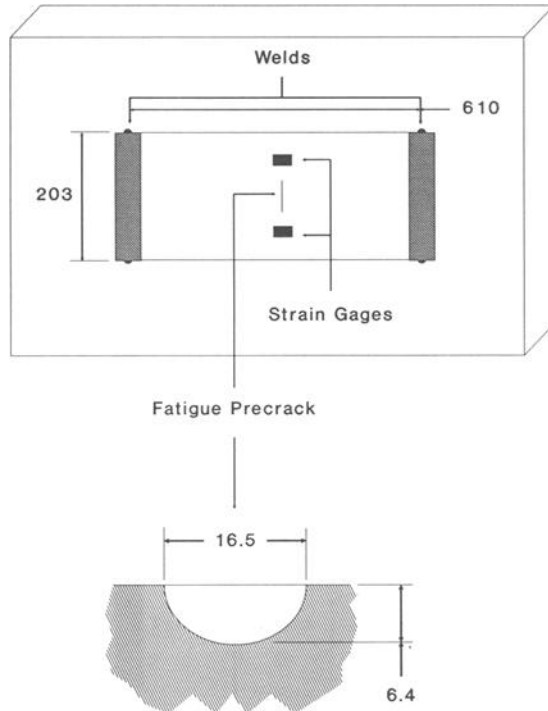


FIG. 3—PS(B) specimen: (a) plan view; (b) detail of precrack at centerline midspan intersection (oriented along midspan). Specimen thickness is 50.8 mm (all dimensions in mm).

## Results and Discussion

Figure 4 compares the typical variation of load, or strain, with time for each of the three specimen types tested. These data indicate that all specimens were loaded at approximately the same rate. The small loading rate variations between the different specimens is not expected to influence the properties measured because the material is not very rate sensitive. As indicated in Fig. 5, the 0.2% offset yield strength and ultimate tensile strength only increase by 12% over a four-order of magnitude increase in loading rate. The yield strength value at the highest loading rate (3.5/s)—675 MPa—was employed in the calculation of  $G$  in Eq 3.

In Fig. 6, the results of the SE(B) fracture tests are presented. The average CVE values shown were determined by testing CVN specimens cut from the fractured SE(B) specimen halves. Here, average values were used for clarity of presentation; data scatter would have to be accounted for prior to engineering use of these, or similar, data. The ordinate values show the total  $J$  absorbed by the specimen prior to section failure ( $J_{crit}$ ). Due to the intergranular fracture mode exhibited by this material, failure was catastrophic for both fully elastic and elastic-plastic loading records.

The data in Fig. 6 indicate that there is no systematic dependence of  $J_{crit}$  on specimen thickness for the deeply cracked SE(B)s. A comparison of the shallow and deep crack SE(B) data indicates that the shallow cracks have considerably more resistance to fracture over the CVE range examined. Moreover, the shallow cracked SE(B)s showed greater sensitivity

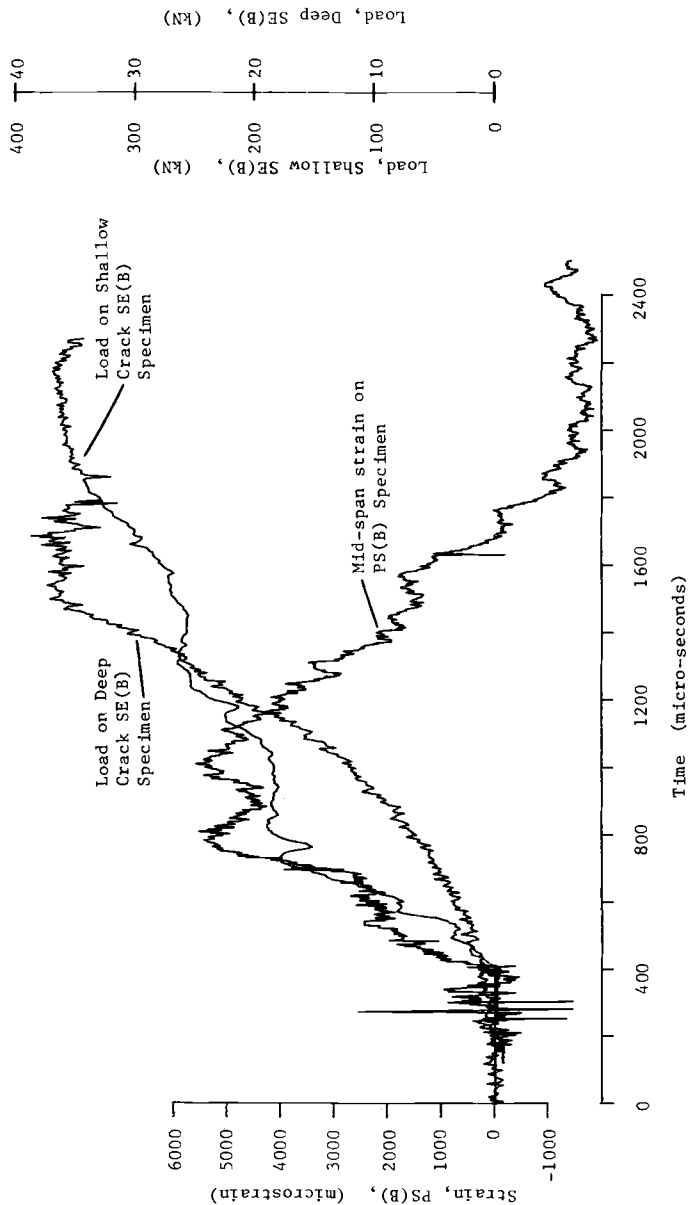


FIG. 4—Typical strain (or time) versus load behavior of deep crack SE(B), shallow crack SE(B), and PS(B) specimens.

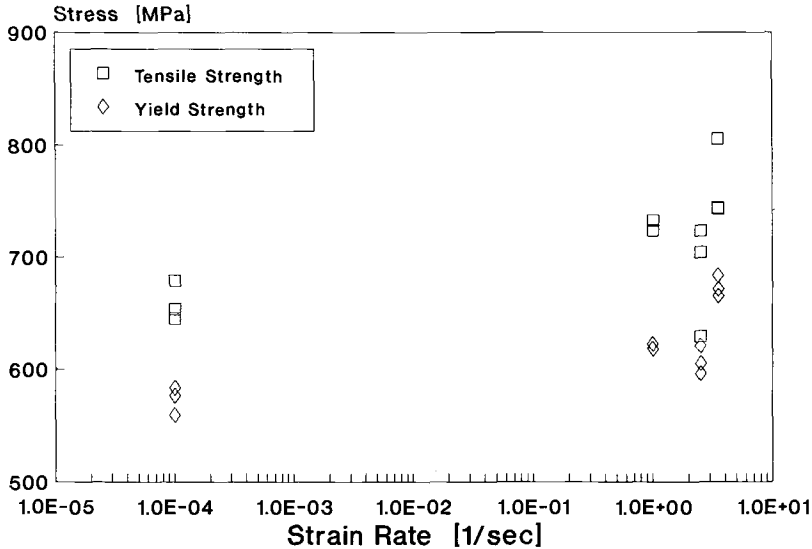


FIG. 5—Variation of 0.2% offset yield strength and ultimate tensile strength with loading rate for embrittled high-strength steel.

to changes in CVE than the more deeply cracked specimens. At an average CVE of 27 J, where the load-displacement behavior was predominantly linear, only a modest increase of  $J_{crit}$  was observed with decreasing crack length. However, at higher CVE (54 J), where elastic-plastic load-displacement behavior was observed, considerably greater increases in  $J_{crit}$  occurred. It is therefore suspected that elevation of  $J_{crit}$  at low CVE is mostly due to a

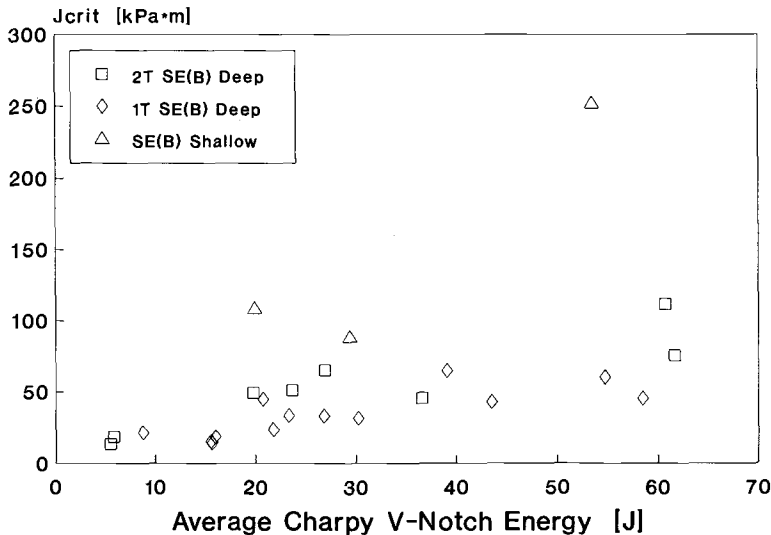


FIG. 6—Variation of the critical  $J$  at fracture with the CVE for deep and shallow crack SE(B) specimens of embrittled high-strength steel.

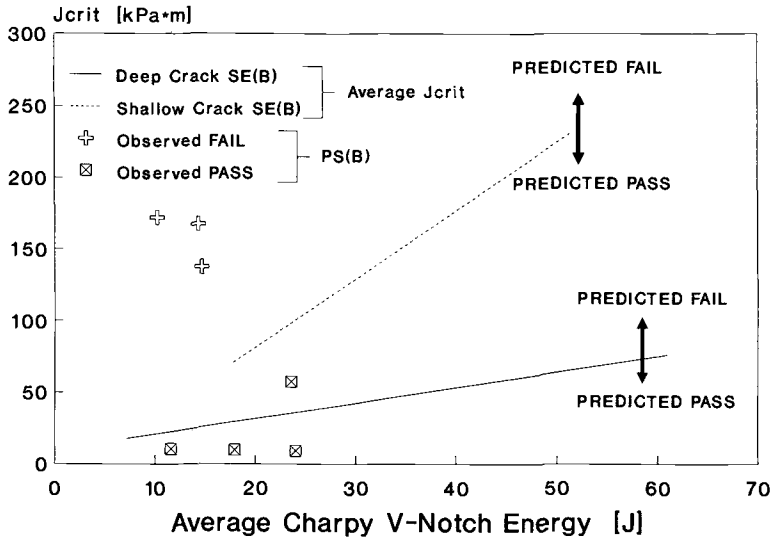


FIG. 7—Comparison of observed PS(B) fracture response to predictions based on data from shallow-crack and deep-crack SE(B) specimens of embrittled high-strength steel.

short crack effect, while the elevation at higher CVE is also attributable to increased plastic energy dissipation.

While the variations of  $J_{crit}$  with CVE and initial crack depth shown in Fig. 6 appear reasonable based on physical considerations, the engineering utility of either data set (shallow crack or deep crack) can only be judged by how well the fracture behavior of a surface crack is predicted. To this end, several PS(B) specimens were tested. The results of these experiments are compared to trend lines drawn through the SE(B) data (Fig. 6) in Fig. 7. The shallow crack SE(B) data predicted the results of all PS(B) experiments correctly, while the deep crack SE(B) data predicted one PS(B) specimen, which actually passed, to fail. (A pass is a specimen for which no crack extension was observed, while a fail is a specimen in which crack propagation completely severed the remaining ligament.) Deep crack SE(B) data predicted PS(B) fracture behavior correctly only when mid span strains in the PS(B) specimens remained below yield level. Thus, while the deep crack SE(B) data provide a conservative assessment of the PS(B) fracture behavior, fracture behavior predictions based on shallow crack SE(B) data were seen to be correct for all PS(B) specimens tested. While this approach lacks the geometry independent qualities of a  $J_{Ic}$  criteria, there seems to be considerable engineering merit in testing a laboratory specimen designed to model a surface flaw.

## Conclusions

For the steel used in this investigation, embrittled to an average Charpy V-notch energy (CVE) between 10 J and 24 J, the following conclusions follow from the data presented herein:

1. Use of the value of the  $J$ -integral at complete specimen separation ( $J_{crit}$ ), measured using deep crack ( $a/W = 0.65$ ) bend specimens, to predict the fracture behavior of part-through surface crack bend [PS(B)] specimens provides conservative results.



2.  $J_{crit}$  values measured using shallow crack bend specimens were consistently higher than deep crack values due to the shorter crack size as well as to increased plastic energy dissipation within the specimen. These higher  $J_{crit}$  values served as better predictors of the PS(B) fracture performance than did comparable deep crack values.

3. Even though  $J_{crit}$  cannot be considered a geometry independent measure of fracture toughness for shallow through cracks, values of this parameter determined using test specimens containing them appear to have considerable engineering utility for predicting the fracture behavior of part-through surface flaws.

## References

- [1] German, M. D. and Shih, C. F., "Requirements for a One Parameter Characterization of Crack Tip Fields by the HRR Singularity," *International Journal of Fracture*, Vol. 17, No. 1, 1981, pp. 27-43.
- [2] Matsoukas, G., Cotterell, B., and Mai, Y.-W., "Hydrostatic Stress and Crack Opening Displacement in Three-Point Bend Specimens with Shallow Cracks," *Journal of Mechanics and Physics of Solids*, Vol. 34, No. 5, 1986, pp. 499-510.
- [3] Zhang, D. Z. and Wang, H., "On the Effect of the Ratio  $a/W$  on the Values of  $d_i$  and  $J_i$  in a Structural Steel," *Engineering Fracture Mechanics*, Vol. 26, No. 2, 1987, pp. 247-250.
- [4] Matsoukas, G., Cotterell, B., and Mai, Y.-W., "Crack Opening Displacement and Hydrostatic Stress," *Engineering Fracture Mechanics*, Vol. 24, 1986, pp. 837-842.
- [5] Matsoukas, G., Cotterell, B., and Mai, Y.-W., "The Effect of Shallow Cracks on Crack Opening Displacement," *Engineering Fracture Mechanics*, Vol. 24, No. 6, 1986, pp. 837-842.
- [6] You, C. P. and Knott, J. F., "Effects of Crack Shape on Fracture Toughness in a High-Strength Structural Steel," *Engineering Fracture Mechanics*, Vol. 24, No. 2, 1986, pp. 291-305.
- [7] Sumpter, J. D. G., " $J_c$  Determination for Shallow Notch Welded Bend Specimens," *Fatigue Fracture in Engineering Material Structures*, Vol. 10, No. 6, 1987, pp. 479-493.
- [8] Hackett, E. M., Joyce, J. A., and Shih, C. F., "Measurement of Dynamic Fracture Toughness of Ductile Materials," *Nonlinear Fracture Mechanics: Volume I—Time-Dependent Fracture*, ASTM STP 995, A. Saxena, J. D. Landes, and J. L. Bassani, Eds., American Society for Testing and Materials, Philadelphia, 1989, pp. 274-297.
- [9] Joyce, J. A. and Hackett, E. M., "An Advanced Procedure for J-R Curve Testing Using a Drop Tower," *Nonlinear Fracture Mechanics: Volume I—Time-Dependent Fracture*, ASTM STP 995, A. Saxena, J. D. Landes, and J. L. Bassani, Eds., American Society for Testing and Materials, Philadelphia, 1989, pp. 298-317.
- [10] Rice, J. R., *Journal of Applied Mechanics*, Vol. 35, 1968, pp. 379-386.
- [11] Kirk, M. T. and Hackett, E. M., "An Evaluation of J-R Curve Testing Using Three-Point Bend Specimens," presented at the 18th National Symposium on Fracture Mechanics, Boulder, CO, June 1985.
- [12] Turner, C. E., "Further Developments on a J-Based Design Curve and Its Relationship to Other Procedures," *Elastic-Plastic Fracture: Second Symposium. Volume II: Fracture Curves and Engineering Applications*, ASTM STP 803, C. F. Shih and J. P. Gudas, Eds., American Society for Testing and Materials, Philadelphia, 1983, pp. II-80-II-102.
- [13] Newman, J. C. and Raju, I. S., "Analysis of Surface Cracks in Finite Plates Under Tension or Bending Loads," NASA Technical Paper 1578, National Aeronautics and Space Administration, Hampton, VA, 1979.

# Measurements of CTOD and CTOA Around Surface-Crack Perimeters and Relationships Between Elastic and Elastic-Plastic CTOD Values

---

**REFERENCE:** Reuter, W. G. and Lloyd, W. R., "Measurements of CTOD and CTOA Around Surface-Crack Perimeters and Relationships Between Elastic and Elastic-Plastic CTOD Values," *Surface-Crack Growth: Models, Experiments, and Structures, ASTM STP 1060*, W. G. Reuter, J. H. Underwood, and J. C. Newman, Jr., Eds., American Society for Testing and Materials, Philadelphia, 1990, pp. 152–176.

**ABSTRACT:** A difficulty associated with predicting structural integrity is that the surface cracks found in structural components are three-dimensional whereas the crack-tip opening displacement (CTOD) and J-integral analytical techniques were derived from two-dimensional theory. This paper provides data from specimens containing surface cracks (aspect ratio either 0.1 or 0.5 and crack depth-to-thickness ratio 0.6); presents measured values of CTOD, crack-tip opening angle (CTOA), and  $\Delta a$ ; provides experimental results relative to the center of rotation and the use of the Newman-Raju solutions for predicting the variation in CTOD around the crack perimeter; and evaluates possible correlations between CTOD, CTOA, and  $\Delta a$ .

**KEY WORDS:** fracture toughness ( $K_{Ic}$ ,  $K_{crit}$ , CTOD, CTOA), surface cracks

## Nomenclature

- $a$  Crack depth, measured normal from cracked plate surface to point of maximum penetration
- $\Delta a$  Generally, crack growth at maximum depth, but used here to include crack growth normal to crack border
- $a'$  Crack depth, measured normal from cracked plate surface to intersection with crack border
- $a_0$  Original crack depth
- $a/2c$  Aspect ratio for semielliptical surface cracks
- $2c$  Crack length
- CMOD Crack-mouth opening displacement
- CTOA Crack-tip opening angle
- CTOD Crack-tip opening displacement

<sup>1</sup> Principal engineer and senior engineer, respectively, Idaho National Engineering Laboratory, EG&G Idaho, Inc., P. O. Box 1625, Idaho Falls, ID 83415-2210.

<sup>2</sup> See the American Society for Testing and Materials (ASTM) Test Method for Plane-Strain Fracture Toughness of Metallic Materials (E 399) and Test Method for  $J_{Ic}$ , a Measure of Fracture Toughness (E 813).

CTOD (90)	CTOD measured at intersection of 90-deg included angle with extrapolated extension of original crack planes in their final position (Fig. 8b)
CTOD (90')	CTOD measured at intersection of 90-deg included angle with actual crack front (Fig. 8a)
CTOD (CT)	CTOD measured at tip of fatigue crack (Fig. 8b)
CVN	Charpy V-notch impact
$E$	Young's modulus
$J$	J-integral
$K$	Applied stress-intensity factor
LN <sub>2</sub>	Liquid nitrogen
$P$	Applied load
$R$	Distance from crack mouth to center of rotation; measurements are made perpendicular to cracked plate surface
$t$	Specimen thickness
$W$	Specimen width
$\delta$	Crack-tip opening displacement, used interchangeably with CTOD
$\delta_{el}$	Elastic component of $\delta$
$\delta_{pl}$	Plastic component of $\delta$
$\delta_t$	$\delta_{el} + \delta_{pl}$
$\nu$	Crosshead displacement
$\theta$	Angular position of a point on crack border; see Fig. 9
$\sigma$	Remote applied stress
$\sigma_{ys}$	Yield strength
$\sigma_{uts}$	Ultimate tensile strength

A numerical approach based on either the J-integral or crack-tip opening displacement (CTOD) is frequently used in predicting the behavior (initiation of crack growth, crack growth, and instability) of a structural component containing a defect and loaded into the elastic-plastic or fully plastic region. The defects actually found in structural components, partial penetrating or completely embedded flaws, are three-dimensional (3-D), whereas the J-integral and CTOD concepts (theory, test procedures, and data) are derived from two-dimensional (2-D) theories.

There is also a substantial difference between estimating a safe condition and predicting the actual failure conditions. For example, it is easier to predict that a structural component will not fail when exposed to a specific set of conditions than it is to predict the critical values of CTOD, crack-tip opening angle (CTOA), or J-integral associated with initiation of crack growth, crack growth, and instability. An associated difficulty is identifying the value of CTOD or  $J$  at a specific location around the circumference of a surface crack as a function of load.

Another major problem is the lack of applicable data from flawed structures for comparison with predictions. This may be overcome by assuming that experimental data generated from plate specimens containing surface cracks are applicable for comparison with predictions. This paper (1) provides experimental measurements of CTOD and CTOA around the circumference of a surface crack as a function of load, (2) provides experimental measurements of distance from crack mouth to center of rotation ( $R$ ) and identifies the limits of applicability for using the Newman-Raju stress-intensity factor equation [1] to predict CTOD distributions for two surface crack configurations, and (3) evaluates possible correlations between applied load ( $P$ ), CTOA, and increment of crack growth ( $\Delta a$ ).

### Materials and Test Procedures

The specimens were fabricated from as-rolled American Society for Testing and Materials (ASTM) A710 Grade A steel. The significant mechanical and physical properties of this material, at 297 K, are yield strength ( $\sigma_{ys}$ ) = 470 MPa, ultimate tensile strength ( $\sigma_{uts}$ ) = 636 MPa, Young's modulus ( $E$ ) = 208.4 GPa, and Poisson's ratio = 0.256. The material chemistry is: 0.05 carbon, 0.47 manganese, 0.010 phosphorus, 0.004 sulfur, 0.25 silicon, 0.74 chromium, 0.85 nickel, 0.21 molybdenum, 1.20 copper, 0.038 columbium, and the balance iron. Figure 1 shows engineering stress-strain and true stress-strain plots obtained at 297 K. When tested in the lower region of the ductile-brittle transition zone (297 K), as defined by results from Charpy V-notch impact tests (CVN), the A710 generally displays elastic or elastic-plastic behavior. Replicate specimens containing surface cracks in the  $T$ - $S$  orientation were fabricated with the configuration shown in Fig. 2. The speci-

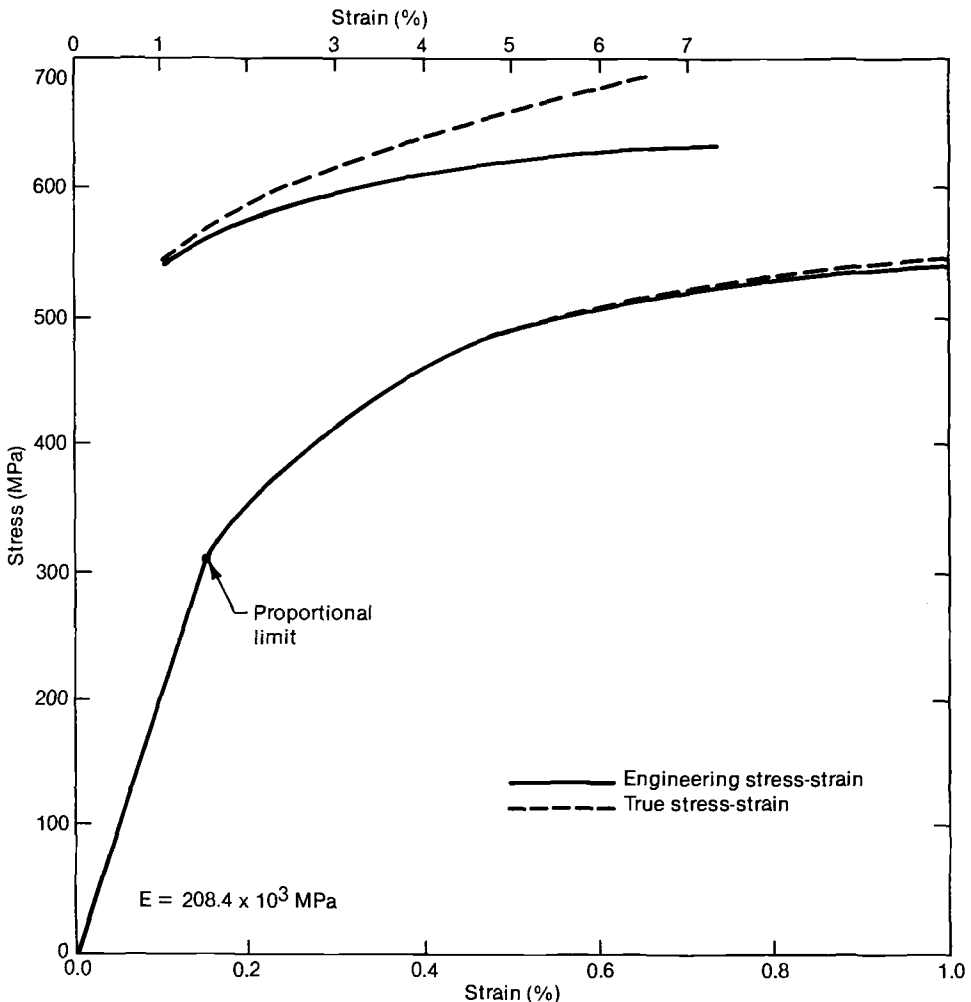


FIG. 1—Stress-strain plot for ASTM A710 steel at 295 K.

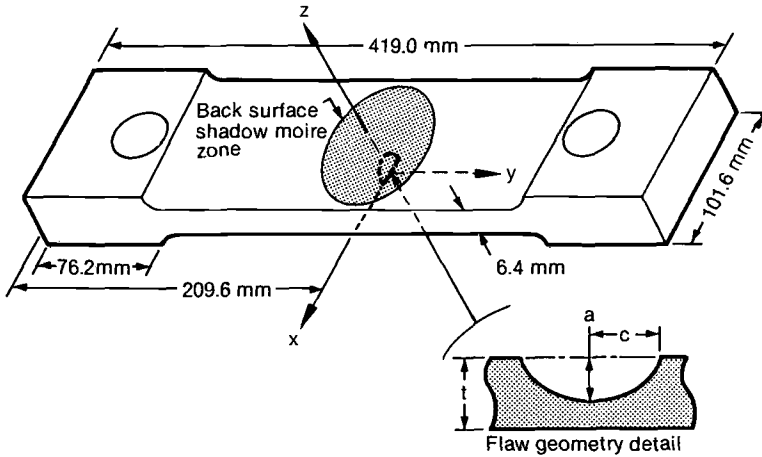


FIG. 2—Configuration of specimens containing surface cracks.

men and fatigue precrack dimensions are presented in Table 1. The specimens had either a crack depth to plate thickness ratio ( $a/t$ ) = 0.63 for  $a/2c$  = 0.12 where  $2c$  is crack length or  $a/t$  = 0.57 for  $a/2c$  = 0.47. These specimens were tested under monotonic loading at 297 K, which corresponds to about 40% of the way up the ductile-to-brittle transition curve, as defined by CVN impact test results. A similar statement is possible based on static tests of standard<sup>2</sup> fracture toughness specimens, though the database is not as complete as the CVN results.

Replicate specimens were tested to varying load-crosshead displacement values. Figures 3 and 4 are typical load-displacement curves ( $\nu$ ) for  $a/2c$  = 0.1 and 0.5, respectively. It was possible to separate the load-displacement plots into the three shown in Fig. 3 and the two shown in Fig. 4. Observe the consistency of these plots, which confirms that the specimens

TABLE 1—Specimen and defect sizes.

Specimen Number	mm					
	$t$	$W$	$a_0$	$2c$	$a/2c$	$a/t$
E-1	6.325	101.62	3.785	32.944	0.115	0.60
E-2	6.325	101.60	3.810	32.995	0.115	0.60
E-4	6.350	101.60	...	32.995	...	...
E-5	6.312	101.62	4.216	33.680	0.125	0.67
E-8	6.312	101.60	4.115	33.147	0.124	0.65
E-9	6.337	101.62	4.191	32.995	0.127	0.66
E-12	6.375	101.60	3.886	33.020	0.118	0.61
E-16	6.414	101.60	3.200	7.722	0.414	0.50
E-20	6.325	101.62	...	7.620	...	...
E-22	6.350	101.60	3.556	7.569	0.470	0.56
E-24	6.312	101.62	3.835	8.179	0.469	0.61
E-25	6.312	101.65	...	7.696	...	...
E-26	6.350	101.60	3.658	7.620	0.480	0.58
E-27	6.325	101.62	3.632	7.544	0.481	0.57
E-28	6.312	101.58	3.861	7.722	0.500	0.61
E-29	6.452	101.60	...	8.230	...	...

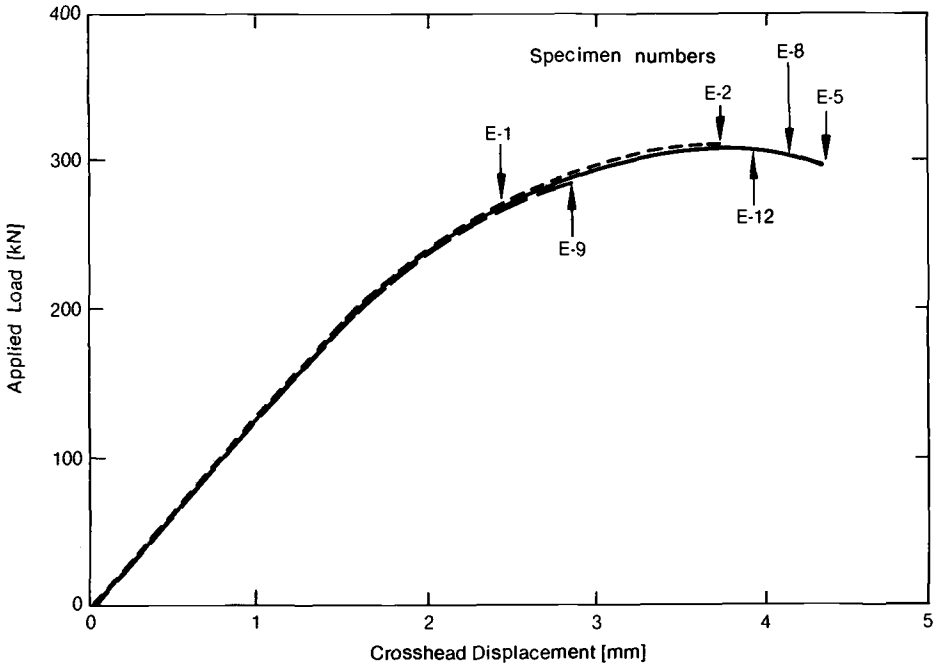


FIG 3—Load-crosshead displacement curves for specimens with  $a/2c = 0.1$ .

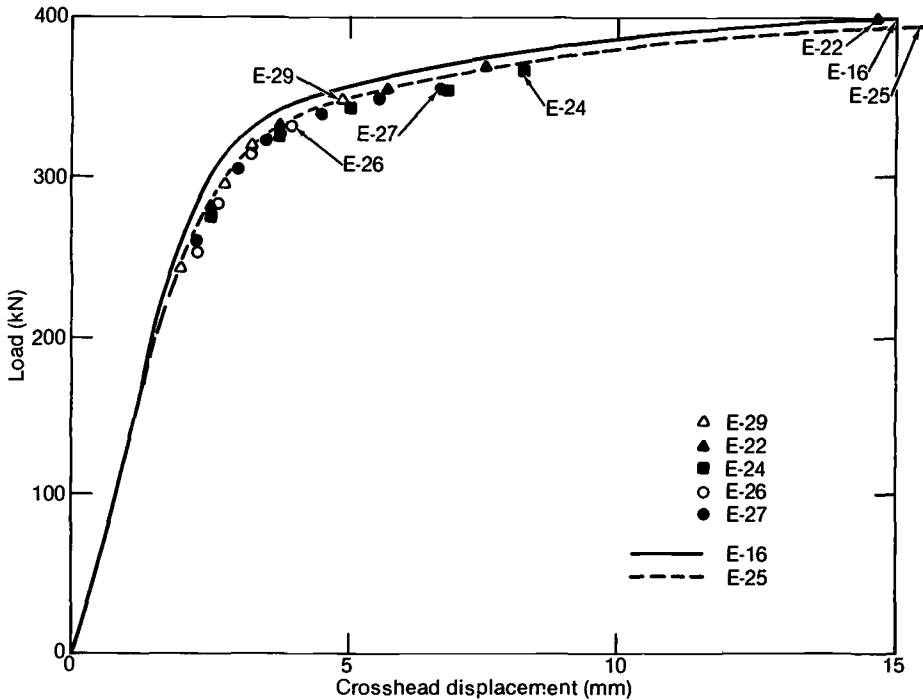


FIG 4—Load-crosshead displacement curves for specimens with  $a/2c = 0.5$ .

were indeed uniform. The points indicated by the arrows identify where the test was terminated for that specific specimen. Symbols in Fig. 4 identify specific locations on the load-displacement plot for the identified specimen; symbols were used because these data were collected using different scales and it was easier to transfer specific points instead of the total curve to the general plot.

Many of these specimens were examined metallographically, after loading, to determine  $\Delta a$ , crack-mouth opening displacement (CMOD), CTOD, CTOA, and the crack tip and back surface configurations as a function of location around the perimeter of the surface crack. The specimens were sliced perpendicular to the plane of the crack and either perpendicular to the cracked plate surface or perpendicular to the crack border. (This is illustrated in Fig. 9 and is discussed later.)

Additionally, microtopographic techniques were used to develop elevation contours, similar to topographic maps, of the fracture surfaces. Detailed explanation of this technology is provided in Kobayashi et al. [2] and Zhang et al. [3]. The first approach used for the microtopographic measurements consisted of loading the specimen to the desired ( $P, \nu$ ) region, unloading, cooling the specimen in liquid nitrogen ( $LN_2$ , a temperature associated with the lower shelf) and loading to failure by cleavage. The second approach consisted of applying fatigue cycles after partial unloading to  $0.85 P_{max}$ , cooling the specimen in  $LN_2$ , and testing to failure. The two approaches provided either cleavage fracture or fatigue crack extension as a boundary outlining the extent of subcritical crack growth that occurred during application of the initial load. These techniques were used to determine if additional plastic deformation occurred during the final loading to failure in  $LN_2$ . No discernible differences in the extent of plastic deformation were observed.

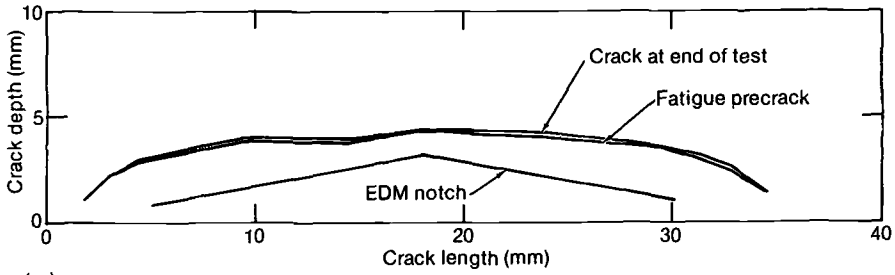
The metallographic sectioning and microtopographic techniques provided that part of CMOD, CTOA, CTOD, etc., associated with plastic deformation. It is assumed that elastic unloading local to the crack tip during specimen unloading is of negligible concern. This will be evaluated in the future.

## Test Results

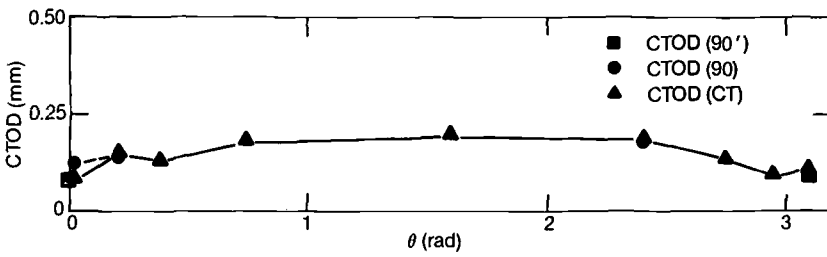
### *Specimens with $a/2c = 0.1$*

Specimens E-5, E-9, and E-12 were examined by microtopographic techniques; measurements were made perpendicular to the crack front. The load-crosshead displacement records are provided in Fig. 3, and the configuration of the original fatigue crack, the extent of subcritical crack growth, CTOD, and CTOA are presented in Figs. 5 through 7 for these three specimens. The load, crosshead displacement, CMOD, and  $\Delta a$  values are given in Table 2. Three different CTOD terms are used in this paper; these are defined in Fig. 8 and in the Nomenclature. CTOD (CT) and CTOD (90°) are standard definitions frequently used. CTOD (90) is an extrapolation method added because it is sometimes difficult to determine the location of the fatigue crack tip on specimens sliced for metallographic examination, and, as suggested in Fig. 8b, the crack front is not applicable for measuring CTOD (90°). In Fig. 8a, CTOD (90) and CTOD (90°) are equivalent, but in Fig. 8b, CTOD (90°) does not exist, which is why CTOD (90) has been added. The CTOD (CT) term in Figs. 8a and 8b are based on using the separation of the fatigue crack tip.

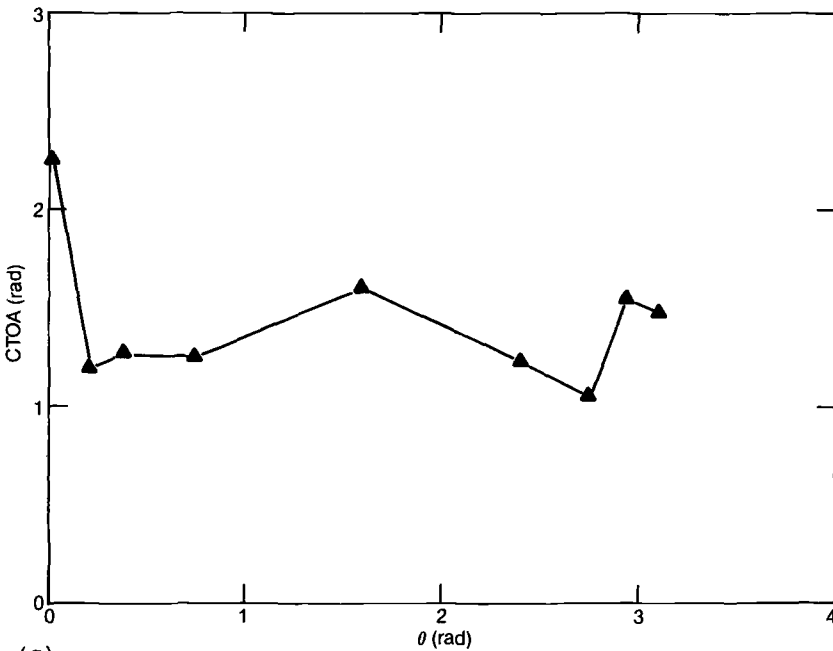
Specimens E-1, E-2, and E-8 were tested to the  $P, \nu$  conditions shown in Fig. 3 and Table 2. These specimens were examined metallographically; the slicing was performed normal to the cracked plate surface. The specimens were examined at specified increments ranging from adjacent to the intersection of the crack with the free surface to the region adjacent to the center of the crack, that is,  $\theta$  ranging from 0 to  $\pi/2$  (Fig. 9). The extent of subcritical



(a)



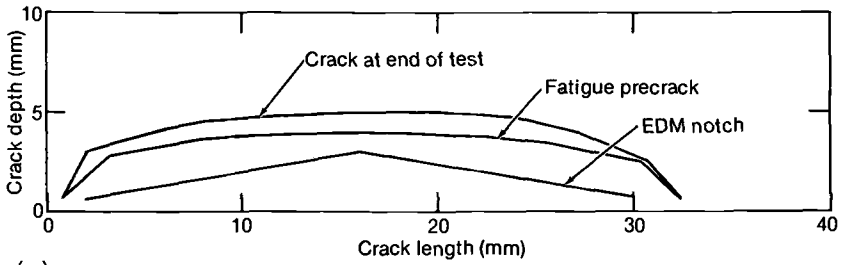
(b)



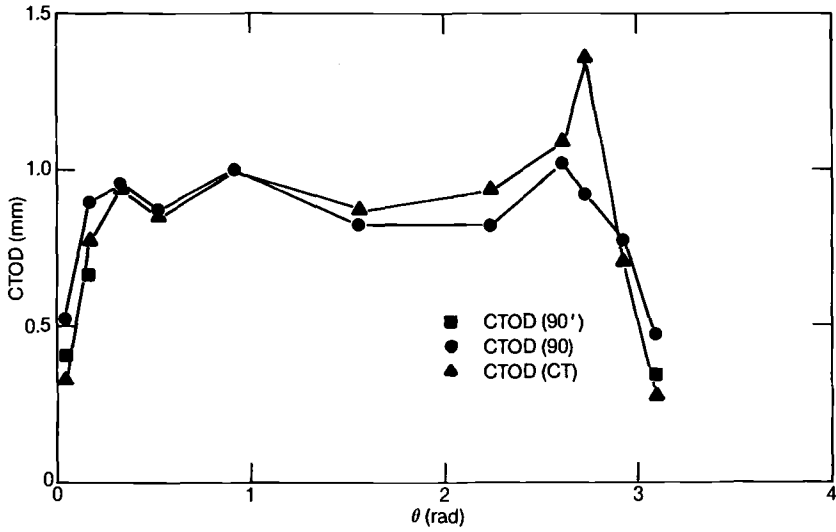
(c)

FIG. 5—Results from topographic measurements for Specimen E-9,  $a/2c = 0.1$ : (a) Crack front configuration and  $\Delta a$ ; (b) CTOD versus  $\theta$ ; (c) CTOA versus  $\theta$ .

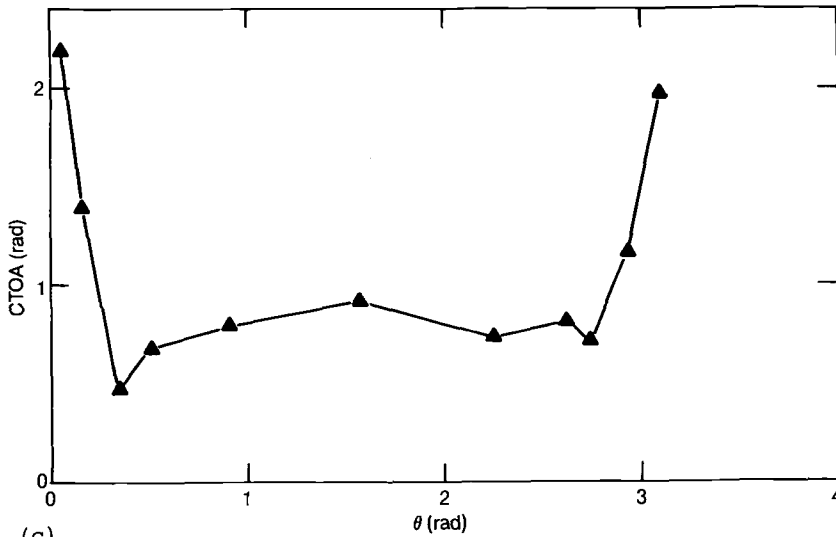




(a)



(b)



(c)

FIG. 6—Results from topographic measurements for Specimen E-12,  $a/2c = 0.1$ : (a) Crack front configuration and  $\Delta a$ ; (b) CTOD versus  $\theta$ ; (c) CTOA versus  $\theta$ .

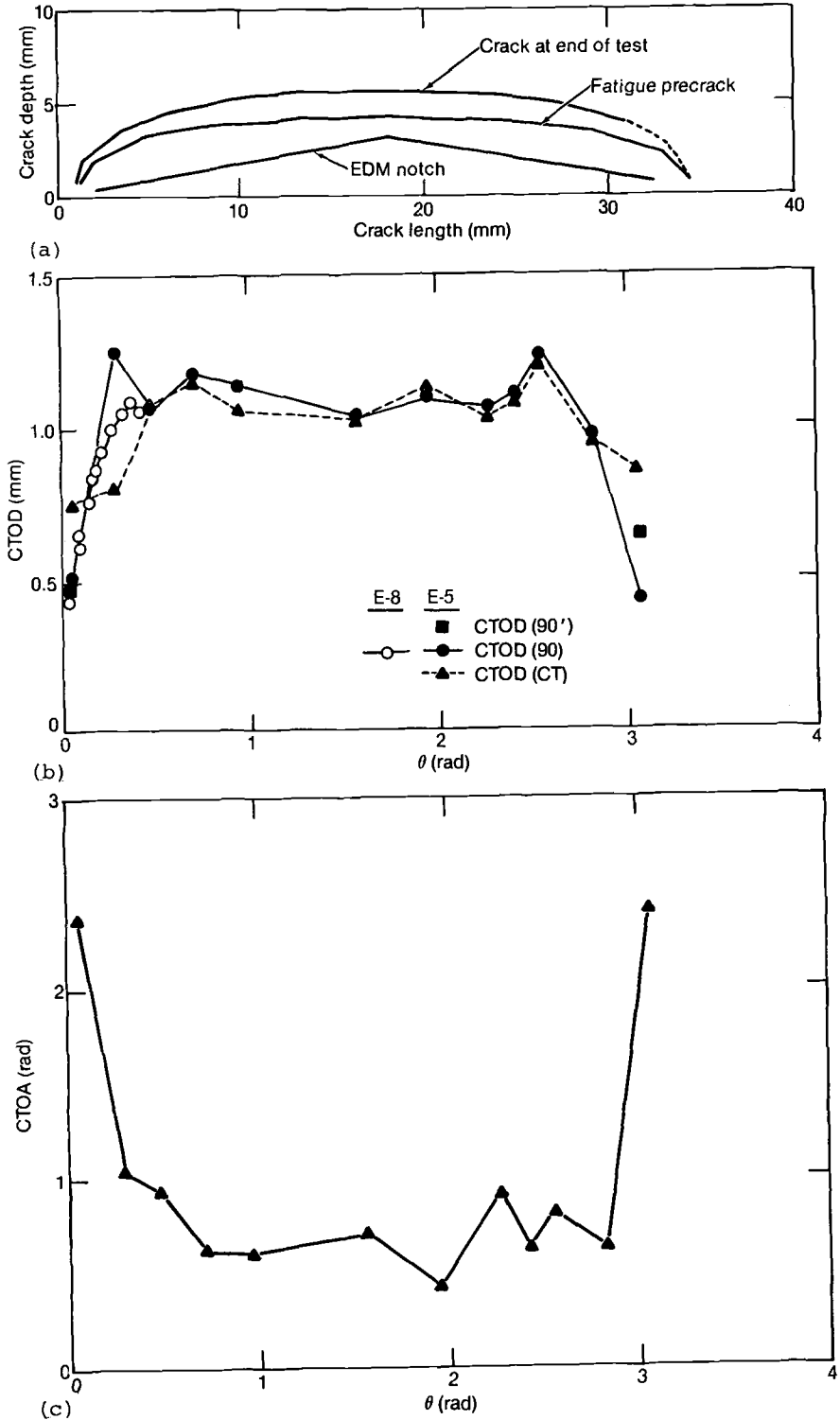
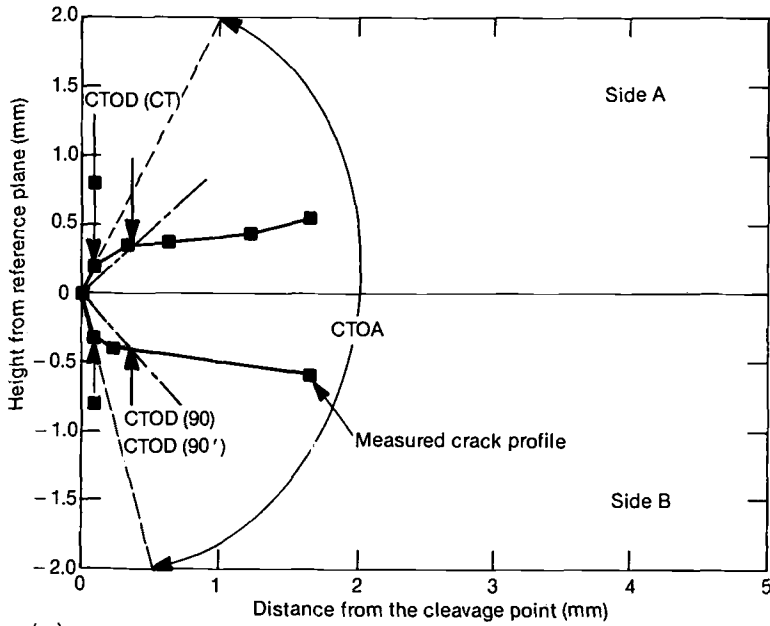
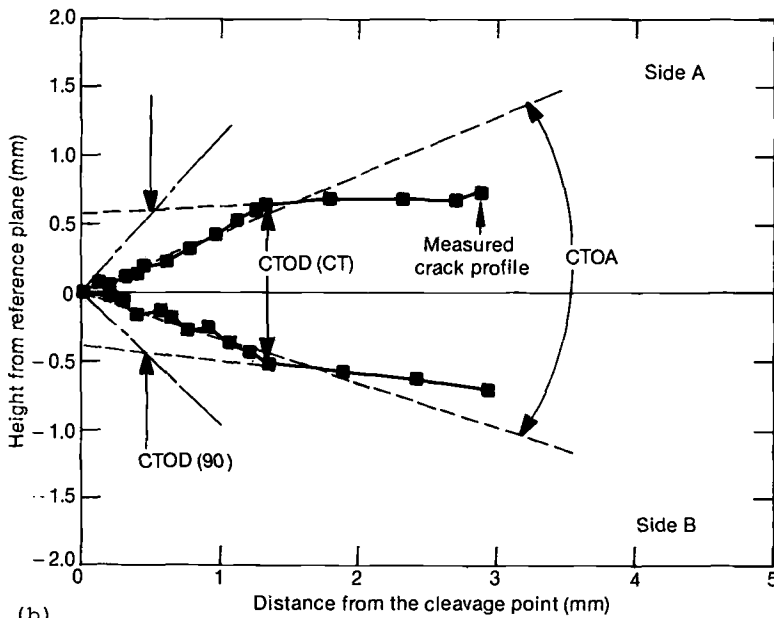


FIG. 7—Results from topographic measurements for Specimen E-5,  $a/2c = 0.1$ : (a) Crack front configuration and  $\Delta a$ ; (b) CTOD versus  $\theta$ ; (c) CTOA versus  $\theta$ .



(a)



(b)

FIG. 8—Crack tip profiles: (a) CTOA and CTOD (CT, 90 and 90'); (b) CTOA and CTOD (CT and 90').

TABLE 2—Summary of load, displacement, and crack parameters for specimens with  $a/2c = 0.1$ .

Specimen Number	Applied Remote Stress, MPa		End of Test, mm		CMOD, mm		$\Delta a^b$ , mm
	Maximum	End of Test	Maximum Crosshead Displacement, $\nu$	Residual Displacement, $\nu$	End of Test	Residual	
E-9 <sup>c</sup>	447.8	447.8	2.941	0.610	0.645	0.526	0.152
E-12 <sup>c,d</sup>	484.8	477.5	4.097	1.9663	1.595	1.501	1.168
E-5 <sup>c</sup>	480.9	460.9	4.440	2.032	2.027	1.933	1.372
E-1 <sup>e</sup>	459.5	459.5	3.556	0.635	...	...	0.038
E-8 <sup>e</sup>	484.4	472.6	4.369	1.880	1.885	1.679	>1.168
E-2 <sup>e,f</sup>	487.1	487.1	3.785	1.092	...	...	0.178
E-4	331.9	331.9	1.857	0.152	0.196	0.070	0.000

<sup>a</sup> These specimens were each subjected to a single loading-unloading cycle.

<sup>b</sup> At maximum crack depth, where  $\theta = \pi/2$ .

<sup>c</sup> Microtopographic technique.

<sup>d</sup> Fatigue cracked to outline  $\Delta a$  due to test.

<sup>e</sup> Sliced perpendicular to free surface.

<sup>f</sup> Sliced perpendicular to crack front.

crack growth and magnitudes of CTOD and CTOA for these specimens are summarized in Table 3. Some values obtained from Specimen E-8 are also presented in Fig. 7b, along with the microtopographic results for Specimen E-5. Specimens E-5 and E-8 were replicates loaded to nearly the same conditions (Table 2); good agreement was obtained with the two examination techniques.

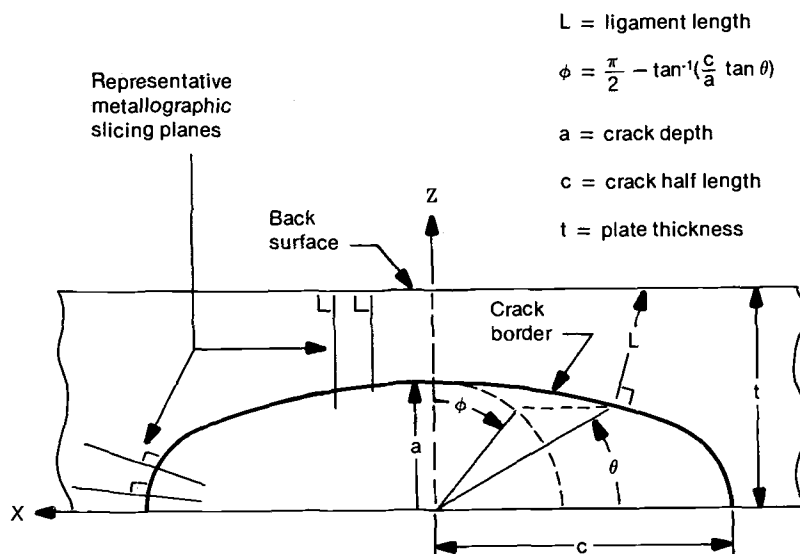


FIG. 9—Schematic showing orientation for metallographic slicing.

TABLE 3—Summary of crack growth and crack tip data.

Specimen Identification	Crack Growth $\Delta a$ , mm			CTOD, mm			CTOA, radians		
	$\theta^a = 0.175$	$\theta = 0.785$	$\theta = 1.571$	$\theta = 0.175$	$\theta = 0.785$	$\theta = 1.571$	$\theta = 0.175$	$\theta = 0.785$	$\theta = 1.571$
E-1	0.010	0.025	0.076	0.112 <sup>b</sup> 0.117 <sup>c</sup>	0.142 <sup>b</sup> 0.147 <sup>c</sup>	0.180 <sup>b</sup> 0.160 <sup>c</sup>	1.86	1.78	1.66
E-2	0.127	0.272	0.152	0.231 <sup>b</sup> 0.343 <sup>c</sup> ...	0.279 <sup>b</sup> 0.445 <sup>c</sup> 0.226 <sup>d</sup>	0.358 <sup>b</sup> 0.445 0.203 <sup>d</sup>	1.74	1.80	1.80
E-8	0.508	1.118	... <sup>e</sup>	0.711 <sup>c</sup>	1.138 <sup>c</sup>	... <sup>e</sup>	1.28	0.73	$\approx 0.7$
E-26	0.076	0.066	0.000	0.041 <sup>b</sup> 0.051 <sup>c</sup>	... 0.079 <sup>c</sup>	0.056 <sup>b</sup> 0.069 <sup>c</sup>	1.07	1.22	2.00
E-27	0.051	0.010	0.025	0.114 <sup>b</sup> 0.102 <sup>c</sup>	0.163 <sup>b</sup> 0.257 <sup>c</sup>	0.188 <sup>b</sup> 0.196 <sup>c</sup>	1.55	1.85	1.9
E-28	0.000	0.023	0.020	0.091 <sup>b</sup> 0.157 <sup>c</sup>	0.104 <sup>b</sup> 0.213 <sup>c</sup>	... 0.206 <sup>c</sup>	1.43	1.80	1.19

<sup>a</sup>  $\theta$  is identified in terms of radians.<sup>b</sup> CTOD (90°).<sup>c</sup> CTOD (90°).<sup>d</sup> CTOD (CT).<sup>e</sup> Not available.*Specimens with  $a/2c = 0.5$* 

Specimens E-16, E-22, and E-24 were also examined by microtopographic techniques, measurements were made perpendicular to the crack front. The load-crosshead displacement records are provided in Fig. 4, and the configuration of the original fatigue crack, the extent of subcritical crack growth, CTOD, and CTOA are presented in Figs. 10 through 12 for these three specimens. The load, crosshead displacement, CMOD, and  $\Delta a$  values are given in Table 4.

Specimens E-26, E-27, and E-28, were tested to the  $P_v$  conditions shown in Fig. 4 and Table 4. These specimens were examined metallographically; the slicing was performed perpendicular to the cracked plate surface. The specimens were examined at specified increments ranging from  $\theta = 0$  to  $\pi/2$ . The extent of subcritical crack growth and magnitudes of CTOD and CTOA for Specimens E-26, E-27, and E-28 are summarized in Table 3.

**Discussion**

Results obtained from these replicate specimens can be used to show crack configuration, the extent of crack growth, CTOA, and CTOD as a function of load. (Data shown in Figs. 3 and 4 and Tables 2 and 4 demonstrate that, in general, replicate specimens were fabricated and tested.) However, it is first necessary to evaluate data generated by the microtopographic technique before establishing possible correlations.

*Evaluation of Microtopographic Measurements*

This technique can be used to measure displacement,  $U_v$ , and crack growth,  $\Delta a$ , at any desired orientation relative to the crack front. In this work the measurements were made

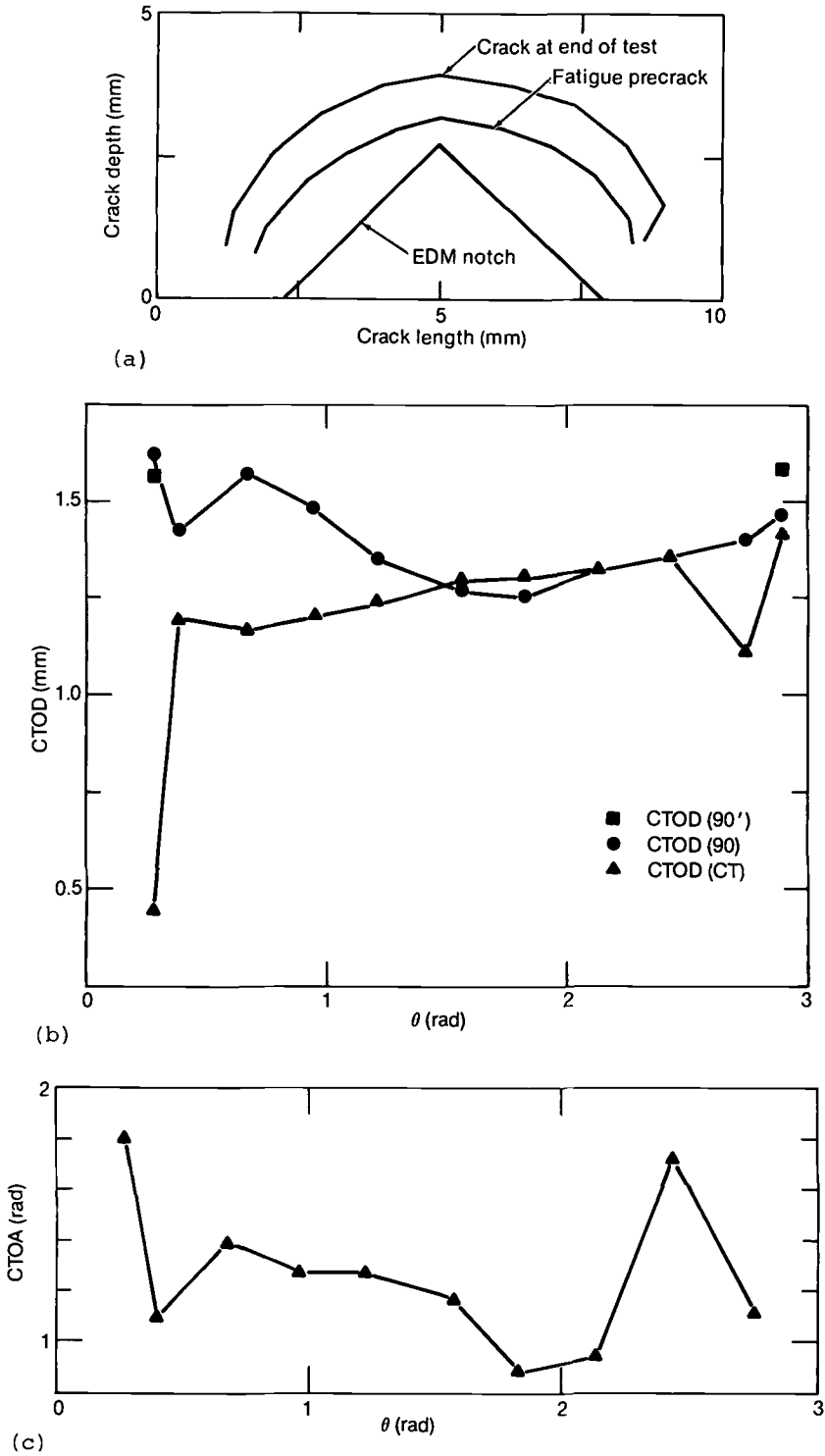


FIG. 10—Results from topographic measurements for Specimen E-16,  $a/2c = 0.5$ : (a) Crack front configuration and  $\Delta a$ ; (b) CTOD versus  $\theta$ ; (c) CTOA versus  $\theta$ .

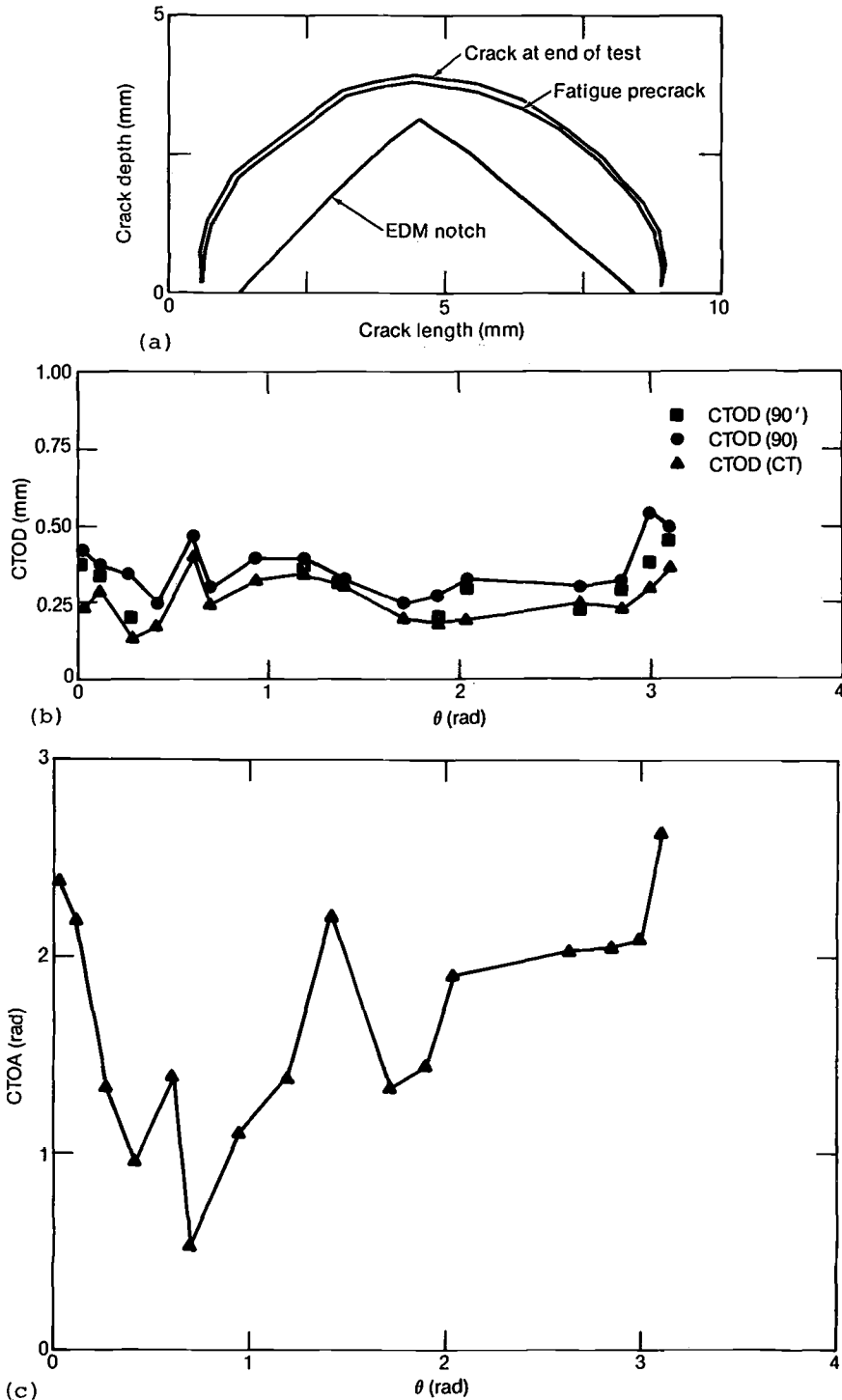


FIG. 11—Results from topographic measurements for Specimen E-24,  $a/2c = 0.5$ : (a) Crack front configuration and  $\Delta a$ ; (b) CTOD versus  $\theta$ ; (c) CTOA versus  $\theta$ .

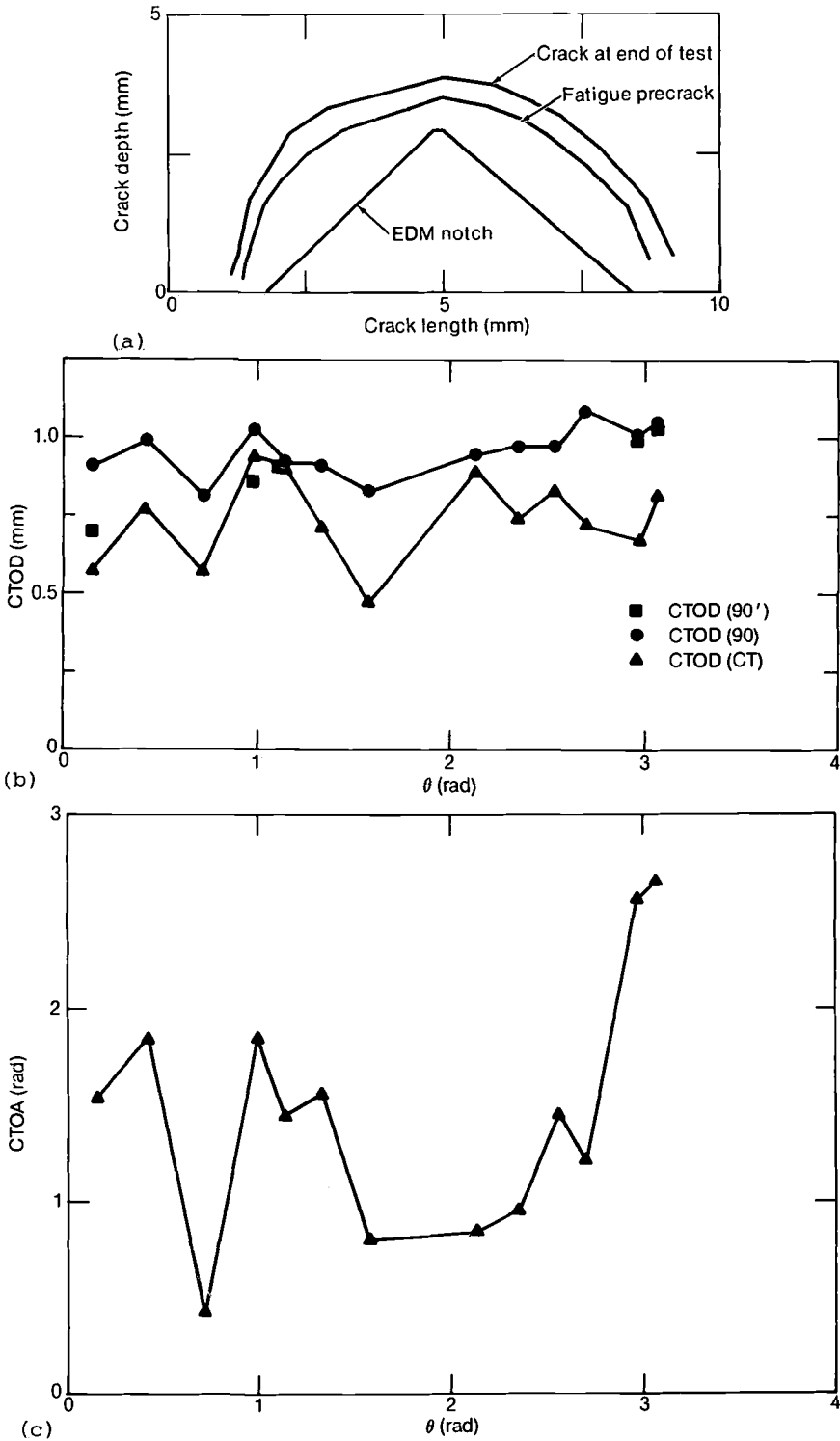


FIG. 12—Results from topographic measurements for Specimen E-22,  $a/2c = 0.5$ : (a) Crack front configuration and  $\Delta a$ ; (b) CTOD versus  $\theta$ ; (c) CTOA versus  $\theta$ .



TABLE 4—Summary of load, displacement, and crack parameters for specimens with  $a/2c = 0.5$ .

Specimen Number	Applied Remote Stress, MPa		End of Test, mm		CMOD, mm		
	Maximum	End of Test	Maximum	Residual	End of Test	Residual	$\Delta a^a$
			Displacement, $\nu$	Displacement, $\nu$			
E-16 <sup>b,c</sup>	623.8	623.8	15.215	12.192	2.205	2.141	0.762
E-22 <sup>c,d</sup>	624.4	624.4	14.707	11.709	...	...	0.381
E-20	345.0	345.0	1.956	...	1.143	...	0.0000
E-24 <sup>c,e</sup>	569.9	569.9	8.230	0.584	...	...	0.127
E-25	615.5	615.5	1.577	1.275	2.588	...	...
E-26 <sup>f,g</sup>	516.1	516.1	4.013	1.473	...	...	0.000
E-27 <sup>f</sup>	553.4	553.4	6.731	3.785	0.564	...	0.025
E-28 <sup>f</sup>	546.5	546.5	NA	NA	0.409	0.351	0.025
E-29	544.4	544.4	5.080	2.261	...	...	...

<sup>a</sup> At maximum crack depth, where  $\theta = \pi/2$ .<sup>b</sup> Microtopographic technique.<sup>c</sup> Fatigue cracked after monotonic loading to outline  $\Delta a$  due to test.<sup>d</sup> Loaded three times:  $P_1 = 355.8$  kN and  $\nu_1 = 5.715$  mm,  $P_2 = 370.1$  kN and  $\nu_2 = 5.385$  mm, and  $P_3 = 406.5$  kN and  $\nu_3 = 9.322$  mm.<sup>e</sup> Loaded two times:  $P_1 = 333.6$  kN and  $\nu_1 = 4.267$  mm and  $P_2 = 367.4$  kN and  $\nu_2 = 8.230$  mm.<sup>f</sup> Sliced perpendicular to free surface.<sup>g</sup> Sliced perpendicular to crack front.

perpendicular to the crack front and taken with respect to a reference plane. It was assumed that the fatigue precrack plane is a common zero elevation point for each measurement line. The microtopographic technique may be also used to measure the extent of the out-of-plane dimpling at the back surface. This was not done for these specimens.

Figures 5 through 7 show that both  $\Delta a$  and the configuration of the surface cracks are generally symmetrical for specimens where  $a/2c = 0.1$ ; Figs. 10 through 12 show less symmetry but not an appreciable difference for specimens where  $a/2c = 0.5$ . The CTOD measurements were observed to be symmetrical and relatively constant for both crack geometries studied, although Specimen E-12 (Fig. 6b) and Specimen E-22 (Fig. 10b) showed some nonsymmetrical and erratic behavior. A comparison was made between CTOD values based on measurements of CTOD (90), CTOD (90'), and CTOD (CT). For  $a/2c = 0.1$ , at low loads, the CTOD values were the same for the CTOD (90) and CTOD (CT) measurement techniques as shown in Fig. 5b for Specimen E-9. At higher loads, the CTOD values were generally the same, but the CTOD (90) values are more symmetrical and less erratic, as shown in Figs. 6b and 7b for Specimens E-12 and E-5, respectively. It was possible to measure CTOD (90') at only a few positions for Specimens E-9, E-12, and E-5, and there was generally good agreement between CTOD (90') and CTOD (CT) except for Specimen E-5 (Fig. 7b). There was no definite trend regarding the magnitude of the numbers relative to each measurement technique.

For  $a/2c = 0.5$  at the lower loads, the trends of CTOD values with respect to position were the same. Values obtained using CTOD (90) and CTOD (90') were always equal to or larger than CTOD (CT), as shown in Fig. 11b for Specimen E-24. At higher loads, the two sets of data [CTOD (90) and CTOD (90')] were in nominal agreement, as shown in

Fig. 12b; however, some disparity can occur as shown in Fig. 10b. In both cases, CTOD (90) and CTOD (90') values were generally larger than CTOD (CT).

The preceding suggests that CTOD measurements based on using a 90 deg included angle [CTOD (90) and CTOD (90')] will be accurate for  $a/2c = 0.1$  at low and high loads, but will not be reliable for  $a/2c = 0.5$ . For  $a/2c = 0.5$ , the ratio of CTOD (90') to CTOD (CT) is nominally 1.1 for both low and high loads. The ratio of CTOD (90) to CTOD (CT) is nominally 1.15 at low loads and 1.25 at high loads. The large difference between CTOD (90) and CTOD (CT) at high loads is not a significant problem since CTOD measurements are generally used only to the point of crack initiation. Crack initiation occurred at  $\sigma$ , ranging from 447.8 to 459.5 MPa and from 516.1 to 546.9 MPa for  $a/2c = 0.1$  and 0.5, respectively (Tables 2 and 4).

The CTOA measurements were observed to be generally symmetrical with respect to  $\theta = \pi/2$ , normal bisector of crack length, and relatively constant for  $a/2c = 0.1$ , but showed substantial nonsymmetrical and erratic results for  $a/2c = 0.5$ . A comparison between these two configurations suggests that the nonsymmetrical and erratic results occur for  $a/2c = 0.5$  because of the high degree of crack curvature and because the maximum constraint occurs at  $\theta$  of approximately  $\pi/3$  and  $2\pi/3$ . For  $a/2c = 0.1$ , the longer crack front approaches a 2-D crack (with substantially less curvature) and the maximum constraint occurs at about  $\theta = \pi/10$  and  $9\pi/10$ . The latter observation is supported in Figs. 5c, 6c, and 7c, where there are considerable changes in CTOA near the surface of the specimen.

#### Determination of $R$

The distance from the crack mouth to the center of rotation,  $R$ , is used to estimate CTOD based on measured values of CMOD. For a surface-flawed specimen exposed to a tensile load, a simplified approach is to assume that  $R$  is a constant for all  $\theta$ . This assumption is appropriate if it can be shown that the portion of the surface crack where  $R$  is essentially constant controls the conditions for initiation of crack growth and subsequent crack extension. Figure 13 shows the approach, based on assuming that similar triangles exist, used to experimentally determine  $R$  from photographs or to calculate  $R$  based on CMOD and CTOD. Figure 14 shows the relationship between  $R$ , normalized by dividing by  $a'$ , and crack perimeter location for each aspect ratio at different applied loads. For those specimens with  $a/2c = 0.1$ , there is a general trend of  $R/a'$  decreasing with increasing  $\theta$  and then remaining constant for  $\theta \geq 0.4$  rad. The ratio  $R/a'$  has a reasonably constant value of 2.20 for Specimens E-1 and E-2 where  $\sigma/\sigma_{ys} = 0.99$  and 1.05, respectively, but increases substantially to 3.0 for Specimen E-8 where  $\sigma/\sigma_{ys} > 1.04$ . The comparison between Specimens E-2 and E-8 suggests that  $\sigma/\sigma_{ys}$  is not completely adequate as the independent variable, since Specimen E-8 experienced maximum load and then a decreasing load before the test was terminated. A better comparison is made by noting that Specimens E-1 and E-2 were subjected to  $\nu = 3.56$  and 3.78 mm, respectively, whereas Specimen E-8 experienced substantially more displacement with  $\nu = 4.37$  mm. An alternate approach using measured values of CTOD and CMOD was also used to calculate  $R/a'$ . These values were somewhat less than the measured values (see the open circles in Fig. 14a).

For those specimens with  $a/2c = 0.5$ , there is also a trend of  $R/a'$  decreasing as  $\theta$  increases to about 1.6 rad (Fig. 14b). The ratio  $R/a'$  is reasonably constant at 1.6 for only a short range of  $\theta$  near 1.7 rad. The results in Fig. 14b suggest no significant differences in  $R/a'$  for specimens loaded to  $\sigma/\sigma_{ys}$  ranging from 1.11 to 1.19. In fact, Specimens E-26 and E-27 experienced substantial differences in applied crosshead displacement since  $\nu = 4.01$

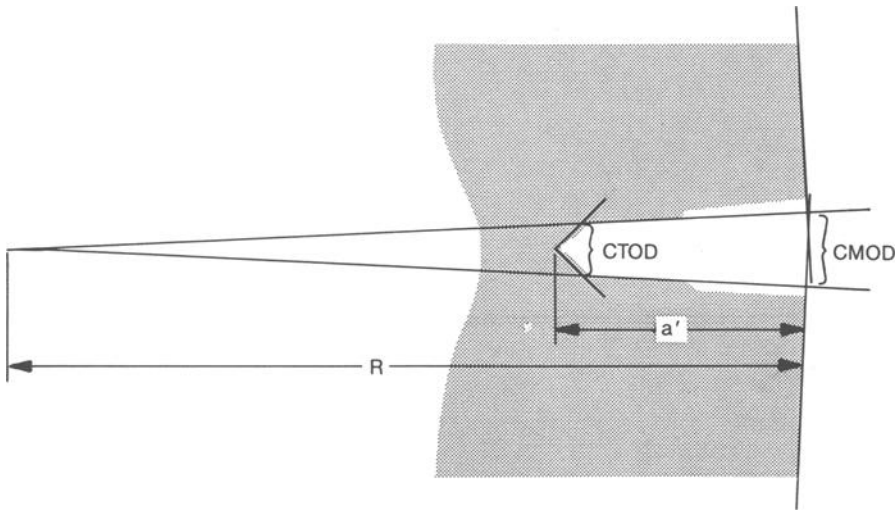


FIG. 13—Schematic showing method for experimental measurement of  $R$ .

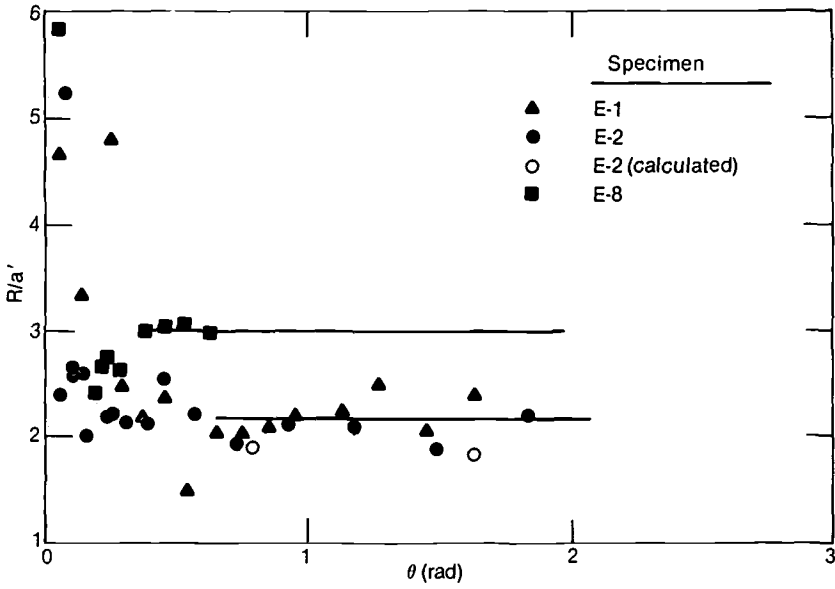
and 6.73 mm, respectively. This suggests that  $R/a'$  is not very sensitive to  $\sigma/\sigma_{ys} < 1.19$  or  $\nu < 6.73$  mm for  $a/2c = 0.5$ .

There is general agreement between the results shown in Figs. 14a and 14b since  $R/a'$  decreased to a nominally constant value. But there are substantial differences in the range of  $\theta$  corresponding to constant  $R/a'$ , as well as in the magnitude of the constant values themselves. The former is related to the length of the crack front having the same size of remaining ligament. This length is longer for Specimen E-8 than for Specimens E-1 and E-2. The longer length also identifies why  $\theta$ , corresponding to a constant  $R/a'$ , was larger for specimens where  $a/2c = 0.1$  than for specimens where  $a/2c = 0.5$ . The increase in the constant value of  $R/a'$  associated with Specimen E-8 shows the effective reduction of out-of-plane bending with increased plasticity.

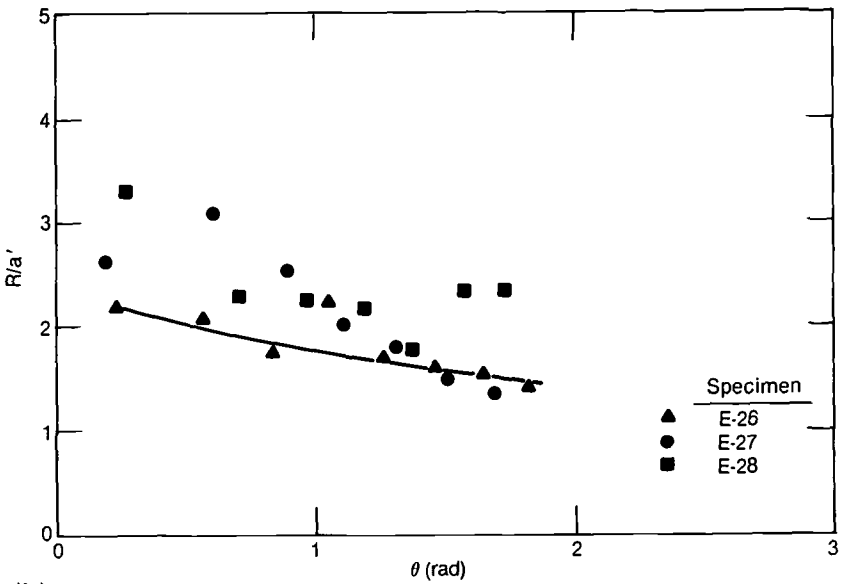
#### Relationship Between $\delta_{pl}$ and $\delta_{el}$

If it is possible to predict a constant value of  $R$  as a function of applied load and flaw configuration in the vicinity of maximum crack depth, it will be possible to predict CTOD at  $\theta = \pi/2$  based on a measure of CMOD (measured on the specimen surface along the normal bisector of the crack length). Therefore, it is desired to identify methods for predicting CTOD ( $\delta_{pl}$ ) around the crack perimeter based on knowing CTOD only in the central region.

The approach evaluated here uses the Newman-Raju equation to calculate  $K$  around the crack perimeter. These values of  $K$  are then used to calculate  $\delta_{el}$  for the same positions where  $\delta_{pl}$  was measured to obtain the ratio  $\delta_{el}/\delta_{pl}$ . This ratio is plotted versus position around the surface crack perimeter in Fig. 15. If  $\delta_{el}/\delta_{pl}$  remains constant as a function of  $\theta$ , then the plastic CTOD ( $\delta_{pl}$ ) follows the same trend as predicted by the Newman-Raju solutions for  $\delta_{el}$ . This provides a basis, when used with  $\delta_{pl}$  at  $\theta = \pi/2$ , for predicting  $\delta_{pl}$  or  $\delta_i$  around the circumference of a surface crack. When the ratio deviates from a constant, then the New-



(a)



(b)

FIG. 14—Plot of normalized  $R$  versus  $\theta$ : (a)  $a/2c = 0.1$ ; (b)  $a/2c = 0.5$ .

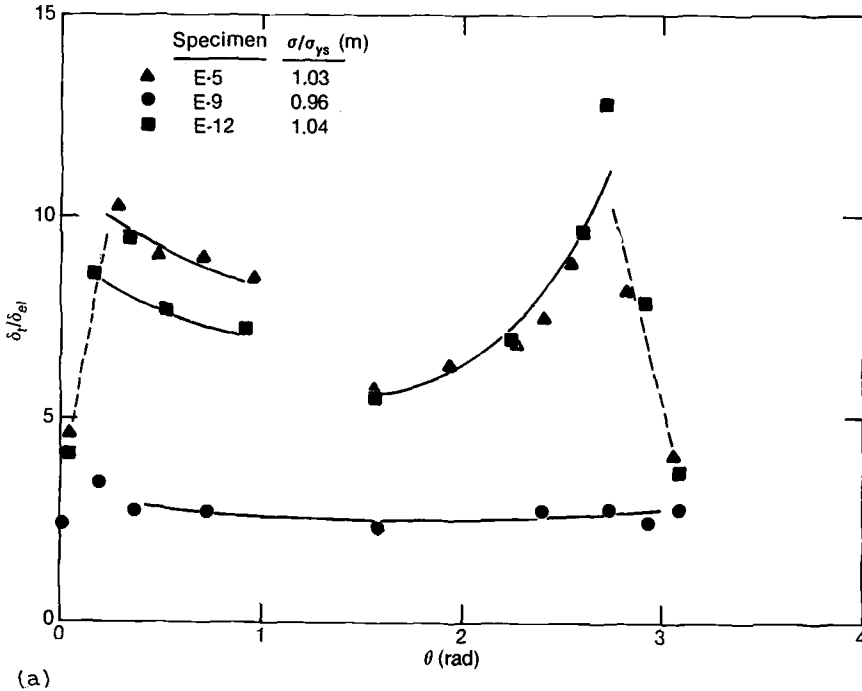


FIG. 15—Plot of normalized  $\delta_i$  versus  $\theta$ : (a)  $a/2c = 0.1$ ; (b)  $a/2c = 0.5$ .

man-Raju solutions can no longer be used for this purpose, that is, it will no longer be possible to predict  $\delta_{pl}$  around the circumference of a surface crack having only  $\delta_{pl}$  in the central region. From Fig. 15a it is apparent that  $\delta_{pl}$  follows the prediction of Newman-Raju up to about gross section yielding, that is,  $\sigma/\sigma_{ys} = 0.96$ . As the applied stress exceeds gross section yielding, there is an increase in  $\delta_i/\delta_{el}$  in the central region as well as larger increases near the free surface, indicating the limit of applicability of this approach for the low-aspect ratio semielliptical flaws has been exceeded. This is true only for this specimen configuration since the loss of constraint, which is related to specimen and defect configuration, will affect the limit. Specimens E-5 and E-12 that were loaded to  $\sigma/\sigma_{ys} = 1.03$  and 1.04, respectively, showed a varying  $\delta_i/\delta_{el}$ , but reasonably good reproducibility between the two specimens.

In Fig. 15b it can be seen that  $\delta_i/\delta_{el}$  increases slightly with increasing stress for  $\sigma/\sigma_{ys}$  up to 1.22 for the semicircular flaws. For these conditions, the distribution of  $\delta_i/\delta_{el}$  with respect to  $\theta$  remains essentially constant. When  $\sigma/\sigma_{ys} \geq 1.3$ , a substantial increase in  $\delta_i/\delta_{el}$  occurs, particularly near maximum depth. This latter observation is probably due to loss of constraint. Parks and Wang [4], using a finite-element technique, predict loss of constraint (loss of Hutchinson-Rice-Rosengren [HRR] field dominance) to occur at about  $\sigma/\sigma_{ys} = 0.85$  and 1.04 for  $a/2c = 0.1$  and 0.5, respectively. For specimens with  $a/2c = 0.5$ , the limit of applicability for using the Newman-Raju solution to predict  $\delta_i$  is  $\sigma/\sigma_{ys} \leq 1.22$ . This limit is applicable only for this specimen configuration, since the loss of constraint will affect the limit. The effect of a loss of constraint at the free surface is evident in both Figs.

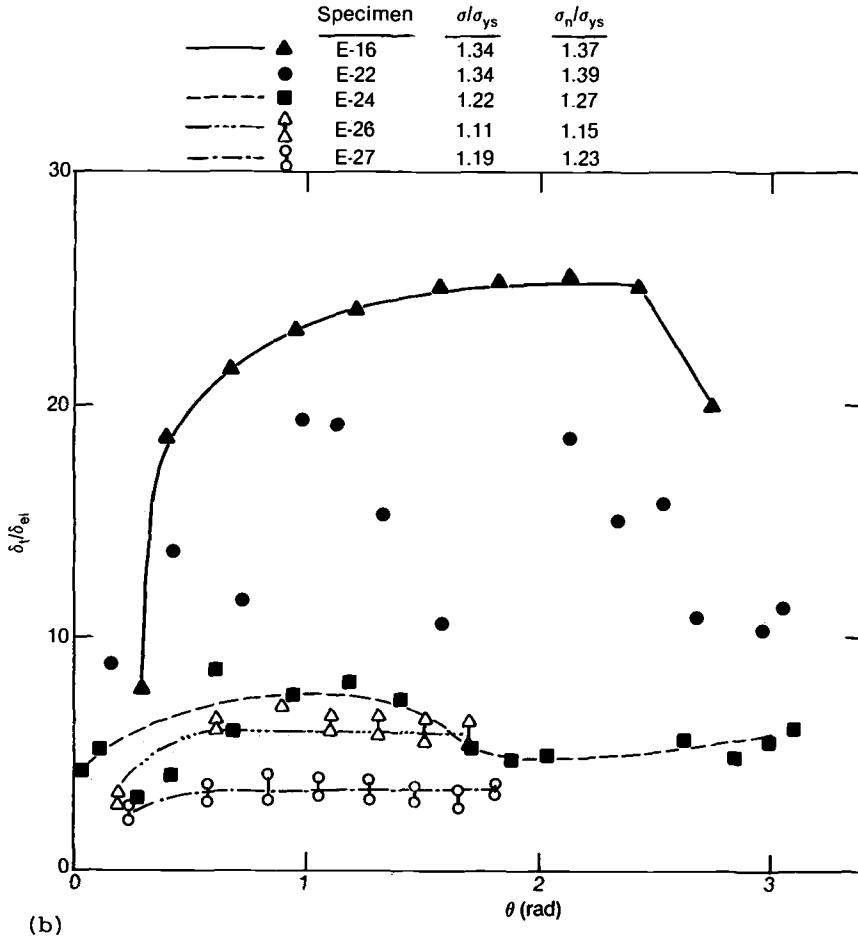


FIG. 15—Continued.

15a and 15b by the decrease in  $\delta_i/\delta_{ei}$  at each end of the figures for six of the eight specimens. Because of the scatter for Specimen E-22, it is not certain if the same trend occurs. The results for Specimen E-24 are questionable if attempting to identify a specific trend.

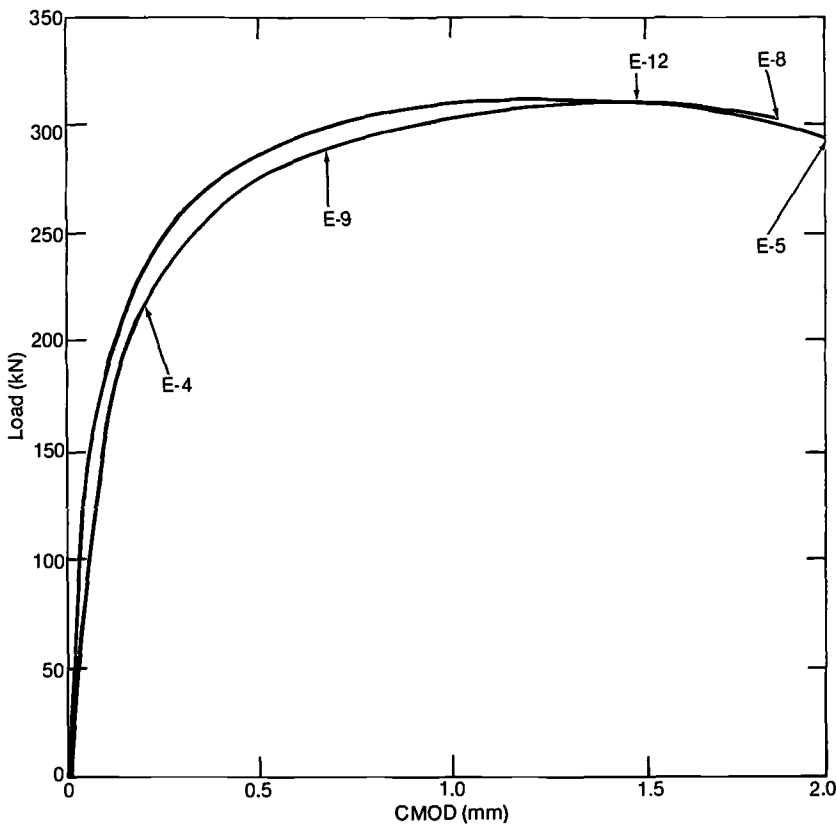
#### Relationship Between Loading Conditions and $\Delta a$ , CTOD, and CTOA

The previous two subsections provided experimental data regarding the distance to the center of rotation  $R$ , and the limits of applicability for using the Newman-Raju stress-intensity factor solutions for calculating CTOD around the perimeter of the surface crack. The relationships between  $P$  and  $\nu$  are shown in Figs. 3 and 4 for specimens with aspect ratios of 0.1 and 0.5, respectively. The crosshead displacement provides a useful qualita-

tive parameter since replicate specimens were tested in the same machine. The compliance for the test machine and associated fixtures is nominally  $1.96 \mu\text{m/kN}$ .

Figure 16a shows good reproducibility, for plots of  $P$  versus CMOD, for Specimens E-5, E-8, E-4, and E-9, but Specimen E-12 differs considerably. This is understandable since the crack depth,  $a$ , is 3.86 mm for Specimen E-12 and is nominally 4.2 mm for Specimens E-5, E-9, and E-8. There is more variation in Fig. 16b because of the large difference in crack depth. At this time, it is not known why the plot for Specimen E-27 falls below that for Specimen E-28, since the latter had the larger initial crack size.

Figure 17 provides plots of CTOA versus  $\Delta a$  for  $a/2c = 0.1$  and  $0.5$ . In Fig. 17a, there is a clear trend of decreasing CTOA with increasing crack growth. This was observed at both  $\theta = \pi/4$  and  $\pi/2$ , which is reasonable for specimens with  $a/2c = 0.1$  since, as was noted earlier, the significant  $\Delta a$  occurs in the central region of the crack border. There is a tendency for CTOA to approach a constant value of 0.7 rad with increasing crack extension. Figure 17b shows considerable scatter, but it is obvious that CTOA is decreasing with increased  $\Delta a$ , and it also appears to be approaching a constant value. Since  $\Delta a \geq 0.5$  mm



(a)

FIG. 16—Plot of load versus CMOD: (a)  $a/2c = 0.1$ ; (b)  $a/2c = 0.5$ .

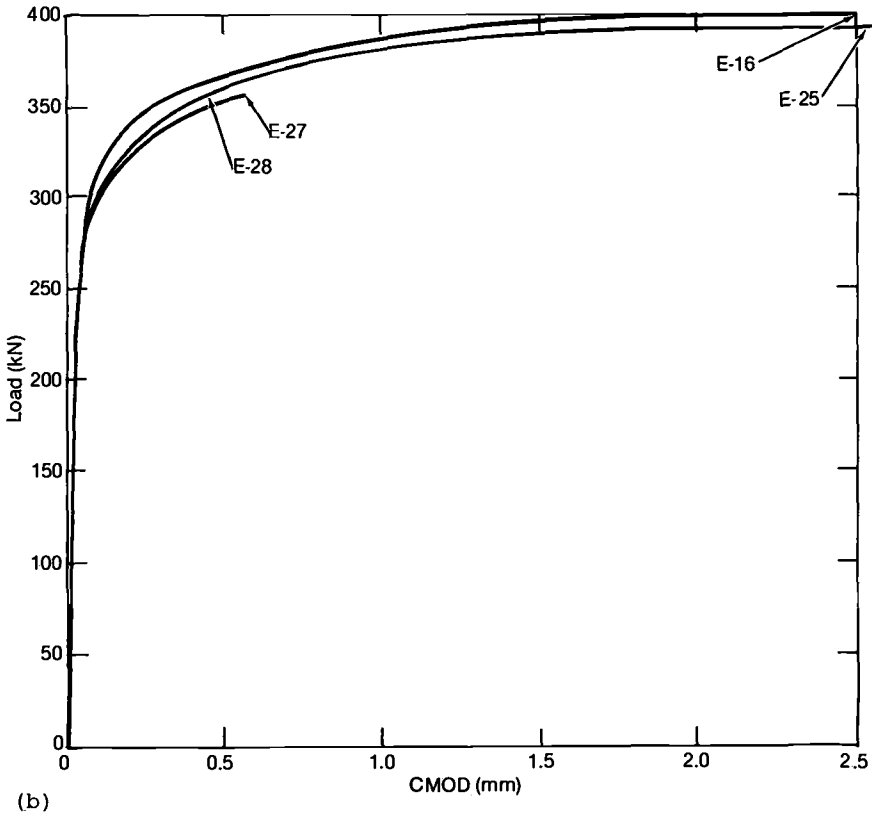


FIG. 16—Continued.

before CTOA decreased to the minimum values, it is expected that loss of constraint affected either the lower limit of CTOA or the amount of  $\Delta a$ , or both. This is hypothesized due to the work of Parks and Wang [4], who have used numerical techniques to predict loss of HRR dominance at  $\sigma/\sigma_{ys} = 0.85$  and  $1.04$  for  $a/2c = 0.1$  and  $0.5$ , respectively. Their predictions were based on the same test specimen geometries, but did not allow for any subcritical crack growth.

### Summary and Conclusions

Experimental measurements of CTOD, CTOA, and  $\Delta a$  around the circumference of surface cracks at different values of  $P/\nu$  for semielliptical and semicircular aspect ratios have been provided. A comparison between CTOD values based on measurements of CTOD (90), CTOD (90'), and CTOD (CT) showed that using the 90-deg included angle concepts provides values comparable with CTOD (CT), for  $a/2c = 0.1$  but not for  $a/2c = 0.5$ . For  $a/2c = 0.5$ , the ratio of CTOD (90') to CTOD (CT) is nominally 1.1 for both low and high loads, and the ratio of CTOD (90) to CTOA (CT) is nominally 1.15 at low loads and 1.25 at high loads. The above illustrates the need to define either a standardized method for measuring CTOD, or minimally, the actual method used in each measurement.



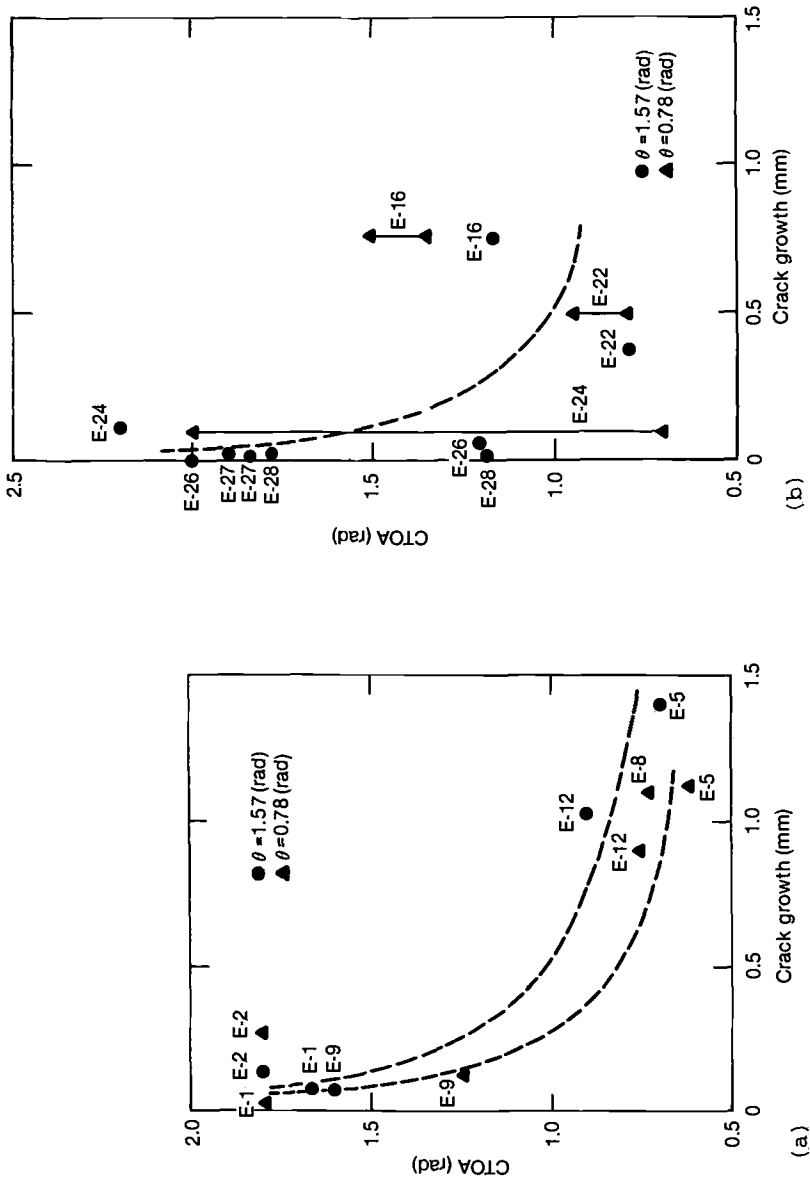


FIG. 17—Plot of CTOA versus  $\Delta a$ : (a)  $a/2c = 0.1$ ; (b)  $a/2c = 0.5$ .

Measurements of CMOD and CTOD were used to show that the distance to the center of rotation ( $R$ ) varied as a function of load, defect geometry, and location around the circumference of the surface crack. For the two aspect ratios studied, a constant  $R/a'$  value may be used for conditions associated with crack initiation regardless of  $\theta$  since the significant  $\Delta a$  occurred in the central region of the crack border.

The Newman-Raju equation may be used to provide useful estimates of  $\delta_{pl}$  and  $\delta_t$  as long as  $\sigma < 0.96 \sigma_{ys}$  for  $a/2c = 0.1$ . For specimens with  $a/2c = 0.5$ , the Newman-Raju equations are adequate for predicting  $\delta_{pl}$  and  $\delta_t$  as long as  $\sigma < 1.22 \sigma_{ys}$ . These two limits correspond to net section stresses of  $1.40 \sigma_{ys}$  and  $1.31 \sigma_{ys}$  for  $a/2c = 0.1$  and  $0.5$ , respectively. These limits are associated with the specific specimen and defect sizes, which affect constraint.

Up to the load associated with crack initiation, it is possible to relate CMOD to CTOD in the maximum depth region of the crack. It is also possible to predict the CTOD around the crack perimeter using the Newman-Raju equation for  $\sigma/\sigma_{ys} < 0.94$  and  $\sigma/\sigma_{ys} < 1.22$  for  $a/2c = 0.1$  and  $0.5$ , respectively. It will be necessary to relate CTOD to constraint before it is possible to predict  $\delta_{crit}$  for crack initiation.

A relationship of decreasing CTOA with increasing  $\Delta a$  has been demonstrated. Currently, it is uncertain how much crack growth is required before attainment of the minimum value of CTOA or how much effect the loss of constraint has on the CTOA.

#### Acknowledgment

This work was supported by the U.S. Department of Energy, Office of Energy Research, Office of Basic Energy Sciences, under DOE Contract No. DE-AC07-76ID01570.

#### References

- [1] Newman, J. C., Jr., and Raju, I. S., *Analysis of Surface Cracks in Finite Plates Under Tension and Bending Loads*, NASA Technical Paper 1578, National Aeronautics and Space Administration, Washington, DC, Dec. 1978.
- [2] Kobayashi, T., Irwin, G. R., and Zhang, X. J., "Topographic Examination of Fracture Surfaces in Fibrous-Cleavage Transition Behavior," *Fractography of Ceramic and Metal Failures, ASTM STP 827*, American Society for Testing and Materials, Philadelphia, 1984, pp. 234-251.
- [3] Zhang, X. J., Armstrong, R. W., and Irwin, G. R., "Cleavage Fracturing Stages at Microsize Inclusions in Pressure Vessel Steel Weldmetal," *Journal of Materials Science Letters*, Vol. 5, 1986, pp. 961-964.
- [4] Parks, D. M. and Wang, Y. Y., "Elastic-Plastic Analysis of Part-Through Surface Cracks," *Proceedings, Symposium on Analytical, Numerical, and Experimental Aspects of Three-Dimensional Fracture Processes*, American Society of Mechanical Engineers, Berkeley, CA, June 1988.

## Surface Cracks in Thick Laminated Fiber Composite Plates

---

**REFERENCE:** Chatterjee, S. N., "Surface Cracks in Thick Laminated Fiber Composite Plates," *Surface-Crack Growth: Models, Experiments, and Structures*, ASTM STP 1060, W. G. Reuter, J. H. Underwood, and J. C. Newman, Jr., Eds., American Society for Testing and Materials, Philadelphia, 1990, pp. 177-193.

**ABSTRACT:** Application of fracture mechanics to through cracks in thin laminated composite plates does not yield good correlation with test data because of large zones of surface damage near the crack tips. However, for thick laminates with through or surface cracks of moderate sizes (of the order of several ply thicknesses), influence of damage zones is usually small and stress analyses based on homogenization assumption and fracture mechanics approach should yield reliable estimates of failure loads. In this paper, stress-intensity factors for elliptic cracks in transversely isotropic (in planes perpendicular to the cracks) and orthotropic media obtained from numerical solutions are reported. In addition, appropriate correction factors to obtain stress-intensity factors for surface cracks of semielliptic shapes are estimated using a limited number of finite-element results. Test data available in literature are correlated with analytical predictions for failure of critical ligaments. Other relevant failure mechanisms are also discussed.

**KEY WORDS:** composite laminates, surface cracks, surface cuts, fracture mechanics, elliptic cracks, semielliptic cracks, homogenization, surface damage

Fracture-mechanics-based methods are not directly applicable for predicting fracture due to through cracks in thin laminates because of considerable surface damage. Semi-empirical corrections are often employed [1]. However, for moderately thick laminates, surface damages are usually limited and direct use of fracture-mechanics-based methods should yield reliable results. Methods to obtain stress-intensity factors for surface cracks in isotropic plates employ various approximate, iterative or finite-element schemes to compute correction factors due to finite thickness and width effects which are applied to the results for elliptic cracks in an infinite medium [2]. Laminated composite plates containing a repeating arrangement of layers can be assumed to be orthotropic (or transversely isotropic with plane of isotropy parallel to laminations), when sizes of cracks are greater than several ply thicknesses. Even with this assumption, the stress field is quite different from that in the isotropic case, although attempts have been made to use the results for isotropic plates to correlate test data for first ligament failure (near the surface) in composite laminates [3-5]. In this study such first ligament failures will be called initial damage or initial failure to distinguish them from final failure, which results in complete loss in load-carrying capacity of the specimen. It should be noted that sometimes initial damage or failure may coincide with final failure. This may happen when load cannot be increased beyond that required to cause initial damage.

<sup>1</sup> Staff scientist, Materials Sciences Corporation, Gwynedd Plaza II, Bethlehem Pike, Spring House, PA 19477.

General approaches for calculation of stress-intensity factors for an elliptic flaw in an anisotropic medium have been suggested in Refs 6 and 7. In this study, we specifically consider transversely isotropic and orthotropic media (with properties of "homogenized" laminates) representative of those used in practice. The crack planes are perpendicular to critical loading directions (0-deg fibers) so that only Mode I effects are present. An explicit expression is given for the transversely isotropic case (plane of isotropy parallel to laminations), where it is necessary to evaluate one definite integral by numerical scheme. Results for orthotropic plates are found to be close to those for transversely isotropic case. It is observed that the stress-intensity factors at the points which correspond to those on the free surface, when one wishes to use these results for the case of semielliptic surface crack (with corrections, as discussed in Ref 2 for isotropic plates), are closer to the through-crack solution as compared to the results in the isotropic case. For obvious reasons, through-crack solutions yield upperbound estimates of intensity factors at the free surface for a surface crack in isotropic as well as orthotropic media and therefore, correction factors (needed to obtain surface-crack solution from that for a crack in infinite medium) estimated from a limited number of three-dimensional finite-element solutions for transversely isotropic plates are found to be smaller than those for surface cracks in isotropic plates. This is a consequence of the fact that the through-the-thickness shear moduli of plates under consideration are extremely low. For the same reason, back surface effects are also found to be small.

The results obtained indicate that failure is expected to occur near the free surface in almost all of the semielliptic flaws considered in Refs 3, 4, and 5, where failure at deepest points are sometimes predicted by the use of isotropic plate results. The correlation of test data with the present solution appears to be much better than that using isotropic plate solution [3]. It is also shown that use of through-crack solution yields reasonable lower-bound estimates in some cases. For some semielliptic flaws, final-failure loads are often higher than those for first-ligament failure (this phenomenon is called "two-part failure" in Ref 4), and sometimes these are found to be lower than the strength of ligaments remaining after initial fracture of layers near the surface. Possible reasons for this phenomenon are also discussed.

### Elliptic Cracks in Orthotropic Media

A review of work on part-through flaws in isotropic plates may be found in Ref 2. It is common to obtain the stress-intensity factors for such flaws by multiplying the known solution of an elliptic crack in an infinite medium by correction factors accounting for front surface, back surface, and finite width effects. The general approach for calculation of stress-intensity factors for an elliptic crack in an infinite anisotropic medium can be found in Refs 6 and 7, and the variation can be expressed by the following formula

$$K(x_1, x_2) = \frac{S\sqrt{\pi a} f(\eta_1, \eta_2)}{\int_0^{\pi/2} f(\eta'_1, \eta'_2) d\phi'} (\eta_1^2 + \eta_2^2)^{-1/4} \quad (1)$$

where

$$\begin{aligned} x_1 &= a \sin \phi, \\ x_2 &= c \cos \phi, \\ \eta_1 &= \sin \phi, \text{ and} \\ \eta_2 &= a \cos \phi / c. \end{aligned}$$

Primed quantities are functions of  $\phi'$  instead of  $\phi$ . Integration with respect to  $\phi'$  is required to evaluate the definite integral in the denominator.

Note that  $x_1$  and  $x_2$  are coordinates of points on the elliptic crack boundary and  $a$  and  $c$  are semi-axes of the ellipse in  $x_1$  ( $\phi = 90$  deg) and  $x_2$  ( $\phi = 0$  deg) directions (Fig. 1). For isotropic materials  $f = G(\eta_1^2 + \eta_2^2)^{1/2}/(1 - \nu)$ ,  $G$  and  $\nu$  being the shear modulus and Poisson's ratio, respectively. No explicit expression of the function  $f$  is available in literature except for isotropic materials. In the Appendix, the method of numerical calculation of  $f$  for orthotropic media and an explicit expression for the transversely isotropic case are given. In what follows, results are given for three specific materials. These results are utilized later for prediction of failure of surface layers (initial damage). In many cases this may also yield the final failure load (except for medium depth flaws in laminated plate specimens with fixed grips). The averaged properties used for calculation of stress-intensity factors are listed in Table 1. The first two materials have been utilized in Refs 3-5. The layup for Material 2 is a bit more complicated than that indicated in the table. However, it is representative of the arrangement near the crack, and it will be seen later from the results that minor differences in properties do not influence the results too much. As shown in Table 1, all materials have high in-plane moduli (2, 3 directions, Fig. 1) but low through-the-thickness modulus (1 direction). They also have low through-the-thickness shear moduli, which have significant influence on the variation of stress-intensity factors for flaws with  $a/c = 1, 0.5$  and 2 shown in Figs. 2, 3, and 4, respectively. For a circular flaw, for example, the solution for isotropic materials indicates that the stress-intensity factor is constant along the periphery (Fig. 2). For the materials under consideration, however, the maximum value is at  $\phi = 0$  deg (corresponding to free surface in part-through flaws), and it is about twice that at  $\phi = 90$  deg, which corresponds to the deepest point in surface flaws. It is clear that more load transfer is occurring in the direction  $x_2$  as compared to the direction  $x_1$  because of low through-the-thickness shear moduli. The same trend follows for the other two values of  $a/c$ . It should be emphasized that even for  $a/c = 0.5$ , the maximum value occurs at  $\phi = 0$  deg, although for isotropic materials the stress-intensity factor at  $\phi = 0$  deg is two thirds that at  $\phi = 90$  deg. This appears to imply that in a majority of

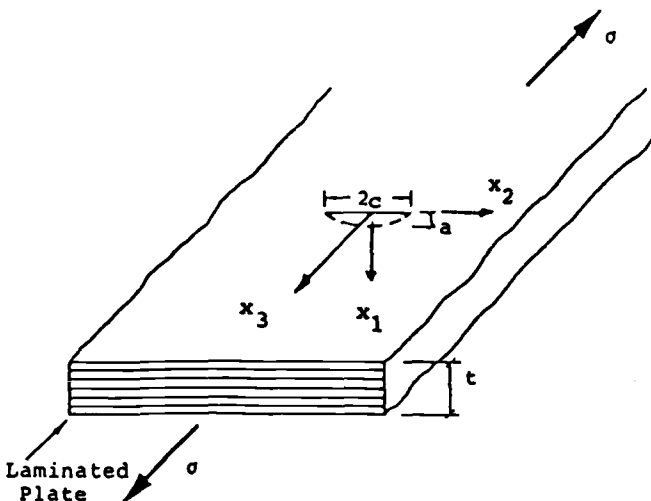


FIG. 1—Part-through flaw in a plate.

TABLE 1—*Properties used for calculations and data correlations.*

Material <sup>a</sup>	Young's Moduli,	Poisson's Ratios	Shear Moduli, GPa	Fracture Toughness, $K_{IC}$ , MPa $\sqrt{m}$	Unnotched Strength, $\sigma_0$ , MPa
	GPa $E_1 E_2 E_3$				
No. 1, transversely isotropic-quasi-isotropic (0/±45/90) layup T300/epoxy	56.7, 56.7, 11.7	0.3, 0.35, 0.35	21.8, 3.67, 3.67	32.9	538
No. 2, orthotropic (±56.5/0) layup AS4/epoxy	38.2, 29.0, 6.90	0.49, 0.17, 0.21	20.0, 3.59, 3.36	30.0	379
No. 3, orthotropic (±70/0) layup T40/epoxy	93.8, 66.1, 12.5	0.21, 0.31, 0.31	17.2, 5.92, 5.49	...	...

<sup>a</sup> 0-deg direction coincides with  $x_3$ -axis, which is perpendicular to the crack plane. All layups are of repeating type.

cases failure will occur first near the surface. This is not in agreement with the results obtained in Refs 3 and 4 where failure near deepest points are predicted for  $a/c < 1$ . This phenomenon also implies that back-surface effects are likely to be small in the materials under consideration.

Also shown in Figs. 2–4 are the limits for through cracks in a plate which is the same for isotropic and anisotropic materials. It can be seen that the stress-intensity factors at  $\phi = 0$  deg for elliptic flaws in orthotropic or transversely isotropic materials are closer to these values than the isotropic solutions. Since these through-crack solutions are the limiting values of stress-intensity factor (SIF) for part-through cracks (at  $\phi = 0$  deg) as  $a/t$  is increased ( $t$  being the thickness), it is expected that the correction factors for obtaining the part-through crack solution near the surface will be smaller than that for isotropic materials. For this reason, only a limited number of finite-element runs were necessary to obtain estimates of the correction factors to consider front- and back-surface effects as discussed in the next section.

### Correction Factors for Surface Flaws

Since the results in the previous section indicate that initial damage (and sometimes final failure as discussed in the introduction section) will occur due to failure of surface layers in a majority of cases, attempts were made in this task to estimate the corrections necessary to obtain the value of SIF at  $\phi = 0$  deg for surface flaws from the solutions in the previous subsection by the scheme

$$K_s = K_e F_c(a/c, a/t) F_w(c/w, a/t) \quad (2)$$

where

- $K_s$  = SIF near surface for elliptic surface flaw in a plate,
- $K_e$  = SIF at  $\phi = 0$  deg (see Figs. 2–4) for infinite medium,
- $F_c$  = correction factor for finite thickness and geometry of the ellipse,
- $a$  = semimajor axis in depth direction,
- $c$  = semimajor axis on surface,
- $t$  = thickness, and
- $F_w$  = correction for finite width =  $(\sec \pi c/w a/t)^{1/2}$ .

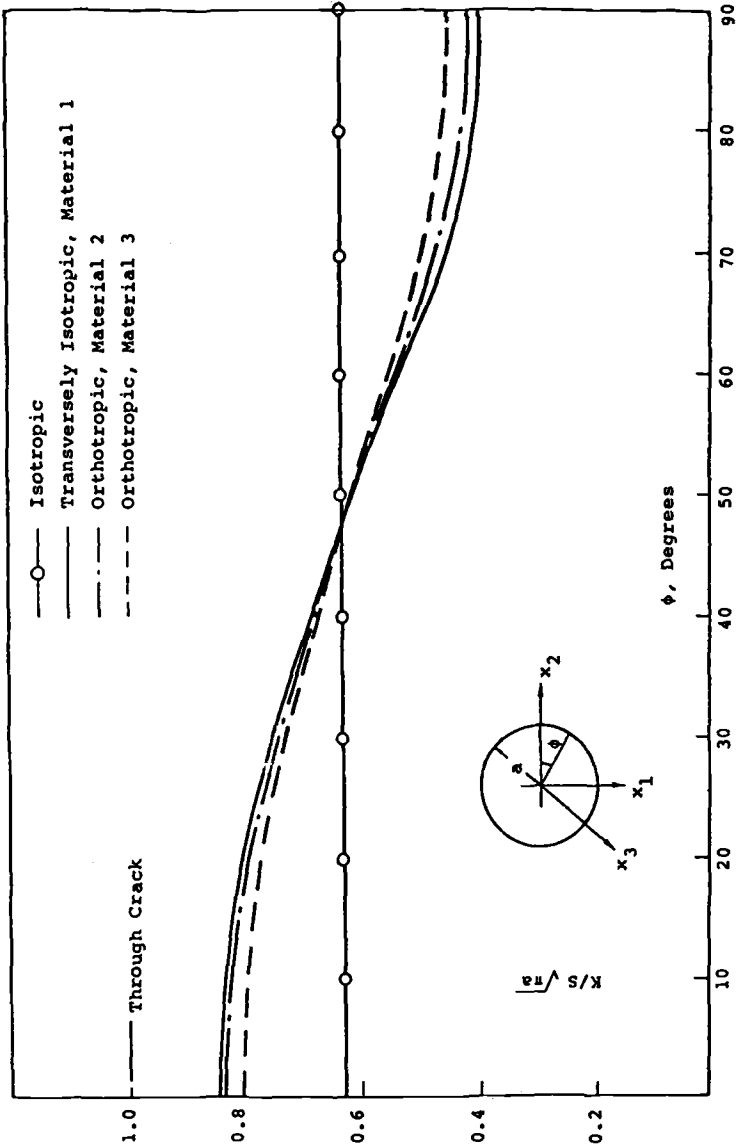


FIG. 2—Stress-intensity factors for a circular crack in infinite media.

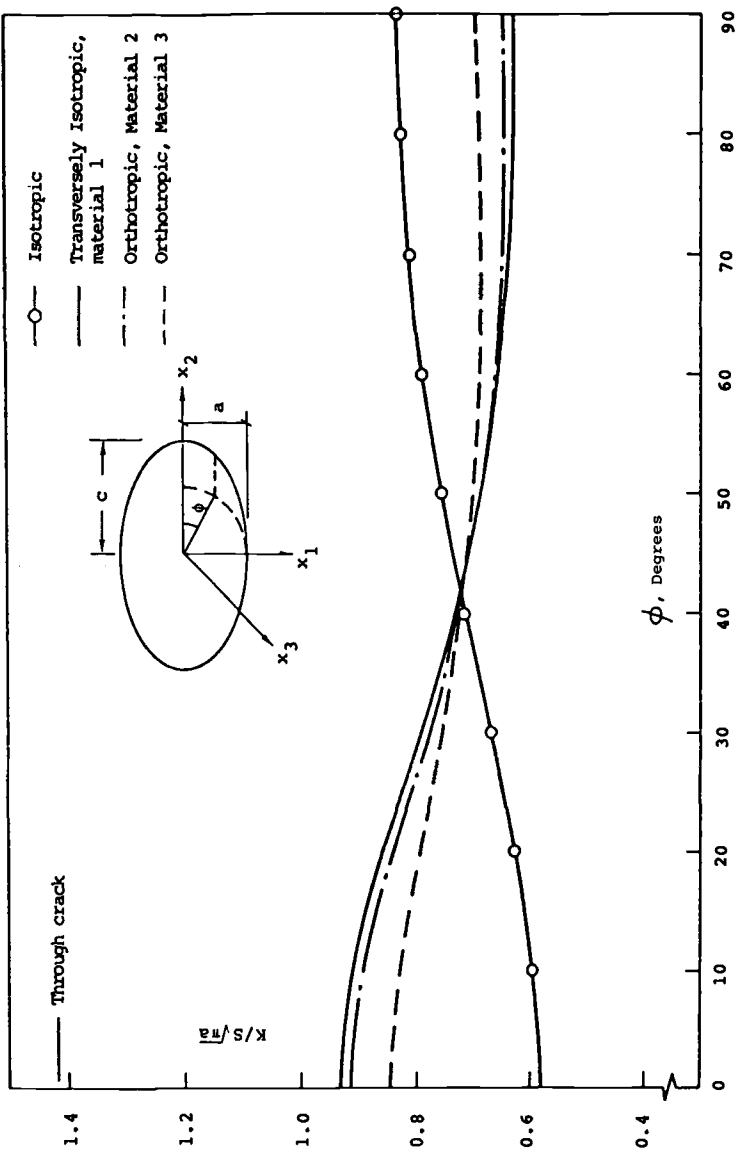


FIG. 3—Stress-intensity factors for elliptical crack ( $a/c = 0.5$ ) in infinite media.



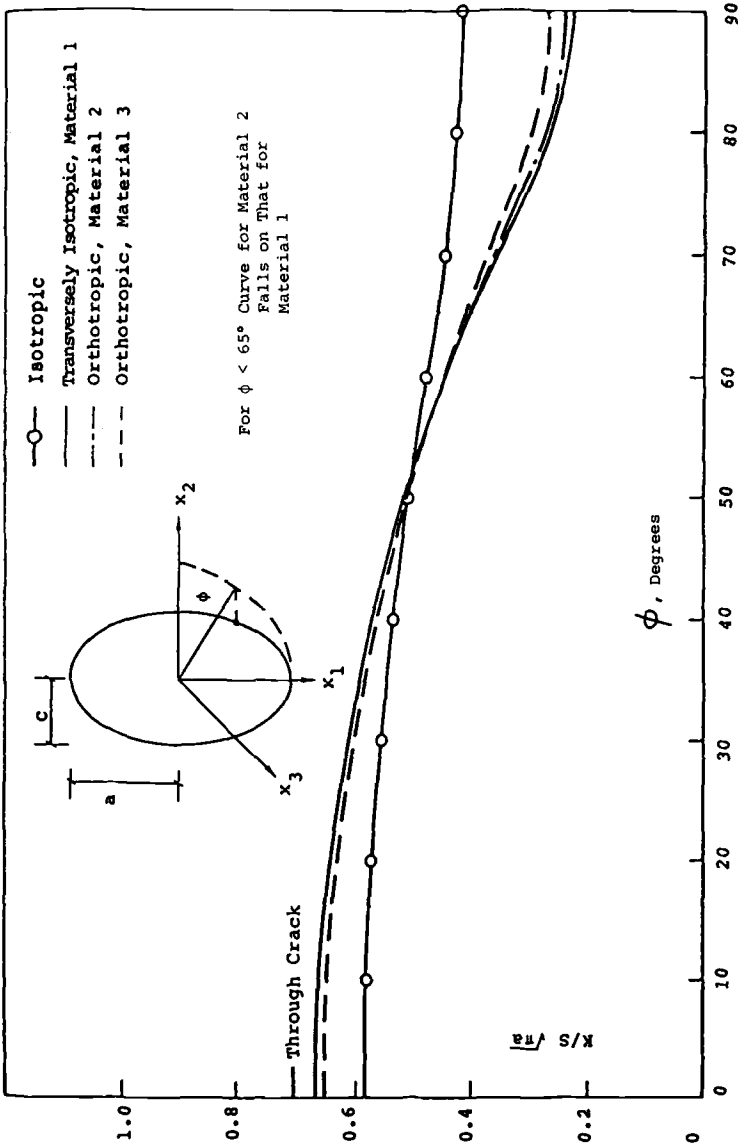


FIG. 4—Stress-intensity factors for elliptic crack ( $a/c = 2.0$ ) in infinite media.

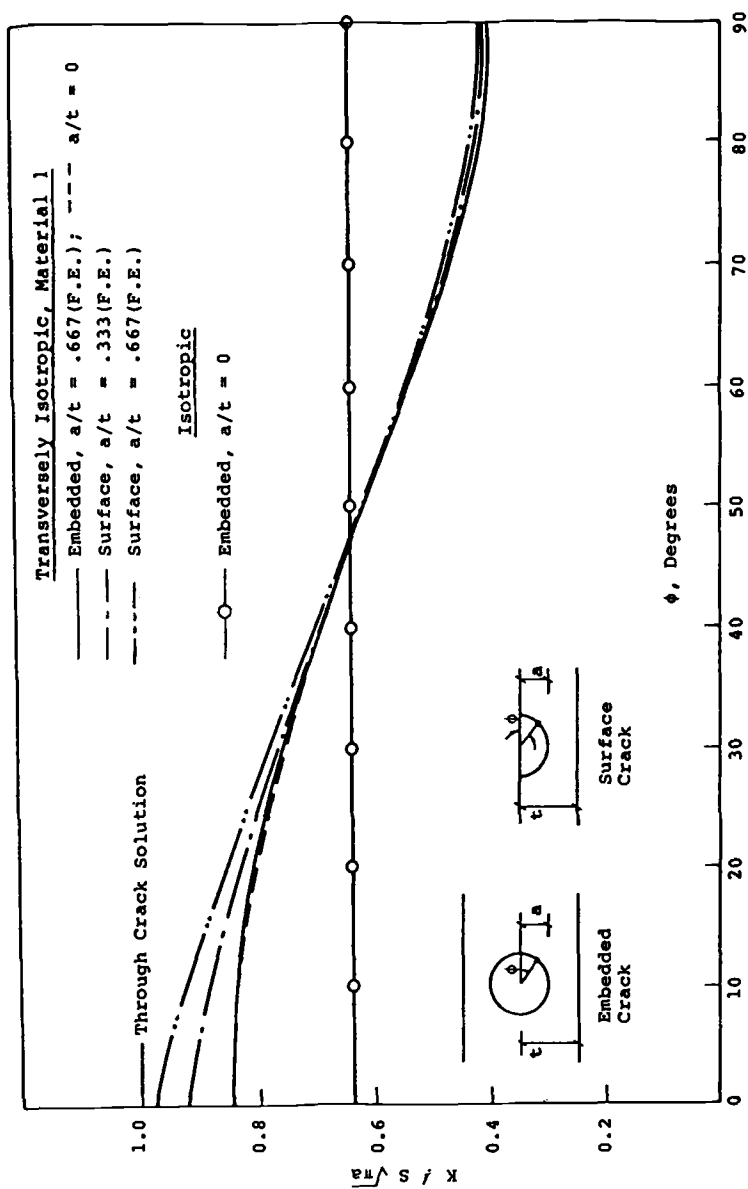


FIG. 5—Stress-intensity factors for circular and semicircular cracks in a transversely isotropic plate.

TABLE 2—Correction factor  $F_c$  determined from finite-element analysis for  $a/c = 1$  compared with isotropic plate result.

Material	$a/t \rightarrow 0$	$a/t = 0.333$	$a/t = 0.667$	Limit for Through Crack
Transversely isotropic, Material 1 (see Table 1)	...	1.09	1.15	1.18
Isotropic [2]	1.14	1.2	1.4	1.57

The correction is taken as the product of a width correction factor  $F_w$  and another factor  $F_c$  to consider front and back surface effects. The factor  $F_w$  is likely to be close to one for small  $2c/w$  ratios, and therefore this factor is taken to be the same as what is usually chosen for isotropic plates [2]. To determine  $F_c$ , we made some three-dimensional finite-element runs for the transversely isotropic material (Material 1) with a semicircular surface flaw. The finite-element code used is an inhouse code employing brick elements with constant strain fields. Since no singular element is utilized, the stress-intensity factors could not be directly calculated. Energy release rate  $G_I$  at any point on the crack periphery was calculated using the well-established procedure of multiplying the concentrated line force at the crack periphery by half of the crack opening displacement gradient in the radial direction at the same location. The line forces were obtained from nodal reaction forces by distributing evenly over the nodal spacing. The intensity factors were obtained from the relationship between  $K$  and  $G_I$  obtained from infinite medium solution (Appendix).

To check the accuracy, the results for  $a/t = \frac{1}{2}$  for an embedded crack (see insert at left in Fig. 5) are compared with the closed-form solution for  $a/t = 0$  (infinite medium) in Fig. 5. It can be seen that the two results are very close to each other, indicating that back-surface influence is negligible for embedded flaws. This is also true for surface flaws (near  $\phi = 90$  deg) as it appears from the comparison of surface flaw solutions for  $a/t = \frac{1}{2}$  and  $\frac{1}{4}$ , shown in the same figure. These results also indicate that as  $a/t$  is increased the SIF at  $\phi = 0$  deg approach the through-crack solution. The rate of increase, however, is slower than that for the isotropic case, since the solution for  $a/t = 0$  for isotropic medium is much lower than that in the transversely isotropic case. The correction factors are shown in Table 2. The factors for transversely isotropic case are not very sensitive to  $a/t$  ratios, and for  $a/t < 0.667$  these are very close to 1.1, a value which is commonly considered as the front-surface correction factor ( $a/t \rightarrow 0$ ) for isotropic plates. Accordingly, for moderate  $a/t$  ratios the correction factors may possibly be estimated from the relation given in Table 3. These relations are chosen to match the correction factors (in the isotropic case) for the two limiting cases  $a/c \rightarrow 0$  and  $c/a \rightarrow 0$  as well as for  $a/c = 1$  (for transversely isotropic case)

TABLE 3—Values of  $F_c$  used for correlation in transversely isotropic and orthotropic materials (see Table 1) for moderate  $a/t$  ratios: for  $a/c < 1$ ,  $F_c \approx 1.24 - 0.14 a/c$ ; for  $a/c > 1$ ,  $F_c \approx 1 + 0.1 c/a$ .

$a/c$	$F_c$	Limit for Through Crack, Material 1
0.2	1.21	2.72
0.5	1.17	1.51
1	1.1	1.18
2	1.05	1.06

when  $a/t$  is small. For physical reasons it appears that the two limiting values should also hold for transversely isotropic case. Since the stress-intensity factors for elliptic cracks in infinite media for the two orthotropic materials are close to those for the transversely isotropic case, the correction factors are also expected to be almost identical. Accordingly, the relations in Table 3 may be assumed to hold. The factors for some  $a/c$  ratios are listed in Table 3 along with the limiting values for through crack. As can be seen for  $a/c \geq 1$ , the correction factors are close to these limiting values. These values were utilized for data correlation studies reported in the next section.

### Correlation with Available Data for Failure of Layers Near the Surface

Tests on quasi-isotropic T300-5208 laminates with  $(0/\pm 45/90)_{10s}$  layup are reported in Ref 3. This material can be considered to be transversely isotropic with elastic properties listed in Table 1 (Material 1). Fracture toughness  $K_Q$  measured from tests with through cracks is also given in Table 1. Predicted values of the ratios of notched strength to unnotched strength to cause fracture of surface layers (close to  $\phi = 0$  deg) obtained by equating the value of  $K$  at  $\phi = 0$  deg (reported in the previous subsection) to  $K_Q$  are plotted in Fig. 6 along with test data. For calculation, the width is taken to be 25.4 mm (1 in.). For closed symbols the width of test specimens was 19 mm (0.75 in.), but for such specimens, values of  $c/w$  are not large enough to cause any significant influence on the results. Test data appear to be in good correlation with predictions except for very small crack sizes where the scatter appears to be greater. For these cases the disagreement may possibly be attributed to the nonhomogeneity in laminated construction, but it should be pointed out that for small  $c/t$  ratios,  $t$  being the laminate thickness, similar deviations from linear-elastic fracture mechanics may be observed even in metal plates because of dominance of inelastic regions near crack tips. Although the material under consideration behaves elastically under extension, some inelastic response may be expected because of the presence of  $\pm 45$ -deg layers, which are subjected to inplane shear, and existence of interlaminar shear stresses. For all practical purposes, the agreement is reasonable and is much better than those based on isotropic plate solutions [3]. Also shown in Fig. 6 are the results obtained on the assumption that the part-through cracks can be replaced by a through crack of length  $2c$ . Because of the possibility of creation of interlaminar delaminations, this solution might possibly be taken as a good lower-bound estimate except for small  $c/t$  ratios.

Similar comparisons for some tests reported in Ref 4 are shown in Fig. 7. The calculations are based on properties listed in Table 1 (Material 2) and the procedure outlined in the previous subsection. It should be noted that the value of  $K_Q$  (Table 1 and Ref 4) was never measured but was estimated in Ref 4 by the procedure outlined there. The differences between test data and predictions for initial damage may possibly be attributed to this fact. However, the differences do not appear to be too large. Also shown in the figure are the predictions obtained by replacing the surface crack by a through crack with the same value of  $c$ , which again provides a lower-bound estimate. In a number of cases for medium  $a/t$  ratios, two-part failures (final failure at a higher load after surface fracture) are reported in Ref 4, and the final failure loads are also plotted in Fig. 7. In some cases these loads are much higher than those to cause fracture of surface layers; an attempt to explain this phenomenon was made in Ref 4. This was investigated in some detail in this study and is described in the next section.

### Delamination Growth after Failure of Surface Layers

In two-part failures suggested in Refs 3 and 4, delaminations are generated separating the fractured surface layers from the remaining layers which remain intact, although the

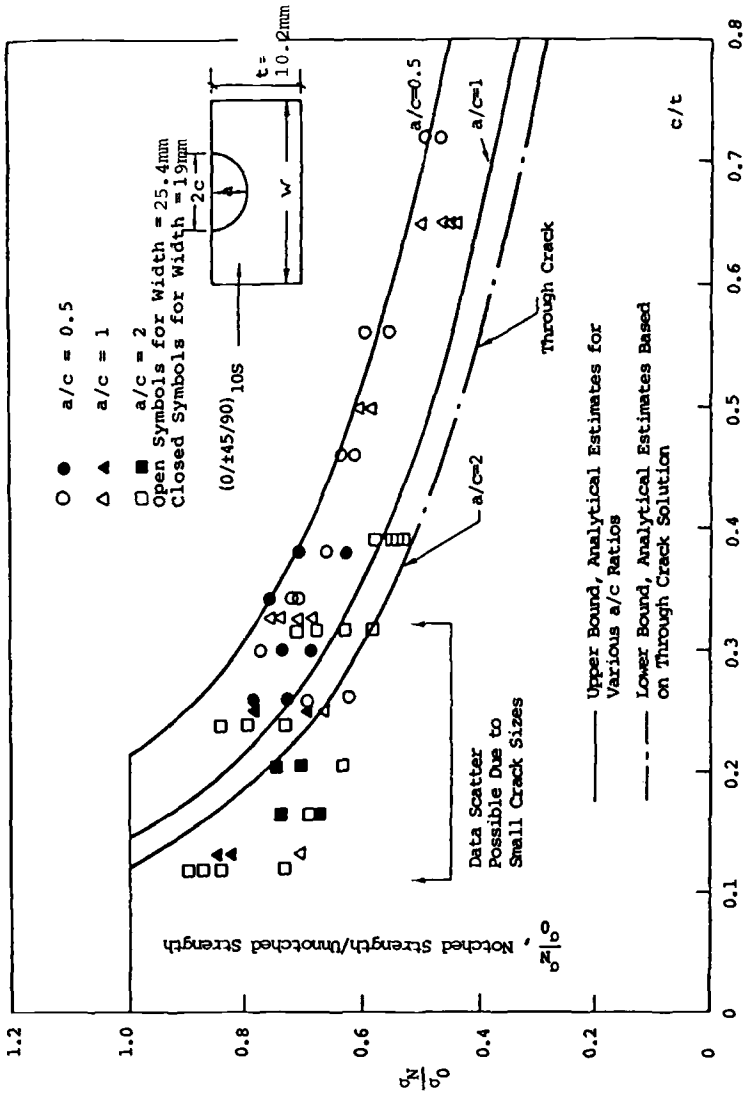


FIG. 6—Test data and fracture-mechanics predictions of effect of surface cracks on initial damage in quasi-isotropic T300/5208 laminates.

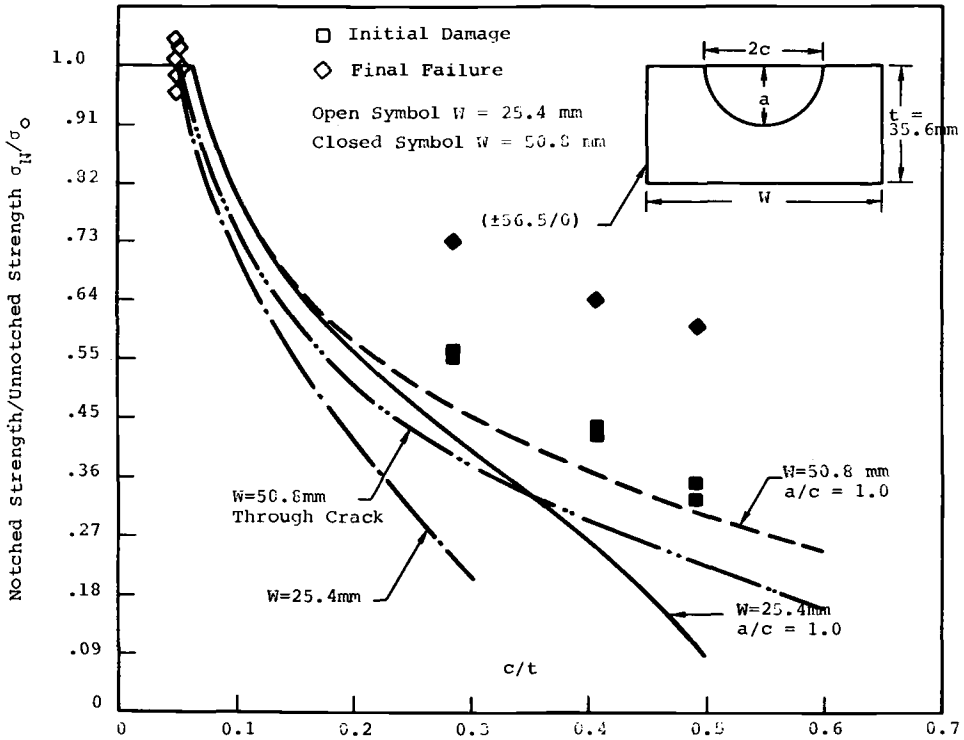


FIG. 7—Test data and predictions of initial damage or fracture of surface layers near the surface for  $a/c = 1.0$ .

delamination depth is not always the same as the cut depth. Sometimes more than one delamination are created. Whatever be the case, if the delaminations extend to the grips and the grips can be considered to be rigid, the final failure loads can be estimated from those of the remaining ligaments subjected to constant axial displacement at the grips. These estimates have been made in Ref 4. However, actual failure loads for two-part failures are sometimes lower than these estimates. An attempt was made in this study to determine the possibility that the delamination could be arrested before they reached the grips and cause failure at loads below those of the remaining ligaments.

Possibilities of delamination growth were examined by the model described in Ref 8. The problem was assumed to be quasi-three-dimensional (all quantities are independent of  $x_2$  coordinate), and a finite-element analysis was utilized to calculate Mode I and Mode II energy-release rate at the tips of delaminations of varying length  $\ell$ . The layup modeled was the same as that used in Ref 4. The cut depth was chosen as 9.91 mm (0.39 in.) and the thickness of the laminate was equal to 35.6 mm (1.4 in.). The stress-analysis method (based on sublaminates assemblage model described in Ref 8) made use of six sublaminates, two above and four below the delamination plane. Specimen lengths (between rigid grips which are pulled apart) of 101.6 mm (4 in. as used in Ref 4) and 406.4 mm (16 in.) were considered. Results showed that the energy-release rates at delamination tip as well as the maximum stresses in the 0-deg layers (average over an element) reduce as the delamination length  $\ell$  increases. For 101.6-mm-long specimens and  $\ell = 35.6$  mm  $G_I = 175$  N/m,  $G_{II} = 2450$  N/m, and the maximum stress in 0-deg layer is equal to 1282 MPa (186 ksi). This

later value is close to the failure stress of the 0-deg layers. It appears, however, that the energy-release rates are too high (a critical value of  $G_{II}^c \approx 1000$  N/m for delamination fracture is possibly appropriate for standard epoxy matrices, see Ref 9) for arresting of delaminations. Moreover, the maximum stress in the 0-deg layers occurs in the elements near the delamination tips, whereas failure of specimens have been reported under the surface cuts [3,4]. It appears, therefore, that if the delaminations do not allow any stress transfer they will grow to the grips. For longer specimens (406.4 mm) the energy-release rates are much higher. It is suggested in Ref 4 that failure occurs (after the delaminations grow to the grips) at loads less than that for remaining ligament failure because the grips are not perfectly rigid. It is most likely, however, that the delaminations created after failure of surface layers do not have smooth surfaces thus allowing transfer of shear stresses. Alternatively, it is possible that instead of delaminations, a highly strained shear transfer region is created where the material (the resin) yields and behaves in a nonlinear fashion. Such damage zones (perpendicular main cracks) are quite common in many epoxy matrix composites as discussed in Refs 10 and 11, and use of such models may yield better correlation with test data for such two-part failures.

## Discussion

Initial damage in the form of fracture of surface layers near part-through semielliptic flaws can be predicted with reasonable accuracy using (a) homogenization assumptions, (b) orthotropic or transversely isotropic elasticity solution for infinite media, (c) correction factors for finite thickness, and (d) fracture mechanics. Loads required to cause initial damage can be much lower than the strengths of the ligaments below the crack for medium-depth flaws (not too shallow or deep). For shallow or deep flaws, failure will occur suddenly and the strength is expected to be higher than that of remaining ligaments. Fracture-mechanics predictions will yield a conservative estimate of the load-carrying capacity for medium-depth flaws. Assumption of through cracks of the same width as the exposed length of the part-through surface flaw can be used to obtain simple but more conservative estimates.

For medium-depth flaws, a two-part failure may occur. Final-failure load is expected to be higher than that for initial damage or fracture of surface layers but may be lower than the strength of the remaining ligaments. Further analytical and experimental studies are required for a better understanding of such two-part failures.

## Conclusions

The results obtained here demonstrate that stress-intensity factors for a majority of semielliptic surface cracks in laminated composites modeled as homogeneous orthotropic plates usually show a maximum value near the surface. This is not observed in isotropic plates when  $a/c < 1$ . Therefore, failure of surface layers (called initial damage) will occur first for a majority of crack configurations in laminates. Because of this fact and because of the crack blunting effect due to creation of damage zones or delaminations below the failed-surface layers, the load-carrying capacity of laminates containing medium-depth flaws is usually greater than the load causing initial damage. Simple formulas for calculation of stress-intensity factors for elliptic flaws in infinite transversely isotropic and orthotropic media as well as estimates of correction factors to consider finite thickness, geometry of the ellipse, and finite width are given. These results can be used to predict failure loads for shallow or deep flaws and obtain conservative estimates of strength of laminates with medium-depth flaws. The predictions will be accurate provided a repeating arrangement

of layers exists and laminate thickness is not small compared to the crack size. This is confirmed by the correlation of analytical predictions with test data reported in the literature. Further studies on two-part failures are, however, required as discussed earlier. It is hoped that the results of this study will be useful for obtaining (1) design guidelines for damage tolerance, (2) accept/reject criteria for manufactured components, and (3) repair/replace criteria for damaged parts in laminated composite structures, which are being used in an increasing number of applications.

### Acknowledgment

This research was supported by HQ, Ballistic Missile Office, Air Force Systems Command, Contract No. F04704-86-C-0141.

## APPENDIX

### Stress-Intensity Factors for an Elliptic Crack in an Orthotropic Medium

The governing equations for three-dimensional elasticity problem of an anisotropic medium are given by

$$\sigma_{jk,k} = 0 \quad (3)$$

$$\sigma_{jk} = C_{jk\ell m} U_{\ell,m} \quad (4)$$

where  $\sigma$ ,  $U$ , and  $C$  denote stresses, displacements, and stiffnesses, respectively, and repeated index indicates summation. Substitution of Eq 4 in Eq 3 yields three second-order partial differential equations in terms of the displacement variables. Taking multiple Fourier transforms of these equations and denoting

$$\tilde{U}_\ell(\xi, x_3) = \frac{1}{2\pi} \int_{-\infty}^{\infty} \int_{-\infty}^{\infty} U_\ell(x_1, x_2) e^{i\xi_1 x_1 + i\xi_2 x_2} dx_1 dx_2 \quad (5)$$

where  $\xi = (\xi_1, \xi_2)$ ,  $x = (x_1, x_2)$  are vectors, and  $i' = \sqrt{-1}$ , one obtains three second-order ordinary differential equations. In what follows we will consider an elliptic crack (with semi-axes  $a_1$  and  $a_2$  oriented in the directions  $x_1$  and  $x_2$ , respectively) in an orthotropic medium subjected to equal and opposite pressure on the crack faces and seek solutions for the half space  $x_3 > 0$ . We introduce the following transformations

$$\begin{aligned} x_i &= a_i x_i' & \text{and} & & \xi_i &= \zeta_i \zeta_i', & i &= 1, 2 \\ x_1' &= r \sin \theta & & & \zeta_1 &= \sin \phi / a_1 \\ x_2' &= r \cos \theta & & & \zeta_2 &= \cos \phi / a_2 \end{aligned} \quad (6)$$

and write the transformed displacements as

$$\tilde{U}_i = \sum_{k=1}^3 \alpha_{ik} C_k e^{-\lambda_k x_3} \quad (7)$$

where the characteristic roots  $\lambda_k$  (with positive real parts) and the eigenvectors  $\alpha_{ik}$  may be evaluated from the following equations obtained by substituting Eq 5 into the differential equations.



$$\begin{bmatrix} (C_{11}\zeta_1^2 + C_{66}\zeta_2^2 - C_{55}\lambda_k^2)((C_{12} + C_{66})\zeta_1\zeta_2)(-i\lambda_k\zeta_1(C_{13} + C_{55})) \\ (C_{66}\zeta_1^2 + C_{22}\zeta_2^2 - C_{44}\lambda_k^2)(-i\lambda_k\zeta_2((C_{23} + C_{44})) \\ (C_{55}\zeta_1^2 + C_{44}\zeta_2^2 - C_{33}\lambda_k^2) \end{bmatrix} \begin{bmatrix} \alpha_{1k} \\ \alpha_{2k} \\ \alpha_{3k} \end{bmatrix} = 0 \quad (8)$$

In Eq 8,  $C_{ij}$  are the stiffnesses in contracted notation. For the transversely isotropic case,  $\lambda_k$ 's are real and we will give a closed form solution of the problem later. For generally orthotropic case,  $\lambda_k$  are not always real and must be evaluated for each value of  $\phi$  by solving the cubic equation involving  $\lambda_k^2$  numerically and taking  $\lambda_k$  as their square roots with positive real parts. For all values of  $\phi$  between 0 deg and 90 deg (except for  $\phi = 0$  deg and 90 deg), one may choose  $\alpha_{3k} = -i'$ ,  $k = 1, 2, 3$  and evaluate  $\alpha_{1k}$ ,  $\alpha_{2k}$  from the first two equations Eq 8. One should note that these two equations may become singular at  $\phi = 0$  deg or 90 deg or both for certain values of  $\lambda_k$ . However, one may obtain a good estimate of  $\alpha_{1k}$ ,  $\alpha_{2k}$  by choosing  $\phi$  close to 0 deg or 90 deg or evaluate them from another pair of equations. We have made use of the first approach by choosing  $\phi$  about 0.5 deg off from 0 and 90°. To evaluate  $C_k$ , we utilize the following conditions at  $x_3 = 0$

$$\tilde{\tau}_{xz} = \tilde{\tau}_{yz} = 0, \quad \tilde{U}_3 = \tilde{W}^* \quad (9)$$

where  $\tilde{W}^*$  is the displacement  $U_3$  at the plane  $x_3 = 0^+$ . Note that  $\tilde{W}^* = 0$  outside the cracked surface. The result (for the choice of  $\alpha_{3k} = -i'$ ) is given by  $C_k = i' \tilde{W}^* C'_k$

$$C'_k = (- (\lambda_\ell \alpha_{2\ell} - \lambda_m \alpha_{2m}) \zeta_1 - (\lambda_m \alpha_{1m} - \lambda_\ell \alpha_{1\ell}) \zeta_2 + \lambda_\ell \lambda_m (\alpha_{1\ell} \alpha_{2m} - \alpha_{1m} \alpha_{2\ell})) / \Delta \quad (10)$$

where  $\ell = 2, m = 3$  for  $k = 1$ ;  $\ell = 3, m = 1$  for  $k = 2$  and  $\ell = 1, m = 2$  for  $k = 3$ , and  $\Delta = \lambda_1 \lambda_2 (\alpha_{11} \alpha_{22} - \alpha_{12} \alpha_{21}) + \lambda_2 \lambda_3 (\alpha_{12} \alpha_{23} - \alpha_{13} \alpha_{22}) + \lambda_3 \lambda_1 (\alpha_{13} \alpha_{21} - \alpha_{11} \alpha_{23})$ .

The transform of  $\sigma_{33}$  as  $x_3 \rightarrow 0^+$  can then be evaluated as

$$\tilde{\sigma}_{33}|_{x_3=0^+} = -\zeta f(\phi) \tilde{W}^* \quad (11)$$

where

$$f(\phi) = \sum_{k=1}^3 (C_{33} \lambda_k - C_{13} \alpha_{1k} \zeta_1 - C_{23} \alpha_{2k} \zeta_2) C'_k \quad (12)$$

It may be noted that since the procedure is numerical, it is not possible to keep track of how  $\alpha_{ik}$  or  $\lambda_k$  for each  $k$  change with  $\phi$ . However, the final result (Eq 11) is not affected since it is obtained by summing over  $k$ .

For transversely isotropic case  $\lambda_k$ 's can be expressed in the following form

$$\lambda_k = \sqrt{\zeta_1^2 / \gamma_k^2 + \zeta_2^2}$$

where

$$\begin{aligned} \gamma_3^2 &= C_{44} / C_{55} \\ \gamma_{1,2}^2 &= \frac{1}{2} [\gamma' + \sqrt{\gamma'^2 - 4C_{22}/C_{11}}] \\ \gamma' &= (C_{11}C_{22} - C_{12}^2 - 2C_{12}/C_{55}) / C_{11}C_{55} \end{aligned} \quad (13)$$

and  $f(\phi)$  in Eq 11 can be expressed as

$$f(\phi) = 2\gamma_3^2 C_{44} \left[ \frac{C_{12} + C_{55}}{2 C_{22}} \frac{\lambda_3^4 (2 - A_1 - A_2) - \xi_2^4 (2 + A_1 + A_2)}{\lambda_1 \lambda_2 (\lambda_1 + \lambda_2)} + \frac{\lambda_3 \xi_2^2}{\lambda_1 \lambda_2 \xi_1^2} (\lambda_3 \lambda_1 + \lambda_3 \lambda_2 - 2\lambda_1 \lambda_2) \right] \quad (14)$$

where  $A_k = (C_{12} + C_{55}) / (C_{55} - C_{22} / \gamma_k^2)$ ;  $k = 1, 2$ .

It should be noted that for  $\xi_1 = 0$ , the limiting form of the second term in Eq 12 must be used:

$$\frac{\lambda_3 \xi_2^2}{\lambda_1 \lambda_2} \left\{ \frac{1}{\lambda_3^2} - \frac{1}{2} \left[ \frac{1}{\lambda_1^2} + \frac{1}{\lambda_2^2} \right] \right\} \quad (15)$$

Inverse transform of Eq 11 yields the following integral equation for evaluation of  $W^*$  within the crack boundaries (or rather over the circle  $0 < r < 1$  onto which the crack is mapped by the transformation 4) for given pressure distribution  $\sigma_{33}(y'_1, y'_2)$  over the unit circle

$$-\sigma_{33}(y') = \frac{1}{4\pi^2} \int_0^\infty \int_0^{2\pi} \xi^2 f(\phi) \int_0^1 \int_0^{2\pi} r W^*(x') e^{i(x'-y') \cdot \xi} d\theta dr d\phi d\xi \quad (16)$$

For constant pressure distribution  $-\sigma_{33}(y') = S$ , it can be shown (the details are omitted here for brevity) that Eq 14 is satisfied by

$$W^* = S(1 - r^2)^{1/2} \int_0^{\pi/2} f(\phi) d\phi \quad (17)$$

Equation 14 is also valid outside the circle, and the singular stress field near but greater than  $r = 1$  can be expressed as

$$\sigma_{33}(r, \theta) = \frac{K(\theta)}{2\pi r'} = \frac{Sf(\theta)(r^2 - 1)^{-1/2}}{\int_0^{\pi/2} f(\phi) d\phi} \quad (18)$$

where  $K$  is the stress-intensity factor and  $r'$  is the distance measured from and normal to the elliptic crack boundary. It follows that

$$K = \frac{S\sqrt{\pi a_1} h(\theta)}{\int_0^{\pi/2} h(\phi) d\phi} g(\theta)^{-1/4} \quad (19)$$

where  $g(\theta) = \sin^2 \theta + a_1^2 \cos^2 \theta / a_2^2$  and  $h(\phi) = a_1 f(\phi) = a_1 f(\xi_1, \xi_2)$ . Therefore,

$$h(\phi) = f(\eta_1, \eta_2) = f(\sin \phi, a_1 \cos \phi / a_2), \quad \eta_i = \xi_i \cdot a_i \quad (20)$$

One should note that we have replaced  $a_1$  by  $a$  and  $a_2$  by  $c$  in Eq 1 of the text. These are the common notations used in the literature for surface cracks. The integral in Eq 19 has to be evaluated by numerical methods, and Simpson's rule has been utilized in this study. Energy-release rate at any point on the crack boundary may be evaluated, if desired, from the expression

$$G_I = \frac{K^2}{2h(\theta)} g(\theta)^{1/2} \quad (21)$$

It may be noted that the function  $h$  for the isotropic case is given by

$$h(\phi) = Gg(\phi)^{1/2}/(1 - \nu) \quad (22)$$

which can be obtained from Eq 14 by an appropriate limiting process and substitution of Eq 22 into Eq 19 yields the well-known result [2].

## References

- [1] Awerbuch, J. and Madhukar, M., "Notched Strength of Composite Laminates: Predictions and Experiments—A Review," *Journal of Reinforced Plastics and Composites*, Vol. 4, 1985, p. 3.
- [2] Newman, J. C., Jr., "A Review and Assessment of the Stress Intensity Factors for Surface Cracks, "Part-Through Crack Fatigue Life Prediction, *ASTM STP 687*, American Society for Testing and Materials, Philadelphia, 1979, p. 16.
- [3] Harris, C. E., Morris, D. H., and Nottorf, E. W., "Analytical and Experimental Investigation of the Notched Strength of Thick Laminates With Surface Notches," *Composite Materials, Testing and Design (Eighth Conference)*, *ASTM STP 972*, American Society for Testing and Materials, Philadelphia, 1988, pp. 298–321.
- [4] Poe, C. C., Jr., Illg, W., and Garber, D. P., "A Program to Determine the Effect of Low Velocity Impacts on Strength of the Filament-Wound Rocket Motor Case for the Space Shuttle," *NASA TM 87771*, National Aeronautics and Space Administration, Washington, DC, July 1986.
- [5] Harris, C. E. and Morris, D. H., "Preliminary Report on Tests of Tensile Specimens With Part-Through Surface Notch for a Filament-Wound Graphite Epoxy Material," *NASA CR172545*, National Aeronautics and Space Administration, Washington DC, March 1985.
- [6] Willis, J. R., "The Stress Field Around an Elliptic Crack in an Anisotropic Medium," *International Journal of Engineering Sciences*, Vol. 6, 1968, p. 253.
- [7] Hoenig, A., "The Behavior of a Flat Elliptical Crack in an Anisotropic Elastic Body," *International Journal of Solids and Structure*, Vol. 14, 1978, p. 925.
- [8] Chatterjee, S. N. and Ramnath, V., "Modeling Laminated Composite Structures as Assemblage of Sublaminates," *International Journal of Solids and Structures*, Vol. 24, 1988, p. 439.
- [9] Chatterjee, S. N., Pipes, R. B., and Blake R. A., Jr., "Criticality of Disbonds in Laminated Composites," *Effects of Defects in Composite Materials*, *ASTM STP 836*, American Society for Testing and Materials, Philadelphia, 1984, p. 161.
- [10] McClintock, F. A., "Problems in the Fracture of Composites With Plastic Matrices," presented at the 4th Symposium on High Performance Composites at St. Louis, MO, Monsanto, CO, and Washington University, 1969.
- [11] Tirosh, J., "The Effect of Plasticity and Crack Blunting on the Stress Distribution in Orthotropic Composite Materials," *Journal of Applied Mechanics*, American Society of Mechanical Engineers, Vol. 40, 1973, p. 785.

Clarence C. Poe, Jr.,<sup>1</sup> Charles E. Harris,<sup>1</sup> and Don H. Morris<sup>2</sup>

## Surface Crack Analysis Applied to Impact Damage in a Thick Graphite/Epoxy Composite

---

**REFERENCE:** Poe, C. C., Jr., Harris, C. E., and Morris, D. H., "Surface Crack Analysis Applied to Impact Damage in a Thick Graphite/Epoxy Composite," *Surface-Crack Growth: Models, Experiments, and Structures, ASTM STP 1060*, W. G. Reuter, J. H. Underwood, and J. C. Newman, Jr., Eds., American Society for Testing and Materials, Philadelphia, 1990, pp. 194–212.

**ABSTRACT:** The residual tensile strength of a thick graphite/epoxy composite with impact damage was predicted using surface crack analysis. The damage was localized to a region directly beneath the impact site and extended only part way through the laminate. The damaged region contained broken fibers, and the locus of breaks in each layer resembled a crack that was nearly perpendicular to the direction of the fibers. In some cases, the impacts broke fibers without making a visible crater. The damage was represented as a semielliptical surface crack of the same width and depth as the cross section of the damage. The maximum length and depth of the damage were predicted using the Theory of Elasticity and a maximum shear stress criterion. The predictions and measurements of strength were in good agreement.

**KEY WORDS:** graphite/epoxy, composite, filament winding, motor case, impact damage, fracture, surface crack

### Nomenclature

$a$	Depth of surface crack or impact damage, m (in.)
$c$	Half-length of surface crack or impact damage, m (in.)
$E$	Young's modulus, Pa (psi)
$E_{xr}$	Young's modulus of remaining ligament in hoop direction, Pa (psi)
$F(a/t, a/c, c/W, \phi)$	Functional in Eqs 6 and 7
$G$	Shear modulus, Pa (psi)
$K$	Stress-intensity factor, $\text{Pa}\sqrt{\text{m}}$ ( $\text{psi}\sqrt{\text{in.}}$ )
$K_Q$	Fracture toughness, $\text{Pa}\sqrt{\text{m}}$ ( $\text{psi}\sqrt{\text{in.}}$ )
$n_0$	Factor in the Hertz law, Pa (psi)
$p$	Contact pressure distribution, Pa (psi)
$p_c$	Average contact pressure, Pa (psi)
$P$	Peak impact force, N (lbf)
$Q$	Shape factor for an elliptical crack
$r_c$	Contact radius, m (in.)
$R_i$	Radius of indenter, m (in.)
$S_{cl}$	Gross stress for failure of first ligament, Pa (psi)

<sup>1</sup> Senior researcher and head, Fatigue and Fracture Branch, respectively, NASA Langley Research Center, Hampton, VA 23665-5225.

<sup>2</sup> Professor, Department of Engineering, Science, and Mechanics, Virginia Polytechnic Institute and State University, Blacksburg, VA 24061.

$S_{cr}$	Gross stress for failure of remaining ligament, Pa (psi)
$t$	Laminate thickness, m (in.)
$W$	Width of specimen in test section, m (in.)
$z_0$	Depth from surface where damage initiates
$\epsilon_{tu}$	Ultimate tensile failing strain of undamaged laminate
$\zeta$	Ratio of damage depth to contact radius, $a/r_c$
$\zeta_0$	Ratio of depth to contact radius where damage initiates, $z_0/r_c$
$\nu$	Poisson's ratio
$\tau_u$	Shear strength, Pa (psi)
$\phi$	Parametric angle of ellipse ( $\phi = 0$ deg and 90 deg correspond to where surface crack intersects free surface and to location of maximum depth, respectively)

### Subscripts

- 1, 2 principal coordinates of the layers (the 1-direction is the fiber direction)
- $x, y$  Cartesian coordinates ( $x$ -direction is hoop direction of FWC laminate)
- $r, \theta, z$  Cylindrical coordinates ( $z$ -direction is normal to plane of laminate)

Lightweight composite cases were developed for the solid-rocket motors of the Space Shuttle. The cases are made of graphite/epoxy using a wet filament-winding process, hence the name filament-wound cases (FWC). Each 3.66-m-diameter (12-ft)<sup>3</sup> motor consists of four cases—a forward case, two center cases, and an aft case—that are joined to short steel rings with pins. The forward and center cases are approximately 7.62 m (25 ft) in length, and the aft case is somewhat shorter. The FWC's are 3.6 cm (1.4 in) thick except very near the ends, where they are thicker to withstand the concentrated pin loads.

Tests [1–4] revealed that impacts by dropped objects such as tools and equipment can reduce the uniaxial tension strength of the FWC laminate, sometimes without even making a visible crater. The damage was localized to a region directly beneath the impact site and extended only partway through the laminate. The damaged region contained broken fibers, and the locus of breaks in each layer resembled a crack perpendicular to the direction of the fibers. Impacts usually cause thin composite laminates to delaminate over a relatively large region. However, the thick FWC did not delaminate extensively, making the damage difficult to detect except with special ultrasonic techniques [5–8].

In the present paper, the impact damage in the FWC laminate is represented as an equivalent surface crack, and the residual strengths are predicted using a surface crack analysis. The stress-intensity factor for a semielliptical surface crack in a homogeneous, isotropic plate is used for the composite plate. The value of fracture toughness was predicted using a general fracture toughness parameter for composite materials. The size of the damage or equivalent surface crack was predicted with the analysis of Ref 9. The analysis uses a maximum shear stress criterion and stresses calculated with Love's solution for pressure applied on part of the boundary of a semi-infinite body. The pressure was calculated using Hertz's law. The predicted strengths are compared with experimental values.

### Material

For the impact investigations [1–4], a 0.76-m-diameter (30-in.), 2.13-m-long (7-ft) full-thickness cylinder was made to represent the region of an FWC away from the ends. The

<sup>3</sup> Original measurements were made in English units and converted to SI units.

cylinder was wound by Hercules Inc. using a wet process and AS4W-12K graphite fiber and HBRF-55A epoxy resin except for the hoop layers, which were hand-laid using prepreg tape. From outside to inside, the orientations of the layers were  $\{(\pm 33.5 \text{ deg})_2/90 \text{ deg}/[(\pm 33.5 \text{ deg})_2/90 \text{ deg}]_3/[(\pm 33.5 \text{ deg})_2/90 \text{ deg}]_7/(\pm 33.5 \text{ deg}/90 \text{ deg})_4/(\pm 33.5 \text{ deg})_2/\text{cloth}\}$ , where the 90-deg layers are the hoops and the  $\pm 33.5$ -deg layers are the helicals. (The layer angles are measured from the hoop direction of the cylinder and from the longitudinal axis of the FWC.) The underlined  $\pm 33.5 \text{ deg}$  helical layers are about 1.6 times as thick as the other helical layers. The cloth layer at the inner surface has an equal number of fibers in the warp and weave directions. The layup is balanced (equal numbers of  $+33.5$  and  $-33.5 \text{ deg}$  layers) but not symmetrical about the midplane. Most of the hoop layers are closer to the inner surface than the outer surface.

None of the specimens from the rings were left for the depley investigation in Ref 9. Consequently, a 30- by 30-mm (12- by 12-in.) plate that had been cut from an actual FWC was used. Because the cylinder was made to represent the FWC, the materials of the plate and cylinder were basically the same. Of course all of the layers of the plate were wound with AS4W-12K graphite fiber and HBRF-55A epoxy, and the radius of curvature of the plates was 1.8 m (6 ft). The layer orientations were also slightly different because the plate came from a FWC with an earlier design. From outside to inside, the layup of the plate was  $\{(\pm 33.5 \text{ deg})_2/90 \text{ deg}/[(\pm 33.5 \text{ deg})_2/90 \text{ deg}]_3/[(\pm 33.5 \text{ deg})_2/90 \text{ deg}]_7/(\pm 33.5 \text{ deg}/90 \text{ deg})_2/\pm 33.5 \text{ deg}/90 \text{ deg}_4/\pm 33.5 \text{ deg}/90 \text{ deg}_2/(\pm 33.5 \text{ deg})_2/\text{cloth}\}$ . The FWC plate has two more hoop layers than the rings, but the outer 55 layers are the same. These differences should not affect the results in Ref 9.

### Test Apparatus and Procedure

The experiments to measure the effect of impact damage on the residual strength of the FWC are described in detail elsewhere [1-4]. Nevertheless, the apparatus and procedure are briefly described here for the convenience of the reader.

#### Impact Tests

The free-falling impacters consisted of a 5-cm-diameter (2-in.) steel rod with a 2.54-cm-diameter (1.00-in.) indenter on the end. Four rods of different lengths were used to give masses of 2.8, 5.0, 9.0, and 18.6 kg (6.1, 11.1, 19.9, and 41.1 lbf), including the indenter. The impacter was instrumented to determine the maximum impact force. Drop heights were varied from 38 to 305 cm (15 to 120 in.) to give kinetic energies from 38 to 446 J (28 to 329 ft-lbf).

The free-falling impacters consisted of a 5-cm-diameter (2-in.) steel rod with a 2.54-cm-diameter (1.00-in.) indenter on the end. Four rods of different lengths were used to give masses of 2.8, 5.0, 9.0, and 18.6 kg (6.1, 11.1, 19.9, and 41.1 lbf), including the indenter. The impacter was instrumented to determine the maximum impact force. Drop heights were varied from 38 to 305 cm (15 to 120 in.) to give kinetic energies from 38 to 446 J (28 to 329 ft-lbf).

Hertz law [10] was used to calculate contact pressures from the impact forces. The pressure between a hemispherical indenter of radius  $R_i$  and a semi-infinite, transversely isotropic body is given by

$$p = \frac{3}{2} p_c \left( 1 - \frac{r^2}{r_c^2} \right)^{1/2} \quad (1)$$

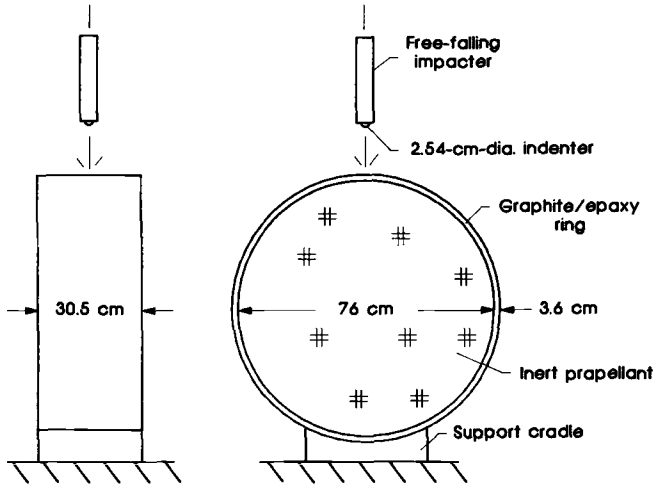


FIG. 1—Impact tests of FWC-like ring.

where

- $r$  = radius measured from the center of the contact site,
- $r_c$  = the contact radius, and
- $p_c$  = average pressure given by

$$p_c = \frac{P}{\pi r_c^2} \quad (2)$$

where  $P$  is the peak or maximum impact force and

$$r_c = \left( \frac{PR_i}{n_0} \right)^{1/3} \quad (3)$$

The value of  $n_0$  can be calculated [10] from the elastic constants of the composite. However, because the transverse Young's modulus of the FWC laminate was not accurately known,  $n_0$  was determined experimentally [9] to be 4.52 GPa (656 ksi).

### Residual Strength Tests

After the two rings were impacted, each one was cut into 44 specimens that were 30.5 cm (12 in.) long and 5.1 cm (2.0 in.) wide. Circular arcs were ground into the specimens' edges to reduce the width in the test section to 3.3 or 3.8 cm (1.3 or 1.5 in.), Fig. 2. The specimens were uniaxially loaded to failure in tension with a 445-kN-capacity (100-kips) hydraulic testing machine. Stroke was programed to increase linearly and slowly with time. Hydraulically actuated grips that simulate fixed-end conditions were used. Otherwise, uniaxial loading would cause bending because the FWC laminate is not symmetrical. Bending does not develop in the pressurized motor case.

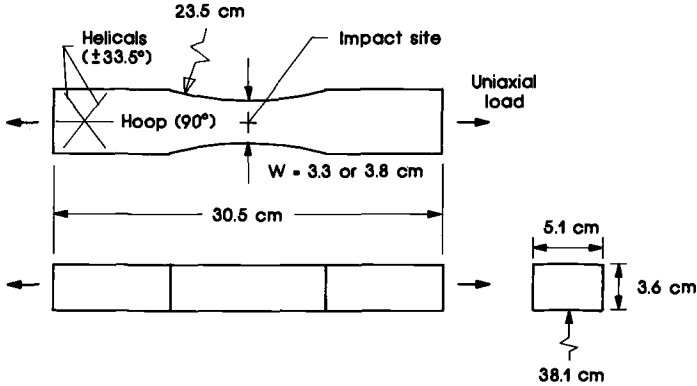


FIG. 2—Sketch of tensile specimen with impact damage.

### Depty Tests

The experiments in Ref 9 were conducted to measure the extent of impact damage by a destructive depty technique. The impacts to the rings could not be directly reproduced with the FWC plate because the stiffness and mass of the plate and rings were different. Thus, we simulated the impacts by statically loading the plate normal to its surface with the indenter. The plate was continuously supported on the opposite surface, and the indenter was applied at the center of each of 36 test squares, where the sides of each square were 3.8 cm (1.5 in.) long. Indenters with diameters of 1.27 and 5.08 cm (0.50 and 2.00 in.) were used in addition to that with a diameter of 2.54 cm (1.00 in.). Contact pressures were calculated from the forces using Eqs 2 and 3. The square specimens were cut from the plate, and the layers were separated using pyrolysis. Damage in contiguous specimens did not overlap. For such a thick laminate, it is believed that the damage (as well as the value of  $n_0$ ) is the same for a simulated impact and an actual impact of low velocity.

### Results and Analysis

This section is divided into two subsections. In the first subsection, the actual impact damage and analysis to predict the size of the damage are described. This analysis is only summarized here; a more detailed description with experimental verification is given in Ref 9. In the second subsection, strengths predicted with the surface crack analysis are presented for both semielliptical surface cuts and impact damage. The surface cut experiments were originally presented in Ref 12 but are summarized here to verify the surface crack analysis and to show how very shallow surface cracks and impact damage were treated.

#### Equivalent Surface Crack for Impact Damage

**Damage Size Measurements**—Radiographs and through-transmission ultrasonic C-scans [5–8] gave no evidence that the impacts caused delaminations. All damage was localized to a region directly beneath the impact site. An example of the type of fiber damage caused by the simulated impacts [9] is shown in Fig. 3. The peak applied force was 66.7 kN (15.0 kips). Photographs of the eight outermost layers of fibers are shown. (There were 76 layers in the laminate.) The contact area is approximately at the center of the first layer. An indentation was readily visible on the surface of the specimen before pyrolysis. Broken



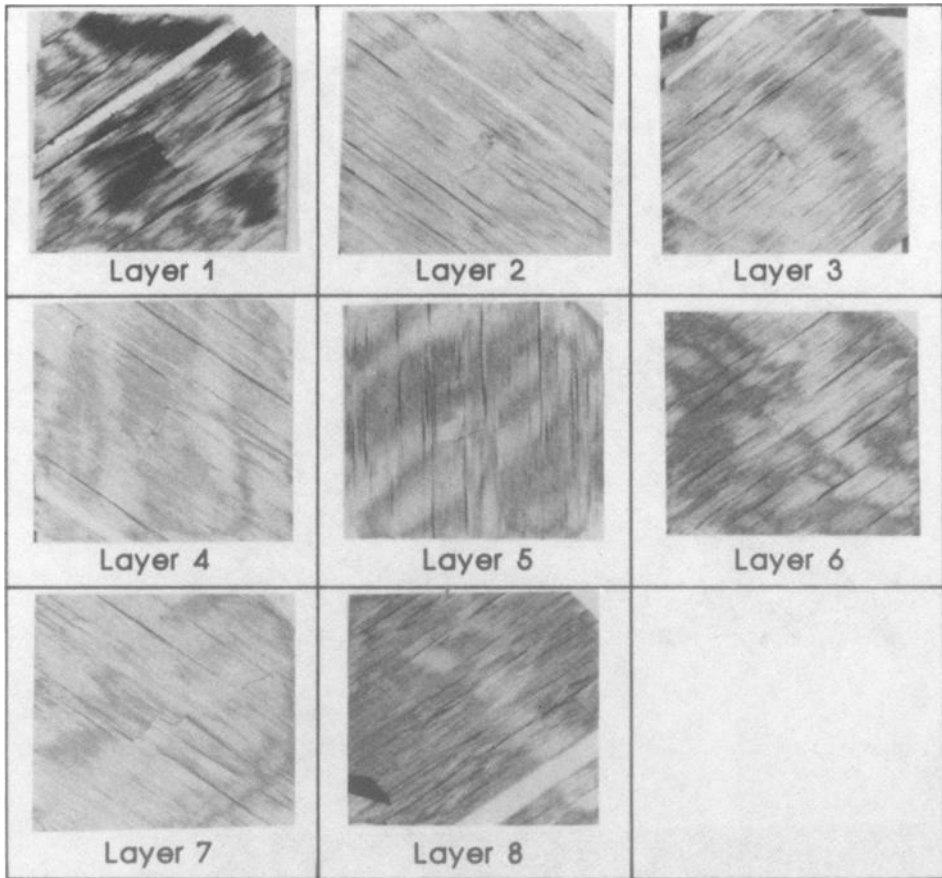


FIG. 3—Fiber damage caused by simulated impact force of 66.7 kN with 2.54-cm-diameter indenter.

fibers are visible in the center of the first seven layers; Layers 8 and below were not damaged. The locus of breaks in each layer resembles a crack, sometimes several closely spaced cracks (barely visible in Layer 4). Sometimes the cracks have a jog, such as in Layer 7. The cracks in each layer are oriented between 56.5 and 90 deg relative to the fiber direction, indicating that the formation of the cracks may be related to the direction of both hoop and helical layers. Thus, the cracks in the various layers are not coplanar and do not make a single surface crack.

Photomicrographs of a highly magnified crack caused by an actual impact [2–4] are shown in Fig. 4. The crack was in Layer 7; Layers 8 and below were not damaged. This specimen was impacted with a 2.54-cm-diameter (1.00-in.) indenter, producing a contact force of 54.3 kN (12.2 kips). Figure 4a shows the entire crack, and Fig. 4b shows a small portion of the crack at an even higher magnification. The fiber breaks caused by the impact resemble those caused by the simulated impact in Fig. 3.

**Damage Size Predictions**—For *ad hoc* assessments of impact damage, it would be sufficient to determine the size with some nondestructive method. However, in order to do sensitivity studies and to design for damage tolerance requirements, an analytical capabil-

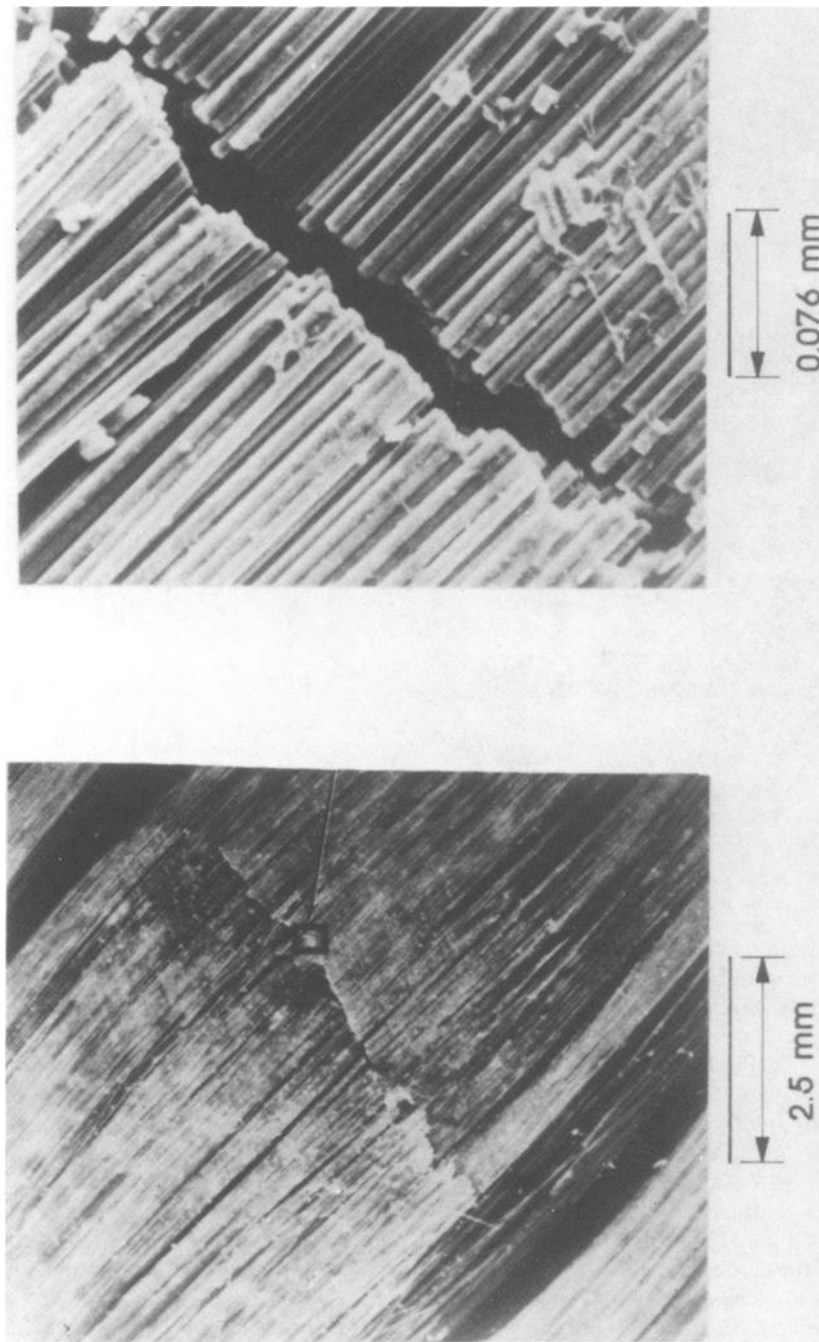


FIG. 4.—Photomicrographs of fiber damage in Layer 7 (the deepest with damage) caused by impact force of 54.3 kN with 2.54-cm-diameter indenter.

ity to predict damage size is necessary. Such a capability was demonstrated in Ref 9 for simulated impacts to an FWC plate. The internal stresses due to the simulated impacts were calculated using Love's solution for a semi-infinite body with pressure on part of the boundary [11]. The pressure distribution is that given by Eq 1. For convenience, the body was assumed to be homogeneous and isotropic. Some discrepancy is expected because the composite plate is layered and nearly transversely isotropic. Even so, it was found that the analysis correctly represented the effect of contact force and indenter radius, which are the important parameters. The extent of the fiber damage was predicted using the maximum shear stress criterion. Except very near the surface, the calculated tension and compression stresses in the fibers were too small to cause the observed fiber damage. It is believed that the fibers away from the surface were broken as a result of shear failures in the epoxy matrix. These shear failures would result in matrix cracks parallel to the fibers, which would be at 56.5 deg to the fibers in the contiguous layers and nearly coincide with the locus of fiber breaks.

Predicted damage contours from Ref 9 are plotted in Fig. 5 using a Poisson's ratio of 0.3 for the FWC laminate. The distance from the surface and from the center of contact are normalized by the contact radius  $r_c$ . The contours are shown for various ratios of the average contact pressure  $p_c$  to the shear strength  $\tau_u$ . Damage initiates below the surface at a distance of 0.482 when the average contact pressure is  $2.15 \tau_u$ . As the pressure increases, the contour increases radially in size until it reaches the surface for  $p_c/\tau_u \approx 5$ . The contours are somewhat elliptical in cross section initially, but become more semielliptical as they approach the surface. Thus, the damage region resembles an ellipsoid or "truncated" ellipsoid.

Crack lengths from two of the 20 deply tests in Ref 9 are plotted against depth in Fig. 6 for simulated impacts. The average contact pressures were 648 and 742 MPa (94.0 and 108 ksi). The corresponding forces were 66.7 and 99.6 kN (15.0 and 22.4 kips), respectively. Note that the crack lengths are not projected onto a single plane (Fig. 6a). The cracks were measured only on the outer side of a layer. In drawing the graph, crack length was assumed to be constant across a layer. The graph shows that the depth and length of the cracks

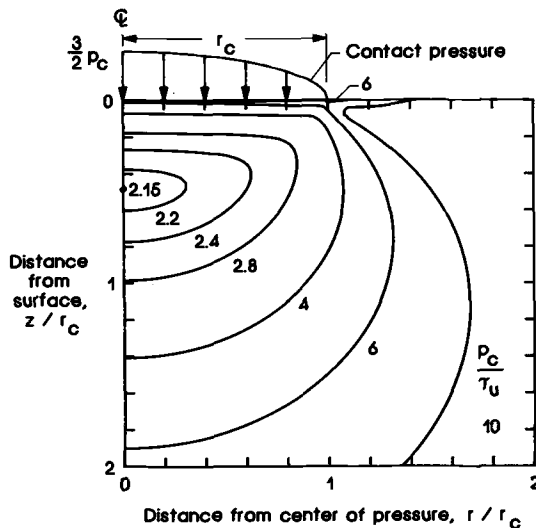


FIG. 5—Damage contours according to Love's solution (Poisson's ratio = 0.3).

increase with increasing contact pressure. Similar results were obtained for other pressures and indenter diameters.

Damage profiles predicted with the maximum shear stress failure criterion are also plotted in Fig. 6. A value of  $\tau_u = 276$  MPa (40 ksi), which gave a good fit to damage depth for these two depley tests, was used to calculate the maximum shear stress with Love's equations. The maximum length of the cracks in Fig. 6 is somewhat larger than predicted. For the damage contours in Fig. 5, the ratio of half-length to depth  $c/a$  is approximately 0.8, where values for the 20 depley tests were typically between 0.8 and 1.4. The predicted damage profile circumscribes the crack lengths fairly well except near the surface, where no damage is predicted. The damage is predicted to initiate at a depth of  $0.482r_c$  and grow toward the surface as pressure is increased. In the depley tests, on the other hand, damage was always found to extend from the first layer down. The damage in the outer layers was probably caused by large inplane compressive stresses  $\sigma_r$  and  $\sigma_\theta$  that diminish rapidly with distance from the surface. The state of stress near the surface is somewhat hydrostatic, causing the maximum shear stress to be relatively small. Away from the surface,  $\sigma_r$  and  $\sigma_\theta$  are small and  $\tau_{\max} \approx 0.5\sigma_z$ , much like the compression test of the disks.

For the 20 depley tests, values of damage depth predicted with  $\tau_u = 228$  and 310 MPa (33 and 45 ksi) gave upper and lower bounds. The tests included three indenter diameters and six values of average contact pressure. Compression tests were conducted on disks taken from the FWC plate, where the load was applied normal to the plane of the laminate.

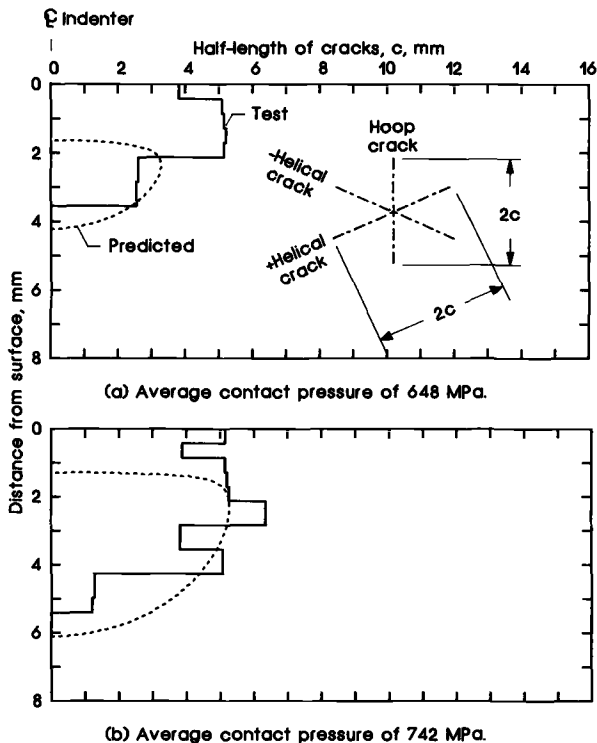


FIG. 6—Comparison of measured and predicted ( $\tau_u = 276$  MPa) damage profiles: (a) average contact pressure of 648 MPa; (b) Average contact pressure of 742 MPa.

The average compression strength was 621 MPa (90 ksi), which corresponds to a maximum shear stress of 310 MPa (45 ksi). Thus, the results of the simulated impacts and the compression tests are in fair agreement. The discrepancy could be caused by the assumption of homogeneity and isotropy in Love's solution.

In the prediction of residual strength, the impact damage was represented as a surface crack oriented normal to the applied load. The depth and length of the crack were taken as those of the damaged region predicted with the maximum shear stress criterion. Thus, the outline of the crack approximately matches the cross section of the damaged region (Fig. 7). It may seem inappropriate at first to assume that the impact damage is equivalent to a surface crack when the cracks in the helical layers do not lie in the plane of the surface crack. However, the stiffness of the helical layers and the stress in the helical layers normal to the surface of the equivalent crack are small compared to the hoop layers. Thus, the helical layers are relatively stress free and ineffective in carrying load across the crack, much as if they were cracked.

The maximum depth of the damage contours in Fig. 5 is given by

$$\left(\frac{1}{2} - \nu_l\right)(1 + \zeta^2)^{-1} + (1 + \nu_l)\left[\zeta \tan^{-1}\left(\frac{1}{\zeta}\right) - \zeta^2(1 + \zeta^2)^{-1}\right] - \frac{4\tau_u}{3p_c} = 0 \quad (4)$$

where  $\zeta = a/r_c$ . The depth  $\zeta_0 = z_0/r_c$ , where damage initiates, is given by

$$0 = 3\zeta_0 - (1 + \nu_l)(1 + \zeta_0^2) \left[ (1 + \zeta_0^2) \tan^{-1}\left(\frac{1}{\zeta_0}\right) - \zeta_0 \right] \quad (5)$$

which corresponds to the location of  $\tau_{\max}$ . The depth of the damaged region or equivalent surface crack was calculated with Eq 4, and the contact pressure  $p_c$  was calculated from the impact force with Eqs 2 and 3 and  $n_0 = 4.52$  GPa (656 ksi). A value of  $\tau_u = 228$  MPa (33 ksi) was assumed because it best represents the minimum contact pressure for damage initiation as well as an upper bound for the damage depth. For convenience, it was assumed that the impact damage has a constant aspect ratio of  $c/a = 1.0$ . As noted previously, the experimental values of  $c/a$  had considerable variation.

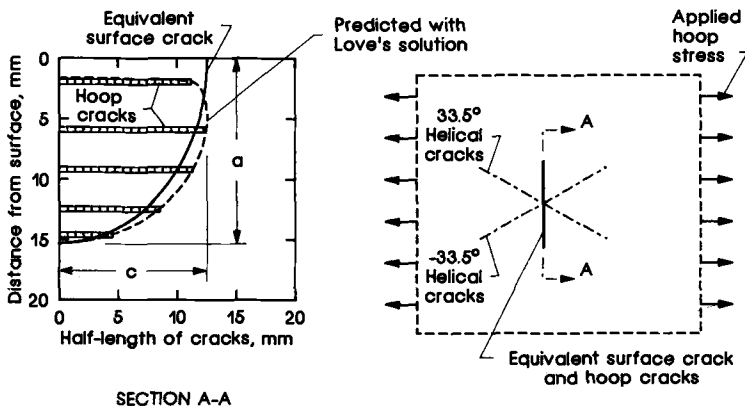


FIG. 7—Equivalent surface crack for impact damage.

### Strength Predictions

Except for very shallow surface cuts or impact damage, the composite laminates failed in two stages: first, the cut or damaged layers broke and delaminated from the undamaged layers; and then, with additional load, the undamaged layers broke (Fig. 8). The two stages of failure are referred to as first- and remaining-ligament failure. For shallow damage, the laminate failed catastrophically in one stage. Specimens with semielliptic surface cuts failed similarly [12]. For quasi-isotropic T300/5208 plates containing surface cuts with  $c/a = 3.8$ , radiographs [13] did reveal delaminations at the maximum depth or bottom of the surface cut prior to failure of the first ligament, but not for specimens with  $c/a < 3.8$ . Radiographs of the FWC specimens were not made prior to failure of the first ligament. But, for specimens with impact damage and surface cuts, there was no visual evidence, nor did load-displacement measurements indicate that delaminations were present prior to when the first ligament failed.

*Surface Crack Analysis for First-Ligament Failure*—Failure of the first ligament was assumed to occur when the maximum stress-intensity factor along the front of the equivalent surface crack exceeded the fracture toughness  $K_{Ic}$ . For an isotropic, homogeneous material, the stress-intensity factor is given [14] by

$$K = S \left( \frac{\pi a}{Q} \right)^{1/2} F(a/t, a/c, c/W, \phi) \quad (6)$$

where

$S$  = remote stress,

$a$  = crack depth,

$2c$  = crack length,

$t$  = plate thickness,

$W$  = plate width,

$Q$  = shape factor, and

$\phi$  = elliptical angle that specifies the location on the crack border.

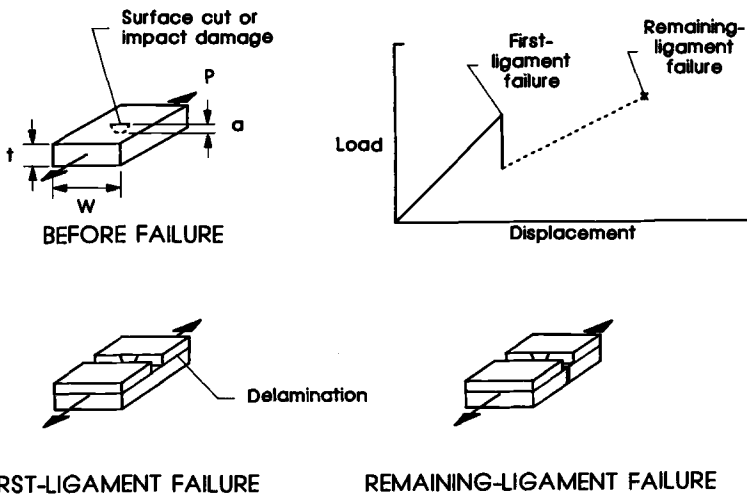


FIG. 8—Two-part failure with surface cut or impact damage.

Where the surface cut intersects the free surface,  $\phi = 0$  deg and, where the depth of the surface cut is a maximum,  $\phi = 90$  deg. The equations for  $Q$  and  $F(a/t, a/c, c/W, \phi)$  are given in Ref 14. Replacing  $K$  with  $K_Q$  in Eq 6 yields the following equation for the failing stress of the first ligament

$$S_{cl} = \frac{K_Q}{\left(\frac{\pi a}{Q}\right)^{1/2} F(a/t, a/c, c/W, \phi)} \quad (7)$$

No fracture tests with through-the-thickness cuts were conducted to determine  $K_Q$  for the FWC laminate. Instead, a value of  $K_Q = 0.949 \text{ GPa } \sqrt{\text{mm}}$  (27.3 ksi  $\sqrt{\text{in.}}$ ) was predicted with a general fracture toughness parameter [1-3,15].

**Maximum Strain Criterion for Remaining-Ligament Strength**—The hoop strain was assumed to be uniform over the remaining ligament, and failure was assumed to be governed by failure of the hoop layers. Thus, the failing strain of the remaining ligament  $\epsilon_{lu}$  is independent of remaining-ligament thickness and is equal to the failing strain of the hoop fibers. Accordingly, the gross stress at failure  $S_{cr}$  is given by

$$S_{cr} = \left(1 - \frac{a}{t}\right) E_{xr} \epsilon_{lu} \quad (8)$$

where  $E_{xr}$  is Young's modulus of the remaining ligament in the loading or hoop direction. Values of  $E_{xr}$ , which vary with remaining-ligament thickness, were calculated [1-4] with lamination theory. A value of  $\epsilon_{lu} = 0.0124$  was derived from unnotched tensile data.

**Strengths with Surface Cuts**—The investigation in Ref 12 was conducted first to study the failure modes of the FWC laminate with part-through cuts and to determine how well strengths could be predicted using Eqs 7 and 8. The specimens that contained the surface cuts were taken from one of the other FWC-like rings that was not impacted. The stress for first- and remaining-ligament failures is plotted against cut depth in Figs. 9a-9d for  $c/a = 0.5, 1.0, 2.0$ , and  $5.7$ . The stresses were divided by an undamaged strength of 379 MPa (55.0 ksi). The plane of the surface cuts was normal to the hoop direction, and the specimens were loaded in the hoop direction. The location and width of the hoop layers are shown on the abscissa to aid in interpreting the results. In most cases, each symbol represents an average of two values. Circular symbols represent 2.5-cm-wide (1.0-in.) specimens, and square symbols represent 5.1-cm-wide (2.0-in.) specimens. The widest specimens were required for the deepest cuts. The open symbols represent first-ligament failure, and the solid symbols represent remaining-ligament failures. For shallow cuts, the first failures were catastrophic and no remaining-ligament strengths are shown. For some of the deeper cuts, remaining-ligament strengths are not shown because the specimens were not reloaded after the first ligament failed. Instead, they were saved for other purposes.

The lines in Figs. 9a-9d represent predictions with Eqs 5 and 6. For first-ligament failure, the dashed lines represent 2.5-cm-wide (1.0-in.) specimens, and the solid lines represent 5.1-cm-wide (2.0-in.) specimens. Except for shallow cuts and  $c/a = 2.0$  with  $W = 2.5$  cm (1.0 in.), the test and predicted values of first-ligament strength are in good agreement. For shallow cuts, the predicted strengths are too large. However, the lines that are drawn tangent to the surface crack equation represent the test values quite well. Notice that the tangent lines were not drawn through the undamaged strength at  $a = 0$ , but through  $a = 1.7$  mm (0.067 in.), which corresponds to the outer surface of the first hoop layer. It was assumed that cuts more shallow than the outer hoop layer would not reduce the strength

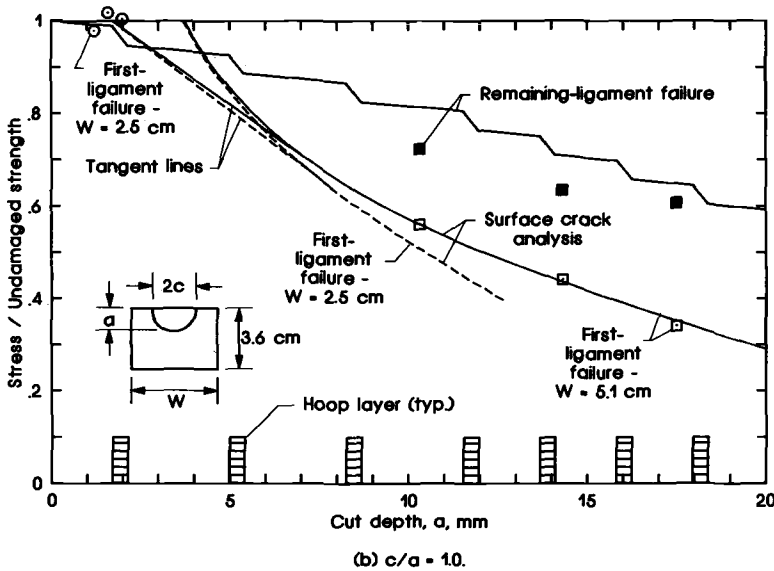
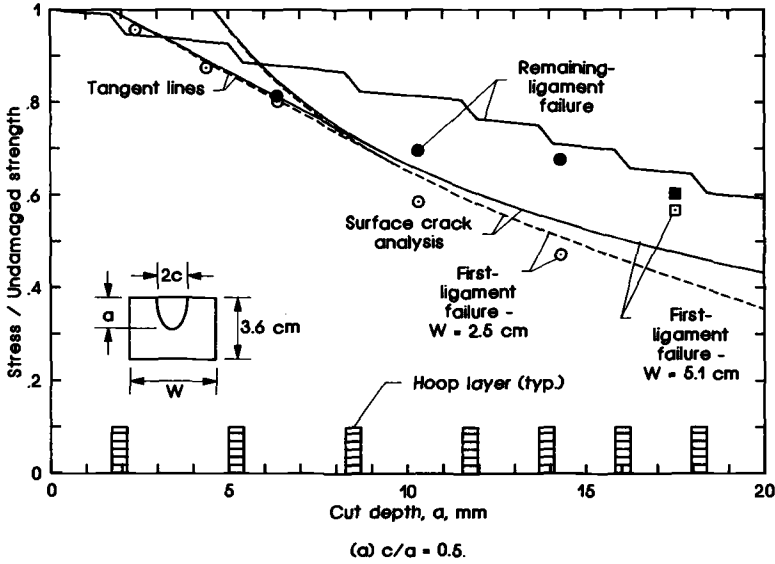


FIG. 9—Average strengths for FWC laminate with surface cuts: (a)  $c/a = 0.5$ ; (b)  $c/a = 1.0$ ; (c)  $c/a = 2.0$ ; (d)  $c/a = 5.7$ .

since the outer helical layers contribute very little to the stiffness of the laminate. These lines correct the surface crack analysis for shallow cracks and are very convenient to construct. For  $c/a = 5.7$ , no tangent line is shown because it virtually coincides with the surface crack equation. Notice in Fig. 9c for  $c/a = 2.0$  that the values of first-ligament strength for  $W = 2.5$  cm (1.0 in.) and the deepest crack are significantly less than the predicted value. These test values seem inconsistent with those for  $W = 5.1$  cm (2.0).



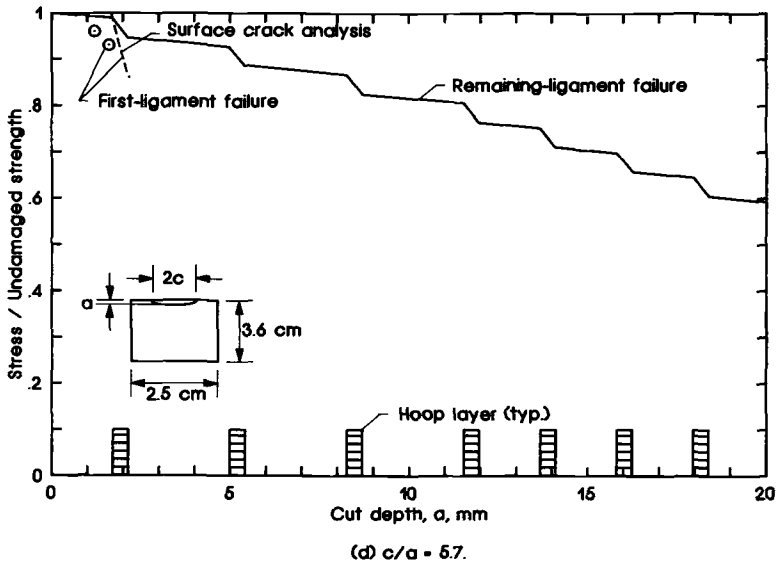
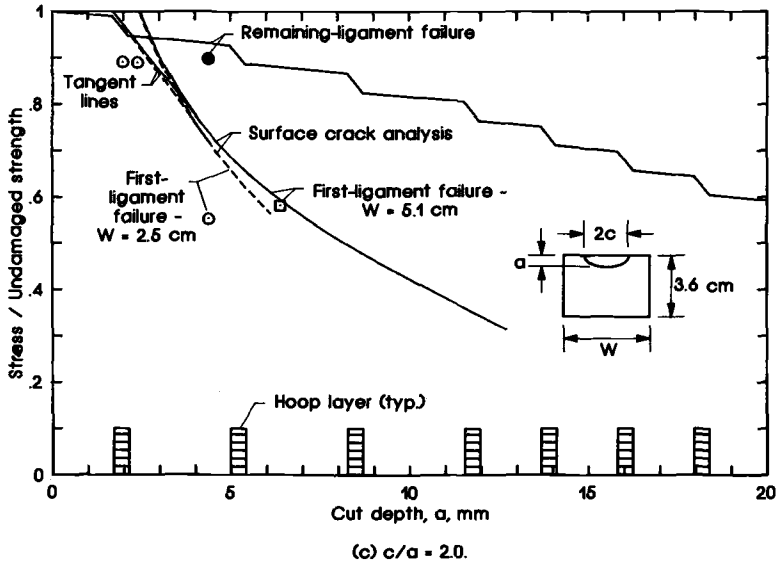


FIG. 9—Continued.

The predicted curve for the remaining ligament in Figs. 9a–9d has a stair-stepped shape because the stiffnesses of the hoop and helical layers are very different. The large drops in stress correspond to removal of the stiff hoop layers, and the small drops correspond to removal of the more flexible helical layers. The curve is convex in the overall sense because most of the hoop layers are closer to the bottom of the laminate. The predictions of remaining-ligament strengths are 5% to 10% larger than the test values. After the first ligament

fails, the load path in the specimens is eccentric. Although the grips are very stiff, they may allow enough bending to cause the test values to be less than the predictions.

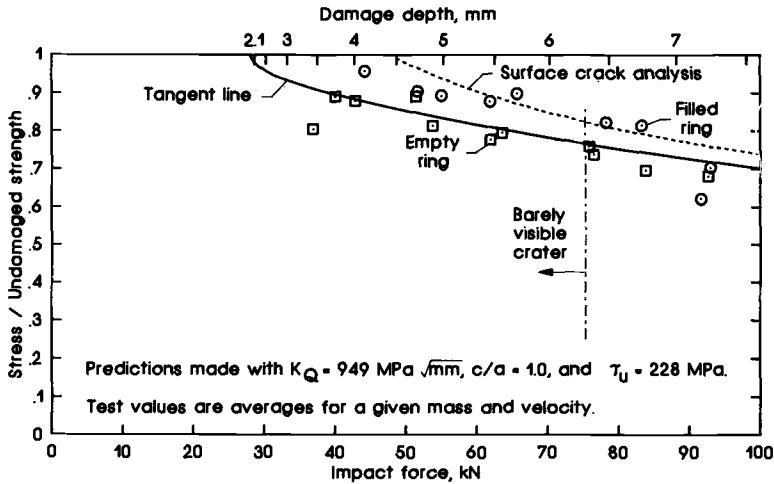
Harris and Morris [13] had equal success in using the surface crack analysis to predict the strength of a 1.0-cm-thick (0.40-in.) T300/5208 graphite/epoxy composite containing semielliptical surface cuts. Strengths of specimens with through-the-thickness cuts were also predicted accurately [16]. The same value of fracture toughness, which was also predicted with a general fracture toughness parameter, was used for the surface cuts and the through-the-thickness cuts.

Recently, Wu and Erdogan [17] and Chatterjee [18] calculated the stress-intensity factor for an orthotropic homogeneous plate with a semielliptical surface crack using a line-spring model and a finite-element model, respectively. In both cases, the isotropic and orthotropic results differ significantly. The agreement between the experiments and isotropic analysis and the discrepancy between the isotropic and anisotropic analyses cannot be resolved at this time. In any event, the experiments validate the use of the isotropic surface crack equations to predict strengths.

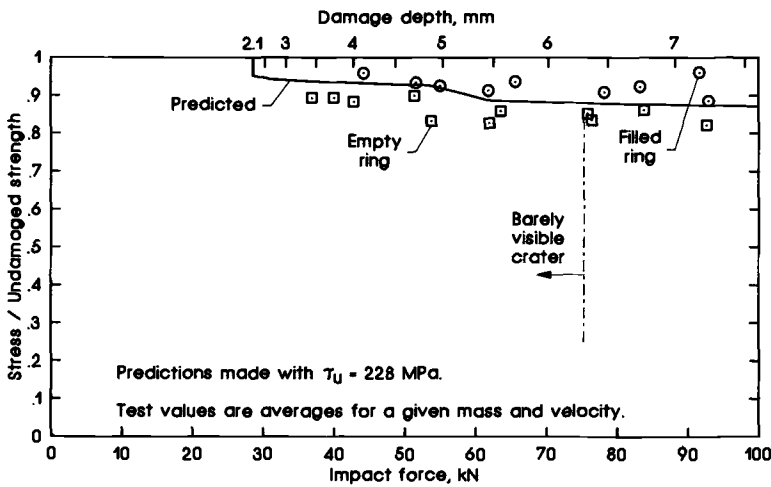
*Strengths with Impact Damage*—The measured and predicted stresses for first- and remaining-ligament failures are plotted against impact force in Figs. 10a–10b, respectively. The stresses were divided by an undamaged strength of 345 MPa (50.1 ksi). The top axis, which is not linear, gives the depth of the damage that is associated with the predictions. Circular symbols were used for the ring filled with inert propellant and square symbols for the empty ring. The specimens had widths of 3.3 and 3.8 cm (1.3 and 1.5 in.). Differences between predictions for the two widths can hardly be discerned. Thus, no distinction is made between predictions for the two widths. Two predicted curves are shown for the first-ligament failures in Fig. 10a: one for the surface crack analysis given by Eq 5 and one for tangent lines like those shown in Figs. 9a–9c. The difference between the tangent line and the surface crack analysis line is significant for the smaller impact forces and damage depths. Damage is predicted to initiate at an impact force of 28.6 kN (6.43 kips) and at a depth of 2.1 mm (0.082 in.), which is below the outer hoop layer. The damage is predicted to be relatively shallow, even for the largest impact forces. For this reason, the strengths were reduced less than 40%. The tangent line agrees with the strengths quite well. The predicted and measured remaining-ligament strengths in Fig. 10b also agree well. The remaining-ligament strengths are significantly larger than the first-ligament strengths for the larger impact forces. Thus, the thick composite laminate affords some degree of damage tolerance not given by conventional metals.

Vertical lines are drawn in Figs. 10a and 10b to indicate that impact forces below 75.2 kN (16.9 kips) caused only slight surface indentations that were barely visible. At this threshold, hoop stresses required to fail the first ligament were less than 80% of the undamaged strength. This impact force corresponds to an average contact pressure of 640 MPa (93 ksi). Recall that a pressure between 408 and 514 MPa (59.2 and 74.6 ksi) was required to initiate fiber damage. Sharper indenters [1] caused more visible surface damage, but the reductions in strength were not much more than those in Figs. 10a and 10b. The analysis used here is capable of predicting the effect of indenter shape on residual strength and contact pressures. Therefore, the analysis can be used for preliminary design and for parametric studies to determine worst conditions and the best materials.

In Figs. 10a and 10b, strengths for the empty ring were about 10% below those for the filled ring. The propellant increased the effective mass of the ring by more than a factor of seven, causing the impact forces for the filled ring to be considerably larger than those for the empty ring. Because the FWC laminate is very thick, the impact damage should be equal in the filled and empty rings for the same impact force. Thus, the difference in



(a) First-ligament failure.



(b) Remaining-ligament failure.

FIG. 10—Measured and predicted strengths for FWC laminate with impact damage: (a) first-ligament failure; (b) remaining-ligament failure.

strengths between the filled and empty rings cannot be explained by the presence of the inert propellant.

## Conclusions

A surface crack analysis was used to predict the residual strength of a thick graphite/epoxy composite after low-velocity impact. The specimens were impacted with a rod that had a 2.54-cm-diameter (1.00-in.) hemispherical indenter mounted on one end. The

impactors were dropped from various heights to give various amounts of damage. The damage was localized to a region directly beneath the impact site. It extended only part way through the laminate. The damaged region contained broken fibers, and the locus of breaks in each layer resembled a crack that was nearly perpendicular to the direction of the fibers. This orientation also nearly coincided with the direction of fibers in contiguous layers. Thus, cracks in layers of different orientations were in different directions. No significant delaminations were detected. The specimens were uniaxially loaded to failure in tension. They failed in two stages—first the damaged layers (first ligament) and then, with increasing load, the remaining undamaged layers (remaining ligament). When the damaged layers failed, they delaminated from the undamaged layers. An analysis was developed to predict the size of damage using Hertz's contact law and the maximum shear stress calculated with Love's solution for pressure applied to part of a semi-infinite body. The analysis was verified by depling specimens and measuring the size of the impact damage. The damage was represented as a semielliptical surface crack of the same width and depth as the cross section of the damage. The stress to fail the first ligament was predicted with a surface crack analysis. The stress to fail the remaining ligament was predicted using a maximum strain failure criterion. The measured and predicted stresses to fail the first ligament of the impacted specimens were in good agreement. The failing stresses of the remaining ligament were a little below the predicted values, perhaps due to bending that was not taken into account.

The analysis, which takes into account the radius of the impactor and the mechanical properties of the composite, can be used for preliminary design and for parametric studies to determine worst conditions and the best materials.

## APPENDIX

TABLE 1—*Properties of constituents of composite.*

	Helical Fiber	Broadgoods Fiber	Matrix
Tensile modulus, GPa (Msi)	228 (33)	228 (33)	2.85 (0.414)
Poisson's ratio	...	...	0.35
Tensile strength, GPa (ksi)	3.96 (574)	.75 (544)	...
Elongation at failure	0.0167	...	...
Density, kg/m <sup>3</sup> (lbm/in. <sup>3</sup> )	1790 (0.0648)	1780 (0.0642)	1230

TABLE 2—*Physical properties of composite.*

Composite density, kg/m <sup>3</sup> (lbm/in. <sup>3</sup> )	1490 (0.05397)
Resin mass fraction	0.3459
Resin volume fraction	0.3845
Fiber volume fraction	0.5449
Void content	0.07062

TABLE 3—Composite lamina properties.

	Unidirectional Broadgoods	Helical Layers	Cut Helical Layers	Cloth
$E_{11}$ , GPa (Msi)	1.06 (15.4)	111 (16.2)	111 (16.2)	59.3 (8.60)
$E_{22}$ , GPa (Msi)	6.39 (0.927)	1.92 (0.278)	1.92 (0.278)	59.3 (8.60)
$G_{12}$ , GPa (Msi)	4.47 (0.649)	4.28 (0.621)	4.28 (0.533)	3.68 (0.533)
$\nu_{12}$	0.275	0.267	0.267	0.0348
Thickness per layer, mm (in.)	0.427 <sup>a</sup> (0.0168)	0.427 (0.0168)	0.711 (0.0280)	0.427 (0.0168)

<sup>a</sup> Equal to three plies of broadgoods.

## References

- [1] Poe, C. C., Jr., Illg, W., and Garber, D. P., "A Program to Determine the Effect of Low-velocity Impacts on the Strength of the Filament-Wound Rocket Motor Case for the Space Shuttle," NASA TM-87588, National Aeronautics and Space Administration, Washington, DC, Sept. 1985.
- [2] Poe, C. C., Jr., Illg, W., and Garber, D. P., "Tension Strength of a Thick Graphite/Epoxy Laminate after Impact by a 1/2-In.-Radius Impactor," NASA TM-87771, National Aeronautics and Space Administration, Washington, DC, July 1986.
- [3] Poe, C. C., Jr., Illg, W., and Garber, D. P., "Strength of a Thick Graphite/Epoxy Laminate after Impact by a Blunt Object," NASA TM-89099, National Aeronautics and Space Administration, Washington, DC, Feb. 1987.
- [4] Poe, C. C., Jr., and Illg, W., "Tensile Strength of a Thick Graphite/Epoxy Rocket Motor Case After Impact by a Blunt Object," 1987 JANNAF Composite Motor Case Subcommittee Meeting, Publication 460, Chemical Propulsion Information Agency, Feb. 1987, pp. 179–202.
- [5] Poe, C. C., Jr., Illg, W., and Garber, D. P., "Hidden Impact Damage in Thick Composites," *Proceedings of the Review of Progress in Quantitative Nondestructive Evaluation*, Vol. 5B, 1986, pp. 1215–1225.
- [6] Madaras, E. I., Poe, C. C., Jr., Illg, W., and Heyman, J. S., "Estimating Residual Strength in Filament Wound Casings from Non-Destructive Evaluation of Impact Damage," *Proceedings of the Review of Progress in Quantitative Nondestructive Evaluation*, Vol. 6B, 1986, pp. 1221–1230.
- [7] Madaras, E. I., Poe, C. C., Jr., and Heyman, J. S., "Combining Fracture Mechanics and Ultrasonics NDE to Predict the Strength Remaining in Thick Composites Subjected to Low-Level Impact," 1986 Ultrasonics Symposium Proceedings, Vol. 86CH2375-4, B. R. McAvoy, Ed., Institute of Electrical and Electronic Engineers, New York, No. 2, 1986, pp. 1051–1059.
- [8] Madaras, E. I., Poe, C. C., Jr., and Heyman, J. S., "A Nondestructive Technique for Predicting the Strength Remaining in Filament Wound Composites Subjected to Low-Level Impact," 1987 JANNAF Composite Motor Case Subcommittee Meeting, Publication 460, Chemical Propulsion Information Agency, Feb. 1987, pp. 249–258.
- [9] Poe, C. C., Jr., "Simulated Impact Damage in a Thick Graphite/epoxy Laminate Using Spherical Indenters," NASA TM-100539, National Aeronautics and Space Administration, Washington, DC, 1988.
- [10] Greszczuk, L. B., "Damage in Composite Materials due to Low-Velocity Impact," *Impact Dynamics*, Wiley, New York, 1982, pp. 55–94.
- [11] Love, A. E. H., "The Stress Produced in a Semi-Infinite Solid by Pressure on Part of the Boundary," *Philosophical Transactions of the Royal Society of London*, Series A, Vol. 228, 1929, pp. 377–420.
- [12] Harris, C. E. and Morris, D. H., "Preliminary Report on Tests of Tensile Specimens with a Part-Through Surface Notch for a Filament-Wound Graphite/Epoxy Material," NASA CR-172545, National Aeronautics and Space Administration, Washington, DC, 1985.

- [13] Harris, C. E. and Morris, D. H., "The Fracture of Thick Graphite/Epoxy Laminates with Part-Through Surface Flaws," *Composite Materials: Fatigue and Fracture, ASTM STP 907*, American Society for Testing and Materials, Philadelphia, 1986, pp. 100-114.
- [14] Newman, J. C., Jr., and Raju, I. S., "Stress-Intensity Factor Equations for Cracks in Three-Dimensional Finite Bodies," *Fracture Mechanics: Fourteenth Symposium—Volume I: Theory and Analysis, ASTM STP 791*, American Society for Testing and Materials, Philadelphia, 1983, pp. I-238-I-268.
- [15] Poe, C. C., Jr., "A Parameteric Study of Fracture Toughness of Fibrous Composite Materials," NASA TM-89100, National Aeronautics and Space Administration, Washington, DC, 1987.
- [16] Harris, C. E. and Morris, D. H., "Fracture Behavior of Thick, Laminated Graphite/Epoxy Composites," NASA CR-3784, National Aeronautics and Space Administration, Washington, DC, 1984.
- [17] Wu, B.-H. and Erdogan, F., "The Surface Crack Problem in an Orthotropic Plate Under Bending and Tension," NASA CR-178281, National Aeronautics and Space Administration, Washington, DC, April 1987.
- [18] Chatterjee, S. N., "Surface Cracks in Thick Laminated Fiber Composite Plates," this volume, pp. 177-193.

## **Fatigue Crack Growth**

## Experimental Evaluation of Stress-Intensity Solutions for Surface Flaw Growth in Plates

---

**REFERENCE:** Carter, D. K., Canda, W. R., and Blind, J. A., "Experimental Evaluation of Stress-Intensity Solutions for Surface Flaw Growth in Plates," *Surface-Crack Growth: Models, Experiments, and Structures*, ASTM STP 1060, W. G. Reuter, J. H. Underwood, and J. C. Newman, Jr., Eds., American Society for Testing and Materials, Philadelphia, 1990, pp. 215-236.

**ABSTRACT:** This combined experimental and analytical study was directed at determining the growth and shape change of surface flaws under axial loading as compared with crack growth data obtained from simple compact tension specimens. The experimental effort aimed at measuring surface flaw crack growth rates for 2219-T851 aluminum specimens. Tests were conducted using constant-amplitude loading with marker bands to measure crack front shape changes.

The analytical effort evaluated available crack growth models and stress-intensity solutions and their ability to predict the growth and shape change of surface flaws. The characterization of surface flaws as semiellipses and the independence of crack growth rate and direction were addressed. The resulting model was successful in predicting growth and shape changes under most conditions. However, due to the variation between surface and depth crack growth rates for surface flaws, it was determined that crack growth data from compact tension specimens could not generally be used to characterize the growth of surface flaws.

**KEY WORDS:** fracture mechanics, fatigue crack growth, surface flaw, aluminum, stress-intensity factor

The most common flaw types observed in aircraft structures are those which have complex shapes such as the bolthole corner flaw or the surface flaw. However, for very practical reasons, most fracture and crack growth data have been generated on simple compact tension (CT) type specimens. Therefore, the ability to predict the growth of cracks of complex shapes, such as surface flaws, from CT crack growth data is of considerable importance. Several authors have addressed this problem [1,2], employing different constraints, stress-intensity solutions, and growth integration techniques.

To conveniently use CT specimen crack growth data for predicting the growth of surface flaws, investigators typically make one or more of the following assumptions:

- (a) the surface flaw assumes a semielliptical shape,
- (b) the flaw shape stays constant at either the initial shape or some arbitrary shape (for example, semicircular),
- (c) the crack growth rate is independent of crack growth direction,
- (d) the crack growth rate is independent of the state of stress (that is, plane stress or plane strain), and
- (e) surface flaw stress-intensity solutions can be used through the entire plate thickness.

<sup>1</sup> Assistant professor, assistant professor, and tenure associate professor, respectively, Department of Engineering Mechanics, U.S. Air Force Academy, Colorado Springs, CO 80840.



These assumptions have proven quite convenient and reasonably accurate in those cases in which the crack dimensions are small compared to the thickness of the structure. However, these assumptions can introduce significant error for larger surface flaws or when trying to model the transition from surface flaws to through flaws. Engle [2] reported predicted lives that were determined from crack growth data to vary from 50 to 250% of actual life using different combinations of these assumptions. Engle also reported that the least variability was obtained with surface flaw growth models which accounted for changing flaw shapes.

The analysis of surface flaw growth is further complicated by the large number of stress intensity formulations reported in the literature. Newman [3] reviewed several available formulations and compared their ability to predict fracture in a brittle epoxy material. He found that the available stress-intensity formulations agreed fairly well for small flaws, but that there was considerable disagreement (up to 80%) for larger flaws. Since small errors in stress intensity can have a considerable impact on predicted crack growth life, the selection of stress-intensity formulation is an important element in a surface flaw growth model.

## Methods and Procedures

### *Objective*

The purpose of this study was to develop and test a model that could accurately predict the growth and shape change of surface flaws under constant-amplitude cyclic tensile loads using the crack growth data obtained from simple CT specimens. In the development of this model, the following questions were addressed:

- (a) Can surface flaws be adequately characterized as semiellipses?
- (b) Is the crack growth rate relatively independent of crack growth direction and state of stress?
- (c) Which of the available stress-intensity formulations results in the most accurate prediction of shape change and crack growth?

### *Summary of Approach*

Because we intended to relate surface flaw growth to CT test results, we selected a material which was characterized in the literature and which had a fairly large amount of consistent CT crack growth data available. 2219-T851 aluminum plate was selected as a material that met these criteria. Surface flaw specimen were designed and precracking procedures were developed to allow constant amplitude fatigue testing of various shape surface flaws. Experimental techniques were developed using marker bands so that both shape change and growth rate of the surface flaws could be monitored. Standard data-reduction techniques were employed with the exception that a number of different stress-intensity solutions were available in the data-reduction program. The program also employed a least-squares-fit routine to extract Paris crack growth constants for growth along the surface ( $dC/dN$ ) and into the specimen ( $da/dN$ ).

A surface-flaw crack growth model was then used to predict both growth rate and shape change. Different stress-intensity solutions were evaluated for their ability to reproduce both shape change and flaw growth rates using CT crack growth rate data from the literature.

### Material Characterization

An aluminum alloy 2219-T851 was used throughout this study. The nominal composition of 2219 is as follows: 6.3% copper; 0.3% manganese; 0.18% zirconium; 0.1% vanadium; 0.06% titanium; and aluminum balance. The rolled plate (3.66 by 1.22 by 0.0254 m) was supplied by Reynolds Aluminum, and all specimens were machined from the same plate.

Extensive testing was done to ensure that the test material was typical of 2219-T851 aluminum. Details of this portion of the study are available elsewhere [4]. Table 1 summarizes the results of the mechanical properties of the as-tested 2219-T851 A1.

### Experimental Procedure

Experimental procedures were developed to verify our predictions of the growth rates and shape change of surface flaws. A summary of the experimental techniques is given below; details of those procedures may be found in Ref 4. Axially loaded surface flaw specimens were machined from the 25.4-mm-thick aluminum plate. The specimens were oriented to allow the growth of two flaws perpendicular to the loading/rolling direction (Fig. 1). The preflaws for crack initiation were introduced by two methods: electro-discharge machining (EDM) and a thin (0.152 mm) circular saw blade.

Cracks were initiated from the preflaws using a Ling Model 390 variable frequency shaker with the specimens mounted such that the first bending mode of vibration caused Mode I crack opening. Final precracking was done in the Monterey servo-hydraulic testing machine in accordance with the work of Hudak et al. [5]. The precracking sequence was terminated with a marker band (30% reduction in load for 5000 cycles) in order to establish initial flaw shape and size by means of post-test fractography.

After precracking, the fatigue crack growth rate testing was initiated at 1 Hz under constant amplitude loading. Various stress ratios and load ranges were tested. Each load range was preceded by a marker band sequence where the maximum and mean loads were decreased by 30% for 3000 to 10 000 cycles (the number of cycles was based on flaw size). The load and resulting stress-intensity range ( $\Delta K$ ) sequence are shown in Fig. 2.

Two systems for crack length measurement were employed. Surface crack width (2C) was monitored with a  $\times 30$  traveling microscope. Also, a compliance technique using displacement gages across the crack mouth was attempted.

The crack growth tests were continued until the largest of the two flaws on each specimen fractured. The smaller flaw was then broken open, and both crack surfaces were photo-

TABLE 1—Summary of mechanical properties testing of 2219-T851 aluminum.

Property	Value
Young's modulus	74.9 GPa
Yield strength (0.2%)	344 MPa
Ultimate tensile strength	430 MPa
Strain hardening exponent	0.10
Strength coefficient	611 MPa
Plane strain fracture toughness (LT) <sup>a</sup>	33.7 MPa $\sqrt{\text{m}}$
Charpy impact energy (LS) <sup>b</sup>	12.2 N·m

<sup>a</sup> LT = longitudinal loading, transverse crack growth.

<sup>b</sup> LS = longitudinal loading, short crack growth.

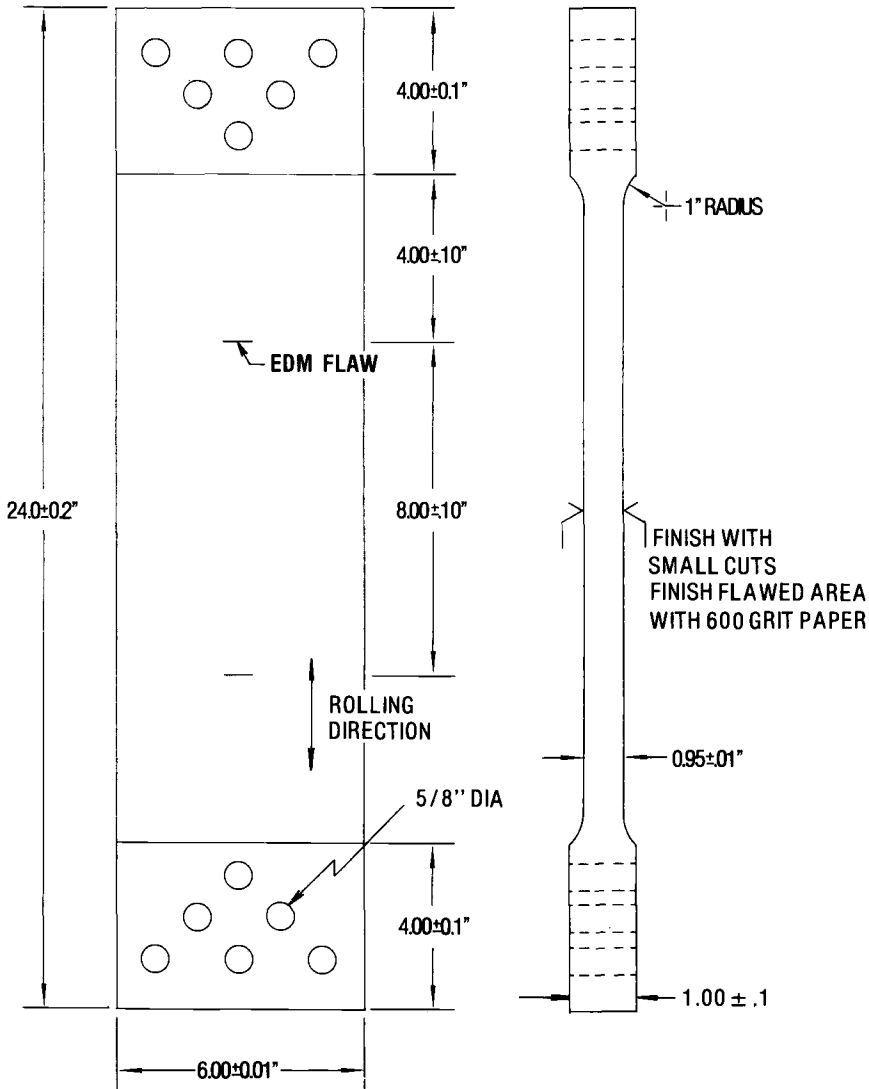
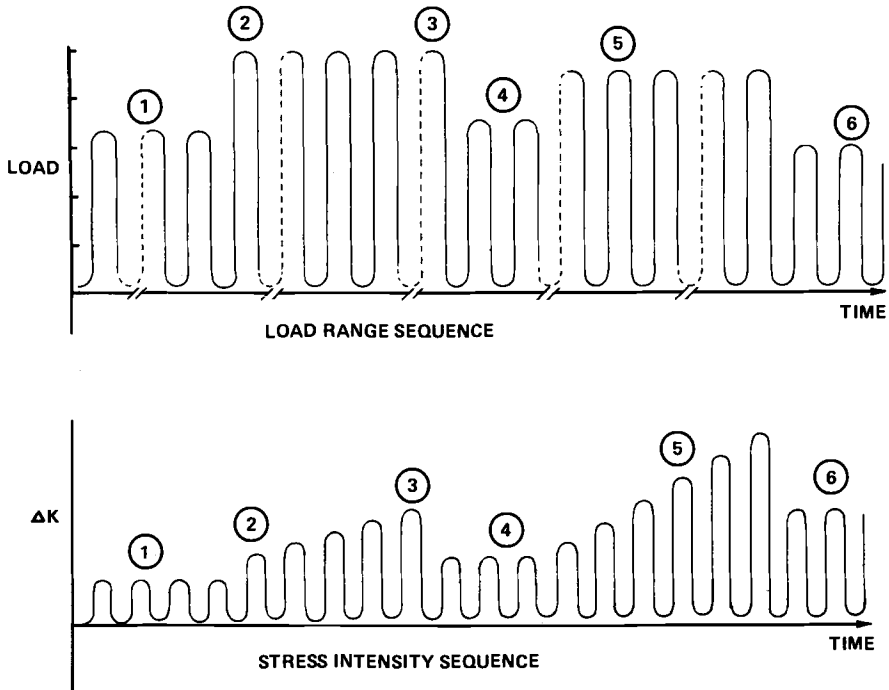


FIG. 1—Fatigue test specimen.

graphed to obtain a permanent record of the marker bands. From enlargements, a visual measurement of marker band depth and a digitized record of flaw shape were made (Fig. 3).

#### Data Reduction

A computer program was developed to take the raw data from the Automatic Test Control program and reduce them to standard  $da/dN$  versus  $\Delta K$  curves. Since the objective of the study was to develop a model to predict surface flaw growth and shape change using CT test data, a "modeling" mode was also developed for the data-reduction program.



- 1) INITIAL MARKER LOAD (20% BELOW TEST LOAD)
- 2) INCREASE LOAD 20% (MEASURE CRACK GROWTH AT INCREMENTS OF  $2C = .01 - .02$  INCH)
- 3) WHEN CRACK HAS GROWN TO THE POINT THAT  $\Delta K$  IS 30% GREATER THAN AT THE BEGINNING OF THE LOAD RANGE, START 2ND MARKER LOAD
- 4) DECREASE MAX AND MEAN LOAD 30% FOR 2ND MARKER BAND
- 5) INCREASE LOAD TO 90% OF THE PREVIOUS LOAD RANGE; GROW CRACK UNTIL  $\Delta K$  INCREASES 30% AGAIN
- 6) REPEAT MARKER BAND

FIG. 2—Load and stress-intensity range sequences.

The basic premise employed in the modeling mode was that crack growth rate as a function of stress-intensity range should be the same at the surface as it is at the deepest point for a surface flaw. If this premise is accurate, then the crack growth rate curves for the surface and depth of a surface flaw should fall on the same line. The modeling mode analyzed different combinations of crack growth rate methods, shape characterization methods, and stress-intensity formulations to find the model which best fit surface flaw data to compact tension results. The best model was later used in the surface flaw growth prediction program.

#### *Calculation of Crack Growth Rate ( $dC/dN$ )*

The raw data for crack growth rate calculations were taken from visual flaw width ( $2C$ ) measurements after a known number of cycles ( $N$ ) of constant amplitude cyclic stress. An

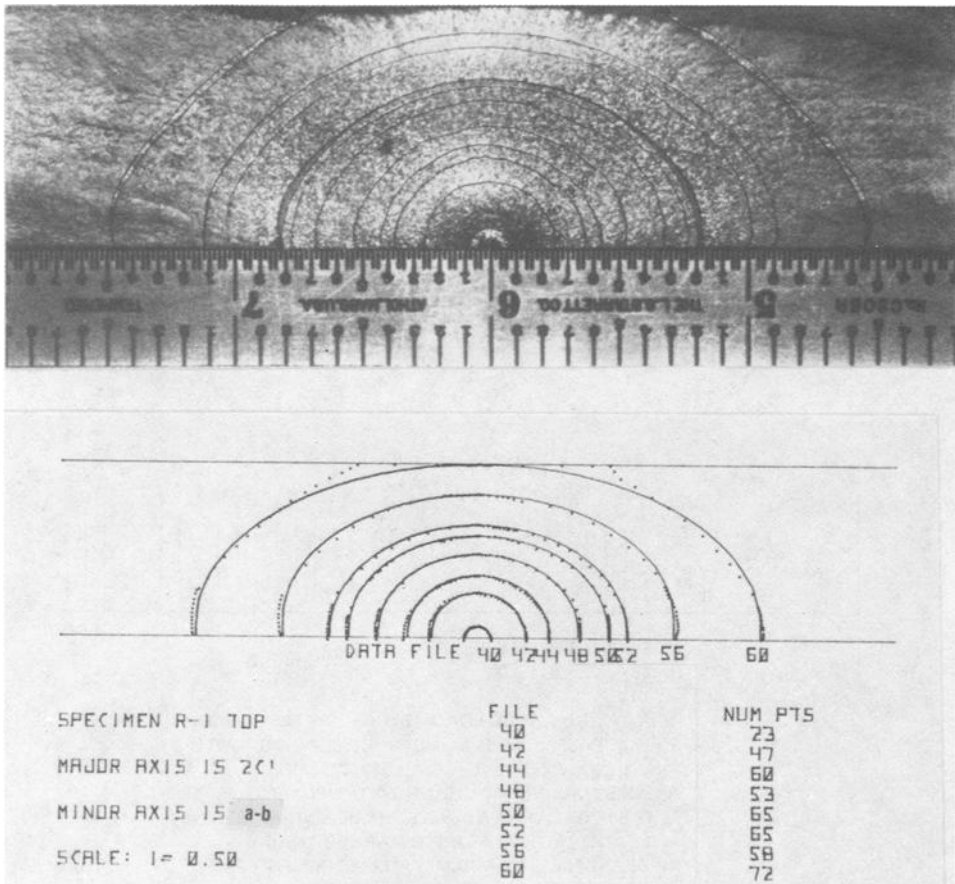


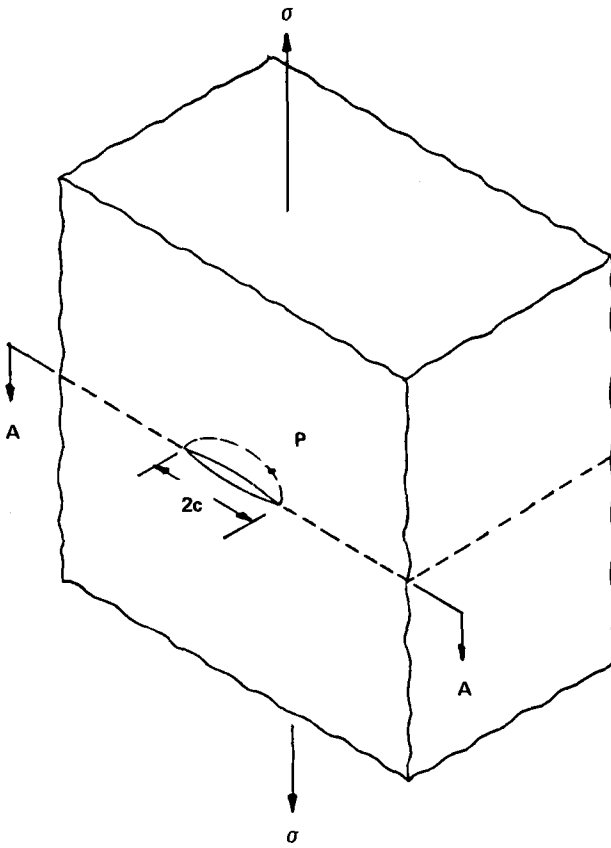
FIG. 3—Typical fracture surface and digitized record.

option to use flaw widths generated from compliance measurements was also developed. However, this option was never employed due to difficulties in calibrating the crack width versus compliance relationship. To determine crack growth rate ( $d(2C)/dN$ ), we initially employed both modified secant and five-point polynomial methods [5]. Since the five-point polynomial method resulted in significantly less scatter, it was used exclusively to calculate crack surface length ( $2C$ ). Therefore,  $d(2C)/dN$  was obtained from the slope of the least-squares fit of a second-order polynomial to five consecutive data points.

To exclude retardation effects resulting from the use of marker bands, we did not use the first data point following the marker band in calculating crack growth rate.

#### *Calculation of Flaw Shape and Growth Rate at Depth ( $da/dN$ )*

Since marker bands were produced only after stress intensity increases of 25 to 30%, the number of marker bands per specimen was only five to eight, depending on the initial flaw size. These bands were used to determine the flaw shape from post-test fractography. Although several methods of shape characterization were investigated, the parameter used for final data reduction was  $(a/2C)$ , where  $(a)$  is the distance from the surface to the deepest point and  $(2C)$  is the width at the surface of the specimen (Fig. 4). A linear interpolation



## COORDINATES OF POINT P

$$x = c \cos \theta$$

$$y = a \sin \theta$$

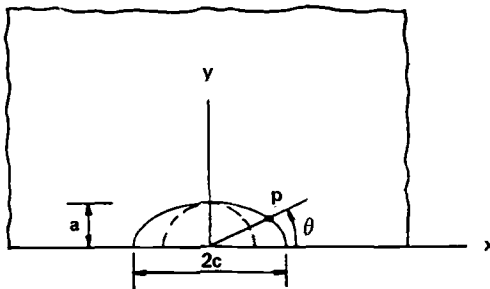


FIG. 4—A small semielliptical crack in uniformly stressed thick structure.

based on measured width ( $2C$ ) was used to get the shape ( $a/2C$ ) for points between marker bands. This method gave consistent results for all but large flaws under high-stress ratio conditions, which resulted in rapid shape changes immediately after marker band placement that prevented accurate interpolation of flaw shapes (Fig. 5).

Once the interpolation of flaw shape ( $a/2C$ ) and the calculation of surface crack growth rate ( $d(2C)/dN$ ) were completed, the crack growth rate at depth ( $da/dN$ ) was calculated as follows

$$da/dN = a/2C \cdot d(2C)/dN \quad (1)$$

This equation results from assuming that the surface flaw has reached an "equilibrium" shape, that is,

$$a/2C \cong \Delta a/\Delta 2C \quad (2)$$

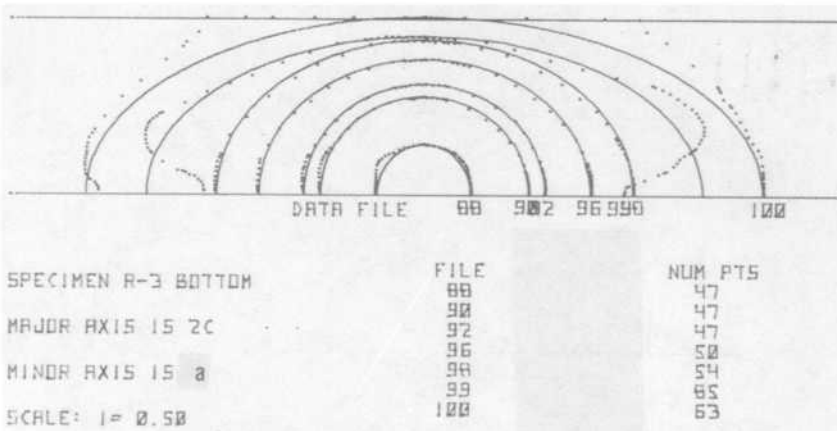
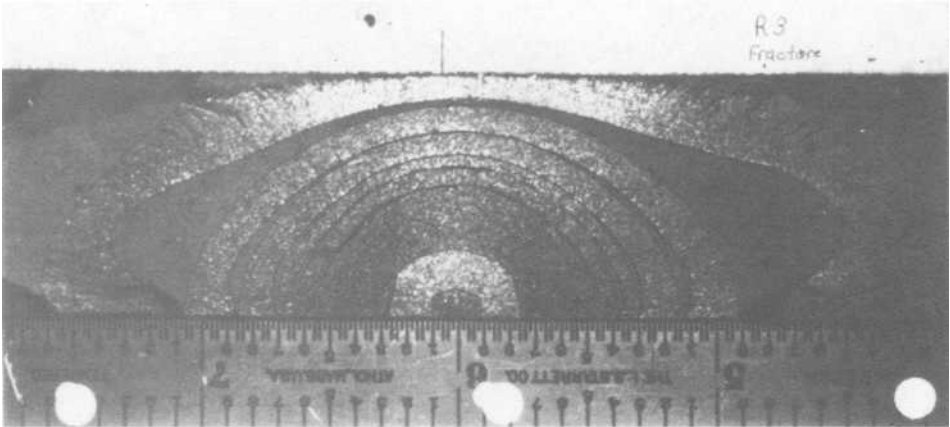


FIG. 5—Example of shape change following marker band placement.

If this is true, then

$$\Delta a \cong (a/2C)\Delta 2C \quad (3)$$

or

$$da/dN \cong (a/2C)(d(2C)/dN) \quad (4)$$

Since the crack growth rate at the depth ( $da/dN$ ) had to be calculated indirectly using interpolated values for  $(a/2C)$ , the accuracy is likely to be less than for  $d(2C)/dN$  values.

### Stress-Intensity Solutions

Many surface-flaw stress-intensity solutions are now published in the literature [5-12]. However, these solutions are not in close agreement (Fig. 6). Several were either usable only over a small range of crack growth or did not allow calculation of stress intensity at both surface and depth. These were eliminated from our study. The four that were finally employed in our data reduction program are shown below.

*Classical Irwin Solution* [6]—(with front and back face corrections)

$$K_I = \sigma \sqrt{\pi a/Q} \cdot f(\theta) \cdot F \cdot M_K \cdot f(W) \quad (5)$$

where

$$F = 1.0 + 0.12(1 - a/2C)^2 \quad [7], \quad (6)$$

$\sigma$  = applied stress,

$a$  = crack depth,

$$Q = \text{shape factor} = \phi^2 - 0.212 (\sigma/\sigma_{ys})^2, \quad (7)$$

$$\phi^2 = 1 + 1.464 (a/C)^{1.65} \text{ for } a/C \leq 1 \quad [9], \quad (8)$$

$$f(\theta) = (a^2/C^2 \cos^2 \theta + \sin^2 \theta)^{1/4}, \quad (9)$$

$$f(W) = \text{width correction} = (\sec \pi C/W)^{1/2}, \text{ and} \quad (10)$$

$M_K$  = back surface correction factor [8].

See Table 2 for  $M_K$  values.

TABLE 2— $M_K$ , back surface correction factor [2,8].

	$a/2C$					
	0.05	0.10	0.20	0.30	0.40	0.50
$a/t$	$M_K$					
0.0	1.00	1.00	1.00	1.00	1.00	1.00
0.1	1.01	1.01	1.01	1.01	1.01	1.00
0.2	1.03	1.03	1.02	1.02	1.01	1.00
0.3	1.06	1.06	1.04	1.03	1.02	1.00
0.4	1.12	1.12	1.08	1.05	1.02	1.00
0.5	1.22	1.18	1.14	1.08	1.03	1.01
0.6	1.34	1.30	1.22	1.13	1.06	1.01
0.7	1.48	1.42	1.31	1.20	1.08	1.02
0.8	1.64	1.57	1.41	1.26	1.13	1.04
0.9	1.77	1.68	1.50	1.32	1.18	1.08
1.0	1.84	1.75	1.59	1.38	1.22	1.10



$$K = S \sqrt{\pi \frac{a}{Q}} F\left(\frac{a}{t}, \frac{a}{c}, \frac{c}{W}, \phi\right)$$

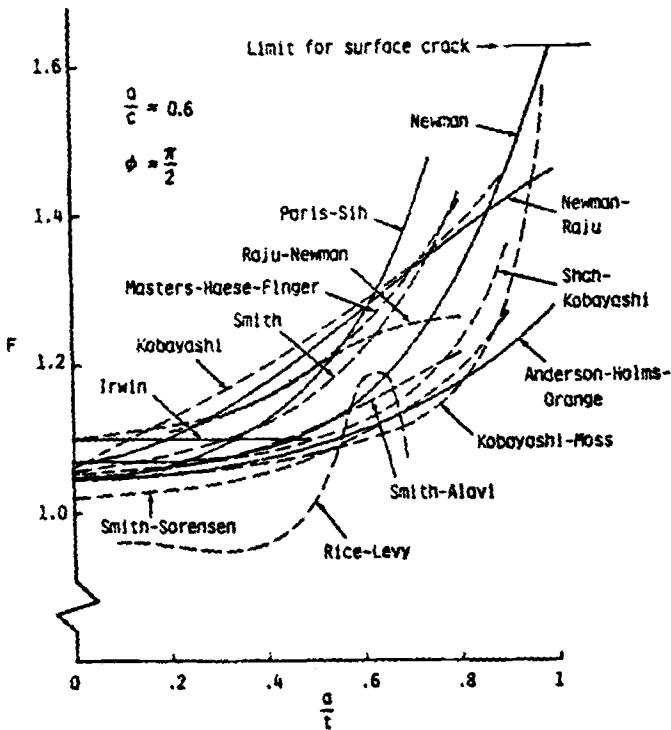
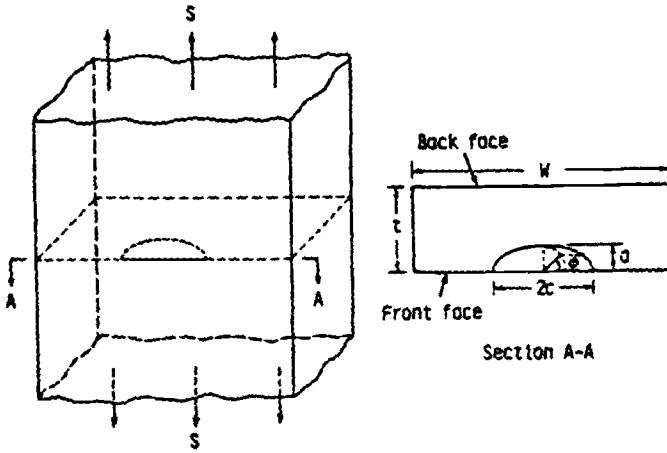


FIG. 6—Surface flaw stress-intensity solutions [3].

*Slice Synthesis Finite-Element Model* [10]—This solution was available in the form of a polynomial fit to the original finite-element results.

$$K_D = \sigma \sqrt{\pi a} \sum_{i=0}^3 \sum_{j=0}^3 A_{ij} (C/a)^{i/2} (a/t)^j \quad (11)$$

$$K_S = \sigma \sqrt{\pi C} \sum_{i=0}^3 \sum_{j=0}^3 B_{ij} (C/a)^{i/2} (a/t)^j \quad (12)$$

where

- $K_D$  = stress intensity at depth ( $\theta = 90$  deg),  
 $K_S$  = stress intensity at surface ( $\theta = 0$  deg),  
 $A_{ij}$  = regression coefficients for  $\theta = 90$  deg, and  
 $B_{ij}$  = regression coefficients for  $\theta = 0$  deg.

See Table 3 for coefficient values.

*Newman-Raju Solution* [11]—This solution was derived from Raju and Newman's three-dimensional finite-element analysis of semielliptical surface cracks and from the work of Gross and Srawley on a single-edge crack.

$$K_I = \sigma \sqrt{\pi a/Q} \cdot f(\theta) \cdot F \cdot f(W) \quad (13)$$

where

$$F = [M_1 + (\sqrt{QC/a} - M_1)(a/t)^P + \sqrt{QC/a} (M_2 - 1)(a/t)^{2P}], \quad (14)$$

$$P = \sqrt{\pi}, \quad (15)$$

$$M_1 = \text{front face correction} = 1.13 - 0.1(a/C) \text{ for } a/C < 1, \quad (16)$$

$$M_2 = \sqrt{\pi}/4 \text{ for } a/C < 1, \quad (17)$$

$$f(W) = (\sec(\pi C/W \cdot \sqrt{a/t}))^{1/2}, \text{ and} \quad (18)$$

$$f(\theta) = (a^2/c^2/\cos^2 \theta + \sin^2 \theta)^{1/4}.$$

TABLE 3—Polynomial coefficients for evaluating surface flaw stress intensities.

i	j							
	A				B			
	0	1	2	3	0	1	2	3
$a \leq C$								
0	-0.333	-1.047	4.618	-3.547	0.426	0.044	-2.109	1.889
1	1.516	1.735	-9.740	8.120	0.654	0.090	3.329	-3.108
2	-0.581	-0.590	5.441	-4.824	-0.385	-0.121	-1.089	1.273
3	0.076	0.026	-0.669	0.669	0.054	0.027	0.096	-0.150
$a > C$								
0	0.0955	-0.0892	0.358	-0.28	0.000788	0.0154	0.00607	0.0177
1	0.634	0.511	-1.875	1.232	0.956	-0.0992	-0.0396	-0.116
2	0.624	-0.681	1.698	-0.1787	0.281	0.167	-0.0356	0.258
3	-0.676	0.385	-0.55	-0.341	-0.494	-0.0426	0.314	-0.268

*Newman-Raju Solution* [12]—This solution is also a fit to earlier finite-element work but is formulated to apply over a larger range of conditions (Eq 13)

$$K_I = \sigma \sqrt{\pi a/Q} \cdot f(\theta) \cdot F \cdot f(W)$$

where

$$F = [M_1 + M_2(a/t)^2 + M_3(a/t)^4] \cdot g \quad (19)$$

$$M_1 = 1.13 - 0.09(a/C), \quad (20)$$

$$M_2 = -0.54 + 0.89/(0.2 + a/C), \quad (21)$$

$$M_3 = 0.5 - 1.0/(0.65 + a/C) + 14(1.0 - a/C)^{24}, \quad (22)$$

$$g = 1 + [0.1 + 0.35(a/t)^2](1 - \sin \theta)^2, \quad (23)$$

$$\theta = 90 \text{ deg at depth and } \theta = 0 \text{ deg at surface,}$$

$$f(\theta) = (a^2/C^2 \cos^2 \theta + \sin^2 \theta)^{1/4}, \text{ and}$$

$$f(W) = (\sec(\pi C/W \cdot \sqrt{a/t}))^{1/2}$$

For comparison purposes, the different stress-intensity solution correction factors were calculated for different shapes ( $a/2C$  ratios) and plotted as a function of fraction of growth through the thickness ( $a/t$ ).

The correction factors used were normalized by dividing the surface flaw stress intensity ( $K_I$ ) by the stress intensity for an equivalent embedded elliptical flaw ( $K_{Ie}$ ) (Fig. 7)

$$K_{Ie} = \sigma \sqrt{\pi a/Q} [a^2/C^2 \cos^2 \theta + \sin^2 \theta]^{1/4} \quad (24)$$

For the  $a/2C = 0.25$  case (Fig. 8), the results are compared to the Society of Experimental Stress Analysis (SESA) Fracture Committee's consensus solution [13]. This comparison illustrates the following points:

- Solutions vary significantly for deep flaws ( $a/t$  approaching 1.0).
- Surface stress intensities are less well behaved than the stress intensity at the deepest point. (The normalized Irwin and Newman-Raju solutions for the surface are not shown because of a problem in the graphing program.)
- The Newman-Raju solution [12] agrees fairly well with the SESA consensus solution at the surface. The Slice Synthesis approach best agrees with the SESA consensus solution at the crack depth.

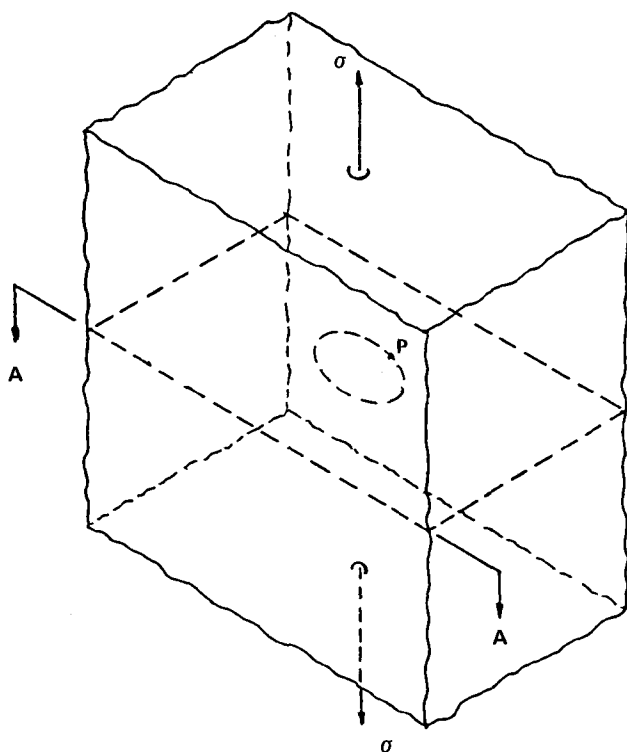
#### Width Correction

Specimen width was fixed at 152 mm. At this width, some form of finite width correction was necessary, at least for the final portions of each test where the flaw width ( $2C$ ) exceeded 20% of the specimen width ( $W$ ). For this purpose, the width correction developed by Newman [14] was used (Eq 18)

$$f(W) = \text{width correction} = [\sec(\pi C/W \cdot \sqrt{a/t})]^{1/2}$$

During reduction of the surface flaw crack data, we found that the use of a width correction had little effect on the slope of  $dC/dN$  versus  $\Delta K$  curves and the resulting crack growth rate "constants."

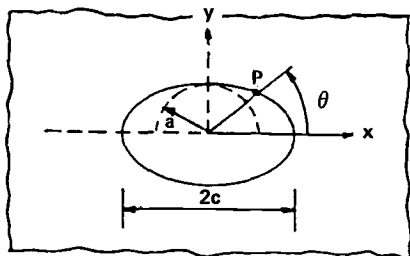
This effect is illustrated in Fig. 9. Although it was not really necessary due to the specimen dimensions, the Newman width correction factor was employed in the final model to make it applicable to a wide range of finite width cases.



COORDINATES OF POINT P

$$x = c \cos \theta$$

$$y = a \sin \theta$$



SECTION A-A

FIG. 7—Embedded elliptical crack geometry.

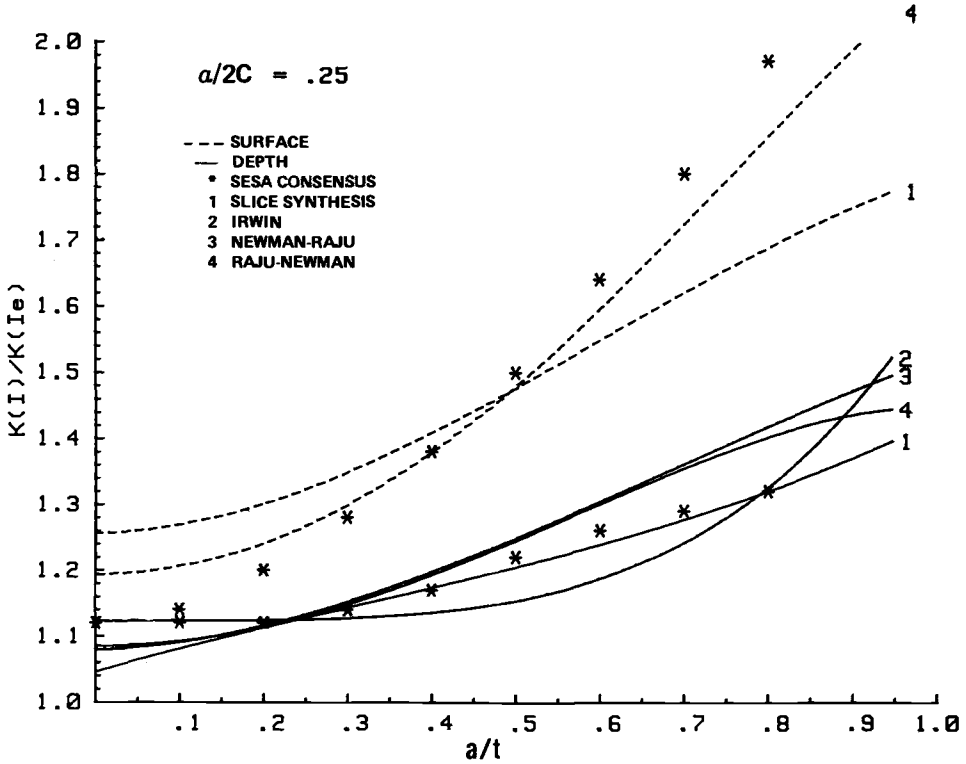


FIG. 8—Surface flaw correction factors for  $a/2C = 0.25$ ,  $2C \ll W$ .

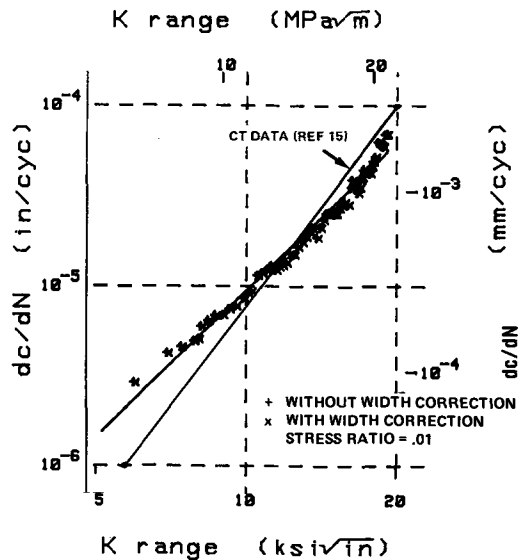


FIG. 9—Effect of width correction on  $dc/dN$  versus  $\Delta K$  plot.

### *Extraction of Paris Constants*

To compare the surface flaw crack growth rate data to CT data from the literature, we included a provision in the data-reduction program to allow extraction of Paris constants. The Paris equations for crack growth rate were

$$dC/dN = C_s \Delta K_s^n \text{ (for growth at the surface), and}$$

$$da/dN = C_D \Delta K_D^n \text{ (for growth at the depth)}$$

The constants were extracted by applying a least-squares linear regression of log growth rate versus log stress-intensity range data. To eliminate the effects of threshold on the Paris constants, the regression did not include data points with  $\Delta K$  less than  $6.6 \text{ MPa } \sqrt{\text{m}}$ . Data on the upper end were not included when  $\Delta K$  exceeded  $22.0 \text{ MPa } \sqrt{\text{m}}$  or  $a/t$  exceeded 0.95.

## **Results and Discussion**

### *Surface Flaw Shape Characterization*

Since one of the objectives of this study was to predict the shape change in surface flaws, the question of surface flaw shape characterization had to be addressed. Typical approaches in the literature are to assume either a semicircular or semielliptical shape. The former assumption can produce adequate results for very small flaws, whereas the latter must be used for most larger surface flaws. To test the applicability of these assumptions, we conducted tests on specimens with shapes of  $(a/2C)$  from 0.25 to 0.65. The use of marker bands allowed for the measurement of shape changes as the flaws progressed through the specimens.

It was apparent from the literature that most surface flaws being reported were not true semiellipses. This was also true in this investigation, since most flaws rapidly assumed a shape that might be described as a partially embedded ellipse with the major axis offset a small distance into the specimen. To quantify this effect, we digitized fractograph marker bands and fitted a true elliptical shape to the digitized points (Fig. 10). To define the flaw shapes more accurately, we employed the following definitions (Fig. 11):

- $a$  = total depth (from surface to deepest point),
- $b$  = offset (from surface to major axis of ellipse),
- $2C$  = maximum width (at major axis), and
- $2C'$  = visually measured width at the specimen surface.

For each specimen, these dimensions were determined for each marker band. Because certain conditions (for example, high load level or high stress ratio) caused significant shape changes to occur during the marker band, the above dimensions were measured for the beginning and end of each marker band. The offset ( $b$ ) is plotted as a function of fraction of distance through the thickness ( $a/t$ ) in Fig. 12. In spite of the wide range of flaw shapes ( $a/2C$  from 0.25 to 0.65), the offset appeared to be very consistent. The offset is independent of  $(a/2C)$  and shows a slight tendency to increase as the flaw progresses through the thickness of the specimen.

The data points in Fig. 12 which are very large offsets [nominally 8.9 to 10.2 mm (0.35 to 0.40 in.)] occurred due to overload effects in the formation of marker bands in the high-stress ratio ( $R = 0.7$ ) specimens.

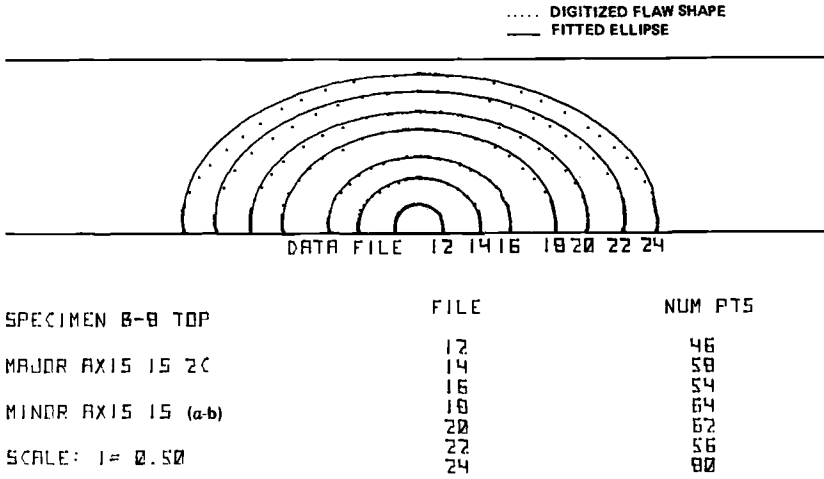


FIG. 10—Partially embedded ellipse fit to marker bands.

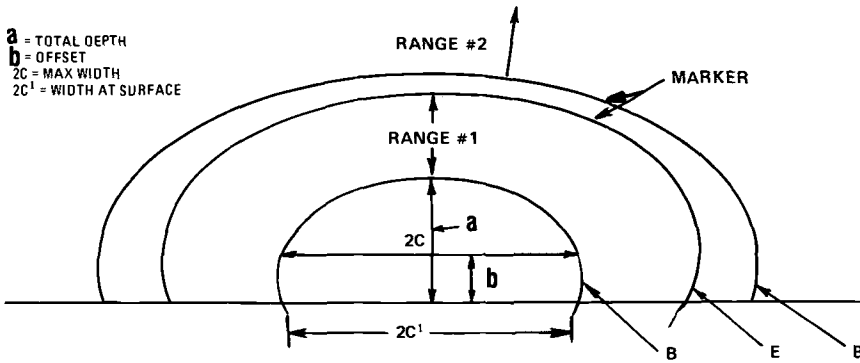


FIG. 11—Flaw shape definitions.

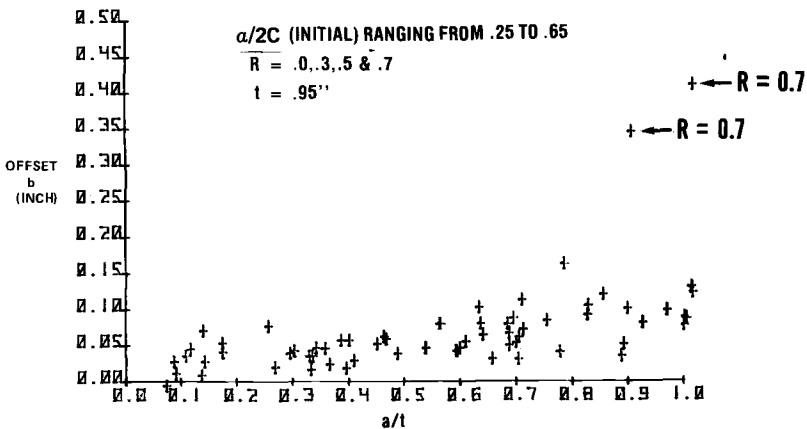


FIG. 12—Offset versus fraction of distance through the thickness.

To determine the best method of shape characterization, we used different techniques to fit elliptical shapes to the digitized marker bands. The two most accurate methods are discussed below.

*Partially Embedded Ellipse with a Minor Axis Equal to  $2(a-b)$  and the Major Axis Equal to the Maximum Width ( $2C$ )* (see Fig. 10)—This method accurately portrays the maximum flaw width, the ellipse offset, and the curling back observed at the surface of most flaws. However, this technique tends to overestimate the total area of the flaw and has two practical drawbacks:

- (a) the maximum flaw width ( $2C$ ) cannot be visually monitored during a test, and
- (b) no existing stress intensity solutions can account for a partially embedded ellipse whose major axis is offset from the specimen surface.

*Semiellipse with Minor Axis Equal to Total Depth ( $a$ ) and Major Axis Equal to the Visually Measured Width at the Surface of the Specimen ( $2C'$ )* (see Fig. 13)—This method has several practical advantages: it is widely used in the literature, it is easy to experimentally measure  $2C'$ , and it is consistent with the assumption of available stress intensity solutions. Since it fails to account for the curling back at the specimen surface (the majority of work reported in the literature) this method tends to underestimate the cracked area. To be consistent with most work in the literature, this method of shape characterization was employed throughout the remainder of this study.

#### Comparison of Surface Flaw and CT Crack Growth Rate Data

When a model for surface flaw growth was being developed, the assumption was made that  $L$ - $T$  orientation compact tension crack growth rate data could be used to predict surface flaw growth in both depth ( $L$ - $S$ ) and width ( $L$ - $T$ ) directions. This implies that crack growth rate differences due to anisotropy and state of stress (plane-stress or plane-strain) are minimal. To check this assumption, we plotted crack growth rate versus stress-intensity range curves comparing surface crack growth rate ( $dC/dN$ ) and depth crack growth rate ( $da/dN$ ). This was done using each of the surface flaw stress-intensity solutions discussed earlier. Typical plots for one of the baseline specimens are illustrated in Fig. 14 using the

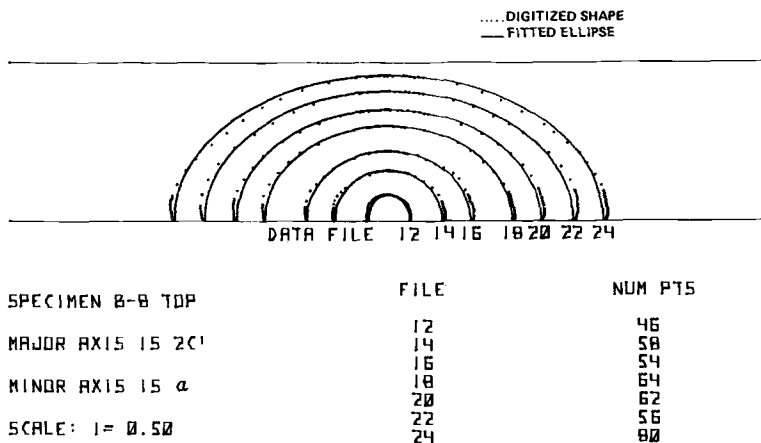


FIG. 13—Standard semiellipse fit to marker bands.



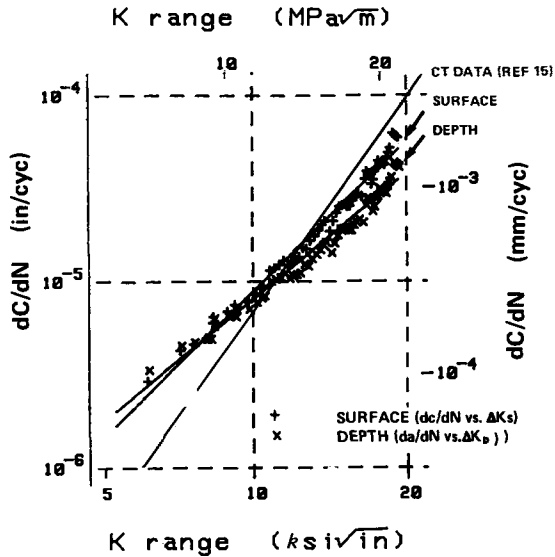


FIG. 14—Surface and depth crack growth rate curves using Raju-Newman [12]  $K$  solution ( $R = 0.1$ ).

Raju-Newman [12]  $K$  solution. In spite of the significant differences among the stress-intensity solutions employed, they provided the following results:

- The slopes of the crack growth rate curves for surface growth were consistently higher than for growth at the depth.
- Over most of the range investigated, the crack growth rate at the surface was higher than at the deepest point for equivalent stress intensity ranges.
- The slopes of the crack growth rate curves for both surface and depth are lower than most  $L$ - $T$  compact tension rate data reported in the literature [15].

These results indicate that the use of CT crack growth rate data to predict the growth and shape change of surface flaws will result in some error. It has not been determined whether the source of this error is due to fundamentally different crack growth rates at surface and depth or due to inaccurate stress-intensity solutions.

#### Surface Flaw Growth Prediction

In order to account for flaw shape change, we developed a two-dimensional growth integration routine for use with CT data from the literature. The model is based on the following premises:

- crack growth rates at the surface and depth are equal for a given value of stress-intensity range and
- shape changes are gradual.

Plots of flaw shapes ( $a/2C$ ) versus  $a/t$  for two initial flaw shapes ( $a/2C$  of 0.2 and 0.6) were prepared for each of the stress-intensity solutions under study (Fig. 15). These were then compared to the actual shape changes observed in the baseline ( $R = 0.1$ ) specimens (Fig. 16). It was noted that the trend of decreasing  $a/2C$  as  $a/t$  increased toward 1.0 was

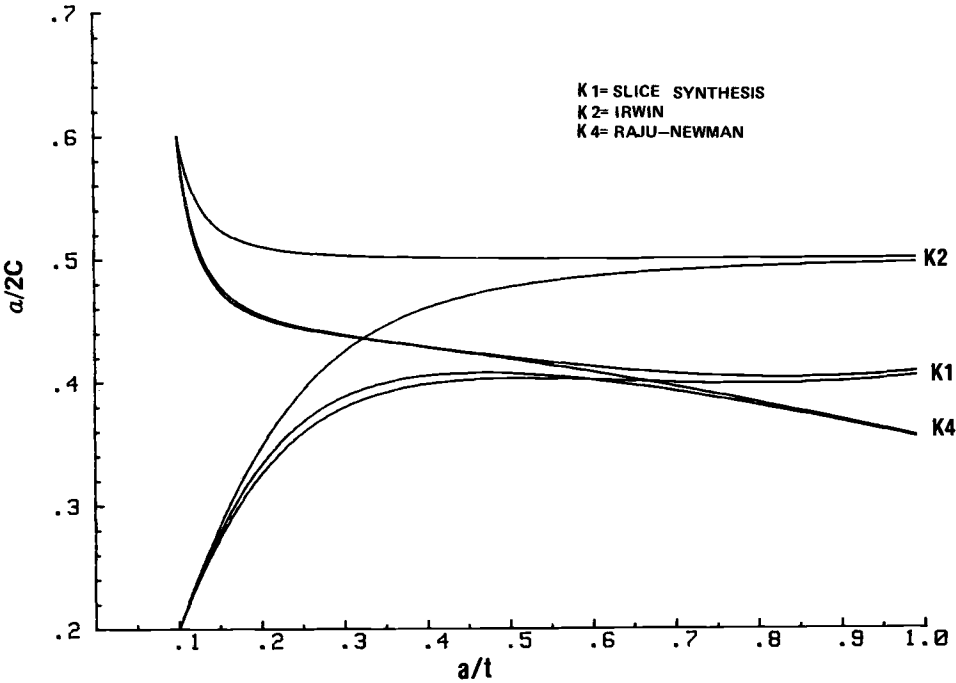


FIG. 15—Predicted shape change versus growth using different stress-intensity solutions.

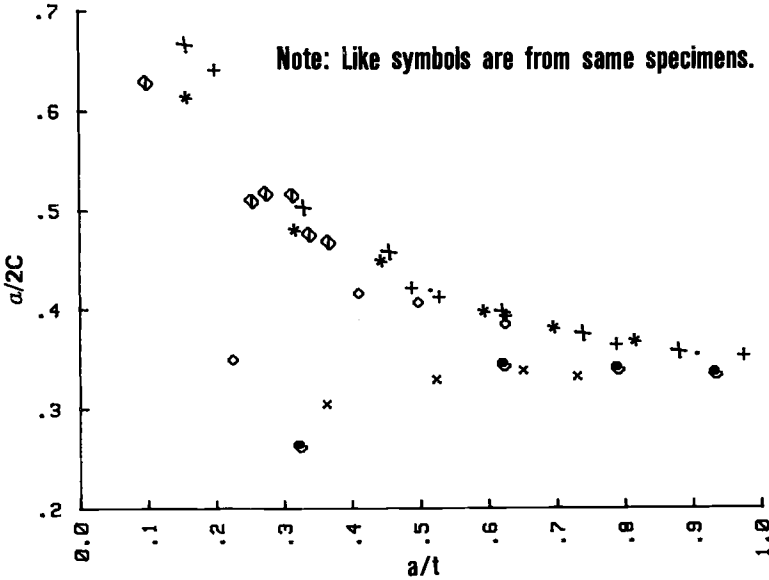


FIG. 16—Shape change versus flaw growth for baseline ( $R = 0.1$ ) specimens.

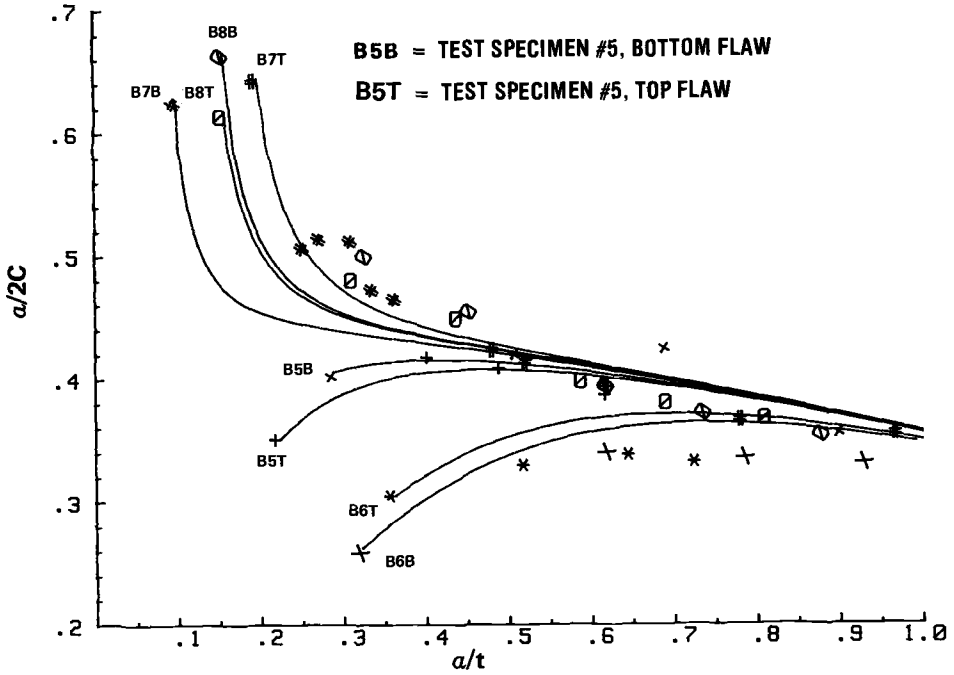


FIG. 17—Predicted versus actual shape change using Raju-Newman [12] solution.

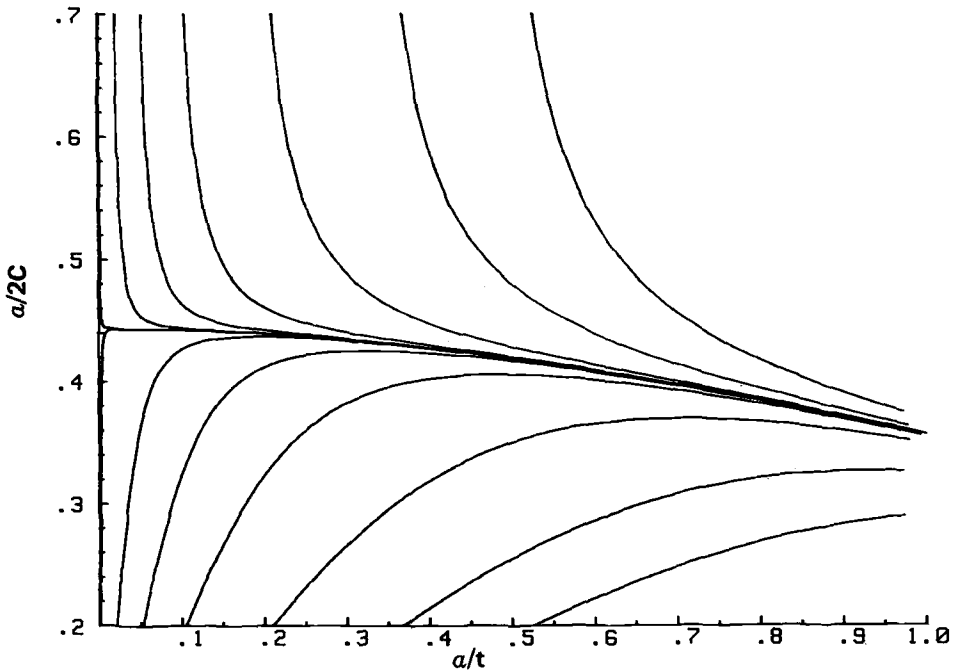


FIG. 18—Predicted shape changes for various initial flaws using Raju-Newman [12] solution.

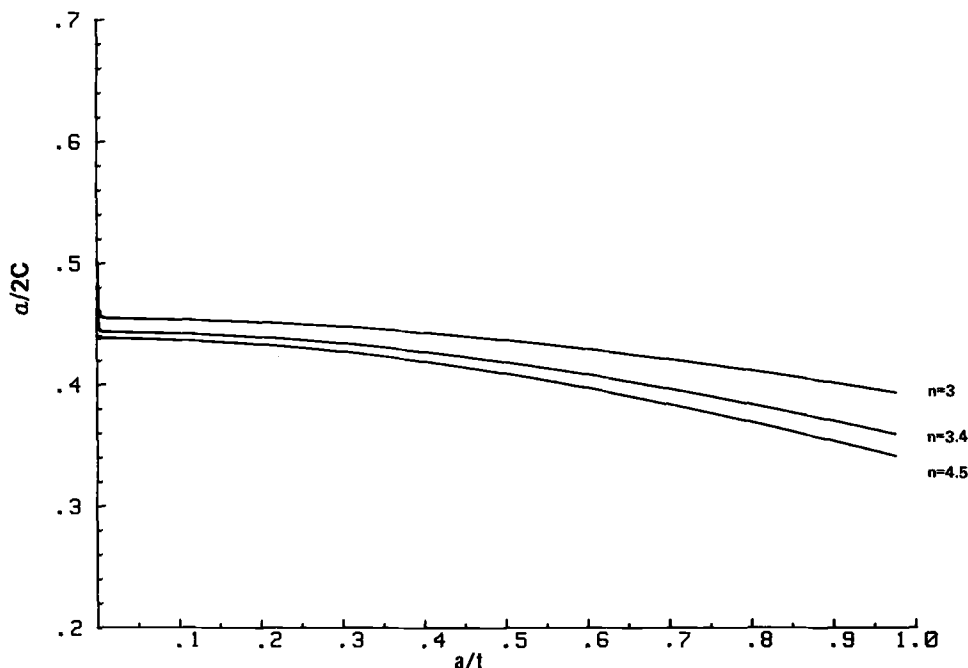


FIG. 19—Predicted equilibrium flaw shape as a function of  $a/t$  and  $n$ .

similar to the shape of the Raju-Newman [12] solution in Fig. 15. When the initial shapes and sizes of the baseline flaws were used as input to the surface flaw growth model (using the Raju-Newman [12] solution), the predicted shape changes generally agreed with the actual changes (Fig. 17). The major discrepancy was that actual flaws did not reach equilibrium shapes as early as predicted.

Whether or not a flaw will ever reach its "equilibrium" shape is a function of the initial size and shape of the flaw. Smaller flaws tended to reach their equilibrium shape much sooner, as shown in Fig. 18. However, equilibrium shape is really a misnomer since the shape is a function of both  $a/t$  and  $n$  (from  $da/dN = C\Delta K^n$ ). This dependency is illustrated in Fig. 19.

## Conclusions

Several conclusions may be drawn from this study concerning the prediction of surface flaw growth in plates of finite thickness and width:

1. Most surface flaws resemble a partially embedded ellipse with the major axis offset into the specimen an amount that increases slightly as the flaw grows.
2. The use of the Raju-Newman [12] stress-intensity formulation to calculate crack growth at surface and depth allowed prediction of surface flaw growth and shape change consistent with those experimentally observed.
3. Crack growth rate data obtained from surface flaws differ from data obtained from compact tension specimens. Furthermore, surface crack growth rate usually exceeded the crack growth rate at the deepest portion of surface flaws. We do not know whether this is

due to fundamentally different growth rates or to inaccuracies in the stress-intensity solutions. Thus, the validity of using standard compact tension specimen growth rate data to predict surface flaw growth is uncertain.

### Acknowledgment

We wish to thank Dr. Ted Nicholas, Metals Behavior Branch, Air Force Wright Aeronautical Laboratories, for his dedicated support of this particular research and for his continued advice and assistance.

### References

- [1] Vroman, G. A., "Life Prediction Analysis of Part-Through Cracks," *Part-Through Crack Fatigue Life Prediction, ASTM STP 687*, J. B. Chang, Ed., American Society for Testing and Materials, Philadelphia, 1979, pp. 89-95.
- [2] Engle, R. M., Jr., "Aspect Ratio Variability in Part-Through Crack Life Analysis," *Part-Through Crack Fatigue Life Prediction, ASTM STP 687*, J. B. Chang, Ed., American Society for Testing and Materials, Philadelphia, 1979, pp. 74-88.
- [3] Newman, J. C., Jr., "A Review and Assessment of the Stress-Intensity Factor for Surface Cracks," *Part-Through Crack Fatigue Life Prediction, ASTM STP 687*, J. B. Chang, Ed., American Society for Testing and Materials, Philadelphia, 1979, pp. 16-42.
- [4] Carter, D. K., Canda, W. R., and Blind, J. A., "Surface Flaw Crack Growth in Plates of Finite Thickness," AFWAL-TR-86-4034, Air Force Wright Aeronautical Laboratories, Materials Laboratory, Wright-Patterson Air Force Base, OH, Jan. 1987.
- [5] Hudak, S. J., Jr., Saxena, A., Bucci, R. J., and Malcolm, R. C., "Development of Standard Methods of Testing and Analyzing Fatigue Crack Growth Data," AFML-TR-78-40, Air Force Materials Laboratory, Wright-Patterson Air Force Base, OH, May 1978.
- [6] Irwin, G. R., "Crack Extension Force for a Part-Through Crack in a Plate," *Journal of Applied Mechanics*, Dec. 1962, pp. 651-654.
- [7] Kobayashi, A. S. and Moss, W. L., "Stress-Intensity Magnification Factors for Surface-Flawed Tension Plate and Notched Round Tension Bar," *Proceedings, Second International Conference on Fracture*, Brighton, U.K., 1969.
- [8] Shah, R. C. and Kobayashi, A. S., "Stress-Intensity Factors for an Elliptical Crack Approach on the Surface of a Semi-Infinite Solid," *International Journal of Fracture*, Vol. 9, No. 2, 1975, pp. 133-146.
- [9] Merkle, J. G., "A Review of Some of the Existing Stress-Intensity Factor Solutions for Part-Through Surface Crack," ONRL-TM-3983, Oak Ridge National Laboratory, Oak Ridge, TN, Jan. 1973.
- [10] Dill, H. D. and Saff, C. R., "Environment-Load Interaction Effects on Crack Growth," AFFDL-TR-78-137, Air Force Flight Dynamics Laboratory, Wright-Patterson Air Force Base, OH, Nov. 1978, pp. 161-182.
- [11] Newman, J. C., Jr., and Raju, I. S., "Analysis of Surface Cracks in Finite Plates Under Tension or Bending Loads," NASA-TM-78805, National Aeronautics and Space Administration, Washington, DC, 1978.
- [12] Newman, J. C., Jr., and Raju, I. S., "Stress Intensity Factor Equations for Cracks in Three-Dimensional Finite Bodies," NASA TM 83200, National Aeronautics and Space Administration, Langley Research Center, Hampton, VA, 1981.
- [13] "Comparison of Numerical Solutions to the Surface Flawed Plate: Benchmark Problem I," J. J. McGowan, Ed., Report of the Society for Experimental Stress Analysis, Fracture Committee, 1980.
- [14] Newman, J. C., Jr., "Predicting Failure of Specimens with Either Surface Cracks or Corner Cracks at Holes," NASA TN D-8244, National Aeronautics and Space Administration, Washington, DC, June 1976.
- [15] Bucci, R. J., "Development of Basic Material(s) Data for Evaluating Crack Growth Life," *Part-Through Crack Fatigue Life Prediction, ASTM STP 687*, J. B. Chang, Ed., American Society for Testing and Materials, Philadelphia, 1979, pp. 47-73.

## A Novel Procedure to Study Crack Initiation and Growth in Thermal Fatigue Testing

---

**REFERENCE:** Marchand, N. J., Dorner, W., and Ilschner, B., "A Novel Procedure to Study Crack Initiation and Growth in Thermal Fatigue Testing," *Surface-Crack Growth: Models, Experiments, and Structures*, ASTM STP 1060, W. G. Reuter, J. H. Underwood, and J. C. Newman, Jr., Eds., American Society for Testing and Materials, Philadelphia, 1990, pp. 237–259.

**ABSTRACT:** An induction heating procedure coupled with an advanced alternating-current potential drop (ACPD) system to study thermal fatigue crack initiation and growth is presented. This technique can be adapted for various specimen geometries and is well suited for studying isotropic as well as anisotropic alloys. Details of the experimental apparatus and ACPD system are given. To illustrate the procedure, the effect of three cyclic thermal histories on the number of cycles to crack initiation of double-edge wedge specimens of IN-100 and MA-6000 superalloys was studied in air. The thermoelasto plastic finite-element analyses (FEA) to determine the critical locations and their respective stress-strain histories are presented. For this particular geometry of specimen, the initiation of microcracks about 10 to 20  $\mu\text{m}$  in length could be detected and crack growth rates lower than 1  $\mu\text{m}/\text{cycle}$  were measured. The experimental results combined with the FEA showed that the peak compressive strains encountered on specimen heat-up are more critical to crack initiation and surface degradation than total stress or strain ranges.

**KEY WORDS:** thermal fatigue, induction heating, crack initiation, crack growth, superalloy, IN-100, finite element, A-C potential drop (ACPD)

The drive toward better performance and fuel economy for aircraft gas turbine engines has resulted in higher turbine inlet temperatures. Currently, the leading and trailing edges of first-stage blades and vanes can rise from 450 to 1100°C in 4 to 10 s during takeoff. During turbine shutdown, after landing and thrust reverse, the airfoil temperature can decrease from 1080 to 450°C in under 15 s [1]. As a result of high metal temperatures and the thermal strains due to temperature transients and internal blade cooling, thermal fatigue, which is a combination of ductility limitations in mechanical behavior and effects of surface degradations, has become the life-limiting phenomenon for gas turbine blades and vanes [2,3]. In this scenario, the ability to detect and analytically predict surface crack initiation and growth is a key technology [3,4].

As reviewed by Holmes et al. [5,6] there are several techniques available for studying thermal fatigue crack initiation. These include gas-burner rigs [7–9] and fluidized beds [10,11]. Gas-burner rigs suffer from high costs and require complex heat-transfer analysis, which makes it difficult to correlate surface degradation with the stress-strain history of

<sup>1</sup> University research fellow, Department of Metallurgical Engineering, Ecole Polytechnique, P.O. Box 6079, Station A, Montreal, PQ, H3C 3A7 Canada.

<sup>2</sup> Project engineer, Motoren und Turbinen Union (MTU), D 8000, München 50, West Germany.

<sup>3</sup> Professor, Department of Materials, Swiss Federal Institute of Technology, Lausanne CH-1007, Switzerland.

test specimens. It should be noted that although burner rigs can simulate the combustion gas composition existing in a turbine, their use has come under considerable debate lately due to the wide differences in test results obtained by different laboratories [8]. The principal reason for the variation in test results, which occurs among rigs which burn the same fuel, is generally attributed to the variation in specimen stress-strain history resulting from the use of various geometries (wedges, squares, circular pins, etc.) and burner-rig velocities. Due to the complex coupled heat-transfer analysis required for the determination of stress-strain history, the stress-strain history of the test specimens is rarely determined except for few exceptions [9]. This makes the transfer of test results to actual gas turbines empirical at best.

The fluidized bed technique has at least two serious drawbacks. First, it is incompatible with corrosive atmosphere testing. Second, it lacks versatility in studying arbitrary temperature histories or mission profiles due to lack of easy control over specimen heating and cooling rates. Further, the potential erosive effect of the alumina particles used in fluidized bed furnaces is now under consideration because it has been shown that oxidation rates are greatly enhanced by impact of hard particles even with moderate velocities [12,13].

Induction heating of a stepped-disk has been shown to be a very efficient alternative to the use of burner-rigs and fluidized beds in thermal fatigue studies [5,6,14]. The induction heating technique [14,15] allows one to subject test specimens to a variety of temperatures and strain histories typical of those encountered by leading and trailing edges of gas turbine blades and vanes. The technique can also be easily modified to allow fatigue testing in inert or corrosive gas atmospheres [5,6].

The purpose of this paper is to describe a computerized testing system capable of detecting surface crack initiation ( $\approx 50 \mu\text{m}$ ) and surface microcrack growth during thermal fatigue. While the main point here is an advanced alternating-current potential drop (ACPD) technique, it will be demonstrated by using it to study the effect of various strain histories on the number of cycles to crack initiation in IN-100 and MA-6000 nickel-based superalloys.

## Experimental Procedure

### *Test Specimen and Testing Apparatus*

For the present study, double-edge wedge specimens were used with edge radii typical of trailing and leading edges of a gas turbine airfoil (Fig. 1). This allowed modeling of the

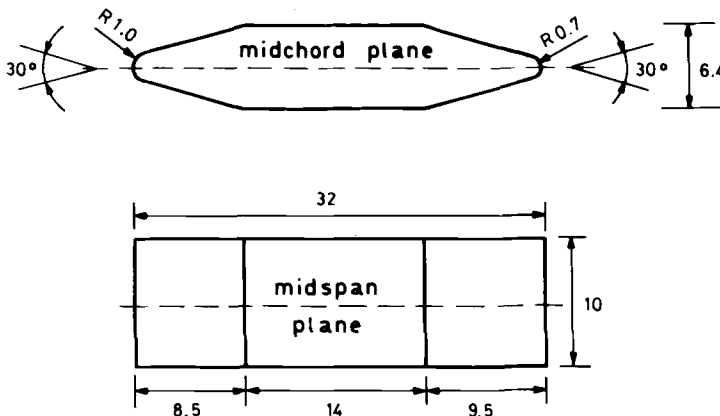


FIG. 1—Geometry of specimen used for testing (in mm).

TABLE 1—*Chemical composition of alloys.*

Alloy	Elements, Weight %											
	Ni	Cr	Co	Mo	Al	Ti	W	C	B	Zr	Ta	Y <sub>2</sub> O <sub>3</sub>
IN-100	Balance	10	15	3.0	5.5	4.7	1.0	0.18	0.014	0.001	...	...
MA-6000	Balance	15	...	2.0	4.5	2.5	4.0	0.05	0.01	0.15	2.0	1.1

TABLE 2—*Alloys' mechanical properties (monotonic).*

Temperature, °C	Ultimate Strength, N/mm <sup>2</sup>	0.02% Yield Strength, N/mm <sup>2</sup>	0.2% Yield Strength, N/mm <sup>2</sup>	Reduction in Area, %
IN-100				
21	986	614	765	14
850	765	607	731	8
925	565	345	462	12
1000	386	200	296	20
MA-6000 <sup>a</sup>				
21	1294	1284	3.5	3.0
538	1156	1011	5.5	4.0
760	976	781	5.5	12.5
982	407	344	12.5	35.0

<sup>a</sup> Longitudinal tensile properties.

5 to 8 s heating and 6 to 30 s cooling experienced by the edges of internally cooled gas turbine airfoils. The specimens were machined from a cast plate (IN-100) about 15 mm in thickness and from an isothermally forged plate (MA-6000) also 15 mm of final thickness. The chemical composition of both alloys is given in Table 1. The tensile properties at room and elevated temperatures are shown in Table 2.

The apparatus which was used consists of a high-frequency oscillator for induction heating, an air compressor for cooling, a programmable high-resolution voltmeter (DVM), an ACPD crack growth monitor, and a mainframe computer [16]. Figure 2 shows the control block diagram for this system.

Thermal fatigue was achieved by inductively heating the double-edge wedge specimens using a Hüttinger<sup>4</sup> solid-state 6.0 kW (200 kHz) induction generator coupled to a special concentrator coil (Figs. 3 and 4). This technique relies on the skin effect obtained with high-frequency induction heating of metals. The skin depth, the depth at which the strength of the magnetic field falls to 0.3679 of its surface value, is given by [17]

$$\delta = (\rho/4\pi^2 \times 10^{-7} \cdot \omega \cdot \mu_r)^{1/2}$$

where

- $\rho$  = resistivity (in  $\Omega \cdot \text{m}$ ),  
 $\omega$  = frequency (in Hz),  
 and  $\mu_r$  = relative permeability ( $\approx 1$  for nonmagnetic materials like IN-100 and MA-600).

<sup>4</sup> Hüttinger GmbH, Model IG 5/200 Hy-A 21-206 B/f-BA 1-8240-10, supplied with a Programmable Eurotherm Temperature Controller, Model 818P.



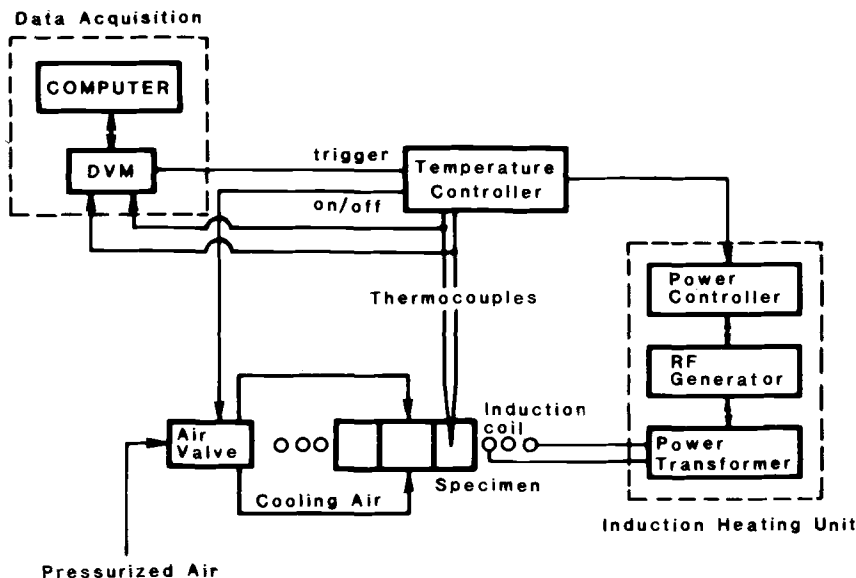


FIG. 2—Block diagram showing control system.

At 200 kHz the skin depth of IN-100 and MA-6000 nickel-base alloys is approximately 1.25 mm [17]. The concentrator coil was machined as to maintain constant coil-to-specimen spacing. This was achieved by using a mold having oversized dimensions of the specimen and 3.0-mm-diameter copper tubing. The air gap between the concentrator coil and specimen surface was 2 mm.

The specimens were positioned in the load coil using two nickel rods (Ni-200) 4 mm in diameter. The bottom one was fixed to an electrically insulated positioner, whereas the top rod was spring-loaded against a central polymeric crossbar (Fig. 3b) to allow free thermal expansion of the rods in the longitudinal direction. Two aluminum forced-air cooling manifolds (Figs. 3 and 4) with center holes to allow the support rods to pass through were used. The cooling manifolds were designed such that high-velocity air, exiting from a 0.5-mm gap about 2 mm from the specimen top (and bottom) surface, impinge and flow along the longitudinal surfaces of the specimen. Varying the airflow through an air valve, and thus through the two manifolds, controls the tensile strains encountered during the cool-down part of the cycle. The air flow is best controlled by the temperature controller, which opens or closes a solid-state relay that drives the power to the air valve. With this technique, the air flow is always synchronized to the temperature cycle and is repeatable. The cooling rate is controlled by the heater ballasting the air blast cooling.

Because of the rapid temperature transients and of the dependence on measured temperatures in the specimen stress-strain histories, extreme care in using thermocouples for temperature measurement and control is required in thermal fatigue testing. Several procedures were used in an effort to increase the accuracy and response time of thermocouple measurements.

To improve the reproducibility of the temperature history from one specimen to another and to increase the contact area between the junction and specimen, we drilled<sup>5</sup> 0.5-mm-diameter by 0.25-mm-deep holes along the specimen at locations shown in Fig. 5. Tem-

<sup>5</sup> Drilled using thin (0.4-mm) electro-discharged-machining (EDM) electrodes.

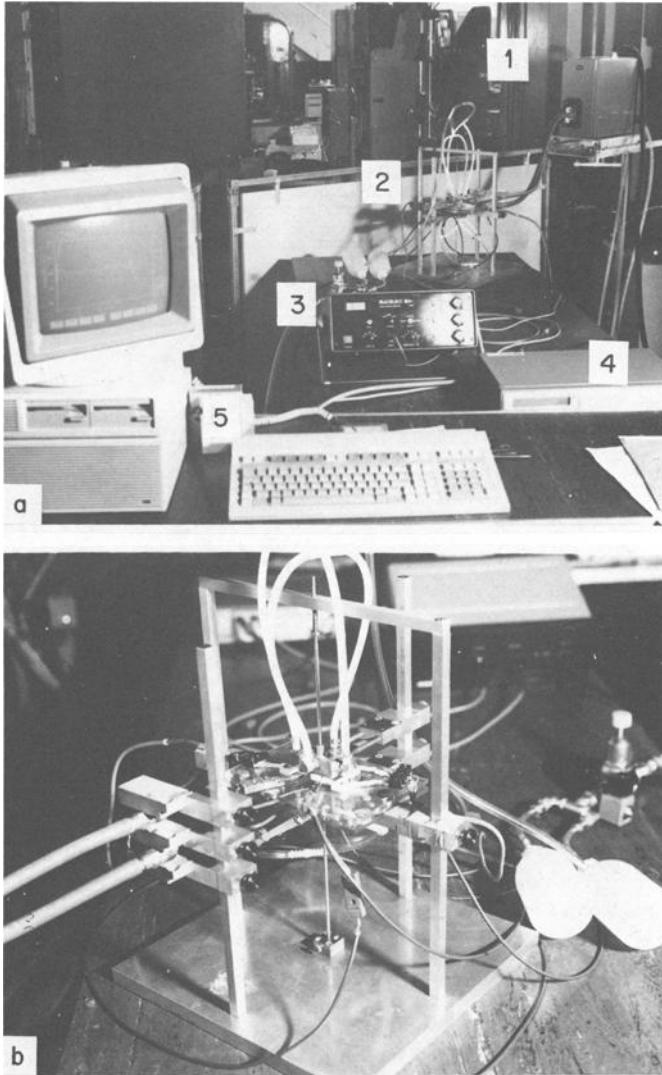


FIG. 3—(a) Overall view of experimental system: 1. induction unit, 2. thermal fatigue apparatus, 3. crack growth monitor, 4. DVM, 5. data acquisition system. (b) Top view of thermal fatigue apparatus.

perature disturbances at the thermocouple mass in the field were also minimized by using fine-gage chromel-alumel thermocouples (0.2-mm wire diameter) with 0.3-mm-diameter ball-junction which were spot-welded into the positioning holes. For calibration of the transients temperature loading, 18 chromel-alumel thermocouples (0.2-mm diameter) were used—their positions are shown in Fig. 5a. The actual tests were performed using six thermocouples positioned along the midspan plane (Fig. 5b). Due to the severity of the temperature range of interest (300 to 1050°C), the 0.2-mm-diameter chromel-alumel thermocouples could be used only for about 24 h before oxidation led to reading errors and

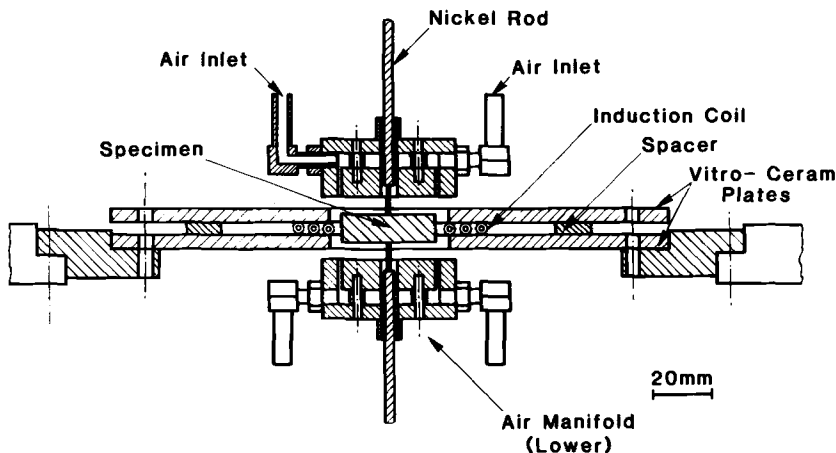


FIG. 4—Schematic of test apparatus for studying thermal fatigue in air.

embrittlement. Thus, for long-time feedback to the temperature controller, Pt/Pt-10% Rh thermocouples (0.2-mm-diameter wire) were used along with 0.3-mm-diameter chromel-alumel thermocouples.

The locations of the thermocouples on the specimen (Fig. 5) were chosen to ensure that the specimen midspan was heated uniformly. The specimens were assumed properly positioned in the focusing inductive coil when the maximum difference in thermocouple outputs located symmetrically about the midchord plane was less than 5°C. Spanwise centering (that is, vertical centering) was also accomplished by comparing the outputs of the thermocouples positioned symmetrically about the midspan plane and by adjusting the height of the specimen such that the maximum difference of outputs was less than 5°C. By comparing the outputs of the thermocouples positioned symmetrically along the midspan, we found that the specimens could be positioned vertically with  $\pm 0.25$ -mm accuracy with respect to the midspan plane.

For the particular specimen geometry and control system used, the testing apparatus was tuned to allow heating from 400 to 1000°C in 5 s with less than 2% overshoot in temperature and cooling from 1000 to 400°C in 15 s with no overshoot in temperature. The thermocouple outputs were digitized (both for calibration and testing) using a ten-channels programmable scanning-DVM (digital voltmeter) set to 10  $\mu$ V resolution and sampling rate<sup>6</sup> of 120 rdg/s. This results in a response time of the thermocouple/data acquisition system (used to record temperature history) better than 0.01 s.

#### *Crack Initiation and Growth Measurements*

Crack initiation and growth measurements during thermal fatigue have been performed mostly by optical measurements [9,10,18,19], either on double-edge wedge or tapered-disc specimens. The resolution claimed for optical measurements is in the range of 100 to 150  $\mu$ m, depending on the crack tips resolution under the thick oxide layer. Further, the measurements of number of cycle to initiate a crack and to grow to a certain size are always

<sup>6</sup> The maximum sampling rate is set by the maximum switching speed of the scanner, which is about 300/s.

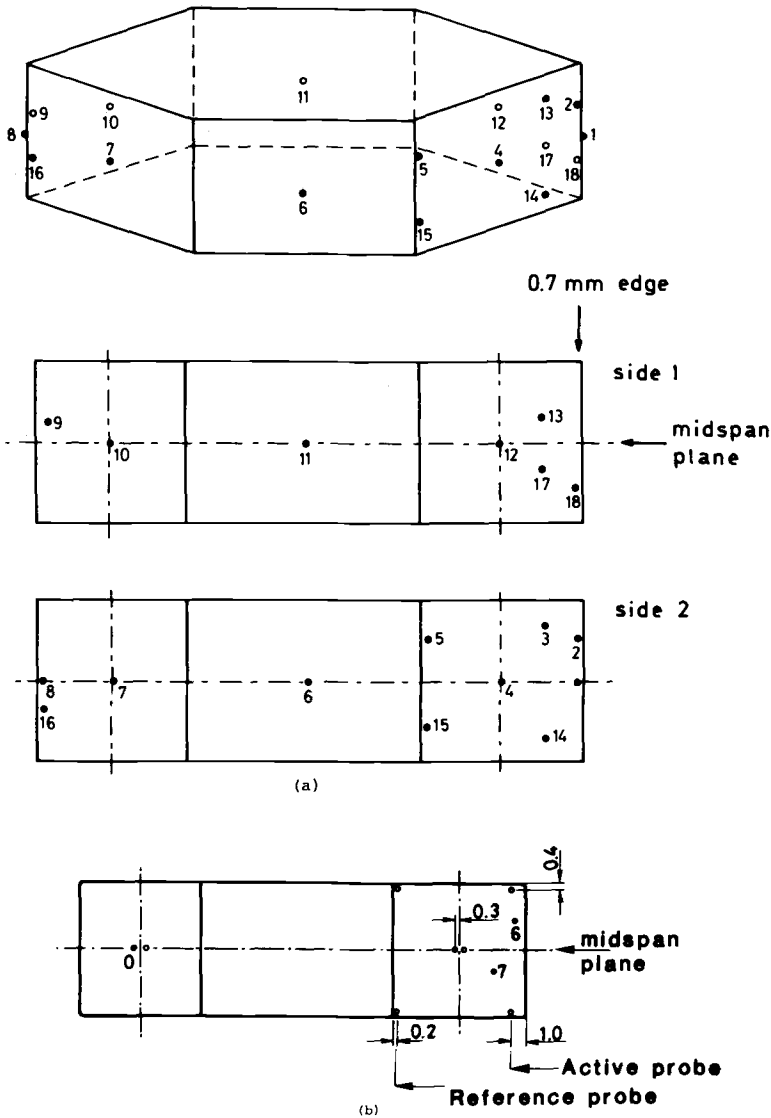


FIG. 5—Position of thermocouples and potential probes: (a) for temperature calibration; (b) for testing.

approximated since optical measurements are performed according to an inspection schedule [18] with a limited number of inspections (normally <20).

There have been a few attempts to measure crack initiation and growth in isothermal and thermal-mechanical fatigue conditions using the potential drop (PD) technique [4,15,20,21]. Although both direct current (d-c) and a-c versions of the PD method have been investigated, the former has found widespread acceptance because of its apparent simplicity. However, the d-c potential drop (DCPD) has several shortcomings with respect to detecting small surface cracks at high temperature [21-24]. The most significant prob-

lem with applying PD methods to thermal fatigue is caused by the temperature coefficient of resistance of nickel-base alloys, which is about  $5 \times 10^{-3} \Omega/\Omega\cdot K$ . This results in a 250% change in potential with a change in temperature of 500 K. In the following, a stable ACPD system with temperature changes is briefly described.<sup>7</sup> The full description of the system is presented elsewhere [25].

For the PD to give a direct measure of the impedance of the specimen, both current and frequency have to be maintained constant to a high degree. Whereas keeping the frequency constant is not a serious problem, the design of a constant a-c current source is far more complex than its d-c counterpart. Further, even if a constant current source can be obtained, variations in  $\mu_r$  and  $\rho$  with temperature are still present. To overcome the above problem, a compensation technique was employed. Potential drops across the specimen edge ( $V_{\text{edge}}$ ) and a reference ( $V_{\text{ref}}$ ), connected at a region of the specimen where the potential is less affected by crack growth, are measured separately. The two signals are electronically subtracted and the resulting signal ( $V_{\text{edge}} - V_{\text{ref}}$ ) can be correlated with crack length. The block diagram of the ACPD system is shown in Fig. 6.

The current source is provided by an a-c power amplifier (B) capable of supplying 2 A at frequencies up to 100 kHz with a voltage gain greater than  $10^5$ . A Wien bridge oscillator (A) provides the controlling input voltage ( $V_{\text{in}}$ ) for the power amplifier which is applied to its noninverting input. The frequency range of the oscillator can be selected from one of six preset values of 0.3, 1, 3, 10, 30, and 100 kHz, and can be maintained stable to better than 0.02%. The specimen is connected in series with a high-stability resistor ( $R_f$ ) across the output of the power amplifier. The voltage drop  $V_f$  ( $V_f = R_f \cdot I$ ) is used as the feedback voltage which is applied to the inverting input of the power amplifier. The amplifier thus amplifies the voltage difference between the two inputs (that is,  $V_{\text{in}} - V_f$ ). Since the amplification (that is, the gain) is very high, this voltage is very small and can be neglected. Thus  $I$ , the current through the specimen which also flows through the feedback resistor  $R_f$ , is proportional to the voltage input  $V_{\text{in}}$  from the oscillator. Since  $R_f$  used is 0.1  $\Omega$ ,  $V_{\text{in}}$  can be varied from 0 to 200 mV to give a constant current of 0 to 2 A. An important advantage of the current feedback technique is that the magnitude of the current  $I$  is maintained constant to better than 0.1% irrespective of the impedance of the test specimen which can change during the test period. Further, it maximizes the high main frequency rejection (50 Hz) and low third-harmonic distortion and these two characteristics have been shown to be highly desirable for ACPD applications [24].

The output signals from the specimen are fed into a dual-inputs, low-impedance, single-winding<sup>8</sup> matching transformer in series with an a-c coupled signal amplifier. The resulting output (subtracted signals) from the transformer is fed into a differential a-c amplifier with adjustable gain between 1 and 1000. The first amplification stage is a-c coupled to a non-inverting amplifier with a gain of  $\approx 7$  through a 10- $\mu\text{F}$  capacitor. Because high linearity at high frequencies and a high dynamic reserve [defined as  $\text{DR} = \log_{10} (V_{\text{noise}}/V_{\text{signal}})$ ] are essential for detecting small surface cracks, synchronous switching was used for rectification.

Rectification by synchronous switching was achieved using two analog complementary metal-oxide semiconductor (CMOS) switches. The output of the oscillator (A) is fed into a phase-locked loop (PLL) system and a voltage-controlled phase shifter to produce two switching signals  $\Phi_1$  and  $\Phi_2 + 90^\circ\text{C}$ , as shown in Fig. 6. These two signals drive the identical CMOS switches. The output from Switch 2, after amplification and smoothing, is fed into

<sup>7</sup> The ACPD system described here is a modified CGM5 crack growth monitor and is a trademark of MATELECT Ltd., 33 Bedford Gardens, London W8-7EF, U.K.

<sup>8</sup> It was later found that a dual-input, double-winding matching transformer provides better long-time stability than that of the single-winding transformer used in this study.

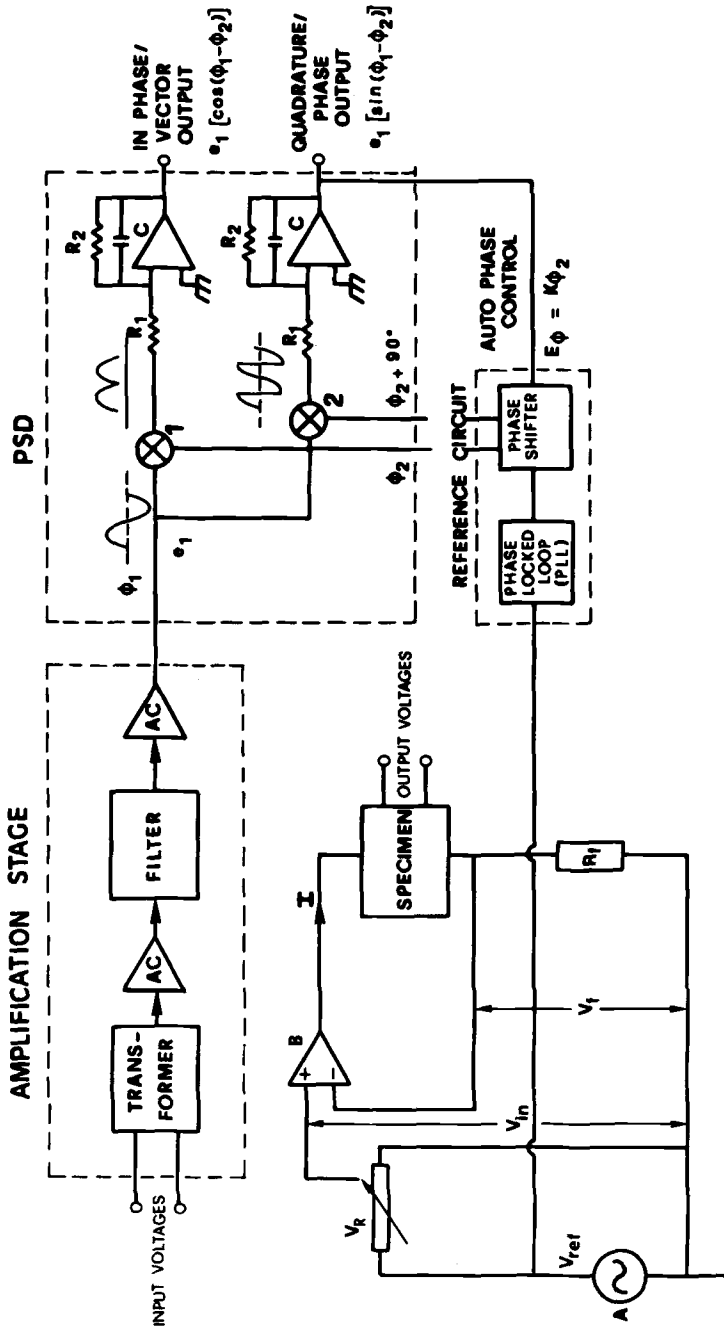


FIG. 6—Block diagrams of ACPD system.

the phase-shifter control input. This feedback loop shifts the phases of the switching signals to make the output of Switch 2 almost zero, that is, exactly in quadrature with the phase of the incoming ACPD signal ( $\Phi_1$ ). The output of Switch 1 is, therefore, in phase with  $\Phi_1$ . Finally, this output is amplified, smoothed by a variable stepped filter, and digitized by a programmable scanning DVM set to 10- $\mu$ V resolution and sampling rate of 120 rdg/s.

For the initial calibration, a double-edge wedge specimen of Nimonic 80 was used. Saw-cuts of 0.5 and 1 mm deep and 0.075 mm wide were used to simulate crack extension. The current and sensing leads were connected as shown in Fig. 5. The current and frequency were varied between 0.5 to 2 A and 10 to 100 kHz. The gain was adjusted to provide sufficient dynamic range and reserve. For the actual specimen geometry and testing conditions it was found that the optimum operating parameters were 1.2 A, 30 kHz, and 70 dB of gain. With these parameters the output for a 1-mm crack is about 700 mV, which results in a resolution better than 10  $\mu$ m (that is, total crack length). Further, the output was found to increase linearly with increasing crack depth.

### Thermal Fatigue Histories

To measure the performance of the ACPD system in detecting crack initiation and growth, the system was used to study the effect of strain histories on surface oxidation and cracking. Two thermal histories were extensively studied both with minimum and maximum temperatures of 400 and 1000°C, and a 60 s hold at 1000°C. A limited number of tests of a third thermal history, denoted FHS (5 s heating, 60 s hold time, and 15 s cooling) were also performed. Figure 7 shows the three cycle types which are labeled FHF (5 s heating, 60 s hold time, and 15 s cooling), SHF (60 s heating, 60 s hold time, and 15 s cooling), and FHS. Here, the temperature histories of the midspan plane (Curve 0) and at two locations (Curves 6 and 7) taken on both sides of the midspan plane (Fig. 5b) are shown. The rapid heating of FHF and slow heating of SHF were included to examine how the magnitude of the compressive edge strains encountered during specimen heat-up affect crack initiation. The fast cooling of FHF and the slow cooling of FHS histories were included to show the effect of tensile strains on thermal fatigue cracking.

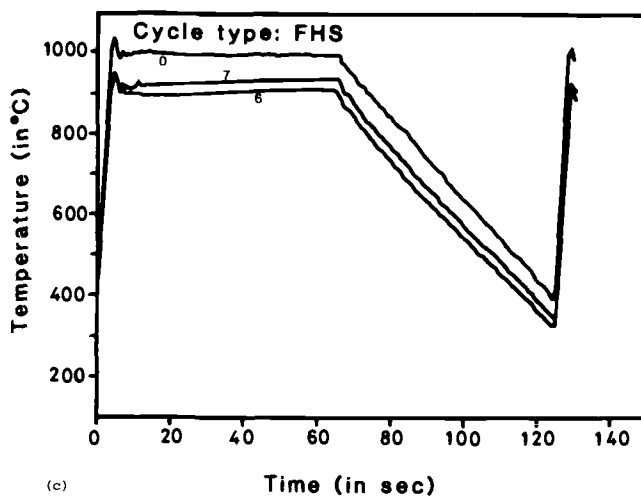
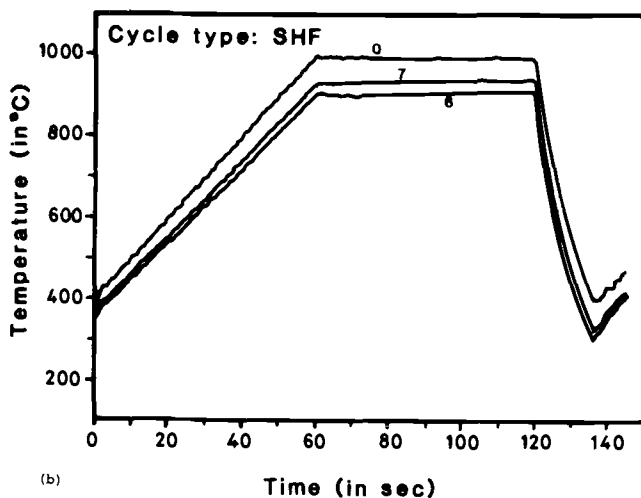
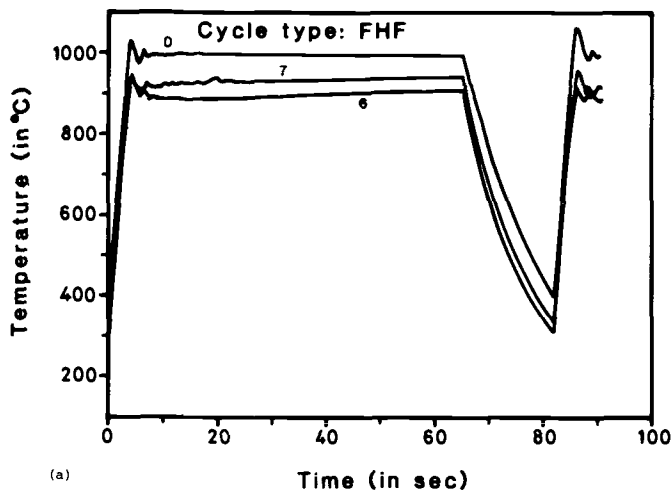
All three thermal histories were investigated using IN-100, whereas only FHF was studied using MA-6000. The latter alloy was tested to study the effect of transverse and longitudinal cracking on the ACPD responses, with fibers (grain structure) either parallel or perpendicular to the midspan plane.

The elastic and elasto-plastic stress-strain histories of the test specimens were determined using the finite-element program ABAQUS [26]. Because of the symmetry, only one-half of the wedge specimen was modeled. The element-type was a 20-node brick element with 27 Gaussian integration points. The model consists of 60 elements (Fig. 8), with a total of 428 nodes and 279 suppressed degrees of freedom for the thermal analyses (out of 428) and 257 suppressed degrees of freedom for the stress-strain analyses (out of 2568).

The calculations were carried out only for IN-100 because the directional properties (elastic modulus and tensile properties) of MA-6000 were not all available. The mechanical and physical properties of the alloy were obtained from Refs 27 and 28<sup>9</sup> and are reproduced in Tables 2 and 3. The transient temperature loadings were determined from thermocouple

<sup>9</sup> The third source of this information was M. Nazmy of Brown, Boveri & Company (BBC), private communication, 1987.

FIG. 7—Temperature histories of double-edge wedge specimens. Position of thermocouples is shown in Fig. 5.





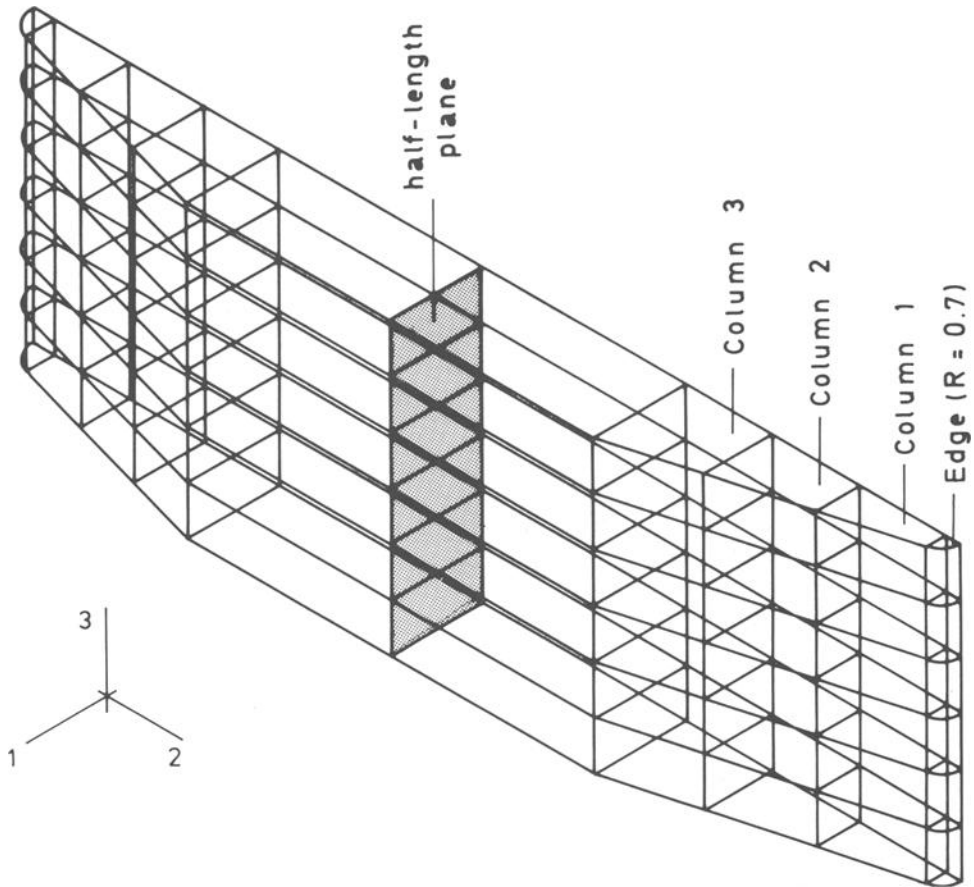


FIG. 8—Finite-element model of the double-edge wedge specimen.

data according to the procedure described in a previous section. The temperature distributions over the entire surface of the specimen were obtained by cross-plotting the thermocouple outputs (and by using interpolated least-squares best-fit parabola between them) and by using the fact that the temperature distributions were almost symmetrical with respect to midchord and midspan planes. All the details concerning the finite-element model, the methods of analysis, and the inputs for the analyses, are given elsewhere [29].

The results of the elastic and elasto-plastic analyses are shown in Figs. 9 and 10, where the stress-strain histories at critical locations for FHF, SHF, and FHS are presented, respectively. Note that for the elastic analyses, the loops are caused by the changing thermal strains in the bulk relative to the periphery and not by the material hysteresis. The strain ranges and mean stress levels for the elastic analyses are about 0.50%, 0.40%, and 0.38%, and  $-270$ ,  $+150$ , and  $-305$  MPa for FHF, SHF, and FHS, respectively. Figure 10 shows the hysteresis loops for the elastic-plastic analyses. As can be seen, ratchetting plastic strain caused the hysteresis loops to shift under cycling, with FHF experiencing the greatest and SHF the least shifting. The long arrows indicate the shifting direction of the hysteresis loops. Comparisons of Figs. 9a with 10a and 9b with 10b show that the stress and strain

TABLE 3—*IN-100 physical properties.*

Temperature, °C	Modulus of Elasticity, N/mm <sup>2</sup>	Mean Coefficient of Thermal Expansion <sup>a</sup> m/m°C	Specific Heat, J/kg	Thermal Conductivity, W/m·K	Poisson Ratio
25	$215 \times 10^3$	...	380	...	0.314
260	$203 \times 10^3$	$13.0 \times 10^{-6}$	...	...	0.317
316	$199 \times 10^3$	$13.1 \times 10^{-6}$	436	...	0.318
371	$197 \times 10^3$	$13.3 \times 10^{-6}$	...	...	...
427	$194 \times 10^3$	$13.5 \times 10^{-6}$	458	15.5	0.322
482	$191 \times 10^3$	$13.7 \times 10^{-6}$	...	...	...
538	$187 \times 10^3$	$13.9 \times 10^{-6}$	480	17.3	0.324
593	$184 \times 10^3$	$14.0 \times 10^{-6}$	...	...	...
649	$180 \times 10^3$	$14.4 \times 10^{-6}$	500	18.9	0.329
704	$177 \times 10^3$	$14.6 \times 10^{-6}$	...	...	...
760	$173 \times 10^3$	$14.9 \times 10^{-6}$	525	21.7	0.333
846	$168 \times 10^3$	$15.4 \times 10^{-6}$	...	...	...
871	$162 \times 10^3$	$15.8 \times 10^{-6}$	545	25.2	0.341
927	$157 \times 10^3$	$16.4 \times 10^{-6}$	...	...	...
962	$151 \times 10^3$	$16.7 \times 10^{-6}$	585	28.8	0.351
1038	$145 \times 10^3$	$17.5 \times 10^{-6}$	...	...	...
1093	$139 \times 10^3$	$18.2 \times 10^{-6}$	605	32.5	0.362

<sup>a</sup> From room temperature to indicated temperature.

ranges from the elastic analyses are within 10% of those computed from the elastic-plastic analyses. However, the mean effective stresses and strains are significantly different. It is important to note that the peak compressive strains ranked (in increasing order) as FHF, FHS, SHF, whereas the peak tensile strains ranked as SHF, FHF, and FHS.

## Results and Discussion

Figure 11 shows examples of temperature and potential histories which took place within one cycle for FHF, SHF, and FHS, respectively. As can be seen, the potential and temperature histories look similar, that is, they show a decrease, a plateau (hold time), and an increase. It thus seems that the dual inputs transformer is not capable of eliminating all the effect of changing temperatures. However, a close look at the changes of potential with time shows that the peaks in the potential histories coincide with the peaks in the stress-strain histories rather than with the temperature. This can be illustrated for FHF for example, by noting that the stress-strain peak in compression occurred after about 4.2 s and that the peak potential also took place after 4.2 s. Recalling that the peak temperature is reached after 5 s (Figs. 7 and 11), one concludes that the ACPD system does fully compensate the changes in temperature and provides a sensitive indication of the strain histories experienced by the specimen.

The performance of the ACPD system in monitoring crack initiation was assessed by plotting the peak potential, the potential after 30-s hold time at 1000°C (mid-hold), and the average value of the plateau, as a function of the number of cycles. Figure 12 plots the average value of the plateau with number of cycles for FHF, SHF, and FHS cycling, respectively. Changes of peak potential and potential at mid-hold are not presented because they show essentially the same information as their corresponding ones in Fig. 12.

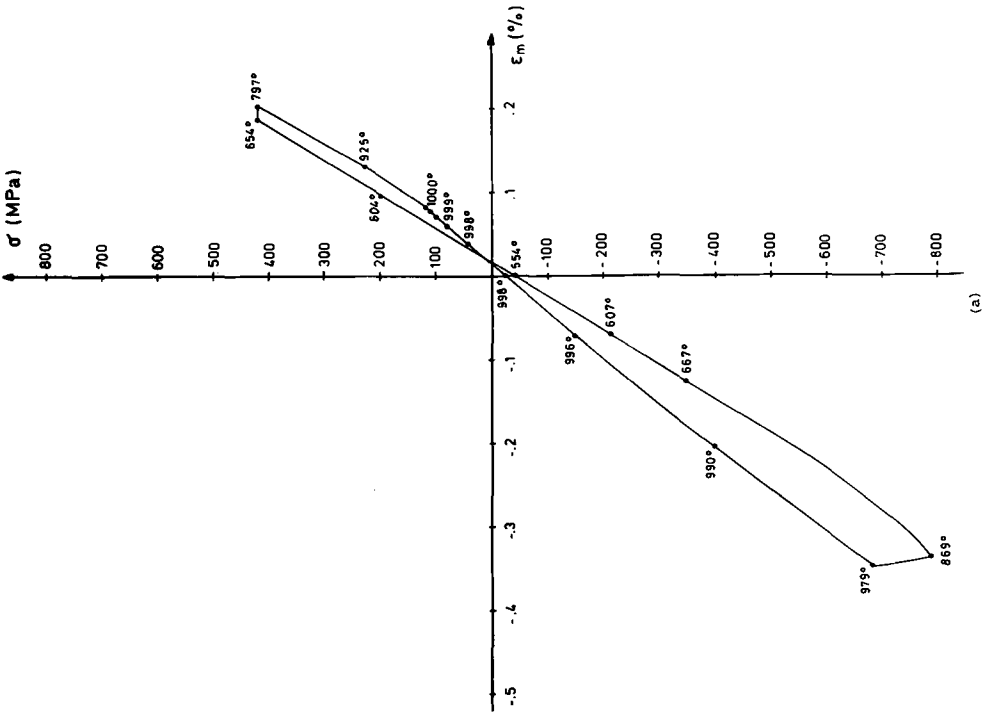
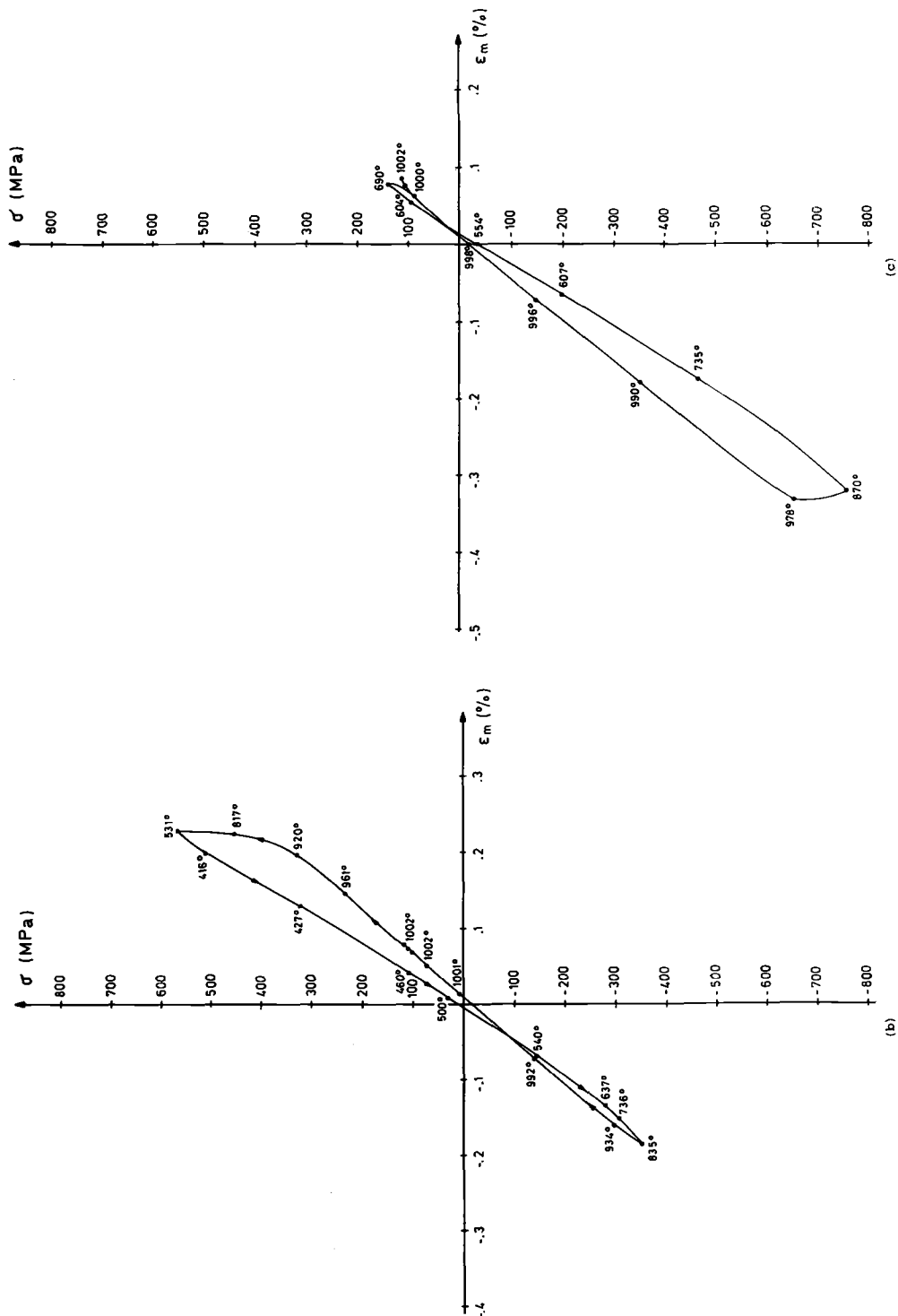


FIG. 9—Stress-strain histories at critical locations determined from thermoelastic analyses: (a) FHF; (b) SHF; and (c) FHS.



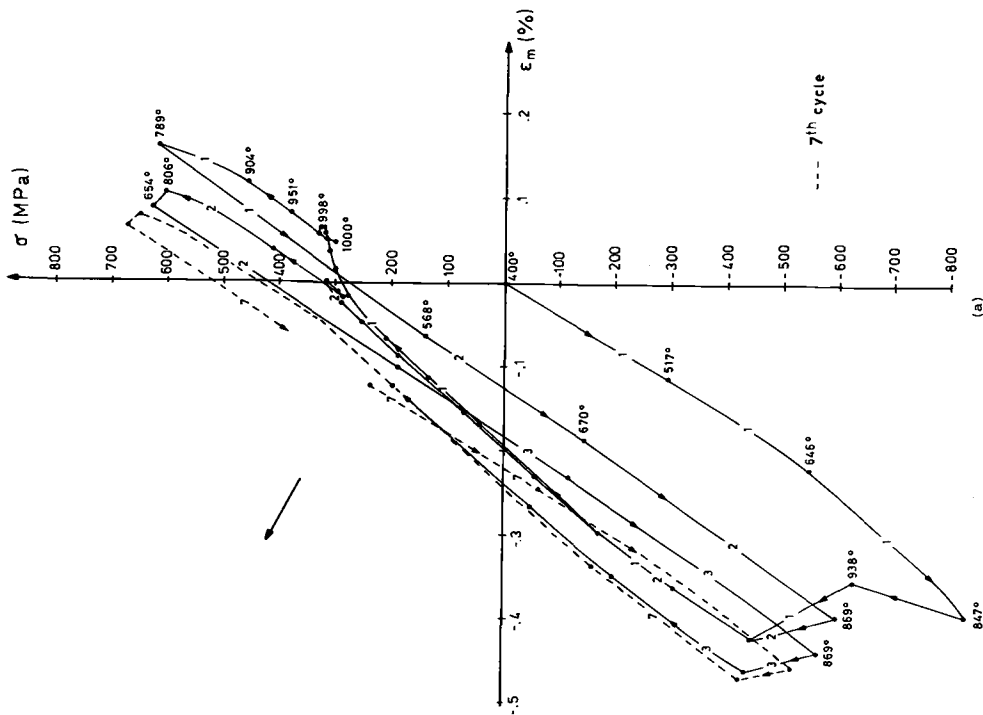
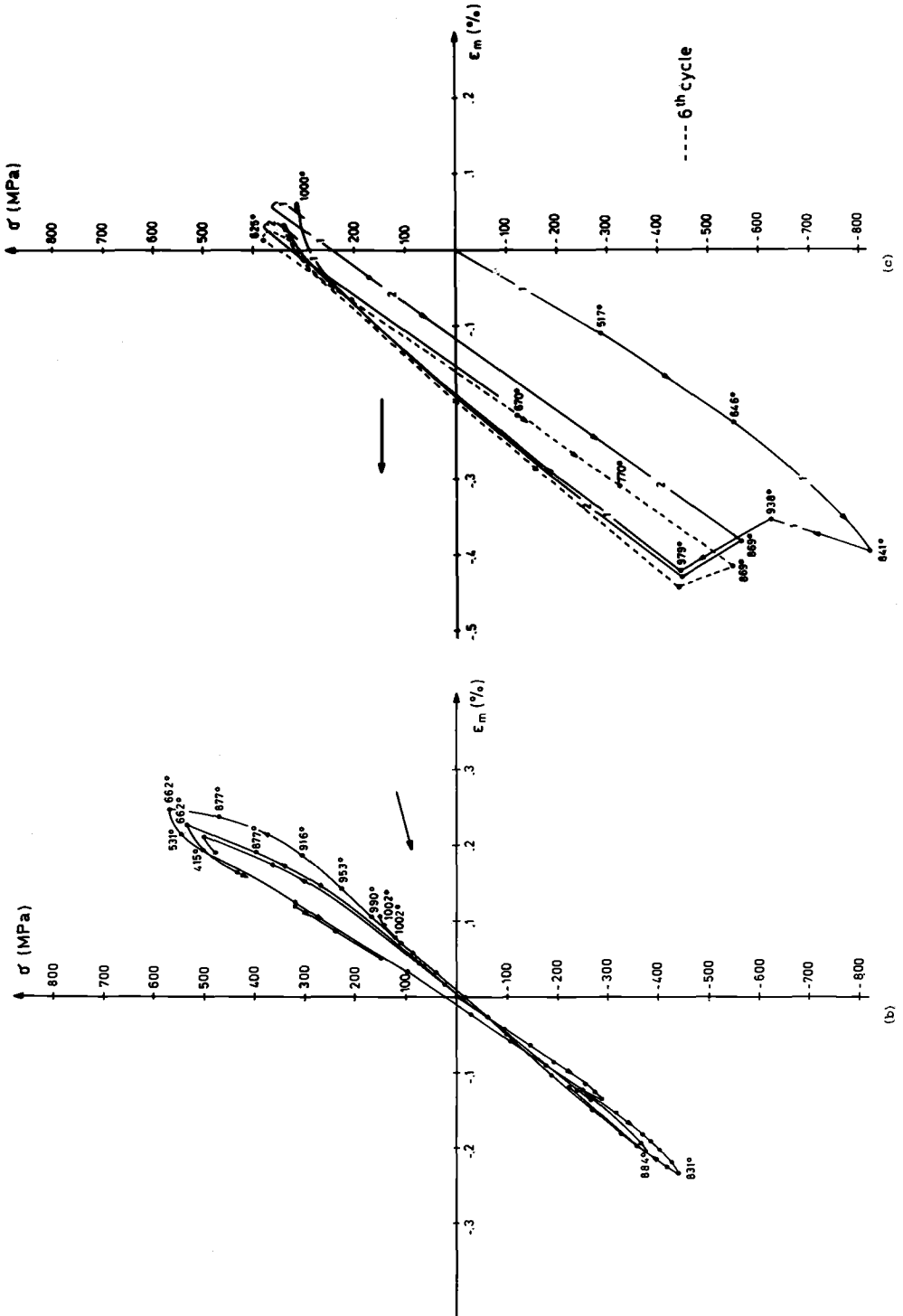


FIG. 10—Stress-strain histories at critical locations determined from thermoelastic-plastic analyses: (a) FHF; (b) SHF; and (c) FHS.



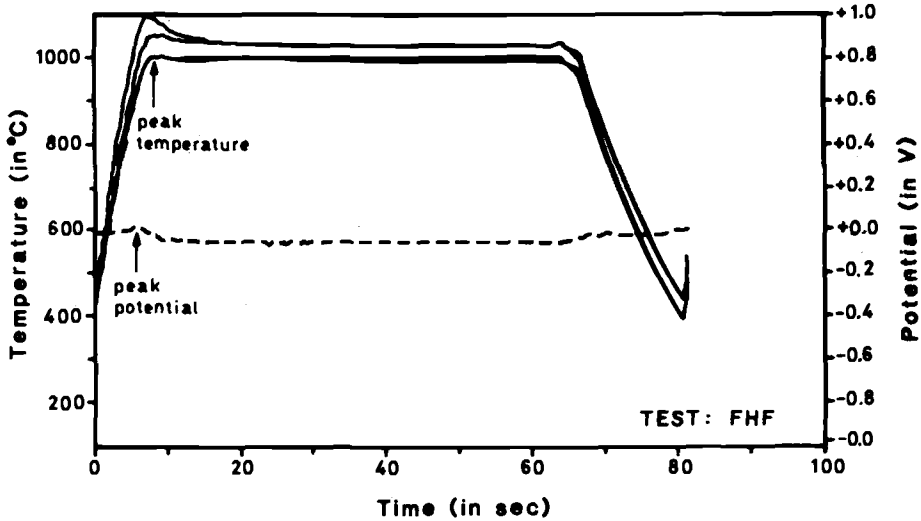


FIG. 11—Example of temperature and potential drop histories within one cycle for IN-100 and FHF cycling.

The following comments can be made concerning the results displayed in Fig. 12. First, it can be seen that there are three regions (or stages) in the potential versus  $N$  curves: An initial stage which corresponds to the thermal shake-down of the specimen (that is, a period in which the specimen, the connecting rods, and the potential probes achieved thermal stability); a second stage during which the potential shows a continuous and smooth increase (or decrease), and a third stage in which the potential significantly departs from Stage II. The final stage characterizes crack growth, whereas the transition between Stages II and III corresponds to the initiation of one or more microcracks. This conclusion was substantiated by microscopic observations which showed microcracking when Stage III was present and no crack if this stage was not observed on the potential versus  $N$  curves.

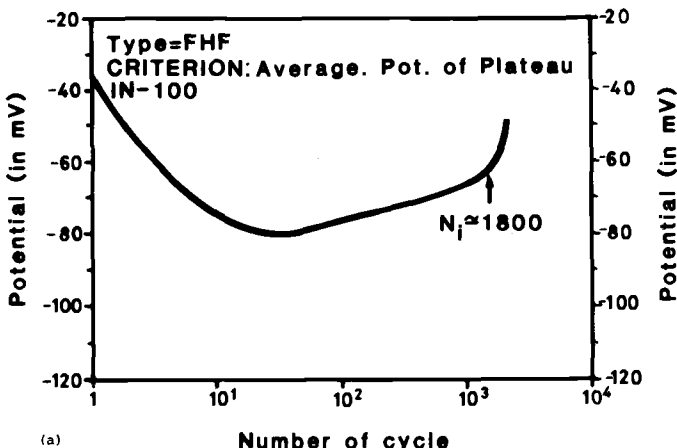


FIG. 12—Potential drop as a function of number of thermal cycle: (a) FHF; (b) SHF; (c) FHS; and (d) MA-6000 FHF.

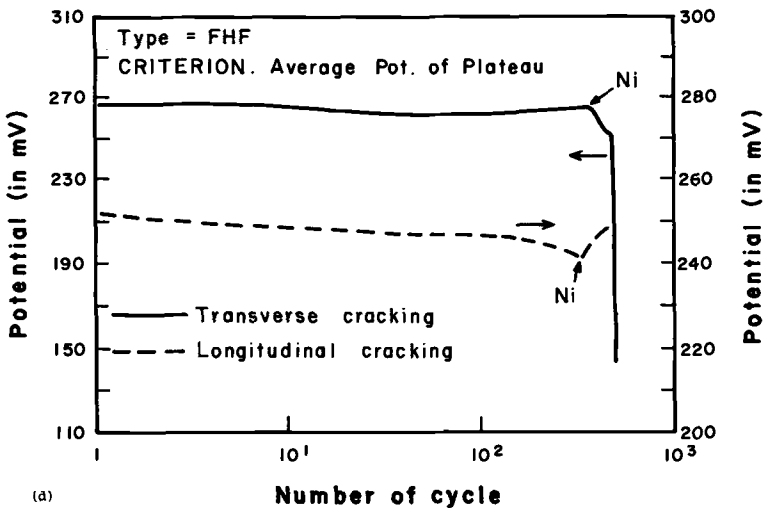
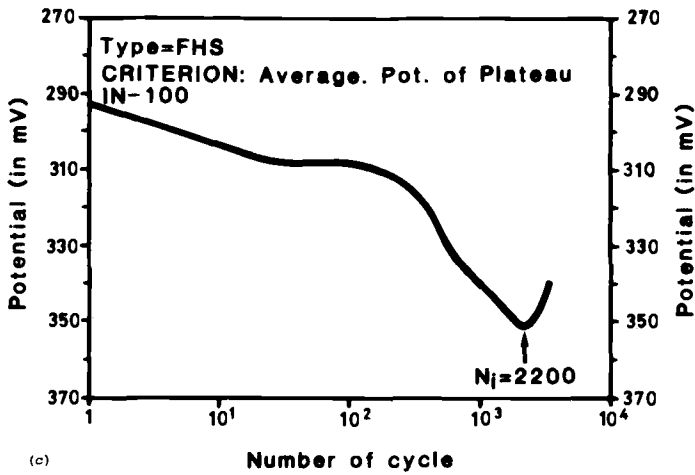
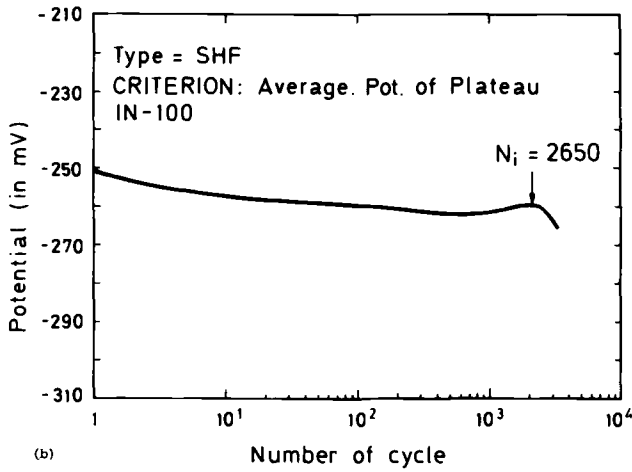


FIG. 12—Continued.



As indicated in Fig. 12, Stage II can either continuously decrease (SHF and FHS of IN-100, FHF of MA-6000) or increase (FHF of IN-100) with increasing number of cycles. This implies that the changes of the reference probes ( $V_{ref}$ ) can be greater or lower than the changes of the active probes ( $V_{edge}$ ). The explanation to these respective changes in potential were again found through microscopic observations. It was observed that when Stage II showed continuous decrease with increasing number of cycles, cracks were only found along the 1.0-mm edge radius (leading edge), whereas cracks at the 0.7-mm edge (trailing edge) were observed if the potential continuously increases. This illustrates that the use of two sets of probes does compensate for the changing temperatures, and allows the sensing of cracks along the opposite edge.

It is worth noting that the observed microcracks in IN-100 were subsurface ones (Fig. 13) with final length (after 3000 cycles) of about 100 to 150  $\mu\text{m}$ . This is in agreement with the finite-element analyses which indicate that the stresses and strains were higher below the surface than at the surface [29]. Further, this observation clearly demonstrates that the ACPD system provides a much more reliable measurement of number of cycles to crack initiation than conventional optical inspections, which obviously fail to pick up the presence of subsurface cracks.

Given the fact that the transition between Stages II and III (the initiation life) occurred near 2000 cycles, it appears that the average crack growth rate can be estimated<sup>10</sup> to be of the order of  $1.0 \times 10^{-4}$  mm/cycle ( $\approx 0.1$   $\mu\text{m}$ /cycle). This is two orders of magnitude lower than the capability of optical measurements [18] in thermal fatigue testing. Of course, for MA-6000, a more brittle material, faster crack growth rates were measured [16].

It is important to emphasize that the ACPD response is very sensitive to the type of microcracks. Hence, for a given thermal history (for example, FHF), transverse cracking led to a sharp but steady decrease in potential (produced by numerous microcracks on the 1.0-mm edge radius), whereas longitudinal microcracks gave rise to a sharp but fluctuating increase of potential (Fig. 12d). These differences in ACPD responses can be attributed to the fact that transverse microcracks add resistances in series with the actual resistance (that is, the resistivity of the material) to the passage of current through the specimen. Thus the total resistance of the 1.0-mm edge radius increases and the net potential ( $V_{edge} - V_{ref}$ ) decreases. On the other hand, longitudinal cracks add parallel resistances to the current with the net result that the total resistance at the 1.0-mm edge radius decreases, leading to an overall increase of the potential. In spite of these results, more work is required to quantify further the changes of potential with types of microcrack. In particular, the problem of cracks at both edges (although not observed in this study) needs to be addressed. In this respect, the use of two sets of probes (working and reference probes), one at each edge of the specimen, should provide valuable information.

Figures 12a–12c show that the number of cycle to crack initiation in IN-100 increases in the following order: FHF, FHS, and SHF. This does not agree with the intuitive argument that the higher the peak tensile stress, the faster should be crack initiation and growth. In fact, this ranking is matched with the ranking of the peak compressive strains. In other words, the lower the peak compressive strain, the shorter the crack initiation life. Thus, it can be concluded that although the peak tensile stresses are likely to be important for crack growth, it is the peak compressive strains encountered during heat-up (and the associated high-temperature damage) that determined the crack initiation life. Holmes and McClintock [5,6,30] also reached a similar conclusion in thermal fatigue testing of monocrystalline René N4.

<sup>10</sup> This is true, assuming that the changes in potential with increasing crack lengths are linear and that the cracks grow parallel to the midspan plane.

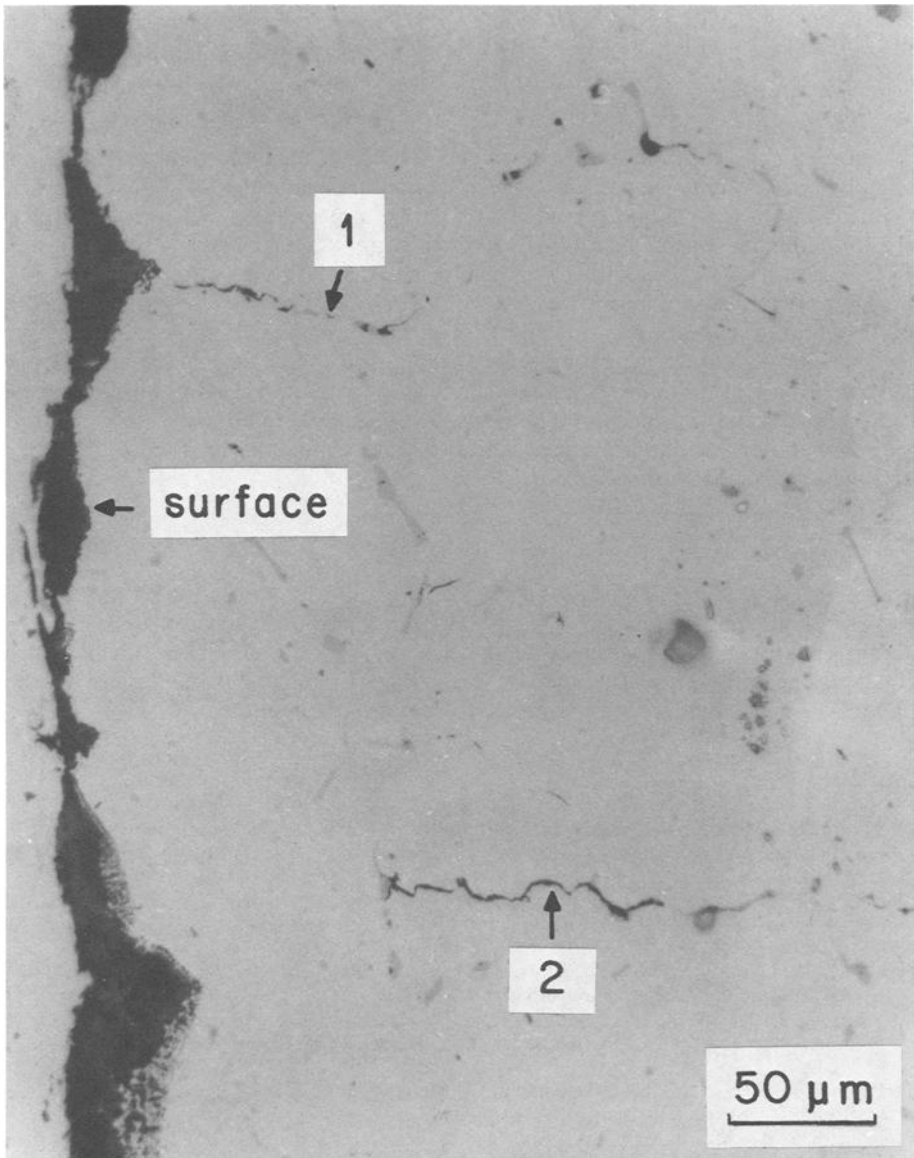


FIG. 13—Subsurface cracks observed in IN-100 (FHF and 3000 cycles).

After completing the tests (that is, after 3000 cycles), the specimens were nickel-plated and then polished parallel to the edge faces down to the midspan plane. Photographs of the surface were taken every 150 to 200  $\mu\text{m}$ . The compressive strains encountered during specimen heat-up produced degradation of the surface in the form of scalloping (Fig. 13). Scalloping was found to increase with increasing peak compressive strain. The slow heat-up (60 s) of SHF produced little surface degradation, and a thick but uniform layer of oxide was formed [31]. Obviously, the oxidation behavior of IN-100 is greatly affected by strain-

ing, which is consistent with other reported data [12,13,30]. The synergistic effect of thermal cycling and oxidation is discussed in detail elsewhere [31].

### Conclusions

Based on a compensation technique, an ACPD system for monitoring crack initiation and growth has been developed and used in thermal fatigue testing of double-edge wedge specimens. The digital output provided an accurate measurement of number of cycles to crack initiation and was unaffected by specimen current and changing temperatures. The ACPD response was also shown to be highly sensitive to the type of microcracks. The inherent sensitivity and stability of the ACPD system could not be fully exploited because the PD output is affected by strain and by the presence of cracks at both edges. Nevertheless, it is believed that the use of two sets of probes, one at each edge of the specimen, will lead to an even better characterization of crack growth in thermal fatigue testing. Finally, the experimental results on IN-100 alloy showed that peak compressive strains encountered on specimen heat-up are more critical to crack initiation and surface degradation than total stress or strain ranges.

### Acknowledgments

It is a pleasure to acknowledge the support for this work provided by the Deutsche Volkswagen Foundation. We greatly appreciate the support of Brown, Boveri, and Company (BBC) through the donation of the materials, and for the supplying of relevant technical data. The authors are also indebted to Dr. B. A. Unvala (Imperial College, London, U.K.) for his help, enlightening comments and fruitful discussions.

### References

- [1] Thulin, E. D., Howe, D. C., and Singer, I. D., "Energy Efficient Engine High Performance Turbine Detailed Design Report," NASA Report CR-165608, Pratt & Whitney Aircraft Group, East Hartford, CT, 1982.
- [2] McKnight, R. L., Laffen, J. H., and Spamer, G. T., "Turbine Blade Tip Durality Analysis," NASA Report CR-165268, General Electric Co., Aircraft Engine Business Group, Cincinnati, OH, 1981.
- [3] Larsen, J. M. and Nicholas, T. in *Engine Cyclic Durability by Analysis and Testing, Proceedings, AGARD Conference, Lisse, The Netherlands, 1984*.
- [4] Remy, L., Reger, M., Reuchet, M., and Rezai-Aria, F. in *High Temperature Alloys for Gas Turbine Applications—1982*, Brunetaud et al., Eds., Riedel, Dordrecht, The Netherlands, 1982, pp. 619–632.
- [5] Holmes, J. W., doctoral thesis, Department of Materials Science and Engineering, Massachusetts Institute of Technology, Cambridge, MA, Sept. 1986.
- [6] Holmes, J. W., McClintock, F. A., and O'Hara, K. S. in *Low Cycle Fatigue: Directions for the Future, ASTM STP 942*, Solomon, Halford, Kalsand, and Leis, Eds., American Society for Testing and Materials, Philadelphia, 1988, pp. 672–691.
- [7] Saunders, S. R. J., Hossain, M. K., and Ferguson, J. M. in *High Temperature Alloys for Gas Turbine Applications—1982*, Brunetaud et al., Eds., Riedel, Dordrecht, The Netherlands, 1982, pp. 177–206.
- [8] *Hot Corrosion Task Force for ASTM Gas Turbine Panel: Round Robin Test*, American Society for Testing and Materials, Philadelphia, PA, 1970.
- [9] Rezai-Aria, F., Rémy, L., Herman, C., and Dambrine, B. in *Mechanical Behaviour of Materials IV*, J. Carlsson and N. G. Ohlson, Eds., Pergamon Press, Oxford, Vol. 1, 1984, pp. 247–253.
- [10] Howes, M. A. H. in *Thermal Fatigue of Materials and Components, ASTM STP 612*, D. A. Spera and D. F. Mowbray, Eds., American Society for Testing and Materials, Philadelphia, 1976, pp. 86–105.

- [11] Bizon, P. and Spera, D. A. in *Thermal Fatigue of Materials and Components*, ASTM STP 612, D. A. Spera and D. F. Mowbray, Eds., American Society for Testing Materials, Philadelphia, 1976, pp. 106–122.
- [12] Tiainen, T., Sintonen, P., Kethunen, P. in *High Temperature Alloys for Gas Turbines and Other Applications*, 1986, W. Betz et al., Eds., Reidel, Dordrecht, The Netherlands, 1986, pp. 1127–1140.
- [13] Kang, C. T., Pettit, F. S., and Birks, N., *Metallurgical Transactions*, Vol. 18A, 1987, pp. 1785–1803.
- [14] Holmes, J. W. and McClintock, F. A. in *Scripta Metallurgica*, Vol. 17, 1983, pp. 1365–1370.
- [15] Marchand, N. J. and Pelloux, R. M., *Journal of Testing and Evaluation*, Vol. 14, 1986, pp. 303–311.
- [16] Dorner, W., “Eine Untersuchung der Risswachstumsmechanismen bei Thermischer Ermüdung,” Diplomarbeit (senior thesis), WWI-Universität Erlangen-Nürnberg, West Germany, Oct. 1987.
- [17] Simpson, J. and Davies, P. in *Induction Heating Handbook*, Chapter 12, McGraw Hill, London, 1979.
- [18] Woodford, D. A. and Mowbray, D. F., *Materials Science and Engineering*, Vol. 16, 1974, pp. 5–43.
- [19] Glenn, R. E. J. in *High Temperature Materials in Gas Turbines*, P. R. Sahm and M. O. Speidel, Eds., Elsevier Science, London, 1974, pp. 257–277.
- [20] Skelton, R. P. in *Mechanical Behavior and Nuclear Application of Stainless Steels at Elevated Temperature*, Metals Society, London, 1981, pp. 19/1–19/12.
- [21] Verpoest, I., Aernoudt, E., Deruythere, A., and Neyrinck, M., *Fatigue of Engineering Materials and Structures*, Vol. 3, 1981, pp. 203–217.
- [22] Druce, C. D. and Booth, J. F. in *The Measurement of Crack Length and Shape during Fracture and Fatigue*, C. J. Beevers, Ed., Engineering Materials Advisory Services, Ltd., West Midlands, U.K., 1980, pp. 57–79.
- [23] Krompholz, K., Grossen, E. D., Ewart, K., and Moritz, E. in *Advances in Crack Length Measurement*, C. J. Beevers, Ed., Engineering Materials Advisory Services, Ltd., West Midlands, U.K., 1982, pp. 231–251.
- [24] Venkatasubramanian, T. and Unvala, B. A., *Journal of Physical Science and Instrumentation*, Vol. 17, 1984, pp. 765–771.
- [25] Marchand, N. J., Unvala, B. A., and Ilschner, B., “An Improved AC Potential Drop System for the Measurement of Short Cracks at Elevated Temperature,” to be published.
- [26] ABAQUS (User's Manual—Version 4.5), Hibbitt, Karlsson, and Sorensen Inc., Providence, RI, July 1985.
- [27] *Metals Handbook. Properties and Selection: Stainless Steels, Tool Materials, and Special Purpose Metals*, Vol. 3, 9th ed., American Society for Metals, 1980, pp. 242–245.
- [28] *Aerospace Structural Metals Handbook*, Vol. 5, 1982 ed., section code 4212, pp. 1–66. Edited by Department of Defense, Army Materials and Structural Mechanics Research Center, Watertown, MA, 02172. Belfour Stulen Pub.
- [29] Marchand, N. J., Dorner, W., and Ilschner, B., “Elastic-Plastic Finite Element Analyses of Thermally Cycled Double-Edge Wedge Specimens,” *Inelastic Behaviour of Solids: Models and Utilization*, G. Cailletaud et al., Ed., MECAMAT, Besançon, France, 1988, pp. 427–444.
- [30] Holmes, J. W. and McClintock, F. A., “The Chemical and Mechanical Processes of Thermal Fatigue Degradation of an Aluminide Coating,” accepted for publication in the *Metallurgical Transactions* (in press).
- [31] Marchand, N. J., Dorner, W., and Ilschner, B., “The Mechanical Processes of Thermal Fatigue Degradation in IN-100 Superalloy,” *Proceedings of the Conference on Constitutive Laws of Plastic Deformation and Fracture*, A. S. Krausz et al., Eds., Martinus Nijhoff, Amsterdam, The Netherlands, in press.

William A. Troha,<sup>1</sup> Theodore Nicholas,<sup>2</sup> and Allen F. Grandt, Jr.<sup>3</sup>

## Observations of Three-Dimensional Surface Flaw Geometries During Fatigue Crack Growth in PMMA

---

**REFERENCE:** Troha, W. A., Nicholas, T., and Grandt, A. F., Jr., "Observations of Three-Dimensional Surface Flaw Geometries During Fatigue Crack Growth in PMMA," *Surface-Crack Growth: Models, Experiments, and Structures, ASTM STP 1060*, W. G. Reuter, J. H. Underwood, and J. C. Newman, Jr., Eds., American Society for Testing and Materials, Philadelphia, 1990, pp. 260–286.

**ABSTRACT:** A series of fatigue crack growth experiments was conducted on a transparent polymer (PMMA) using a surface flaw geometry in bending. A Newton interferometric technique was used to measure crack opening displacements and closure for four different loading histories. Results are presented for conditions of constant applied stress-intensity factor along the crack face free surface, at the crack tip in the depth direction, for constant applied load range, and for a block loading sequence.

Three distinct crack geometries are identified and are found to be a function of crack size. The crack opening displacement patterns are found to be strongly influenced by the formation of a void internal to the crack. Three distinct closure loads are identified and measured for surface flaws of various crack depths and aspect ratios. The various closure loads are used to define effective stress-intensity ranges. Life predictions, crack growth rates, and aspect ratios are used to evaluate the applicability of the various closure loads at different locations. It is found that the same closure load does not determine the best value of effective stress intensity at all points along the crack tip in the surface flaw geometry.

**KEY WORDS:** fatigue crack closure, fracture mechanics, surface flaw, polymethylmethacrylate, Newton interferometer, crack opening displacement, life prediction, effective stress-intensity range

Closure measurements have been used to consolidate fatigue crack growth data by numerous investigators [1,2] since the introduction of the crack closure concept by Elber [3] in the early 1970s. The basis of the closure concept is the recognition that the crack remains closed during a portion of the load cycle. This leads to an "effective" stress-intensity range which governs crack growth behavior. The effective stress-intensity range is lower than the applied range when the load at which closure occurs is above the minimum load in the fatigue cycle. In trying to apply the closure concept to experimental data, it has become evident that lack of a definitive definition of crack closure load level has caused inconsistencies in evaluating experimental results. In a recent investigation by the authors [4], closure load levels were found to vary with the location around a surface flaw in a

<sup>1</sup> Turbine development engineer, Wright Research and Development Center (WRDC/POTC), Wright-Patterson Air Force Base, OH 45433.

<sup>2</sup> Senior scientist, Wright Research and Development Center (WRDC/MLLN), Wright-Patterson Air Force Base, OH 45433.

<sup>3</sup> Professor and head, School of Aeronautics and Astronautics, Purdue University, West Lafayette, IN 47907.

transparent material. Further, crack closure at one location does not always significantly affect the stress intensity at another location. Conversely, closure at a distant location could shield the crack at a second location, even though the latter location did not experience closure. This investigation was undertaken to shed further light on the development of closure in surface flaws under a variety of loading conditions and to evaluate the applicability of the closure concept to fatigue crack growth data.

The surface flaw (part-through-crack) was selected to investigate the effect of closure on fatigue crack growth rate because of its occurrence in many engineering applications. Although a common crack type, the amount of crack closure information available on surface flaws in comparison to through-thickness cracks is relatively small. This is due to the three-dimensional complexities of surface flaw crack opening displacement and stress-intensity factor solutions around the crack boundary, as well as the difficulties in measuring these quantities experimentally. To address questions concerning crack opening displacements, we used an optical interference method with transparent polymer specimens to map the fatigue crack opening displacement contours of surface flaws. Crack closure loads at different locations and crack growth rates were determined experimentally. An analytical approach for predicting crack growth rate and aspect ratio using the three closure load definitions was used in a life prediction scheme. The analysis is presented only as an example since the data generated in this investigation are not independent.

### Experimental Approach

Experiments were conducted using a transparent polymethylmethacrylate (PMMA) material in bending using a laser interferometry system to measure crack opening displacements. The experimental procedure is described in detail in a prior publication [4]. The polymeric PMMA material was selected because of its transparent qualities and its demonstrated fracture-mechanics characteristics [5–7]. Experiments were conducted using both constant load ( $P$ ) and constant stress-intensity factor ( $K$ ) load cycles as well as a block loading sequence. The experiments were performed on a closed-loop MTS fatigue machine with a 22.2-kN (5000-lb) load cell and four-point bending fixture. An  $x$ - $y$  directional traveling microscope was used to make visual measurements of the surface flaw depth  $a$  and the surface crack length  $2c$  (Fig. 1). Visual observations of optical interference fringes produced by the crack opening profile were used to determine closure/opening load levels. Although opening and closure loads are used interchangeably here, a small amount of hysteresis was noted in the crack displacements when the load was increased (opening) versus a decreasing load (closure). The measurements reported in this paper will all be crack opening load levels.

Tests were conducted with 19 by 76 by 178 mm (0.75 by 3 by 7 in.) specimens at a cyclic frequency of 4 Hz at a stress ratio,  $R$ , of 0.035. This relatively slow cyclic fatigue rate was chosen to minimize crack tip heating, and thus avoid introduction of potential time-dependent phenomena. A crack initiation site (0.13 mm deep by 1.5 mm long) was scribed on the specimen surface using a knife edge. Precracking followed American Society for Testing and Materials (ASTM) standard load-shed practices for a through-thickness crack using a load level below 80% of material yield strength. Four types of tests were conducted. Two tests maintained a constant value of stress intensity at a specific location. One involved keeping  $K_a$  constant, while the other maintained  $K_c$  constant, where  $a$  is the location of the crack tip in the depth direction, normal to the surface and  $c$  is at the crack tip along the free surface. The fatigue load was reduced throughout the two constant- $K$  tests in order to maintain a constant stress-intensity factor of 659.3 kPa·m<sup>1/2</sup> (600 psi·in.<sup>1/2</sup>) at the given locations. The amount of load shedding was determined by measuring  $a$  and  $c$  with a trav-

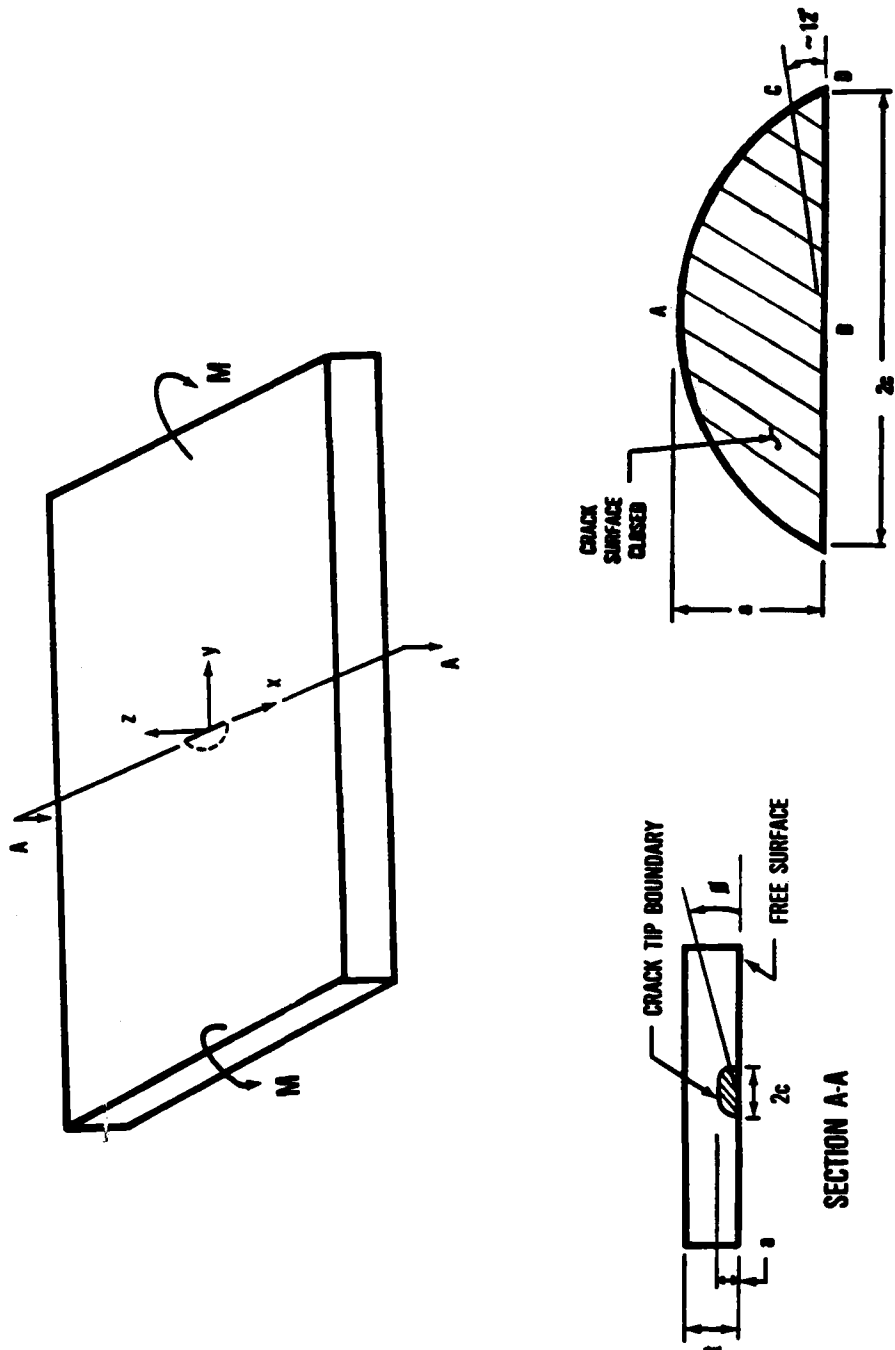


FIG. 1—Surface crack fatigue specimen.

eling microscope and calculating stress-intensity factors using the Newman-Raju  $K$  solutions [8]. A third test was conducted using a constant value of maximum moment of 72.7 N·m (644 in·lb). The fourth test involved a block loading sequence as illustrated in Fig. 2.

The PMMA specimens were annealed at 100°C for 24 h prior to precracking and sealed with a desiccating material at the crack face to minimize humidity effects during the test.

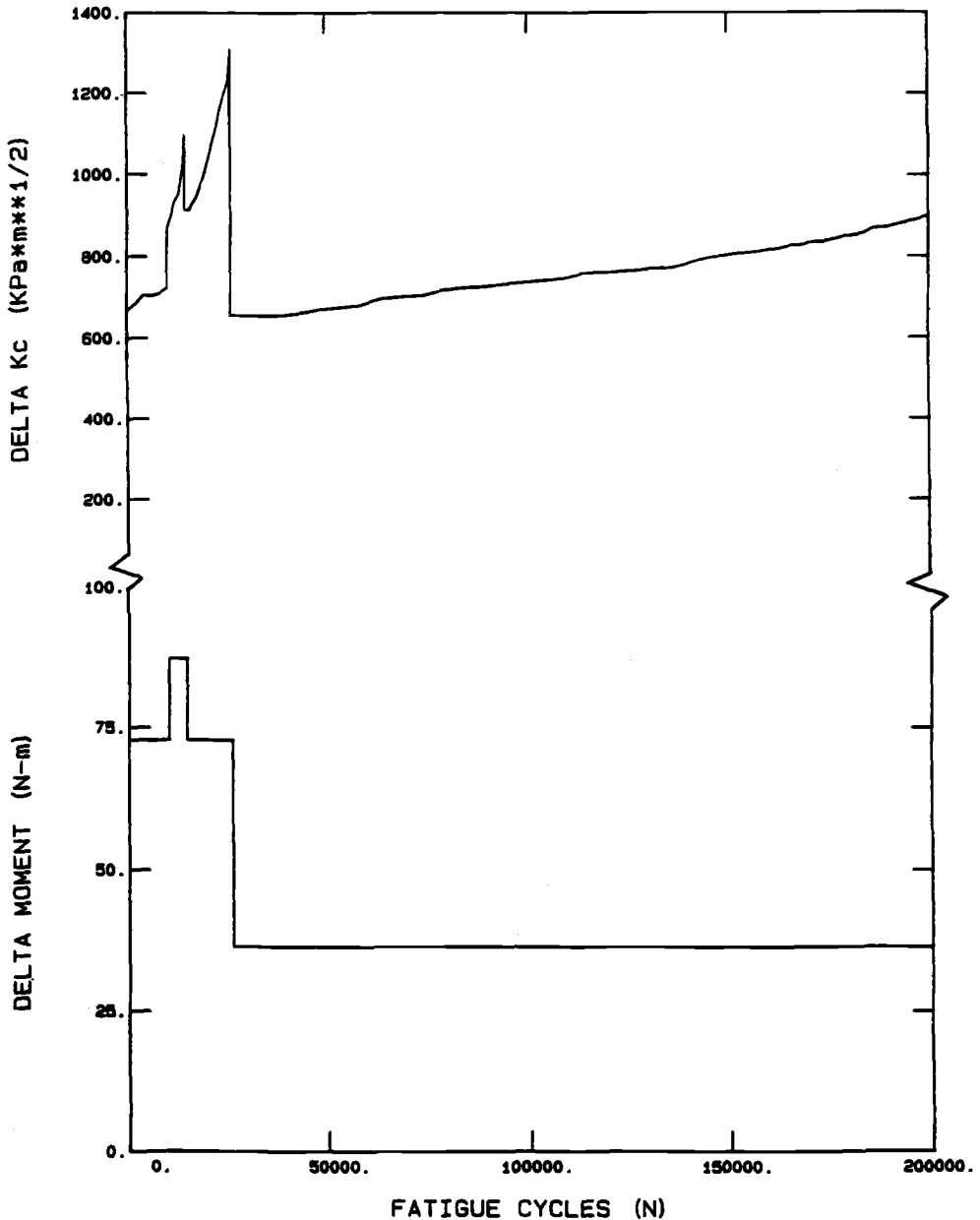


FIG. 2—Block loading sequences used in test program.



Crack dimensions were calibrated using known reference marks on the specimen. Surface flaw crack opening displacement (COD) measurements were made on crack shapes (aspect ratios) and sizes in the range of  $0.97 > a/c > 0.50$  and  $0.05 < a/t < 0.43$  (where  $t$  is the plate thickness). A laser interferometer system and camera were used to record optical interference fringe patterns under various applied loads during fatigue cycling. By counting the interference fringe order  $n$ , displacement changes of  $3.16 \times 10^{-4}$  mm ( $1.25 \times 10^{-5}$  in.) could be resolved.

### COD Profiles

The experimental investigation identified three primary crack types which were observed to be consistent for all tests. Four crack tip locations identified in Fig. 1 will be referred to extensively throughout this report. Location A defines the maximum crack depth location, Location B the midpoint of the crack free-surface, Location C is approximately 12 deg from the crack tip free-surface, and Location D is located at the crack tip free-surface. Crack lengths along the free surface (BD) are referred to as being in the  $c$  direction, consistent with standard nomenclature. The three crack types are shown schematically in Fig. 3 for a zero applied load. The figure is divided into two parts to describe the differences between "crack geometry" and observed "fringes" patterns. The cross-hatched area illustrates that the two mating crack surfaces are closed (in contact). The clear area (not cross-hatched) illustrates that the crack surfaces are separated, and is referred to in this report as a geometric "void." The dotted "fringe order" lines represent contours of constant crack opening displacement (COD) patterns. The terminology "void" is used in the remainder of this paper to describe a displacement hump which is internal to the crack mating surfaces. This internal void displacement is always open once formed, even under zero load.

A Type I crack (Fig. 3a) is defined as the crack geometry where the two mating surfaces are fully closed under zero load. This crack type is typically modeled as an elastic COD pattern. The Type I crack was observed in all four tests for smaller cracks having an  $a/t$  value less than 0.095. As the crack grew in size due to fatigue cycling, a Type II crack was formed (Fig. 3b). This change in crack geometry occurs when the crack internal surfaces separate and form a displacement "void" close to the crack tip at Location A. The pattern

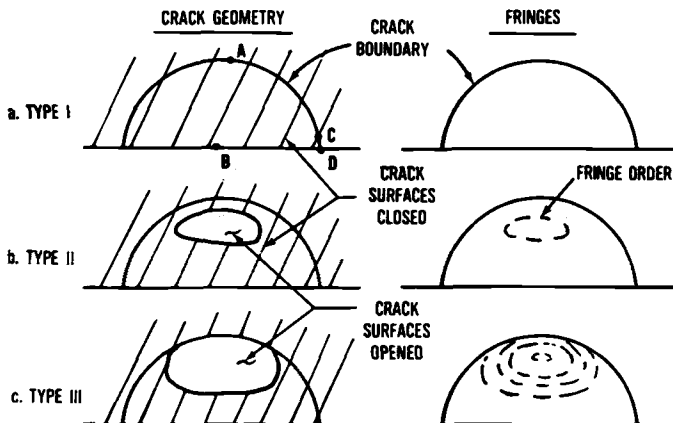


FIG. 3—Schematic of COD patterns under zero load for the three crack types—Types I, II, and III.

is distinguished by the interference fringe order contours under zero load. The uniqueness of a Type II crack is that under zero load the crack tip boundary is fully closed, while there is an internal nonzero displacement void area separating the two crack surfaces. In the four tests, a Type II crack formed at an  $a/t$  ratio ranging from 0.068 to 0.095. As the crack continues to grow due to fatigue cycling, the void area and height also increase, forcing the crack tip at Location A to separate and remain open even under zero applied load. This characteristic crack tip opening is defined as a Type III crack (Fig. 3c). In the four tests, a Type III crack was formed when the  $a/t$  range was between 0.139 and 0.189 for all tests.

Another means of visualizing the three void types is by slicing the crack between Locations A and B (Fig. 1) as schematically depicted in Fig. 4. For a Type I crack (Fig. 4a), the crack mating surfaces are completely closed under zero load. With increased crack growth, a Type II crack develops when the crack surfaces separate (forming an internal void area) while the crack tip boundary remains closed (Fig. 4b). As the crack continues to grow, a Type III crack is formed when the void size is sufficiently large to open the crack tip at Location A (Fig. 4c). The percent of crack tip boundary  $AD$  which is open for a Type III crack at zero load depends on the crack size. For example, the crack tip boundary between Locations A and D is open 17% for a newly formed Type III crack ( $a/t = 0.156$  and  $a/c = 0.652$  from the constant  $\Delta K_d$  test). When the crack reached the size of  $a/t = 0.180$  and  $a/c = 0.677$ , 30% of the  $AD$  boundary is open. With continued fatigue cycling, 65% of the  $AD$  boundary is open for a crack size of  $a/t = 0.260$  and  $a/c = 0.650$ . This opening of the crack tip boundary between Locations A and D results from an increase in void surface area and internal displacement with crack growth. Table I lists the measured crack lengths when transition occurred between crack Types I and II and between Types II and III. The crack transition size was found to correlate most favorably with  $a/t$ .

A general trend in crack aspect ratio ( $a/c$ ) was noted in the experimental results, where  $a/c$  for a Type I crack is higher than for a Type II, and  $a/c$  for a Type II crack is higher than for a Type III. Although it can be speculated that this trend is caused by the stress being larger at the crack free-surface than at the depth position due to the bending, the stress-intensity solutions do not bear out this concept, especially for small cracks. The experimental aspect ratio data are summarized in Fig. 5, which plots the data as a function of (dimensionless) crack depth. It can be seen that, for all four tests,  $a/c$  is continually decreasing. The only exception to this is the block loading test, where overload considerations and resultant crack growth retardation along the free surface become important. The

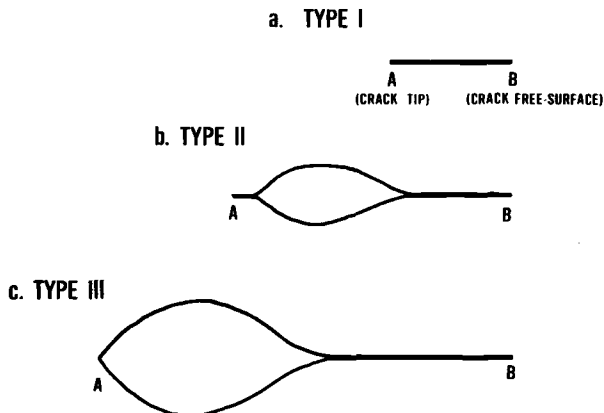


FIG. 4—Schematic of COD patterns under zero load along a cross section between A and B for the three crack types.

TABLE 1—Crack dimensions when transition occurs from a Type I and II, and from a Type II and III crack.

Transition to	<i>a</i>	<i>c</i>	<i>a/c</i>	<i>a/t</i>
TYPE II CRACK				
constant $\Delta K_d$	0.051	0.058	0.872	0.068
constant $\Delta K_a$	0.060	0.075	0.840	0.084
constant load	0.071	0.084	0.845	0.095
block load	0.052	0.075	0.693	0.069
TYPE III CRACK				
constant $\Delta K_d$	0.117	0.180	0.652	0.156
constant $\Delta K_a$	0.127	0.153	0.833	0.169
constant load	0.104	0.149	0.698	0.139
block load	0.142	0.202	0.705	0.189

circled region in Fig. 5 is a region of common crack size which is used in comparisons later on.

Another feature of the crack profile is the size and location of the internal void which is typical of a Type II or Type III crack. It was noted that for low load levels, the void maximum displacement is located internal to the crack surfaces and is closer to the crack tip (Location A) than the crack free-surface (Location B). With an applied load, the void maximum displacement moves away from the Location A crack tip and toward the crack free-surface at Location B. It was also observed that as the crack increases in size the void maximum displacement point increases in height and moves away from the crack tip and toward the crack free-surface. Three primary observations can be made about the void maximum displacement point from the experimental data:

- (1) the void is closer to the crack tip (Location A) for smaller cracks,
- (2) the void height is lower for smaller cracks than for larger cracks at an equivalent applied load, and
- (3) as load is applied, the void height increases and moves away from the crack tip and toward the crack free-surface.

To compare the void displacement patterns for all tests, a common crack aspect ratio ( $a/c$ ) and  $a/t$  value was chosen as shown in Fig. 5. The common point selected from this figure was  $a/c = 0.69$  and  $a/t = 0.19$ . Comparison of the void displacement patterns, showing both maximum displacement and location, is shown in Fig. 6. The data are shown for different values of applied load for all four tests. The reference line segment is drawn for the constant  $\Delta K_d$  data and is found to fit the other data sets quite well. It can be seen from this plot that the void movement toward the crack free-surface with applied load is consistent for various load histories. However, the applied moment required to achieve a given displacement (shown in parentheses) varies with load history. That is, to achieve a void maximum displacement of 13 fringe orders requires an applied moment at 15 N·m (132 in.·lb) for the constant  $\Delta K_d$  test, but only 8.2 N·m (73 in.·lb) for the constant  $\Delta K_a$  test. In all the tests, three primary observations of the void COD pattern were noted:

- (1) under zero load, the void maximum displacement is a direct function of crack size,
- (2) under zero load, the void maximum displacement location relative to the crack tip (Location A) is a direct function of crack size, and
- (3) with applied load, the void maximum displacement increases, and moves away from the crack tip and toward the crack free-surface (Location B).

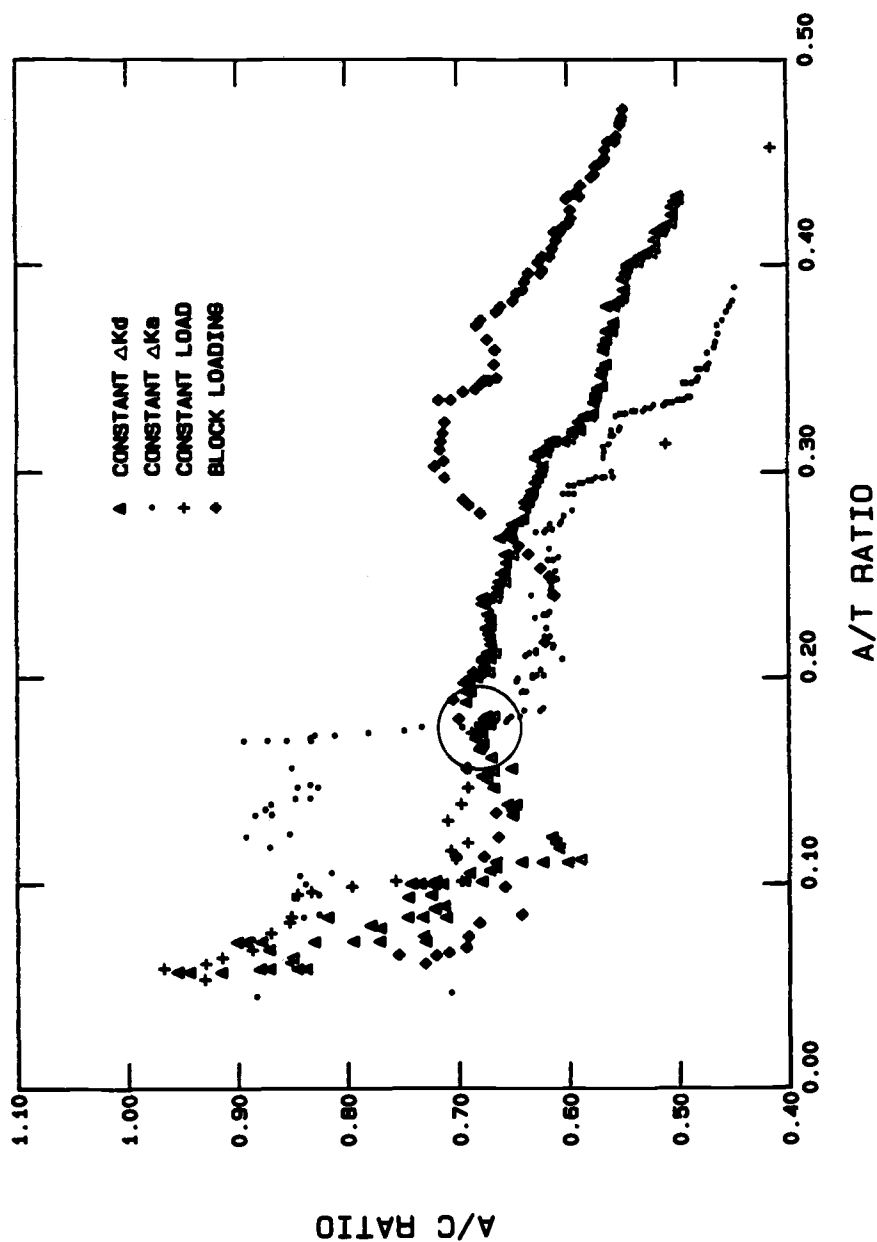


FIG. 5—Experimental values of crack aspect ratio ( $a/c$ ) as a function of dimensionless crack depth ( $a/t$ ) for all four tests. Circle identifies common crack size at which COD values are compared.

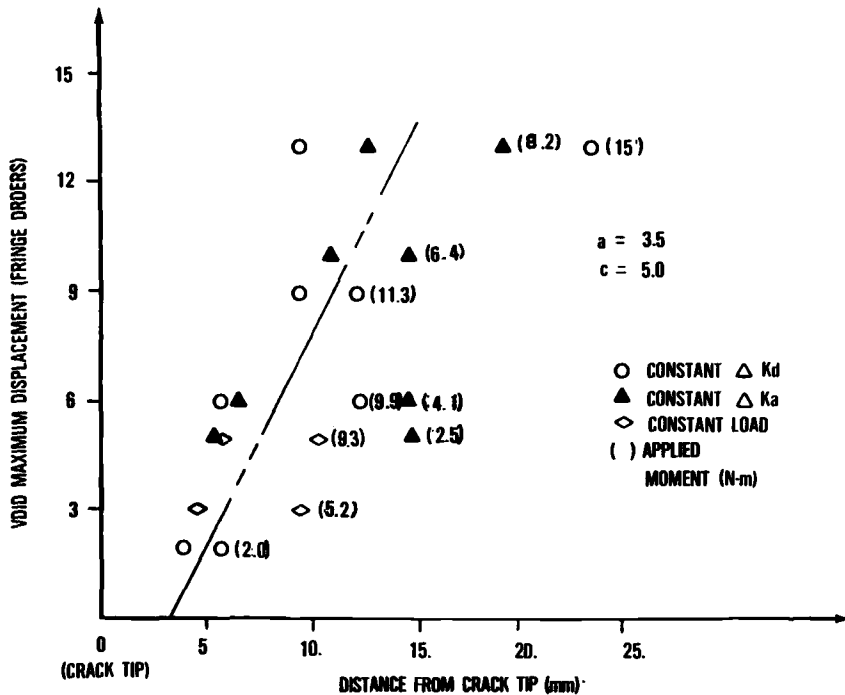


FIG. 6—Magnitude and location of void maximum displacement at several load levels for three tests. Numbers in parentheses represent applied bending moment.

### Crack Closure/Opening Loads

This experimental investigation identified three primary closure loads which are considered important for the understanding of fatigue crack growth. How these closure loads correlate with the three crack types described previously forms the basis for the eventual development of a life prediction scheme. The identification of three distinct closure loads raises several questions concerning their relationship to the standard definition of closure load (defined from a load versus displacement plot). In reality, the potential for having more than one closure load for the same crack size is not hypothetical. Several closure load values can be generated using the standard definition of closure if different measurement locations are used. This sensitivity to measurement location has been discussed by several investigators using clip gages, back face strain, and interferometry techniques [9-11]. These considerations will be evaluated more fully in the next section when the definitions of  $\Delta K_{eff}$  are considered.

Three primary closure loads ( $aP_{op}$ ,  $bP_{op}$ , and  $cP_{op}$ ) are defined in this investigation. The  $aP_{op}$ ,  $bP_{op}$ , and  $cP_{op}$  closure loads are defined here as the loads needed to open the crack surfaces ( $P_{op}$ ) at the A, B, and C locations, respectively, as shown in Fig. 1. Location C is the last portion of the crack surface to completely open under an applied load, and is typically located 12 to 15 deg into the specimen thickness from the crack free-surface. Figure 7 schematically illustrates the relationships between the three closure loads ( $aP_{op}$ ,  $bP_{op}$ , and  $cP_{op}$ ) and the three crack opening displacement types (Types I, II, and III). For a Type I crack (Fig. 7a), the crack surfaces are closed under zero load. As load is applied the crack remains closed until a load level of  $bP_{op}$  is reached, and the crack begins to open at the

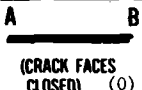
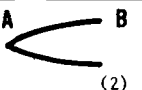










APPLIED LOAD CRACK TYPE	ZERO LOAD	a Pop	b Pop	c Pop
a. TYPE I $aP_{op} = cP_{op}$ $bP_{op} < aP_{op}$	 (0)	 (2)	 (1)	 (2)
b. TYPE II $aP_{op} < bP_{op} < cP_{op}$	 (0)	 (1)	 (2)	 (3)
c. TYPE III $aP_{op} = 0$ $bP_{op} < cP_{op}$	 (0)	 (0)	 (1)	 (2)

FIG. 7—Schematic of COD profiles between A and B for the three crack types at zero load and at each of the defined opening load levels ( $aP_{op}$ ,  $bP_{op}$ , and  $cP_{op}$ ). (NOTE: Numbers in parentheses indicate sequence of crack opening.)

crack free-surface (Location B). With increased load, the crack opens symmetrically inward and is fully open at Locations A and C at the same load level ( $aP_{op} = cP_{op}$ ). For a Type II crack, a void formation has developed internal to the crack surfaces as shown for zero load in Fig. 7b. The crack boundary and free-surface are closed (Locations A, B, and C) under zero load. With load application, Location A opens at a load level of  $aP_{op}$ . At the  $bP_{op}$  load level, the crack free-surface begins to open at Location B and is completely open between A and B; however, the crack tip is closed at Location C. At the  $cP_{op}$  load level, the crack surfaces are completely open. For a Type II crack,  $cP_{op} > bP_{op} > aP_{op}$ . For a Type III crack, Location A is always open, while Locations B and C are closed under zero load. Therefore, the  $aP_{op}$  load level is zero for a Type III crack. Location B begins to open at the  $bP_{op}$  load level, and at  $cP_{op}$  the crack is completely open. Thus,  $aP_{op} = 0$  and  $cP_{op} > bP_{op}$ .

Closure loads were obtained at the three Locations A, B, and C for each of the four tests. A typical set of data which illustrates the trends discussed in the preceding paragraph, shown for the case of the constant  $\Delta K_d$  test, is presented in Fig. 8. A feature which was apparent in most of the data is illustrated in this figure whereby the trend in closure load changes in progressing from a Type II crack to a Type III crack. The trend of a generally decreasing value of the closure load with increase in crack depth is also apparent in Fig. 8.

The absolute value of one of the closure loads ( $cP_{op}$ ) is presented for all four tests in Fig. 9. Similar results were obtained for the  $aP_{op}$  and  $bP_{op}$  closure loads. From these data, several observations were made. First, closure load absolute values decrease with increasing crack size. Second, the  $bP_{op}$  and  $cP_{op}$  load levels are higher for the constant load and block loading tests than for the constant stress-intensity factor tests. In comparing trends from the constant  $\Delta K_d$  test with the constant  $\Delta K_a$  tests, it was noted that  $bP_{op}$  and  $cP_{op}$  are higher for the constant  $\Delta K_d$  tests than for the constant  $\Delta K_a$  tests. When comparing the constant load test (continually increasing  $\Delta K$ ) with the constant  $\Delta K_d$  test, it was found that the constant load test closure loads are consistently higher than the constant  $\Delta K_d$  levels. This is to be expected since the plastic zone size is continually increasing while the constant  $\Delta K_d$  plastic zone remains constant after precracking. It was also found that  $aP_{op}$  and  $bP_{op}$  closure loads follow the same slope once a Type II crack is formed. Further, when comparing the

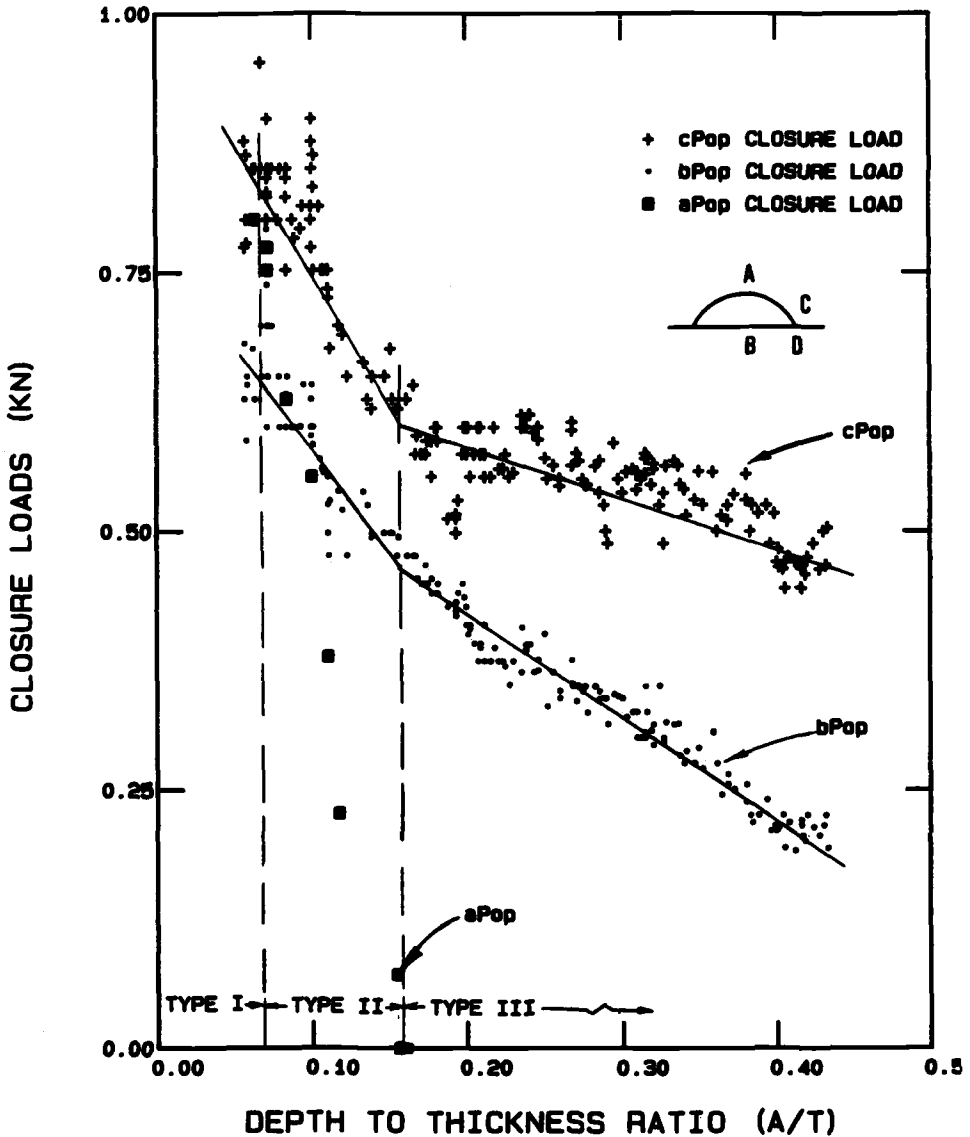


FIG. 8—Closure loads ( $aP_{op}$ ,  $bP_{op}$  and  $cP_{op}$ ) as a function of crack depth for the constant  $\Delta K_d$  test.

constant load test with the block loading test, it was noted that  $cP_{op}$  values for the block loading test are only slightly higher than the constant load test during the Types I and II crack formation. Once a Type III crack is formed, the closure loads are the same. Finally,  $cP_{op}$  is relatively constant for the constant load test until a Type III crack is formed. For the block loading test, abrupt increases in applied load cause  $cP_{op}$  to increase, whereas decreases in applied load cause  $cP_{op}$  to decrease.

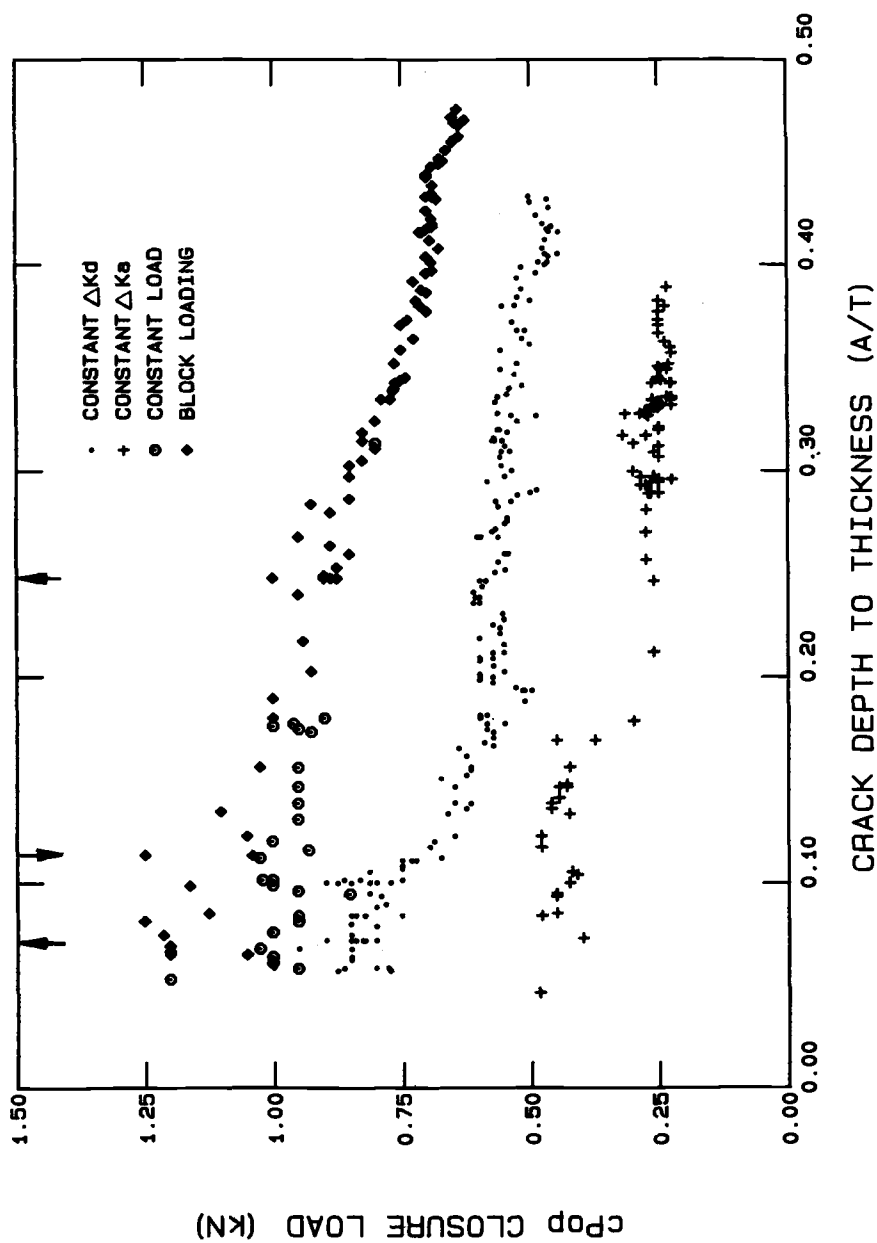


FIG. 9—Experimental data for  $cP_{op}$  as a function of crack size for all four tests. (NOTE: arrows at the top represent changes in block loading sequence).



Comparison of the closure load ratio ( $cP_{op}/P_{max}$ ) for all four tests is shown in Fig. 10. In three of the four tests (constant  $\Delta K_c$ , constant load, and block loading) average closure load ratio values of approximately 0.28 are obtained for  $0.0 < a/t < 0.20$  (during transition between crack Types I and II). The constant  $\Delta K_c$  test is at a level of approximately 0.14. This result is somewhat surprising, considering that the precracking procedure in the four tests were nominally the same. It appears that the closure which developed during precracking had a major influence in the subsequent closure load ratio. The only exception to the relative constancy of closure load ratio in any given test was for the case of the block loading test. Here, with a major  $P_{max}$  load reduction of 50% at  $a/t = 0.25$ , an abrupt change in  $cP_{op}/P_{max}$  occurs. Since  $K_{cl}$  is assumed to be a continuous function, the sudden jump in closure load ratio is expected. However, this ratio does not return to the original level for an amount of crack extension of approximately  $a/t \approx 0.2$ . This corresponds to at least 20 plastic zone sizes. This is similar to observations by Ashbaugh [12] when testing through-thickness CT specimens of Inconel 718 material. He observed that with a 60% reduction in load level for a test at  $R = 0.1$ , the crack was required to grow twice its length or many plastic zone sizes in order to return to the original closure load ratio.

The closure load data can also be presented in the form of stress intensity at a closure load level. Such a plot, as a function of crack depth, is presented in Fig. 11. The stress intensity at the free surface, Location C, is calculated from the value of  $cP_{op}$ . The dotted lines shown through the various data sets were polynomial fits to the data which were used later in life-prediction calculations.

### Effective Stress-Intensity Factors

The complexity of defining stress-intensity factor as a function of applied load and the difficulties of using the opening loads to calculate the actual  $K$  are illustrated schematically for a Type III crack in Fig. 12. Starting at maximum load, the stress intensity at Location A (the crack tip in the depth direction) is calculated using the solution for a surface flaw based on the applied load and the crack dimensions. As load is decreased, the  $K$  versus  $P$  plot is linear, based on that same  $K$  solution, as shown in the figure. Geometrically, when the load decreases to  $cP_{op}$ , the crack tip at Location C just starts to close, while the crack at A remains open. As load continues to decrease, the amount of crack face which is closed in the vicinity of Location C continues to increase. At any time, the slope of the  $K$  versus  $P$  curve depends on the  $K$  solution corresponding to the instantaneous geometry of the portion of the crack that remains open. As more and more of the crack closes, the stress intensity at A per unit applied load decreases since Location A is now shielded more by the partially closed crack. The actual stress-intensity solution is not known since this is now a complex geometry. When the unloading reaches the value  $bP_{op}$ , the entire crack free-surface is closed, but the interior is open. The stress intensity per unit load is further decreased due to shielding of the crack from the applied load, and the slope of the  $K$  versus  $P$  curve is even lower. Finally, further unloading results in more of the crack interior becoming closed, with a corresponding decrease in the slope of the curve as depicted in Fig. 12. When the load finally reaches  $P_{min}$ , the crack tip at A is still open and  $K$  remains nonzero. The effective stress intensity at A at each of the three opening loads is shown pictorially in Fig. 12, but  $K$  solutions are not available to calculate the exact values as shown by the dashed line.

It is apparent from the foregoing discussion that the calculation of an effective stress intensity for the surface flaw, given the closure load data at the three Locations A, B, and C, is a formidable task. There are four primary considerations in defining an effective

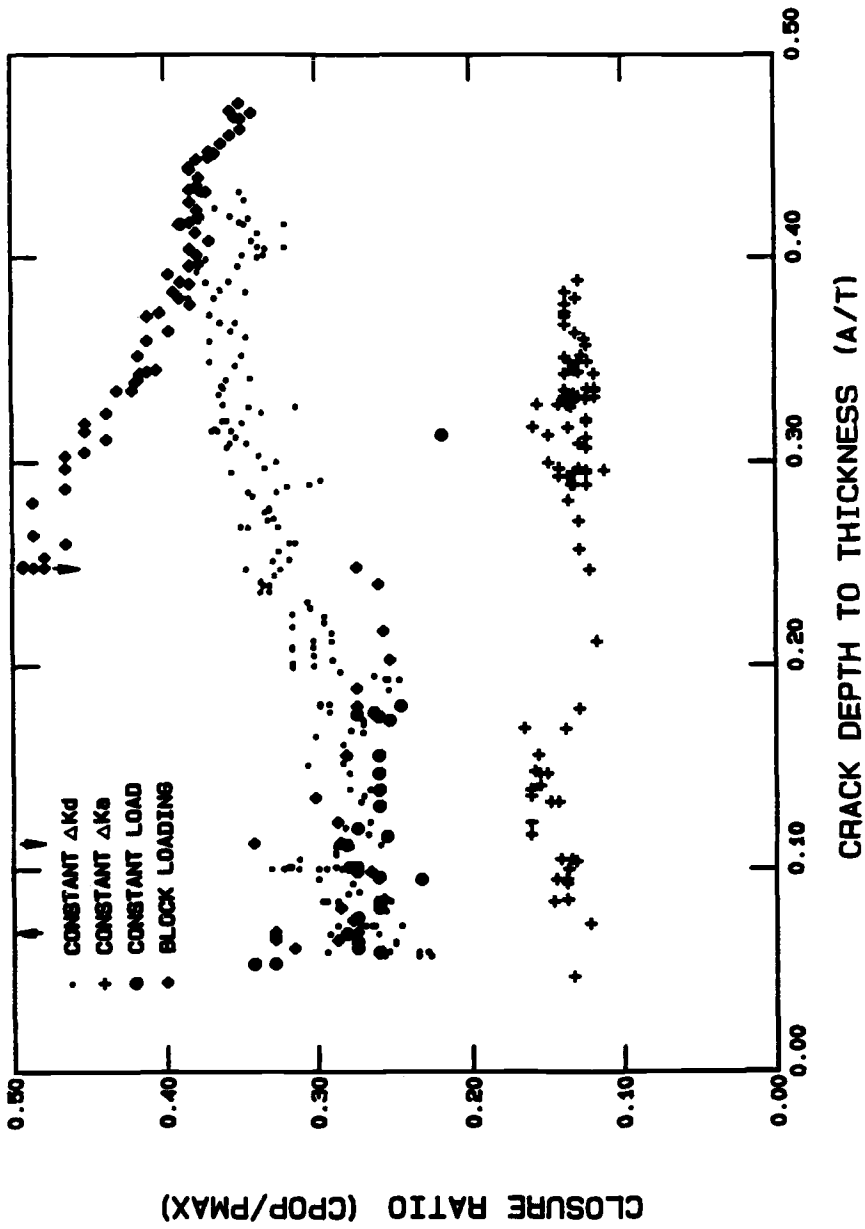


FIG. 10—Experimental data for the ratio  $cP_{op}/P_{max}$  as a function of crack size for all four tests.

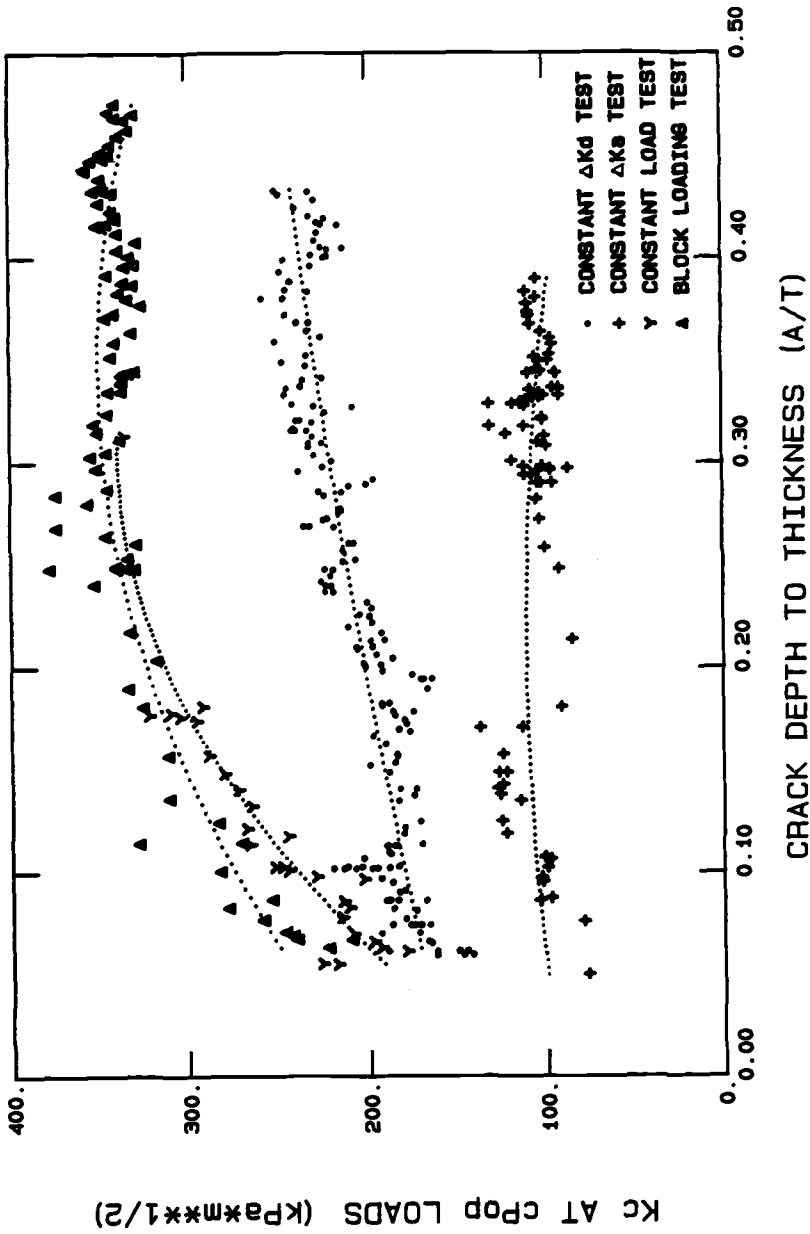


FIG. 11—Stress-intensity factor at the crack tip free surface,  $K_{cp}$ , at the  $cP_{op}$  load level as a function of crack size for all four tests.

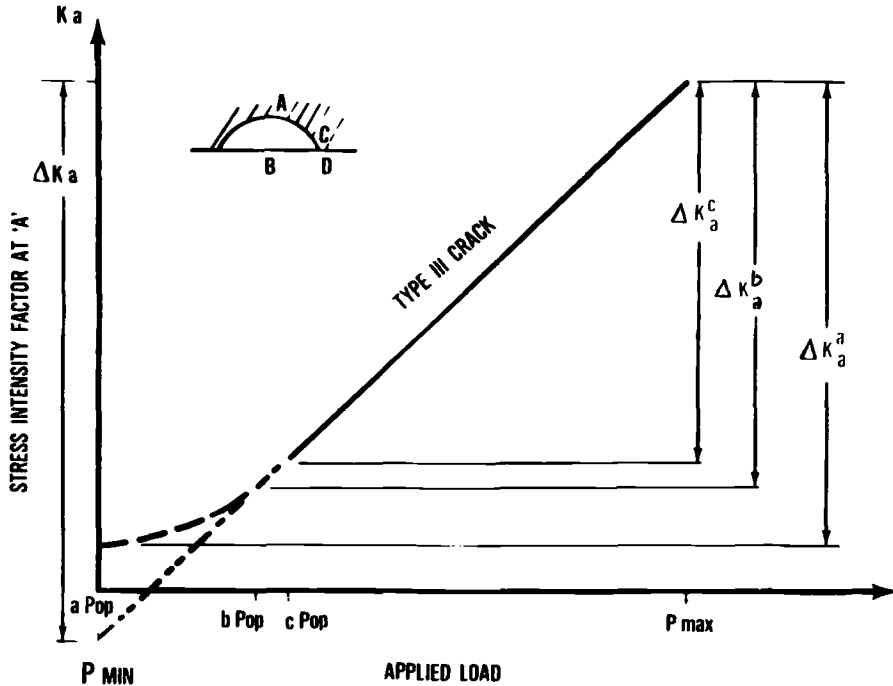


FIG. 12—Schematic representation of stress intensity at A as a function of applied load. Effective stress-intensity ranges due to the three closure loads are shown.

stress-intensity range,  $\Delta K_{\text{eff}}$ , which must be addressed in order to develop a life prediction methodology:

1. The closure load range ( $P_{\text{max}} - P_{\text{cl}}$ ), where  $P_{\text{cl}}$  is one of the three measured closure loads ( $aP_{\text{op}}$ ,  $bP_{\text{op}}$ , or  $cP_{\text{op}}$ ).
2. The location at which  $K$  is being calculated (that is, crack tip Location A or D). (Note that the closure load is measured at Location C, away from the surface, while the crack length along the surface is measured at Location D.)
3. The COD associated with a particular crack tip location and crack size (that is, crack Types I, II, and III).
4. The stress-intensity factor solution used to calculate  $K$ .

Addressing the previously mentioned four areas in a systematic manner requires a concise set of definitions. The first two points can be addressed by organizing the data in a matrix of closure load and crack tip location. This format requires a set of definitions which will be used extensively throughout the remainder of this report. The closure load used in the calculation is denoted by a superscript, the crack tip location by a subscript, thus  $\Delta K$  and  $\Delta K_{\text{eff}}$  are defined as follows:

*Applied Stress-Intensity Factor ( $\Delta K$ ):*

$\Delta K_a$  = applied  $\Delta K$  at Location A due to ( $P_{\text{max}} - P_{\text{min}}$ )

$\Delta K_c$  = applied  $\Delta K$  at Location C due to ( $P_{\text{max}} - P_{\text{min}}$ )

*Effective Stress-Intensity Factor ( $\Delta K_{\text{eff}}$ ):*

$\Delta K_{a \text{ eff}}^a$  = effective  $\Delta K$  at Location A due to  $(P_{\text{max}} - aP_{\text{op}})$

$\Delta K_{a \text{ eff}}^b$  = effective  $\Delta K$  at Location A due to  $(P_{\text{max}} - bP_{\text{op}})$

$\Delta K_{a \text{ eff}}^c$  = effective  $\Delta K$  at Location A due to  $(P_{\text{max}} - cP_{\text{op}})$

$\Delta K_{c \text{ eff}}^c$  = effective  $\Delta K$  at Location C due to  $(P_{\text{max}} - cP_{\text{op}})$

or

$\Delta K_{j \text{ eff}}^i$  = effective  $\Delta K$  at Location  $j$  due to  $(P_{\text{max}} - iP_{\text{op}})$

where  $i = a, b$  or  $c$  to define the closure load, and  $j = a$  or  $c$  to define the crack tip Location A or C, respectively.

The third and fourth considerations are interrelated in that the COD profile will provide guidance as to the stress-intensity factor which best fits the situation. This point can best be illustrated by considering one of the crack types and the associated stress intensity solution for a specific point. We choose a Type II crack and consider the stress intensity at the depth, A. A Type II crack is distinguished by the formation of a "void" internal to the crack surfaces while the crack tip boundary is closed under zero load. This "void" formation complicates the definition of  $K$  around the crack tip boundary because the load required to open the crack tip at Location A ( $aP_{\text{op}}$ ) is different from the load required to open Location C ( $cP_{\text{op}}$ ). Therefore, for applied loads between  $aP_{\text{op}}$  and  $cP_{\text{op}}$ , the crack tip is open at Location A while it is closed at Location C. This forms a crack tip boundary which is "partially open" and "partially closed" (as opposed to "fully open"), for which there are no  $K$ -solutions known to be available.

The COD process for a Type II crack is shown schematically in Fig. 13, where  $K_a$  is plotted as a function of applied load. The opening process is separated into four regions such that: Region (1) is between a load of zero and  $aP_{\text{op}}$ , Region (2) between  $aP_{\text{op}}$  and  $bP_{\text{op}}$ , Region (3) between  $bP_{\text{op}}$  and  $cP_{\text{op}}$ , and Region (4) between  $cP_{\text{op}}$  and  $P_{\text{max}}$ . The hypothesized "partially open"  $K$ -level experienced by the crack tip in the closure load regions (1) to (3) is identified on the plot by the heavy dotted and dashed line, respectively. The solid line (Region 4) represents available "fully open"  $K$ -solutions when the crack is completely open, that is, for loads greater than  $cP_{\text{op}}$ .

In Region 1, the crack tip boundary is closed at zero load. Upon load application, the internal void increases in size and initially opens the crack tip at Location A at a load level of  $aP_{\text{op}}$ . Since the crack tip is closed below  $aP_{\text{op}}$ ,  $K_a$  is undefined and remains unchanged. The  $K_a$  variation with load is depicted by a dotted line. As load is increased above  $aP_{\text{op}}$ , the void increases in size until it reaches the crack free-surface (Location B) at the  $bP_{\text{op}}$  load level. Below  $bP_{\text{op}}$ , the crack free-surface is closed while the crack tip boundary is open between Locations A and C, and results in the specimen geometry being relatively stiff. Therefore, changes in  $K_a$  with increased load are very small, as well as being nonlinear because of the continual change in crack geometry between  $aP_{\text{op}}$  and  $bP_{\text{op}}$  (Region 2). As load is increased above  $bP_{\text{op}}$ , changes in  $K_a$  are expected to be much greater with applied load since the geometry is more compliant due to the crack free-surface being open. Between  $bP_{\text{op}}$  and  $cP_{\text{op}}$  (Region 3), the crack surfaces and tip boundary continue to open until the  $cP_{\text{op}}$  load is reached and the crack is fully open. Between  $aP_{\text{op}}$  and  $cP_{\text{op}}$ ,  $K_a$  variations with load are not known to be available for partially-open cracks as shown by a heavy dashed line. Between  $cP_{\text{op}}$  and  $P_{\text{max}}$  (Region 4),  $K_a$  (solid line) is linear with applied load since the crack is fully open and the geometry remains constant. That is, the slope of the linear portion of the  $K_a$  versus applied load curve is proportional to the geometry factor corresponding to a fully open surface flaw, and  $K_a$  can be defined using available  $K$ -solu-

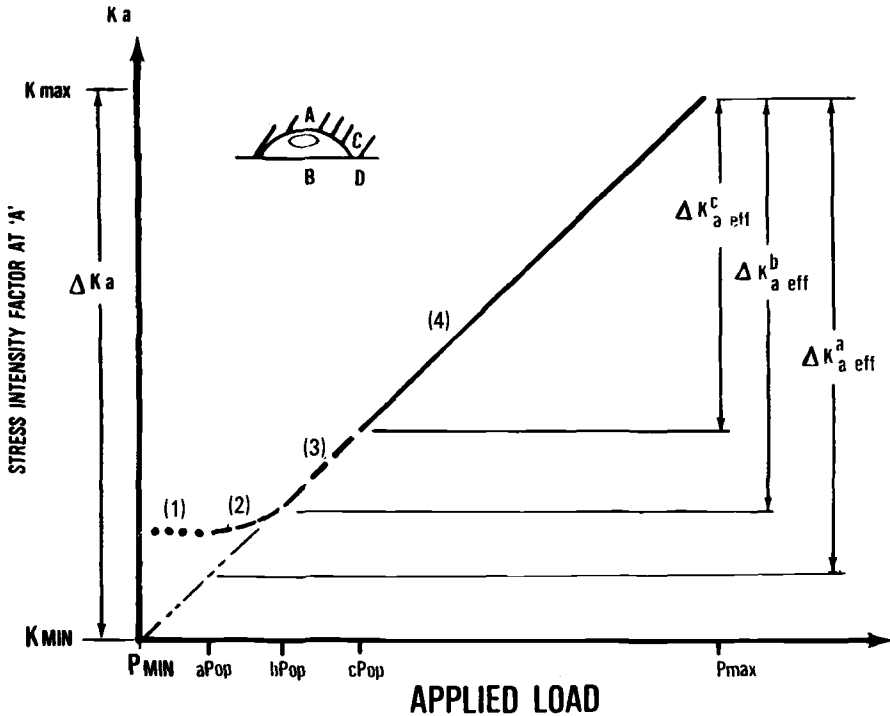


FIG. 13—Schematic representation of  $K$  as a function of applied load for a Type II crack at A. Significance of the three definitions of  $\Delta K_{a\text{ eff}}$  is shown.

tions. In summary, changes in actual  $K_a$  are nonlinear with respect to applied load between zero and  $cP_{op}$  because of the continually changing crack geometry with increasing load.  $K_a$  is hypothesized to remain constant between a load of zero and  $aP_{op}$  (Region 1), and to continue along a nonlinear path (Regions 2 and 3) until it reaches the  $cP_{op}$  load. It then becomes linear (Region 4) up to and including the maximum applied load.

Referring to Fig. 12 again, the effective stress-intensity ranges at Location A are shown corresponding to each of the measured closure loads. As pointed out earlier, these ranges are not readily calculated except for  $\Delta K_a^c$ . The quantities which can be calculated readily are the linear values of  $\Delta K_{a\text{ eff}}^i$  as defined above, with  $i = a, b$  or  $c$ . The relationship between the actual  $K_a^i$  experienced by the crack tip at Location A (Fig. 12) and the calculated  $\Delta K_{a\text{ eff}}^i$  can be seen in Fig. 13. Here, the three separate  $\Delta K_{a\text{ eff}}^i$  definitions are shown. These quantities are based on calculations using available fully open  $K$ -solutions and measured closure loads ( $aP_{op}$ ,  $bP_{op}$ , and  $cP_{op}$ ). It would appear from Fig. 13 that the "best" value to represent the effective value of  $\Delta K$  at Location A would be  $\Delta K_{a\text{ eff}}^b$  which is based on the use of the  $bP_{op}$  closure load at Location B. Note that all three of the  $\Delta K_{a\text{ eff}}^i$  definitions provide values which are less than the applied  $\Delta K_a$  values defined by  $K_{\max} - K_{\min}$ .

In comparison,  $\Delta K_c$  at Location C is much simpler to evaluate than  $\Delta K_{a\text{ eff}}$ . Here, the crack is closed at Location C until the  $cP_{op}$  load level is reached (defined as the last portion of the crack surfaces to open). Thereafter, the crack is fully open and  $\Delta K_c^c$  is calculated from available formulae using an effective load range of  $P_{\max} - cP_{op}$ . This analysis is valid for all three crack types.

### Fatigue Crack Growth Rates

Recognition of the three crack types, and their influence on COD, closure loads, and effective stress-intensity factor, raises a number of questions concerning the prediction of fatigue crack growth rate (FCGR). One of the more significant questions deals with selecting the load range which "best" defines an effective stress-intensity factor using fully open  $K$ -solutions. The approach for selecting this "best" effective load range is based on correlating experimental FCGR data. The evaluation is conducted using experimental FCGR data along with the effective stress-intensity factor definitions discussed previously. Available  $K$ -solutions will be used to bound the crack growth rate predictions by evaluating various effective load ranges.

Selecting the optimum closure load ( $P_{cl}$ ) can be accomplished by evaluating the ability of several  $\Delta K_{eff}$  definitions to correlate FCGR data into the specimen depth ( $da/dN$ ) and along the crack free-surface ( $dc/dN$ ). The selection of the most representative closure load range to match the experimental data is based on the correlation of predicted  $da/dN$  and  $dc/dN$  from all test conditions using several definitions of  $\Delta K_{eff}$ . The matrix of  $\Delta K_{eff}$  definitions is based on the use of the  $bP_{op}$  and  $cP_{op}$  closure loads at Locations A and C. From the discussion in the previous section, the logical selection for correlating  $da/dN$  data is  $\Delta K_{a\ eff}^b$ , and for  $dc/dN$  is  $\Delta K_{c\ eff}^c$ .

The FCGR data,  $da/dN$ , are plotted in Fig. 14 as a function of applied  $\Delta K$  for the four tests. Crack growth rates are calculated using a modified incremental polynomial smoothing routine developed by Larsen [13]. The average growth rates are approximately a factor of two lower than data generated by Perez [14] using through-thickness CT specimens from the same sheet of PMMA as was used in these experiments. A fair amount of scatter is seen in the data from the four different test conditions. For two of the tests,  $\Delta K$  remained fairly constant for portions of the test although the growth rates under those conditions are seen to vary by well over a factor of two.

The same data are plotted in Fig. 15 as a function of effective stress intensity, using  $\Delta K_{a\ eff}^b$  as the correlating parameter. That is using the  $bP_{op}$  closure load to define  $K_{cl}$  at Location A where  $\Delta K_{a\ eff}^b = K_{a\ max} - K_{a\ cl}^b$ , discussed above. The use of an effective stress-intensity factor which accounts for crack closure is seen to consolidate the data slightly better. In particular, the growth rates obtained under nominally constant  $\Delta K$  conditions are no longer as scattered. The through-thickness CT results are also plotted on this figure for reference (dashed line). Although the through-thickness CT data appear to agree well with the surface flaw data, the CT data are not corrected for closure (since no closure measurements were obtained on the CT tests) and thus are plotted as a function of applied  $\Delta K$ . Any closure in the CT tests would tend to move the curve to the left in Fig. 15. Most of the surface flaw data would then lie below the CT data, an observation consistent with that made from the data based on applied  $\Delta K$  in Fig. 14. Similar plots were made of  $da/dN$  against  $\Delta K_{eff}$  using the other closure load  $cP_{op}$ . Although the data are not presented here, it can be stated that the correlation of  $da/dN$  data from the four tests was not as good when using the  $cP_{op}$  closure load.

The FCGR data along the free surface,  $dc/dN$ , are presented in Fig. 16 as a function of applied  $\Delta K$  for all four tests. There is a small amount of scatter in these results. Using the reasoning that  $cP_{op}$  should be used to obtain the "best" value of an effective stress-intensity range, Fig. 17 is presented to illustrate the consolidation of the data. The scatter from test to test is seen to be minimized significantly. The reference CT curve is also shown. Comparison of the results of  $da/dN$  in Fig. 15 with those of  $dc/dN$  in Fig. 17 shows that the growth rates in the depth and surface directions are approximately equal when plotted

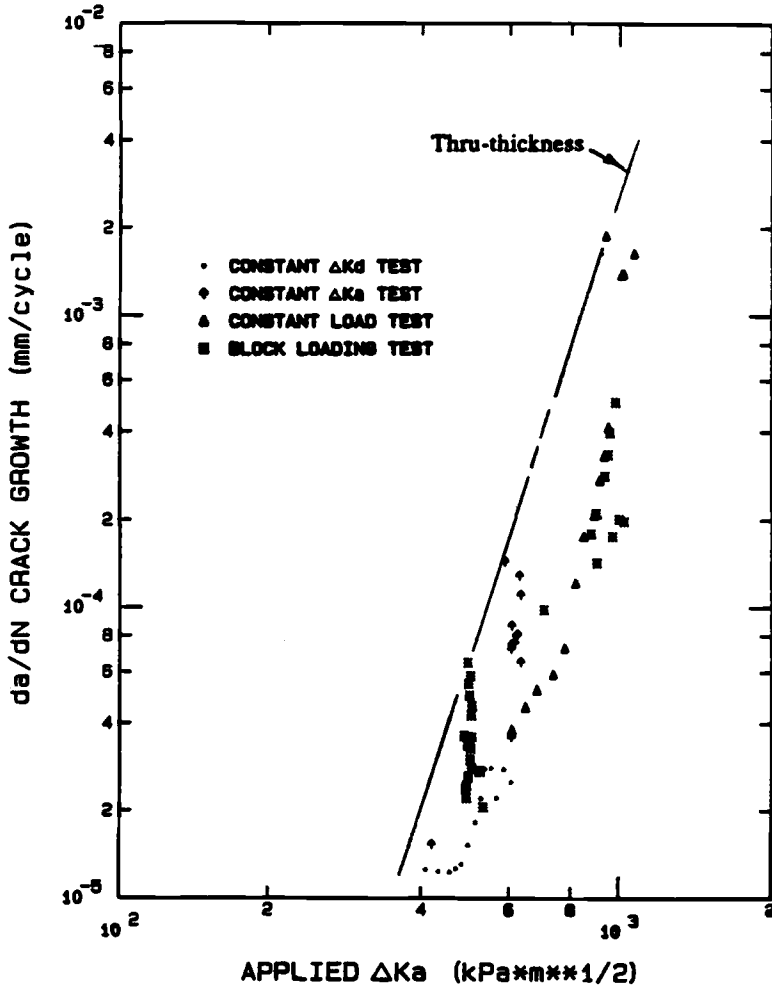


FIG. 14—Crack growth rate at Location A as a function of applied stress-intensity range for all four tests.

against the appropriate  $\Delta K_{\text{eff}}$ . A similar plot of  $dc/dN$  was made using  $bP_{\text{op}}$  as the closure load in the  $\Delta K_{\text{eff}}$  calculation. The correlation of the data from the four tests was even better than in Fig. 17, although the physical significance of using  $bP_{\text{op}}$  as the effective closure load at Location C is totally lacking.

#### Crack Growth Predictions

The usefulness of the preceding correlations for predicting fatigue crack growth (FCG) can be evaluated by comparing experimental measurements with analytical predictions of crack aspect ratio and the number of cycles to reach a given crack length. The computa-



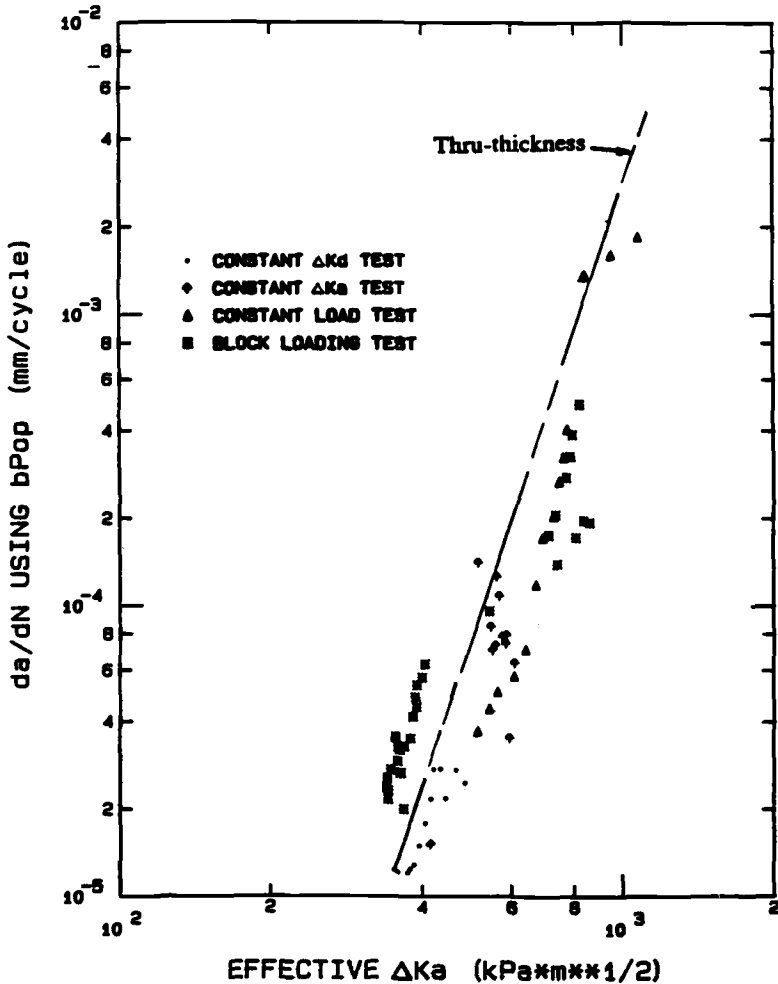


FIG. 15—Crack growth rate at Location A as a function of effective stress-intensity range based on  $\Delta K_{a,cl}^b$  for all four tests.

tions are carried out using a numerical integration of crack growth rates, the Newman-Raju stress-intensity solution for a surface flaw, and a straight line fit to the experimental FCGR data; that is, a Paris law representation. The numerical comparisons are made for two cases using applied  $\Delta K$  and for three cases using corrected constants derived from  $\Delta K_{eff}$  definitions described in the previous section. Since the closure load corrected constants (fits of data plotted against  $\Delta K_{eff}$ ) are derived from this investigation and are not independent, the calculations are presented as an illustration of the approach rather than as a true prediction.

The analytical program calculates stress-intensity factors in the  $a$  and  $c$  directions using the Newman-Raju boundary correction factors at  $\Phi = 90$  and  $0$  deg, respectively. The model uses either the applied stress-intensity factor range of  $(K_{max} - K_{min})$ , or effective

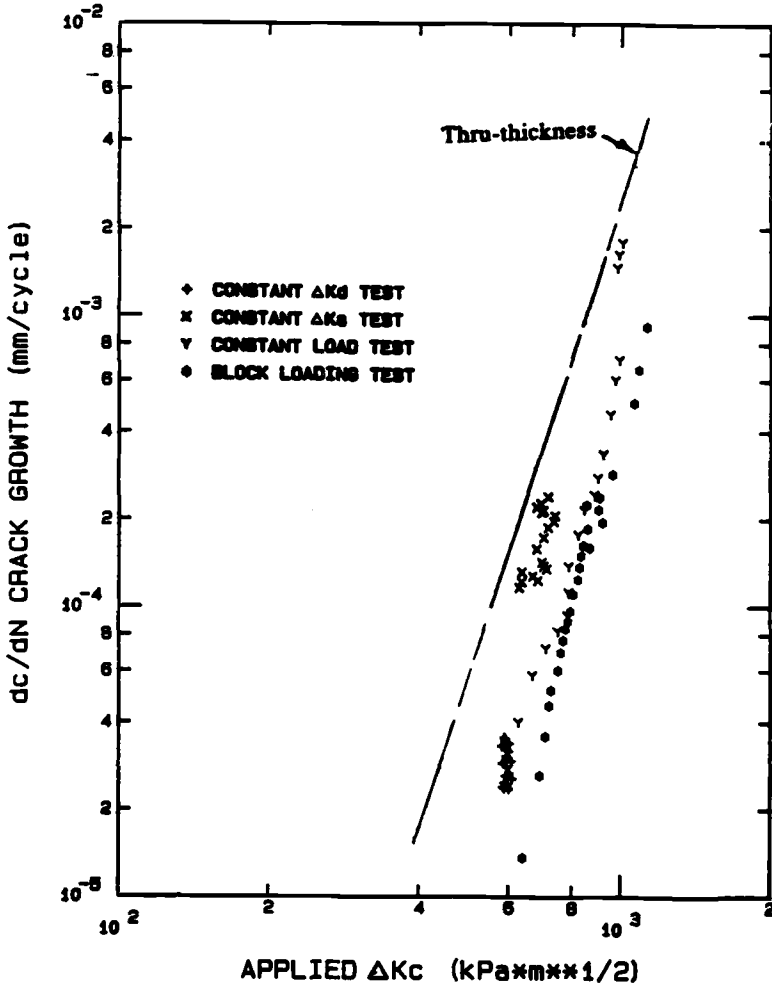


FIG. 16—Crack growth rate at Location C as a function of applied stress-intensity range for all four tests.

stress-intensity factor range of  $(K_{\max} - K_{cl})$ . The crack growth rates are represented as

$$dc/dN = C_c (\Delta K_{c \text{ eff}}^i)^{n_c} \quad (1)$$

$$da/dN = C_a (\Delta K_{a \text{ eff}}^i)^{n_a} \quad (2)$$

where  $i = a, b$  or  $c$ ,  $C_c$  and  $n_c$  are Paris law constants generated from FCGR data along the crack free-surface, and  $C_a$  and  $n_a$  from data in the depth direction. The constants can be generated independently when  $da/dN$  and  $dc/dN$  data are available as in Figs. 14 and 16. Although the analytical formulation was set up to recognize these potential differences in growth rates in the two directions, this investigation used  $C_a = C_c$  and  $n_a = n_c$  since they were approximately equal.

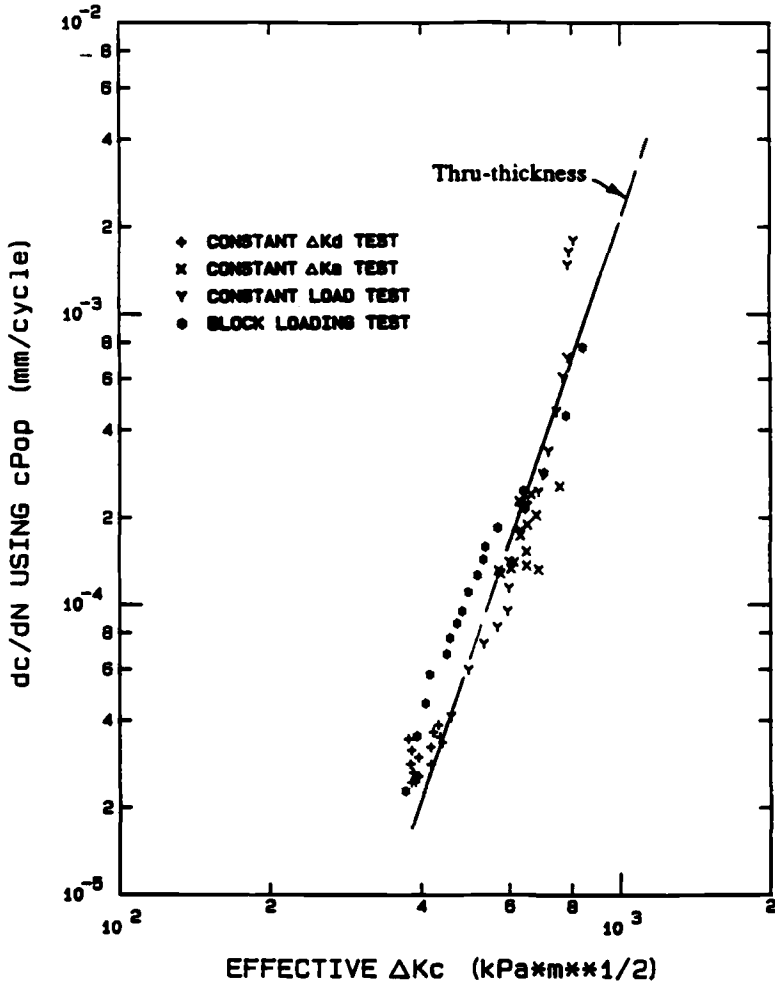


FIG. 17—Crack growth rate at Location C as a function of effective stress-intensity range based on  $\Delta K_{eff}$  for all four tests.

Calculations were made using five different combinations of Paris law constants ( $C$  and  $n$ ) and closure load, which were then compared with experimental results. Two of these combinations included “uncorrected” constants developed for applied loads, and three using closure “corrected” constants generated from  $\Delta K_{eff}$  plots. The uncorrected constants are from through-thickness data [14], and surface flaw data from this investigation. The corrected constants were from fits to both  $da/dN$  and  $dc/dN$  data using  $bP_{op}$  and  $cP_{op}$  separately; that is, one calculation used  $\Delta K_a^b$  and  $\Delta K_c^b$ , and the other  $\Delta K_a^c$  and  $\Delta K_c^c$ . The final calculation used  $bP_{op}$  for the  $da/dN$  and  $cP_{op}$  for the  $dc/dN$  calculations, or  $\Delta K_a^b$  and  $\Delta K_c^c$  as discussed above. The constant  $\Delta K_d$  test results were used for these sample calculations after eliminating precracking effects.

The analytical results for aspect ratio ( $a/c$ ) and cycles to achieve a given crack length ( $N$ ) are compared in Table 2 at several crack depths ( $a/t$ ). The results are presented as a ratio of the predicted quantity (subscript  $p$ ) to the experimental quantity (subscript  $e$ ).

TABLE 2—Comparison of experimental and predicted aspect ratios and cycles to a given crack depth using applied and effective stress intensities to obtain Paris law constants.

Condition	$a/t$	$(a/c)_p/(a/c)_e$	$N_p/N_e$
APPLIED LOAD (UNCORRECTED CONSTANTS)			
Through-thickness	0.1	1.10	0.16
	0.2	1.00	0.24
	0.4	0.87	0.23
Surface flaw	0.1	1.09	0.53
	0.2	0.99	0.77
	0.4	0.84	0.77
CLOSURE LOAD (CORRECTED CONSTANTS)			
$bP_{op}$	0.1	1.09	0.70
	0.2	1.01	0.97
	0.4	0.91	0.89
$cP_{op}$	0.1	1.09	0.50
	0.2	1.01	0.79
	0.4	0.92	0.95
$bP_{op}$ and $cP_{op}$	0.1	1.02	0.56
	0.2	0.97	0.82
	0.4	0.98	0.87
EXPERIMENTAL RESULTS			
	$a/t$	$(a/c)_e$	$N_e(\text{cycles})$
	0.1	0.72	57 000
	0.2	0.68	140 000
	0.4	0.54	480 000

Here, cycle prediction improvements due to the use of correlated Paris law constants for an effective load range versus an applied load range (uncorrected constants) are readily apparent. However, the ability to predict aspect ratio is not as apparent. The aspect ratio predictions are better shown in Fig. 18, which illustrates that several of the calculation results are equivalent: (1) the two calculations using the nominal applied  $\Delta K$  uncorrected constants for "through-thickness" and "surface flaws," and (2) the two calculations using the corrected constants of " $bP_{op}$ " ( $\Delta K_a^b$  and  $\Delta K_c^b$ ) or " $cP_{op}$ " ( $\Delta K_a^c$  and  $\Delta K_c^c$ ) for both  $da/dN$  and  $dc/dN$ . Although all of these combinations are quite good, using " $bP_{op}$  and  $cP_{op}$ " for  $da/dN$  ( $\Delta K_a^b$ ) and " $cP_{op}$ " for  $dc/dN$  ( $\Delta K_c^c$ ), respectively, provided the "best" overall crack growth match. In general, all of the analytical results using an effective load range provided a better match with experimental data than the nominal applied load range.

The results presented in Fig. 18 indicate that the fully open  $K$ -solutions are adequate to provide quite good crack growth predictions for various combinations of Paris law constants based on detailed closure load measurements. The questions then arise as to how good are the predictions if only Paris law constants are available and an assumed constant (not a function of crack length) closure load ratio ( $P_{cl}/P_{max}$ ) is used in the FCGR calculations. Results of this approach are presented in Table 3 using corrected Paris law constants from through-thickness and surface flaw tests. Two combinations of constant closure load ratios were considered: (1) 30% for both  $da/dN$  and  $dc/dN$ , and (2) 20% for  $da/dN$  and 30% for  $dc/dN$ , which represents a best average for the experimental data. It would appear from these results that either approach (1) or (2) mentioned previously are equivalent for predicting FCGR of surface flaws in bending when an assumed closure load is used with corrected Paris law constants.

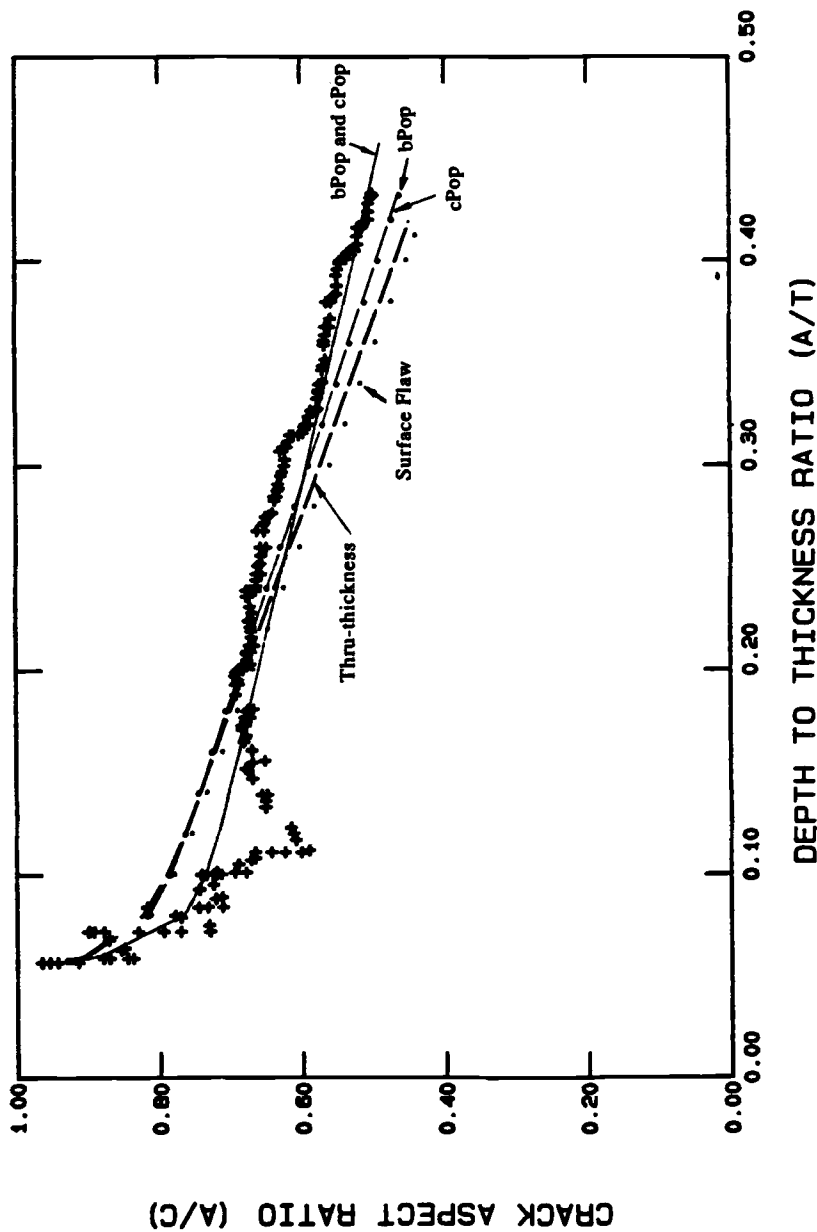


FIG. 18—Comparison of predictions and experimental data for aspect ratio as a function of crack depth for constant  $\Delta K_d$  test.

TABLE 3—Comparison of experimental and predicted aspect ratios and cycles to a given crack depth using a constant  $P_{cl}/P_{max}$  value.

Condition	$a/t$	$(a/c)_p/(a/c)_e$	$N_p/N_e$
SURFACE FLAW			
$P_{cl}/P_{max} = 0.3$	0.1	1.07	0.42
	0.2	0.98	0.68
	0.4	0.87	0.89
$P_{cl}/P_{max} = 0.2 \text{ and } 0.3$	0.1	1.09	0.52
	0.2	0.99	0.76
	0.4	0.85	0.77
THROUGH-THICKNESS			
$P_{cl}/P_{max} = 0.3$	0.1	1.10	0.19
	0.2	1.00	0.28
	0.4	0.87	0.28
$P_{cl}/P_{max} = 0.2 \text{ and } 0.3$	0.1	1.10	0.19
	0.2	1.00	0.28
	0.4	0.87	0.28

## Conclusions

Experimentally measured COD profiles identified three patterns (referred to here as crack Types I, II, and III) which directly influence closure load level and crack tip stress-intensity factor in the nonlinear closure region. The COD patterns (that is, crack types) were found to be a function of crack depth ( $a/t$ ) and not load history. The Types II and III COD patterns are identified by a "void" area which separates the crack interior surfaces while the crack free-surface is closed under zero load. Upon loading, the crack Types II and III open from the internal crack tip outward toward the crack free-surface. The middle of the crack free-surface opens first, with the last portion of the crack internal surfaces opening at 12 to 15 deg from the crack free-surface. This crack tip boundary opening pattern is referred to as "partially open" in the closure load region since the crack tip is open at certain locations while it is closed at other locations.

Closure load measurements were made at three crack surface locations. One closure load corresponds to complete opening of the crack surface. The other two correspond to complete opening of the deepest portion of the crack tip and opening at the crack middle free-surface. The closure load ratios ( $P_{cl}/P_{max}$ ), and inherent closure load stress-intensity factor ( $K_{cl}$ ) levels, were found to be a function of crack size and load history. As the crack grows in size, the "void" area increases in size, causing a decrease in closure/opening load level and an increase in crack displacement. These COD patterns have a direct impact on crack tip stress-intensity factor in the closure load region.

Correlation of closure load measurements with the three crack types is essential to the development of a  $\Delta K_{eff}$  definition. The correlation of FCGR with several definitions of  $\Delta K_{eff}$  (using closure load measurements and available fully open  $K$ -solutions) found the crack middle free-surface closure load measurement ( $bP_{op}$ ) produced the least scatter when compared with experimental results. The closure load corresponding to complete opening of the crack surfaces ( $cP_{op}$ ) also produced good correlation. Evaluation of FCG using several  $\Delta K_{eff}$  definitions found that use of a different closure load at two different crack tip locations provided the best prediction. That is,  $da/dN = f(P_{max} - bP_{op})$ , and  $dc/dN = f(P_{max} - cP_{op})$ .

## References

- [1] *Mechanics of Fatigue Crack Closure*. ASTM STP 982, J. C. Newman, Jr., and W. Elber, Eds., American Society for Testing and Materials, Philadelphia, 1988.
- [2] Suresh, S. and Ritchie, R. O., "Near-Threshold Fatigue Crack Propagation: A Perspective on the Role of Crack Closure," *Fatigue Crack Growth Threshold Concepts*, D. L. Davidson and S. Suresh, Eds., The Metallurgical Society of the American Institute of Mining, Metallurgical, and Petroleum Engineers, Warrendale, PA, 1984, pp. 263-279.
- [3] Elber, W., "Fatigue Crack Closure Under Cyclic Tension," *Engineering Fracture Mechanics*, Vol. 2, 1970, pp. 37-45.
- [4] Troha, W. A., Nicholas, T., and Grandt, A. F., Jr., "Three-Dimensional Aspects of Fatigue Crack Closure in Surface Flaws in Polymethylmethacrylate Material," *Mechanics of Fatigue Crack Closure*, ASTM STP 982, J. C. Newman, Jr., and W. Elber, Eds., American Society for Testing and Materials, Philadelphia, 1988, pp. 598-616.
- [5] Grandt, A. F., Jr., and Sinclair, G. M. "Stress Intensity Factor for Surface Cracks in Bending," *Elevated Analysis and Growth of Cracks*, ASTM STP 513, American Society for Testing and Materials, Philadelphia, 1972, pp. 37-58.
- [6] Hertzberg, R. W., Manson, J. A., and Wu, W. C., "Structure of Polymers and Fatigue Crack Propagation," *Progress in Flow Growth and Fracture Toughness Testing*, ASTM STP 536, American Society for Testing and Materials, Philadelphia, 1973, pp. 391-403.
- [7] Hertzberg, R. W. and Manson, J. A., *Fatigue of Engineering Plastics*, Academic Press, New York, 1980.
- [8] Newman, J. C. and Raju, I. S., "An Empirical Stress-Intensity Factor Equation for the Surface Crack," *Engineering Fracture Mechanics*, Vol. 15, 1981, pp. 185-192.
- [9] Elber, W., "The Significance of Fatigue Crack Closure," *Damage Tolerance in Aircraft Structures*, ASTM STP 486, American Society for Testing and Materials, Philadelphia, 1971, pp. 230-242.
- [10] Sharp, W. N., Jr., and Grandt, A. F., Jr., "A Laser Interferometric Technique for Crack Surface Displacement Measurements," *Proceedings of the 20th International Instrumentation Symposium of the Instrument Society of America*, Albuquerque, NM, May 1974.
- [11] Newman, J. C., Jr., "A Finite Element Analysis of Fatigue Crack Closure," *Mechanics of Crack Growth*, ASTM STP 590, American Society for Testing and Materials, Philadelphia, 1976, pp. 291-301.
- [12] Ashbaugh, N. E., "Evaluation of Crack Closure," presented at American Institute of Astronautics and Aeronautics Mini-Symposium, Wright-Patterson Air Force Base, OH, March 1984.
- [13] Larsen, J. M., "An Automated Photomicroscopic System for Monitoring the Growth of Small Fatigue Cracks," *Fracture Mechanics; Seventeenth Volume*, ASTM STP 905, American Society for Testing and Materials, Philadelphia, 1986, pp. 226-238.
- [14] Perez, R., "Initiation, Growth and Coalescence of Fatigue Cracks," M.S. thesis, School of Aeronautics and Astronautics, Purdue University, West Lafayette, IN, Aug. 1983.

## Some Special Computations and Experiments on Surface Crack Growth

---

**REFERENCE:** Prodan, M. and Radon, J. C., "Some Special Computations and Experiments on Surface Crack Growth," *Surface-Crack Growth: Models, Experiments, and Structures, ASTM STP 1060*, W. G. Reuter, J. H. Underwood, and J. C. Newman, Jr., Eds., American Society for Testing and Materials, Philadelphia, 1990, pp. 287–302.

**ABSTRACT:** The new method of surface crack growth calculation under linear elastic fracture mechanics (LEFM) conditions facilitates the use of stress-intensity factor  $K$  (and in particular its  $\Delta K$  range) as a tool to estimate the fatigue life of cracked plates under tensile loads. This is made possible by determining a set of parameters in order to obtain equal  $\Delta K$  values and analogous crack propagation rates in two widely different specimen geometries, a plate and a standard compact type (C(T)) specimen. A comparison of fatigue lives with equivalent crack growth for both types of specimen suggests that in using the proposed procedure, the significance of  $\Delta K$  values in a part-through crack is closely related to that of a through crack in a C(T) specimen.

In analyzing the surface crack growth under elastic-plastic conditions, it should be necessary to use  $J$  values in a different way than in LEFM. Appropriate references to both problems are quoted.

**KEY WORDS:** three-dimensional crack problems, fatigue, specimen-to-structure correlation, stress-intensity factor  $K$ , energy integral  $J$ , surface crack, pressure vessels, pipes

### Nomenclature

$a, a_i$	Depth of part-through surface crack (plate); length of through-thickness crack (C(T) specimen)
$c, c_i$	Half-length of part-through surface crack (plate)
$\Delta F$	Cyclic load (force)
$h$	Half-length of plate
$K$	Stress-intensity factor
$\Delta K, \Delta K_i$	Stress-intensity factor range
$i$	Index (counter)
$t$	Thickness
$W$	Width of C(T) specimen; half-width of plate
$\eta$	Load per unit thickness of C(T) specimen
$\Delta\sigma$	Stress range
C(T)	Compact type (ASTM E 399-81)
$\varphi$	Parametric angle of ellipse
LEFM	Linear elastic fracture mechanics

<sup>1</sup> Leader of group, Fracture and Damage Mechanics, Sulzer Bros., Ltd., 8401 Winterthur, Switzerland.

<sup>2</sup> Honorary research fellow, Department of Mechanical Engineering, Imperial College of Science and Technology, London, SW7 2BX, U.K.



ASME American Society of Mechanical Engineers  
 $J$  Path-independent line integral; energy rate  
 COD Crack opening displacement

Interest in part-through cracks has a long, well-documented history. The most common flaws in structural components are part-through surface cracks and internal cracks of more or less elliptical shape. The importance of such cracks has been recognized for many years, not only in the context of elastic and plastic fracture, but also in fatigue and creep crack growth. This paper deals with semielliptical surface cracks in plates subjected to monotonic and cyclic tension.

The evaluation of the stress-intensity factor  $K$  or the energy integral  $J$  along the crack front of a part-through crack is a complex, three-dimensional problem. Several reference solutions may be found in the literature; those of Raju and Newman [1] for the  $K$  factor and Yagawa and Ueda [2]<sup>3</sup> for the  $J$ -integral are particularly well known and extensively applied. Raju and Newman's solution [1] has been used in the present work. It has been assumed that the stress-intensity range  $\Delta K$  plays a dominant role in the fatigue growth of surface cracks.

### Computations of Fatigue Crack Growth

Figure 1 shows a cross section of a specimen in the plane of the crack and illustrates the local application of the crack propagation law in the form

$$\frac{dl(\varphi)}{dN} = f[\Delta K(\varphi)] \quad (1)$$

on the assumption that  $\Delta K$  plays a dominant role in describing crack growth, thus predicting fatigue life.

Several calculation methods for stress-intensity factors are available in the literature. The theoretical-experimental procedure presented here uses the readily available solutions of Raju and Newman [1] and Irwin [3].

An iterative scheme with equidistant steps in the direction of the crack depth is used to calculate the growth of a crack. The following two operations are necessary to proceed in the calculation of crack length  $c$  (paragraph *a*) and  $\Delta K$  (paragraph *b*) from state  $(i - 1)$  to state  $(i)$ :

(*a*) *Calculation of the Crack Half Length  $c_i$*

$$c_i = c_{i-1} + (a_i - a_{i-1}) \left( \frac{a_{i-1}}{c_{i-1}} \right)^{m/2} \quad (2)$$

from the known crack depth  $a_i$  and the results of the previous step,  $c_{i-1}$  and  $a_{i-1}$ , using a material-dependent exponent  $m/2$  ( $2 < m < 5$ , for example,  $m = 3$ ). Equation 2 was deduced from equations established by Irwin [3] and Paris [4] in the following way: Irwin's equation [3] is

$$K = \frac{\sigma \sqrt{\pi a}}{\Phi} \left[ \left( \frac{a^2}{c^2} \right) \cos^2 \varphi - \sin^2 \varphi \right]^{1/4} \quad (3)$$

<sup>3</sup> Yagawa, G. and Ueda, H., private communication, 1987.

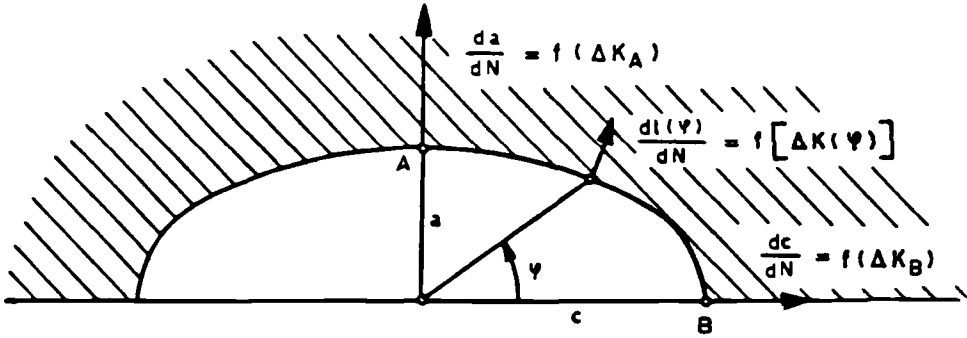


FIG. 1—Fatigue crack growth of a surface crack in isotropic material (resistance to crack propagation is considered to be independent of direction).

where  $\Phi$  is a complete elliptic integral of the second kind

$$\Phi = \int_0^{\pi/2} \left( \sin^2 \varphi + \left( \frac{a}{c} \right)^2 \cos^2 \varphi \right)^{1/2} d\varphi \quad (4)$$

For the crack in the  $c$ -direction and  $\varphi = 0$ , the  $K$ -value is

$$K_0 = \frac{\sigma \sqrt{\pi a}}{\Phi} \cdot \left( \frac{a}{c} \right)^{1/2}$$

Similarly, for the crack in the  $a$ -direction and  $\varphi = \pi/2$ ,

$$K_{\pi/2} = \frac{\sigma \sqrt{\pi a}}{\Phi}$$

Using the Paris equation [4] we obtain

$$\frac{\Delta c}{\Delta N} = C \cdot \Delta K_0^m$$

$$\frac{\Delta a}{\Delta N} = C \cdot \Delta K_{\pi/2}^m$$

Dividing the previously mentioned expressions we have

$$\frac{\Delta c}{\Delta a} = \left( \frac{\Delta K_0}{\Delta K_{\pi/2}} \right)^m$$

and since from Eq 3

$$\frac{\Delta K_0}{\Delta K_{\pi/2}} = \left( \frac{a}{c} \right)^{1/2}$$

therefore

$$\frac{\Delta c}{\Delta a} = \left( \frac{a}{c} \right)^{m/2}$$

as shown rearranged in Eq 2 with quoted indices.

(b) *Calculation of  $\Delta K_I$  from  $\Delta\sigma$ ,  $c$ , and  $a$ , Using the Finite-Element Solution [1] or Irwin's Equation [3]*—This calculation is performed in the following simplified manner: Fig. 2 shows the surface crack in a tension plate with the relevant notation. In contrast with Fig. 1,  $\varphi$  is now not the polar coordinate, but the parametric angle; see inset in Fig. 2.

The application of the finite-element solution [1] is preferable because of a wider validity range than the closed analytical solution [3].

According to Raju and Newman, the stress-intensity factor  $K$  is

$$K = \frac{\sigma \sqrt{\pi a}}{\Phi} F\left(\frac{a}{c}, \varphi, \frac{a}{t}\right) \quad (5)$$

where  $c/W \leq 0.25$  and  $c/h \leq 0.25$ . The correction factors

$$F\left(\frac{a}{c}, \varphi, \frac{a}{t}\right) = \frac{K \cdot \Phi}{\sigma \sqrt{\pi a}} \quad (6)$$

are given in Table 1.

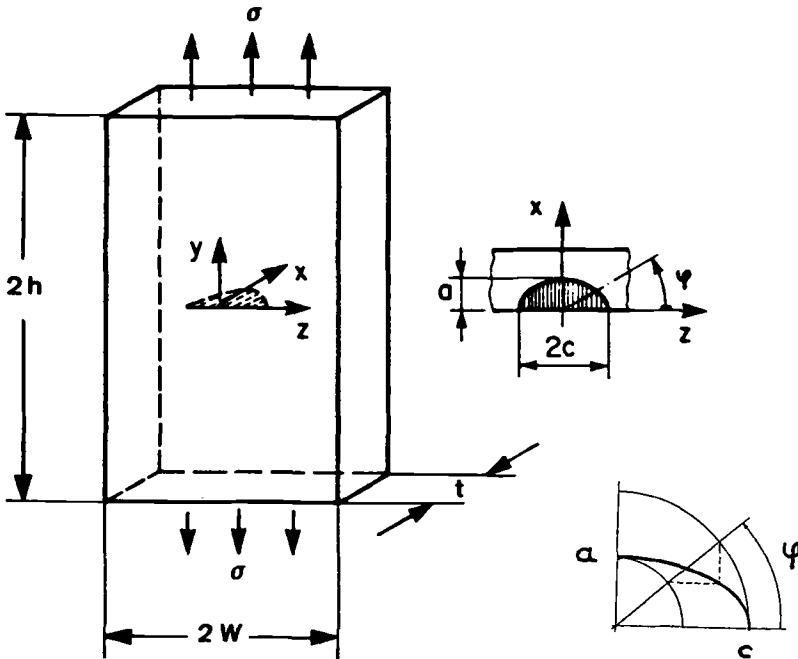


FIG. 2—Surface crack in a tension plate.

TABLE 1—Correction factors  $F\left(\frac{a}{c}, \varphi, \frac{a}{t}\right)$  from Ref 1.

a/c	a/t	$\varphi$ [°]								
		0.00	11.25	22.50	33.75	45.00	56.25	67.50	78.75	90.00
0.20	0.20	0.617	0.650	0.754	0.882	0.990	1.072	1.128	1.161	1.173
0.40	0.20	0.767	0.781	0.842	0.923	0.998	1.058	1.103	1.129	1.138
0.60	0.20	0.916	0.919	0.942	0.982	1.024	1.059	1.087	1.104	1.110
1.00	0.20	1.174	1.145	1.105	1.082	1.067	1.058	1.053	1.050	1.049
2.00	0.20	0.821	0.749	0.740	0.692	0.646	0.599	0.552	0.512	0.495
0.20	0.40	0.724	0.775	0.883	1.009	1.122	1.222	1.297	1.344	1.359
0.40	0.40	0.896	0.902	0.946	1.010	1.075	1.136	1.184	1.214	1.225
0.60	0.40	1.015	1.004	1.009	1.033	1.062	1.093	1.121	1.139	1.145
1.00	0.40	1.229	1.206	1.157	1.126	1.104	1.088	1.075	1.066	1.062
2.00	0.40	0.848	0.818	0.759	0.708	0.659	0.609	0.560	0.519	0.501
0.20	0.60	0.899	0.953	1.080	1.237	1.384	1.501	1.581	1.627	1.642
0.40	0.60	1.080	1.075	1.113	1.179	1.247	1.302	1.341	1.363	1.370
0.60	0.60	1.172	1.149	1.142	1.160	1.182	1.202	1.218	1.227	1.230
1.00	0.60	1.355	1.321	1.256	1.214	1.181	1.153	1.129	1.113	1.107
2.00	0.60	0.866	0.833	0.771	0.716	0.664	0.610	0.560	0.519	0.501
0.20	0.80	1.190	1.217	1.345	1.504	1.657	1.759	1.824	1.846	1.851
0.40	0.80	1.318	1.285	1.297	1.327	1.374	1.408	1.437	1.446	1.447
0.60	0.80	1.353	1.304	1.265	1.240	1.243	1.245	1.260	1.264	1.264
1.00	0.80	1.464	1.410	1.314	1.234	1.193	1.150	1.134	1.118	1.112
2.00	0.80	0.876	0.839	0.775	0.717	0.661	0.607	0.554	0.513	0.496

In a particular case for  $K_{\min} = 0$ , the cyclic stress-intensity factor  $\Delta K$  can be written as

$$\Delta K = K_{\max} - K_{\min} = K_{\max} = K \quad (7)$$

### Optimization Method

A sufficient number of pairs  $(\Delta K_i, a_i)$  being determined, the parameters of the equation

$$\Delta K = \frac{\Delta F}{t \sqrt{W}} f\left(\frac{a}{W}\right) \quad (8)$$

(currently used for compact type (C(T)) specimens, see ASTM Test Method for Plane-Strain Fracture Toughness of Metallic Materials [E 399-81]) can be adjusted to fit this set of information.  $\Delta F$ ,  $t$ ,  $a$ , and  $W$  are the notations for the load range, thickness, crack length, and width of the C(T) specimen, respectively. The expression

$$f\left(\frac{a}{W}\right) = \frac{\left(2 + \frac{a}{W}\right) \left(0.886 + 4.64 \left(\frac{a}{W}\right) - 13.32 \left(\frac{a}{W}\right)^2 + 14.72 \left(\frac{a}{W}\right)^3 - 5.6 \left(\frac{a}{W}\right)^4\right)}{\left(1 - \frac{a}{W}\right)^{3/2}} \quad (9)$$

is specified in ASTM E 399-81 (where  $0.2 \leq a/W \leq 0.8$ ).

By combining the two purely multiplicative factors in Eq 8 and transforming the coordinate origin, we obtain

$$\Delta K = \frac{\eta}{\sqrt{W}} f\left(\frac{a_0 + a'}{W}\right) \quad (10)$$

where

$$\begin{aligned} \eta &= \frac{\Delta F}{t}, \\ a_0 + a' &= a, \\ a' &= \sum_{i=1}^n \Delta a_i, \text{ and} \\ \Delta a_i &= a_i - a_{i-1}. \end{aligned}$$

Thus the parameters  $W$ ,  $a_0$ , and  $\eta$  can be used to reproduce the two key values for a plate geometry, namely  $a$  and  $\Delta K$ , in the C(T) specimen. For optimization of the process, the steepest descent method and a modified Newton-Raphson minimization scheme were used in the following way. The growing crack shapes and the respective  $K$ -values can be computed for the plate using Eqs 2 and 5. A typical example is shown in Fig. 3 (full-line curve). Here the crack starter (spark-eroded notch) was  $a_0 = 2$  mm and  $2c_0 = 14$  mm for a plate 150 mm wide, 20 mm thick, and 800 mm long. The crack growth was divided into nine steps from  $a_i = 4$  mm to  $a_{\text{end}} = 20$  mm when the crack reached the other side of the plate. All the steps are plotted in Fig. 3 as a full line.

In the next step, the initial values for the C(T) specimen were chosen as follows

$$W \geq \frac{5}{3} t = \frac{5}{3} \cdot 20 \approx 33 \text{ mm}$$

Say  $W = 50$  mm. Then  $a_0 \geq 0.2 W = 10$  mm.

Say  $a_0 = 10$  mm. Then

$$\eta = \frac{\Delta \sigma (W - a_0)^2}{2(2W + a_0)} = \frac{250(50 - 10)^2}{2(100 + 10)} \approx 1800 \frac{N}{\text{mm}}$$

Using these results, we computed  $\Delta K$ -values for all appropriate values of  $a$  from  $a = a_1 = 4$  mm up to  $a = a_{\text{end}} = 20$  mm,  $\Delta a = 2$  mm for the plate and  $a - a_0 = a_1 - 10 = 4$  mm up to  $a - a_0 = a_{\text{end}} - 10 = 20$  mm or  $a_1 = 14$  mm up to  $a_{\text{end}} = 30$  mm,  $\Delta a = 2$  mm for the C(T) specimen. The differences  $[\Delta K_{\text{plate}} - \Delta K_{\text{C(T)}}]$  were then computed and the expression

$$\sum_1^n [(\Delta K_{\text{plate}} - \Delta K_{\text{C(T)}})/\Delta K_{\text{plate}}]^2$$

compared with an originally chosen value of 0.015 for the illustrated example.

Since the differences were very high, higher than this prescribed value of 0.015 for the relative error squares, the iterative computation followed using the modified initial values of  $W$ ,  $a_0$ , and  $\eta$ . After an appropriate number of iteration steps, the most suitable values

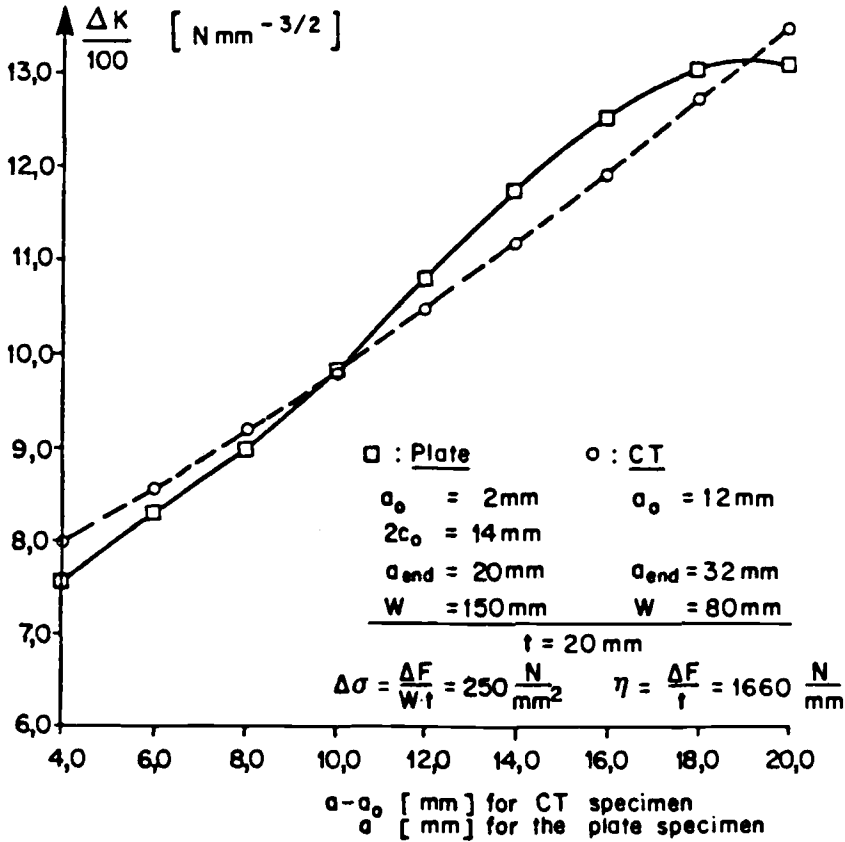


FIG. 3—Calculated  $\Delta K$  values of a growing surface crack in a plate at its deepest point (Fig. 2) and of an optimally adjusted C(T) specimen.

for the C(T) specimen were

$$W = 80 \text{ mm}, \quad a_1 = 16 \text{ mm}, \quad a_{\text{end}} = 32 \text{ mm}, \quad \Delta a = 2 \text{ mm}, \quad a_0 = 12 \text{ mm}$$

and

$$\eta = 1660 \frac{\text{N}}{\text{mm}} \cdot \sum_1^n [(\Delta K_{\text{plate}} - \Delta K_{\text{C(T)}}) / \Delta K_{\text{plate}}]^2 = 0.012$$

See also Table 2.

Additional specific details of the above procedure may be obtained in Refs 5 and 6. The influence of each independent variable may be specified as follows:

(a)  $W$  influences the function

$$\frac{\eta}{\sqrt{W}} f\left(\frac{a_0 + a'}{W}\right)$$

TABLE 2—Tabulated results illustrated in Fig. 3.

$(a - a_0)$ C(T) Specimen, mm $a$ Plate, mm	$\Delta K$ , N mm <sup>-3/2</sup>	
	Plate	C(T) Specimen
4	752	797
6	833	857
8	898	919
10	982	983
12	1079	1050
14	1174	1120
16	1254	1195
18	1304	1275
20	1308	1362

in both the vertical and the horizontal directions. This function is given by Eq 10 and illustrated in Fig. 3<sup>4</sup> where  $\Delta K$  is represented in the vertical direction, and  $(a)$  or  $(a - a_0)$  in the horizontal direction.

(b)  $\eta$  influences only the vertical scale.

(c) Referring to Eqs 8 to 10 it will be observed that the value of  $a_0$  will influence all three factors, namely,  $a/W$ ,  $f(a/W)$ , and  $\Delta K$ . Consequently, it will also influence the slope of the  $\Delta K$  versus  $(a - a_0)$  of the C(T) specimen. The section of the Curves  $\Delta K$  versus  $(a - a_0)$  and  $\Delta K$  versus  $a$  shown in Fig. 3 suggests that their slopes are nearly equal.

In order to obtain the initial estimates of  $W$ ,

$a_0$ , and  $\eta$ , we can use the following values:

(a) Equal thickness for C(T) specimen and plate is recommended. Then  $W \geq 5/3 t$  will be valid.

(b)  $a_0 \geq 0,2 W$

(c) 
$$\eta = \frac{\Delta\sigma \cdot (W - a_0)^2}{2(2W + a_0)}$$

where  $\Delta\sigma$  is the stress range in the uncracked region of the plate. This expression is derived from an elementary mechanics consideration of the stress distribution in the C(T) specimen.

Using the process described in detail in Refs 5 and 6 and previously, we start with the initial values of  $W$ ,  $a_0$ , and  $\eta$  thus obtained. The optimization algorithms are repeatedly applied until either a chosen local sum of the squares of the deviations

$$\sum_1^n [(\Delta K_{\text{plate}} - \Delta K_{\text{C(T)}})/\Delta K_{\text{plate}}]^2$$

<sup>4</sup> Editorial comment: The example results summarized in Fig. 3 illustrate the central idea of the investigation, that is, an experimental evaluation on the hypothesis that three-dimensional surface crack growth is controlled by  $\Delta K$  in the same way as two-dimensional straight-fronted crack growth. The generally good agreement of  $\Delta K$  versus  $a$  curves for the two types of specimens supports this hypothesis. The use of an appropriate, only at first sight arbitrary value of  $a - a_0$  in plotting the compact tension results has an emphasizing effect on the important comparison of the slopes of the two curves and on the conclusion that crack growth is controlled by  $\Delta K$ .

is obtained or a predetermined number of iteration steps accomplished. In this expression,  $\Delta K$  values are those used in fatigue cycling and will be replaced by the values of  $K$  in static applications.

The above method of iteration will reduce substantially the error of the inappropriate choice of the initial values of  $W$ ,  $a_0$ , and  $\eta$  and the squares of the deviations

$$\sum_1^n [(\Delta K_{\text{plate}} - \Delta K_{\text{C(T)}})/\Delta K_{\text{plate}}]^2$$

It should be remembered that only the change in the values  $W$ ,  $a_0$ , and  $\eta$  in the C(T) equation (Eq 8) is necessary because the plate values are those given in the actual engineering part investigated (designed).

### Computational and Experimental Results

To illustrate the preceding procedure, we present an example in Fig. 3 and Table 2. The material used was a fine-grain structural steel BH 43W (German Standard (DIN) (St E 43 or USA equivalent steel ASTM A 572 Grade 60). The  $\Delta K$ -values of the growing part-through crack in the plate were calculated using the finite-element solution [1].

The present aim was to establish a one-to-one correspondence between the fatigue growth rates of a part-through crack in a plate and a through crack in a C(T) specimen. As far as the crack shape was concerned, good agreement was obtained on the basis of the local Paris law [4] (Fig. 1). However, the comparison of the cyclic tests performed on a plate and optimally corresponding C(T) specimen revealed a substantial discrepancy (Fig. 4a). This may be attributed to various causes, including locally varying stresses and material properties, incomplete crack propagation algorithms, and insufficient control of experimental conditions, for example, unwanted bending effects.

Figure 3 illustrates experimental evaluation of the hypothesis that three-dimensional surface crack growth is controlled by  $\Delta K$  in the same way as two-dimensional straight-fronted crack growth. The generally good agreement between the C(T) specimen and the surface-cracked specimen results in Figs. 4a and 4b supports this hypothesis. As explained next, the error in Fig. 4b is reduced by the omission of data associated with crack initiation and the early stages of crack growth.

With reference to the incomplete crack propagation algorithms, it will be observed that when the experimental values of  $a$  and  $c$  in Table 3 are compared with computations using Eq 2, substantial discrepancies may occur. Relatively small differences in the crack shape could produce larger differences in  $\Delta K$  and  $N$ . A new computation for Fig. 3 using the experimental  $a$  and  $c$  values would provide a scatter band for this geometry.

In an earlier work [7], fatigue growth rates of through cracks were studied in a center-cracked tension specimen M(T) and a C(T) specimen, while avoiding bending by anti-buckling plates. It was found that in the whole length of Paris's regime the C(T) tests showed lower crack growth rates than the M(T) tests. A similar result, caused however by different reasons, was found in the present study, Figs. 4a and 4b. One of the experimental problems in these tests is the measurement of the crack depth. Here a crack-measuring system based on potential technique was applied. Although a potential measurements method has been used for many years, the present application was described in detail in Ref 9 and was used for all the tests reported here. This technique is particularly suitable for the depth of crack measurement since the disturbances of the electrical field are drastically reduced [9]. Also, on-line strain-gage measurements helped to reduce undesirable bending effects in the loaded plates.



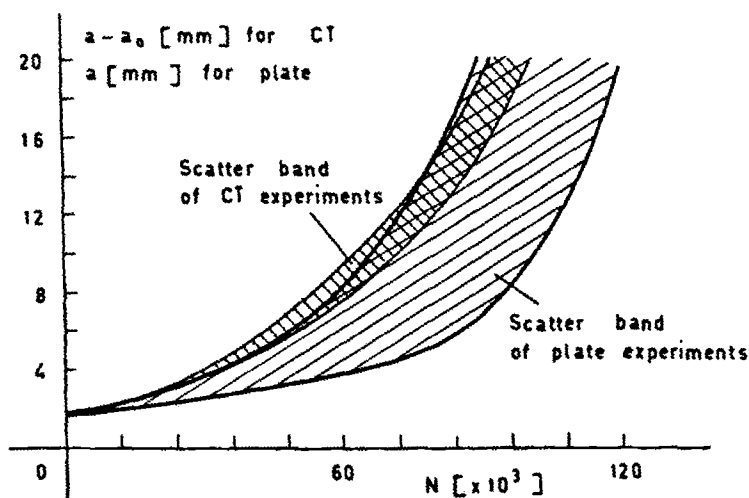


FIG. 4a—Crack propagation in tension plates and optimally adjusted C(T) specimens.

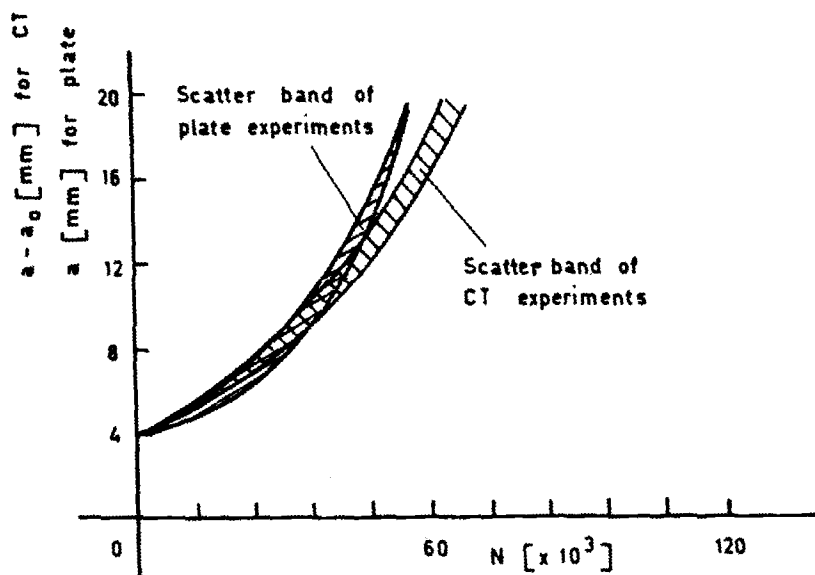


FIG. 4b—Transformations of crack growth curves (see Fig. 4a) to the origin at  $N = 0$  and crack depth of 4 mm.

TABLE 3—*Tension plates experimental results (Fig. 4).*

<i>a</i> , mm	<i>N</i>	<i>c</i> , mm	<i>a</i> , mm	<i>N</i>	<i>c</i> , mm
PLATE SPECIMEN NO. 1			PLATE SPECIMEN NO. 3		
1.79	0	7.0	1.61	0	7.0
2.24	10 000	7.0	1.73	3 000	7.0
2.84	20 000	7.0	2.01	10 000	7.0
3.57	30 000	7.15	2.43	20 000	7.0
4.49	40 000	7.5	2.91	30 000	7.0
4.93	45 000	7.7	3.33	40 000	7.0
6.79	60 000	9.1	3.62	50 000	7.0
7.48	65 000	9.85	3.92	60 000	7.05
8.68	70 000	10.55	4.35	70 000	7.20
10.03	75 000	11.95	5.20	80 000	7.45
11.62	80 000	13.35	6.86	90 000	8.25
13.50	85 000	15.20	9.51	100 000	9.90
14.18	87 000	16.60	13.48	110 000	13.30
14.58	88 000	17.80	16.21	115 000	16.20
15.53	90 000	18.80	17.49	117 000	17.35
16.36	91 400	19.45	18.85	119 000	19.60
17.07	92 500	20.80	19.56	120 000	20.95
18.32	94 300	22.70			
PLATE SPECIMEN NO. 2			PLATE SPECIMEN NO. 4		
			1.95	0	7.0
2.13	0	7.0	2.14	10 000	7.0
2.31	10 000	7.0	2.58	20 000	7.0
2.83	20 000	7.0	3.28	30 000	7.0
3.68	30 000	7.0	4.34	40 000	7.0
4.74	40 000	7.05	5.10	50 000	7.2
6.33	50 000	7.45	6.20	60 000	7.6
8.33	60 000	8.70	8.04	70 000	9.2
10.99	70 000	10.65	10.68	80 000	11.4
14.87	80 000	14.25	15.28	90 000	15.5
16.69	84 000	16.95	15.65	90 500	16.8
17.86	86 000	17.75	16.70	92 500	17.6
18.78	87 500	18.80	18.42	94 000	18.4
20.08	89 500	20.95	18.34	95 000	18.95
			18.48	96 000	19.6
			18.79	97 000	20.4
			18.94	97 500	20.8
			19.23	98 500	21.5

For the loading and geometry conditions in these experiments, see Fig. 3. The scatter bands of the  $a = f(N)$  diagrams are illustrated in Fig. 4a and show a great similarity for all four plates and three C(T) tests. The scatter bands of the  $(a - a_0) = f(N)$  diagrams are illustrated in Fig. 4a.

In another earlier work [8] the notch opening displacement at seven positions was measured in notched and surface precracked tension plates, using a specially developed miniature COD meter.

A total of five COD tests with tension plate specimens were performed in air at room temperature. Afterwards C(T) specimens were taken from the tested plates, two samples from each plate specimen. Similarly to  $K$  and  $\Delta K$ , generally good agreement of COD was found for the two types of specimen "plate" and C(T). The COD tests belonged to the same experimental program as the fatigue crack growth tests with plates and C(T) specimens for investigating some additional particular problems.

Further application of this method might help to clarify the influence of a locally varying crack resistance along the crack front mentioned earlier. Figure 4a shows, however, that by using C(T) specimen data for the prediction of fatigue growth of surface cracks, the results will be on the safe side.

TABLE 4—Experimental results for three adjusted C(T) specimens (see also Figs. 3 and 4a).

$(a - a_0)$ , mm	$N$		
	No. 1	No. 2	No. 3
3.0	24 000	24 000	24 000
3.5	28 470	30 575	30 475
4.0	29 510	35 550	35 175
4.5	31 950	40 300	39 250
5.0	35 640	43 825	43 175
5.5	40 775	47 275	46 775
6.0	42 050	50 375	50 150
6.5	45 020	53 500	53 550
7.0	47 500	56 700	56 175
7.5	51 955	59 150	59 025
8.0	53 235	61 875	61 825
8.5	56 705	64 275	64 475
9.0	57 875	66 875	66 975
9.5	60 390	69 150	69 450
10.0	61 855	71 225	71 675
10.5	65 045	73 625	73 725
11.0	66 150	75 575	75 850
11.5	68 790	77 600	77 700
12.0	70 200	79 500	79 200
12.5	72 755	81 275	81 225
13.0	73 830	82 950	82 800
13.5	76 035	84 800	84 625
14.0	77 670	86 275	86 300
14.5	79 205	87 800	87 725
15.0	79 935	89 350	89 175
15.5	81 230	90 900	90 625
16.0	82 175	92 275	91 925
16.5	84 010	93 575	93 300
17.0	84 800	94 850	94 625
17.5	86 240	96 000	95 800
18.0	87 320	...	96 900
18.5	88 370	...	98 025
19.0	89 305	...	...

Referring again to Fig. 4a, it will be noted that by starting the count of load-cycles  $N$  at the moment when both cracks have a depth of 4 mm ( $a$  for the plate,  $a - a_0$  for the C(T) specimen), we obtain a substantial reduction in scatter. This manipulation, though somewhat arbitrary at first sight, makes clear that the congruence between the two types of experiments is remarkably good when neglecting their initial phases (Fig. 4b).

Figure 5 shows a comparison of the observed crack growth with an engineering proposal assuming a constant  $a/c$  ratio as postulated in the American Society of Mechanical Engineers (ASME) Boiler and Pressure Vessel Code, Section XI. This assumption may sometimes be very far from correct, depending on the crack depth-to-length ratio and the geometry of the plate. Consequently, the number of cycles between the observed position of the crack and its critical state may be dramatically overestimated.

Figure 6 compares the detectable and critical crack size for two cases of semi-elliptical and semi-circular crack,  $K_{Ic} = 4000 \text{ N/mm}^{3/2}$ ,  $\sigma = 350 \text{ N/mm}^2$ , and  $t = 100 \text{ mm}$ . In contrast to those in Fig. 5, the crack sizes in Fig. 6 were computed on the assumption of a constant  $a/c$  ratio as suggested in the ASME Code.

Figures 7 and 8 illustrate the experimental setup and four macrofractographs of tension plate specimens, respectively. The initial geometries of the plate specimens, Fig. 8, were identical (20 by 150 by 800 mm); they contained a starter notch  $a_0 = 2 \text{ mm}$  and  $2c_0 = 14 \text{ mm}$ , growing under identical testing conditions (for details see also Fig. 3). The cyclic frequency was 6 Hz, the stress ratio  $R = \sigma_{\min}/\sigma_{\max}$  was 0.06. Note that the fatigue crack growth behavior was reproduced to a high degree of accuracy.

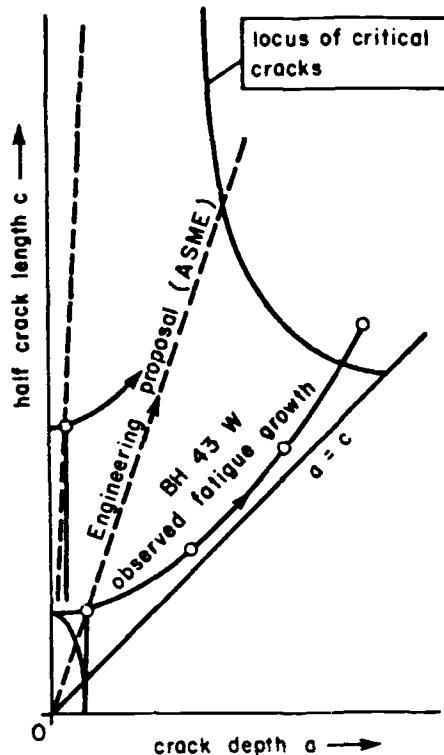


FIG. 5—Fatigue growth of surface cracks towards critical size. Comparison of experimental results with ASME Code, Section XI.

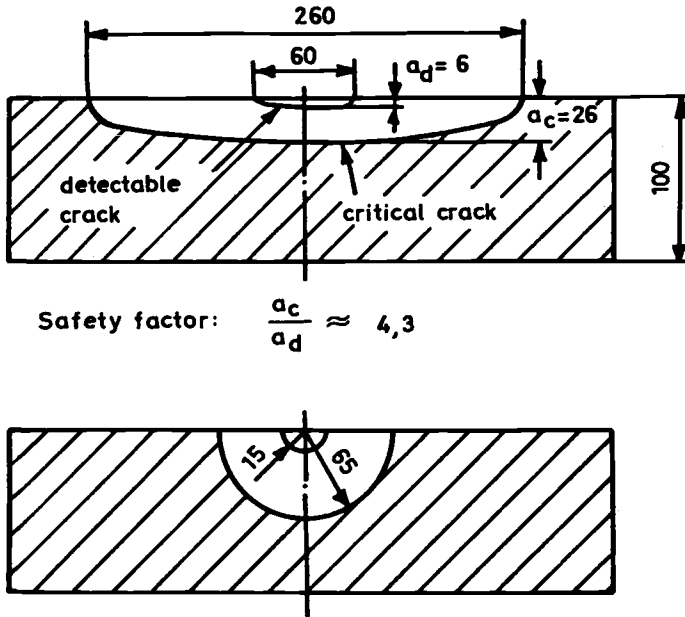


FIG. 6—Two examples of critical and detectable crack sizes: (a) semi-elliptical and (b) semicircular cracks.

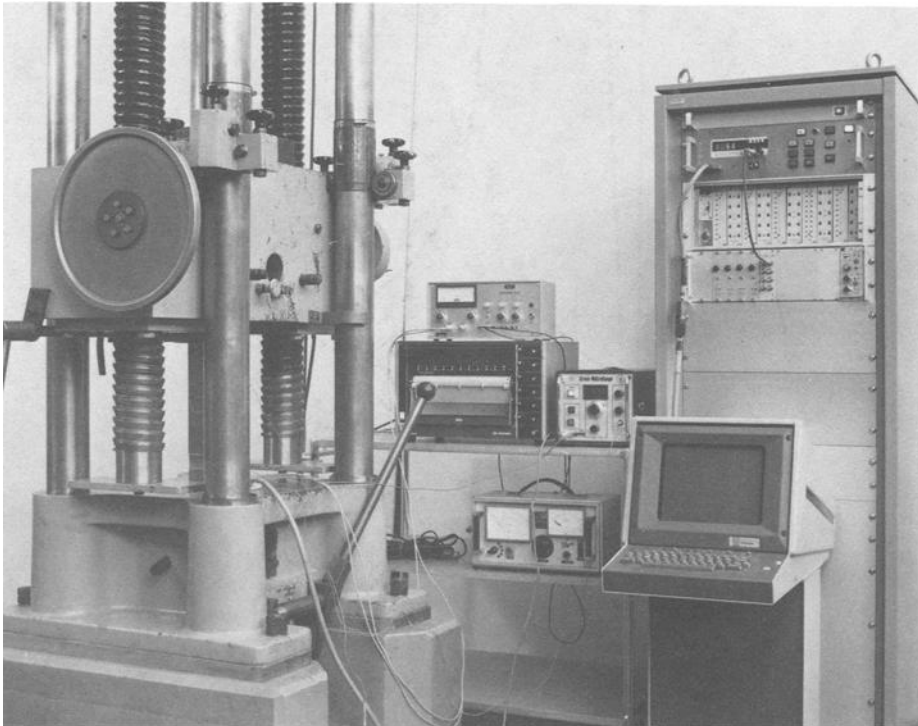


FIG. 7—Experimental setup for tests with tension plates.

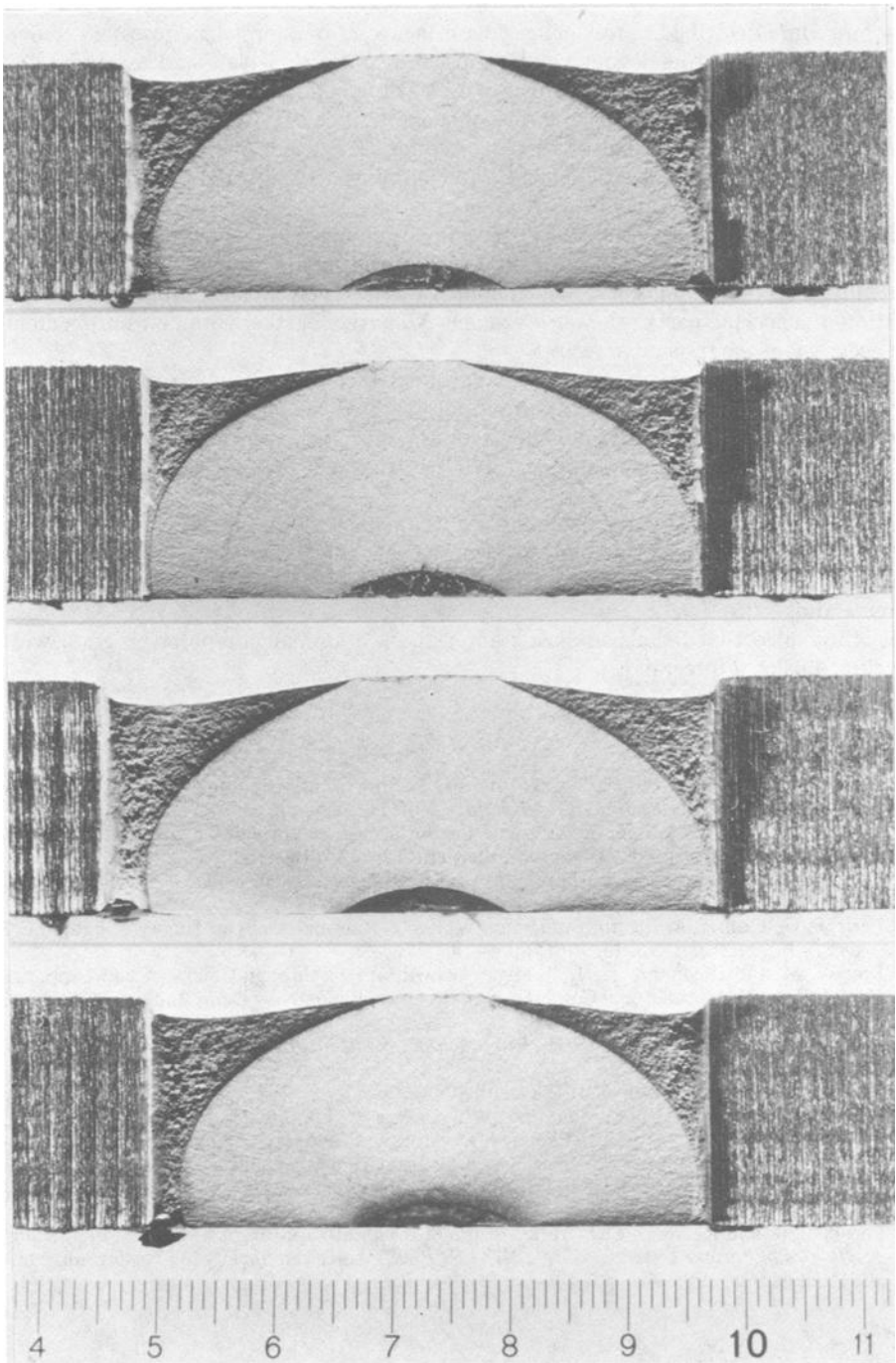


FIG. 8—Fracture surfaces of four tension plates specimens.

## Conclusions

A procedure described in this paper determines a set of parameters necessary to obtain equal  $\Delta K$  values and analogous crack propagation rates in a plate and a standard C(T) specimen. A comparison of the number of cycles obtained for the equivalent crack growth in both types of specimens suggests that the significance of  $\Delta K$  values in a part-through crack is closely related to that in a C(T) specimen. The experimental results obtained in the fatigue tests performed with the plates and appropriately adjusted C(T) specimens indicate that this hypothesis may be correct.

It is a common practice to use a C(T) specimen geometry to investigate a very large part of  $da/dN$  versus  $\Delta K$  curve. However, the crack growth in a real structure may occur only in a limited section of this curve. The method described here enables a more precise investigation of a specific part of the  $da/dN$  versus  $\Delta K$  curve together with an improvement in the accuracy of the respective results.

Although these observations were made under idealized circumstances (air environment, room temperature, constant-amplitude loading), the transferability of the results obtained using this approach should be valid also for more complicated service conditions, such as in a water reactor environment (300°C, 140 bar) and at variable-amplitude loadings [5,8].

As already shown by others, the fatigue experiments with the tension plates may be also regarded as a suitable experimental verification of the linear elastic  $K$ -solution of Raju and Newman [1]. Other solutions are being analyzed at present, also for surface cracks under pure bending [9].

It is intended that for elasto-plastic application, a similar computer program will be developed using  $J$ -integral<sup>5</sup> [2].

## References

- [1] Raju, I. S. and Newman, J. C., "Stress-Intensity Factors for a Wide Range of Semi-elliptical Surface Cracks," *Engineering Fracture Mechanics*, Vol. 11, 1979, pp. 817-829.
- [2] Yagawa, G. et al., "A Parametric Study on the Surface Crack Growth," *Transactions, SMiRT-9*, Vol. G, F. H. Wittman, Ed., Balkema, Rotterdam, 1987, pp. 189-194.
- [3] Irwin, G. R., "Crack-extension Force for a Part-through Crack in a Plate," *Journal of Applied Mechanics*, Vol. 4, 1962, pp. 651-654.
- [4] Paris, P. C., Gomez, M. P., and Anderson, W. E., "A Rational Analytic Theory of Fatigue," *The Trend in Engineering*, Vol. 13, 1961, pp. 9-14.
- [5] Prodan, M. and Erismann, T. H., "Fatigue Growth of Part-through Cracks: A New Approach," *Proceedings, 6th International Conference on Fracture (ICF6)*, New Delhi, India, 1984, pp. 1927-1934.
- [6] Aday, P. R. and Dempster, M. A. H., *Introduction to Optimization Methods*, Chapman and Hall, London, 1978.
- [7] Rhodes, D. and Radon, J. C., "Effect of Some Secondary Test Variables on Fatigue Crack Growth," *Fracture Mechanics: Fourteenth Symposium. Volume II: Testing and Application, ASTM STP 791*, 1983, American Society for Testing and Materials, Philadelphia, pp. II 33-II 46.
- [8] Prantl, G. and Prodan, M., "The Crack Opening Displacement of Semi-elliptical Surface Cracks," *Fracture and Fatigue*, J. C. Radon, Ed., Pergamon Press, Oxford, U.K., and New York, 1980, pp. 185-193.
- [9] Foroughi, R. and Radon, J. C., "Crack Closure Behavior of Surface Cracks Under Pure Bending," *Mechanics of Fatigue Crack Closure, ASTM STP 982*, American Society for Testing and Materials, Philadelphia, 1988.

<sup>5</sup> See footnote 3.

## Influences of Crack Closure and Load History on Near-Threshold Crack Growth Behavior in Surface Flaws

**REFERENCE:** Jira, J. R., Nagy, D. A., and Nicholas, T., "Influences of Crack Closure and Load History on Near-Threshold Crack Growth Behavior in Surface Flaws," *Surface-Crack Growth: Models, Experiments, and Structures*, ASTM STP 1060, W. G. Reuter, J. H. Underwood, and J. C. Newman, Jr., Eds., American Society for Testing and Materials, Philadelphia, 1990, pp. 303-314.

**ABSTRACT:** Fatigue crack growth threshold tests are conducted on a high-strength titanium alloy using a surface flaw specimen geometry. A laser interferometer is used to monitor crack-mouth opening displacements, from which compliance determined crack length is computed. Four types of loading history involving both increasing- and decreasing- $\Delta K$  are used to reach a threshold condition. Two of the test conditions maintain constant  $K_{\max}$  under computer control. Crack closure is obtained from the load-displacement plots and used to determine an effective stress-intensity range,  $\Delta K_{\text{eff}}$ . Results from all four test types indicate that a single value of an effective stress-intensity range is obtained which is independent of stress ratio,  $R$ , or load history. Crack growth rate data in the near-threshold regime, on the other hand, appear to have a dependence on  $R$  even when  $\Delta K_{\text{eff}}$  is used as a correlating parameter.

**KEY WORDS:** fatigue crack growth, threshold, surface flaw, crack closure, effective stress intensity

The determination of near-threshold crack growth behavior in structural materials is important in damage-tolerant-based life predictions of high-cycle fatigue limited components in aircraft and turbine engine applications. Since a large portion of the life of a component may be spent at very low crack growth rates, accurate knowledge of the near-threshold growth rate behavior is important for life prediction. Further, for very high-frequency loading applications, such as turbine blades which may see vibratory stresses in the kilohertz regime, knowledge of a true threshold stress intensity ( $\Delta K_{\text{th}}$ ) below which a defect or crack will not propagate to failure is necessary.

The threshold stress-intensity factor range,  $\Delta K_{\text{th}}$ , defines a condition below which a crack will not propagate or, alternately, propagates at an arbitrarily slow growth rate defined as  $10^{-10}$  m/cycle. The standard method of determining  $\Delta K_{\text{th}}$  is to conduct a decreasing  $\Delta K$  test on a specimen at a constant value of stress ratio,  $R$ , following a history of maximum  $K$  in the form

$$K = K_0 \exp[C(a - a_0)] \quad (1)$$

<sup>1</sup> Materials research engineer and senior scientist, respectively, Wright Research and Development Center, Materials Laboratory (MLLN), Wright-Patterson Air Force Base, OH 45433.

<sup>2</sup> Graduate student, Air Force Institute of Technology, Wright-Patterson Air Force Base, OH 45433.



where  $K_0$  and  $a_0$  are the initial values of the stress intensity and crack length, respectively, and  $C$  is a load-shedding constant which is supposed to be no less than  $C = -0.08/\text{mm}$  [ASTM Standard Test Method for Measurements of Fatigue Crack Growth Rates (E 647-86A)]. When such a test is performed, a crack is grown at an ever decreasing growth rate until sufficient data are obtained to either determine or extrapolate to the threshold value which is commonly defined as a growth rate of  $10^{-10}$  m/cycle. The crack also continues to grow at an ever decreasing growth rate through a region of previously deformed material. A wake of plastically deformed material is left behind the crack, leading to crack closure in the near-threshold regime [1]. The extrapolation of data obtained under such conditions to a condition of the incipient growth of an initial defect which has *not* been previously propagating is certainly a question. The load-history effects and any subsequent closure development in a load-shedding test can generally be expected to be different than what might be found in a nonpropagating, preexisting flaw. One concept which has been proposed is that the effective stress-intensity range,  $\Delta K_{\text{eff}}$ , approaches zero as the threshold is approached. If this is the case, the incipient growth of an initial defect which has not previously propagated could occur at an arbitrarily low load since such a crack will not yet have developed any closure. This, in fact, is the basis for much of the reasoning used to explain the anomalous high growth rates of small cracks and the observations that small cracks propagate at stress intensities below the long crack threshold value [2-4].

Another question to be raised in the determination of threshold values is the uniqueness of such values based on a standard load-shedding test. Thus, it would be important to know at which  $\Delta K$  levels a crack would start to propagate if the load were gradually increased from below threshold and how those values compare with ones obtained from a standard decreasing  $\Delta K$  test. It is also of interest to see if threshold values obtained from that type of loading were dependent on the history of the increasing load or the method by which the initial flaw was obtained.

There have been a number of investigations which have addressed the question of the effect of loading history on the determination of a threshold below which cracks will not propagate. Cadman et al. [5] found that the threshold values obtained in a decreasing  $\Delta K$  test depended on the  $K$ -reduction rate (the constant  $C$  in Eq 1) and recommended that such rate should be reported as part of the test procedure. They suggested that the threshold value was not a material property since it depended on the history of loading. Doker et al. [6] found in a conventional decreasing  $\Delta K$  threshold test that the threshold depended on stress ratio,  $R$ . They suggested that this dependence on  $R$  is, in reality, a presentation of the closure behavior of the material. They introduced a test technique in which  $K_{\text{max}}$  was maintained constant while  $K_{\text{min}}$  was increased. In this increasing  $R$  type of test, it was suggested that a true material threshold can be obtained only when the  $K_{\text{max}}$ -values were high enough to avoid closure (load history) effects. This same test procedure was used later by Doker and Peters [7] to extend the data base to a number of other materials. Herman et al. [8] also noted that the conventional decreasing  $\Delta K$  threshold test, when conducted at low  $R$ , could lead to nonconservative estimates of the materials inherent fatigue resistance. This was attributed to crack closure which is observed to increase during a standard (decreasing  $\Delta K$ , constant  $R$ ) threshold test, leading to a decrease in  $\Delta K_{\text{eff}}$  and a corresponding reduction in growth rate. They also proposed the use of a constant  $K_{\text{max}}$ , increasing  $R$  test, pointing out that a further advantage of such a test is that the stress-intensity reduction rate can assume large values without introducing false conditions. Their stress gradient followed the form

$$\Delta K = \Delta K_0 \exp[C(a - a_0)] \quad (2)$$

Values of  $C$  between  $-0.06$  and  $-0.4 \text{ mm}^{-1}$  were used without any noticeable difference in growth rate. This test technique was also suggested as a method for obtaining data from conventional long crack specimens which closely simulate the fatigue crack growth behavior of small cracks [9]. Castro et al. [10] defined a "fatigue tolerance range" similar to a conventional threshold ( $10^{-10} \text{ m/cycle}$ ), which represents conditions for the nonpropagation of a fatigue crack. Using four different loading histories, they found that this tolerance range depends on the amplitude of the cyclic plastic zone from the prior loading history. The differences in their results were explained by the differences in damage states due to both the  $K_{\max}$  and  $\Delta K$  from the prior fatigue cycles.

In a prior investigation, an increasing  $\Delta K$  test was used to determine thresholds in a high-strength titanium alloy [11]. The results of that study indicated that the use of an effective stress-intensity factor,  $\Delta K_{\text{eff}}$ , which accounts for crack closure effects, enabled consolidation of threshold values from both increasing and decreasing  $\Delta K$  tests into a single value. In those experiments, the stress ratio,  $R$ , was maintained constant at a value of 0.1. The variation of threshold  $\Delta K$  with  $R$  was not addressed. Further, the possible influences of loading history, including that of the precracking procedure for the increasing  $\Delta K$  tests, was not determined.

To address the question of the influences of prior loading history and stress ratio on threshold, we conducted a series of experiments on surface flaws in a high-strength titanium alloy, Ti-6Al-2Sn-4Zr-6Mo. Four different load histories were examined which included both increasing and decreasing  $\Delta K$  test types. The influence of crack closure was examined through the use of an effective stress-intensity factor.

### Experimental Approach

All testing was performed on the alloy Ti-6Al-2Sn-4Zr-6Mo. The material and heat treatment were the same as those used in previous studies [12,13]. Threshold testing was performed using two specimen geometries, a small and a large surface-flaw specimen. Both specimens have rectangular cross sections. The small surface-flaw specimen [12] employs a mild notch to facilitate natural initiation of surface cracks. This geometry allows cracks of surface lengths as small as 0.075 mm to be studied. The large surface-flaw specimen [13] utilizes a semicircular electro-discharge machined (EDM) notch approximately 0.1 mm deep by 0.2 mm wide and having a height of 0.07 mm for crack initiation. Surface-crack sizes ranging from 0.4 mm to as large as 8 mm were studied using this geometry. The gage sections of all specimens of both geometries were electropolished to a depth of at least 0.20 mm to eliminate surface residual stresses.

Most of the tests reported in this investigation were conducted on the large rectangular specimens unless otherwise noted. Precracking for both specimen geometries was accomplished using fully reversed axial loading ( $R = -1.0$ ) at  $\sigma_{\max} = 0.6 \sigma_y$  ( $\sigma_y = \text{yield stress} = 1158 \text{ MPa}$ ) for the small-crack specimens and  $\sigma_{\max} = 0.3 \sigma_y$  for the large-crack specimens. The specimens were tested under full computer control using a laser interferometric displacement gage (IDG) to measure crack-mouth opening displacement (CMOD) [14,15]. For the small-crack specimens, natural crack initiation was detected by periodic visual inspection during the constant amplitude precracking. For the large-crack specimens, abrupt changes in compliance across the EDM starter notch indicated crack initiation which was verified by visual inspection. Crack length was determined from compliance measurements of load-CMOD by fitting a straight line to the linear portion of the curve. Crack closure loads were determined as the load at which the load-CMOD curve displayed the first deviation from linearity on unloading. The extremely high resolution of the IDG,

which allowed displacements to be measured to an accuracy of  $0.01\text{ }\mu\text{m}$ , enabled accurate determination of the closure loads and provided crack length measurements that were accurate to within approximately  $1\text{ }\mu\text{m}$ .

Four types of loading histories were employed; the first two were constant  $R$  tests and the second two were variable  $R$ . The four test types are shown schematically in Fig. 1 and summarized in Table 1. The first (Type I) test was the standard decreasing  $\Delta K$  test described by Eq 1. The load was shed at a constant value of  $R$  until the growth rate dropped to below  $10^{-10}\text{ m/cycle}$ . The load was then maintained constant while the crack continued to grow under increasing  $\Delta K$  to complete the test. Data were obtained under this test condition for values of  $R$  of 0.1, 0.5, and 0.8. The second (Type II) constant  $R$  test was an increasing  $\Delta K$  test. In this case, the specimen was precracked at negative  $R$  and then tested at a positive value of  $R$  of either 0.1 or 0.5. The initial  $\Delta K$  was chosen to be below threshold

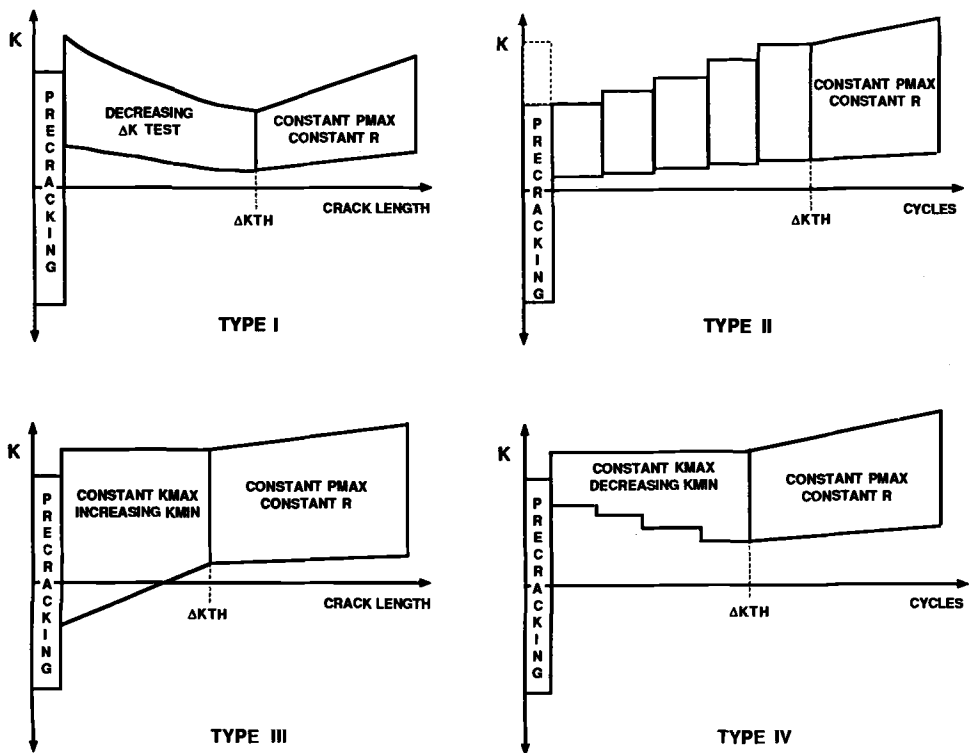


FIG. 1—Schematic of loading history used in four test types in experimental investigation.

TABLE 1—Test conditions for the four types of threshold tests.

Type	$\Delta K$	$K_{max}$	$R$
I	decreasing	decreasing	constant
II	increasing	increasing	constant
III	decreasing	constant	increasing
IV	increasing	constant	decreasing

and sufficient cycles were applied to validate that the crack was not growing above a rate of  $5 \times 10^{-11}$  m/cycle. The  $\Delta K$  value was then increased slightly and the procedure repeated. When crack growth was finally detected, the test was continued under constant load amplitude to obtain near-threshold growth rate data. The last two types of tests were conducted under variable  $R$  conditions using a condition of constant  $K_{\max}$  [16,17]. In the Type III decreasing  $\Delta K$  test,  $K_{\min}$  was increased linearly with crack length until threshold was reached. The test was then continued at the threshold  $R$  under constant load range. In the Type IV increasing  $\Delta K$  test,  $K_{\min}$  was decreased linearly with crack length until the crack started to grow. As in the Type II test, initiation of crack growth was defined as when the growth rate reached a value of  $5 \times 10^{-11}$  m/cycle. After this point, the load range was maintained constant. In all of the tests, closure loads were measured continuously. The data obtained include  $\Delta K_{th}$ ,  $\Delta K_{eff,th}$ , and  $da/dN$  as a function of both  $\Delta K$  and  $\Delta K_{eff}$ .

In both the Type II and Type IV increasing- $\Delta K$  threshold tests, the initial maximum loading was such that the applied  $\Delta K$  was well below the threshold as determined in compact type (C(T)) tests. Thirty crack length measurements were made using the IDG system with a minimum of additional fatigue cycling. A linear regression and standard deviation calculation on these 30 points supplied a measure of the reproducibility of the crack length measurements for a given crack and experimental setup. A value for the number of cycles,  $N$ , necessary to establish a growth rate above threshold, was then determined. The test proceeded by applying blocks of  $N$  cycles with crack length measurements every  $N/30$  cycles. After each block of  $N$  cycles, a linear regression on the preceding 30  $a-N$  points was made. If the slope of the data indicated a negative growth rate or a growth rate below threshold, the load was incremented to increase the applied  $\Delta K$  and the process was repeated. If a growth rate above threshold was indicated, the crack was grown at the current maximum load under constant amplitude conditions.

## Results and Discussion

Data from the load-shedding portion of a Type I test are presented in Fig. 2 as a function of  $\Delta K_{eff}$  as determined from the closure measurements. The solid line in the figure represents the trend for data obtained from C(T) specimens in an earlier investigation on the same material for the same value of  $R = 0.1$  [13]. It can be seen that both the growth rates over the entire range of  $\Delta K$  as well as the value for the threshold effective stress intensity are nearly the same for the two different specimen geometries. Similar results were obtained for tests conducted at  $R = 0.5$  and  $R = 0.8$ . In these latter tests, no closure was observed, thus applied and effective stress-intensity values were identical. These data compared well with C(T) data obtained at  $R = 0.5$  where there was also no closure observed. The data for the values of  $\Delta K$  at threshold, defined as a growth rate of  $10^{-10}$  m/cycle, are summarized for all of the Type I tests in Fig. 3. For reference purposes, the effective and applied stress-intensity values from C(T) tests are also shown. It can be seen that the use of  $\Delta K_{eff}$  consolidates all the data into a single value for the threshold stress intensity, consistent with the C(T) data. Use of  $\Delta K$ , without consideration for crack closure, does not provide a single value for threshold stress intensity.

The results for the value of the threshold stress intensity from the Type II increasing  $\Delta K$  tests are summarized in Fig. 4. Values using both applied  $\Delta K$  and effective  $\Delta K$  based on closure measurements are shown for the seven tests performed along with the reference C(T) data. All of these tests, with the exception of one, were conducted on small, naturally initiated cracks without the use of a starter notch [11]. For these tests, both  $\Delta K$  and  $\Delta K_{eff}$  appear to be equally good correlating parameters to obtain a single threshold value which is consistent for both surface flaws and C(T) specimens. All tests were run at  $R = 0.1$  and,

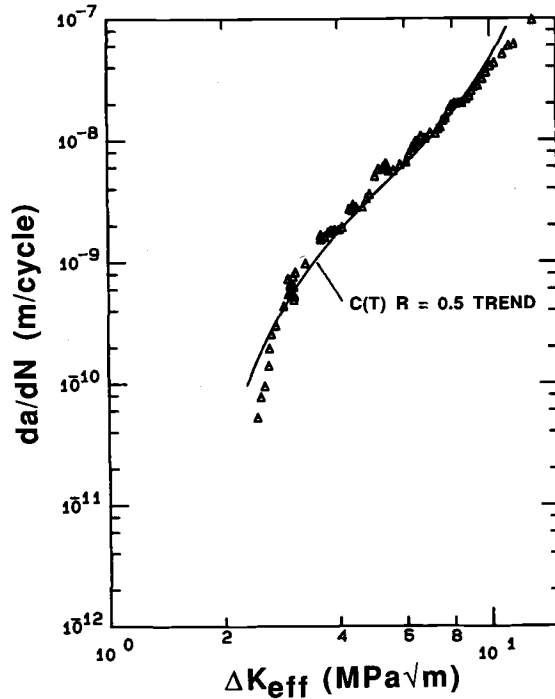


FIG. 2—Crack-growth-rate data for Type I test at  $R = 0.1$  as a function of  $\Delta K_{eff}$ .

in all cases, closure developed after the precracking at  $R = -1.0$ . Data for two of the specimens in Fig. 4 show lower bounds on the threshold value. In both cases, the specimen failed prematurely at another crack so that a threshold value had not yet been established for the crack under observation.

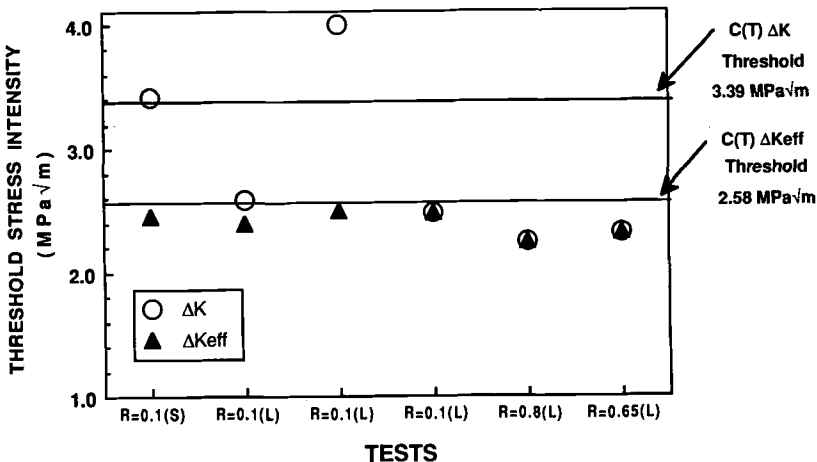


FIG. 3—Summary of test results for threshold stress intensity from Type I tests.

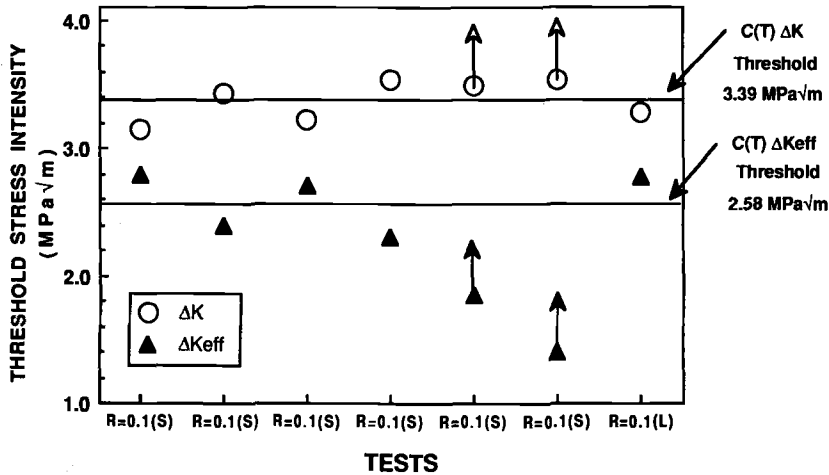


FIG. 4—Summary of test results for threshold stress intensity from Type II tests.

The Types III and IV tests were conducted to evaluate the role of prior loading history on the threshold under both decreasing and increasing  $\Delta K$  test conditions. In a Type I test, the crack is growing into a region with a plastic zone size, dependent on maximum  $K$ , which is larger than that created by new growth at a lower value of  $K_{max}$ . Although guidelines have been developed to minimize the prior loading history effect by controlling the rate of load shedding, the history effect cannot be eliminated completely. In the Type II test, in most cases, the initial crack growth occurred at a value of  $K_{max}$  which was below that applied during the reversed loading precracking procedure. Thus, the crack started to grow into a plastic zone which was larger than that which would be developed by the growing crack. In the Type III tests, the plastic zone ahead of the crack was kept constant as the crack grew at a decreasing rate, while in the Type IV test, the plastic zone due to precracking was smaller than that due to the first increment of crack extension as threshold is approached with increasing  $\Delta K$  loading.

Typical growth rate data from a Type III test are presented in Fig. 5 for a specimen which was grown initially at  $R = 0.3$  and reached threshold at  $R = 0.44$ . The constant load, increasing  $\Delta K$ , part of the test was carried out at a constant value of  $R = 0.44$ . The data in Fig. 5 are corrected for closure and plotted against  $\Delta K_{eff}$ . It can be seen that the decreasing and increasing  $\Delta K$  growth rate data near threshold collapse into a single curve which falls on the C(T) trend line for  $R = 0.5$  where there was no closure. At the initial higher growth rates during the decreasing  $\Delta K$  portion of the test, the growth rate data do not fall on a single curve. These data represent a condition of negative  $R$  for the initial portion of the test and an increasing  $R$  as the test proceeds at decreasing growth rates. The lack of consolidation of the data into a single curve may be due to the inability to determine the true closure load from load-CMOD data on a surface flaw geometry, or the influence of  $R$  or mean load on the growth rate, even when corrected for closure. It is of importance to note that the only case where crack growth rate data could not be consolidated into a single curve using  $\Delta K_{eff}$  to account for crack closure occurred at negative values of  $R$ . The data for threshold from all of the decreasing  $\Delta K$  tests, Types I and III, are summarized in Fig. 6 along with the relevant C(T) data. Threshold stress intensity is plotted against  $R$  to examine any effect due to mean load. It can be seen that a single value of threshold of approximately  $2.3 \text{ MPa} \sqrt{m}$  is obtained from all of the tests when using an effective stress inten-

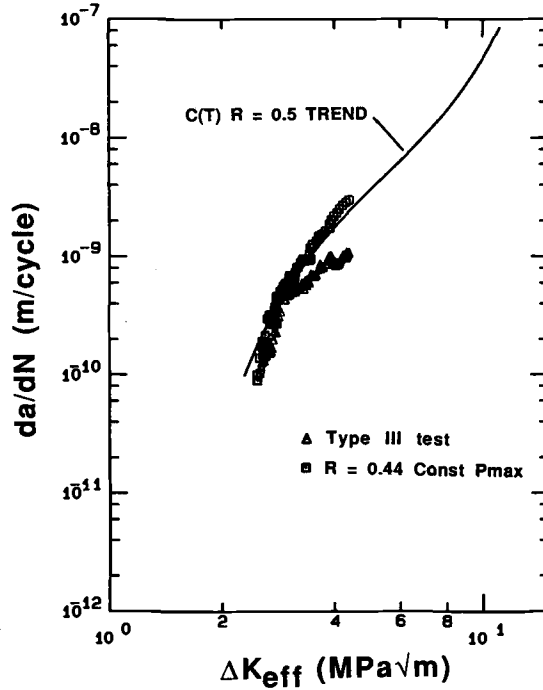


FIG. 5—Crack-growth-rate data for a Type III test as a function of  $\Delta K_{eff}$ .

sity which accounts for closure effects. If closure is not considered, then the threshold value appears to increase with decrease in  $R$  below  $R = 0.4$ . Above this value of  $R$  there is no closure so that applied and effective stress intensity are identical and there is no variation with  $R$ .

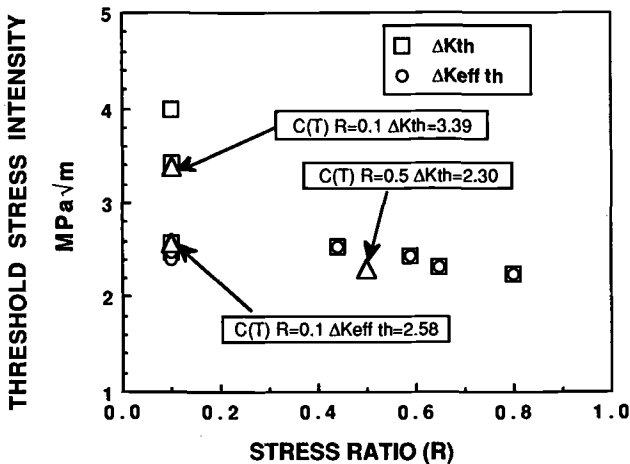


FIG. 6—Summary of test results for threshold stress intensity as a function of  $R$  from decreasing  $\Delta K$  tests. (Type I and Type III) Data from reference  $C(T)$  tests are shown as triangles.

The last type of test, Type IV, involved an increase in  $\Delta K$  while maintaining  $K_{\max}$  constant until the crack reached a growth rate in excess of  $5 \times 10^{-11}$  m/cycle. The extreme precision of the IDG allowed these very low growth rates to be observed without having to apply an unreasonably large number of cycles at each load condition. Each subsequent loading block was applied at a lower value of  $R$  as shown in Fig. 1. Results of crack growth rate from a typical test of this type are shown in Fig. 7 as a function of  $R$ . The initial block of cycles was applied at  $R = 0.70$ , from which it was determined that the crack was not growing above the established threshold level. Seven more blocks of cycles were applied, each one at a slightly lower value of  $R$  or slightly higher  $\Delta K$ . Although the crack was apparently growing during this entire procedure, the data obtained in real time during the test established only that the crack growth rate had not exceeded a value of  $10^{-10}$  m/cycle. After the test had been completed, plots such as that of Fig. 7 were constructed to interpolate the value of  $R$  (and  $\Delta K$ ) for threshold. These same data, plotted as a function of growth rate using incremental polynomial fitting, are shown in Fig. 8 as a function of  $\Delta K$ . Since there was no observed closure, effective and applied stress intensities are identical. It can be seen that the growth rate data above threshold follow the C(T) trend line quite closely. The values for threshold as a function of  $R$  for all of the increasing  $\Delta K$  tests are summarized in Fig. 9. With the exception of one test at  $R = 0.2$ , the effective stress intensity appears to consolidate all of the data into a single value for threshold. The anomalous test showed very little closure and thus an unexpectedly high value for  $\Delta K_{\text{eff}}$ . The growth rate data for this test did not consolidate with the C(T) data at  $R = 0.5$  [16], again indicating that closure should have been expected. In fact, if a closure level of approximately  $1 \text{ MPa } \sqrt{\text{m}}$  were present, both the effective threshold value and the growth rate data would have been consistent with the remaining data when using an effective stress intensity factor. This would lead one to believe that closure may not be easily detected in surface flaws for stress ratios in the vicinity of 0.2. For larger values of  $R$ , there is no apparent closure. For smaller values of  $R$ , closure is readily detected. In this intermediate region, the extent of closure may be inadequate to detect with a mouth-opening displacement gage, no matter how precise it is.

Finally, all of the threshold values are summarized in Fig. 10 as a function of  $R$ . Again, with the exception of a single data point, all of the data indicate a unique value of an

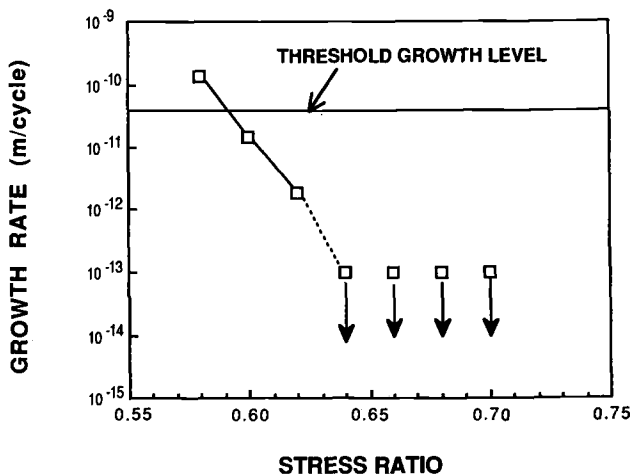


FIG. 7—Crack growth rate as a function of  $R$  for a Type IV threshold test.



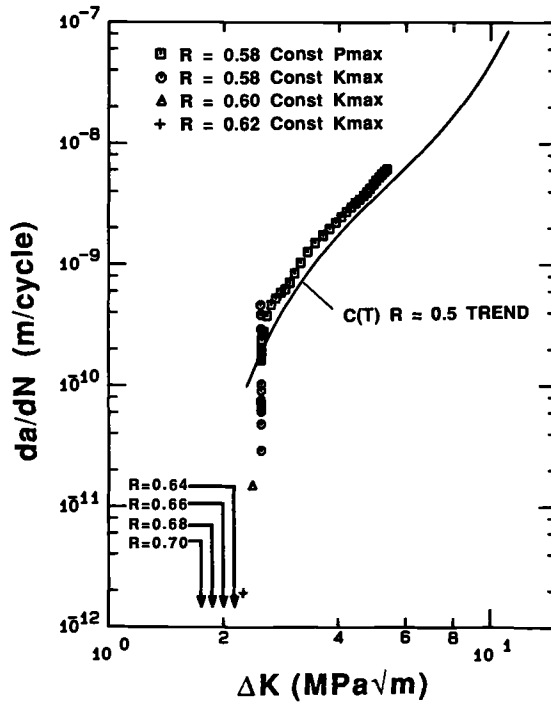


FIG. 8—Crack-growth-rate data for a Type IV test as a function of  $\Delta K$ .

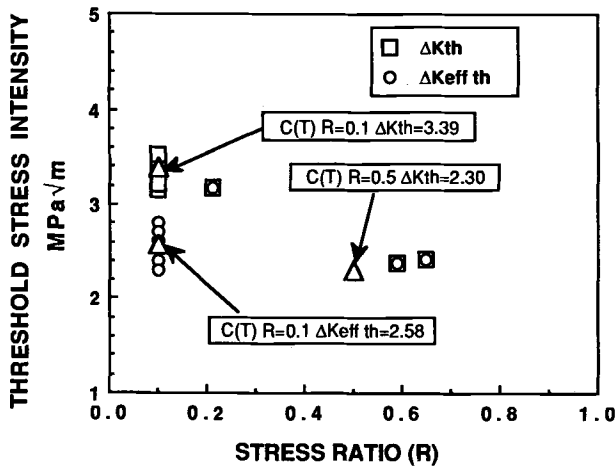


FIG. 9—Summary of test results for threshold stress intensity as a function of  $R$  from increasing  $\Delta K$  tests. (Type II and Type IV) Data from reference  $C(T)$  tests are shown as triangles.

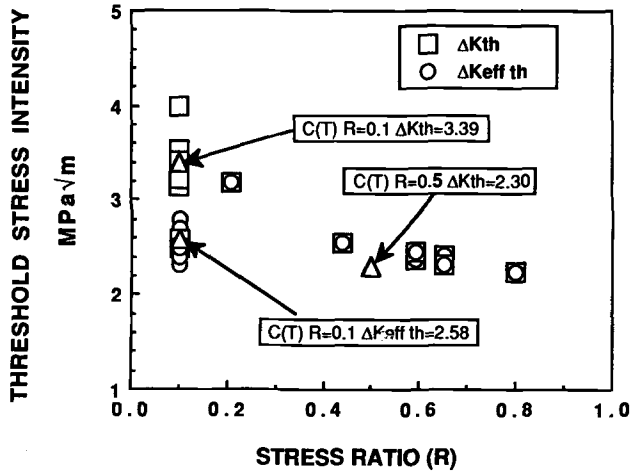


FIG. 10—Summary of all test results for threshold stress intensity as a function of stress ratio ( $R$ ).

effective stress-intensity factor of approximately  $2.30 \text{ MPa}\sqrt{\text{m}}$ . These data are obtained from the four types of tests and indicate that loading history can be completely accounted for when determining threshold if crack closure is taken into account.

### Summary and Conclusions

The threshold stress intensity can be determined from tests which involve either decreases in  $\Delta K$  through a load-shedding procedure or the incipient growth from a precrack in which  $\Delta K$  is gradually increased until crack growth is detected. The use of an effective stress-intensity factor, which accounts for crack closure, allows the determination of a threshold value which appears to be independent of stress ratio, loading history, and test type.

Crack growth rate data are consolidated reasonably well into a single curve in the near-threshold regime using  $\Delta K_{\text{eff}}$  as the correlating parameter. At growth rates above threshold, in the vicinity of  $10^{-9} \text{ m/cycle}$ , the use of  $\Delta K_{\text{eff}}$  does not consolidate the data into a single curve. This may be either a mean load effect or a reflection of the inability to accurately determine crack closure loads using CMOD measurements in a surface flow geometry.

Crack growth rate data in the near-threshold regime and values of the threshold stress-intensity factor obtained from surface flaw geometries are consistent with similar data obtained from experiments using C(T) specimens. The threshold values and growth rates can be consolidated through the use of the effective stress intensity factor for both specimen geometries.

### References

- [1] Suresh, S. and Ritchie, R. O., "Near-Threshold Fatigue Crack Propagation: A Perspective on the Role of Crack Closure," *Fatigue Crack Growth Threshold Concepts*, D. L. Davidson and S. Suresh, Eds., The Metallurgical Society of the American Institute of Mining, Metallurgical and Petroleum Engineers, Warrendale, PA, 1984, pp. 263–297.

- [2] Hudak, S. J., Jr., "Small Crack Behavior and the Prediction of Fatigue Life," *Transactions, American Society of Mechanical Engineers, Journal of Engineering Materials Technology*, Vol. 103, 1981, pp. 26-35.
- [3] Miller, K. J., "The Short Crack Problem," *Fatigue of Engineering Materials and Structures*, Vol. 5, 1982, pp. 223-232.
- [4] Suresh, S. and Ritchie, R. O., "Propagation of Short Fatigue Cracks," *International Metallurgical Review*, Vol. 25, 1984, pp. 445-476.
- [5] Cadman, A. J., Brook, R., and Nicholson, C. E., "Effect of Test Technique on the Fatigue Threshold  $\Delta K_{th}$ ," *Fatigue Thresholds: Fundamentals and Engineering Applications*, J. Backlund, A. F. Blom, and C. J. Beevers, Eds., Engineering Materials Advisory Services, Ltd., West Midlands, U.K., 1981, pp. 59-75.
- [6] Doker, H., Bachmann, V., and Marci, G., "A Comparison of Different Methods of Determination of the Threshold for Fatigue Crack Propagation," *Fatigue Thresholds: Fundamentals and Engineering Applications*, J. Backlund, A. F. Blom, and C. J. Beevers, Eds., Engineering Materials Advisory Services, Ltd., West Midlands, U.K., 1981, pp. 45-57.
- [7] Doker, H. and Peters, M., "Fatigue Threshold Dependence on Material, Environment and Microstructure," *Fatigue 84*, C. J. Beevers, Ed., Engineering Materials Advisory Services, Ltd., West Midlands, U.K., 1984, pp. 275-285.
- [8] Herman, W. A., Hertzberg, R. W., and Newton, C. H., "A Reevaluation of Fatigue Threshold Test Methods," *Fatigue 87*, Vol. 2, R. O. Ritchie and E. A. Starke, Jr., Eds., Engineering Materials Advisory Services, Ltd., West Midlands, U.K., 1987, pp. 819-828.
- [9] Herman, W. A., Hertzberg, R. W., and Jaccard, R., "A Simplified Laboratory Approach for the Prediction of Short Crack Behavior in Engineering Structures," *Fatigue Fracture in Engineering Materials and Structures*, 1988.
- [10] Castro, D. E., Marci, G., and Munz, D., "Threshold and Non-Propagation of Fatigue Cracks under Service Loading," *Fracture Mechanics: Nineteenth Symposium, ASTM STP 969*, T. A. Cruse, Ed., American Society for Testing and Materials, Philadelphia, 1987, pp. 818-829.
- [11] Jira, J. R., Nicholas, T., and Larsen, J. M., "Fatigue Thresholds in Surface Flaws in Ti-6Al-2Sn-4Zr-6Mo," *Fatigue 87*, Vol. 3, Addendum, R. O. Ritchie and E. A. Starke, Jr., Eds., Engineering Materials Advisory Services, Ltd., West Midlands, U.K., 1987, pp. 1851-1860.
- [12] Larsen, J. M., Jira, J. R., and Weerasooriya, T., "Crack Opening Displacement Measurements on Small Cracks in Fatigue," *Fracture Mechanics: Eighteenth Symposium, ASTM STP 945*, D. T. Read and R. P. Reed, Eds., American Society for Testing and Materials, Philadelphia, 1987, pp. 896-912.
- [13] Jira, J. R., Larsen, J. M., and Nicholas, T., "Effects of Closure on the Fatigue Crack Growth of Surface Flaws in a Titanium Alloy," *Mechanics of Fatigue Crack Closure, ASTM STP 982*, J. C. Newman and W. Elber, Eds., American Society for Testing and Materials, Philadelphia, 1988, pp. 617-635.
- [14] Sharpe, W. N., Jr., and Ward, M., "Benchmark Cyclic Plastic Notch Strain Measurements," *Transactions, American Society of Mechanical Engineers, Journal of Engineering Materials and Technology*, Vol. 105, 1983, pp. 235-241.
- [15] Hartman, G. and Nicholas, T., "An Enhanced Laser Interferometer for Precise Displacement Measurements," *Experimental Techniques*, Vol. 11, No. 2, 1987, pp. 24-26.
- [16] Mall, S., Nagy, D. A., and Jira, J. R., "A Comparison of Different Test Techniques On Fatigue Threshold Behavior of Surface Flaws in a Titanium Alloy," presented at the 7th International Conference on Fracture, Houston, TX, April 1989.
- [17] Nagy, D. A., "Threshold Fatigue Crack Growth in Ti 6Al-2Sn-4Zr-6Mo," M.S. thesis, Air Force Institute of Technology, Wright-Patterson Air Force Base, OH, Dec. 1987.

## Growth of Surface Cracks Under Fatigue and Monotonic Increasing Load

---

**REFERENCE:** Hodulak, L., *Growth of Surface Cracks Under Fatigue and Monotonic Increasing Load*, "Surface-Crack Growth: Models, Experiments, and Structures, ASTM STP 1060, W. G. Reuter, J. H. Underwood, and J. C. Newman, Jr., Eds., American Society for Testing and Materials, Philadelphia, 1990, pp. 315-332.

**ABSTRACT:** An engineering assessment of the life time and failure conditions for components with surface cracks can be easily done using a personal computer program. The methods, assumptions and the modeling of surface crack growth used in the program are briefly described.

A more detailed comparison of calculated and observed growth of surface cracks under fatigue and monotonic increasing load shows some phenomena, which are not completely understood as yet. They are discussed in connection with the constraint variation along the crack front. Some results on constraint at the front of surface cracks and on the  $J$ - $R$  curves for surface cracks in tension plates are given.

**KEY WORDS:** surface crack, failure assessment, constraint, fatigue,  $J$ - $R$  curves

In assessing life time and failure conditions of components with defects we usually have to deal with small part-through-wall defects. Therefore methods for the prediction of sub-critical and critical growth of surface cracks are required. In this paper some aspects of surface crack behavior are summarized.

The first part of this paper deals with the quick and easy estimation scheme for fracture behavior of components with surface cracks, using a computer program based on approximate methods. Calculational results are shown with the example of a cracked steel valve casing. In the second part, the crack shape development of surface cracks under fatigue is discussed in connection with constraint, and some results on the stress state ahead of surface crack fronts are given. The third part of the paper deals with the measurement of the tearing resistance for surface cracks in plates and with the geometry dependence of  $J$ - $R$  curves.

### Assessment of Components with Surface Cracks

For the failure assessment of cracked components of metallic materials, concepts and calculation methods of elastic and elastic-plastic fracture mechanics are available. In particular, the stress-intensity factor  $K$  and the  $J$ -integral may be used as parameters describing the loading and the material resistance in the fracture process. For specific geometries with surface cracks there are tabulated values or equations fitting finite element results for these loading parameters (for example, [1]).

<sup>1</sup> Senior scientist, Fraunhofer-Institut für Werkstoffmechanik, Freiburg, Federal Republic of Germany.

Published methods and solutions are used in the personal computer program "IWM-VERB," which provides a tool for fast failure assessments of cracked components [2]. Before demonstrating performance of the program by comparing calculations and experimental results for a component with a surface crack, the underlying assumptions and idealizations will be briefly described and their justification will be discussed.

### *Calculation Program and Methods Used*

**Geometry of Surface Crack**—Both real defects found during nondestructive evaluation and hypothetical cracks are modeled as planar, having semielliptic contours and being loaded normal to the crack plane.

For a best estimate the dimensions of the semielliptical crack may be determined according to Fig. 1. The length  $2c$  is the mean value of the maximum crack extension in the length direction and the crack extension at the surface of the body; the crack depth  $a$  is the maximum depth of the smoothened contour of the real crack. For a conservative estimate, well known procedures according to Refs 3,4 can be used.

The shape of real cracks usually deviates little from a semiellipse as long as plastic deformations in the crack vicinity are small. In case of large deviations, the modeling by an ellipse according to Fig. 1 is a possible rough approximation.

**Evaluation of Loading Parameters**—The stress-intensity factor  $K_{\text{appl}}$  is evaluated for the apex and the surface points of the crack as a function of geometry and loading based mainly on results from Refs 1,5,6. The elastic-plastic loading parameter  $J_{\text{appl}}$  is approximately evaluated for the depth direction, using a failure assessment diagram with assessment lines according to Refs 7,8. Limit load formulae from Refs 9,10 are used.

Instead of using just local values a more substantiated procedure would be the evaluation of an average value of  $K_{\text{appl}}$  or  $J_{\text{appl}}$  in the surroundings of  $\phi = 0$  and  $\pi/2$  (as in Ref 11), because there is an interaction of the adjacent parts of the crack front. The differences in the fatigue crack shape development, due to the use of local or averaged stress-intensity values shown on an example in Fig. 2, are, however, rather small. Surprisingly, the tendency of the crack shape development agrees better with the calculation using local values. In these calculations, no modifications of stress-intensity factors as in Eq 1 have been done.

Although the calculation program was designed to make best estimates, the  $J_{\text{appl}}$  values are overestimated by the program due to conservative assessment lines from Refs 6, 7 and the conservative limit load solutions used. "Conservative" means here shifting the results towards a safe assessment, for example, underestimating critical loads or critical crack sizes.

**Evaluation of the Fatigue Crack Growth**—The crack growth is stepwise evaluated along two specific directions (length and depth) only using the Paris law. These simplifying assumptions have to be justified by a good agreement of calculations with experimental results.

**Evaluation of Critical Conditions**—Critical conditions are assessed in the depth direction only. The evaluation is based on elastic-plastic fracture mechanics using two-criteria approach. The fracture toughness is characterized by  $K_{Ic}$  or  $J_I$  and  $J$  resistance curve ( $J$ - $R$

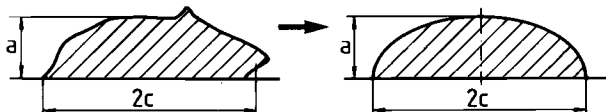


FIG. 1—Idealization of surface crack contour.

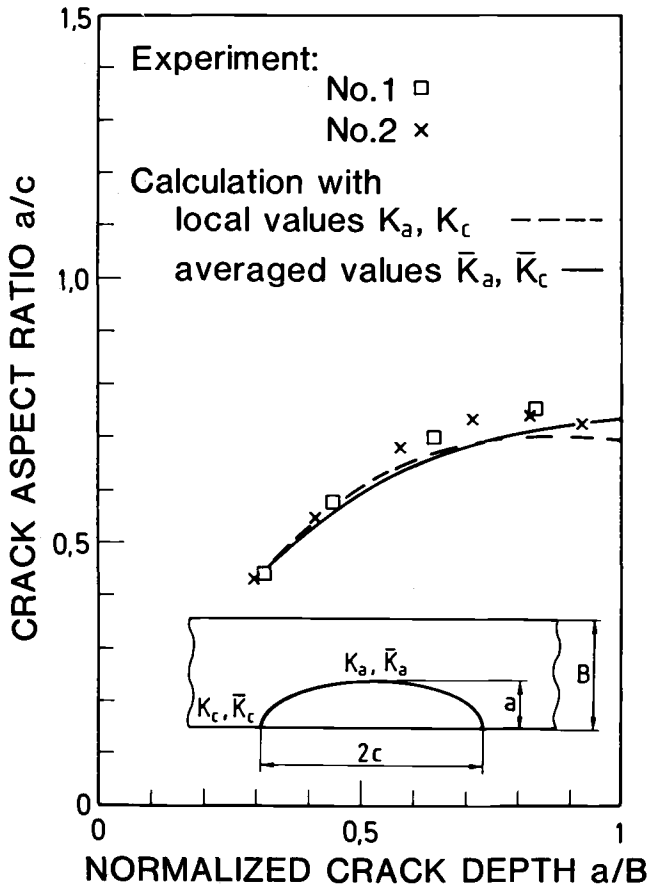


FIG. 2—Calculated and observed crack shape development in tension plates under fatigue with load ratio  $R = 0.1$ . Calculation with local (Program "IWM-VERB") and averaged stress-intensity factor (SIF) values. In both cases SIF is calculated with equations from Ref 1 and Paris' relation for the crack growth is used.

curve). When calculating stable crack growth a constant crack length, or a constant crack aspect ratio  $a/c$  is assumed.

Omitting the analysis for the surface points of the crack is justified for geometries available in the present version of the calculation program (no bending loads or significant stress gradients) and for  $a/c < 1$  (which can be assumed at the absence of stress gradients). The somewhat higher loading parameters for the length direction as for the depth direction at  $a/c \approx 1$  are compensated by fracture resistance, being higher at the surface of the body, than for the depth direction, as a result of different stress state.

#### Failure Assessment of a Valve Casing

The possibilities and limitations of the computer program-based fracture-mechanics failure assessment were tested by comparing pre- and post-test calculations, with the experimentally observed fracture behavior of a cast steel valve case with a surface crack [12]. Detailed material characterization and accompanying model experiments on a plate and a

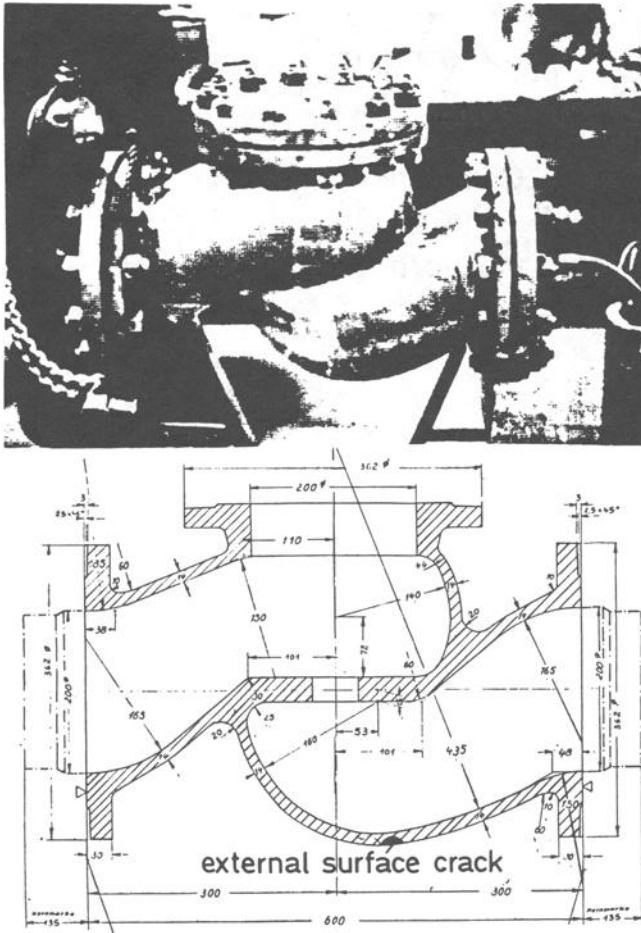


FIG. 3—Valve casing (wall thickness 12.5 mm) of cast steel, with an external surface crack and modeling of the cracked part of it (encircled) [12].

pipe of the same material, with the same thickness and initial crack have been performed to promote understanding of differences between calculations and experimental results.

The valve and simple geometries used to model the critical part of the valve with a crack (in the figure encircled) can be seen in Fig. 3. For a very conservative assessment, an axial crack in an cylindrical shell can be used. A cracked spherical shell as a model with overestimate failure pressure. For a realistic calculation therefore an elliptical shell of revolution with a meridional crack was used.

The results of pre-test calculations are compared with the experimental results in Table 1. Despite the complicated geometry of the valve, realistic predictions were obtained for the fatigue crack extension, the failure loads of the surface crack, and the through crack. The through crack has been tested after sealing the leak.

The lead-before-break behavior of the cracked valve casing was very close to conditions at which the failure mode changes. It means that a relatively small inaccuracy in the predicted crack shape development would result in the prediction of break instead of leak.

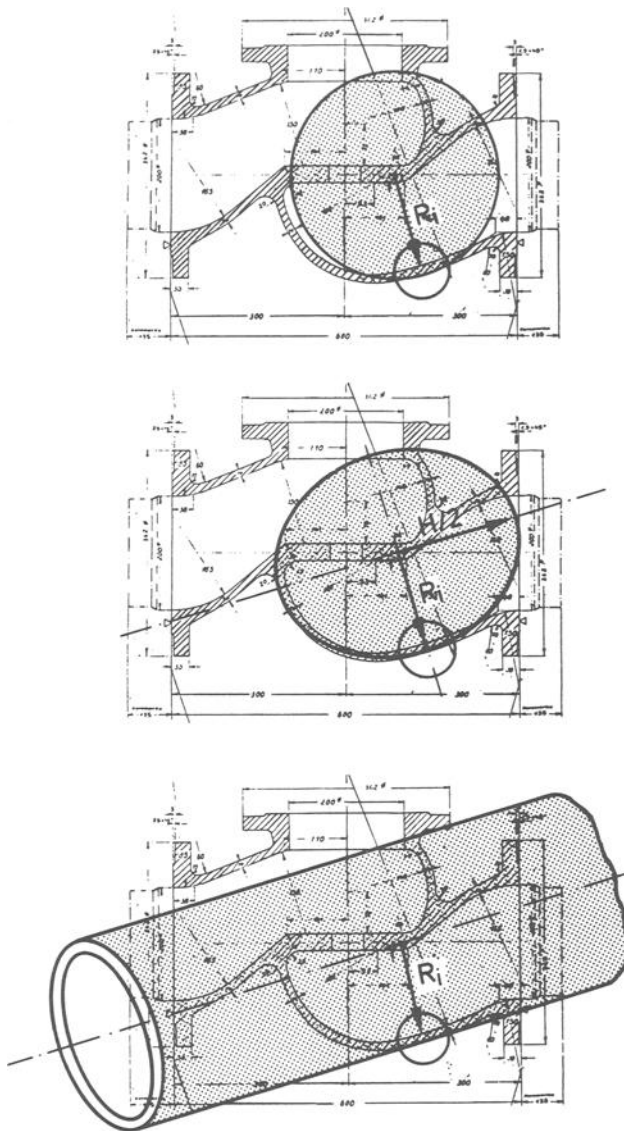


FIG. 3—Continued.

### Crack Shape Development Under Fatigue Loading

#### *Correction for Variation of Stress State*

It has been shown that the development of the crack shape aspect ratio  $a/c$  in tension plates under fatigue loading not only depends on initial geometry, but also on the load level [13], or on the stress ratio  $R = \sigma_{\min}/\sigma_{\max}$  [14]. This was explained as a result of the different stress states along the crack front [13] and in terms of crack closure [14].



TABLE 1—Fatigue crack extension and failure pressure for a valve with a surface crack. Comparison of pre-test calculations with experimental results.

	Calculation	Experiment	Ratio Calculation/ Experiment
INITIAL CRACK: $a = 3$ mm $c = 15$ mm			
Crack after 172 630 cycles			
$a$ [mm]	6.6	9.3	
$c$ [mm]	16.9	18.2	
$da$ [mm]	3.6	6.3	0.57
$dc$ [mm]	1.9	3.2	0.59
SURFACE CRACK: $a = 9.3$ mm $c = 18.2$ mm			
Failure pressure [MPa]	30.4	42.0	0.72
Failure mode	leak	leak	
THROUGH CRACK: $c = 17.1$ mm			
Failure pressure	35.7	44.5	0.80

According to the crack closure model, an  $R$ -dependent correction of the crack growth rate at the specimen surface was proposed in [15]: the stress-intensity factor range  $\Delta K_c$  at specimen surface is multiplied by the crack-closure factor ratio  $\beta_R$ ,

$$\beta_R = 0.9 + 0.2 \cdot R^2 - 0.1 \cdot R^4 \quad (1)$$

when inserted in a crack growth equation.

#### Comparison with the Experiment

The growth of surface cracks under uniform fatigue loading in high strength 12% chromium steel (German designed X20 CrMoV 12) (yield stress  $\sigma_y = 510$  MPa), was measured on plates with thickness of 20 mm and width of 120 mm. The same starter cracks  $a = 3.5$  mm,  $2c = 18$  mm, and the same amplitude  $\sigma_{\max} - \sigma_{\min}$ , but different load ratios,  $R = 0.1$  and  $R = 0.6$ , were used. The maximum nominal stresses were  $0.5 \cdot \sigma_y$  and  $0.9 \cdot \sigma_y$ , respectively. The crack growth rates in stress-intensity factor region used can be described by

$$da/dN = C \cdot \Delta K^n \quad (2)$$

where  $C = 6.37 \cdot 10^{-9}$ ,  $n = 2.90$ , and  $C = 7.17 \cdot 10^{-9}$ ,  $n = 3.11$  for  $R = 0.1$  and  $R = 0.6$ , respectively, from tests on CT-specimens.

A comparison of the crack shape development calculated using  $\beta_R$  and observed in experiments in Fig. 4 shows an excellent agreement for low  $R$  values and some deviations for high  $R$  values. A possible reason for these deviations is the fact that the differences of the stress state for crack depth and length depend not only on  $R$ , but on the maximum stress as well.

In the theoretical approach for the derivation of relation (Eq 1) crack growth directions  $a$  and  $c$  are associated with the limiting conditions of plane strain and plane stress, respectively. This can be regarded as a first approximation. The actual situation at the crack front may be obtained from finite-element calculations.

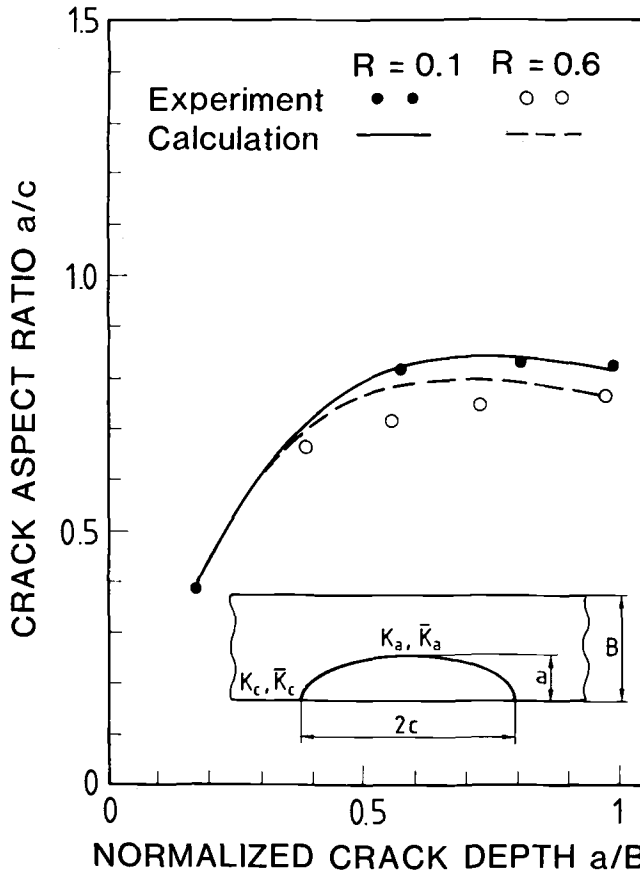


FIG. 4—Influence of the stress ratio  $R$  on the shape development of fatigue cracks. Calculations and experiment.

#### Constraint Variation Along Crack Front

Stresses obtained in linear elastic three-dimensional finite-element calculations for plates with surface cracks were evaluated to quantify constraint along the crack front. As an example principal stresses  $\sigma_1$ ,  $\sigma_2$ , and  $\sigma_3$  ahead of the crack front in the crack plane (actual evaluation points were gaussian points located very closely to the crack plane), were evaluated in terms of hydrostatic stress  $\sigma_H = \sigma_1 + \sigma_2 + \sigma_3$ , and von Mises' stress  $\sigma_M = \sqrt{((\sigma_1 - \sigma_2)^2 + (\sigma_2 - \sigma_3)^2 + (\sigma_3 - \sigma_1)^2)}$  for a surface crack  $a = 15$  mm,  $2c = 44$  mm in a plate 25 mm thick and 150 mm wide of (22 NiMoCr 37 steel). The evaluations are shown in Fig. 5 (top). The stress state at the distance of 0.3 and 1 mm from the crack front is plotted as a function of elliptic angle  $\phi$ , between plate surface ( $\phi = 0$ ) and crack apex ( $\phi = \pi/2$ ). In this plot, all points on the straight line from the origin have the same state of stress (the inverse value of the slope of this line is the factor of tri-axiality  $h = \sigma_H/\sigma_M$  introduced in Ref 16). It can be seen that the stress state shifts its position between plane strain and plane stress, as the angle  $\phi$  decreases. This shift is smaller and stress states are nearer to plane strain if the distance from the crack front is smaller. The effect is more pronounced for the same crack in a pipe (bottom of Fig. 5).

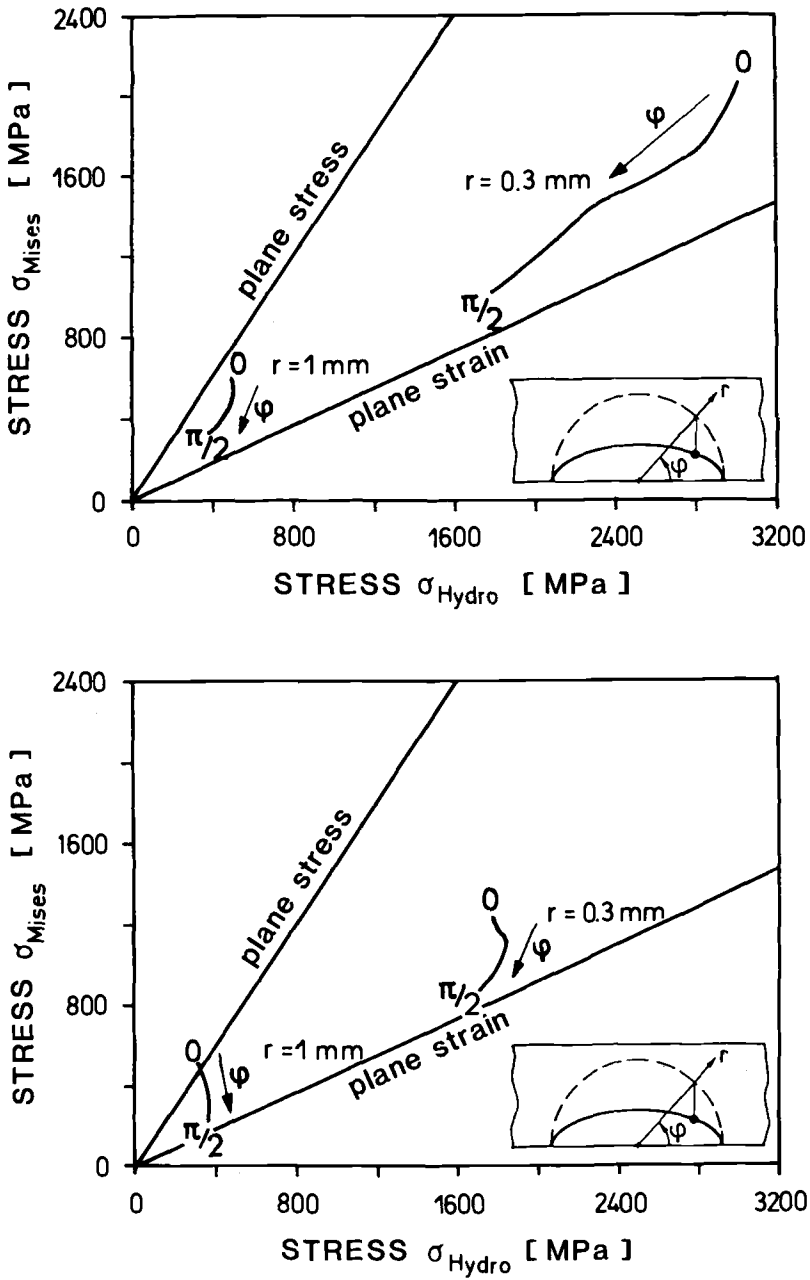


FIG. 5—Stress state in ligament, near the crack front of surface cracks in plate (top) and pipe (bottom). Results for varying crack front location  $\phi$  and distance from the crack front  $r$ .

For the use of the tri-axiality factor  $h$  (also called constraint parameter in this paper) as an additional parameter influencing fracture process, the mean value of this parameter in the process zone has to be considered. The process zone size will again depend on the degree of plastification, that is, on the load level during the subcritical crack growth and at the onset of fracture. For low load levels there will be only small variation of the constraint along the crack front, with  $h$ -values differing very little from the plane strain  $h$  value. With increasing load, the constraint variation along the crack front will increase and the  $h$  values will shift towards the plane stress  $h$  value (recall Fig. 5).

Regarding crack shape development during fatigue, it can be expected that the crack closure effects, which depend on the constraint distribution along the crack front, will depend not only on the stress ratio  $R$ , but on the maximum stress as well.

The variation of the constraint along the crack front and its dependence on the geometry and loading of the cracked component is illustrated in Fig. 6 in terms of the normalized constraint parameter  $h_n$ , defined as  $h_n = h/h_{\text{plane strain}} = (\sigma_H/\sigma_M)/(\sigma_H/\sigma_M)_{\text{plane strain}}$ . The increase of the constraint in the sequence—plate, pipe, CT-specimen, large vessel—can be explained in the following way:

The plate under tension and the pressurized pipe, have the same geometry in the crack plane, but different loading: two-axial tension in the pipe increases constraint parameter, compared to uniaxial tension in the plate. This effect becomes stronger with increasing distance from the crack front. Still higher constraint in the CT-specimen is most probably caused by the straight crack front and the bending type of loading. In the case of the pressure vessel, there is a long part of the crack front with very small curvature and two-axial loading.

The effect of the crack shape on the constraint at the crack front can be seen in Fig. 7. Constraint evaluation from finite element calculation of a surface crack with irregular shape in a nozzle under internal pressure and thermal shock loading [17] shows the same dependence on crack front shape as stress-intensity factor does: a local minimum at the convex part of the crack front with minimum radius of curvature (Positions 8–9 in Fig. 7) and a local maximum at the part of the crack front, which is slightly concave (Position 5). From the two loading cases—internal pressure and thermal shock—the higher constraint is obtained for the latter case with higher biaxiality of loading. Since the evaluations have been done some distance from the crack front (0.4 mm), where the singular type of stress distribution is less dominant, the biaxial loading rises the values of the constraint parameter to exceed the plane strain value.

The influence of the crack shape and loading on constraint increases with increasing distance from the crack front. Thus, the effects on crack growth and fracture will be larger in cases with larger process zones (for example, at extended plastic deformations). Some evidence of it is given by comparison of fracture resistance curves, measured on cracks with different shapes. One of these experiments was re-evaluated in Ref 18 by means of three-dimensional elastic-plastic finite-element calculations and the application of a model, utilizing the triaxiality factor  $h$ , for a constraint dependent evaluation of the stable crack growth.

### Fracture Resistance Curves of Surface Cracks

Differences in the state of stress at the crack front are also considered as a reason for the geometry dependency of the  $J$  resistance curves ( $J$ - $R$  curves) and for the ductile crack growth under monotonically increasing load.  $J$ - $R$  curves are used as a material characterization in the upper shelf toughness region. Experiments show that lower bound  $J$  resist-

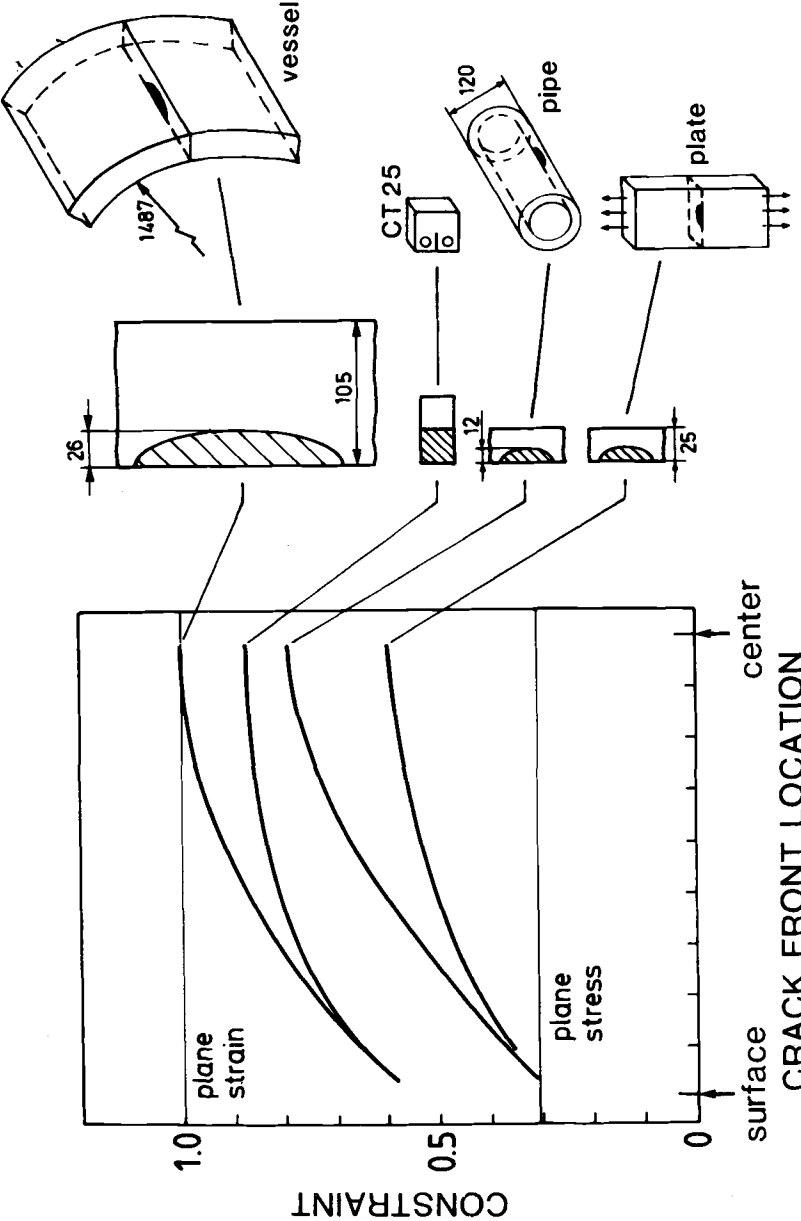


FIG. 6—Variation of the constraint parameter  $h_n$  along the crack front in three-dimensional cracked bodies.

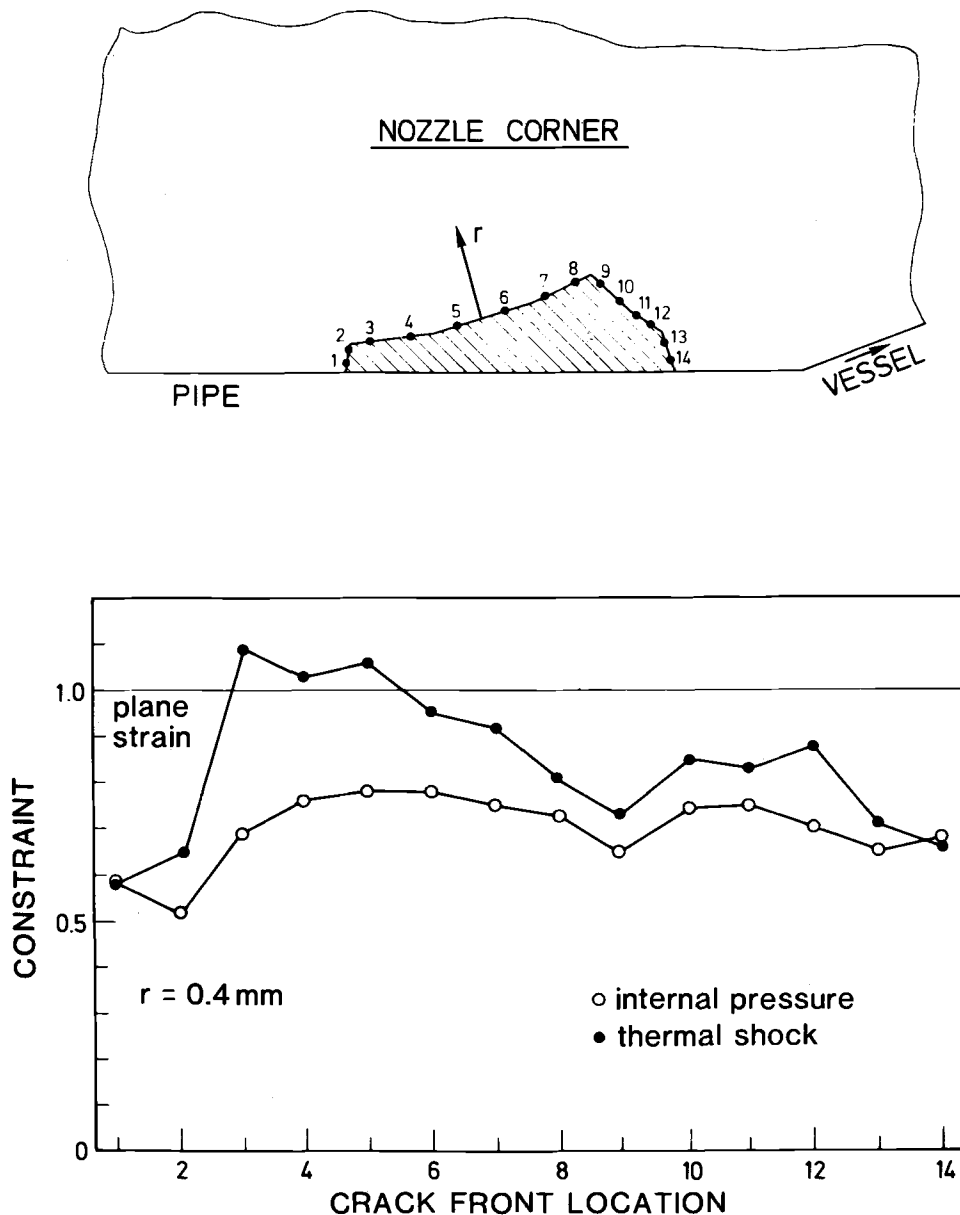


FIG. 7—Variation of the constraint parameter  $h_n$  along the crack front of a surface crack in a nozzle under internal pressure and thermal shock.

ance curves can be measured on deeply notched side-grooved CT-specimens. The  $J$ - $R$  curves measured according to the requirements of the ASTM Test Method for Determining  $J$ - $R$  curves (E-1152) are not geometry dependent and characterize the  $J$  resistance for the plane strain conditions. The knowledge on  $J$  resistance curves describing adequately fracture behavior of components with surface cracks is very limited.

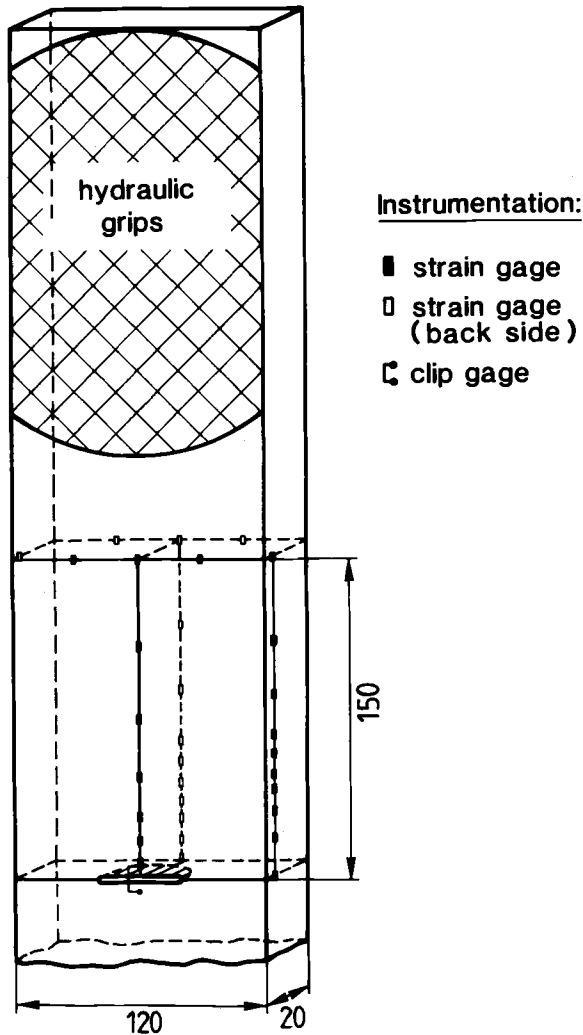


FIG. 8—Geometry and instrumentation of plates with surface cracks for measurement of  $J$ -R curves.

Using two approximate methods [19,20],  $J$  resistance curves have been measured for tension plates with surface cracks. The plate geometry and instrumentation with strain gages and with a CMOD gage is shown in Fig 8. The dimensions of the surface cracks can be found later in Fig. 11. The material investigated at RT was a high toughness pressure vessel steel, German designation 22 NiMoCr 3 7.

#### Determination of $J$ -Integral

**Garwood Method**—Approximate equations for determination of the  $J$ -integral of surface cracks in plates from force-displacement curve were derived by Garwood [19]. In the expression of  $J$ -integral in terms of  $\eta$ -functions

$$J = (\eta_e U_e + \eta_p U_p) / (BW - A) \quad (3)$$

it was assumed  $\eta_e = \eta_p$  and  $\mu_p$  was approximate calculated from a postulated force-displacement curve (see Fig. 9 also for symbols used). In the calculation of  $\eta_p$ , we replaced the relation for an extended surface crack of length  $a$

$$J_p = -(\partial U_p / \partial a) \Big|_{q_p}^B \quad (4)$$

by the relation for a surface crack with finite length and crack area  $A$

$$J_p = -(\partial U_p / \partial A) \Big|_{q_p} \quad (5)$$

and obtained

$$J = (p_n \cdot q_n / (WB - \pi ac/2) + \sigma_y \cdot q_p) / 2 \quad (6)$$

which we used for evaluation of  $J$ -integral.

The displacement  $q_n$  was determined from strains measured along lines  $S_1$ ,  $S_3$  (Fig. 9) and CMOD. It was corrected by the subtraction of displacement of the plate without a crack at the same gage length. To determine the plastic part of displacement  $q_p$

$$q_p = q_n - q_e \quad (7)$$

the elastic part  $q_e$  was calculated from measured elastic compliance.

*Read Method*—The  $J$ -integral is calculated as contour integral

$$J = \int_S (w \cdot dy - T \cdot (\partial v / \partial x) ds) \quad (8)$$

along  $S = S_1 + S_2 + S_3$  (Fig. 9) and the strain energy density  $w$  is approximately determined from strain components  $\epsilon_y$  measured along the integration path  $S_1 + S_2$  with strain gages [20]. The second term in Eq 8 is approximately calculated from strains  $\epsilon_f$ ,  $\epsilon_b$ , and displacements  $v_f$ ,  $v_b$  at the front and back side of the plate, at the end and at the beginning of the path  $S_2$  as

$$\int_{S_2} T \cdot (\partial v / \partial x) ds = (\epsilon_f + \epsilon_b) \cdot E \cdot (v_b - v_f) \quad (9)$$

The strain energy density was calculated using Eq 10

$$w = \int \sigma_y \cdot d\epsilon_y \quad (10)$$

with stress component in  $y$  direction  $\sigma_y$ , obtained from the stress-strain relation.

### Experiments and Results

In the experiments, the load was increased slowly under CMOD control and partial unloadings were done as in the standard unloading-compliance method, following the ASTM test proposal [21]. Smooth and side grooved CT-specimens 20 mm thick of the same material were tested in order to get a baseline for comparison.



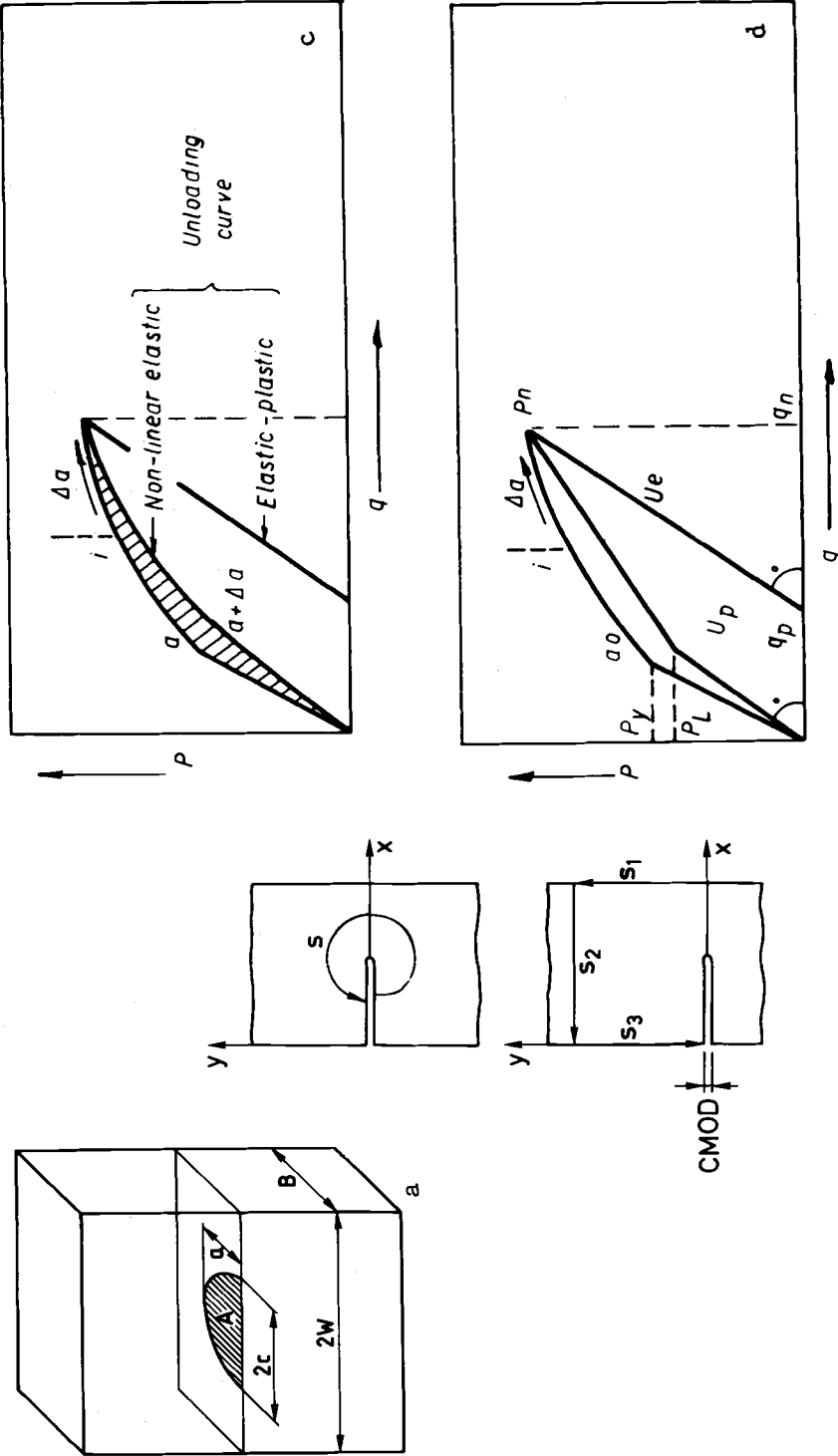


FIG. 9—Schematics to description of methods for measurement of the J-integral: (a) geometry of the cracked plate, (b) integration paths for determination of the J-integral, (c) postulated and actual load-displacement record [19], and (d) approximation to the load-displacement curve [19].

For each of the two crack geometries investigated, two experiments were done. On prints of fracture surfaces in Fig. 10, spark-eroded notches, fatigue crack extensions, and crack extensions during monotonic increasing load (dark areas) can be seen.

The  $J$  resistance for the surface cracked plates determined by two methods is shown in Fig. 11. The  $J$  values are plotted only for crack extensions measured on the fracture sur-

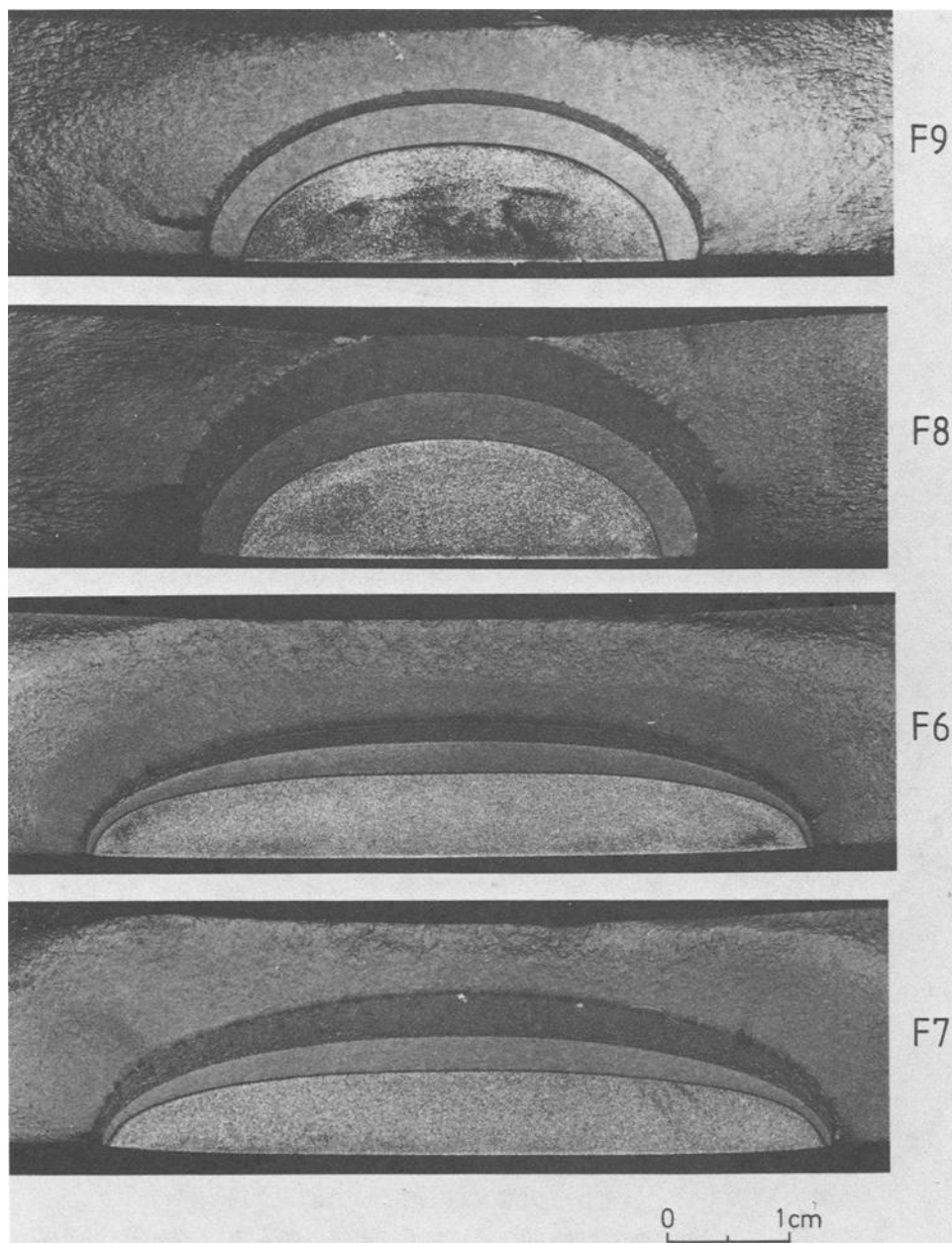


FIG. 10—Fracture surfaces of tension plates with surface cracks.

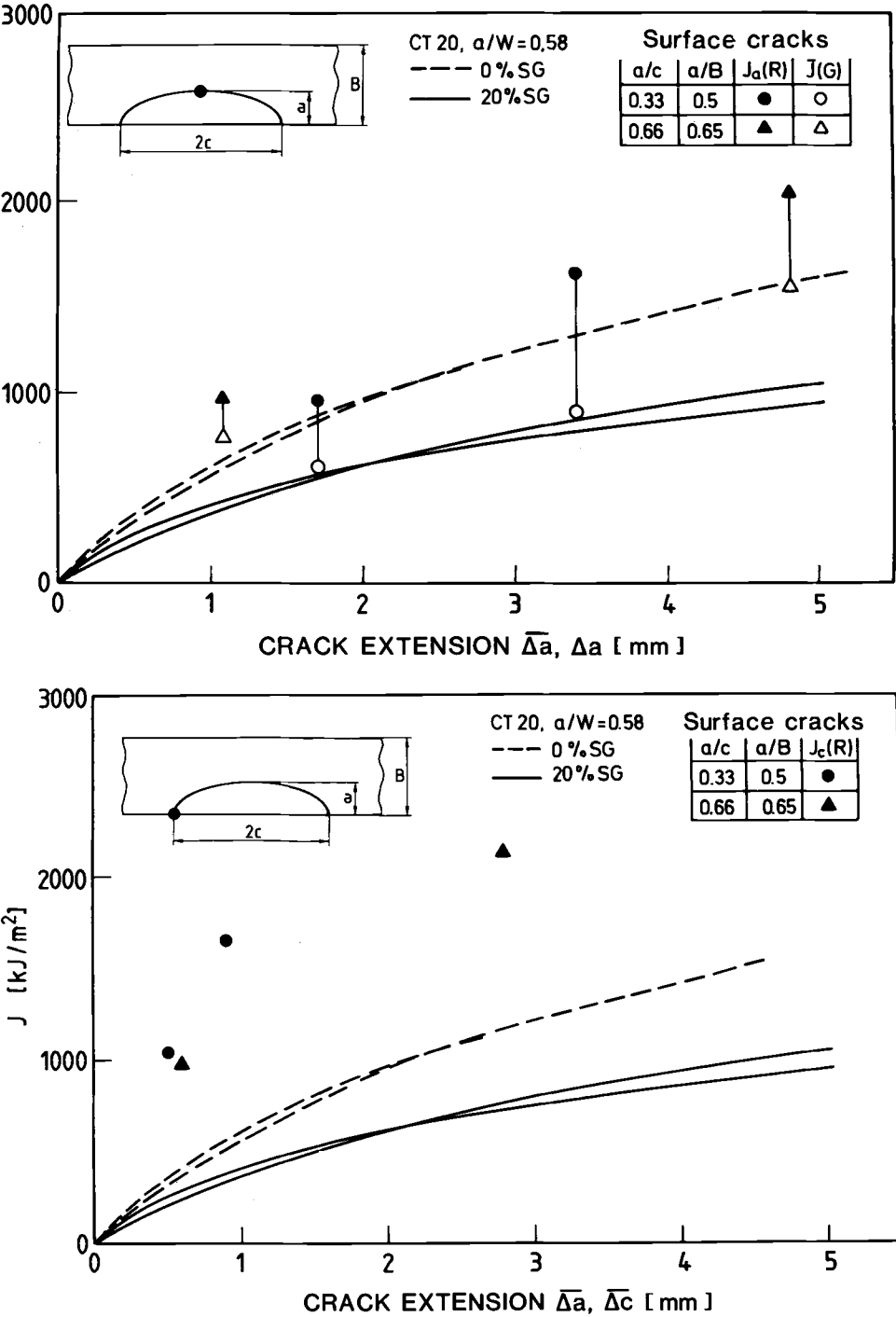


FIG. 11—J resistance curves measured in apex (top) and at specimen surface (bottom) of surface cracks in plates, in comparison with J-R curves measured on smooth and side-grooved compact tension specimens.

faces, as the crack extensions measured by the method of unloading compliance were not reliable, due to large plastic deformations of the ligament.

The  $J$  values obtained by the Garwood method are systematically lower than the values obtained by the Read method. Independent on the method, the two results show the same tendency: decrease of  $J$ - $R$  values on the apex of surface cracks with decreasing aspect ratio  $a/c$ . For the crack front at the plate surface, this tendency is reversed. These phenomena can be explained by the dependence of the constraint on the local radius of curvature of the crack front: with a decreasing local radius of curvature, the constraint parameter decreases (recall Fig. 7).

A comparison with  $J$ - $R$  curves generated on smooth and side-grooved compact tension specimens is somewhat questionable, since different methods of evaluation have been used. Therefore, the Garwood method and the Read method were tested on finite-element results for a similar plate with a surface crack. It was found [22], that the Read method overestimated and the Garwood method underestimated the  $J$ -integral. The results of this comparison and of Fig. 11 indicate that the  $J$  resistance for surface cracks investigated is higher than  $J$  resistance measured on side-grooved CT-specimens. This is in agreement also with the constraint arguments in Fig. 7.

## Conclusions

An engineering assessment of fatigue crack growth and failure conditions, of components with surface cracks can easily be done using a personal computer program, if an appropriate model of the cracked part of the component has been chosen.

The dependence of the crack shape development under fatigue on the ratio  $R = \sigma_{\min}/\sigma_{\max}$  can be better understood, analyzing the actual variation of the stress state in the process zone along the crack front. Following this approach the crack shape development depends not only on  $R$ , but on the load level (for example,  $\sigma_m = (\sigma_{\min} + \sigma_{\max})/2$ ) as well.

From testing of tension plates with surface cracks, higher  $J$  resistance curves have been obtained than those measured on standard side-grooved CT-specimens. The  $J$ - $R$  curves depend on the crack aspect ratio  $a/c$ .

## References

- [1] Newman, J. C. and Raju, I. S., "Stress-Intensity Factor Equations for Cracks in Three-Dimensional Finite Bodies," *Fracture Mechanics: Fourteenth Symposium, ASTM STP 791*, American Society for Testing and Materials, Philadelphia, 1983, pp. I-238-I-265.
- [2] Hodulak, L., "Development and Application of Failure Assessment Programs for Personal Computers," Structural Failure, Product Liability and Technical Insurance, *Proceedings*, 2nd International Conference, July 1-3 1986, pp. 373-382.
- [3] American Society of Mechanical Engineers Boiler and Pressure Vessel Code, Section XI.
- [4] Guidance on Some Methods for the Derivation of Acceptance Levels for Defects in Fusion Welded Joints," BSI Published Document PD 6483, British Standard Institution, 1980.
- [5] Lim, E. Y. et al., "Approximate Influence Functions for Part-Circumferential Interior Surface Cracks in Pipes," *Fracture Mechanics: Fourteenth Symposium, ASTM STP 791*, American Society for Testing and Materials, Philadelphia, pp. I-281-I-296.
- [6] Newman, J. C. and Raju, I. S., "An Empirical Stress-Intensity Factor Equation for the Surface Crack," *Engineering Fracture Mechanics*, Vol. 15, 1981, pp. 185-192.
- [7] Milne, I. et al., "Assessment of Structures Containing Defects," Report R/H/R6-Rev. 3, Central Electricity Generating Board, May 1986.
- [8] Kumar, V., German, M. D., and Shih, C. F., "An Engineering Approach for Elastic-Plastic Fracture Analysis," EPRI Report NP-1931, Electric Power Research Institute, Palo Alto, CA., July 1981.
- [9] Harrison, R. P. et al., "Assessment of Structures Containing Defects," Report R/H/R6-Rev. 2, Central Electricity Generating Board, 1980.

- [10] Kiefner, J. F. et al., "Failure Stress Levels of Flaws in Pressurized Cylinders," *Progress in Flaw Growth and Fracture Toughness Testing, ASTM STP 536*, American Society for Testing and Materials, Philadelphia, 1973, pp. 461-481.
- [11] Besuner, P. M., "Residual Life Estimates for Structures with Partial Thickness Cracks," *Mechanics of Crack Growth, ASTM STP 590*, American Society for Testing and Materials, Philadelphia, 1976, pp. 403-419.
- [12] Blauel, J. G. et al., "Bruchmechanische Analyse von Sicherheit und Lebensdauer einer Regelmatur aus Stahlguss," *Bauteil und Bauteilprüfung*, DVM-Tag 1988, DVM-Verlag, Berlin, 1988H.
- [13] Hodulak, L., Kordisch, H., Kunzelmann, S., and Sommer, E., "Growth of Part-Through Cracks," *Fracture Mechanics: Eleventh Conference, ASTM STP 677*, American Society for Testing and Materials, Philadelphia 1979, pp. 399-410.
- [14] Jolles, M. and Tortoriello, V., "Effects of Constraint Variation on the Fatigue Growth of Surface Flaws," *Fracture Mechanics: Fifteenth Symposium, ASTM STP 833*, American Society for Testing and Materials, Philadelphia, 1984, pp. 300-311.
- [15] Newman, J. C., Jr., and Raju, I. S., "Prediction of Fatigue Crack-Growth Patterns and Lives in Three-Dimensional Cracked Bodies," *Proceedings, 6th International Conference on Fracture*, New Delhi, India, 4-10 December 1984, pp. 1597-1608.
- [16] Clausmayer, H., *Konstruktion*, Vol. 20, 1968, pp. 395-401.
- [17] Schmitt, W., Blauel, J. G., and Hodulak, L., "Analysis of the Propagation of a Natural Flaw in a Nozzle Corner under Cyclic Thermal Loading," *Proceedings, 3rd German-Japanese Joint Seminar on Research of Structural Strength and NDE Problems in Nuclear Engineering*, August 1985, Stuttgart, West Germany.
- [18] Kordisch, H., Sommer, E., and Schmitt, W., "The Influence of the Triaxiality on Stable Crack Growth," *Proceedings, 13th MPA-Seminar*, August 1987, Stuttgart, W. Germany, paper also to be published in *Nuclear Engineering and Design*.
- [19] Garwood, S. J., "Measurement of Crack Growth Resistance of A 533 B Wide Plate Tests," *Fracture Mechanics: Twelfth Conference, ASTM STP 700*, American Society for Testing Materials, Philadelphia, 1980, pp. 271-295.
- [20] Read, D. T., "Experimental Method for Direct Evaluation of the J-Contour Integral," *Fracture Mechanics: Fourteenth Symposium, ASTM STP 791*, American Society for Testing Materials, Philadelphia, 1983, pp. II-191-II-213.
- [21] Albrecht, P. et al., "Tentative Test Procedure for Determining the Plane-Strain  $J_I$ -R Curve," *Journal of Testing and Evaluation*, Vol. 10, 1982, pp. 251-254.
- [22] Hodulak, L. and Stöckl, H., "Determination of J Resistance Curves on Plates with Surface Cracks," IWM report W 11/85, Institut für Werkstoffmechanik, Freiburg, 1985 (in German).

## Experimental Investigation of Subcritical Growth of a Surface Flaw

---

**REFERENCE:** Ramulu, M., "Experimental Investigation of Subcritical Growth of a Surface Flaw," *Surface-Crack Growth: Models, Experiments, and Structures*, ASTM STP 1060, W. G. Reuter, J. H. Underwood, and J. C. Newman, Jr., Eds., American Society for Testing and Materials, Philadelphia, 1990, pp. 333–347.

**ABSTRACT:** The early stage of initiated fatigue crack propagation from a notch root is investigated. The fatigue crack initiation and dependency of growth rates on initial flaw sizes were tested by using compact-type specimens with a keyhole notch in 7075-T6 aluminum alloy. Each of the specimen keyhole notches was indented with a probe with the included angle at the tip of 30, 45, or 60 deg, machined out of a tempered drill rod. Special attention is given to the transition crack length where small crack growth merges into a long crack growth under constant load control at room temperature. Measurements from scanning electron microscopy and macroscopic measurements made by a traveling microscope showed that the short crack growth is dependent on the initial flaw size, load ratio, and the material characteristics. The transition crack length between short crack and long crack behavior is found to be about 1 to 2 mm.

**KEY WORDS:** fatigue, fatigue crack growth rates, notches, flaws, small cracks, indents, transition crack length, linear-elastic fracture mechanics, load ratio

It has been observed that fatigue cracks are initiated at geometric stress raisers characterized by sudden changes in member cross sections such as notches and holes. The cracks propagate from these highly stressed regions and continue through the specimen cross section until final fracture occurs. However, physically small cracks whose length was less than 1 mm were found to exhibit growth rates far in excess of those of larger cracks ( $\geq 5$  mm) subjected to the same stress-intensity factor range  $\Delta K$  [1–25]. Short cracks which initiate at discontinuities such as notches may not continue to grow across the specimen if the notch is very sharp and the nominal stress range is sufficiently small [6–8]. Recent experimental studies [4–13] on the initiation and growth of fatigue cracks in a wide range of materials have revealed that cracks of length less than 3 mm, initiated near regions of surface roughening caused by dislocations or at inclusions and grain boundaries, propagate at rates which are different from those of equivalent long cracks when characterized in terms of linear elastic fracture mechanics concepts. This variation in growth rate, however, is seen to occur at stress-intensity ranges well below the fatigue threshold stress-intensity range. The initial higher growth rate of the short cracks reduces progressively and finally merges with the growth rates above the threshold values. A similar observation was made by the authors [26–29] in blunt notched compact specimens of aluminum alloy. This phenomenon appeared to be caused by the plastic field at the notch and the control condition local to the crack tip. Lankford [9,13] reported recently the influence of microstructure on

<sup>1</sup> Assistant professor, Mechanical Engineering, FU-10, University of Washington, Seattle, WA 98195.

the initiation and growth of small cracks. An excellent review and bibliography on the subject can be found in Refs 1-3, 11, 12, and 16. From the reviews, the range of materials and test conditions studied in individual investigations was generally too limited to derive consistent conclusions. Moreover, most engineering structures have superficial flaws on the surface and these are a consequence of material processing techniques [2]. It has been verified that such inherent flaws can cause the initiation and propagation of fatigue cracks. In the investigation related to the growth rate of such flaws, no information is available that describes the precise effects of flaw size on crack propagation. It appears at the present time that there are problems in defining the unique characteristics and controlling parameters for short cracks propagating in the stress field at the root of a notch.

This paper presents and discusses experimental results on the nucleation and continued growth of short cracks from notches in 7075-T6 aluminum alloy. One of the objectives of this research is to elucidate the dependency of minimum crack growth rate,  $da/dN$ , on the shape and size of small cracks. Specimens and test conditions were chosen to examine two aspects considered significant with regard to microcrack growth and the observed non-unique correlation of  $\Delta K$  and  $da/dN$ . In order for us to have a better understanding of the growth phenomena for short surface fatigue cracks, an experimental study has been conducted to examine the microscopic events which occur during the growth of a small surface crack. This study then addresses two questions, namely, what are the controlling parameters which affect the growth of short cracks and at what length does the short crack make the transition where the linear-elastic fracture mechanics (LEFM) approach can predict the fatigue life of the structure?

### Experimental Procedure

A single plate of commercially obtained 7075-T6 aluminum alloy plate provided the compact type tension specimens used in the experiments. Specimen thickness was chosen as 6.35 mm to ensure propagation under plane-strain conditions. Table 1 gives the material properties of the testing material 7075-T6 aluminum alloy. The compact specimens were fabricated from 7075-T6 aluminum and contained a keyhole notch. The hole was reamed and electropolished to minimize residual stresses.

In order to study dependency of crack growth rates on initial flaw sizes, the specimens had to be configured to introduce the initial indents. For this, a hole was machined in each specimen, the diameter of which was equal to that of the probe used to introduce the indents. Figure 1 details the specimen configuration; Fig. 2 shows the shape and configuration of a probe and the location of the indent. The probe shown in Fig. 2a was machined out of a tempered drill rod which had a conical point, the included angle at the tip being 30, 45, and 60 deg. The probe was inserted in a slot machined into the specimen and a compressive force applied to introduce an indent into the surface of the "keyhole notch" as shown in Fig. 2b. The indent size is a function of the compressive force applied to the probe. Three indent sizes were introduced for each probe angle by applying loads of 223 N, 334 N, and 445 N. The indent provided a stress concentration at the center of the circular notch. This ensured that the crack would start from the mid-thickness of the hole

TABLE 1—Material properties of 7075-T6 aluminum alloy.

Young's modulus	$E = 72 \text{ GPa}$
Yield strength	$S_y = 480 \text{ MPa}$
Poisson's ratio	$\nu = 0.33$
Fracture toughness	$K_{Ic} = 27 \text{ MPa}$

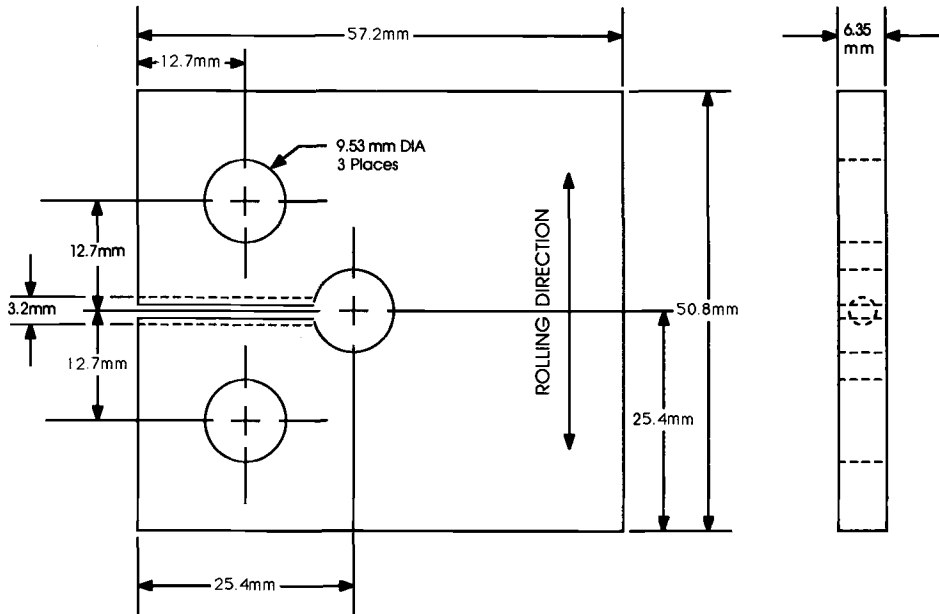


FIG. 1—Fatigue test specimen configuration.

instead of one of the corners of the specimen or any other asymmetric location in the keyhole notch.

All specimens were polished using 320- and 400-grit emery papers perpendicular and parallel to the crack direction, respectively. This was followed by final polishing with 600-grit emery paper perpendicular to the crack direction. The direction of the final polish lines helped to identify the crack tip while making measurements at larger values of crack length. After preparation, the specimens were mounted in the MTS servo-hydraulic machine, in air, at room temperature, 21°C. A constant loading was applied in all cases. The loading in each case was sinusoidal with the stress ratio  $R$  maintained positive at all times. Frequency of all tests was 15 Hz. A total of eleven tests were conducted with variable flow

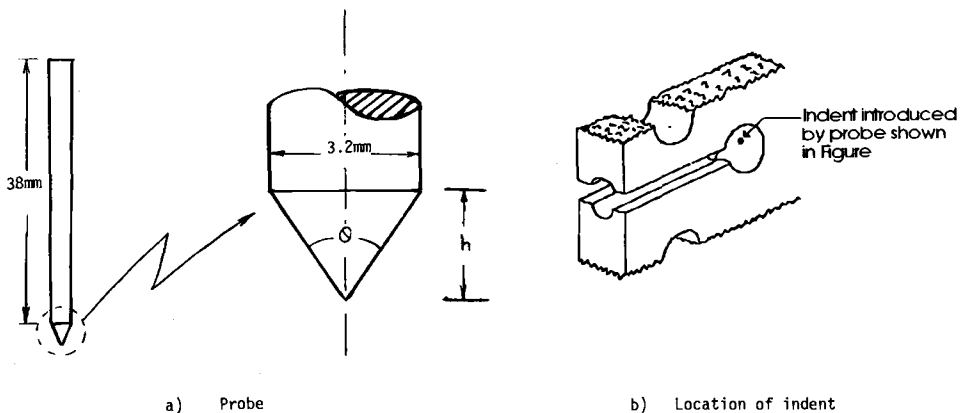


FIG. 2—Shape and configuration of a probe.



sizes generated by the indents. For 30- and 60-deg indent flawed specimens, the stress ratio  $R$  was held constant at 0.33, and for the 45-deg indent specimens the  $R$  was 0.50. The mean force applied was 5.34 kN, and force amplitudes maintained at 1.78 kN and 2.67 kN, respectively. The crack length was measured with a Gaertner horizontally traveling microscope of  $\times 100$  magnification, which has a least reading of 0.025 mm. Crack measurements were taken on both sides of the specimen; therefore, the tests were stopped in order to take the required dual measurements. A tension load, exceeding not more than 60 to 70% of maximum load, was applied during the crack length measurements, in order to minimize any hold time effects and for better observation of crack tip position. Each of these specimens was fatigued in laboratory air to determine the influence of the respective indent size on the initial growth rate of cracks. The effect of an initial flaw size on the resulting crack propagation rate has been observed and the growth rate is correlated with the crack length.

Scanning electron microscopy (SEM) has been used to observe the microscopic crack growth mechanisms of specimens of varying initial flaw sizes. Fractographic features of fracture surfaces and microcrack growth rates were evaluated by measuring striations near the tip of an indent. Micromasurements from SEM are correlated with those of the macro-measurements made from a traveling microscope.

## Results

Table 2 gives a summary of test conditions and the load cycles at a detectable crack length of  $>0.05$  mm and the final fracture. The short crack, which emanated radially from the indent, penetrated through the thickness and exhibited typical fan morphology. The results of fatigue crack growth presented in the following section were used only when the cracks grew larger than 0.05 mm on the front and back side surface of the specimen. This arbitrary criterion was adopted to minimize the error in crack length measurement as well as to account for the through-the-thickness crack profile. Instantaneous growth rates were computed for very small crack lengths using data obtained from SEM.

### Fatigue Crack Growth Rate

Figure 3 shows the normalized crack length,  $a/a_f$ , versus normalized number of load cycles,  $N/N_f$ , to failure in an indented keyhole-notched compact-type specimen, where  $a$  is

TABLE 2—Summary of test conditions and initiation-fracture results.

Specimen No.	Probe Angle, deg	Indent Load, N	Mean Force, kN	Force Amplitude, kN	N Initiation, <sup>a</sup> Cycles	N <sub>f</sub> Fracture, Cycles
1	60	334	5.34	not constant	8 470	14 490
2	60	445	5.34	2.67	8 350	8 460
3	60	445	5.34	1.78	21 100	22 610
4	45	223	5.34	1.78	22 470	23 730
5	45	334	5.34	1.78	22 210	24 050
6	45	223	5.34	1.78	21 540	23 300
7	45	445	5.34	2.67	19 910	20 980
8	30	223	5.34	2.67	21 910	23 460
9	30	334	5.34	2.67	18 450	20 070
10	30	445	5.34	2.67	16 770	17 850
11	60	223	5.34	2.67	15 910	16 640

<sup>a</sup>The term initiation denotes first-time observed crack length,  $a \geq 0.05$  mm.

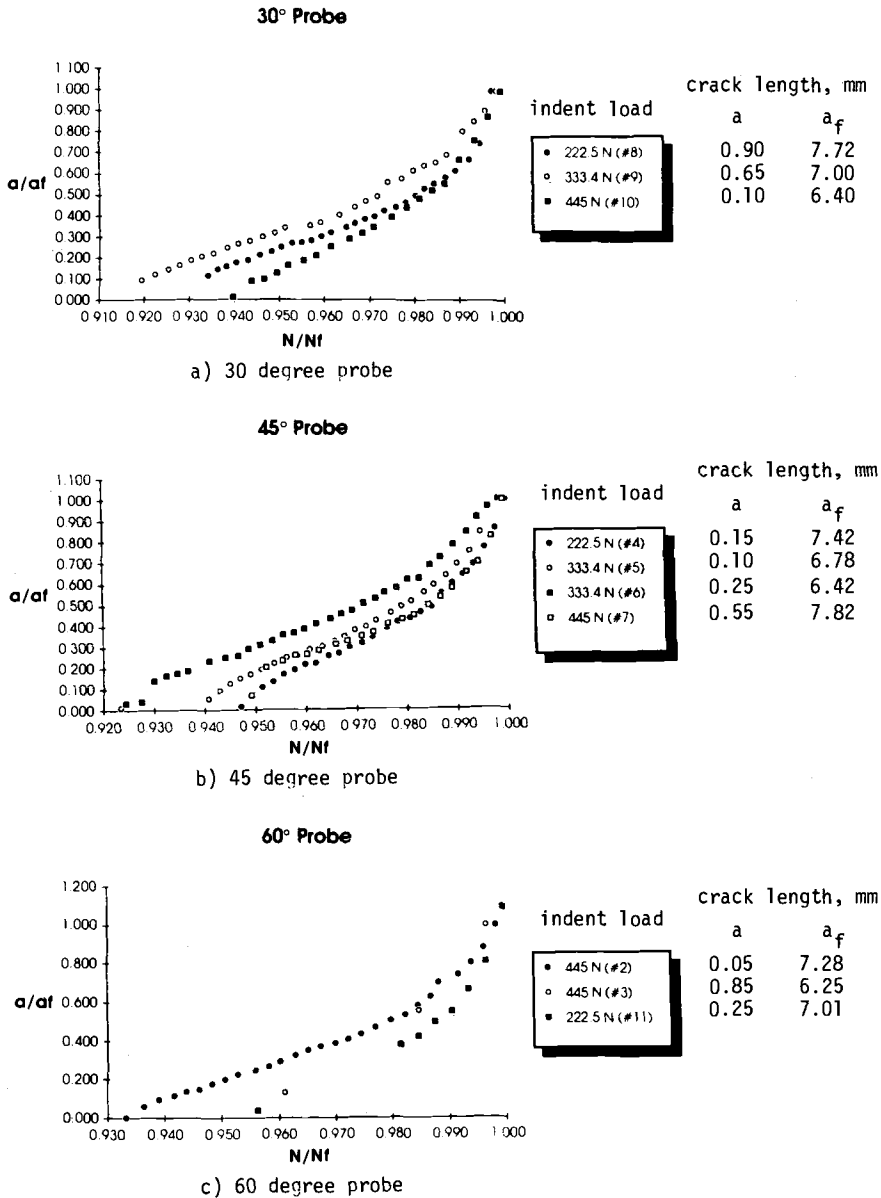
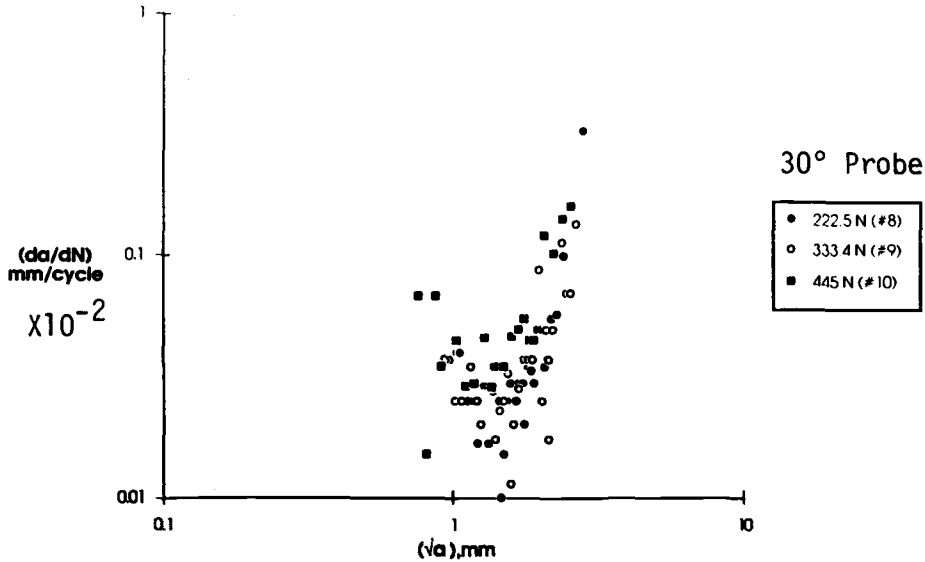


FIG. 3—Normalized crack length versus normalized load cycles.

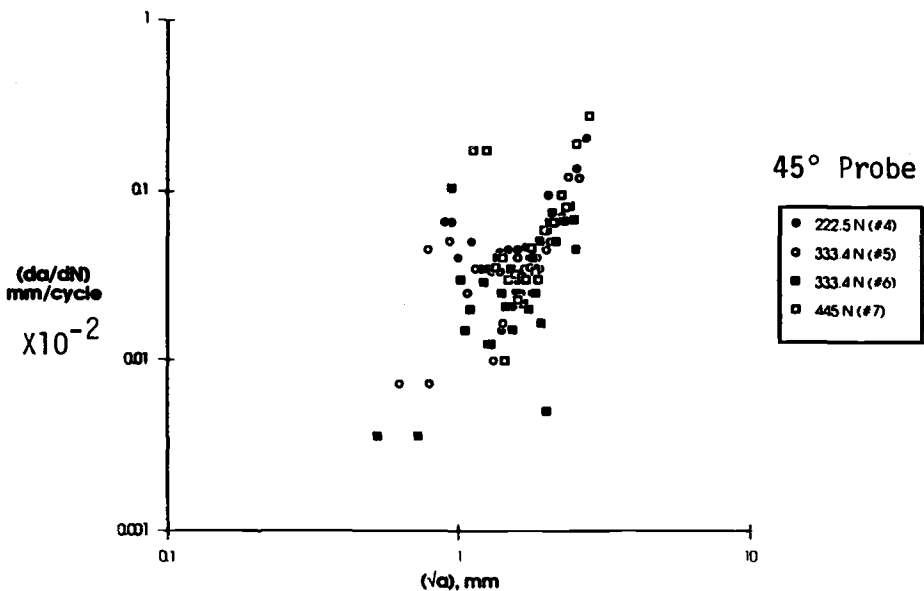
the crack length,  $N$  is the elapsed load cycles, and the subscript  $f$  is used to identify the crack length and the corresponding load cycles at final fracture. Three or four tests were conducted for each indent generated by using 30, 45, and 60-deg probes and the results of each one plotted in Figs. 3a–3c, respectively, identifying different initial indent loads with different symbols. Note that most of the fatigue life is spent in initiating the crack irrespective of the initial size of the defect. The term “crack initiation” herein denotes the formation of a crack about 0.05 mm. Regardless of the initial indent size, a distinct slope

in the crack growth is observed immediately upon crack initiation. The slope was very large initially; that is, the crack grew very quickly as soon as it was initiated, then the crack growth slowed down and flattened out. As the crack length increased, the slope of the curves again increased until the final fracture occurred.

Figure 4 shows the propagation rates, calculated from the raw data, presented as the



a)  $R = 0.33$



b)  $R = 0.50$

FIG. 4—Fatigue crack growth rate,  $da/dN$ , as a function of crack length.

variation in crack growth rate as a function of the square root of crack length from the indent tip. The decrease in crack growth rates after crack initiation is obvious in all the cases. The minimum crack growth rate appears to be at a point where the "short crack" and "long crack" growth data intersect. The growth rate of cracks initiated from the notch root, initially high,  $6 \times 10^{-7}$  m/cycle, then decreases toward a minimum  $1 \times 10^{-7}$  m/cycle, and finally increases. The defects generated by the indents in the keyhole notch did depict its influence on the growth rate, as seen in Figs. 4a–4c for 30, 45, and 60 deg, respectively. From these figures, it is seen that deceleration in crack growth rate is a function of the initial indent load. Note also that the crack length from the tip of the indent at which the growth rate is a minimum is seen to decrease with increasing initial indent size. The crack extension at which the short crack growth rate reaches minimum seems to vary prior to merging into a long crack growth rate. However, this variation is not large but appears to be between 1 to 2 mm.

There is a large scatter in the crack growth data for physically short cracks (that is,  $< 1$  mm), and the scatter is diminished when the crack length exceeded about 5 mm. The magnitude of minimum crack growth rate is varied with respect to the nature of the flaw generated by initial indent loads. In order to extrapolate the effect of initial indent severity on the growth rate curves, the indent loads were compared with corresponding crack lengths at which growth rates were a minimum. This dependence may be observed in Fig. 4 and is found to be approximately linear in nature. This indicates that within a certain limiting indent size, "small crack" growth rate data approach those of "long cracks" sooner if the initial indent load or the initial defect size is larger.

### Fractography

In order to assess the validity of the macromasurements, we examined the fatigued surfaces fractographically. Representative fractographic results are shown in the following paragraphs for 30, 45, and 60-deg indent flaws. Depending on the stress level and defect size, almost all of the fractured components possessed varying amounts of flat and slant

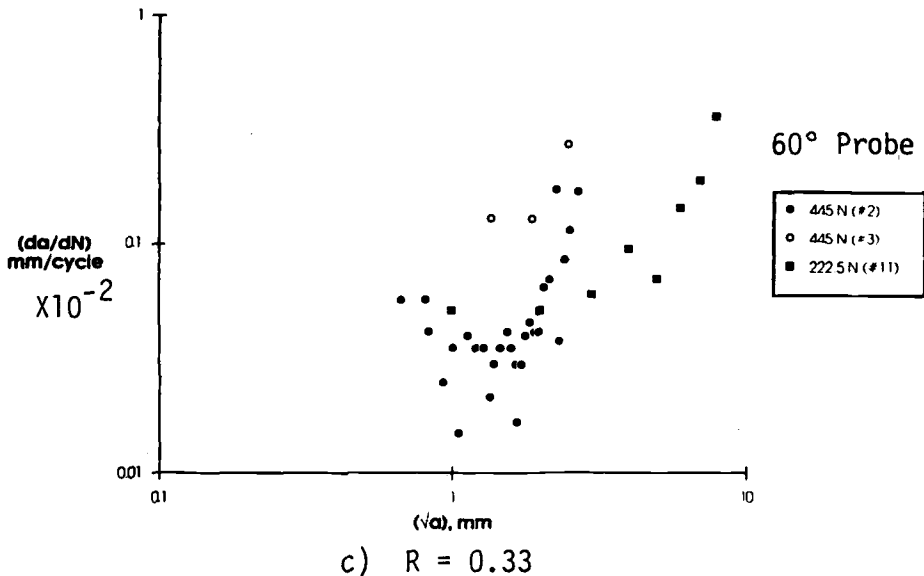


FIG. 4—Continued.

fracture. Consequently, a fatigue crack started out at 90 deg to the plate surface but completed its propagation at 45 deg to the surface. A typical fatigue crack surface with an indent and without an indent is shown in Fig. 5. A short crack which emanates from an unindented keyhole notch, shown in Fig. 5a, spread in a radial or fan-like morphology and mingled at steps in the fracture surface, whereas the crack generated from an indent on the keyhole notch spread initially in a conical shape and reaches in steps a semielliptical to through-the-thickness crack.

Fractographic analysis of the striation spacings was performed using SEM. All fractographs were taken using either a 20- or 25-deg tilt to limit possible distortions of striation spacings used to calculate fatigue crack propagation rates. Micrographs obtained from SEM were used to compute growth rates at very small crack lengths. Essentially, it was observed that fatigue crack growth occurred mainly by the mechanisms of striation formation. The spacing of the striations was in reasonable agreement with the growth rates obtained from the Gaertner horizontally traveling microscope at larger crack lengths.

Figure 6 presents a good visual comparison of the difference on the fatigue crack growth rates at different crack lengths for Specimen 8 with an initial indent load of 223 N in 30-deg indent flaws. Fatigue striations are well defined near the tip of the indent and as close as 1.38 mm from the notch or 0.92 mm from the indent tip. The locations of micrographs, Figs. 6b–6f, are shown on the fatigue surface of the photomicrograph Fig. 6a. Figure 7 shows typical fatigue striations at various locations in a 45-deg indent flaw with an initial indent load of 334 N in Specimen 5. Figure 7a shows the observed striations locations presented in Figs. 7b–7e. The crack growth rates computed from these striations range from  $9.9 \times 10^{-8}$  m/cycle to  $1.8 \times 10^{-7}$  m/cycle, corresponding to small crack,  $a$ , values. The  $da/dN$  versus  $\sqrt{a}$  obtained from the micrographs agreed reasonably well with the corresponding macro measurements made since the striations locations are around the transition region. Figure 8a shows the locations where scanning electron micrographs of the fatigue surface of Specimen 11 were taken. Specimen 11 was subjected to an initial indent load of 223 N, as shown in Table 2. Figures 8b–8c show the typical striations observed at the transitional zone located in Fig. 8a. Crack length and corresponding microscopic crack growth rates have good agreement with the data of Fig. 4c.

Figure 9 is presented for the visual comparison of crack growth rates calculated by the macromasurements and micromasurements observed in a 60-deg indent with an initial indent load of 334 N in Specimen 1. Within the permitted experimental conditions, there is an excellent agreement between the SEM measurements and the measurements made by traveling microscope. It is indeed the crack growth decelerated to a minimum value at a crack length of 1.7 or 1.4 mm from the tip of the indent. Crack propagation is found to be due to the striation mechanism. Striation measurements consistently showed slightly lower growth rates for short cracks of less than 450  $\mu\text{m}$  in length, but there was no noticeable change observed for long cracks of length greater than 2.5 mm. The low growth rates for physically small cracks are possible because striations are influenced by grain orientation, presence of inhomogeneity, and the severe strain field experienced by the short crack.

## Discussion

The basic data for this study are shown in Fig. 3 and were obtained by measuring the crack extension after a selected number of load cycles. The microscopic crack extension obtained from SEM measurements coincided with the macroscopic values, and, therefore, the extension of the curves into a very small crack range could be undertaken with confidence. In order to assess the influence of plastic zones on the crack lengths, the plastic zone size was calculated and compared. The depth of indented flaws was measured optically

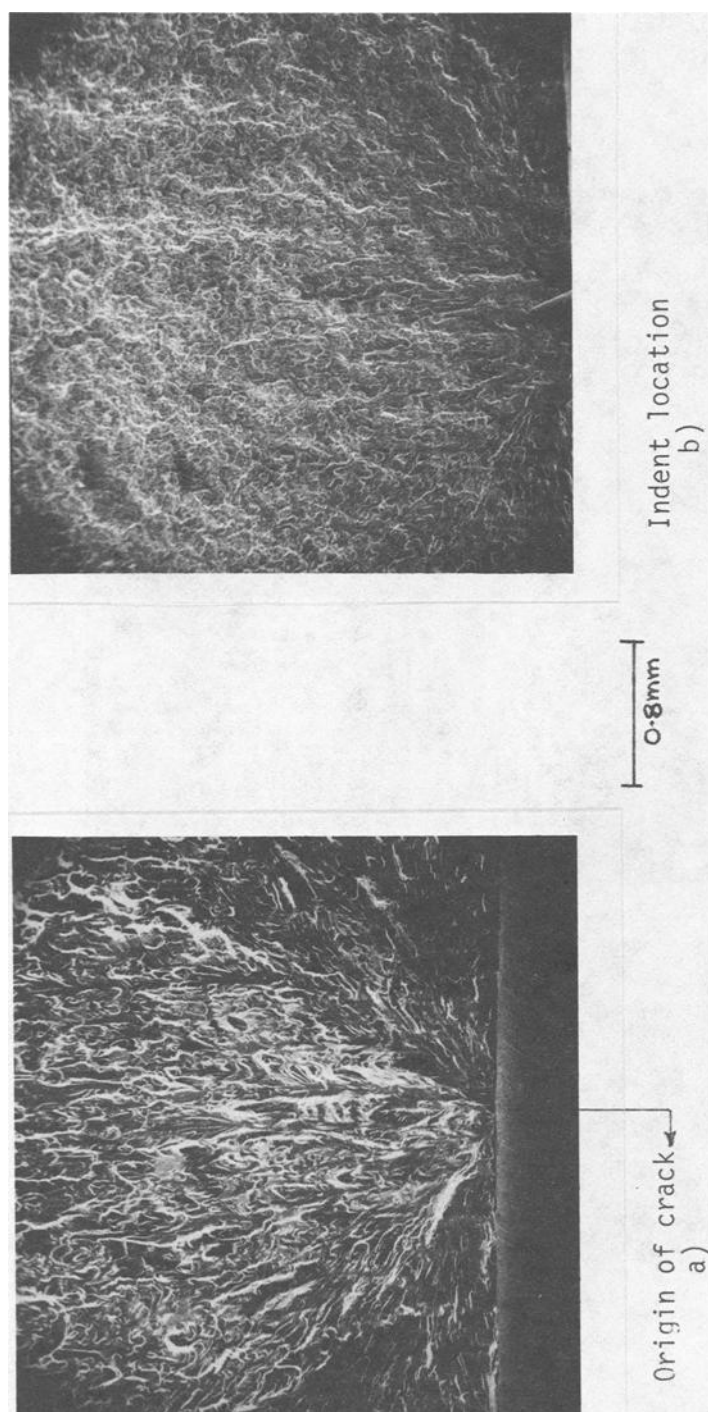


FIG. 5—Photomicrographs of fatigue crack initiation: (a) smooth notch, (b) indent notch.

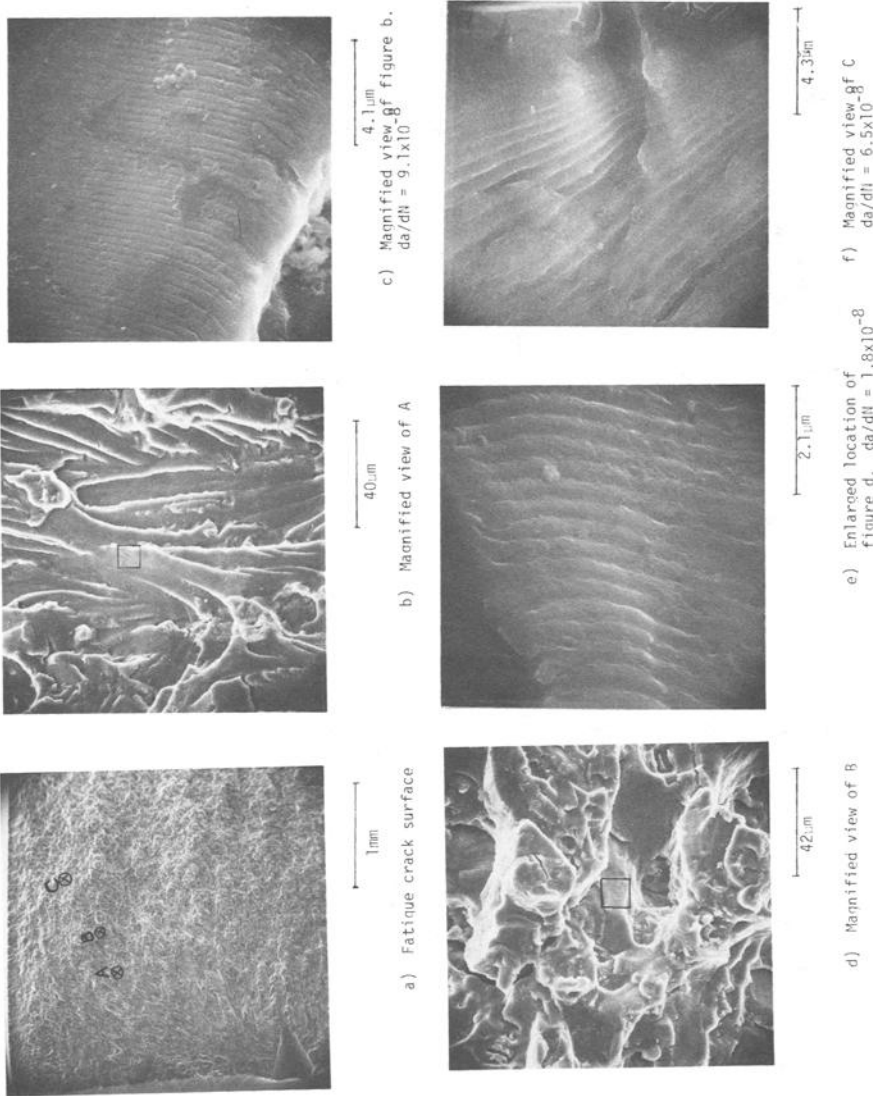
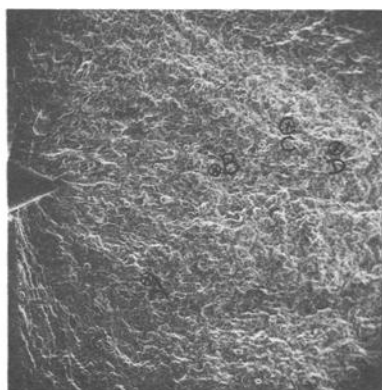
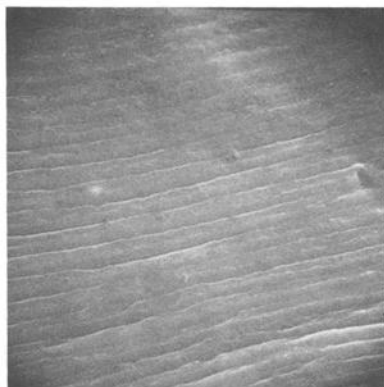


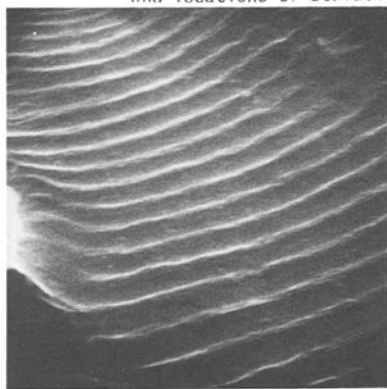
FIG. 6—Typical fractographic observations in 7075-T6 aluminum alloy. Initial flaw was introduced by 30-deg probe with a load of 223 N.



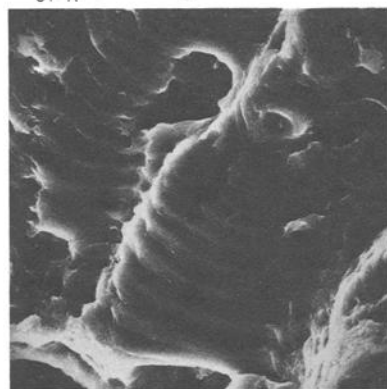
a) Fatigue crack surface and locations of striations



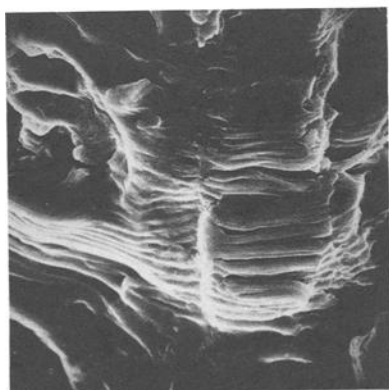
b) Magnified view of A }  $da/dN = 6 \times 10^{-8}$



c) Magnified view of B }  $da/dN = 9 \times 10^{-8}$



d) Magnified view of C. }  $da/dN = 1.6 \times 10^{-7}$



e) Magnified view of D. }  $da/dN = 1.8 \times 10^{-7}$

FIG. 7—Typical fractographic observations in 7075-T6 aluminum alloy. Initial flaw was introduced by 45-deg probe with a load of 334 N.





FIG. 8—Typical fractographic features observed in 60-deg indent specimen of 7075-T6 aluminum alloy.

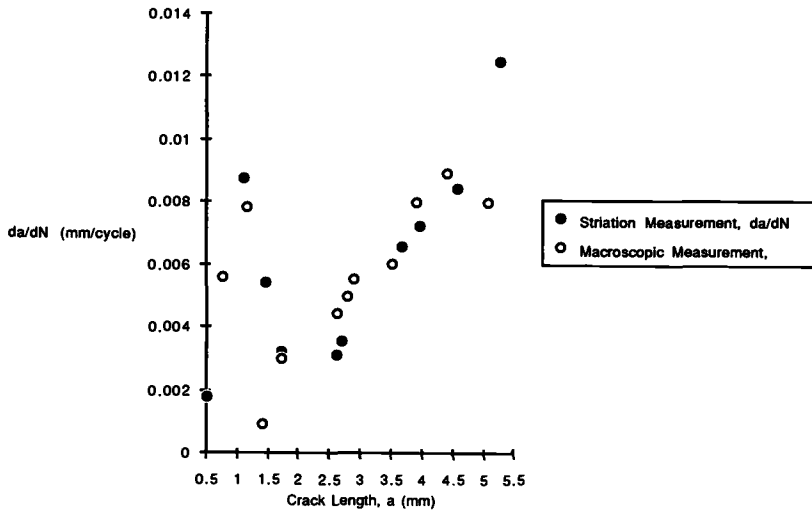


FIG. 9—Fatigue crack growth rate,  $da/dN$ , versus crack length,  $a$ . Specimen No. 1, 60-deg indent, with an initial indent load of 334 N.

and varied between 0.156 to 0.6 mm. Using the highest stress-intensity factor  $K$  value of  $19 \text{ MPa}\sqrt{\text{m}}$  for the physically short cracks with the yield strength  $S_y = 480 \text{ MPa}$ , the plane-stress plastic zone radius,  $r_y$  when

$$r_y = \frac{1}{2\pi} \left( \frac{K_{\max}}{S_y} \right)^2$$

was 0.2 mm. This is sufficiently less than the crack lengths encountered in this study.

The crack extension,  $a$ , at which the growth rate reaches a minimum, seems to depend on the material and load ratio [7,9,15]. From the nature of physically short cracks, as outlined by previous investigations, it was expected that a characteristic crack length could exist for a given material and load conditions. The  $da/dN$  versus  $\sqrt{a}$  data shown in Fig. 4 indeed show not only the influence of load ratio but also the initial flaw size on minimum crack growth. SEM measurements of microcrack growth, shown in Figs. 6–9, agreed very well with that of Fig. 4. The transition from short crack to long crack does not occur at a unique crack length, but exists over a small range of crack lengths of 1 to 2.5 mm and agrees with the SEM measurements shown in Fig. 9. As a first estimation, the transition crack length may be obtained as the average of the observed transition lengths; approximately  $1.5 \times 10^{-3} \text{ m}$ . A calculation based on Smith and Miller [6,7], the theoretical predictions yield a transition length of 1.38 mm for the specimen configuration and loading conditions employed in this study. These estimates are close to the observed value for the transition crack length. It is clear from these data, and our previous investigations on key-hole-notched compact specimens [26,27,29], that the transition distance from small crack behavior to long crack behavior varies; it appears to depend on the stress ratio and the initial flaw size. This indeed implies that in aluminum alloys, small cracks seem to lack a threshold altogether, so that no such simple determination in terms of  $\Delta K$  is possible. The reasons could be use due to the strain field experienced by the short cracks. This strain field is determined by the grain boundary population along the crack front in addition to the slip processes that are activated in the crystal ahead of the crack. It is important to point

out here that there was no attempt made to correlate the growth rate of short and long fatigue cracks by stress-intensity factor because the flaws were initially of a three-dimensional nature. Studying the nature of crack propagation by fractography indeed shows that the early stage of crack growth has depicted the conical crack profile from the indent. The surface defects generated by the indents are three-dimensional in nature, and, therefore, the analysis must be done on a three-dimensional basis, as suggested in Ref 12. This will enhance our understanding about the nature of short fatigue crack growth. The study is in progress and will be reported in the future.

### Conclusions

1. Experimental data show that when characterized in terms of the same linear-elastic fracture mechanics parameter, short fatigue cracks grow at rates faster than long cracks. The growth rates then decrease to a minimum before converging with long crack data.
2. The crack growth rate appears to be a minimum at a point where the "short crack" and "long crack" growth data intersect. The minimum value of crack growth rate decreases with increasing initial indent severity.
3. Scanning electron microscopy indicates that fatigue cracks in air propagate by a mechanism involving the formation of microstriations on the fatigue surface.
4. The results of this research suggest that an initial flaw has an effect on the behavior of short fatigue cracks in 7075-T6 aluminum alloy. The variation in crack growth rates is found to be a function of initial indent severity.

### Acknowledgment

The author wishes to acknowledge Professor Raymond Taggart for helpful discussions and Mr. K. Lu, undergraduate student, for his assistance in conducting experiments.

### References

- [1] Suresh, S. and Ritchie, R. O., *International Metals Review*, Vol. 29, 1984, pp. 445-476.
- [2] Leis, B., Hopper, A. T., Ahamad, J., Broek, D., and Kanninen, N. F., *Engineering Fracture Mechanics*, Vol. 23, No. 1, 1986, pp. 883-898.
- [3] Dowling, N. E. and Wilson, W. K. in *Engineering Fracture Mechanics*, Vol. 20, No. 3, 1984, pp. 569-572.
- [4] El Haddad, M. H., Topper, T. H., and Smith, K. N., *Engineering Fracture Mechanics*, Vol. 2, 1979, pp. 573-584.
- [5] Hammouda, M. M. and Miller, K. J. in *Elastic-Plastic Fracture, ASTM STP 668*, American Society for Testing and Materials, Philadelphia, 1979, pp. 703-719.
- [6] Smith, R. A. in *Fatigue Mechanisms: Advances in Quantitative Measurement of Physical Damage, ASTM STP 811*, American Society for Testing and Materials, Philadelphia, 1983, pp. 264-279.
- [7] Smith, R. A. and Miller, K. J., *International Journal of Mechanical Science*, Vol. 20, 1978, pp. 11-22.
- [8] Dowling, N. E. in *Fracture Mechanics, ASTM STP 677*, American Society for Testing and Materials, Philadelphia, 1979, pp. 247-273.
- [9] Lankford, J., *Fatigue of Engineering Material and Structures*, Vol. 5, 1982, pp. 233-248.
- [10] Morris, W. L., James, M. R., and Buck, O., *Engineering Fracture Mechanics*, Vol. 18, 1983, pp. 871-877.
- [11] Smith, C. W. in *Experimental Mechanics*, Vol. 28, No. 2, 1988, pp. 194-200.
- [12] Newman, J. C. and Raju, I. S., *Advances in Fracture Research (ICF6)*, Vol. 3, 1984, pp. 1597-1608.
- [13] Lankford, J., *Fatigue of Engineering Materials and Structures*, Vol. 8, No. 2, 1985, pp. 161-175.
- [14] Lankford, J., *Engineering Fracture Mechanics*, Vol. 9, 1977, pp. 617-624.

- [15] Tanaka, K., Nakai, Y., and Yamashita, M., *International Journal of Fracture*, Vol. 17, 1981, pp. 519–533.
- [16] Suresh, S., *Metallurgical Transactions*, Vol. 14A, 1983, pp. 2375–2385.
- [17] Lankford, J., *Fatigue of Engineering Material and Structures*, Vol. 6, 1983, pp. 15–31.
- [18] Hudak, S. J. *Transactions*, American Society of Mechanical Engineers, *Journal of Engineering Material Technology*, Vol. 103, 1981, pp. 26–35.
- [19] Ritchie, R. O. and Suresh, S., *Material Science and Engineering*, Vol. 57, 1983, pp. L27–L30.
- [20] Suresh, S. and Ritchie, R. O., *Metallurgical Transactions*, Vol. 13A, 1982, pp. 937–940.
- [21] Tanaka, K. and Nakai, Y., *Fatigue of Engineering Materials and Structures*, Vol. 6, 1983, pp. 315–321.
- [22] Dowling, N. E. in *Cyclic Stress-Strain and Plastic Deformation Aspects of Fatigue Crack Growth*, ASTM STP 637, American Society for Testing and Materials, Philadelphia, 1977, pp. 97–121.
- [23] Schijve, J. in *Fatigue Thresholds*, J. Baeklund, A. F. Blom, and C. J. Beevers, Eds., Vol. 2, 1982, pp. 881–908.
- [24] Gangloff, R. P. in *Fatigue Crack Growth Measurement and Data Analysis*, ASTM STP 738, American Society for Testing and Materials, Philadelphia, 1981, pp. 120–138.
- [25] Shimada, H. and Yasubumi, F., *Engineering Fracture Mechanics*, Vol. 19, 1984, pp. 41–48.
- [26] Ramulu, M. and Taggart, R., *Fatigue Life: Analysis and Prediction*, V. S. Goel, Ed., American Society for Metals, 1986, pp. 117–122.
- [27] Ramulu, M. and Jenkins, M. G., *Scripta Metallurgica*, Vol. 21, No. 2, 1987, pp. 187–190.
- [28] Ramulu, M., *Experimental Techniques*, Vol. 11, No. 6, 1987, pp. 32–34.
- [29] Ramulu, M., *Experimental Mechanics*, Vol. 28, No. 2, 1988, pp. 214–220.

# Measurement and Analysis of Surface Cracks in Tubular Threaded Connections

---

**REFERENCE:** Newport, A. and Glinka, G., "Measurement and Analysis of Surface Cracks in Tubular Threaded Connections," *Surface-Crack Growth: Models, Experiments, and Structures, ASTM STP 1060*, W. G. Reuter, J. H. Underwood, and J. C. Newman, Jr., Eds., American Society for Testing and Materials, Philadelphia, 1990, pp. 348–364.

**ABSTRACT:** The results from fatigue tests on large-scale, hollow-threaded connections are presented. The fatigue crack depths and profiles were monitored during the tests using the alternating-current (a-c) field measurement technique. The crack growth data have been used to validate the weight function approach used in conjunction with a through-thickness stress distribution to calculate suitable stress-intensity factors for threaded connections.

**KEY WORDS:** threaded connections, stress analysis, fatigue, a-c field measurement, stress-intensity factors, weight function

## Nomenclature

- $A$  Crack area
- $A_i$  Pin cross-sectional area at Tooth  $i$
- $a$  Crack depth
- $C$  Paris's equation parameter
- $c$  Half crack length measured on the surface
- $K$  Stress-intensity factor
- $K_t$  Stress concentration factor in a notch
- $K_{ti}$  Stress concentration factor at Tooth  $i$
- $K_{tmin}$  Stress concentration factor at minimum applied load
- $K_{tmax}$  Stress concentration factor at maximum applied load
- $K_Q$  Stress-intensity factor at Point Q' for embedded elliptical crack
- $N$  Number of cycles
- $m$  Paris's equation exponent
- $S_i$  Nominal stress at Tooth  $i$
- $S_{mi}$  Mean nominal stress at Tooth  $i$
- $S_t$  Nominal stress in a notch tip
- $S_{tmin}$  Nominal stress under minimum applied load
- $S_{tmax}$  Nominal stress under maximum applied load
- $t$  Pin wall thickness
- $x$  Distance from notch tip

<sup>1</sup> Research assistant, Department of Mechanical Engineering, University College London, Torrington Place, London WC1E 7JE, U.K.

<sup>2</sup> Associate professor, Department of Mechanical Engineering, University of Waterloo, Ontario, Canada N2L 3G1.

$Y$	Geometric correction factor for stress intensity
$\sigma_i$	Maximum local stress at Tooth $i$
$\sigma_{mi}$	Mean local stress at Tooth $i$
$\sigma_x, \sigma_y$	Stress components
$\sigma_{ymin}$	Notch stress under minimum applied load
$\sigma_{ymax}$	Notch stress under maximum applied load
$\Delta K$	Stress-intensity factor range
$\Delta S_i$	Nominal stress range at Tooth $i$
$\sum P_i$	Sum of tooth loads from Tooth 1 to Tooth $i$
$\rho$	Notch root radius

Tubular threaded connections, such as those used in drilling pipes, the end closure of pressure vessels, and the tension legs of floating offshore structures, experience high local stress concentrations in the fillet radius at the base of the loaded tooth flank [1,2]. Consequently, when such a connection is subjected to cyclic loading, high local stress ranges may occur in the fillet radius. It is also known that the tooth loads are not uniformly distributed, the largest load occurring on the tooth farthest from the free end of the male portion of the connection [3]. The largest local stress range occurs at this tooth [1,2], and it is in the fillet radius of this pitch that fatigue cracks usually initiate [4].

The traditional approach to predicting the fatigue life of threaded connections is to use empirically derived  $S/N$  curves. However, due to the extensive variety of shapes of these tubular connections, and also due to their large scale and different levels of initial pretorque (preload), obtaining a comprehensive set of these curves can prove expensive. An alternative is to use the local strain approach to predict the fatigue life to crack initiation and a fracture-mechanics approach to predict the crack propagation life.

The aim of this paper is to present a model for fatigue crack growth analysis making it possible to predict crack growth periods for given initial and critical crack sizes. The model includes a brief description of a hybrid stress calculation technique and the calculation of stress-intensity factor for surface cracks using a "weight function." The calculated stress-intensity factors are validated against experimental data obtained from fatigue tests on full-scale, threaded connections. The experimental data were obtained by monitoring crack sizes and crack shape evolution throughout the tests using the alternating-current (a-c) field measurement technique [5].

## Stress Distribution

Because of the local nature of fatigue the first step in any fatigue life analysis must be the determination of the local stress range to which the critical section of the component is subjected. In the present analysis this is undertaken in two stages. In the first stage, a hybrid finite-element-analogue technique is used to determine the distribution of maximum local stress in the fillet radius of the threaded connection. In the second stage, the analysis is extended to calculate the through-thickness stress distribution on the expected crack plane. The through-thickness stress distribution is used later in the study to calculate appropriate stress-intensity factors.

## Surface Stress Distribution

The local surface stress distribution along the thread is determined using a hybrid finite-element-analogue technique [6], which has been previously validated against results from

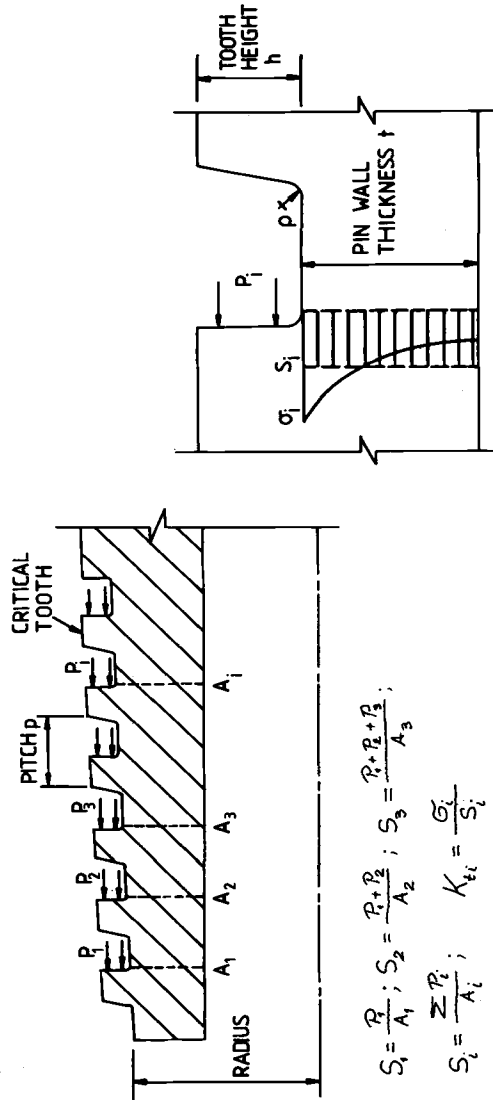


FIG. 1—General thread geometry and notation.

a three-dimensional (3-D) photoelastic model. References 6 and 7 contain a full description of the analogue load distribution model.

In the hybrid stress analysis technique, the analogue model allows the tooth load distribution to be determined. The connection is assumed to be axisymmetric, and the thread is represented as a mechanical system composed of rigid levers joined by springs. The springs represent the stiffness of the elements of pin, box, and teeth. The stiffnesses of the individual elements are modeled as a single spring. The distribution of load on the teeth is determined by an analogy of this system with an electrical network. The finite-element analysis is used to derive stress concentration factors only, and, consequently, it is not necessary to model the whole threaded coupling. An axisymmetric analysis of three teeth is used in the analysis, and stress concentration factors are calculated for different ratios of axial load  $\sum P_i$  to tooth load  $P_i$  because stress concentration factor is dependent on this ratio [6]. The stress concentration factor  $K_{ti}$  is defined as the ratio of the maximum local stress near Tooth  $i$  to the nominal stress  $S_i$  in the pin body at tooth  $i$  (Fig. 1).

$$K_{ti} = \frac{\sigma_i}{S_i} \quad (1)$$

where

$$S_i = \frac{\sum P_i}{A_i} \quad (2)$$

Once the tooth load distribution is known, the nominal stress at each tooth can be determined as can the ratio of axial load to tooth load. The peak local stress at each tooth can then be calculated as the product of the stress concentration factor for the appropriate ratio of axial load to tooth load and the nominal stress at that tooth:

$$\sigma_i = K_{ti} \cdot S_i \quad (3)$$

The finite-element mesh for the thread tested as part of the study reported here is shown in Fig. 2.

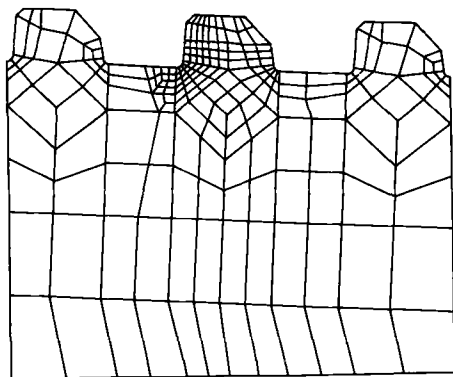


FIG. 2—Finite-element mesh.



*Through-Thickness Stress Distribution*

The stress field ahead of a tooth fillet can be described by equations that were derived to describe the stress field ahead of a notch [8]. For  $K_t < 4.5$

$$\sigma_x = \frac{K_t S_t}{2} \left[ \left( \frac{x}{\rho} + 1 \right)^{-2} - \left( \frac{x}{\rho} + 1 \right)^{-4} \right] \quad (4a)$$

$$\sigma_y = \frac{K_t S_t}{2} \left[ \frac{1}{3} + \frac{1}{2\sqrt{2}} \left( \frac{x}{\rho} + \frac{1}{2} \right)^{-1/2} + \frac{1}{4\sqrt{2}} \left( \frac{x}{\rho} + \frac{1}{2} \right)^{-3/2} + \frac{1}{6} \left( \frac{x}{\rho} + 1 \right)^{-2} + \frac{1}{2} \left( \frac{x}{\rho} + 1 \right)^{-4} \right] \quad (4b)$$

or  $K_t > 4.5$ ,

$$\sigma_x = \frac{K_t S_t}{2} \left[ \frac{1}{2\sqrt{2}} \left( \frac{x}{\rho} + \frac{1}{2} \right)^{-1/2} - \frac{1}{4\sqrt{2}} \left( \frac{x}{\rho} + \frac{1}{2} \right)^{-3/2} + \frac{1}{2} \left( \frac{x}{\rho} + 1 \right)^{-2} - \frac{1}{2} \left( \frac{x}{\rho} + 1 \right)^{-4} \right] \quad (5a)$$

$$\sigma_y = \frac{K_t S_t}{2} \left[ \frac{1}{\sqrt{2}} \left( \frac{x}{\rho} + \frac{1}{2} \right)^{-1/2} + \frac{1}{2\sqrt{2}} \left( \frac{x}{\rho} + \frac{1}{2} \right)^{-3/2} \right] \quad (5b)$$

The equations give a maximum error of 10% over a distance of  $3\rho$  from the notch tip. Figure 3 shows a comparison of the stress field ahead of the tooth fillet calculated from Eqs 5a and 5b and by the finite-element technique. It will be noted that good agreement occurs

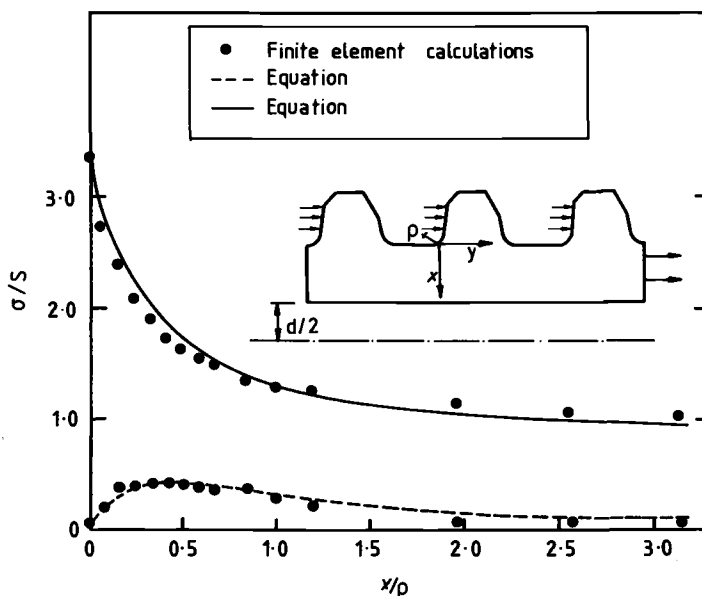


FIG. 3—Through-thickness stress field ahead of a tooth fillet, normalized with respect to nominal stress  $S$ .

between the two. The stress distribution beyond the region influenced by the fillet radius  $\rho$  (that is, for distances  $x > 3\rho$ ) can be assumed to be either uniform or linear depending on the ratio of axial load  $\sum P_i$  to tooth load  $P_i$ .

### Stress-Intensity Factor Calculation

There is no general closed solution for the formulation of stress-intensity factors under nonuniform stress fields, and consequently a numerical technique must be used. One such technique based on the weight function method [9] is used in this study. The weight function can be regarded as the stress-intensity factor for a pair of unit-splitting forces acting on the crack surfaces and may be used in the derivation of stress-intensity factors for any other stress system acting on the crack surfaces by integrating over the crack area provided the stress system on the potential crack plane is known.

$$K = \int_A W_{Q\sigma}(x, y) dA \quad (6)$$

A general weight function for an embedded flaw in a flat plate was proposed by Oore and Burns [10] based on an examination of the structure of known weight functions for various crack shapes and is of the form

$$W_{QQ'} = \frac{\sqrt{2}}{\pi \ell_{QQ'}^2} \frac{1}{\left[ \oint \frac{ds}{\rho_Q^2} \right]^{1/2}} \quad (7)$$

where, as shown in Fig. 4,  $Q'$  is the point on the crack front at which  $K_{Q'}$  must be computed, and  $Q$  is the point on the crack surface at which  $P$ , a pair of symmetric opening forces, act. The  $\ell_{QQ'}$  and  $\rho_Q$  denote, respectively, the distances between  $Q$  and  $Q'$ , and between  $Q$  and the point  $S$  at the centroid of the elemental length  $ds$  of the crack front. The resulting stress-intensity factor  $K_{Q'}$  at  $Q'$  is given by

$$K_{Q'} = P W_{QQ'} \quad (8)$$

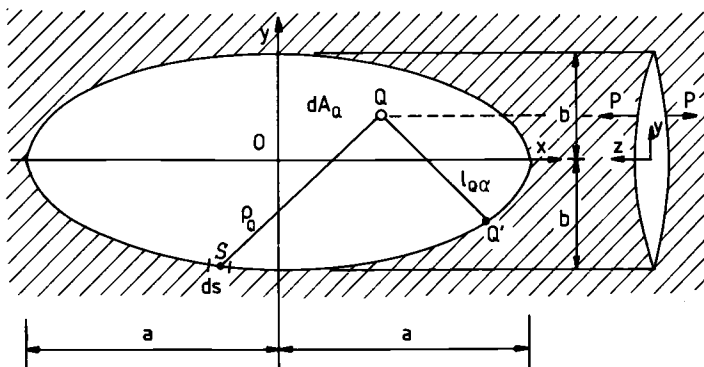


FIG. 4—Notation for the elliptical crack weight function.

Therefore, for an arbitrary normal stress field,  $\sigma_Q(x, y)$  Oore and Burns [10] argued that an estimate of the stress-intensity factor  $K_{Q'}$ , at the point  $Q'$  should be given by the integral

$$K_{Q'} = \int \int_A \frac{\sqrt{2} \sigma_Q dA_Q}{\pi \ell_{QQ'}^2 \left[ \int \frac{ds}{\rho_Q^2} \right]^{1/2}} \quad (9)$$

In order to determine the stress-intensity factor for a surface semi-elliptical crack, Oore and Burns [10] proposed the following modification to the results for the embedded flaw

$$K_s = MK_e \quad (10)$$

where

$K_s$  = stress-intensity factor for a surface crack,

$M$  = boundary correction factor due to the free surface and finite specimen dimensions, and

$K_e$  = stress-intensity factor of the embedded crack with the same half geometry and loading.

In this study,  $M$  was estimated from the stress-intensity formulation proposed by Newman and Raju [11] for a surface semi-elliptical crack under uniform tensile stresses.

The stress-intensity factors for the fatigue cracks in the threads were calculated using the generalized weight function (9) in combination with the through-thickness stress field given by Eq 5b. The stress was assumed to be the nominal stress once it had decayed to this value. Stress-intensity factors were calculated for a range of crack depths using aspect ratios which were taken from an empirical relationship obtained from the test results reported in the next section.

Assuming the stress-intensity factors to be of the form

$$K = Y\sigma\sqrt{\pi a} \quad (11)$$

values of the geometric correction factor  $Y$  were calculated as a function of  $a/t$ . These values can be used to assess the accuracy of the technique by a comparison with experimental values.

## Experimental Study

In order to verify the theoretical predictions of stress-intensity factor, we conducted three fatigue tests on large-scale tubular connections and the crack shape evolution monitored. The connections used were vinyl acetate monomer (VAM) joints, which are thin-walled connections incorporating an external coupling. These connections are commonly used in piping applications, and a joint of the VAM type is shown in Fig. 5. All joints were manufactured from API C75 steel. Each specimen was pre-loaded to a different level. The initial preload was achieved by applying a torque to the joint. The preload was the highest in Specimen No. 1 and the lowest in Specimen No. 3. The cyclic axial loading was applied to the specimens using a 1000-kN capacity servohydraulic test machine. Table 1 gives details of the stresses in each joint calculated by the hybrid finite element-analogue technique described in the Surface Stress Distribution subsection. It is worth noting that the stress concentration calculated as the ratio of stress ranges  $\Delta\sigma_i/\Delta S_i$  is 4.1, while the stress

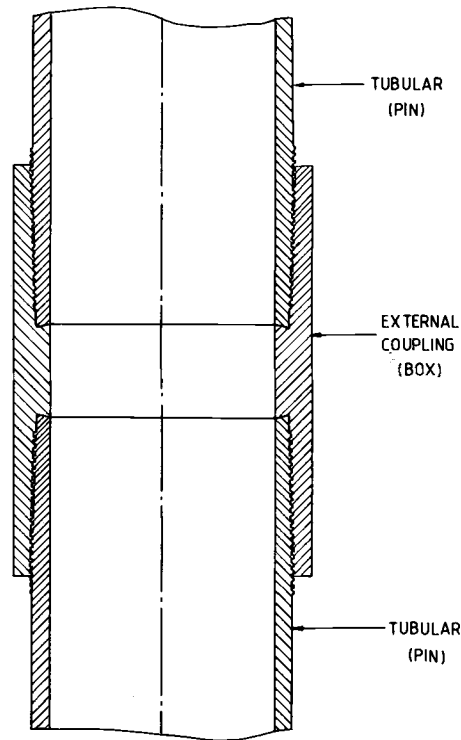


FIG. 5—VAM threaded connection.

concentration based on mean stress  $\sigma_{m,i}/S_{m,i}$  is 19.5. The smaller value of cyclic stress concentration factor  $\Delta\sigma_i/\Delta S_i$  is due to the beneficial effect of the preload. More detail discussion regarding the preload effect is given in Ref 12. It is apparent that the local cyclic stress range of 700 MPa is entirely within the linear-elastic stress range for the API C75 steel, noting that the yield strength  $\sigma'_{ys}$  under cyclic loading is twice the monotonic value. However, the first stress excursion experienced by the material in the critical tooth fillet of Specimen 1 was theoretically from 0 to 2380 MPa and from 0 to 2095 MPa in the case of Specimen 3. Therefore, localized plastic yielding will have occurred in the critical tooth fillet during this first load reversal.

The specimens were periodically removed from the test machine, opened, and inspected using a system based on the alternating-current (a-c) field measurement technique. A schematic drawing of the inspection system is shown in Fig. 6. The section of joint is rotated

TABLE 1—Details of applied nominal and local cyclic stresses in tested VAM joints.<sup>a</sup>

Specimen No.	Nominal Stress Range, $\Delta S_i$ , MPa	Nominal Mean Stress, $S_{m,i}$ , MPa	Local Stress Range, $\Delta\sigma_i$ , MPa	Local Mean Stress $\sigma_{m,i}$ , MPa
1	170	104	700	2030
2	170	104	700	1905
3	170	104	700	1745

<sup>a</sup> Material: Steel API C75;  $\sigma_{ys} = 517\text{--}621$  MPa;  $\sigma_{uts} = 655$  MPa.

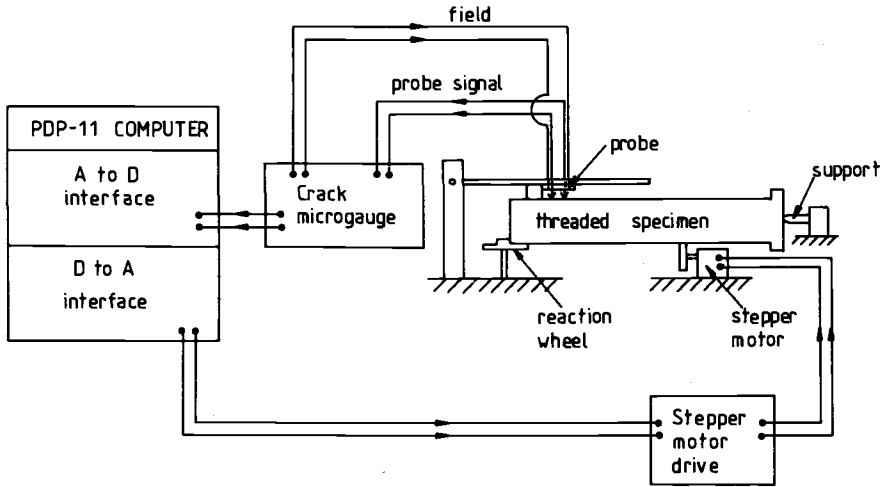


FIG. 6—Schematic of the a-c field measurement inspection rig.

by a stepper motor under computer control, and the a-c field voltage is measured by a probe contacting on the top surfaces of the threads. The probe setup is shown in Fig. 7. The field voltage is induced in the connection by a high-frequency current passing through wires set in the probe housing. The probe is machined with a mating thread profile and is constructed so that the probe contacts are on adjacent thread crowns. In this way, rotation of the joint causes the probe to traverse along the thread, recording the variation of measured voltage. The reading of voltage and position is stored automatically on a PDP11/02 computer.

On completion of testing, the joints were destructively sectioned and the measured crack profiles were compared with the final predictions from the a-c field measurements. Agreement was good for crack length, but the a-c field measurement technique had slightly underpredicted the depth. The error in predicted depth is thought to be due to the use of

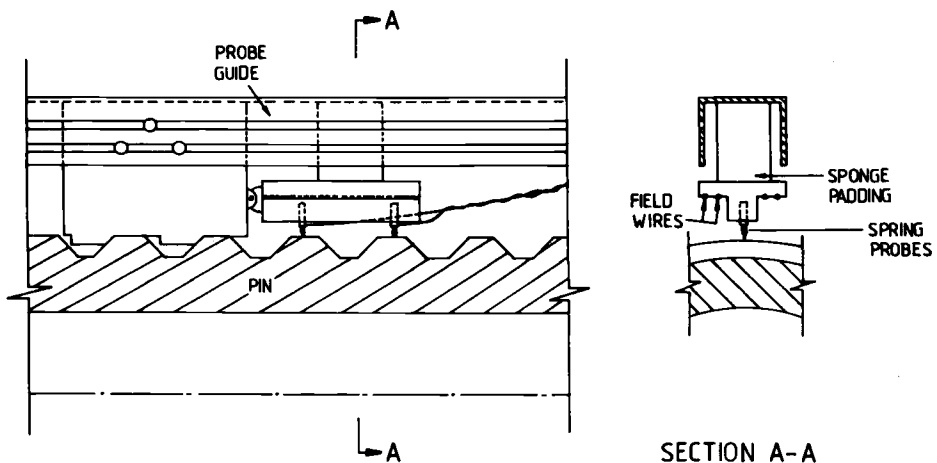


FIG. 7—A-c field measurement probe.

an induced electric field voltage. Consequently, a calibration curve of actual depth versus measured depth was produced and the measured crack profiles corrected. Figure 8 shows the set of crack evolution profiles obtained from the a-c field measurement results for Specimen 2. It will be noted that three cracks were present but that one dominated. It was characteristic for all specimens that the fatigue crack initiation occurred almost simultaneously at several locations, resulting in relatively long cracks with aspects ratios  $0.06 \leq a/c \leq 0.40$ . From the crack profiles it was possible to derive curves of maximum crack depth versus number of cycles; these are shown in Figs. 9 to 11. This fatigue crack growth data can be interpreted to give the experimental stress-intensity factor range which is assumed to be of the form

$$\Delta K = Y \Delta S \sqrt{\pi a} \quad (12)$$

therefore

$$Y = \frac{\Delta K}{\Delta S \sqrt{\pi a}} \quad (13)$$

Using the Paris [13] crack growth equation

$$\frac{da}{dN} = C(\Delta K)^m \quad (14)$$

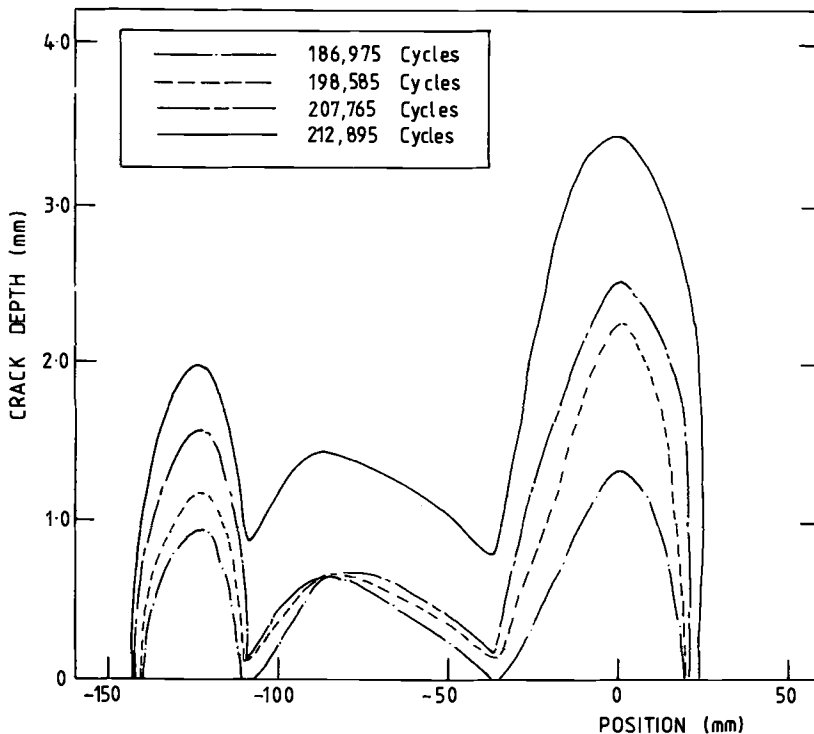


FIG. 8—Crack evolution profiles.

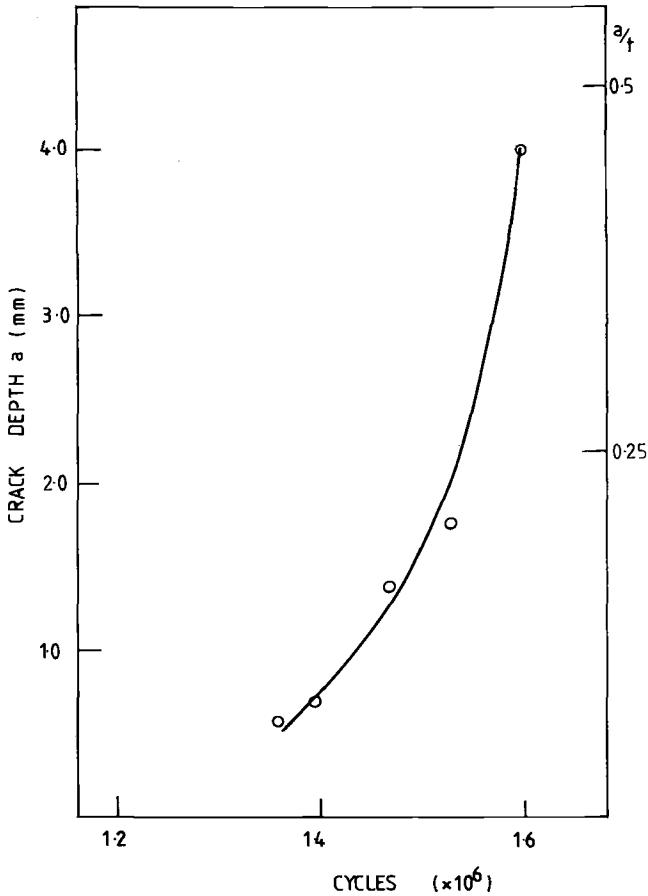


FIG. 9—Crack depth versus number of cycles for Specimen 1.

we obtain the expression

$$Y = \frac{\left( \frac{1}{C} \left( \frac{da}{dN} \right) \right)^{1/m}}{\Delta S \sqrt{\pi a}} \quad (15)$$

The material constants  $C$  and  $m$  are not known for the API C75 steel from which the VAM joints were manufactured. Therefore, it was decided to use the mean value of the data produced by Barsom [14] for high-strength steels, that is,  $C = 9.51 \times 10^{-11}$  and  $m = 2.25$  for  $\Delta K$  measured in  $\text{MPa}\sqrt{\text{m}}$  and  $da/dN$  in  $\text{m/cycle}$ .

To calculate a value of  $Y$  using the weight function, it is necessary to know the value of aspect ratio  $a/c$  corresponding to the crack depth  $a$ . The values of aspect ratio used in this study were those obtained experimentally from the crack evolution profiles. Aspect ratio  $a/c$  is shown as a function of crack depth for all three specimens in Fig. 12.

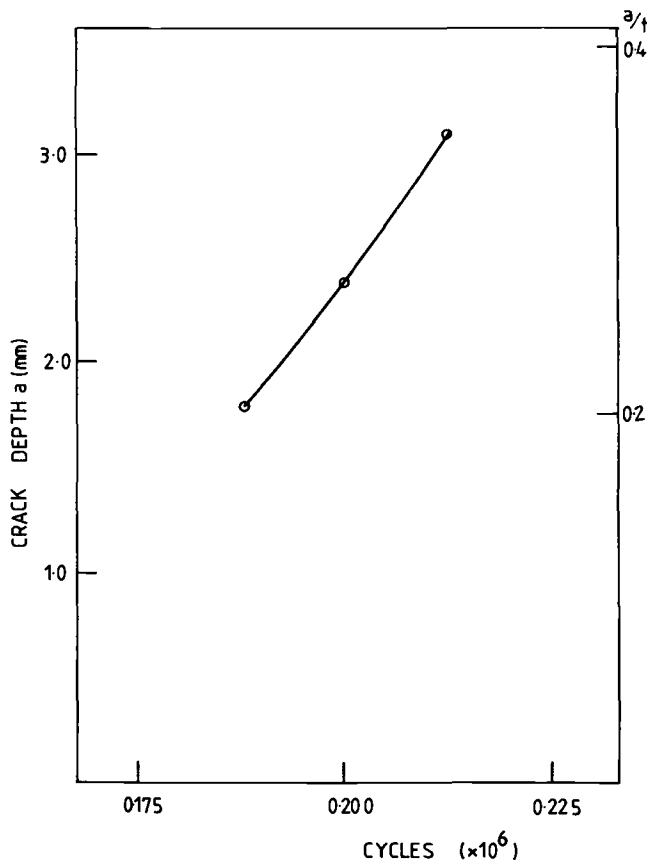


FIG. 10—Crack depth versus number of cycles for Specimen 2.

The theoretically obtained  $Y$  values from the weight function technique are compared with the experimentally obtained  $Y$  values in Figs. 13 to 15, where they are plotted as a function of  $a/t$ .

It is apparent that both the calculated and experimentally obtained geometric correction factors  $Y$  showed similar features and trends. The geometric factor  $Y$  decreases initially as the crack depth increases and then increases slightly as the crack approaches the opposite free surface, that is, the inner surface of the tube. The initial decay of the  $Y$  factor was due to the sharp decreases in stresses away from the tooth fillet in which region high-stress concentrations occurred. It should also be noted that the crack was probably propagated through a monotonic plastic zone caused by the first load reversal as mentioned earlier. On the other hand, the increase in the geometric factor  $Y$  for cracks deeper than 50% of the wall thickness was slightly higher than in the case of surface semi-elliptical cracks in smooth pipes [15] under tensile load. It is also felt that the bending stress component resulting from the bending of the tooth as a cantilever may change with the crack depth because of changes in the tooth stiffness. Additionally, the decreasing tooth stiffness may change the preload effect. Therefore, it is worth emphasising that the three specimens



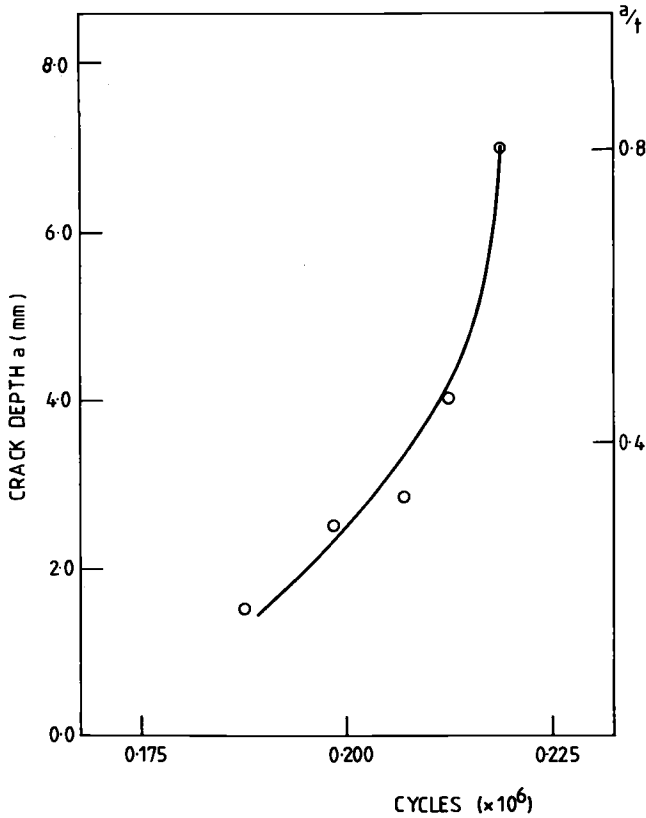


FIG. 11—Crack depth versus number of cycles for Specimen 3.

under discussion were tested under different preloads, with the lowest and highest preload applied to the third and first specimens, respectively.

Nevertheless, the calculation of stress intensity for cracks in threaded connections seem to be possible by using the weight function (7), but the input data regarding stress level and stress distribution require detailed studies. The weight function can be used satisfactorily for calculating stress intensity factors despite the inaccuracies indicated lately by Desjardins et al. [16].

### Discussion

The theoretical calculations consisted of calculations of surface stress using a hybrid analogue-finite-element model followed by the calculation of the through-thickness stress distribution in the critical section. The stress analysis was further complicated by the fact that the stress concentration factor at the critical location was found to be dependent on the applied load level and the preload. Thus the local stress in the tooth fillet had to be calculated for maximum and minimum load level for each particular level of preload.

It should be also noted that the weight function used above is of an approximate nature and may underestimate stress-intensity factors for deep semi-elliptical cracks under bend-

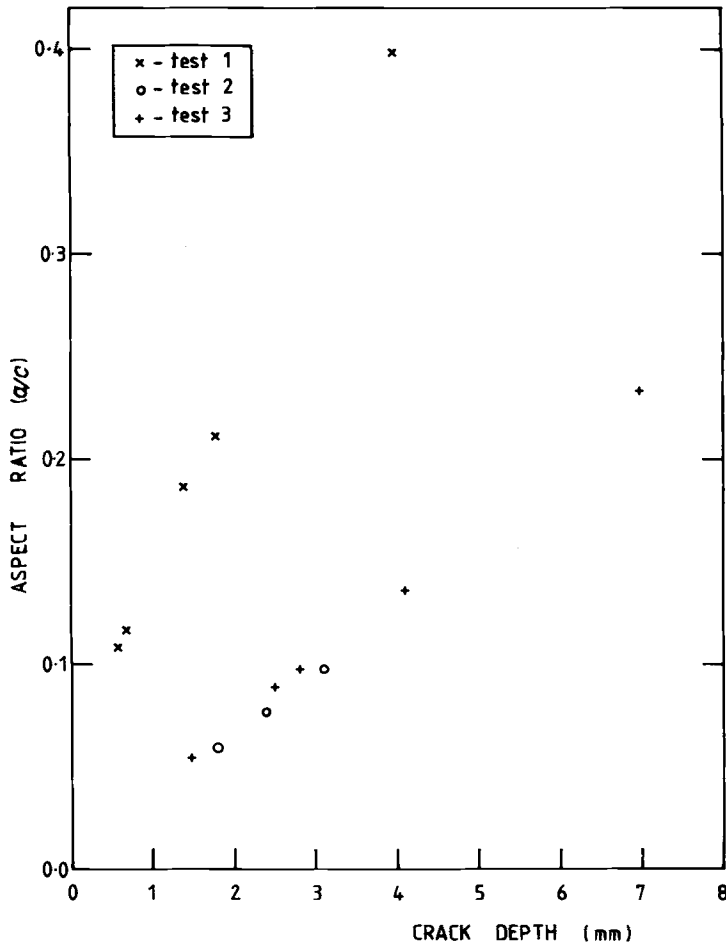


FIG. 12—Aspect ratio as a function of crack depth.

ing loading as reported in Ref 16. Furthermore, the weight function was derived for cracks in smooth flat plates only. The analysis of fatigue crack growth in threaded connections is also complicated by the intricate stress analysis that is required to calculate the surface stress at the critical location. A further complication in this particular study was the lack of suitable material data for the test specimen steel.

Nevertheless, despite these obvious approximations, the calculated stress-intensity factors showed the same trends as the experimental results, and even quantitative agreement was reasonable. Therefore, the technique described above may be used in the optimization of threaded connections and also for comparative studies. However, it should be noted that in certain cases the technique underestimates the geometric correction factor  $Y$ . Consequently, further refinement of the method may be useful before using it in a predictive capacity. The advantage of the presented methodology lies in the cheap and fast calculation of tooth load distribution and through-the-thickness stresses and relatively simple stress-intensity calculations based on the weight function.

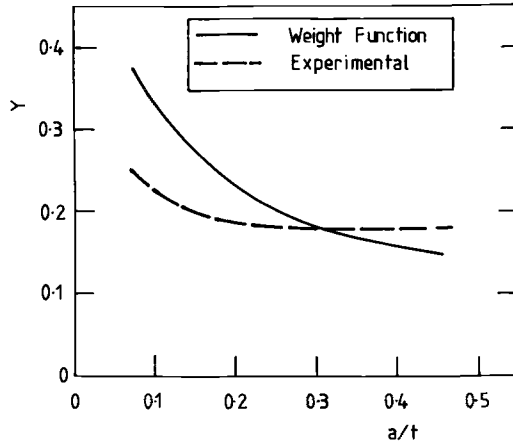


FIG. 13—Comparison of experimental and theoretical variation in geometric stress-intensity calibration factor for Specimen 1.

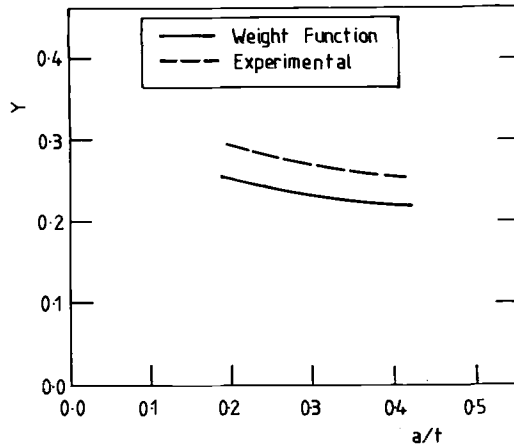


FIG. 14—Comparison of experimental and theoretical variation in geometric stress-intensity calibration factor for Specimen 2.

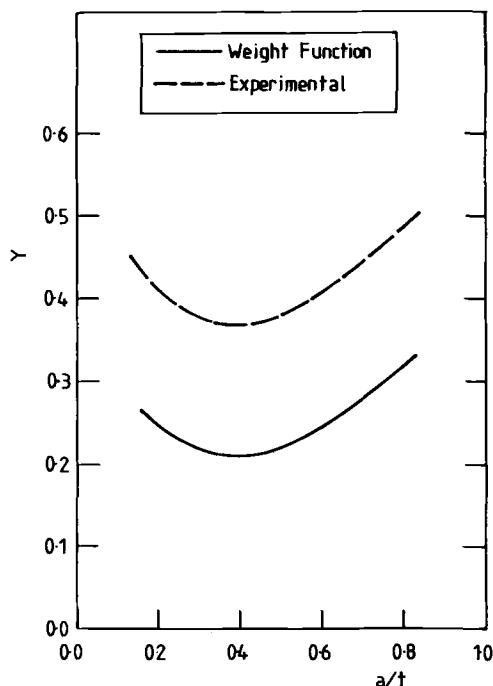


FIG. 15—Comparison of experimental and theoretical variation in geometric stress-intensity calibration factor for Specimen 3.

## Conclusions

1. The stress distributions in the critical sections can be satisfactorily calculated using the hybrid analogue-finite-element model.
2. Fatigue crack profiles in large threaded connections can be satisfactorily measured using the a-c field measurement technique. Several small cracks initiated almost simultaneously in the critical tooth fillet, resulting in a relatively long macrocrack with aspect ratios  $a/c$  varying from 0.06 up to 0.40.
3. The weight function technique used in conjunction with a through-thickness stress field description can be satisfactorily applied to the prediction of stress-intensity factors for threaded connections. However, in certain cases the stress-intensity factor is underestimated, which will lead to overestimates of fatigue life.

## Acknowledgment

A major part of the work reported in this paper was conducted by both authors during their employment at the Department of Mechanical Engineering, University College London, London, United Kingdom.

## References

- [1] Hetenyi, M., "The Distribution of Stress in Threaded Connections," *Experimental Stress Analysis*, 1943, pp. 147-156.

- [2] Brown, A. P. C. and Hickson, C. W., "A Photoelastic Study of Stresses in Screw Threads," *Proceedings of the Institution of Mechanical Engineers*, Vol. 1B, 1952, pp. 605-608.
- [3] Sopwith, D. G., "The Distribution of Load in Screw Threads," *Proceedings of the Institution of Mechanical Engineers*, Vol. 159, 1948, pp. 373-383.
- [4] Birger, I. A., "Extending Life of Threaded Joints by Increasing Thread Root Radius," *Russian Engineering Journal*, Vol. 48, 1968, pp. 50-52.
- [5] Dover, W. D., Collins, R., and Michael, D. H., "The Use of A-C-Field Measurements for Crack Detection and Sizing in Air and Underwater," *Transactions of the Royal Society*, London, Vol. A320, 1986, pp. 271-283.
- [6] Newport, A., Topp, D. A., and Glinka, G., "The Analysis of Elastic Stress Distribution in Threaded Tether Connections," *Journal of Strain Analysis*, Vol. 22, No. 4, 1987, pp. 229-235.
- [7] Newport, A., "Stress and Fatigue Analysis of Threaded, Tether Connections," PH.D. thesis, University College London, Department of Mechanical Engineering, London, 1989.
- [8] Glinka, G. and Newport, A., "Universal Features of Elastic Notch-Tip Stress Fields," *International Journal of Fatigue*, Vol. 9, No. 3, 1987, pp. 143-150.
- [9] Bueckner, H. F., "A Novel Principle for the Computation of Stress-Intensity Factors," *Zeitschrift für Angewandte Mathematik und Mechanik*, Vol. 50, 1970, pp. 529-546.
- [10] Oore, M. and Burns, D. J., "Estimation of Stress-Intensity Factors for Embedded Irregular Cracks Subjected to Arbitrary Normal Stress Fields," *Transactions, American Society of Mechanical Engineers, Journal of Pressure Vessel Technology*, Vol. 102, No. 2, 1980, pp. 202-211.
- [11] Newman, J. C. and Raju, I. S., "An Empirical Stress-Intensity Factor Equation for the Surface Crack," *Engineering Fracture Mechanics*, Vol. 15, No. 1, 1981, pp. 185-192.
- [12] Newport, A. and Glinka, G., "The Effect of Preload on The Local Cyclic Stresses in Tubular Threaded Connections," 1989, American Society for Mechanical Engineers, *Journal of Offshore Mechanics and Arctic Engineering*, to be published.
- [13] Paris, P. C. and Erdogan, F., "A Critical Analysis of Crack Propagation Laws," *Transactions, American Society of Mechanical Engineers, Journal of Basic Engineering*, Vol. 5, No. 4, 1963, pp. 528-534.
- [14] Barsom, J. M., "Fatigue Crack Propagation in Steels of Various Yield Strength," *Transactions, American Society of Mechanical Engineers, Journal of Engineering for Industry*, Vol. 93, No. 4, 1971, p. 190.
- [15] Raju, I. S. and Newman, J. C., "Stress-Intensity Factor for Circumferencial Surface Cracks in Pipes and Rods Under Tension," *Fracture Mechanics; Seventeenth Volume, ASTM STP 905*, J. H. Underwood et al., Eds., American Society for Testing and Materials, Philadelphia, 1986, pp. 789-808.
- [16] Desjardins, J. L., Lambert, S. B., Burns, D. J., and Thompson, J. C., "A Weight Function Technique for Surface Cracks with Application, to Welded Joints," *Proceedings, Conference on Fatigue of Offshore Structures*, W. D. Dover and G. Glinka, Eds., London, Engineering Materials Advisory Services, Ltd., West Midlands, U.K., Sept. 19-20 1988.

## Propagation of Surface Cracks in Notched and Unnotched Rods

---

**REFERENCE:** Caspers, M., Mattheck, C., and Munz, D., "Propagation of Surface Cracks in Notched and Unnotched Rods," *Surface-Crack Growth: Models, Experiments, and Structures, ASTM STP 1060*, W. G. Reuter, J. H. Underwood, and J. C. Newman, Jr., Eds., American Society for Testing and Materials, Philadelphia, 1990, pp. 365–389.

**ABSTRACT:** Stress-intensity factors for surface cracks in cylindrical bars have been calculated applying the method of weight functions. The weight function was obtained from the crack opening displacement of a reference load using the finite-element method. The results can be used for the prediction of growth rates and the shapes of the developing crack front for cracks in notched and unnotched cylindrical bars under arbitrary loading conditions. The predictions have been compared with experimental results.

**KEY WORDS:** surface cracks, fatigue crack growth, stress-intensity factors

Failures caused by fatigue crack propagation are often found in components with circular cross sections such as shafts, bolts, screws, or wires. These may be unnotched cylindrical rods or rods with circumferential notches. Different crack shapes have been observed [1], which are dependent on the geometry of the component (for example, type of notch) and on the type of loading (for example, uniaxial tension or bending). Considering all possible crack shapes, two main classes can be defined as shown in Fig. 1. Cracks with a concave crack front are called "almond"-shaped cracks; those with a convex crack front are called "sickle"-shaped cracks. The limiting case between both types is the straight fronted crack.

To predict the remaining life of a component with an initial crack it is necessary to calculate the crack growth rate of the two-dimensional cracks from the basic material behavior obtained from tests with standard specimens. This requires the knowledge of the stress-intensity factors of the cracks as a function of their geometries.

For specific geometries, results can be found in the literature [2–13]. In this paper, results are presented for a great variety of geometries applying the method of weight functions. Thus, stress-intensity factors can be calculated for arbitrary stress distributions, also including notch stresses or thermal stresses. From these results, crack growth rate predictions have been made and compared with experimental results.

### Weight-Function Method for the Calculation of Stress-Intensity Factors

The weight-function method for the calculation of stress-intensity factors was developed by Bückner [14] and Rice [15]. Cruse and Besuner [16,17] applied the method to two-

<sup>1</sup> Research engineer and group leader, respectively, Nuclear Research Center, Postfach 3640, D-75 Karlsruhe, West Germany.

<sup>2</sup> Professor, University of Karlsruhe, and division head, Nuclear Research Center, Postfach 3460, D-75 Karlsruhe, West Germany.

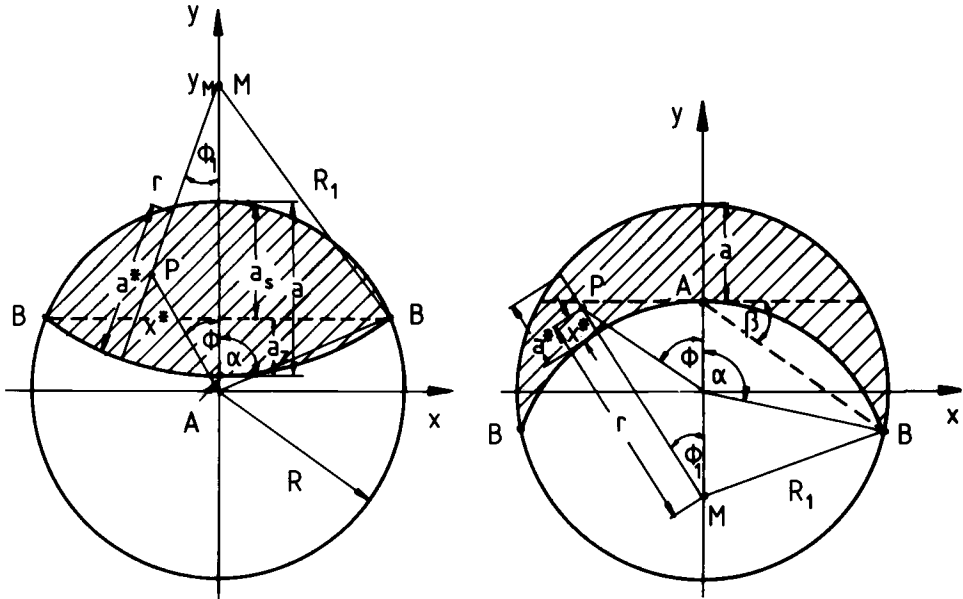


FIG. 1—Almond- and sickle-shaped crack.

dimensional cracks (3D-problem). Further results on the problem of weight function for 3D-problems are discussed by Rice [18], Sham [19], and Vainshtok and Varfolomeyev [20].

For a 2 D-problem, the Mode I stress-intensity factor for an arbitrary loading is given by

$$K_I' = \frac{H}{K_{Ir}} \int_0^a \sigma(x) \frac{\partial u_r(x, a)}{\partial a} dx \quad (1)$$

with  $H = E/(1 - \nu^2)$  for plane strain and  $H = E$  for plane stress.

$K_{Ir}$  and  $u_r(x, a)$  are the stress-intensity factor and the crack opening displacement, respectively, for a reference loading for which usually a constant stress is chosen.  $\sigma(x)$  is the stress distribution at the location of the crack in the uncracked body. The integration is performed over the crack length. The stress-intensity factor  $K_{Ir}$  can be obtained from the  $u_r$ -field if in Eq 1,  $K_I$  is replaced by  $K_{Ir}$ . Then  $\sigma(x)$  is the reference stress distribution  $\sigma_r(x)$ . For  $\sigma_r(x) = \sigma_0 = \text{const}$ ,  $K_{Ir}$  is given by

$$K_{Ir}^2 = H \sigma_0 \int_0^a \frac{\partial u_r}{\partial a} dx \quad (2)$$

This relation enables the calculation of  $K_{Ir}$  from the displacement field  $u_r$ .

For a 3-D problem, a two-dimensional crack is considered. The stress-intensity factor usually varies along the crack front. For the cracks in the cylinders, two special locations are considered here, the surface Points B and Point A of the center of the crack with the local values of the stress-intensity factors  $K_A$  and  $K_B$ . Instead of using these local values for the prediction of the crack growth behavior, Cruse and Besuner used the "local averaged" values  $K_A^*$  and  $K_B^*$ .

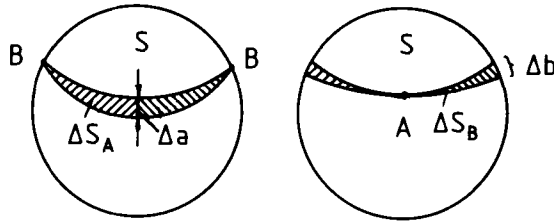


FIG. 2—Virtual crack extension for calculation of energy release rate.

The derivation of these values is best explained with the energy release rate. In Fig. 2, two virtual crack extensions are considered. In one the crack is fixed at the Points B and extended in depth at Point A. The energy release rate then is given by

$$G_{IA} = \int_S \sigma(x,y) \frac{\partial u(x,y)}{\partial S_A} dS \quad (3)$$

where

$S$  = crack area,  
 $\partial S_A$  = virtual crack growth increment, and  
 $u(x,y)$  = crack opening displacement caused by stress  $\sigma(x,y)$ .

For the second virtual crack extension, the crack is fixed at Point A and extended along the surface of the cylinder at the Points B. Then

$$G_{IB} = \int_S \sigma(x,y) \frac{\partial u(x,y)}{\partial S_B} dS \quad (4)$$

Equations 3 and 4 correspond to Eq 2 for a 2 D-problem. From  $G_{IA}$ , a stress-intensity factor  $K_{IA}$  can be calculated

$$K_{IA}^* = (G_{IA} \cdot H)^{1/2} \quad (5)$$

It can be shown [16] that  $K_{IA}$  defined in this way can be also obtained from

$$K_{IA}^{*2} = \frac{1}{\Delta S_A} \int K_I^2(s) d\Delta S_A \quad \text{for } K_I > 0 \quad (6)$$

where  $K_I(s)$  is the stress-intensity factor along the crack front and  $\Delta S_A$  is the virtual crack extension. Similar relations can be written for  $K_{IB}$ .

The weight function concept in terms of energy release rate reads

$$G_{IA} \cdot G_{IA,r} \geq \left[ \int \frac{\partial u_r(x,y)}{\partial S_A} \sigma(x,y) dS \right]^2 \quad (7)$$

It can be shown that in Eq 7, the sign of equality can be used with only a small error [21]. Then Eq 7 reads in terms of  $K$

$$K_{IA}^* = \frac{H}{K_{IA,r}^*} \int \sigma(x,y) \frac{\partial u_r(x,y)}{\partial S_A} dS \quad (8a)$$



and for Point B

$$K_{IB}^* = \frac{H}{K_{IB,r}^*} \int \sigma(x,y) \frac{\partial u_r(x,y)}{\partial S_B} dS \quad (8b)$$

### Stress-Intensity Factors

All cracks are described by a circular crack front in fairly good agreement with experimental findings. The cracks are characterized (Fig. 1) by either the crack depth  $a$  and the crack angle  $\alpha$  or the crack radius  $R_1$  and the coordinate  $y_M$  of the center  $M$  of the crack radius. For sickle-shaped cracks  $y_M < 0$  and for almond cracks  $y_M > 0$ . For sickle cracks, an angle  $\beta$  is also introduced (Fig. 1), which is related to  $a$  and  $\alpha$  by

$$\beta = \tan^{-1} \frac{1 - a/R - \cos \alpha}{\sin \alpha} \quad (9)$$

where  $R$  is the radius of the cylinder. For almond-shaped cracks, the crack depth  $a$  is written as

$$a = a_s + a_z = R(1 - \cos \alpha) + a_z \quad (10)$$

where  $a_s$  is the depth of the straight fronted crack corresponding to the crack angle  $\alpha$ .

For a given crack angle  $\alpha$ , sickle-shaped cracks have a crack depth in the range

$$0 < \frac{a}{R} < 1 - \cos \alpha$$

The calculations for the almond-shaped cracks have been performed in the range

$$1 - \cos \alpha < \frac{a}{R} < \sin \alpha + 1 - \cos \alpha$$

The upper limit is given by the semi-circular crack front.

A point of the crack area is characterized by the polar coordinates  $r, \Phi_1$  with the center  $M$ . Alternatively to  $r$ , the coordinate

$$x^* = R_1 - r \quad (11)$$

is introduced, which starts from the crack front and is directed perpendicular to the crack front. Alternatively to  $\Phi_1$ , and angle  $\Phi$  as shown in Fig. 1 can be used, with  $0 \leq \Phi \leq \alpha$ .

As a reference loading case, uniaxial tension was chosen. The loading condition was a constant force acting at the cylinder ends, which induces a bending moment because of the eccentric position of the crack. The length-to-diameter ratio was chosen to be high enough to avoid any influence on the crack opening displacement.

To obtain an analytical relation between the crack opening displacement  $u(x,y)$  and the crack parameters first 3D-finite-element-method calculations were carried out for a set of different values of  $a$  and  $\alpha$ . In Fig. 3,  $u_r = u_{r0}$  at the surface of the cylinder ( $x^* = a^*$ ) is

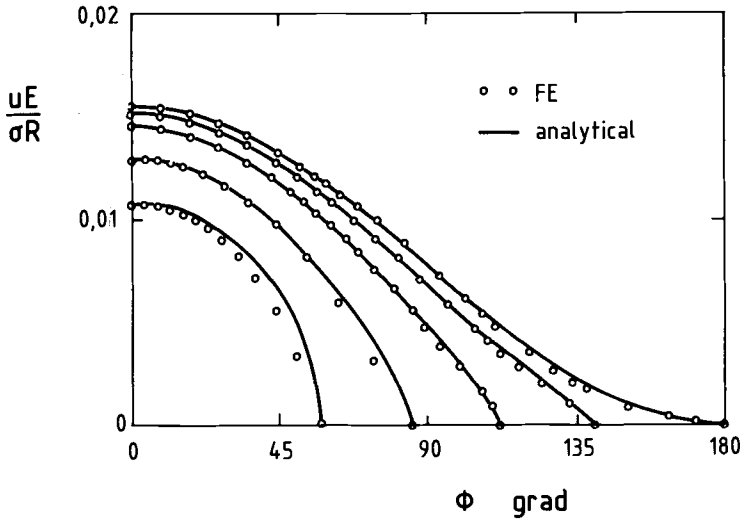


FIG. 3—Crack opening displacement at surface of cylindrical rod for cracks with  $a/R = 0.4$  and different crack angles  $\alpha$  and tension loading.

plotted versus  $\Phi$ . The finite-element results could be described by

$$u_{ro} = u_{\max} \left[ 1 - \left( \frac{\Phi}{\alpha} \right)^2 \right]^{1/2} \quad (12a)$$

for the almond-shaped cracks and by

$$u_{ro} = u_{\max} \left\{ \left[ 1 - \left( \frac{\Phi}{\alpha} \right)^2 \right]^{1/2} (1 - C) - \frac{\cos \alpha + \cos \Phi}{1 - \cos \alpha} \cdot C \right\} \quad (12b)$$

where

$$C = \left[ \frac{\alpha - \alpha_s}{\alpha_e - \alpha_s} \right]^{1/4} \quad (12c)$$

and  $\alpha_e$  is equal to  $\Pi$  for fully opened cracks and to  $\alpha_c$  for cracks under compression (see below) for the sickle-shaped cracks.  $\alpha_s$  is given by  $\cos \alpha_s = 1 - a/R$ .

$u_{\max}$  is the displacement for  $x = 0$  and  $y = R$ . Figure 3 also contains the analytical relations of Eq 12.

Figure 4 shows the displacement along the normal to the crack front ( $x^*$ -coordinate). This displacement could be described by

$$u_r = u_o \left( \frac{x^*}{a^*} \right)^{1/2} \quad (13)$$

Special problems resulting from application of this relation for deep almond-shaped cracks are discussed in Ref 22. After these relations had been set up, only  $u_{\max}$  was calculated for

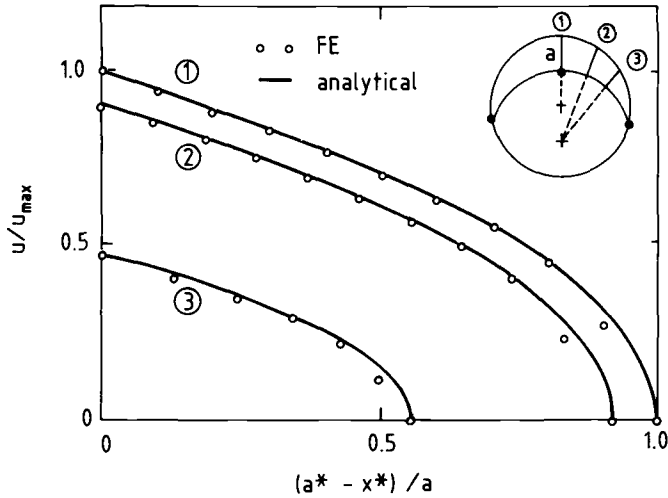


FIG. 4—Crack opening displacement perpendicular to crack front for tension loading.

all possible geometries, and polynomial expressions were fitted to the results

$$u_{\max} = \frac{\sigma R}{E} \sum_{i=0}^4 \sum_{j=1}^5 C_{ij} \left( \frac{a_z}{R} \right)^i \left( \frac{\alpha}{\Pi} \right)^j \quad (14a)$$

for almond-shaped cracks

$$u_{\max} = \frac{\sigma R}{E} \sum_{i=1}^6 \sum_{j=0}^4 C_{ij} \left( \frac{a}{R} \right)^i \left( \frac{\beta}{\Pi} \right)^j \quad (14b)$$

for sickle-shaped cracks. The coefficients  $C_{ij}$  are given in Table 1.

For sickle-shaped cracks with large crack angles, the crack is under compression at Point B. The critical angle  $\alpha_c$  beyond which a compressive region occurs is shown in Fig. 5.

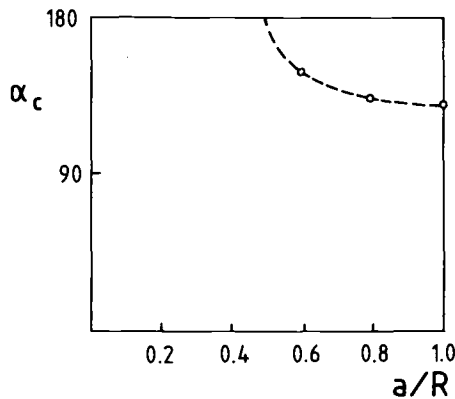


FIG. 5—Critical crack angle  $\alpha_c$  for compression at Point B under tension loading.

TABLE 1—Coefficients  $C_{ij} = C(ij)$  for crack opening displacement.

Almond Crack	Sickle Crack
$C(0,1) = 2.7948$	$C(1,0) = 2.15958$
$C(0,2) = -37.9847$	$C(1,1) = 2.38033$
$C(0,3) = 323.733$	$C(1,2) = -10.4227$
$C(0,4) = -964.272$	$C(1,3) = 29.1113$
$C(0,5) = 1\,137.37$	$C(1,4) = -28.7039$
$C(1,1) = 50.6964$	$C(2,0) = 13.4394$
$C(1,2) = -434.276$	$C(2,1) = 1.50796$
$C(1,3) = 1\,746.73$	$C(2,2) = 9.16937$
$C(1,4) = -3\,457.44$	$C(2,3) = -22.8641$
$C(1,5) = 3\,161.96$	$C(2,4) = 91.3211$
$C(2,1) = -173.246$	$C(3,0) = -112.586$
$C(2,2) = 1\,847.97$	$C(3,1) = 61.3479$
$C(2,3) = -7\,245.92$	$C(3,2) = 10.5490$
$C(2,4) = 12\,340.9$	$C(3,3) = -262.417$
$C(2,5) = -7\,051.4$	$C(3,4) = 1\,320.29$
$C(3,1) = 459.276$	$C(4,0) = -2\,900.30$
$C(3,2) = -5\,622.2$	$C(4,1) = 2\,884.80$
$C(3,3) = 26\,001.0$	$C(4,2) = -1\,074.37$
$C(3,4) = -53\,898.0$	$C(4,3) = -40.2488$
$C(3,5) = 42\,182.4$	$C(4,4) = 844.926$
$C(4,1) = -438.504$	$C(5,0) = -4\,564.65$
$C(4,2) = 5\,529.6$	$C(5,1) = 10\,292.2$
$C(4,3) = -26\,102.6$	$C(5,2) = -10\,485.2$
$C(4,4) = 54\,794.0$	$C(5,3) = 3\,935.03$
$C(4,5) = -42\,918.0$	$C(5,4) = 37.7223$
	$C(6,0) = -788.763$
	$C(6,1) = 4\,455.96$
	$C(6,2) = -10\,388.3$
	$C(6,3) = 10\,844.5$
	$C(6,4) = -4\,148.12$

For all cracks, stress-intensity factors associated to Points A and B were calculated applying Eq 3 for tension loading and Eq 8 for bending. They are presented in dimensionless form as

$$F_{A,B} = \frac{K_{A,B}^*}{\sigma \sqrt{a\Pi}} \quad (15)$$

The results obtained for individual cracks were curve-fitted by polynomial expressions: Almond-shaped cracks

$$F = f_C \cdot f_D + f_E \quad (16)$$

$$f_C = \sum_{i=0}^5 C_i \left( \frac{\alpha}{\Pi} \right)^i \quad (17)$$

$$f_D = \sum_{i=0}^5 D_i \left( \frac{a}{R} \right)^i \quad (18)$$

$$f_E = E_0 + \sum_{i=1}^3 \sum_{j=1}^3 E_{ij} \left( \frac{\alpha}{\Pi} \right)^i \left( \frac{a}{R} \right)^j \quad (19)$$

## Sickle-shaped cracks

$$F = \frac{f_C \cdot f_D + f_E}{f_N} \quad (20)$$

$$f_C = \sum_{i=0}^5 C_i \left( \frac{\beta}{\Pi} \right)^i \quad (21)$$

$$f_D = \sum_{i=0}^5 D_i \left( \frac{a}{R} \right)^i \quad (22)$$

$$f_E = E_0 + \sum_{i=1}^3 \sum_{j=1}^3 E_{ij} \left( \frac{\beta}{\Pi} \right)^i \left( \frac{a}{R} \right)^j \quad (23)$$

$$f_N = \sum_{i=0}^3 N_i \left( \frac{a}{R} \right)^i \quad (24)$$

The coefficients are given in Tables 2 and 3.

In Figs. 6–9, the coefficients  $F_A$  and  $F_B$  are plotted versus the crack depth  $a/R$  for different crack angles for tension and bending loading. The lower bound curve for  $a/R$  for the almond-shaped cracks (dashed curve) corresponds to the crack with a straight crack front. In case of tension loading, the curves are dashed where the crack at Point B is under com-

TABLE 2—Coefficients for stress-intensity factor of almond-shaped crack.

	Tension		Bending	
	$F_A$	$F_B$	$F_A$	$F_B$
C(0)	0.284891	−0.174778	−1.27178	0.534850
C(1)	−2.29584	0.171504	−1.76705	−1.80967
C(2)	4.20991	6.18611	0.109108	0.978850
C(3)	−1.03836	−10.6026	3.21155	−1.83945
C(4)	−15.9721	−39.8776	30.0692	−1.97111
C(5)	30.4747	80.7728	74.3460	7.53119
D(0)	−0.057374	2.32806	−0.398249	−0.706977
D(1)	−12.0294	−15.9156	1.31880	6.28759
D(2)	13.4820	44.0288	−2.50969	−25.0751
D(3)	−6.70042	−36.7323	2.52467	42.7418
D(4)	4.98501	−13.9354	−1.57768	−32.1517
D(5)	−1.97201	15.4674	0.369476	7.84860
E(0)	1.08053	0.791439	−0.239241	0.740317
E(1,1)	−4.63021	−0.253200	3.07184	−0.048047
E(1,2)	2.39022	2.81767	−1.32857	1.77526
E(1,3)	0.0	0.0	0.0	0.0
E(2,1)	−3.33244	−0.420148	4.70852	−6.46038
E(2,2)	4.95148	1.25604	−13.5632	3.71890
E(2,3)	0.0	0.0	0.0	0.0
E(3,1)	15.8171	7.80674	16.5175	2.35524
E(3,2)	16.0412	−15.5394	1.36243	8.38177
E(3,3)	−12.9077	11.2836	9.22057	−12.6500

TABLE 3—Coefficients of stress-intensity factor of sickle-shaped crack.

	Tension		Bending	
	$F_A$	$F_B$	$F_A$	$F_B$
C(0)	0.196093	3.90271	1.00593	0.651468
C(1)	0.017962	-4.76498	0.139264	0.398816
C(2)	5.72210	0.271554	-6.70529	-6.76962
C(3)	-21.8804	-39.1609	9.81534	5.44538
C(4)	87.6494	173.342	-0.829499	15.0154
C(5)	-63.7666	5.64194	-1.27203	-16.9295
D(0)	0.023081	-0.0017082	1.67224	1.43102
D(1)	0.158383	-0.0356006	0.918626	-0.398409
D(2)	2.29000	2.52726	0.303356	1.41702
D(3)	1.94650	-3.93215	2.38413	-0.767647
D(4)	4.91535	4.63433	-1.32019	-0.043943
D(5)	-0.763835	0.0	0.0	0.386336
E(0)	0.959233	0.784279	0.759813	-0.245881
E(1,1)	3.03306	-5.43769	11.1843	-2.56652
E(1,2)	1.69247	8.60220	2.89672	-1.12218
E(1,3)	0.0	15.7460	-4.19099	0.0
E(2,1)	-6.03316	27.5570	-30.5130	2.04720
E(2,2)	4.96290	26.9794	-14.3987	17.8284
E(2,3)	0.0	-61.3896	56.4413	0.0
E(3,1)	-9.61249	-47.9063	19.4660	2.29894
E(3,2)	7.36898	-54.4771	39.7278	-21.1347
E(3,3)	-153.724	-104.485	-88.8442	-4.24542
N(0)	1.0	1.04043	2.51162	1.0
N(1)	0.0	0.834666	3.17928	0.0
N(2)	0.0	2.58231	0.086776	0.0
N(3)	0.0	0.812281	-1.64956	0.0

pression. For this situation, the applicability of the weight function method is doubtful. Therefore, also the results for bending loading with large crack angles, where the crack tip is under compression, may not be exact.

For components with circumferential notches, stress-intensity factors can be calculated applying Eqs 3 and 8, if the stress distribution in the uncracked component is known. As an example, results are presented for the notch geometry shown in Fig. 10. The stress distribution obtained from finite-element analysis is given in Fig. 10. With these stresses the stress-intensity factors have been calculated. The results are shown in Figs. 11–14.

### Prediction of Crack Growth Rate and Developing Crack Shape

The change of the crack geometry starting from an initial crack was calculated applying the following procedure and assumptions [23]:

- The crack front can be described as a circle.
- The material is homogeneous and isotropic.
- No effect is exerted by the stress state (plane stress/plane strain). Assumptions *b* and *c* result in a  $da/dN$ - $\Delta K$ -relation independent of the location of the crack front and the direction of crack growth.
- The crack extension is calculated for the deepest Point A and the surface Points B only. Starting from an initial crack of the size given by  $a_i$  and  $b_i$  (or  $\alpha_i$ ), the crack

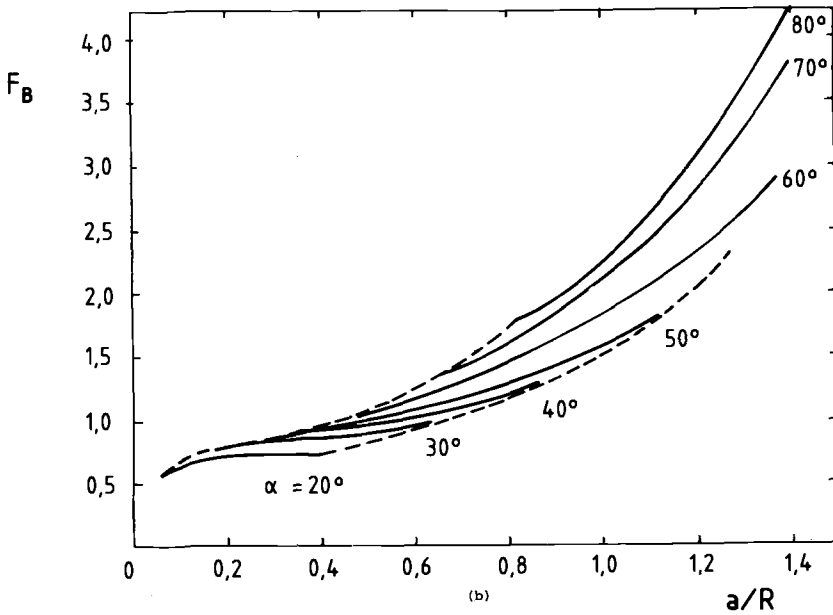
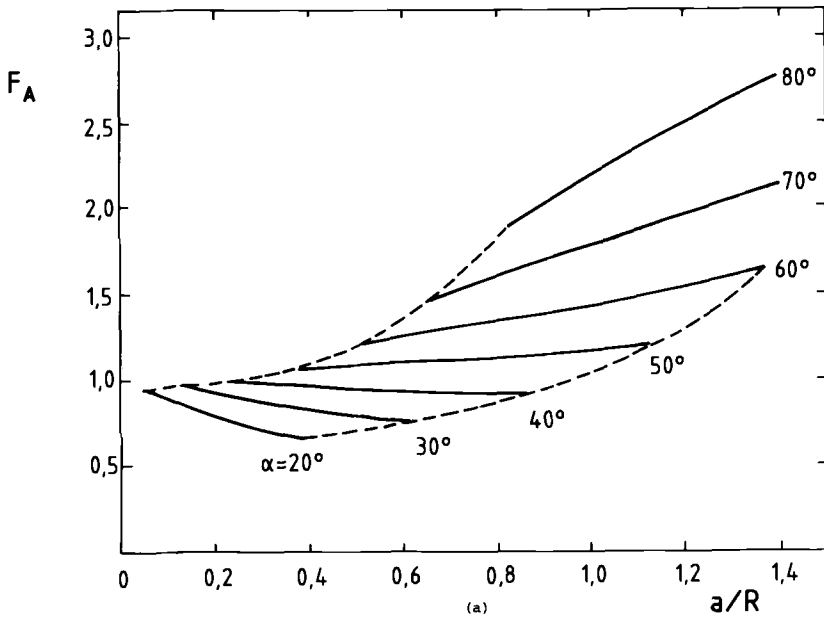


FIG. 6—Stress-intensity factor coefficient for almond-shaped cracks under tension loading.

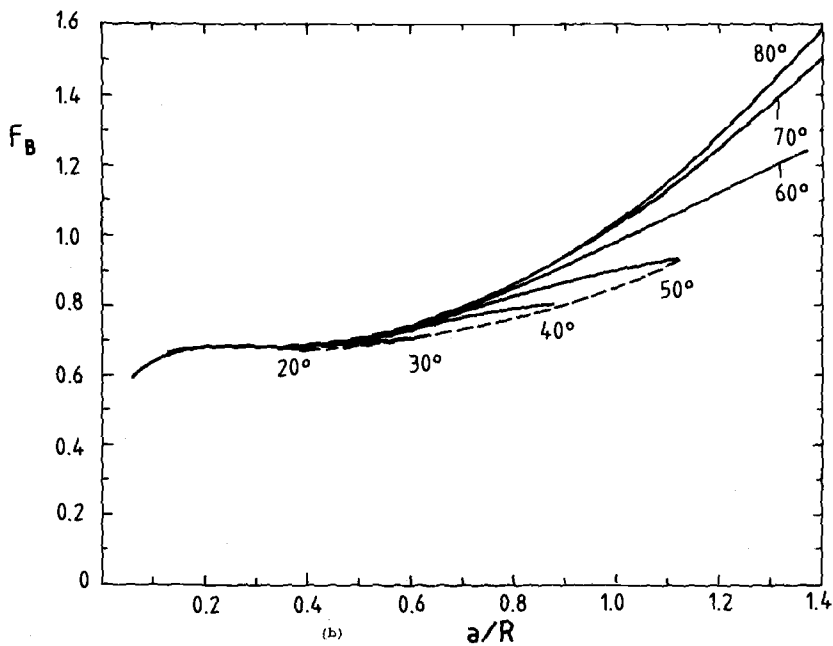
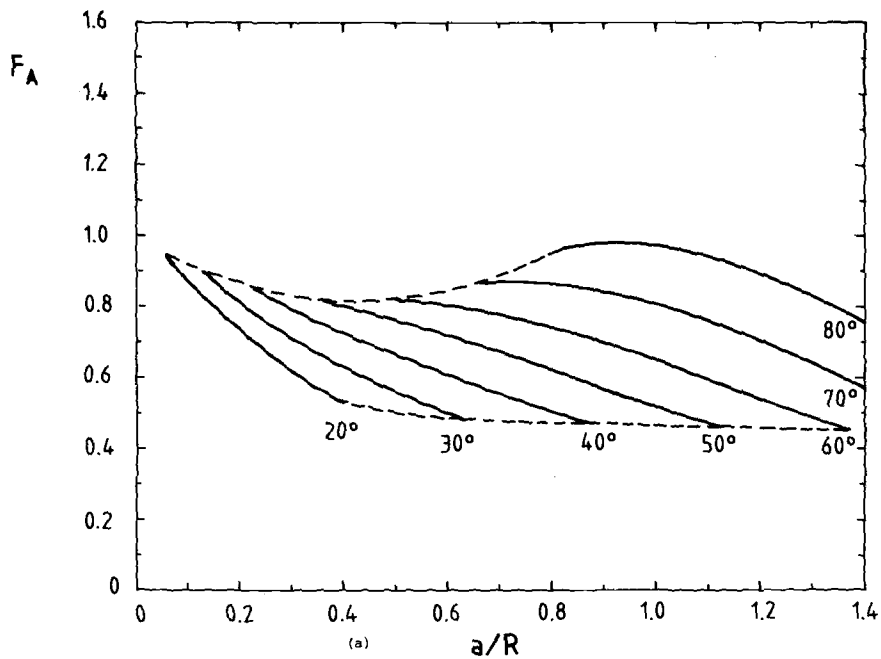


FIG. 7—Stress-intensity factor coefficient for almond-shaped cracks under bending loading.



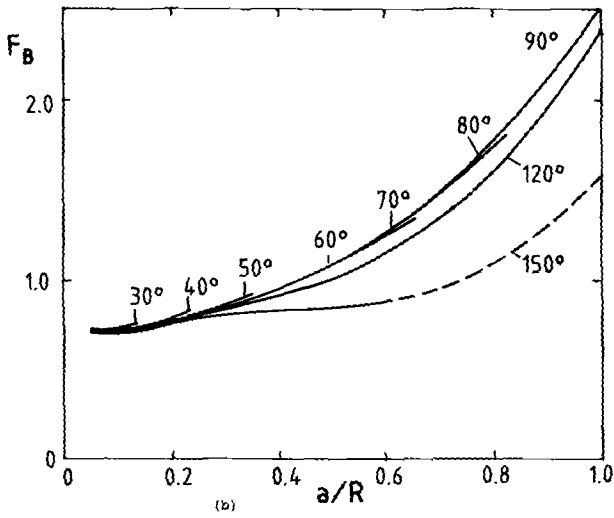
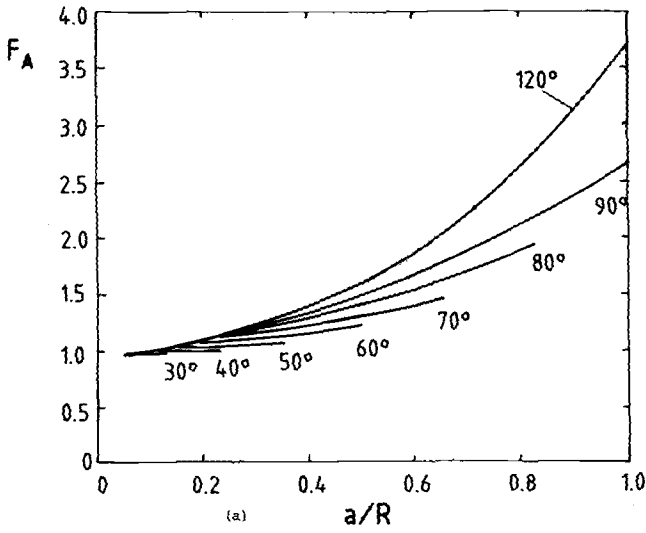


FIG. 8—Stress-intensity factor coefficient for sickle-shaped cracks under tension loading.

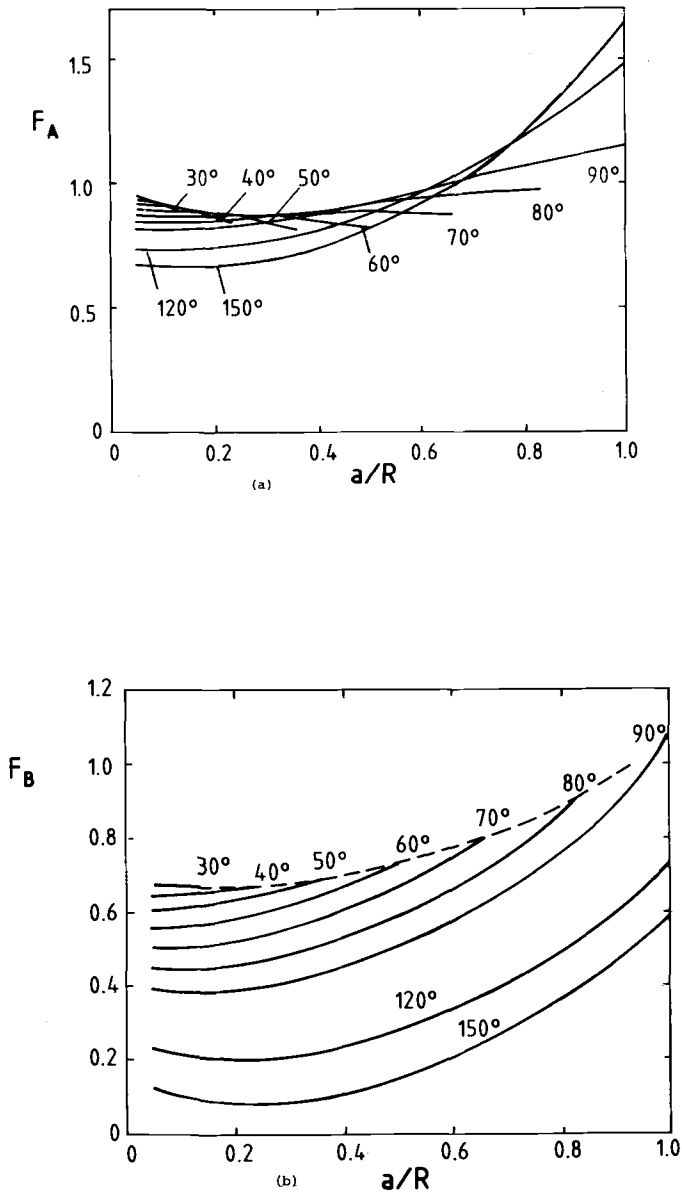


FIG. 9—Stress-intensity factor coefficients for sickle-shaped cracks under bending loading.

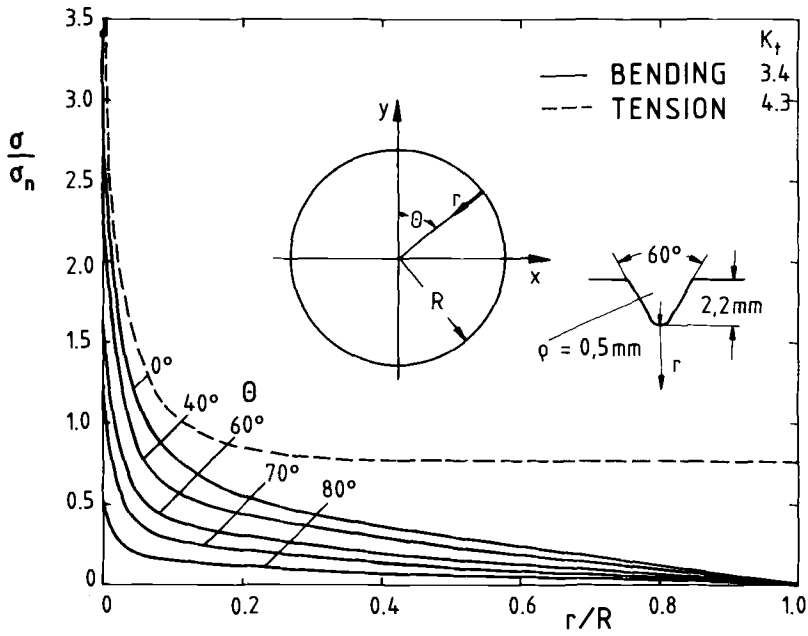


FIG. 10—Stress distribution in uncracked notched bar for tension and bending loading.

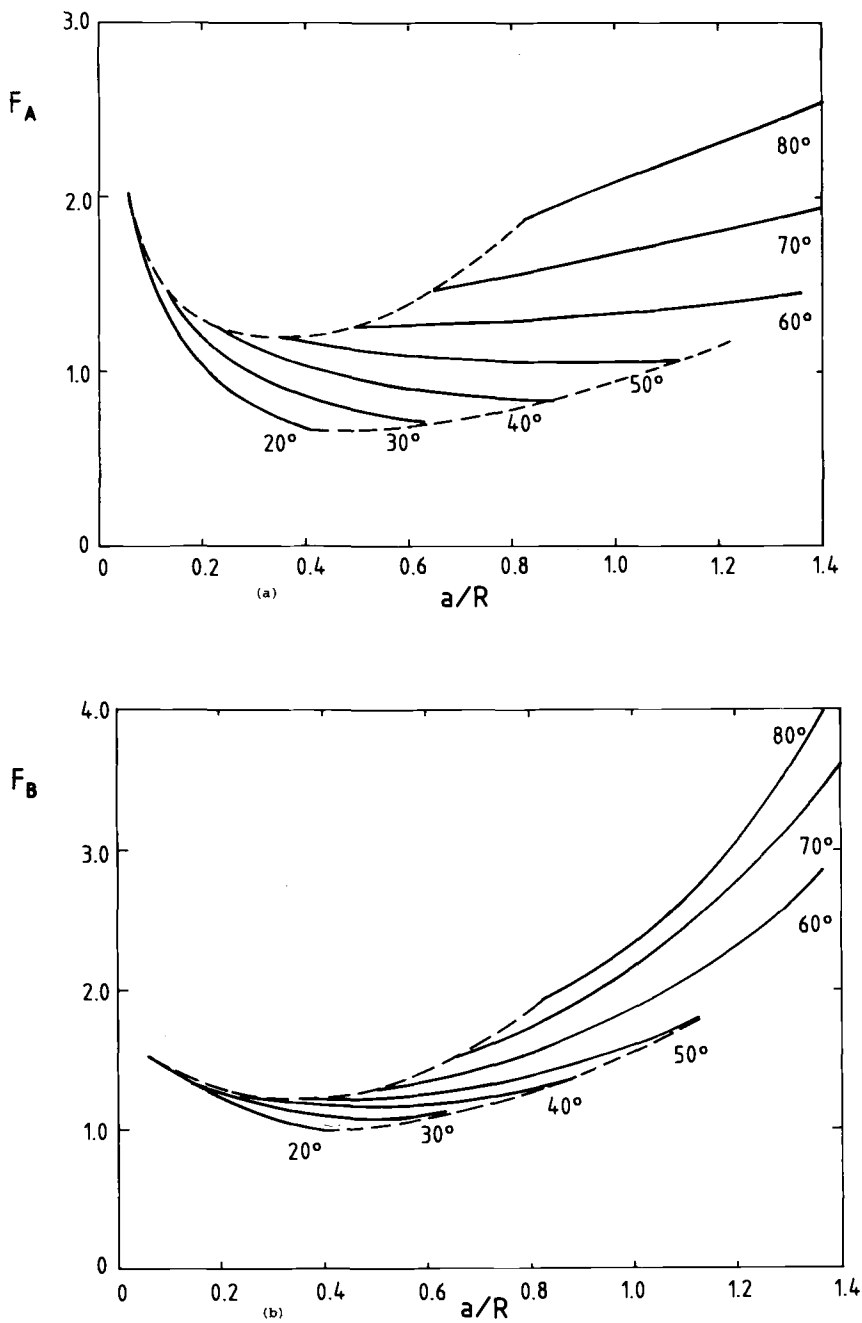


FIG. 11—Stress-intensity factor coefficient for almond-shaped cracks in notched bar under tension loading.

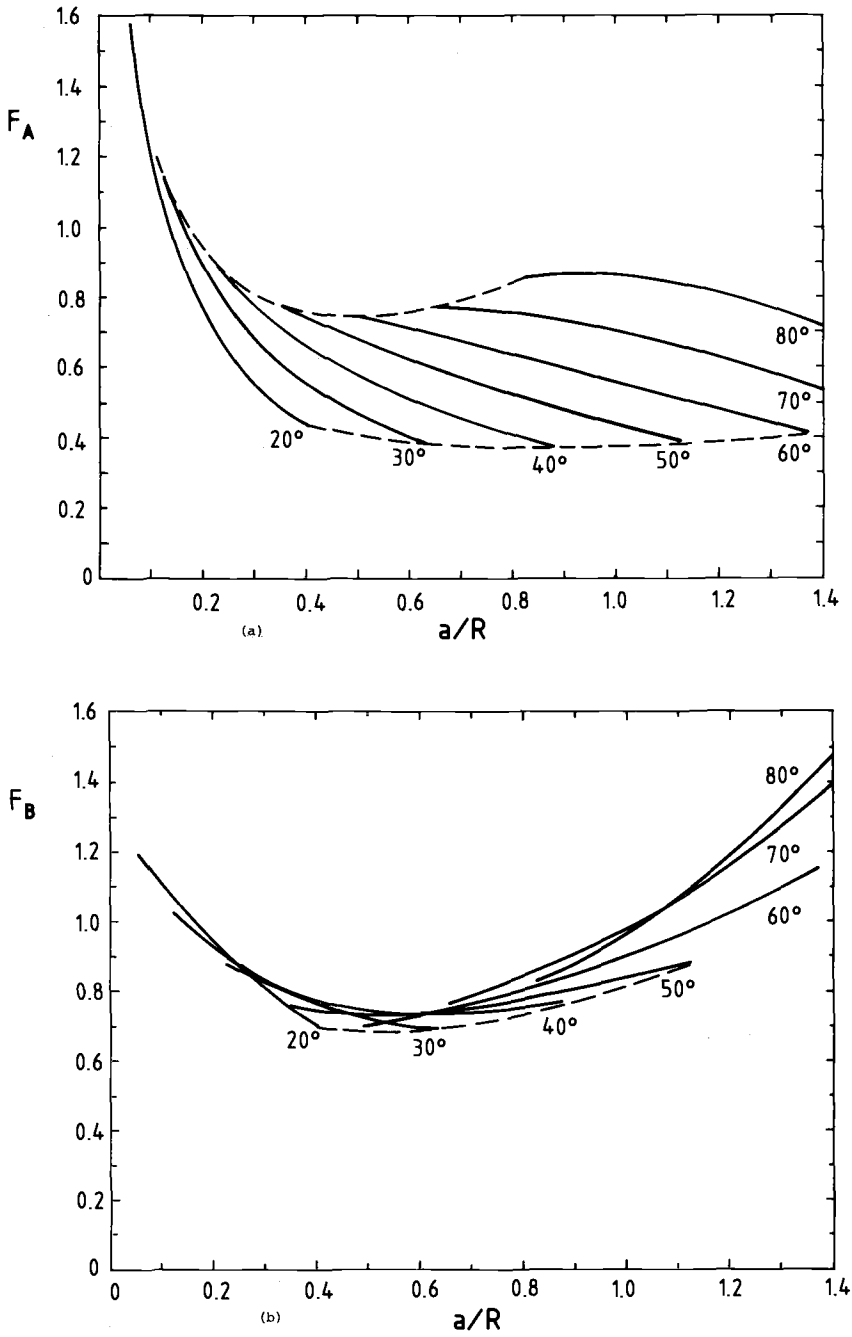


FIG. 12—Stress-intensity factor coefficient for almond-shaped cracks in notched bar under bending loading.

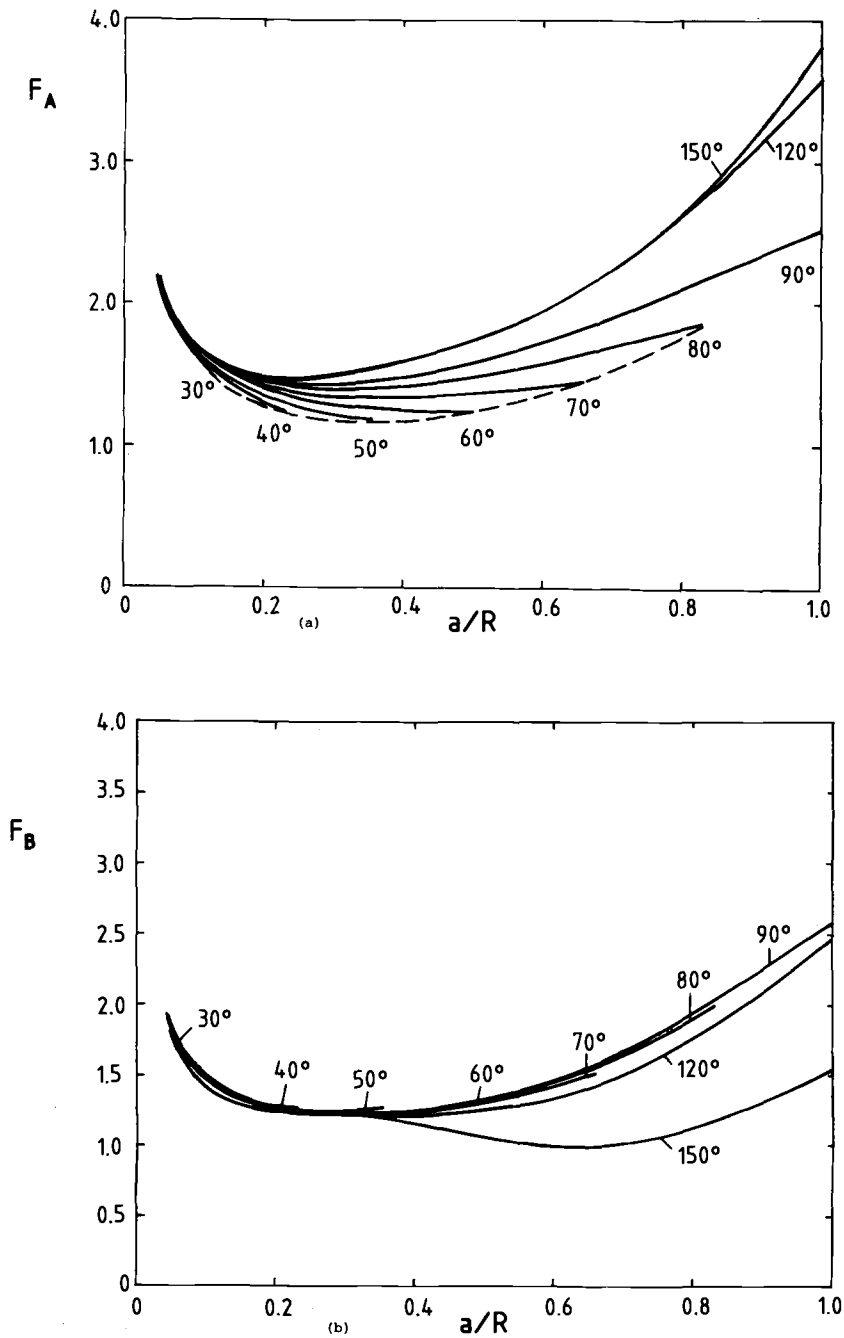


FIG. 13—Stress-intensity factor coefficient for sickle-shaped cracks in notched bar under tension loading.

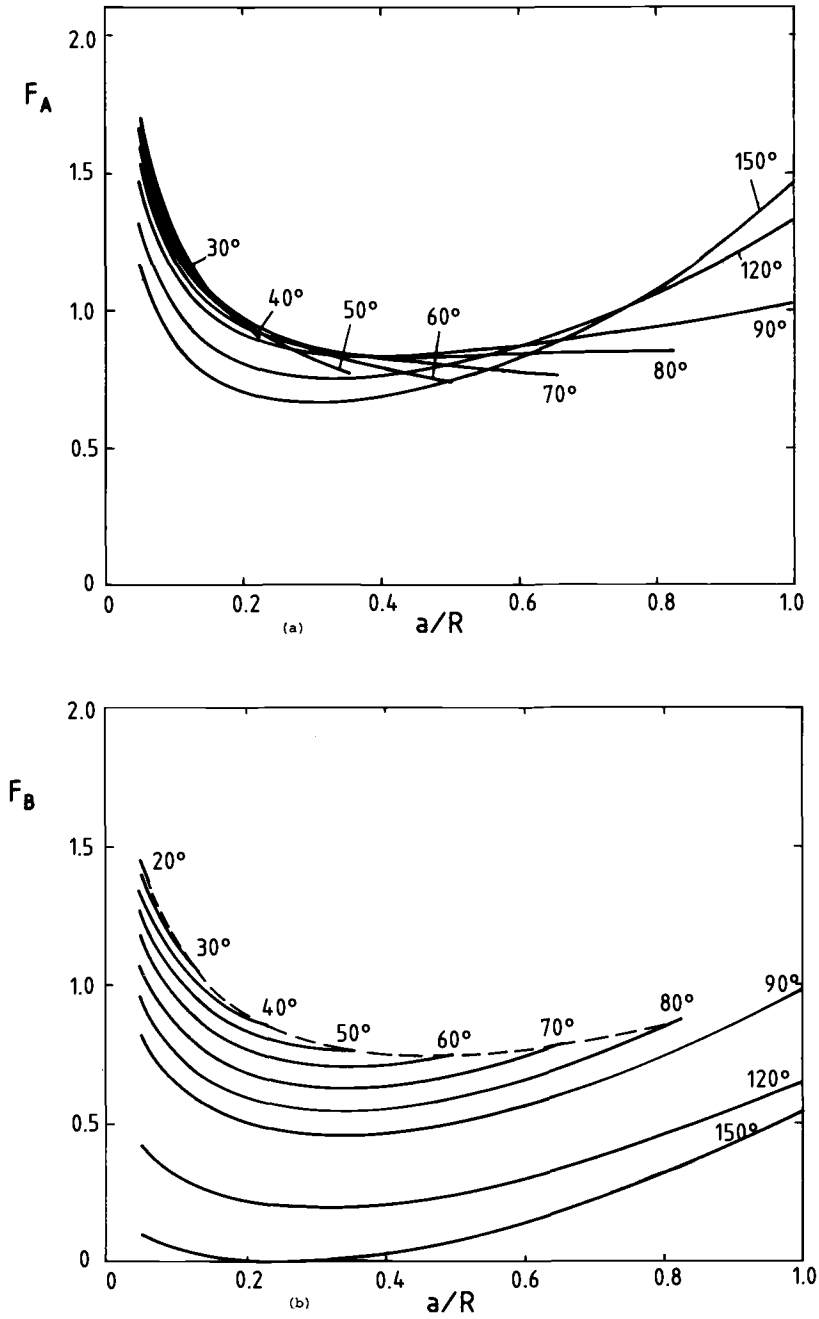


FIG. 14—Stress-intensity factor coefficient for sickle-shaped cracks in notched bar under bending loading.

extensions  $\Delta a$  and  $\Delta b$  are calculated for the first load cycle applying the  $da/dN$ - $\Delta K$  relation for the material and for  $\Delta K_A$  and  $\Delta K_B$  calculated with  $a_i$  and  $b_i$ . The new  $\Delta K_A$  and  $\Delta K_B$  are calculated with  $a = a_i + \Delta a$  and  $b = b_i + \Delta b$ , and then the crack extensions for the next cycles are obtained.

The predicted change in the shape of the crack depends on the type of loading and of the crack growth relation. If the  $da/dN$ - $\Delta K$ -relation can be described by the Paris relation

$$\frac{da}{dN} = C(\Delta K)^m$$

the crack shape is independent of the parameter  $C$  and weakly dependent on the parameter  $m$ , as can be seen from Fig. 15. In this figure, the ratio  $a/b$  is plotted versus the relative crack depth for different initial crack geometries for the unnotched rod under cyclic tensile and bending loading.

## Experimental Results

### Material, Specimens, and Testing Procedure

Specimens were machined from rods of 35 mm diameter of a chromium-molybdenum steel (German designation 42CrMo4). Metallographic examinations and hardness measurements showed that the material was very homogeneous.

To determine the  $da/dN$ - $\Delta K$ -relation for the chromium-molybdenum steel, we machined specimens with length 50 mm, height 30 mm, and thickness 30 mm. Fatigue tests were performed with  $R = 0.5$  in four-point-bending. Crack growth rates were measured applying the electrical potential method in combination with beach marks, which were obtained by periodic increase in  $R$ -ratio. In the range of  $20 \text{ MPa } \sqrt{\text{m}} < \Delta K < 80 \text{ MPa } \sqrt{\text{m}}$ , the Paris relation could be applied with  $C = 6 \cdot 10^{-11}$ ,  $m = 2.18$  (units: MN and m).

The cylindrical bars were 30 mm in diameter. The notched specimens had a notch diameter of 25.6 mm; the notch geometry is shown in Fig. 10. They were tested under cyclic tension with  $R = 0.5$  and in cyclic bending. The high  $R$ -value was chosen in order to exclude crack closure effects.

The specimens for tensile cycling had a total length of 600 mm and free length between the grips of 400 mm. The four-point bending was performed with a lower span of 350 mm and an upper span of 150 mm.

Electroerosive starter notches of different shapes were introduced. Also for these specimens the electrical potential method and beach marks were used for crack growth measurements.

### Crack Geometry and Crack Growth Rate

The developing crack geometry for the unnotched bars is shown in Fig. 16. Figure 17 shows the measured  $a/b$ -ratio plotted versus the crack depth for the unnotched specimens. A good agreement with the predicted curves of Fig. 15 can be seen. The first open symbol characterizes the erosive notch; the first filled symbol characterizes the first beach mark.

In Fig. 18, the measured crack growth rates  $da/dN$  (center of the specimen) and  $db/dN$  (surface) are plotted versus  $\Delta K$ . The diagrams also show the curve for the four-point-bend specimens with the straight crack front. Again, an excellent agreement can be found.



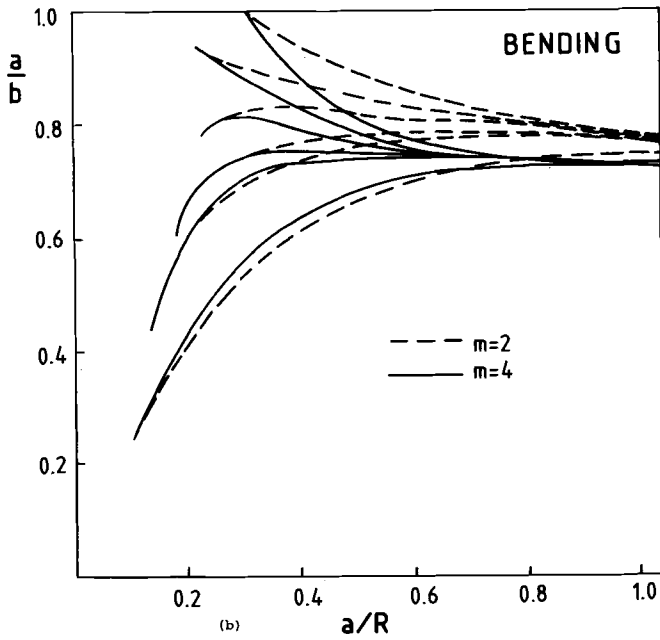
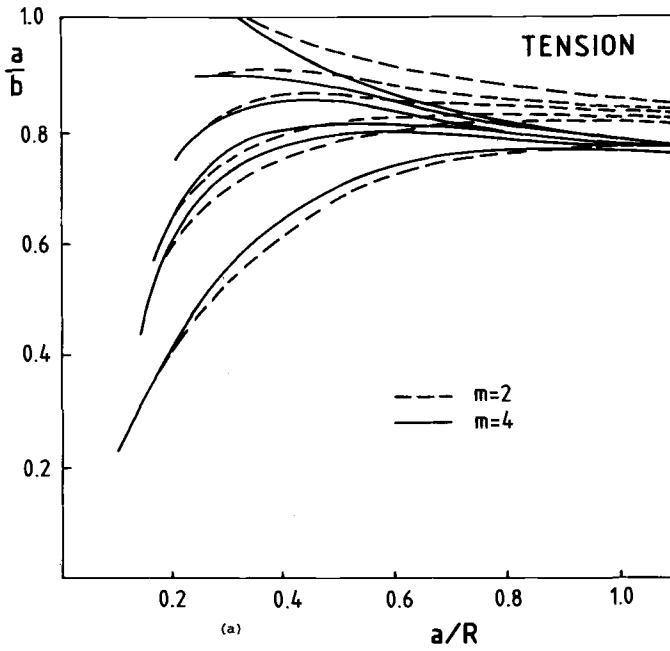


FIG. 15—Predicted change in crack geometry for unnotched rods for Paris relation.

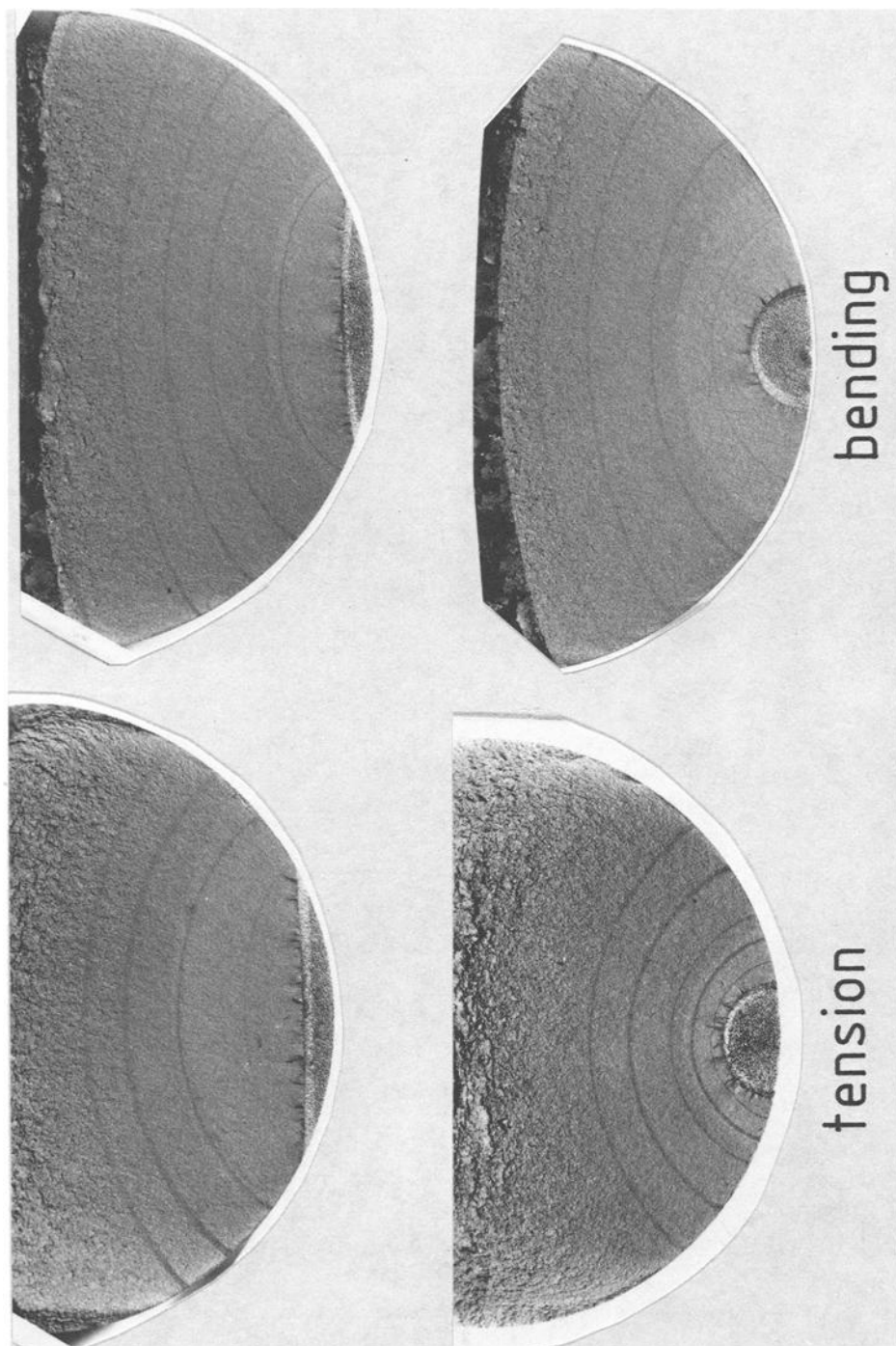


FIG. 16—Fatigue fracture areas with beach marks.

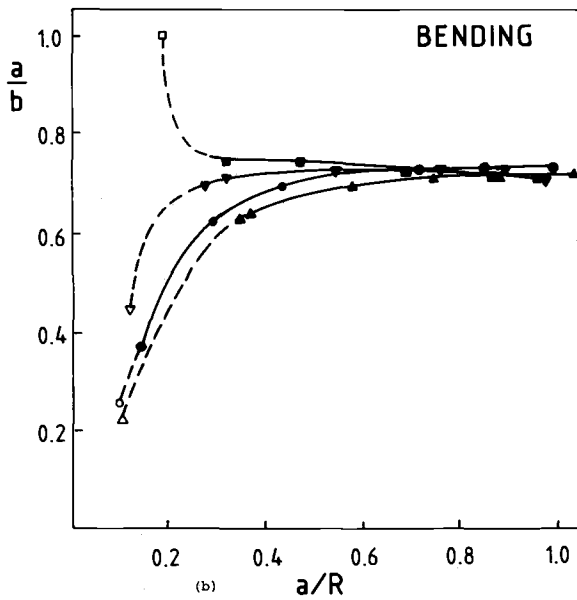
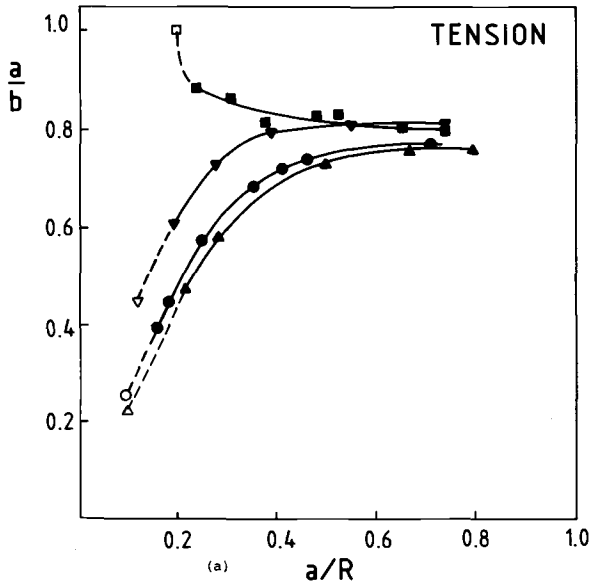


FIG. 17—Observed change of crack shape for unnotched specimens (open symbols: starting crack).

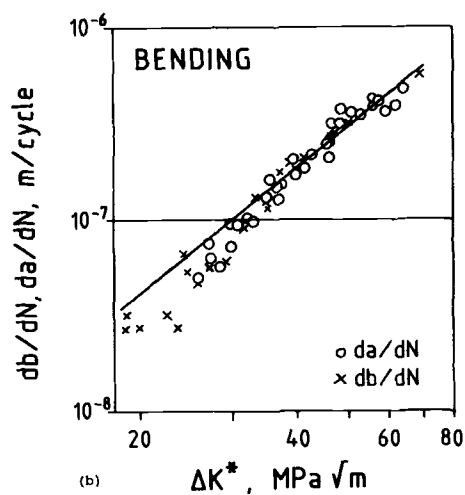
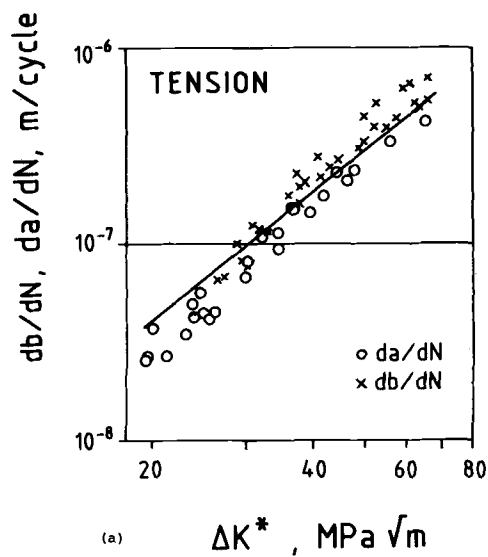


FIG. 18—Crack growth rates at surface ( $db/dN$ ) and at midpoint ( $da/dN$ ) for unnotched specimens under tension and bending loading (straight line: results from specimens with rectangular cross section and straight crack).

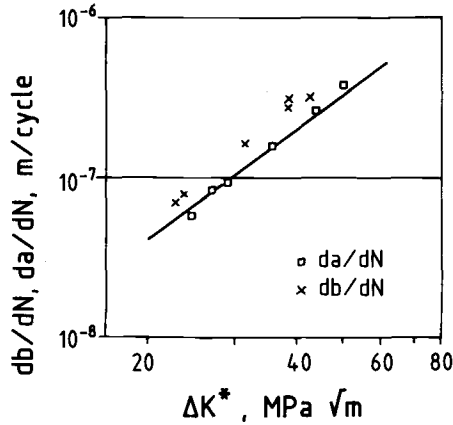


FIG. 19—Crack growth rates for notched specimens under bending loading (straight lines as in Fig. 18).

For the notched bars the measured crack growth rate for bending loading is shown in Fig. 19. Whereas for the central part of the specimen the agreement with the curve from the straight cracks is good at the surface, a faster crack growth rate is observed. This may be due to crack initiations at the root of the sharp notches.

## Conclusions

Weight functions have been calculated for two-dimensional surface cracks in cylindrical bars with circular cross sections for a great variety of crack shapes. The calculations are based on approximate crack opening displacement fields obtained by finite-element results. The method was applied for the calculation of energy release rates or stress-intensity factors at the surface and in the midsection of the crack. Predictions of the crack growth rate and the development of the shape of fatigue cracks have been compared with experimental results and found to be in good agreement.

## References

- [1] Fuchs, H. O. and Stephens, R. T., *Metal Fatigue in Engineering*, Wiley, New York, 1980.
- [2] Blackburn, W. S., *Engineering Fracture Mechanics*, Vol. 8, 1976, pp. 731-736.
- [3] Wilhem, D., Fitzgerald, J., Carter, I., and Dittmer, D., *Advances in Fracture Research*, Vol. 1, 1980, pp. 112-121.
- [4] Athanassiadis, A., Boissenot, J., Brevet, P., Francois, D., and Rahavinaivo, A., *International Journal of Fracture*, Vol. 17, 1981, pp. 553-566.
- [5] Nezu, K., Machida, S., and Nakamura, H., in *Proceedings, 25th Japan Congress on Material Research—Metallic Materials*, 1982, pp. 87-92.
- [6] Salah el din, A. S. and Lovegrave, J. M., *International Journal of Fatigue*, Vol. 3, 1981, pp. 117-123.
- [7] Bush, H., *Journal of Testing and Evaluation*, Vol. 9, 1981, pp. 216-223.
- [8] Ouchterlony, F. in *Fracture Mechanics for Ceramics, Rocks, and Concrete, ASTM STP 745*, American Society for Testing and Materials, Philadelphia, 1981, pp. 237-256.
- [9] Daoud, O. and Cartwright, D., *Engineering Fracture Mechanics*, Vol. 19, 1984, pp. 701-707.
- [10] Mackay, T. and Alperin, B., *Engineering Fracture Mechanics*, Vol. 21, 1985, pp. 391-397.
- [11] Mattheck, C., Morawietz, P., and Munz, D., *International Journal of Fatigue*, Vol. 7, 1985, pp. 45-47.

- [12] Forman, R. and Shivakumar, K. in *Fracture Mechanics: Seventeenth Volume, ASTM STP 905*, American Society for Testing and Materials, Philadelphia, 1986, pp. 59-74.
- [13] Raju, I. and Newman, J. in *Fracture Mechanics: Seventeenth Volume, ASTM STP 905*, American Society for Testing and Materials, Philadelphia, 1986, pp. 789-805.
- [14] Bueckner, H. F., *Zeitschrift für Angewandte Mathematik und Mechanik*, Vol. 50, 1970, pp. 529-546.
- [15] Rice, J. R., *International Journal of Solids and Structures*, Vol. 8, 1972, pp. 751-758.
- [16] Cruse, T. and Besuner, P., *Journal of Aircraft*, Vol. 12, 1975, pp. 369-375.
- [17] Besuner, P. M. in *Mechanics of Crack Growth, ASTM STP 590*, American Society for Testing and Materials, Philadelphia, 1976, pp. 403-419.
- [18] Rice, J. R., *Transactions, American Society for Mechanical Engineers, Journal of Applied Mechanics*, Vol. 52, 1985, pp. 571-579.
- [19] Sham, T. L., *International Journal of Solids and Structures*, Vol. 23, 1987, pp. 1257-1372.
- [20] Vainshtok, V. A. and Varfolomeyev, I. V., *International Journal of Fracture*, Vol. 35, 1987, pp. 175-186.
- [21] Fett, T., Mattheck, C., and Munz, D., *International Journal of Fracture*, Vol. 40, 1989, pp. 307-313.
- [22] Caspers, M., *Fortschritt Berichte VDI*, Series 18, No. 44, VDI-Verlag, 1987.
- [23] Görner, F., Mattheck, C., and Munz, D., *Zeitschrift für Werkstofftechnik*, Vol. 14, 1983, pp. 11-18.

# Theoretical and Experimental Analyses of Surface Fatigue Cracks in Weldments

---

**REFERENCE:** Niu, X. and Glinka, G., "Theoretical and Experimental Analyses of Surface Fatigue Cracks in Weldments," *Surface-Crack Growth: Models, Experiments, and Structures, ASTM STP 1060*, W. G. Reuter, J. H. Underwood, and J. C. Newman, Jr., Eds., American Society for Testing and Materials, Philadelphia, 1990, pp. 390–413.

**ABSTRACT:** The stress-intensity factor for a semi-elliptical surface crack in T-butt welded joints has been studied by using the weight function approach. The weight functions for cracks in welded joints have been derived by employing the method proposed by Petroski-Achenbach. The calculated stress-intensity factors were compared with those obtained from the variable-amplitude fatigue tests conducted on a series of T-butt welded joints. It has been shown that the weight functions provided sufficiently accurate solutions, in terms of the agreement between the calculated and measured stress-intensity factors and fatigue crack propagation lives. The method proved to be useful in studying weld plate thickness and weld geometry effects on fatigue crack growth in welded joints.

**KEY WORDS:** fatigue, welded joints, crack growth, semi-elliptical surface cracks, weight function, stress-intensity factor, variable loading history

## Nomenclature

- $a$  Crack depth for a semi-elliptical surface crack
- $a_0$  Initial crack depth
- $da/dN$  Crack growth rate
- $C$  Paris equation parameter
- $c$  Half crack length of a semi-elliptical surface crack
- $E$  Modulus of elasticity
- $E_n$  Euler number
- $F_s^\alpha$  Geometric stress-intensity correction factor for a crack emanating from an angular corner  $\alpha$  in a semifinite plate with a step
- $F_s^{90}$  Geometric stress-intensity correction factor for a crack emanating from right-angle corner in a semifinite plate with a step ( $\alpha = 90^\circ$ )
- $h$  Weld leg length
- $h_k$  Stress-intensity factor due to stress rise  $h_k$
- $h_s$  Individual rise in stress history or stress cycle
- $H$  Generalized modulus of elasticity:
  - $H = E$ —for plane strain
  - $H = E/(1 - \nu^2)$ —for plane strain

<sup>1</sup> Research assistant, Department of Mechanical Engineering, University College London, Torrington Place, London WC1E 7JE, U.K.

<sup>2</sup> Associate professor, Department of Mechanical Engineering, University of Waterloo, Waterloo, Ontario, Canada N2L 3G1.

$K_h$	Stress-intensity factor due to nominal average stress $S_h$
$\Delta K_h$	Range of stress-intensity factor due to nominal average stress range $\Delta S_h$
$\Delta K_{cal}$	Stress-intensity factor range calculated using the weight function $m_s^w$
$\Delta K_{exp}$	Experimental stress-intensity factor range obtained from fatigue crack growth data
$K_e^p$	Stress-intensity factor for an edge crack in a long strip
$K_e^w$	Stress-intensity factor for an edge crack emanating from weld toe
$K_{new}$	Stress-intensity factor corresponding to local stress system $\sigma_{new}(x)$
$K_r$	Reference stress-intensity factor corresponding to local reference stress $\sigma_r(x)$
$K_s^p$	Stress-intensity factor for a semi-elliptical surface crack in a finite-thickness plate
$K_s^w$	Stress-intensity factor for a semi-elliptical surface crack emanating from weld toe
$m(x,a)$	Weight function
$m_e^w(x,a,\alpha)$	Weight function for an edge crack emanating from an angular corner $\alpha$ in a long strip with a step
$m_e^p(x,a)$	Weight function for an edge crack in a long strip
$m_s^w(x,a,\alpha)$	Weight function for a semi-elliptical surface crack emanating from an angular corner $\alpha$ in a long strip with a step and finite thickness $t$
$m_s^p(x,a)$	Weight function for a semi-elliptical surface crack in a finite-thickness plate
$N$	Number of load cycles
$N_0$	Number of reference load cycles
$n$	Paris's equation exponent
$R = S_{min}/S_{max}$	Nominal load-stress ratio
$S$	Nominal stress
$S_h$	Nominal weighted average stress
$\Delta S_h$	Nominal weighted stress range
$\Delta S_{rms}$	Root mean square stress value of stress ranges
$S_{max}$	Maximum peak stress in the stress history
$t$	Joint thickness
$u_r(x,a)$	Crack-opening displacement function corresponding to reference stress-intensity factor $K_r$
$Y$	Geometric stress-intensity correction factor
$\alpha$	Weld angle or angular corner angle
$\phi = \pi^2/4$	Value of elliptical integral of second and for a circular crack
$\nu$	Poisson's coefficient
$\rho$	Weld toe radius
$\sigma_{new}(x)$	New distribution of stresses normal to prospective crack plane and corresponding to stress-intensity factor $K_{new}$
$\sigma_0$	Characteristic stress or nominal stress at weld toe

It has been recognized that a large proportion of the total fatigue life of a welded structure is usually spent on propagation of a crack [1,2] initiated at the weld toe. Therefore the prediction of fatigue life of a welded joint has to be based on accurate analysis of fatigue crack growth in the highly stressed region near the weld. Fracture-mechanics models are often used for such analyses, which require calculations of stress-intensity factors for relevant crack-load configurations. Such calculations are difficult due to the fact that three-



dimensional stress analysis has to be employed since semi-elliptical surface cracks are very often encountered in engineering practice.

It is known that the stress-intensity factor for a crack in a welded joint depends on the global geometry of the joint, the weld profile, and the type of loading. Therefore, calculation of stress-intensity factors even for one type of weldment such as the T-butt welded joint requires detailed analysis of several parameters, including plate thickness, weld thickness, weld angle, weld toe radius, and loading system. In addition, it is often necessary to include residual stresses into the analysis for they may significantly influence both the fatigue crack growth rate [3] and the critical crack size [4]. For these reasons it is necessary to derive appropriate formulae which enable the stress-intensity factors to be calculated for a variety of loading systems and geometric parameters. Derivation of such formulae can be approached by using the weight function method [5,6].

The weight functions for cracks in welded joints have been derived by the authors and are discussed in the paper. The weight functions were used for calculating stress-intensity factors necessary for fracture mechanics modeling of fatigue crack growth behavior.

The theoretical crack growth analysis was carried out by numerical integration of Eq 1 proposed by Paris [7]

$$\frac{da}{dN} = C(\Delta K)^m \quad (1)$$

The experimental investigation of "surface crack growth" required complex crack measurement techniques to be employed because the crack shape evolution had to be monitored with sufficient accuracy. Because the crack front was not visible to optical devices, some alternative nondestructive methods had to be employed. In the investigation under discussion, the Alternating Current Potential Drop (ACPD) method [8,9] was used taking advantage of the "skin effect." This method made it possible to monitor crack initiation and crack shape evolution due to cyclic loading and subsequently to validate the theoretical results.

### Calculation of Stress-Intensity Factors for Semi-Elliptical Surface Cracks in T-Butt Welded Joints

The T-butt welded joint is one of configurations very often used in welded structures and therefore it can be applied for modeling of a variety of welded joints encountered in practice. It is known that fatigue cracks usually initiate at the weld toe (Fig. 1) and propagate through the thickness under the dominant effect of the Mode I stress system.

Although a number of stress-intensity factor handbooks have been published, appropriate formulae are still not available for many welded configurations. For this reason it was necessary to derive formulae which enabled the stress-intensity factor to be calculated for a variety of loading and geometric parameters. This was achieved by first deriving appropriate weight functions [5,6] defined in a general form

$$m(x,a) = \frac{H}{K_r} \frac{\partial u_r(x,a)}{\partial a} \quad (2)$$

In order for the weight function 2 to be derived, a reference stress-intensity factor  $K_r$  for a given geometry under simple stress system  $S$  needs to be known (Fig. 2) together with

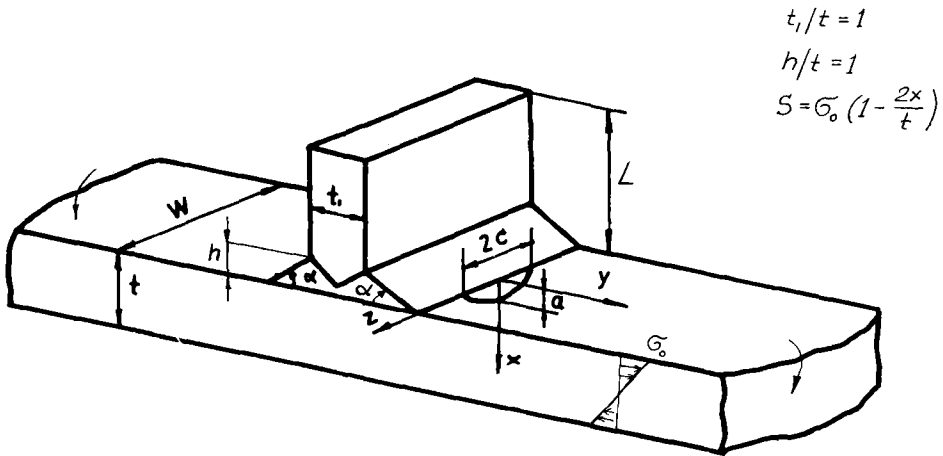


FIG. 1—Geometry of a T-butt welded with a surface semi-elliptical crack.

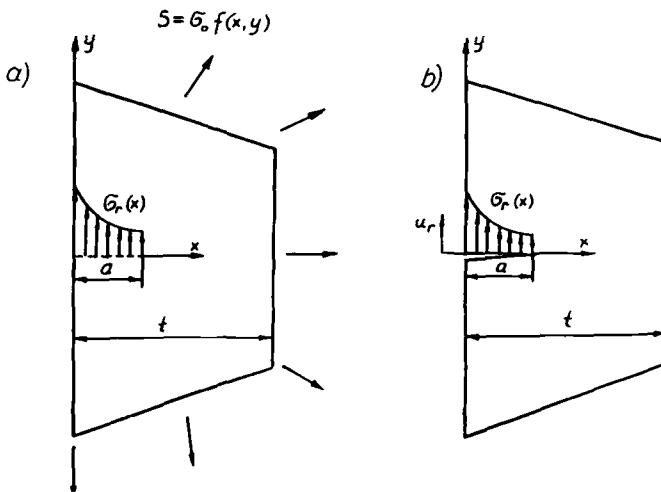


FIG. 2—Stress system  $S$ ,  $\sigma_r(x)$  and displacement  $u_r$  necessary for the derivation of the weight function  $m(x,a)$ ; (a) reference stress  $\sigma_r$  in the uncracked body; (b) notation and quantities necessary for calculating the stress-intensity factor.

the corresponding crack-opening displacement field  $u_r(x,a)$ . Even though the stress-intensity factors are known for many crack geometries and load cases, the displacements are only available for a very few special cases. Therefore, the method developed by Petroski and Achenbach [10] was used to calculate the crack opening displacement from the known reference stress-intensity factor  $K_r$ . The stress-intensity factor for a given stress field  $\sigma_{\text{new}}(x)$  could then be calculated from Eq 3

$$K_{\text{new}} = \int \sigma_{\text{new}}(x) m(x,a) dx \quad (3)$$

*Stress-Intensity Factors for Edge Cracks Emanating from the Weld Toe in a T-Butt Joint*

It was shown [11,12] that the Petroski-Achenbach method can be successfully applied to a variety of problems despite its limitations discussed in Refs 12 and 13. Therefore this method was employed [14] for derivation of the weight function for an edge crack in a T-butt welded joints as shown in Fig. 3. The final version of the derived weight function was given in the form (4).

*The weight function for an edge crack emanating from an angular corner in a finite thickness plate*

$$m_e^w(x, a, \alpha) = \frac{F_s^\alpha}{F_s^{90}} M(x, \alpha, 90) \quad (4)$$

where

$$M(x, \alpha, 90) = \frac{2}{\sqrt{2\pi(a-x)}} \left[ 1 + M_{e1}^w \left( \frac{a-x}{a} \right) + M_{e2}^w \left( \frac{a-x}{a} \right)^2 \right] \quad (5)$$

$$M_{e1}^w = 0.6643 - 12.7438 \left( \frac{a}{t} \right)^{1.5} + 397.8081 \left( \frac{a}{t} \right)^{3.0} - 3285.1810 \left( \frac{a}{t} \right)^{4.5} \\ + 14\,162.5870 \left( \frac{a}{t} \right)^{6.0} - 30\,127.1580 \left( \frac{a}{t} \right)^{7.5} + 25\,119.5351 \left( \frac{a}{t} \right)^{9.0}$$

$$M_{e2}^w = 0.1117 + 3.8570 \left( \frac{a}{t} \right)^{1.5} - 47.1626 \left( \frac{a}{t} \right)^{3.0} + 285.4393 \left( \frac{a}{t} \right)^{4.5} \\ - 646.6118 \left( \frac{a}{t} \right)^{6.0} + 934.4538 \left( \frac{a}{t} \right)^{7.5} - 596.8319 \left( \frac{a}{t} \right)^{9.0}$$

$$\frac{F_s^\alpha}{F_s^{90}} = 1 + \left( \frac{6\alpha}{\pi} - 2 \right) \left[ 1 - f \left( \frac{a}{h} \right) \right] \quad (6)$$

$$f \left( \frac{a}{h} \right) = 1.0355 - 3.3324 \left( \frac{a}{h} \right)^{0.5} + 21.5999 \left( \frac{a}{h} \right)^{1.0} - 58.8513 \left( \frac{a}{h} \right)^{1.5} \\ + 81.6246 \left( \frac{a}{h} \right)^{2.0} - 56.9396 \left( \frac{a}{h} \right)^{2.5} + 15.8784 \left( \frac{a}{h} \right)^{3.0}$$

Since the stress-intensity factor can be written in the form

$$K = \sigma_0 \sqrt{\pi a Y} \quad (7)$$

it is sufficient to present only the geometric factor  $Y$ .

The stress-intensity factors for edge cracks in T-butt weldments calculated by using the weight function (4) were validated [14] against known finite-element data. It was also demonstrated [14] that the weight function (4) can be used for estimation of the weld angle  $\alpha$  and the weld toe radius  $\rho$  effects on stress-intensity factors. Examples of such effects are shown in Figs. 4 and 5.



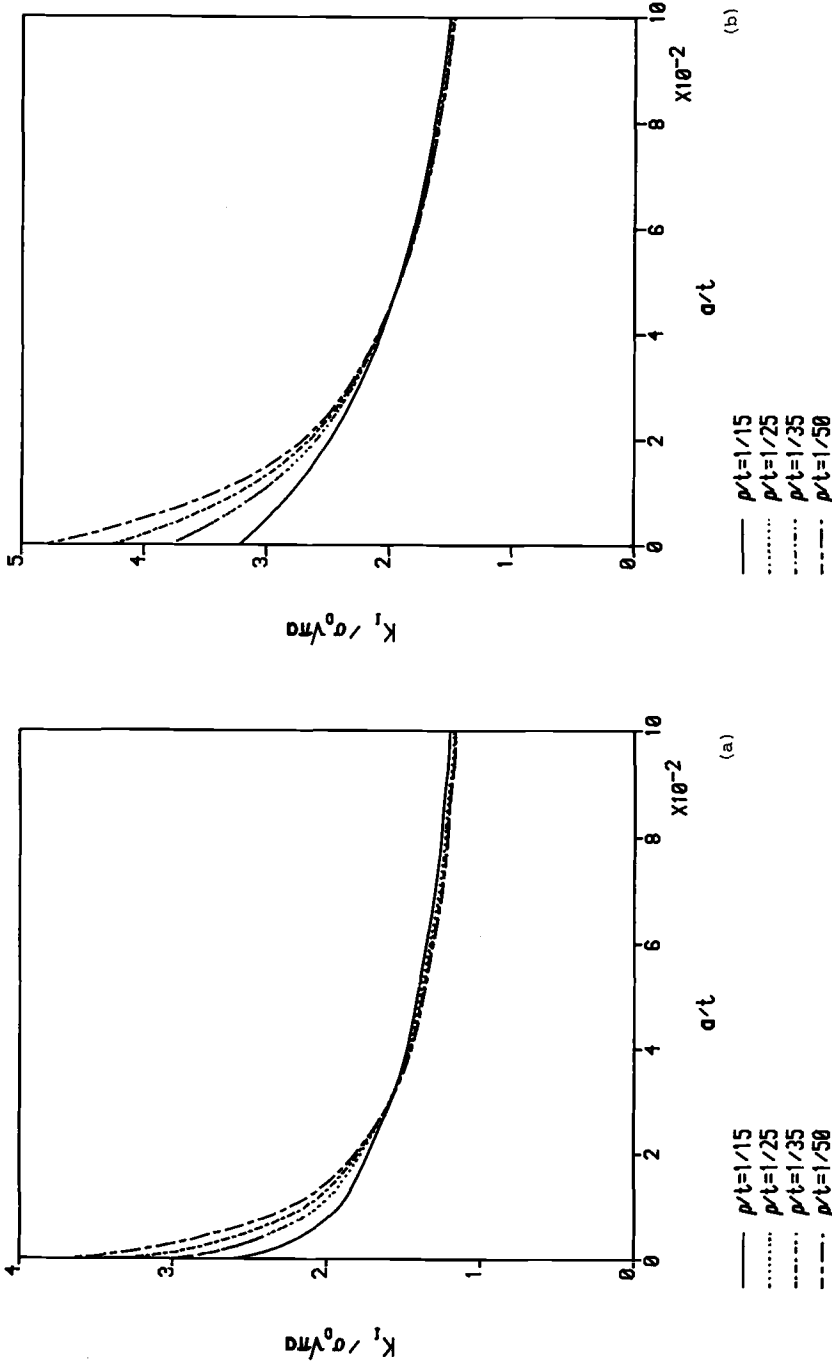


FIG. 4—Effect of the weld toe radius  $p$  on the stress-intensity factor for an edge crack in a T-butt joint under bending load: (a) for  $\alpha = 30$  deg, (b) for  $\alpha = 60$  deg.

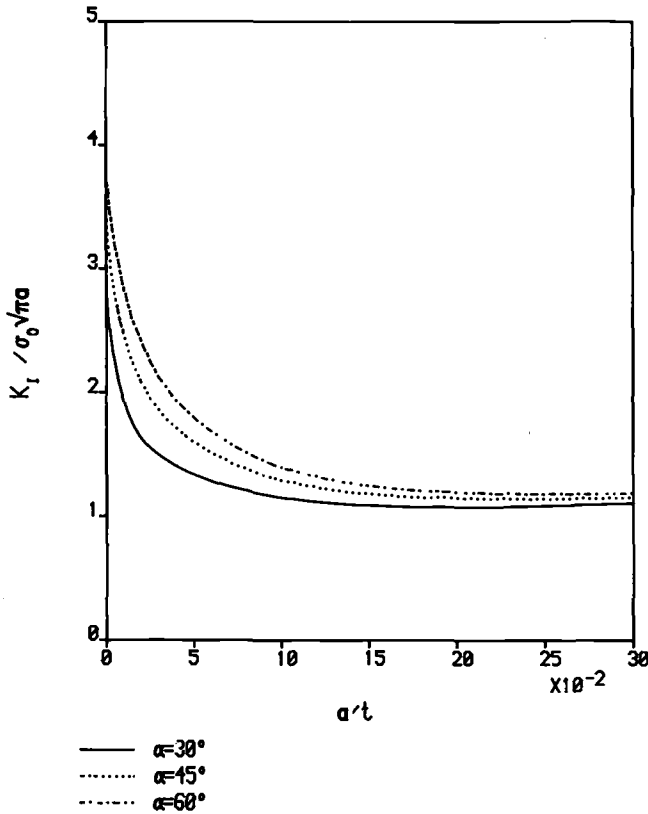


FIG. 5—Effect of the weld toe angle  $\alpha$  on the stress-intensity factor for an edge crack in a T-butt joint under bending load; for  $\rho/t = 1/25$ .

Consequently, the calculation of the stress intensity factor  $K_s^w$  requires three weight functions to be known, that is,  $m_e^w$ ,  $m_e^p$ , and  $m_s^p$ . Whereas the weight function  $m_s^w$  for a semi-elliptical crack in a T-butt joint is not needed. The weight function  $m_e^w$  for an edge crack in a T-butt joint is given by relation 4. The weight function  $m_e^p$  for an edge crack in a plate has been derived earlier by Bueckner [17].

*The weight function for an edge crack in a finite-thickness plate*

$$m_e^p(x, a) = \frac{2}{\sqrt{2\pi(a-x)}} \left[ 1 + M_{e1}^p \left( \frac{a-x}{a} \right) + M_{e2}^p \left( \frac{a-x}{a} \right)^2 \right] \quad (10)$$

where

$$M_{e1}^p = 0.6147 + 17.1844 \left( \frac{a}{t} \right)^2 + 8.7822 \left( \frac{a}{t} \right)^6$$

$$M_{e2}^p = 0.2502 + 3.2899 \left( \frac{a}{t} \right)^2 + 70.0444 \left( \frac{a}{t} \right)^6$$

The method of deriving the weight function  $m_s^p(x, a)$  for a surface crack in a flat plate has been described in Ref 15. The closed form expression for this weight function is given as follows:

*The weight function for a semi-elliptical surface crack in a finite thickness plate*

$$m_s^p(x, a) = \frac{1}{\sqrt{2\pi(a-x)}} \left[ 1 + M_{s1}^p \left( \frac{a-x}{a} \right) + M_{s2}^p \left( \frac{a-x}{a} \right)^2 \right] \quad (11)$$

where

$$M_{s1}^p = A + 3B - 4,$$

$$M_{s2}^p = 5 \left[ \frac{\sqrt{2}\pi}{4} F \left( \frac{a}{t} \right) - \frac{A-1}{3} - B \right],$$

$$A = 0.5 \left( \frac{\pi c}{W} \right) \sqrt{\frac{a}{t}} \operatorname{tg} \left( \frac{\pi c}{W} \sqrt{\frac{a}{t}} \right) + 4 \frac{d_2 \left( \frac{a}{t} \right)^2 + 2d_3 \left( \frac{a}{t} \right)^4}{d_1 + d_2 \left( \frac{a}{t} \right)^2 + d_3 \left( \frac{a}{t} \right)^4},$$

$$B = \frac{5\sqrt{2}\pi}{8QF \left( \frac{a}{t} \right)} \sum_{n=0}^{10} \sum_{m=1}^5 \frac{\left( \frac{\pi c}{W} \right)^{2n} \cdot E_{2n} (-1)^n}{(2n)!} \frac{C_m}{2m+n} \left( \frac{a}{t} \right)^{2m+n-2},$$

$$F \left( \frac{a}{t} \right) = \left[ d_1 + d_2 \left( \frac{a}{t} \right)^2 + d_3 \left( \frac{a}{t} \right)^4 \right] \sqrt{\sec \left( \frac{\pi c}{W} \sqrt{\frac{a}{t}} \right)} / \sqrt{Q},$$

$$d_1 = 1.13 - 0.09 \left( \frac{a}{c} \right); d_2 = -0.54 + \frac{0.89}{0.2 + (a/c)},$$

$$d_3 = 0.5 - \frac{1.0}{0.65 + a/c} + 14 \left( \frac{c-a}{c} \right)^{24},$$

$$Q = 1.0 + 1.464 (a/c)^{1.65}; \text{ for } a \leq c,$$

$$C_1 = d_1^2; C_2 = 2d_1 d_2; C_3 = d_2^2 + 2d_1 d_3; C_4 = 2d_2 d_3; C_5 = d_3^2, \text{ and}$$

$$E_n - \text{Euler numbers, } E_0 = 1; E_2 = -1, E_4 = 5, E_6 = -61, E_8 = 1385,$$

$$E_{10} = -50521. \dots$$

Finally, the expression for the weight function  $m_s^w(x, a, \alpha)$  has also been derived in a closed form 11a [18].

*The weight function for a semi-elliptical surface crack emanating from an angle in a finite thickness plate*

$$m_s^w(x, a, \alpha) = \frac{2}{\sqrt{2\pi(a-x)}} \left[ 1 + M_{s1}^w \left( \frac{a-x}{a} \right) + M_{s2}^w \left( \frac{a-x}{a} \right)^2 \right] \quad (11a)$$

where

$$M_{s1}^w = A_r + 3B_r - 4,$$

$$M_{s2}^w = 5 \left[ \frac{\sqrt{2}\pi}{4} F_r \left( \frac{a}{t} \right) - \frac{A_r - 1}{3} - B_r \right],$$

$$A_r = \frac{2 \cdot F_r^1 \left( \frac{a}{t} \right) \cdot \frac{a}{t}}{F_r \left( \frac{a}{t} \right)}, \text{ where } F_r^1 \left( \frac{a}{t} \right) = \frac{\rho F(a/t)}{\rho(a/t)},$$

$$B_r = \frac{5\sqrt{2}\pi \int_0^{a/t} F_r^2 \left( \frac{a}{t} \right) \cdot \left( \frac{a}{t} \right) \cdot d \left( \frac{a}{t} \right)}{8 \left( \frac{a}{t} \right)^2 \cdot F_r \left( \frac{a}{t} \right)}, \text{ and}$$

$$F_r \left( \frac{a}{t} \right) = \frac{2\sqrt{2} \frac{F_s^a}{F_s^{90}} \frac{15 + 5M_{e1}^w + 3M_{e2}^w}{15 + 5M_{e1}^p + 3M_{e2}^p} (15 + 5M_{s1}^p + 3M_{s2}^p)}{15\pi \frac{F_s^a}{F_s^{90}} \frac{15 + 5M_{e1}^w + 3M_{e2}^w}{15 + 5M_{e1}^p + 3M_{e2}^p} (15 + 5M_{s1}^p + 3M_{s2}^p)}.$$

Comparison of stress-intensity factors calculated from the weight function and finite-element data [16] showed excellent agreement (Figs. 6a and 6b).

It is also found that the weld toe angle  $\alpha$  effect on the stress intensity factor was noticeable for cracks of relative depth of  $a/t < 0.35$ . The effect was more significant for long surface cracks with low aspect ratio  $a/c = 0.2$ . The effect of the weld toe radius  $\rho$  (Figs. 7a and 7b) was similar to that of edge crack and negligible for cracks of relative depth  $a/t > 0.05$ . The effect in general was independent of the crack aspect ratio  $a/c$ .

The correction factor  $Y$  in Figs. 6a to 7b was multiplied by parameter  $\sqrt{\phi}$  in order to compare the calculated stress-intensity factors with the finite-element data by Bell [16], who normalized his results in respect to the circular "penny-shape" crack under tension.

It is very often assumed that the stress-intensity factor for a crack in a notched element such as the T-butt joint can be calculated using the flat plate weight function  $m_s^p$  and the stress distribution  $\sigma(x)$  derived from the uncracked notched body. However, one has to bear in mind that the stress-intensity factor is a quantity which is dependent on both stress and geometry. Therefore, using the weight functions derived for plates may lead to noticeable errors in spite of the fact that the notched body stress field is taken into account. The differences in stress-intensity factors calculated on the basis of weight functions  $m_s^p$  and  $m_s^w$  are shown in Fig. 8. It is apparent that application of the "flat plate weight function"  $m_s^p$  would lead, in general, to an overestimation of the stress-intensity factor for a crack in the T-butt joint.

## Experiments

### Specimens and Material

The specimens tested were T-butt welded plate joints made of British Standards Institution, Low Alloy Steels, (BS 4360: 50D, 1984.) The material properties and the standard chemical composition are given in Tables 1 and 2, respectively. The specimens were 1000 mm long and 100 mm wide, with the "T" attachment welded at the center (Fig. 1). A series



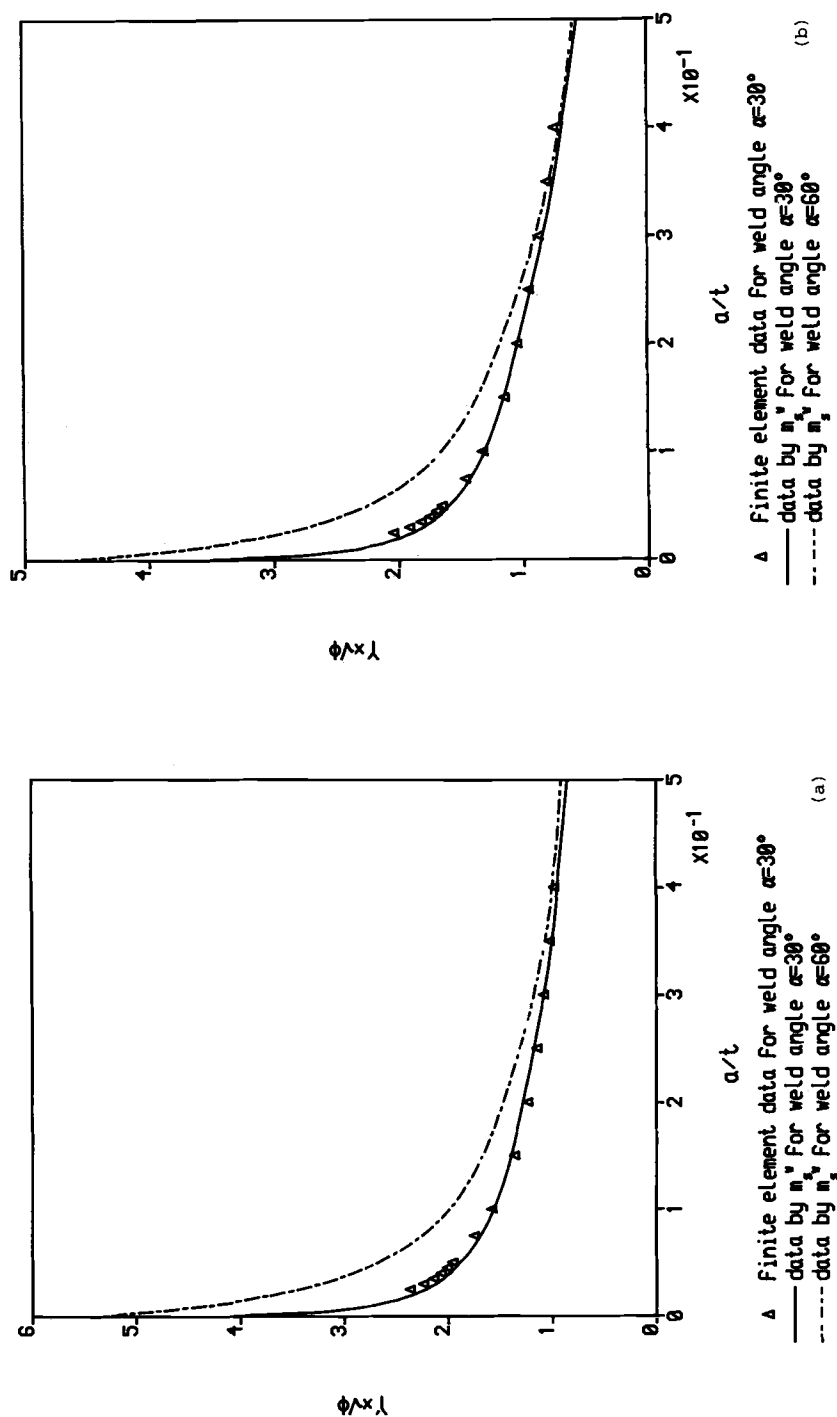


FIG. 6—Effect of the weld angle  $\alpha$  on stress-intensity factor at the deepest point of semi-elliptical crack in a T-butt welded joint under bending loading: (a) for  $a/c = 0.25$  and  $\rho/t = 1/25$ ; (b) for  $a/c = 0.5$  and  $\rho/t = 1/25$ .

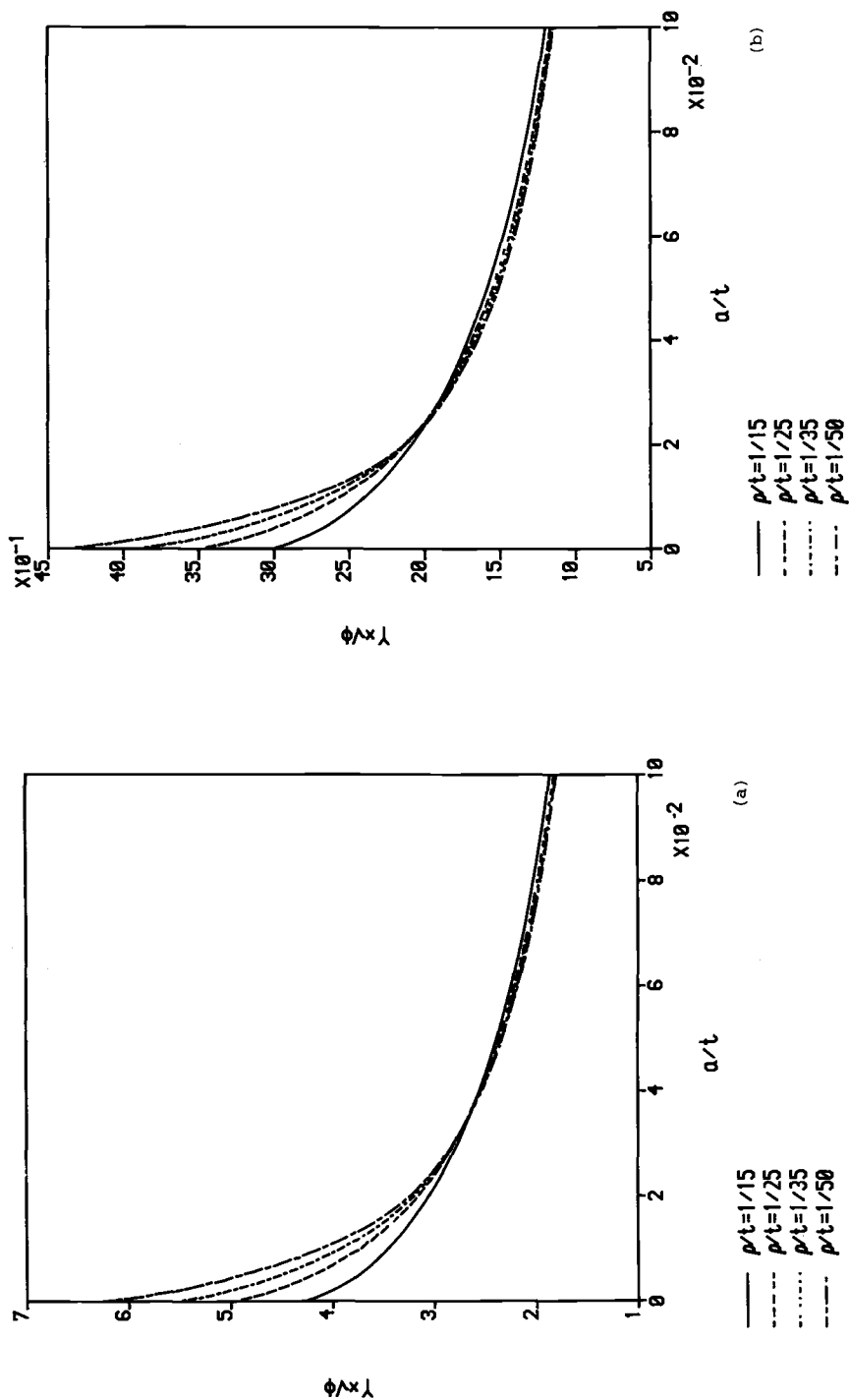


FIG. 7—Effect of the weld toe radius  $\rho$  on stress-intensity factor at the deepest point of semi-elliptical crack in a T-butt joint under bending load; (a) for  $\alpha = 45$  deg and  $a/c = 0.25$ ; (b) for  $\alpha = 45$  deg and  $a/c = 0.8$ .

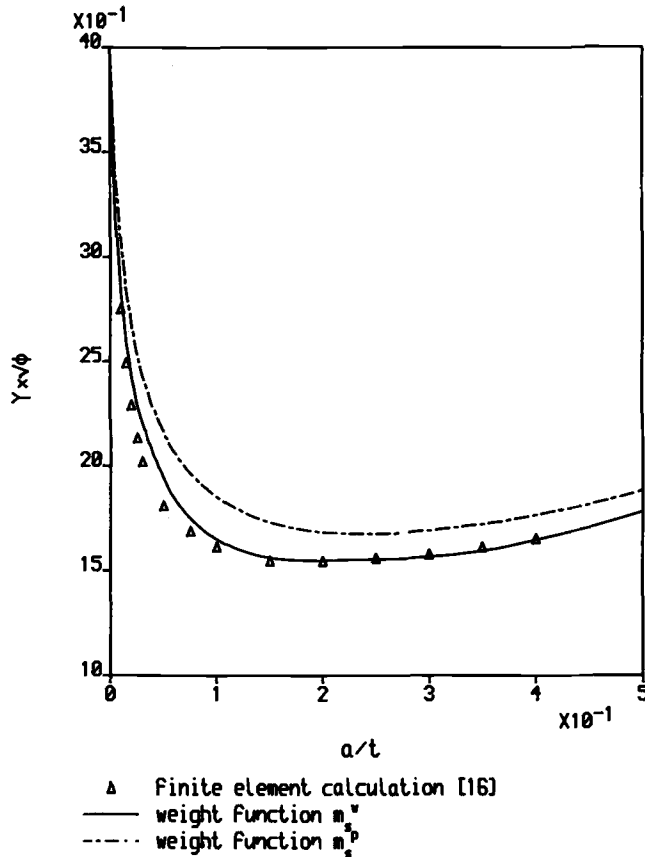


FIG. 8—Effect of the weight function type on the calculated stress-intensity factor at the deepest point of semi-elliptical crack in a T-butt joint under tension load, in relation to the finite-element data [16]; for  $\alpha = 45$  deg,  $c/a = 0.33$ ,  $\rho/t = 1/25$ .

of specimens of plate thickness varying from  $t = 30$  mm up to  $t = 70$  mm was tested. The specimens were welded manually with full weld root penetration. Three types of welds were produced with nominal weld angles of  $\alpha = 30$  deg,  $\alpha = 45$  deg, and  $\alpha = 60$  deg. The specimens were tested under variable amplitude four-point bending with the load ratio  $R \geq 0$ . The welds on one side of the joints were ground at toe areas in order to avoid simultaneous crack initiation on both sides of the attachment, so that the measuring device only needed to be mounted on one side of the specimen. All specimens were post-weld heat

TABLE 1—Mechanical properties of BS 4360: 50 D steel.

Yield strength	$\sigma_Y = 345$ MPa
Ultimate strength	$\sigma_{UTS} = 450/620$ MPa
Reduction of cross section area	$A = 18\%$
Paris Equation parameter <sup>a</sup>	$C = 8.02 \times 10^{-12}$
Paris Equation exponent	$m = 2.96$

<sup>a</sup> For  $da/dN$  in m/cycle and  $\Delta K$  in MPa  $\sqrt{m}$ .

TABLE 2—Chemical composition.

Chemical Component	Content, Weight %
Carbon	0.18 max
Silicon	0.1/0.5
Manganese	1.5 max
Niobium	0.1 max
Vanadium	0.1 max
Sulfur	0.04 max
Phosphorus	0.04 max

treated to release the residual stresses due to welding. The specimens were kept in a furnace for about 6 h at the temperature of approximately 620°C. Weld toe radii and weld angles were measured for each specimen.

#### *Test Conditions and Test Rig*

All specimens were tested in air under variable-amplitude loading defined by the power spectrum density function shown in Fig. 9. The magnitude of the nominal mean bending stress was  $S_m = 150$  MPa. The root mean square nominal stress was  $S_{rms} = 65$  MPa, with a clipping ratio of  $S_{max}/S_{rms} = 2.87$ . All tests were conducted in load control mode using computer-controlled actuator. The frequency varied from 0 to 2.5 Hz. A computer package [19] was used for the signal generation and data acquisition. The software was linked with a specially built Alternative Current Potential Drop System [9] for detection, measurement, and monitoring of crack shape evolution. The standard crack microgage [9] has been used for the generation and measurement of the alternating-current (a-c) field. As shown in Fig. 10, a special double probe head (three contact points) with sliding spring contacts has been constructed and this was attached to a lead screw driven by a computer-controlled stepping motor. The probe head contained a flat coil which was used to induce the a-c field in the specimen. The switching unit controlled by the computer made it possible to mea-

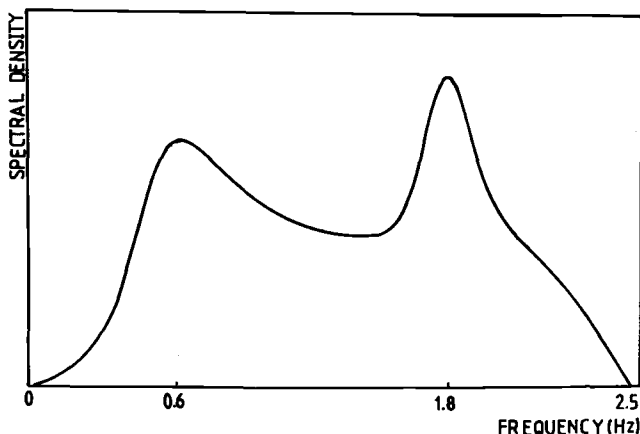


FIG. 9—Power spectrum density function for the stress history used in testing.

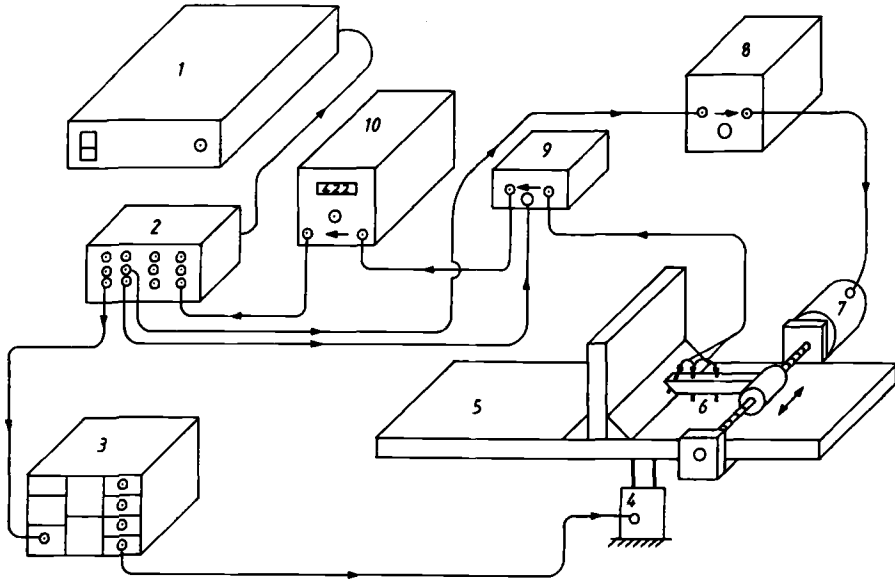


FIG. 10—Automatic system for two-dimensional fatigue crack shape evolution monitoring: 1-computer PDP-11; 2-interface; 3-servohydraulic controller; 4-piston; 5-specimen; 6-probe; 7-stepping motor; 8-stepping motor driver; 9-switching unit; 10-microgate.

sure the cross crack and off crack a-c voltage probe using the same crack microgate at required positions. The probe head was periodically driven across the specimen in steps of 1 mm during the fatigue test so that the a-c field along the weld toe could be measured and monitored. The data from each scan, corresponding to one pass over the specimen width (100 mm), were stored on a disk and subsequently analyzed. The final output from the computer was in the form of a graph showing the crack depth against the distance along the weld toe.

Several successive scans taken periodically allowed the fatigue crack shape evolution to be examined during test; a typical example of the results is shown in Fig. 11. The accuracy of the system [9] was of the order of 10% for cracks deeper than 2 mm.

#### *Analysis of Variable-Amplitude Stress History: The Weighted Average Stress Range*

Because there is no general approach for all types of variable-amplitude loading, it is necessary to identify the main features of each particular case. It was shown [20,21] that in the case of loading histories for offshore structures, such as the one under consideration, some simplifications can be made by using so called "weighted average stress range." It is considered in this theory that each rise or cycle will cause a small crack increment.

$$da = C(h_k)^m \quad (12)$$

where

$$h_k = h_s \sqrt{\pi a} Y \quad \text{and} \quad \frac{da}{dn} = C(h_k)^m$$

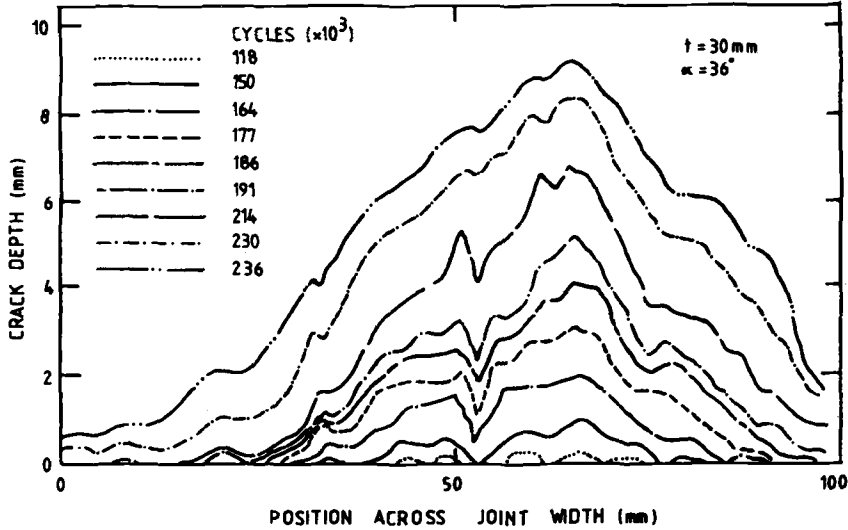


FIG. 11—Crack shape evolution recorded with the ACPD system; T-butt welded joint under variable-amplitude bending load,  $t = 30$  mm,  $\alpha = 36$  deg.

The average over  $M$  cycles will be

$$\bar{da} = \frac{\sum_{i=0}^M C(h_k)_i^m}{M} = C(\bar{h}_k^m) \quad (13)$$

This average stress-intensity range  $\bar{h}_k^m$  can be reinterpreted as an average effective stress-intensity factor  $K_h$

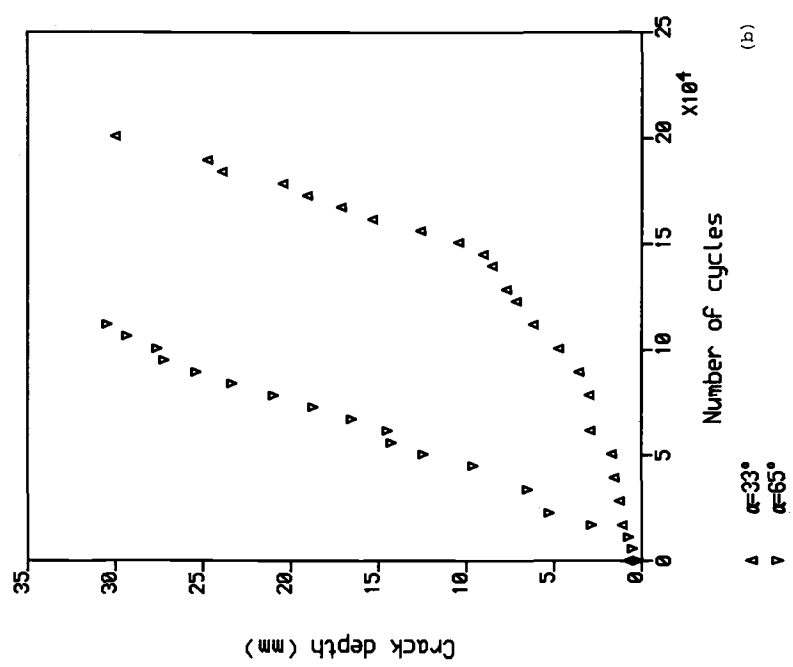
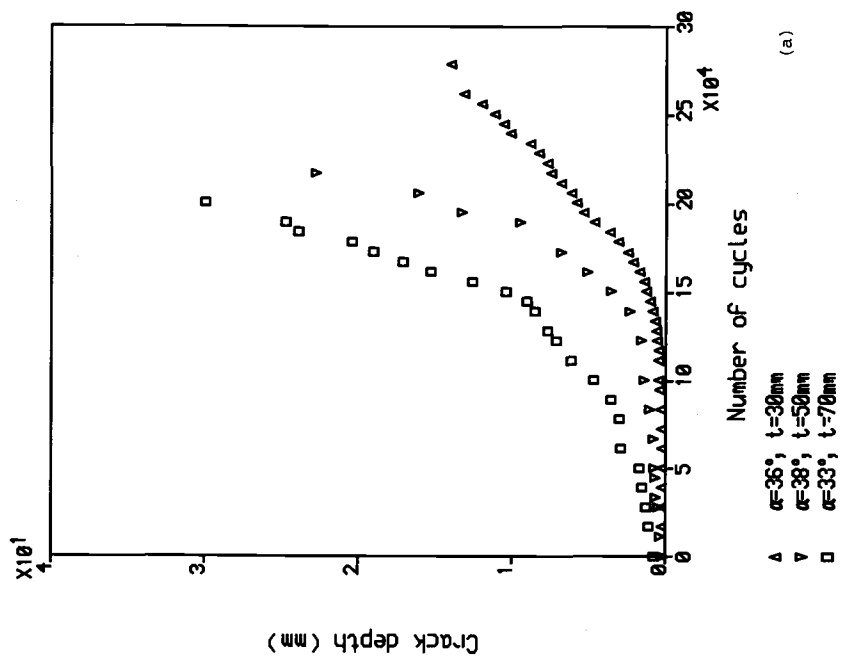
$$\Delta K_h = \sqrt[m]{\frac{\sum_{i=1}^M (h_k)_i^m}{M}} = \bar{h}_s^m \sqrt{\pi a} Y = \Delta S_h \cdot \sqrt{\pi a} Y \quad (14)$$

where

$$\bar{h}_s^m = \Delta S_h = \sqrt[m]{\frac{\sum_{i=1}^M (\Delta S_i)^m}{M}} \quad (15)$$

The fatigue analysis can therefore be based on the single stress range  $\Delta S_h$  weighted by the material property  $m$  while the individual stress ranges are calculated according to the "rainflow counting procedure" [22]. The average weighted stress range used in this study was  $S_h = 175$  MPa calculated for  $m = 2.96$ .

It was shown [20–22] that this technique successfully correlated fatigue crack growth data for several variable amplitude loading spectra. Therefore, the weighted stress range  $\Delta S_h$  and the stress-intensity factor  $\Delta K_h$  were used for further theoretical calculations.



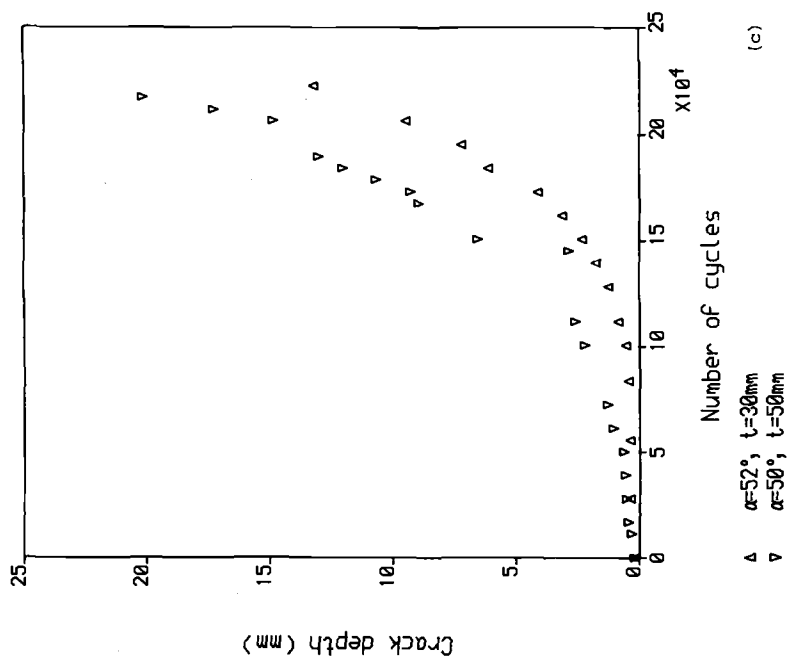


FIG. 12—Maximum crack depth versus number of cycles for T-butt welded joints under variable-amplitude bending load; with  $S_{ms} = 65 \text{ MPa}$ , clipping ratio 2.87,  $\Delta S_h = 175 \text{ MPa}$ : (a) for weld angle  $\alpha = 33\text{--}38 \text{ deg}$  and different plate thicknesses; (b) for constant thickness  $t = 70 \text{ mm}$  and two weld angles  $\alpha = 33 \text{ deg}$  and  $65 \text{ deg}$ ; and (c) for variable plate thickness and weld angle  $\alpha = 50 \text{ deg}$ .



### Experimental Data

The successive crack shape contours (Fig. 11) monitored periodically throughout the tests made it possible to derive empirical relations between the maximum crack depth versus the number of applied loading cycles. The same curves were also used to determine the fatigue life of a specimen after the crack had penetrated a half of the plate thickness. The example sets of " $a$  versus  $N$ " data shown in Fig. 12a were obtained from specimens made of three different plate thicknesses. Similar curves were also constructed for specimens with different weld angles  $\alpha$ , as shown in Fig. 12b. Additional data obtained from welds with the angle  $\alpha = 50$  deg is shown in Fig. 12c.

It should be noted that the weld toe angle  $\alpha$  and the weld toe radius  $\rho$  varied along the weld. Therefore, the nominal values quoted here represent average values based on several measurements over the specimen width of 100 mm.

The  $a$ - $N$  diagrams shown in Figs. 12a and 12b were subsequently used for calculating the experimental crack growth rate  $da/dN$  and the experimental stress-intensity range  $\Delta K_{\text{exp}}$

$$\Delta K_{\text{exp}} = \sqrt[m]{\left(\frac{da}{dn}\right)/C} \quad (16)$$

The data shown in Fig. 12a illustrate the detrimental effect of increasing plate thickness. All three specimens were tested under the same stress history and all of them were proportionally scaled regarding the plate thickness and weld dimensions.

The weld angle effect on fatigue crack growth in 70-mm-thick T-butt joint is shown in Fig. 12b. The welds in both specimens had the same leg lengths but obviously different weld heights measured along the T-attachment.

However, it should also be noted that at early stages of fatigue crack growth, several small cracks initiated almost simultaneously along the weld toe. Therefore, the experimentally determined stress-intensity factor ranges should be considered as stress-intensity factor ranges for the deepest cracks subject to possible influence of the colinear smaller cracks. As the cracks grew deeper, a single crack of approximately semi-elliptical shape was finally developed. Therefore, the fracture mechanics modeling based on a single crack analysis seems to be more appropriate for deep cracks.

The calculated stress-intensity ranges  $\Delta K_{\text{exp}}$  versus experimental data  $\Delta K_{\text{exp}}$  are shown in Fig. 13. The agreement was within 30% for all specimens and crack depths. The  $\pm 30\%$  scatter could result from a number of sources such as errors in measuring the weld geometry and crack depth, the difference between the idealized semi-elliptical crack and real crack shape, etc. Nevertheless, such scatter can be considered to be small taking into account the number of geometric parameters and the variable amplitude loading.

### Calculations Versus Experiment

Calculations of fatigue lives were executed by integration of Paris's Eq 1 using the stress-intensity factor range  $\Delta K_h$  given by Eq 14. The calculations were conducted assuming the initial crack length and depth  $c = 0.2$  mm and  $c = 0.2$  mm, respectively, which were the crack size and shape of the smallest detectable crack. All calculations were carried out until the crack depth was a half of the plate thickness, that is, up to  $a = t/2$ . However, in most cases several small cracks initiated almost simultaneously along the weld toe. Therefore, the analysis based on a growth of a single crack did not seem to be adequate because subsequent crack coalescence resulted in sudden change in the aspect ratio  $c/a$  that could not

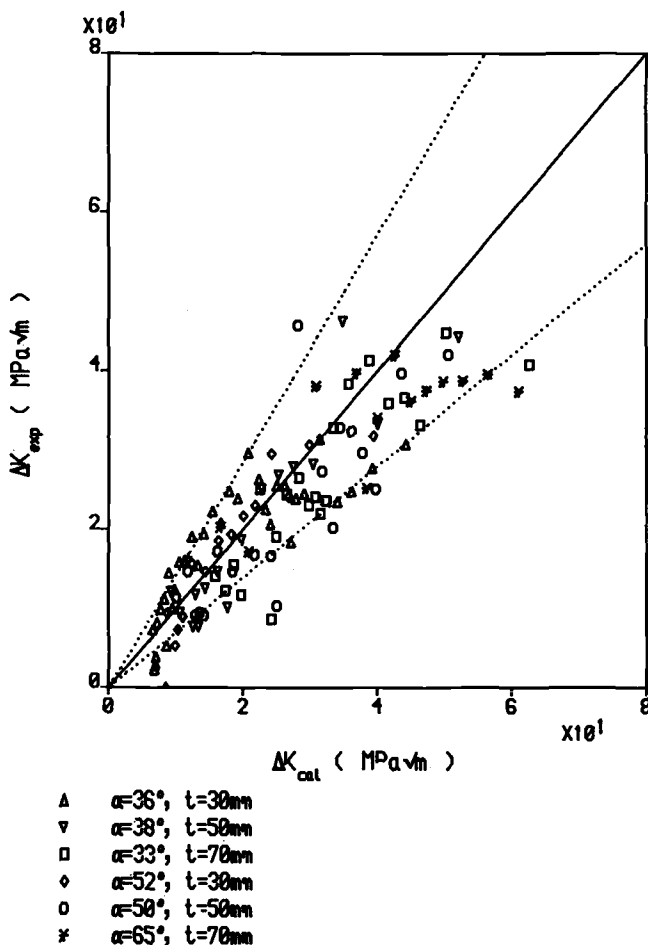


FIG. 13—Comparisons of calculated and experimental (fatigue crack growth based) stress-intensity factor ranges for T-butt welded joints under variable-amplitude bending.

be characterized correctly by the single crack model. In order to account for this effect the experimentally derived [24] aspect ratio versus crack depth (17) was used.

$$a/c = e^{-ka} \quad (17)$$

where  $k = 2.915 \times 10^{-6} (\Delta S_h)^2 \cdot \sqrt{t}$  for  $a$  and  $t$  in millimetres and  $\Delta S_h$  in MPa.

Thus, the stress-intensity factor for the deepest crack point was calculated using the weight function 11a, the empirical Eq 17, and the average weighted stress range. The comparison of calculated and experimental fatigue crack growth lives is shown in Fig. 14. In general, less than  $\pm 30\%$  error was found for all specimens used in the study. One of the important factors leading to this correlation was the empirical support of the theoretical analysis by implementation of Eq 17.

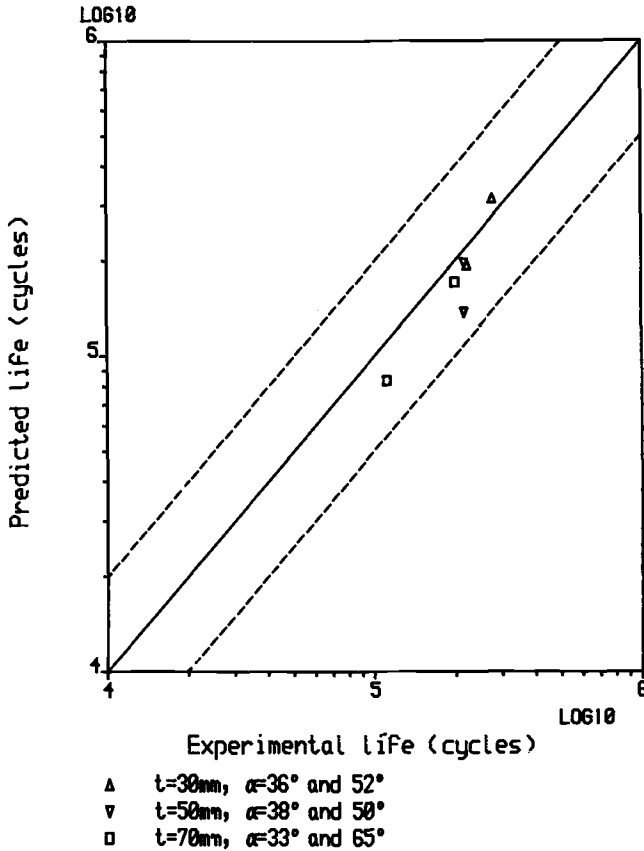


FIG. 14—Comparisons of calculated and experimental fatigue crack growth lives of T-butt welded joints under variable-amplitude bending load.

It was also shown in Fig. 8 that application of the "flat plate" weight function  $M_s^p$  led to an overestimation of the stress-intensity factor  $K$ . Data shown in Fig. 15 demonstrate this effect in terms of the fatigue crack growth life of T-butt specimens tested under constant amplitude bending load. It is worth noting that a few percent error in estimation of the stress-intensity factor may accumulate to result in 20% to 50% difference in predicted lives. The predictions based on the weight function  $m_s^w$  derived for a surface crack in a weldment resulted in a better correlation with the experimental data for both constant and variable amplitude loading. Finally, the weight function  $m_s^w$  was used for analysis of the weld angle and weld toe effects on fatigue crack growth lives. The data shown in Figs. 14 and 15 were obtained for the whole range of weld angles  $\alpha = 30$  to  $60$  deg and plate thickness  $t = 30$  to  $70$  mm. It is apparent that application of the weight function  $m_s^w$  (Eq 11a) led to a more accurate estimation of fatigue lives for constant amplitude loading.

Despite the visible scatter, the theoretical analysis led to a reasonably good estimation of geometrical effects on fatigue crack growth lives both in qualitative and quantitative terms. Thus the technique can be used for estimation of the weld profile effect on fatigue lives of welded joints consisting of fillet welds. Also, the same approach can be used for studying thickness effect [23] on fatigue life of welded joints.

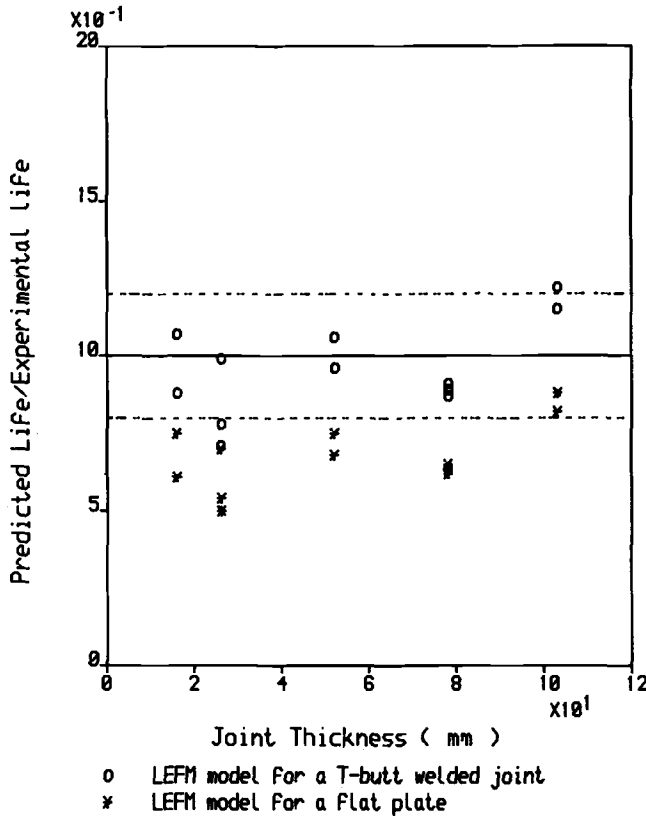


FIG. 15—Effect of the weight function type on calculated fatigue crack growth lives of T-butt welded joints in relation to experimental data [16] obtained under constant-amplitude bending; Calculated for  $a_0 = 0.2$  mm,  $\rho = 1.1$  mm, and weld angle  $\alpha = 39$  deg.

## Discussion

Fatigue crack growth analysis requires several input data such as material properties, stress-intensity factor, initial crack size, and critical crack size or fracture toughness to be known. The quality of the final result depends on the quality of each of them. The material crack growth data and the stress-intensity factor seem to be understood well and may be the most reliable parameters in the whole model. Unfortunately, the important data regarding the initial crack size are rather arbitrarily chosen and subjective depending upon the investigator. The whole problem is even more complex in welded structures because of the simultaneous initiation, growth, and subsequent coalescence of multiple cracks. Therefore, the most frequently used single-crack fracture-mechanics approach needs to be complemented by additional experimental data such as Eq 17. The alternative approach is to use multiple-crack fracture-mechanics models [25], but the complexity of such analyses does not make them sufficiently attractive for engineering practice at present. An additional difficulty is that one does not know how many cracks are to be initiated along a given weld toe. Therefore, more experimental data on initiation and growth of surface cracks in weldments are required. This indicates that the emphasis should be put on further

development of nondestructive testing techniques necessary to support such investigations and fracture-mechanics analyses.

### Conclusions

It has been shown that the weight functions derived herein lead to a sufficiently accurate, for engineering applications, estimation of stress-intensity factors for surface cracks in weldments. These functions allow the stress-intensity factor to be analyzed with respect to several geometrical and loading parameters such as weld toe, radius, weld angle, plate thickness, and combinations of tension and bending loads.

It was found that the weld angle had a more significant effect on the fatigue life than the weld toe radius.

The variable-amplitude crack growth due to offshore loading histories, such as the one used in the paper, can be analyzed by means of the average weighted stress range excluding the load interaction and mean stress effects.

The initiation and growth of multiple surface cracks in a weldment makes it difficult to predict crack growth and crack shape evolution by using the single-crack fracture-mechanics model. Therefore, the single-crack model requires complementary experimental data such as the crack aspect ratio versus crack depth.

### Acknowledgment

A major part of the work reported in this paper was conducted by both authors during their employment at the Department of Mechanical Engineering, University College London, London, United Kingdom.

### References

- [1] Jakubczak, H. and Glinka, G., "Fatigue Analysis of Manufacturing Defects in Weldments," *International Journal of Fatigue*, Vol. 8, No. 2, 1986, pp. 51-57.
- [2] Yee, R. et. al., "Thickness Effect and Fatigue Crack Development in Welded T-joint," presented at the International Conference on Offshore Mechanics and Arctic Engineering (OMAE), American Society of Mechanical Engineers, Houston, 7-12 Feb. 1988.
- [3] Glinka, G., "Residual Stresses in Fatigue and Fracture: Theoretical Analyses and Experiments," *Advances in Surface Treatment—Residual Stresses*, A. Niku-Lari, Ed., Pergamon Press, New York, Vol. 4, 1987, pp. 413-454.
- [4] Glinka, G., Gmur, Z., and Swiderski, Z., "An Examination of Mixed Fatigue-Tensile Surface Crack Growth in Rails," *Engineering Fracture Mechanics*, Vol. 20, No. 1, 1984, pp. 103-112.
- [5] Bueckner, H. F., "A Novel Principle for the Computation of Stress Intensity Factors," *Zeitschrift für Angewandte Mathematik und Mechanik*, Vol. 50, No. 9, 1970, pp. 129-146.
- [6] Rice, J. R., "Some Remarks on Elastic Crack-Tip Stress Field," *International Journal of Solids and Structures*, Vol. 8, No. 5, 1972, pp. 751-758.
- [7] Paris, P. and Erdogan, F., "A Critical Analysis of Crack Propagation Laws," *Transactions, American Society of Mechanical Engineers, Journal of Basic Engineering*, Vol. 85, No. 4, 1963, p. 538.
- [8] Dover, W. D., Collins, R., and Michael, D. M., "The Use of AC-Field Measurements for Crack Detection and Sizing in Air and Underwater," *Transaction of the Royal Society*, London, Vol. A320, 1986, pp. 217-283.
- [9] Dover, W. D., Glinka, G., and Collins, R., "Automated Crack Detection and Monitoring of Crack Shape Evolution in Tubular Welded Joints and T-butt Welds," *Proceedings, International Conference on Non-Destructive Testing in the Fitness-for-Purpose Assessment of Welded Constructions*, The Welding Institute, London, 20-22 Nov. 1984, pp. 83-90.
- [10] Petroski, H. J. and Achenbach, J. D., "Computation of the Weight Function from a Stress Intensity Factor," *Engineering Fracture Mechanics*, Vol. 10, No. 2, 1978, pp. 257-266.

- [11] Mattheck, C., Morawietz, P., and Munz, D., "Stress Intensity Factor at the Deepest Point of a Semi-Elliptical Surface Crack in Plates under Stress Gradients," *International Journal of Fracture*, Vol. 23, No. 2, 1983, pp. 210-212.
- [12] Niu, X. and Glinka, G., "On the Limitations of the Petroski-Achenback Crack Opening Displacement Approximation for the Calculation of Weight Function," *Engineering Fracture Mechanics*, Vol. 26, No. 5, 1987, pp. 701-706.
- [13] Fett, T. and Mattheck, C., "On the Calculation of Crack Opening Displacement from the Stress Intensity Factor," *Engineering Fracture Mechanics*, Vol. 27, No. 6, 1987, pp. 697-715.
- [14] Niu, X. and Glinka, G., "The Weld Profile Effect on Stress Intensity Factors in Weldments," *International Journal of Fracture*, Vol. 35, No. 1, 1987, pp. 3-20.
- [15] Niu, X. and Glinka, G., "Semi-elliptical Surface Crack Stress Intensity Factor for Welded Joints," *International Journal of Fracture*, Vol. 40, No. 2, 1989, pp. 255-270.
- [16] Bell, R., "Determination of Stress Intensity Factors for Weld Toe Defects," Final Report, BSS 22ST. 23440-2-1083/7, Faculty of Engineering, Carleton University, Ottawa, Oct. 1985.
- [17] Bueckner, H. F., "Weight Function for the Notched Bar," *Zeitschrift für Angewandte Mathematik und Mechanik*, Vol. 51, 1971, pp. 97-109.
- [18] Niu, X. and Glinka, G., "Weight Functions for Edge and Surface Semi-Elliptical Cracks in Flat Plates and Plates with Corners," *Engineering Fracture Mechanics*, 1989, accepted for publication.
- [19] Broome, D. R., Dharmavasan, S., and Dover, W. D., "The Use of Digital Techniques in the Large Scale Fatigue Testing of Tubular Joints," *Proceeding of the International Conference SEECON '83 on Digital Techniques in Fatigue*, London, 28-30 March 1983, pp. 330-347.
- [20] Hibberd, R. D. and Dover, W. D., "The Analysis of Random Load Fatigue Crack Propagation," *Fracture 1977*, Vol. 2, Fourth International Congress on Fracture, Waterloo, Ont., Canada, 1977.
- [21] Dover, W. D. in *Variable Amplitude Fatigue of Welded Structures in Fracture Mechanics: Current Status, Future Prospects*, R. A. Smith, Ed., Pergamon Press, New York, 1979, pp. 125-147.
- [22] Glinka, G. and Kam, J. P., "Rainflow Counting Algorithm for Very Long Stress Histories," *International Journal of Fatigue*, Vol. 9, No. 3, 1987, pp. 223-228.
- [23] Niu, X. and Glinka, G., "Weld Geometry Effects on Fatigue Life Under Variable Amplitude Loading," *Proceedings*, 3rd International Spring Meeting on Fatigue Crack Growth Under Variable Amplitude Loading, American Society for Testing and Materials, Paris, 15-17 June 1988.
- [24] Vosikovsky, O., Bell, R., Burns, D. J., and Mohaupt, U. H., "Fracture Mechanics Assessment of Fatigue Life of Welded Plate T-joints, Including Thickness Effect," in *Proceedings*, Behavior of Offshore Structures Conference (BOSS), Amsterdam, 1985, pp. 453-464.
- [25] Bell, R., Vosikovsky, O., Burns, D. J., and Mohaupt, V. H., "A Fracture Mechanics Model for Life Prediction of Welded Plate Joints," *Proceedings*, 3rd International ECSC Offshore Conference on Steel in Marine Structures (SIMS'87), C. Noordhoek and J. de Back, Eds., Elsevier, Amsterdam, 1987, pp. 901-910.

## Author Index

### A

Andersson, Borje, 77-97

### B

Blind, John A., 215-236

Blom, Anders F., 77-97

### C

Canda, William R., 215-236

Carter, Dale K., 215-236

Caspers, Michael, 365-388

Chang, Che W., 99-110

Chatterjee, Sailendra N., 177-193

Chiang, Fu Pen, 112-128

### D

Dally, J. W., 130-140

Dorner, Wilhelm, 237-258

### G

Glinka, Grzegorz, 348-363, 390-412

Grandt, Allen F., Jr., 49-61, 260-285

### H

Hackett, Edwin M., 142-151

Harris, Charles E., 194-211

Hodulak, Ludvik, 315-331

### I

Ilschner, Bernhard, 237-258

### J

Jira, Jay R., 303-313

### K

Kirk, Mark T., 142-151

### L

Li Yingzhi, 63-76

Lloyd, Wilson R., 152-176

### M

Marchand, Norman J., 237-258

Mattheck, Claus, 365-388

Morris, Don H., 194-211

Munz, Dietrich, 365-388

### N

Nagy, Dale A., 303-313

Newman, James C., Jr., 3-5, 34-47

Newport, Andrew, 348-363

Nicholas, Theodore A., 260-285, 303-313

Niu, Xiaon, 390-412

### O

Olinkiewicz, JoAnne C., 112-128

### P

Parks, David M., 9-30

Perez, Rigo, 49-61

Poe, Clarence C. Jr., 194-211

Prodan, Miklos, 287-302

### R

Radon, John C., 287-302

Raju, I. S., 34-47

Ramulu, Mamidala, 333-347

Reuter, Walter G., 3-5, 152-176

Rezvani, Mohamed, 99-110

### S

Saff, Charles R., 49-61

Sciammarella, C. A., 130-140

Shareef, I., 130-140

Shivakumar, K. N., 34-47

Smith, C. William, 99–110  
Swedlow, J. L., iii–iv

**T**

Tan, P. W., 34–47

Tippur, H. V., 112–128  
Troha, William A., 260–285

**U**

Underwood, John H., 3–5



# Subject Index

## A

- ABAQUS program, 246–249
- A* derivation, 14–17
- Alloys
  - chemical composition, 239
  - surface crack testing of cylindrical rods, 383–388
  - threshold testing, 305–306
- Almond-shaped crack
  - bending loading coefficients, 375
  - stress-intensity factor coefficient, 366, 368–372
  - tension loading coefficients, 374
- Alternating-current (A-C) field measurement
  - schematic, 355–356
  - tubular threaded connections, 348–363
- Alternating-current (A-C) potential drop (ACPD)
  - crack initiation and growth measurement, 242–246
  - test specimen and apparatus, 238–242
  - thermal fatigue histories, 246–249
  - thermal fatigue testing, 237–258
  - weldment surface crack analysis, 403–404
- Aluminum alloys
  - fractographic analysis, 340, 342–344
  - subcritical surface flaw growth, 334–336
  - surface flaw analysis, 216–236
- Anisotropic alloys, 237–238
- Antisymmetric loading, 13–14
- Aspect ratio, 360–361
- ASTM Standards
  - A 572, 295
  - A 710, 154
  - E 399–81, 291
- ASTM Test Methods
  - E 1152, 325
  - E 647–86A, 304

## Asymptotic technique

- eigenfunction expansion, 66–67
  - HRR dominance in tensile-loaded surface cracks, 23–24
- Average crack growth rate, 256–258

## B

- Beach marks, 383, 385
- Bending
  - almond-shaped cracks, 375
  - notched bar almond-shaped cracks, 380
  - notched bar sickle-shaped cracks, 382
  - sickle-shaped cracks, 377
  - uncracked notched bar, 378
- Block loading sequences
  - crack growth retardation, 265–266
  - surface flaw geometries, 262–264
- Boundary correction factors, 41–46
- Boundary-layer effect
  - finite-element models and methods, 37–40
  - stress-intensity factors, 94–96

## C

- Center of rotation, 168–170
- Charpy-V notch testing
  - crack-tip opening displacement values, 154–155
  - impact toughness, 142–150
- Circumferentially cracked pipe, 21–22
- Closure loads
  - effective stress-intensity factors, 272–277
  - surface flaw geometry, 268–272
- Compact-type (CT) specimens
  - fatigue crack growth rates, 278–279
  - subcritical surface flaw growth, 333–346
  - surface crack growth computations, 287–302
  - surface flaw analysis, 215–236
- Complementary metal-oxide semiconductor (CMOS) switches, 244–246
- Complex load, corner crack stress-intensity factors, 53–56

Composite laminates  
   near-surface layer failure, 186–189  
   properties, 210–211  
   surface cracks, 177–193  
 Condensation technique, stress-intensity  
   analysis, 69–70  
 Constraint parameter  
   crack front, 321–324  
   internal pressure and thermal shock, 323,  
     325  
   three-dimensional crack bodies, 323–324  
 Continuum analysis, 21–22  
 Convergence, 82–83  
 Coordinate system  
   fracture analysis, 64–66  
   in-plane displacement measurement in  
     PVC pipe, 137–138  
 Corner crack  
   schematic, 49–50  
   stress-intensity factors, 49–61  
   two-degree-of-freedom, 50–51  
 Corner singularities, 13–14  
 Correction factors  
   stress-intensity solutions, 226–227  
   surface flaws, 180, 185–186  
   tubular threaded connections, 359–360  
 Crack aspect ratio, 265–268  
 Crack border-free surface intersection  
   effects, 99–108  
 Crack closure/opening loads, 268–273  
 Crack closure threshold testing, 303–314  
 Crack geometry, 383–388  
 Crack growth  
   crack-tip opening displacement values,  
     162–163  
    $dC/dN$  calculation, 219–220  
   predictions, 279–285, 373–383  
   surface crack testing of cylindrical rods,  
     383–388  
   thermal fatigue testing, 237–258, 242–  
     246  
 Crack half length calculation, 288–290  
 Crack initiation, 237–258  
 Crack-mouth opening displacement  
   (CMOD)  
   load history and closure, 305–306  
   surface flaw analysis, 112, 117–120  
 Crack shape  
   almond and sickle-shaped, 365–366  
   crack front constraint variation, 323–  
     324  
   fatigue loading, 319–323  
   prediction, 373–383  
   stress-intensity factors, 40–46  
 Crack size, 40–46

Crack-tip-opening angle (CTOA), 3–4,  
   152–176  
 Crack-tip opening displacement (COD)  
   effective stress-intensity factors, 272–277  
   measurement, 3–4, 152–176  
   surface flaw geometries, 264–265  
   testing parameters, 298–302  
   values, 162–163  
 Critical conditions, failure assessment, 316–  
   317  
 Curvilinear coordinates, 64–66  
 Cylindrical bars, surface crack growth, 365–  
   388

## D

Damage size measurements, 198–200  
 Damage size predictions, 199–203  
 Delamination growth, 186–189  
 Depley tests, filament wound cases, 198  
 Depth crack growth rate ( $da/dN$ ), 231–232  
 Dimensionless displacement solution, 68–  
   69  
 Dimensionless stress-intensity factors, 73–  
   74  
 Direct current (D-C) potential drop, 243–  
   244  
 Domain integrals, 14–17  
 Double-beam illumination technique, 137–  
   139  
 Double-edge wedge specimen, 247–248  
 Double-exposure holography, 138–139  
 Dynamic loading, 142–150

## E

Edge stress-intensity factor, 86–96  
 Effective stress distribution, 123, 125, 127  
 Eigenfunction expansion, 66–69  
 Eigenvalues  
   algorithm for linear-elastic fracture  
     mechanics, 103  
   in-plane displacement measurement,  
     133–134  
   least-squares in-plane displacement  
     measurement, 139  
   semi-elliptical surface crack analysis, 84–  
     85  
 Elastic behavior  
   crack-tip opening displacement, 152–176  
   surface crack analysis, 9–30  
   thermal fatigue testing, 246–253  
 Elastic-plastic analysis  
   crack-tip opening displacement values,  
     152–176

rapidly-loaded surface crack specimens,  
142–150  
surface crack review, 9–30  
thermal fatigue testing, 246–253  
Elastic stress fields, 77–97  
Electro-discharge machining (EDM), 217–  
218  
Elliptical cracks  
  composite laminates, 177–193  
  orthotropic media, 178–180  
  stress-intensity factors, in orthotropic  
  medium, 190–193  
  weight function, 353–354  
Embedded elliptical crack geometry, 226–  
227  
Energy release rate, 367  
Equilibrium equations, 65–66  
Equivalent surface crack, 198–203  
Exact solutions behavior, 78–81

## F

Failure assessment  
  calculation programs, 316–317  
  valve casing, 317–319  
Fatigue crack closure, 260–285  
Fatigue crack growth  
  aluminum plate surface flaw analysis,  
  217–218  
  computations and experiments, 3–4,  
  287–302  
  crack length, 338–339, 345–346  
  failure assessment, 316  
  maximum crack versus number of cycles,  
  357–360  
  plates, 215–236  
  predictability, 278–285  
  subcritical surface flaw growth, 333–339,  
  346  
  three-dimensional surface flaw  
  geometries, 260–285  
  threshold tests, 303–314  
Fatigue crack initiation, 340–341  
Fatigue loading, 319–323  
Fatigue testing  
  subcritical surface flaw growth, 334–336  
  surface crack growth, 315–331  
  tubular threaded connections, 348–363  
  vinyl acetate monomer (VAM) joints,  
  354–360  
Fiber damage, 198–200  
Filament-wound cases (FWC)  
  damage size and prediction tests, 199–  
  203  
  deply tests, 198  
  impact testing, 195–211  
  residual strength tests, 197–198  
Finite-element analysis  
  convergence properties of  $p$ -version, 82–  
  83  
  correction factor, 185  
  crack-tip opening displacement values,  
  171–172  
  HRR dominance in tensile-loaded  
  surface cracks, 23–24  
  plastically deformed surface flaw, 112–128  
   $p$ -version, 81–82  
  slice synthesis, 225  
  special computations, 290–291  
  stress-intensity factors, 57–58  
  surface flaw, 34–47, 112–128  
  thermal fatigue testing, 237–258  
  three-dimensional, 36–40, 122–128  
Finite-element mesh  
  stress-intensity factors, 70–71  
  tubular threaded connections, 351–352  
First-ligament failure, 204–205  
Flat plate weight function, 399, 402, 410  
Flow theory of plasticity, 19–20  
Fluidized bed technique, 237–238  
Fractography, 339–344  
Fracture analysis  
  dimensionless stress-intensity factors, 70–  
  74  
  eigenfunction expansion, 67–69  
  finite-element mesh and special element,  
  70  
  governing equations in curvilinear  
  coordinates, 64–66  
  monotonic loading, 329–330  
  rapidly loaded surface-cracked specimens,  
  142–150  
  stress-intensity factors in surface cracks,  
  69–74  
  three-dimensional bodies with surface  
  crack, 63–76  
Fracture mechanics  
  composite laminates, 177–193  
  linear-elastic, 10–14  
  near-surface layer failure, 186–189  
  optical stress analysis, 99–110  
  prediction for rapidly-loaded surface  
  crack specimens, 142–150  
  semi-elliptical surface crack analysis, 77–  
  97  
  three-dimensional geometries, 260–285  
Fracture resistance curves, 323–324  
Free surface-crack border intersection, 134  
Frozen stress algorithm, 102  
Frozen stress analysis, 108–110

## G

- Garwood  $J$ -integral equation, 326–328
- Geometry
  - failure assessment, 316
  - tubular threaded connections, 350–351
- Goursat-Kolosov stress functions, 131–134
- Graphite/epoxy composite
  - constituent properties, 210
  - impact damage, 194–211
  - physical properties, 210
  - strength predictions, 204–209

## H

- Hertz's law, 195
- Holes, surface and corner cracks, 35
- Holographic interferometry, 130–140
- Homogenization assumption, 178–193
- Hooke's law, 65–66
- HRR dominance, 171–172
- Hybrid analogue-finite-element model, 360–361
- Hybrid stress analysis, 350–351
- Hydrostatic stress, 321–323

## I

- "Ill-shaped" elements, 37–38
- Impact damage
  - equivalent surface crack, 198–203
  - filament-wound cases, 196–197
  - strength predictions, 208–209
  - surface crack analysis, 194–211
- Incompressibility, 86–94
- Indent notch, 333–346
- Induction heating, thermal fatigue crack, 237–258
- Initiation-fracture testing
  - smooth and indent notch, 340–341
  - subcritical surface flaw growth, 336–338
- In-plane displacements, 130–140
- Interferometric displacement gage (IDG), 305
- Inverse square-root singularity, 133–134
- Irwin stress-intensity solution, 223–225
- Isotropic alloys, thermal fatigue testing, 237–238

## J

- $J_{crit}$  value, 146–150
- $J$ -integral
  - crack-tip opening displacement values, 152–176

- Garwood method, 326–328
- rapidly loaded surface-cracked specimens, 142–150
- Read method, 327
- surface crack growth computations, 20–22, 287–302
- surface flaw analysis, 112, 117–122
- $J$ - $R$  curve
  - geometry and instrumentation, 326
  - $J$  curve comparison, 329–331
  - monotonic increasing load, 323–331
- $J$  resistance curve,  $J$ - $R$  curve comparison, 329–331

## L

- Lamé coefficient, curvilinear coordinates, 65–66
- Laplace equations, 78–81
- Lead-before-break behavior, 318–319
- Least squares, in-plane displacement measurement, 134–137
- Ligament failure
  - composite laminate surface cracks, 177–178
  - surface cuts, 205–208
- Linear elastic fracture mechanics
  - algorithms, 100–103
  - nonsingular effect, 103–104
  - semi-elliptical surface crack analysis, 78
  - subcritical surface flaw growth, 333–346
  - surface crack growth computations, 10–14, 287–302
- Line-spring analysis, 17–21
- Load displacement curves, 156–157
- Loading history
  - CTOD and CTOA values, 172–176
  - surface crack growth and, 304–314
- Loading parameters, 316
- Load ratio, 333–346
- Local-global analysis, 63–76
- Locking effects, 82
- Love's solution, 201–202

## M

- Magnification factors, 92–93
- Maximum strain criterion, 205
- Maxwell-Betti reciprocity theorem, 83–84
- Metallographic slicing, 157, 162
- Microcrack initiation, 254–257
- Microtopographic techniques, 157–161, 163–167
- Moiré interferometry
  - in-plane displacement measurement, 134–137

optical analysis, 110  
 surface flaw analysis, 113–114  
 Monotonic loading  
   models and experiments, 2–3  
   surface crack growth, 315–331  
 Motor cases, impact damage analysis, 195–211  
 M(T) crack specimens, 295–296

## N

Near free surface effects, 30  
 Near-surface layer failure, 186–189  
 Near-threshold crack growth behavior, 303–314  
 Near-tip problem geometry and notation, 100–101  
 Newman-Raju solution  
   crack-tip opening displacement values, 169–172  
   fatigue crack growth rate prediction, 280–282  
   stress-intensity analysis, 225–226  
 Newman width correction factor, 226, 228  
 Newton interferometry, 260–285  
 Newton-Raphson minimization, 292–293  
 Nodal-force method, 38–40  
 Nondimensional stress-intensity factors, 54–61  
 Nonsingular effect, linear elastic fracture mechanics, 103–104  
 Notched rods, surface crack growth, 365–388  
 Notches  
   subcritical surface flaw growth, 333–346  
   size, stress-intensity factors, 40–46  
 Numerical differentiation, 117

## O

Optical analysis  
   free-surface effects on cracks, 99–110  
   frozen stress analysis, 108–110  
   plastically deformed surface flaw, 112–128  
 Optical spatial filtering, 113–115  
 Optimization, special computations, 291–295  
 Orthotropic media  
   elliptic cracks, 178–180  
   stress-intensity factors, 190–193

## P

Paris equations  
   failure assessment, 316  
   fatigue crack growth rate prediction, 282–284

surface flaw crack growth, 229  
 tubular threaded connections, 357–358  
 unnotched rods, 383–384  
 weldment surface crack analysis, 408–411

Partially embedded ellipse, 230–231

Part-through cracks

  fracture behavior predictions, 146–148  
   line-spring analysis, 17–21  
   orthotropic media, 179–180

Phase-locked loop (PLL) system, 244–246

Plasticity, surface flaw analysis, 112–128

Plates

  dimensionless stress-intensity factors, 73  
   surface and corner cracks, 35, 215–236

PMMA polymer surface crack growth geometries, 260–285

Poisson's ratio

  eigenvalues, 84–85  
   magnification factor, 92  
   semi-elliptical surface crack analysis, 78

Polynomial coefficients, 225–226

Potential drop technique, 243–244

Power-law deformation theory, 19–20

Power spectrum density function, 403–404

Pressure vessels, 287–302

*p*-version finite element method  
   convergence properties, 82–83  
   reliability, 96–97

## R

Raju-Newman solution

  surface and depth crack growth rate curves, 232

  surface crack shape change, 234–235

Read *J*-integral equation, 327

Refined polariscop schematic, 109

Remaining-ligament strength criterion, 205

Residual tensile strength

  filament-wound cases, 197–198  
   graphite/epoxy composite, 194–211

Root-mean-square relations, 52

## S

Scanning electron microscopy, 334–346

Semicircular crack fronts, 25–29

Semicircular edge notch, 40–46

Semi-elliptical cracks

  composite laminates, 177–193  
   convergence properties, 82–83  
   eigenvalue determination, 84  
   exact solutions behavior, 78–81  
   finite-element mesh models, 90–96  
   HRR dominance, 25–29

Semi-elliptical cracks—*continued*

- model problem, 84–90
  - numerical solutions, 77–97
  - p*-version of finite-element method, 81–82
  - stress-intensity factors, 41–46, 83–84
  - surface flaw shape characterization, 229–231
  - T-butt welded joints, 392–399
  - weight function stress-intensity factor, 354
  - welded joints, 390–412
- Sickle-shaped cracks
- bending loading, 377
  - stress-intensity factor coefficients, 366, 368–373
  - tension loading, 376
- Simplified models, surface crack analysis, 17–22
- Single-edge notch bend (SEB)
- deep cracked, 144–148
  - shallow cracked, 145–148
- Single-edge notched (SEN), 18–19
- Singular integral, finite-element hybrid (SIFEH), 12
- linear-elastic fracture mechanics, 11–13
- Slice synthesis technique
- corner crack stress-intensity factors, 56–59
  - finite-element model, 225
  - stress-intensity factors, 56–59
- Society of Experimental Stress Analysis
- consensus solution, 226–228
- Special element properties, finite-element mesh and, 70–71
- Specimen geometry
- surface flaw analysis, 113–114, 116
  - thermal fatigue testing, 238–239
- Specimen-to-structure correlations, 287–302
- Square-root singularity, 79–81
- Strength predictions, 208–209
- Stress analysis
- surface crack, 2
  - tubular threaded connections, 348–363
- Stress distribution, 349–353
- Stress gradients, 49–61
- Stress-intensity factor
- calculations, 52–53
  - circular crack, 180–181
  - closure-load data, 272–277
  - computations and experiments, 287–302
  - contour integral calculation, 83–84
  - corner cracks, 49–61
  - distribution, 107–108

- edge cracks, 394–395
  - elliptic and semi-elliptic flaws, 178, 180, 182–183, 190–193
  - high-order special element, 69–70
  - infinite media, 180–183
  - in-plane displacement measurement, 130–140
  - loading parameter evaluation, 316–317
  - nondimensional, 54–59
  - notched and unnotched rods, 365–388
  - orthotropic medium, 190–193
  - plates, 215–236
  - semicircular edge notch, 40–46
  - subcritical surface flaw growth, 345–346
  - surface crack, 34–47
  - T-butt welded joints, 392–399
  - three-dimensional finite-element analysis, 36–38, 36–37
  - transversely isotropic media, 180, 184
  - threshold testing of crack closure and load, 303–314
  - tubular threaded connections, 348–363
  - weight-function calculation method, 365–368
  - weldment fatigue cracks, 390–412
- Stress-intensity solutions
- Irwin solution, 223–225
  - Newman-Raju solution, 225–226
  - surface flaw analysis, 223–226
- Stress ratio (*R*)
- crack closure behavior, 304–314
  - crack shape development under fatigue loading, 320–321
- Stress state variation correction, 319–320
- STRIPE program, 81–82
- Subcritical growth, surface flaw, 333–346
- Superalloys, thermal fatigue testing, 237–238
- Surface crack growth
- computational and experimental results, 295–302
  - elastic and elastic-plastic behavior, 9–30
  - failure assessment, 315–319
  - fatigue crack growth computations, 288–291
  - fracture analysis of three-dimensional bodies, 63–76
  - HRR dominance, 24–29
  - line-spring analysis, 17–21
  - monotonic increasing load, 315–331
  - optimization method, 291–295
  - plastic hinges, 21–22
- Surface cuts, strength predictions, 205–208

Surface flaw, 112–128  
 correction factors, 180, 185–186  
 CT crack growth rate data, 231–232  
 growth predictions, 232–235  
 plates, 215–236  
 shape and growth rate at depth ( $da/dN$ ), 220–223  
 subcritical growth, 333–346  
 shape characterization, 229–231  
 size and subcritical growth, 333–346  
 three-dimensional geometries, 260–285  
 threshold testing of crack closure and load, 303–314  
 Surface layer failure, 186–189  
 Surface stress distribution, 349–351

## T

T-butt welded joint  
 edge crack, 394–395  
 semi-elliptical surface cracks, 392–399  
 Tensile-loaded surface cracks, 22–29  
 Tension loading  
 almond-shaped cracks, 374  
 notched bar almond-shaped cracks, 379  
 notched bar sickle-shaped cracks, 381  
 plastically deformed surface flaw, 112–128  
 sickle-shaped cracks, 376  
 surface cracks in cylindrical rods, 370–372  
 uncracked notched bar, 378  
 Thermal fatigue testing, 237–258  
 Thick-shell isoparametric elements, 69–70  
 Threaded connections, surface cracks, 348–363  
 Three-dimensional crack problems  
 computations and experiments, 287–302  
 evaluation of, 37–40  
 fracture analysis, 63–76  
 geometries, 260–285  
 singular integral formulations, 12  
 stress-intensity factor, 36–37  
 surface flaws, 12, 36–40, 112  
 Threshold testing, fatigue crack growth, 303–314  
 Through-thickness stress distribution, 352–353  
 “Thumbail” cracks, 100–106  
 Transition crack length, subcritical surface flaw growth, 333–346

Tri-axiality factor, crack front constraint variation, 323  
 Tubular threaded connections, 348–363  
 Turner’s Engineering  $J$  approach, 146–147  
 Two-part failure  
 elliptic and semi-elliptic flaws, 178  
 medium-depth flaws, 189

## U

Unnotched rods, surface crack growth, 365–388

## V

Valve casing failure assessment, 317–320  
 Variable-amplitude stress history, 405–408  
 Variable eigenvalue algorithm, 100  
 Variable loading history, 390–412  
 Vertex-edge intensity factor, 88–96  
 Vertex intensity factor, 86–90  
 Vinyl acetate monomer (VAM) joints, 354–360  
 Virtual-crack-closure technique (VCCT), 38–40  
 Virtual crack extension, 14–17  
 Virtual grating schematic, 110  
 Von Mises’ stress, crack front constraint variation, 321–323

## W

Weighted average stress range, 405–408  
 Weight function  
 corner crack, 49–52  
 edge crack, 394–395, 397–398  
 flat plate, 399, 402, 410  
 notched and unnotched rods, 365–388  
 semi-elliptical surface crack, 398–399  
 stress-intensity factors, 58–59, 365–368  
 tubular threaded connections, 348–363  
 welded joints, 390–412  
 Weld angle, stress-intensity factor, 400  
 Weldments, surface fatigue cracks, 390–412  
 Weld toe radius, stress-intensity factor, 401  
 Westergaard approach, in-plane displacement measurement, 130–134  
 Width correction, stress-intensity solutions, 226–228  
 Wien bridge oscillator, thermal fatigue testing, 244–245

